INVESTIGATING THE MECHANISTIC REGULATION OF HOMOLOGOUS RECOMBINATION

A doctoral dissertation presented by
Stefan Braunshier
M.Sc. in Biochemistry, Ludwig-Maximilian-Universität, München
Born on 28.03.1997
Citizen of Romania

Under the supervision of
Prof. Dr. Petr Cejka
Prof. Dr. Arianna Calcinotto
Prof. Dr. Grzegorz Ira

Submitted to the
Faculty of Biomedical Sciences
Università della Svizzera italiana

For the degree of
Ph.D. in Biomedical Sciences

August 2026

To all my special people

Summary

DNA double-strand breaks are among the most deleterious types of DNA damage and must be repaired rapidly and efficiently. The two main repair pathways, homologous recombination (HR) and non-homologous end-joining (NHEJ), are in a delicate and dynamic competition for repair choice. NHEJ is a fast, broadly accessible, and energetically efficient repair mechanism, but it can introduce insertions or deletions that can lead to mutations. Alternatively, HR is slower, cell-cycle restricted, and requires multiple enzymatic steps, yet it provides high-fidelity repair by using the sister chromatid as a template to restore the original DNA sequence. The dynamic equilibrium between these repair pathways is regulated on multiple levels. Mechanistically, the earliest stages of repair are shaped by the competition between DNA end resection mediated by MRX-pSae2 in yeast and the DNA end-binding and scaffolding activities of the Ku heterodimer, a central component of NHEJ.

In this thesis, I provide insight into the molecular mechanisms of this competition and several aspects of repair pathway commitment. We found that synapsis of the DNA ends is refractory to resection. I demonstrated that Ku-bound DNA ends remain susceptible to endonucleolytic incision, but the exonuclease activity of MRX-pSae2 alone cannot efficiently remove the Ku protein block. Ku displacement requires the presence of Replication protein A (RPA). RPA acts *in cis* and stimulates the exonuclease activity of MRX-pSae2. I further showed that RPA interacts with both MRX and Sae2 through the DBD-F of Rfa1, although this interaction is functionally dispensable. Our data suggest the existence of transient interaction sites between MRX-pSae2 and the Rfa3 subunit that mediate this functional interplay, as deletion of Rfa3 from the trimer abolished the stimulatory effect of RPA. Furthermore, we showed that partially resected DNA can still undergo end-joining in the absence of RPA.

Following initial processing by MRN-pCtIP in human cells, repair proceeds to long-range resection mediated by DNA2-WRN or DNA2-BLM and EXO1. Although HR can be divided into multiple stages, these steps are mechanistically interconnected, creating a more complex regulatory network than initially anticipated. We showed that BRCA1-BARD1, a complex involved in antagonizing the activity of 53BP1 and promoting RAD51-mediated strand exchange, also promotes long-range resection. Specifically, BRCA1-BARD1, together with MRN and CtIP, stimulates DNA2-WRN-mediated resection. My contribution to this collaborative project was to investigate the effect of the BRCA1 complex on EXO1. I showed that BRCA1-BARD1 enhances EXO1 nuclease activity. In contrast to DNA2-WRN, EXO1 is not further stimulated by the addition of MRN or CtIP. I also found that the BRCA1 complex does not affect the exonuclease activity of MRE11-RAD50 and thus might not play a role during short-range resection.

Resection generates long stretches of RPA-coated ssDNA. In the next stage, RPA is replaced by RAD51, which forms a nucleoprotein presynaptic filament. The stability of the RAD51 presynaptic filament is a critical determinant of successful HR completion. Consequently, a wide range of cellular factors regulate filament assembly, stability, and disassembly. Data from our collaborators indicated that deletion of the FIGNL1 anti-recombinase can reverse the HR defects and mitigate genomic instability in BRCA2-deficient cells. My contribution to this project was the *in vitro* characterization of FIGNL1. I showed that FIGNL1 can remove RAD51 from ssDNA, rendering it susceptible to nuclease degradation. I found that FIGNL1 interacts with RAD51 through the FRBD domain predominantly in a monomer-to-monomer manner, although interactions between FIGNL1 oligomers and RAD51 monomers were also detected. Using pull-down assays with recombinant proteins, I also described the interaction between FIGNL1 and MMS22L-TONSL, another factor that promotes RAD51-ssDNA filament formation at stalled replication forks. I observed that this interaction is also dependent on the FRBD domain of FIGNL1 and is disrupted by the presence of RAD51, potentially through competition for the binding site. Collectively, this work advances our mechanistic understanding of how DNA double-strand break repair pathways are coordinated and regulated to maintain genome stability.

Abbreviations

ATM	Ataxia-telangiectasia mutated
ATR	Ataxia-telangiectasia and Rad3 related
bp	Base pair
BTRR	BLM-TopIIIα-RMI1-RMI2
CDK	Cyclin-dependent kinase
CST	CTC1-STN1-TEN1
D-loop	Displacement loop
DDR	DNA damage response
dHJ	Double Holliday junction
DSB	Double-Strand Break
dsDNA/ssDNA	double-stranded/single-stranded DNA
HR	Homologous recombination
LRR	Long-range resection
MMEJ	Microhomology-mediated end-joining
MRX	Mre11-Rad50-Xrs2
MRN	MRE11-RAD50-NBS1
NHEJ	Non-homologous end-joining
RPA	Replication protein A
nt	nucleotide
SDSA	Synthesis-dependent strand annealing
SRR	Short-range resection
SSA	Single-strand annealing
STR	Sgs1-Top3-Rmi1

Table of Contents

1.Introduction 7
1.1. Non-homologous end-joining 9
1.2. Homologous recombination 11
1.2.1 Short-range resection 13
1.2.2. Long-range resection 14
1.2.3. Strand invasion 15
1.2.4. Processing of the double Holliday junction 16
1.3. Regulation of homologous recombination 17
1.3.1. Kinase-mediated control of resection 18
1.3.2. BRCA1-BARD1 and 53BP1 19
1.3.3. The relationship between HR and NHEJ 20
1.3.4. Regulation of presynaptic filament stability 21
1.4. The MRX-(p)Sae2 complex 23
1.5. Replication protein A and DNA repair 26
1.5.1. The structure of RPA 27
1.5.2. The role of RPA in DSB repair 29
2.Aim of the thesis 31
3.Results 32
3.1. NHEJ-mediated DNA synapsis and RPA-driven MRX exonuclease balance DNA end resection to control DSB repair pathway choice 32
3.2. Mechanism of BRCA1–BARD1 function in DNA end resection and DNA protection 102
3.3. FIGNL1 inhibits homologous recombination in BRCA2 deficient cells by dissociating RAD51 filaments 140
4.Discussion and outlook 203
4.1. The sequential model of NHEJ and HR 203
4.2. The role of BRCA1-BARD1 in long-range resection 206
4.3. The role of the FIGNL1 anti-recombinase in RAD51 filament dynamics 207
5.References 210
6.Acknowledgements 239

1. Introduction

For billions of years genetic information has been stored in DNA and RNA molecules. In fact, the emergence of RNA, which is widely regarded to be the genetic precursor of DNA in the context of the RNA world hypothesis (Bartel et al., 1993, Robertson and Joyce, 2012), is often considered the first step in the origins of life. Accordingly, all life contains a genome, in the form of DNA (and RNA in some viruses), which encodes all the proteins that drive cellular processes. Moreover, especially in multicellular organisms, the genome also contains regulatory information, in the form of epigenetic modifications, including parent-of-origin marks at imprinted genes, as well as chromatin states that influence gene expression programs underlying differentiation and apoptosis (programmed cell death) (Jaenisch and Bird, 2003). As organisms became more complex, their genetic information increased, leading to ever larger genomes. *E. coli* DNA is roughly 4.6 million base pairs (Mbp) in size (Blattner et al., 1997); *S. cerevisiae*, around 12 Mbp (Goffeau et al., 1996), while humans have a staggering 3.2 billion base pairs-long genome (Lander et al., 2001). Due to the central role of DNA, the cells have also evolved mechanisms that ensure genomic integrity, by maintaining the fidelity of the DNA sequence (Ciccia and Elledge, 2010).

Paradoxically, it is commonly accepted that mutations in the DNA sequence stand at the core of the evolutionary process (Lynch, 2007). However, excessive DNA damage is a perpetual danger to the cell, and, if left unrepaired, can cause mutations which might eventually lead to catastrophic failures of cellular processes, and therefore cell death, or, perhaps even worse, a radical rewiring of these processes as in the case of cancer cells (Hanahan and Weinberg, 2011, Lindahl, 1993, Negrini et al., 2010). Moreover, while not all diseases are caused by inherited genetic defects, most have a genetic component which influences our susceptibility to the disease and our response to treatment (Visscher et al., 2017). This highlights the need for efficient surveillance of DNA integrity and accurate DNA repair (Tong et al., 2024).

Each cell incurs between several thousand and one million DNA lesions per day (Lodish et al., 2004, Lindahl, 1993, Chen et al., 2024). The sources of DNA damage can be classified as exogenous, including radiation (X-rays, UV light) or chemical agents such as cisplatin, or endogenous, arising from reactive oxygen species (ROS) generated during cellular metabolism, or from errors in DNA-related processes, such as replication (Chatterjee and Walker, 2017) (Figure 1). DNA double-strand breaks (DSBs) are among the most harmful types of DNA damage and can lead to gross genomic rearrangements (Tubbs and Nussenzweig, 2017). Depending on the nature of the DNA ends, DSBs can be classified as “clean” if the ends are chemically compatible with DNA ligation, or “dirty” if they contain additional chemical modifications or are covalently attached to proteins, as in the case of faulty topoisomerase reactions (Tse et al., 1980, Olive et al., 1990). DSBs can be further distinguished based on the number of DNA ends available for repair: one-

ended DSBs typically arise during DNA replication and cannot be repaired by direct ligation, whereas two-ended DSBs can be channeled through different repair pathways (Scully et al., 2024, Chapman et al., 2012b).

DSBs can be repaired by two main and evolutionarily conserved pathways: non-homologous end-joining (NHEJ) and homologous recombination (HR) (Ranjha et al., 2018). These pathways will be discussed in more detail in the following sections. Briefly, NHEJ relies on the direct ligation of the DNA ends to restore the integrity of the double helix. This process is simple and requires the action of relatively few enzymes. Consequently, it is also fast and can be completed in as little as a 30 minutes (Mao et al., 2008). However, high kinetics and low complexity come at a cost, making NHEJ a highly mutagenic pathway that can generate short deletions or insertions at the break site (Lieber, 2010). At its worst, NHEJ may even cause genomic rearrangements if breaks from different chromosomes are erroneously joined (Bhargava et al., 2017, Chiarle et al., 2011). In contrast, HR is a much slower process, often requiring hours to complete, and involves a complex orchestration of repair factors (Mao et al., 2008). However, HR provides significantly more accurate repair by employing a homologous DNA strand as template. Due to this limitation, HR is primarily active in the S and G2 phases of the cell cycle, where a fully homologous template, in the form of a sister chromatid, is available,

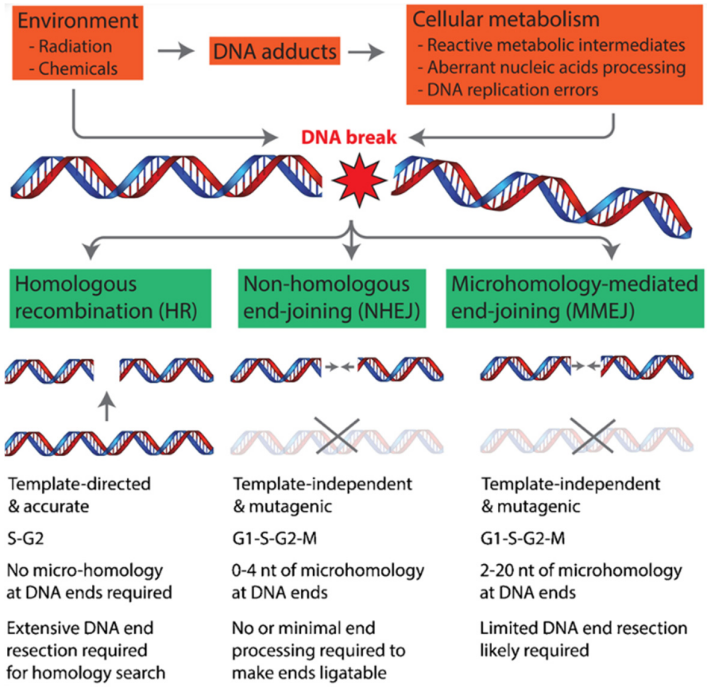

Figure 1: An overview of DNA damage sources leading to double-strand breaks and the main repair pathways.

DSBs can be caused by endogenous or exogenous insults to the genetic material. Repair can be carried through homologous recombination, which is accurate, but restricted to the S-G2 phases of the cell cycle due to the limited availability of a template strand. NHEJ can also be employed to ligate the broken DNA ends. Even though NHEJ is active throughout the whole cell cycle, it is mutagenic and can cause insertions or deletions in the DNA. Lastly, MMEJ, often considered a branch of NHEJ and similarly mutagenic, relies on limited end resection revealing existing microhomologies in the vicinity of the DNA ends to mediate annealing and ligation. From (Reginato and Cejka, 2020).

whereas NHEJ can act throughout the entire cell cycle (Symington, 2014). While both pathways are versatile, HR can also act on one-ended breaks, which, as mentioned previously, cannot be resolved by NHEJ (Chapman et al., 2012b).

Understanding the mechanisms of these pathways allows us to exploit them in the context of therapeutic strategies. A common oncological treatment relies on the use of DNA-damaging drugs that preferentially affect rapidly dividing cancer cells and often has severe side-effects. Targeted therapies, in contrast, are more specific and act on defined molecular alterations in cancer cells, including defects in DNA repair pathways (Jackson and Bartek, 2009, Pilie et al., 2019). Therefore, to gain further clinical benefits, it is crucial to deepen our knowledge of the DNA repair network. This task is made easier by the conserved nature of these pathways (Mimitou and Symington, 2009, Krogh and Symington, 2004), which enables us to draw some important general conclusions through the study of model organisms, such as *Saccharomyces cerevisiae* (budding yeast).

1.1. Non-homologous end-joining

The NHEJ factors as well as the repair mechanisms are highly conserved across eukaryotes. This section will describe the factors present in yeast, with comparisons to the human system (Figure 2). The process begins with the detection of the DNA ends by the Ku70-Ku80 complex. This heterodimer is conserved in humans and has a central β-barrel structure that allows it to bind at the break site in a sequence-independent manner by slipping the DNA end through this ring (Walker et al., 2001). As such, double-stranded DNA (dsDNA) ends are the preferred substrates of Ku. Furthermore, Ku can slide on the DNA, suggesting that multiple heterodimers can load on DNA ends (Blier et al., 1993). The Ku ring has a defined polarity, with the C-terminus of Ku80 facing the break site and the C-terminus of Ku70 facing away from the DNA end (Walker et al., 2001). The main function of Ku in NHEJ is to protect the DNA ends from nuclease degradation (Clerici et al., 2008, Mimitou and Symington, 2010) and to act as a recruitment platform for the other repair factors (Zhang et al., 2007, Chen and Tomkinson, 2011). In mammals, Ku is part of the DNA-PK complex, together with the kinase DNA-PKcs, which is lacking in yeast and whose function is performed by other NHEJ factors (Emerson and Bertuch, 2016, Ceccaldi et al., 2016). Apart from its role in NHEJ, Ku is also involved in telomere maintenance (Ribes-Zamora et al., 2013, Ribes-Zamora et al., 2007) and loss of human Ku is lethal in mammalian cells due to telomeric function deficits (Wang et al., 2009).

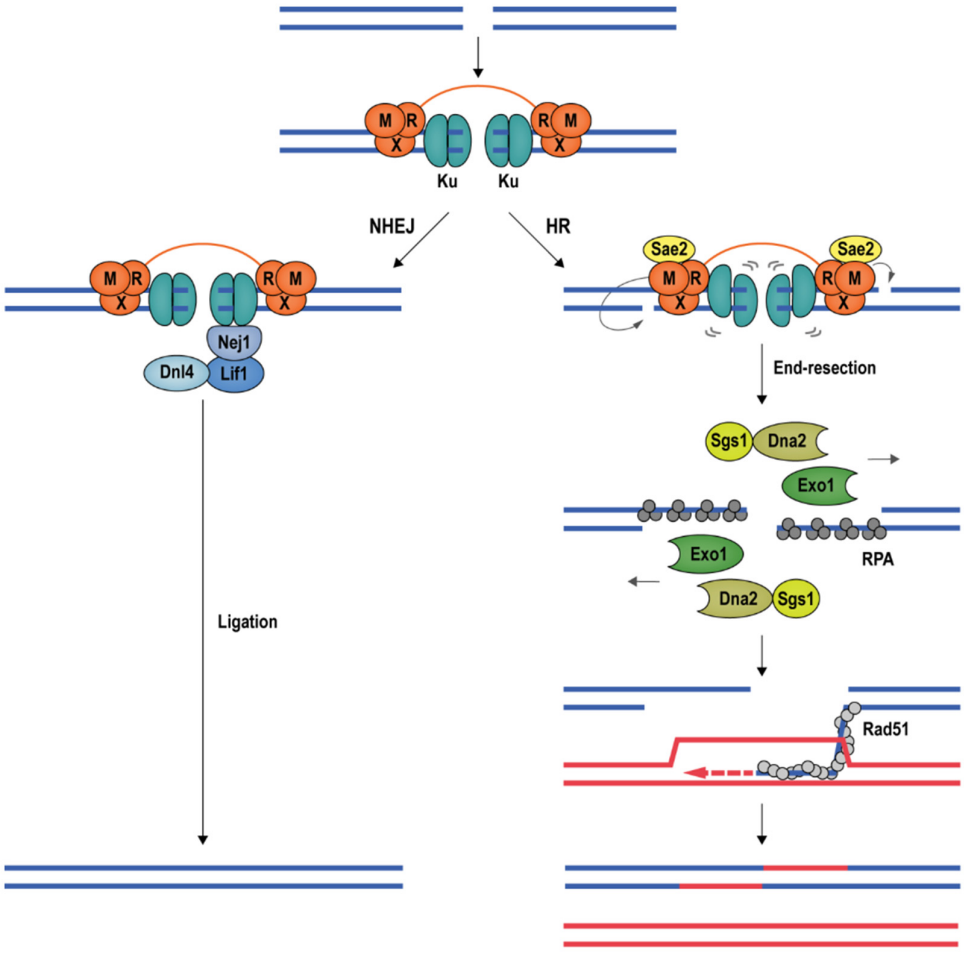

Figure 2: The main steps and factors involved in the early stages of NHEJ and HR.

The Ku heterodimer is the first responder to DSBs due to its high affinity for DNA ends. MRX is also quickly recruited and tethers the broken ends. During NHEJ, Ku acts as a scaffold for the other end-joining factors, Nej1 and Dnl4-Lif1 which ligate the broken DNA. On the other hand, resection, initiated by MRX-Sae2, is slower and channels repair to HR. The MRX-Sae2 complex is highly versatile and can process Ku-bound DNA ends, creating an entry point for Exo1 or Dna2-Sgs1-mediated long-range resection. This creates overhangs initially coated by RPA. RPA is exchanged with the Rad51 recombinase, which catalyzes strand exchange and homology search, forming a D-loop. DNA synthesis from the invading strand restores sequence integrity, and resolution of recombination intermediates completes repair. From (Fontana et al., 2018).

After recognition, Ku recruits Dnl4-Lif1 and Nej1 (Zhang et al., 2007, Chen and Tomkinson, 2011). Dnl4 is an ATP-dependent DNA ligase that does not act in replication but is strictly required for end-joining (Wilson et al., 1997) and interacts with the C-terminus of Yku80 (Palmbos et al., 2008). Dnl4 also strongly interacts with Lif1, to the extent that Dnl4 alone is not stable on its own (Herrmann et al., 1998). This association is similar in the human variants, LIG4 and XRCC4 (Chiruvella et al., 2014). The association of Dnl4-Lif1 with Ku at the break site stabilizes the end-joining assembly and has a further protective effect against nucleases (Zhang et al., 2007, Chen and Tomkinson, 2011).

Another interacting partner of Dnl4-Lif1 is Nej1 (XLF in humans), which is required for efficient NHEJ (Frank-Vaillant and Marcand, 2001, Valencia et al., 2001, Kegel et al.,

2001). Nej1 can form homodimers (Deshpande and Wilson, 2007) and physically interacts with both Lif1 (Deshpande and Wilson, 2007, Sulek et al., 2007, Ooi et al., 2001, Mahaney et al., 2014) and Yku70 (Chen and Tomkinson, 2011). This interaction further stabilizes the complex (Chen and Tomkinson, 2011) and genetic evidence shows that Nej1 plays a further role in inhibiting end resection (Sorenson et al., 2017, Mojumdar et al., 2022). Additionally, Nej1 promotes the reactivation of Dnl4 (Ellenberger and Tomkinson, 2008, Chen and Tomkinson, 2011).

Interestingly, the last key player of the NHEJ core in yeast is the Mre11-Rad50-Xrs2 (MRX) complex (D'Amours and Jackson, 2002). Although its main role is in the initial end-resection step of HR, deletion of MRX subunits decreases the efficiency of NHEJ *in vivo* (Zhang and Paull, 2005, Schiestl et al., 1993, Moore and Haber, 1996). The predominant model is that MRX acts by bridging the DNA ends (Chen et al., 2005, Chen et al., 2001), although end-tethering can still be carried out by Ku-Dnl4-Lif1 in its absence (Grob et al., 2012). MRX also stimulates the ligase activity of Dnl4-Lif1 *in vitro* (Chen et al., 2001), and the Xrs2 subunit of the complex interacts with Lif1 (Palmbos et al., 2005, Matsuzaki et al., 2008). In humans, MRE11-RAD50-NBS1 (MRN) has not been shown to be as important for end tethering (Soutoglou et al., 2007), and instead, DNA-PKcs plays a key role in synapsis within the NHEJ machinery (Graham et al., 2016).

In the case of “dirty” or similarly incompatible DNA ends, limited processing of the DNA needs to occur before ligation. The yeast Pol4 (or Polλ and Polμ in humans) can fill in 5’ overhangs (Wilson and Lieber, 1999, Tseng and Tomkinson, 2002, Bebenek et al., 2005), or the DNA can be degraded by the yeast Rad27 (FEN1), whose endonuclease activity can remove flaps (Wu et al., 1999). In humans, a nuclease called Artemis, which has no equivalent in yeast, is also involved in removing various DNA modifications (Ma et al., 2002). Limited DNA resection at the ends can also channel repair through alternative NHEJ (alt-NHEJ) (Lee and Lee, 2007). This pathway relies on existent microhomologies between the ends and is especially favored if the break site is located at repetitive DNA sequences (Sinha et al., 2016, Sfeir and Symington, 2015). The microhomologies can be 2-20 bp long and can require the resection of up to a few hundred base pairs (Ma et al., 2003). As a result, alt-NHEJ, also called microhomology-mediated end joining (MMEJ), often results in deletions. MMEJ also relies on factors that are not part of canonical NHEJ, such as Pol32 (a Polδ subunit) and Cdc9 (a DNA ligase I homolog) (Lee and Lee, 2007, Ma et al., 2003). In humans, the functions of these proteins are performed by Polθ and XRCC1-Ligase III complex (Simsek et al., 2011, Kent et al., 2015, Ceccaldi et al., 2015).

1.2. Homologous recombination

Similarly to NHEJ, homologous recombination (HR) is also a highly conserved repair pathway, with most of the core components having broadly similar functions in organisms ranging from bacteria to humans (San Filippo et al., 2008, Kowalczykowski, 2015). However, in contrast to NHEJ, HR-mediated repair is highly accurate as it requires

a template DNA molecule to reestablish the correct sequence at the break site (Jasin and Rothstein, 2013). This requirement restricts HR to cell phases where such homologous DNA, usually the sister chromatid, is available (the S-G2 phases) (Schlacher et al., 2011, Jeggo et al., 2011). HR also requires much more extensive processing of the break during the DNA end resection step, making it generally slower than NHEJ (Mao et al., 2008, Cejka, 2015). Even though, by and large, HR is accurate, recombination with template sequences other than the sister chromatid can lead to mutations, including loss of heterozygosity events (Reginato and Cejka, 2020, Kawale and Sung, 2020). Remarkably, the cell has taken advantage of this potential to generate genetic diversity during meiosis in a tightly regulated process. During meiotic prophase I, programmed DSBs occur through the action of Spo11/SPO11 at specific recombination hotspots across the genome. These breaks are then channeled through HR, with the template DNA being the homologous chromosome, instead of the sister chromatid. This process generates crossover events between the chromosomes, promoting genetic exchange during sexual reproduction and is one of the driving factors for evolution (Lam and Keeney, 2014, Borde and de Massy, 2013, Zickler and Kleckner, 2015).

Summarily, the mechanism of HR begins with end resection (Figure 2), in which the DNA is nucleolytically processed by various enzymes to produce 3' single-stranded DNA overhangs coated by Replication Protein A (RPA). Based on the extent of DNA degradation, resection can be divided into two stages: short-range and long-range resection (Cejka, 2015). RPA plays an important role in regulating both stages of resection and will be covered more in detail in a separate section. RPA is subsequently exchanged with the key recombinase Rad51 (RAD51 in humans), forming a nucleoprotein filament primed for homology search and strand invasion. During this step, the Rad51-coated DNA scans for a homologous DNA sequence, typically on the sister chromatid, to serve as a template. The invasion produces a structure called a displacement loop (D-loop). Once the template is engaged, DNA synthesis then extends the invading 3' end and accurately restores the missing genetic information (Jasin and Rothstein, 2013, San Filippo et al., 2008, Ranjha et al., 2018). Repair can then proceed through Synthesis-Dependent Strand Annealing (SDSA) where the newly synthesized strand is displaced from the D-loop and is allowed to anneal to the other resected end of the DNA break, leading predominantly to non-crossover products. Alternatively, the second end of the break can be captured by the displaced D-loop intermediate in a process called second-end capture. After further DNA synthesis and ligation, a double Holliday junction (dHJ) is formed. This intermediate can be resolved by various mechanisms, leading to either crossover or non-crossover products. While SDSA is preferred in mitotic cells, meiosis predominantly involves dHJs that are biased toward crossover outcomes (Mitchel et al., 2010, Zakharyevich et al., 2012, Matos et al., 2011).

1.2.1 Short-range resection

Short-range resection (SRR) is the first step of HR and often commits repair to this pathway. It is carried out by the Mre11-Rad50-Xrs2/MRE11-RAD50-NBS1 complex together with the accessory factor Sae2/CtIP and is limited to the vicinity of the break (Mimitou and Symington, 2008, Cannavo and Cejka, 2014). *In vivo* studies in yeast revealed that in the absence of long-range resection, MRX can process hundreds of bases and is sufficient to support HR (Zhu et al., 2008). In yeast, short-range resection is primarily required for "dirty" ends, whereas for "clean" breaks the nuclease activity of Mre11 is not required (Moreau et al., 1999, Llorente and Symington, 2004, Zhu et al., 2008, Mimitou and Symington, 2010). In humans, resection initiation is entirely dependent on the nuclease of MRE11 (Shibata et al., 2014, Sartori et al., 2007, Deshpande et al., 2020), partially due to the higher concentration of the NHEJ factor KU (Beck et al., 2011). In fact, when Ku is overexpressed in yeast, Mre11 becomes necessary for the processing of "clean" ends (Mimitou and Symington, 2010).

Short-range resection begins with the introduction of a nick on the 5'-terminated strand next to the DNA ends by the endonuclease activity of the MRX/MRN complex (Figure 3), which is stimulated by phosphorylated Sae2/CtIP (pSae2/pCtIP) (Cannavo and Cejka, 2014). This is followed by exonucleolytic degradation in the 3' to 5' direction (i.e., toward the DNA end) by the Mre11 nuclease (Paull and Gellert, 1998, Garcia et al., 2011, Shibata

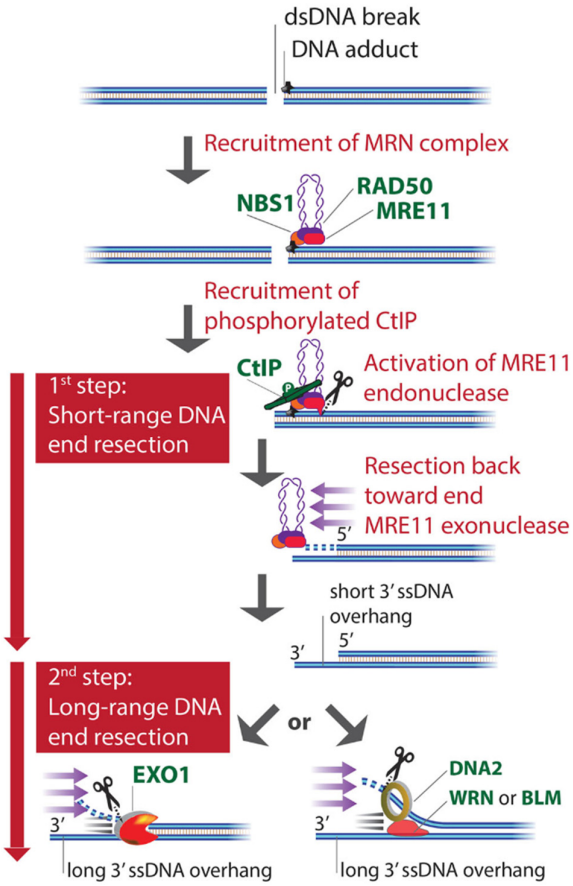

Figure 3: An overview of the bidirectional resection model.

In the process of short-range resection, MRX/MRN, in conjunction with phosphorylated Sae2/CtIP endonucleolytically incises the 5'-terminated strand in the vicinity of the DNA end. The subsequent 3' to 5' exonuclease activity of the resection complex resects the DNA towards the end, creating an entry point for the long-range resection enzymes Exo1/EXO1 and Dna2-Sgs1/DNA2-BLM or DNA2-WRN, which degrade the DNA in the 5' to 3' direction. From (Ranjha et al., 2018).

et al., 2014). This model of short-range is similar in humans (Deshpande et al., 2016, Anand et al., 2016). Moreover, protein blocks, particularly Ku/KU, further activate the endonuclease activity of MRX-pSae2/MRN-pCtIP (Wang et al., 2017, Reginato et al., 2017). MRX-pSae2 is also required for the resection of Spo11-bound DNA ends during meiosis (Neale et al., 2005, Keeney and Kleckner, 1995, Keeney et al., 1997, Moreau et al., 1999) and, in fission yeast, for the removal of Top2 adducts from DNA (Hartsuiker et al., 2009). In the latter case, a similar role is performed in humans by the MRN-pCtIP complex (Hoa et al., 2016). Mechanistically, short-range resection generates an entry point for long-range resection to extend DNA degradation in the 5' to 3' direction (i.e., away from the DNA end) (Cannavo et al., 2019, Reginato et al., 2017).

1.2.2. Long-range resection

Long-range resection (LRR) is performed in the 5' to 3' direction by the nucleases Exo1/EXO1 and Dna2/DNA2. Whereas Exo1 can degrade ssDNA within dsDNA, Dna2 can only act on ssDNA, and, as such, is functionally coupled with the helicase Sgs1 (BLM or WRN in humans) (Tran et al., 2002, Lee Bi et al., 2002, Gravel et al., 2008, Zhu et al., 2008, Mimitou and Symington, 2008, Sturzenegger et al., 2014, Bae et al., 1998). While SRR only resects tens to hundreds of nucleotides near the break site, LRR can process up to tens of kilobases of DNA, leading to long 3' overhangs coated with RPA (Zhu et al., 2008, Mimitou and Symington, 2008). Contrary to SRR, LRR is more sensitive to "dirty" DNA ends and requires the action of MRX-pSae2/MRN-pCtIP to bypass protein blocks (KU) or chemical modifications (Shim et al., 2010, Myler et al., 2017, Reginato et al., 2017, Deshpande et al., 2020).

Sgs1 is a RecQ family helicase and translocates on the 3'-terminated strand in a 3' to 5' direction (Bennett et al., 1998). It interacts with and is stimulated by Top3-Rmi1, forming the heterotrimeric STR complex. This complex can disassemble D-loops and dissolve dHJ intermediates, leading to non-crossover outcomes (Fasching et al., 2015, Cejka et al., 2010b, Cejka et al., 2012). In humans, BLM and WRN are the RecQ family homologs of Sgs1 (Myung et al., 2001). WRN additionally contains a unique exonuclease domain at the N-terminus whose role in cellular processes remains poorly understood (Huang et al., 1998). Dna2/DNA2 possesses both helicase and nuclease domains; however, its helicase activity functions primarily as a translocase and cannot efficiently unwind dsDNA (Bae et al., 1998, Masuda-Sasa et al., 2006, Levikova et al., 2013, Miller et al., 2017). Thus, during resection Dna2/DNA2 functions in concert with Sgs1/BLM and WRN (Nimonkar et al., 2011, Cejka et al., 2010a, Sturzenegger et al., 2014). Beyond its role in

HR, Dna2/DNA2 is involved in DNA replication, where it processes Okazaki fragments. In this context, its endonuclease activity removes long 5'-flaps generated during strand displacement synthesis by DNA polymerase δ (Kao et al., 2004, Masuda-Sasa et al., 2006, Bae et al., 1998).

Exo1/EXO1 is a member of the Rad2/XPG family of proteins which possess both 5' to 3' exonuclease and 5' flap endonuclease activities. Exo1/EXO1 is a very processive dsDNA exonuclease and does not strictly require the activity of other proteins (Lee Bi et al., 2002). Nevertheless, studies have shown that BLM interacts with and can stimulate the activity of EXO1 (Nimonkar et al., 2008, Nimonkar et al., 2011).

The short-range and long-range resection are functionally coupled steps. The MRX/MRN complex serves as a recruitment platform for LRR enzymes and stimulates resection mediated by both Exo1/EXO1 and Dna2-Sgs1/DNA2-BLM (Shim et al., 2010, Gobbini et al., 2018, Cannavo et al., 2013, Cejka et al., 2010a, Nimonkar et al., 2011). In addition, CtIP promotes the recruitment and translocase activity of DNA2 (Ceppi et al., 2020, Daley et al., 2017, Hoa et al., 2015). Similarly, yeast Sae2 can activate resection mediated by Exo1 and Dna2 (Nicolette et al., 2010, Daley et al., 2017). Resection is further coupled with downstream strand invasion, as BRCA1-BARD1, a complex involved in the strand invasion step, stimulates the helicase activity of WRN and BLM and the nuclease activity of EXO1 (Ceppi et al., 2024, Salunkhe et al., 2024).

One outstanding question in the field is why a non-essential but highly conserved process such as long-range resection is maintained in HR, given that the limited resection that occurs during short-range resection is sufficient to produce a substrate for the downstream steps of HR (Zhu et al., 2008). However, the length of the 3' ssDNA overhang is one of the factors that can promote more efficient and accurate homology search by modulating RAD51 filament stability (Renkawitz et al., 2014, Qi et al., 2015). Moreover, extensive resection may channel repair away from the mutagenic MMEJ (McVey and Lee, 2008), which operates at short resection lengths, but also enables the mutagenic single-strand annealing (SSA) pathway once sufficient resection has exposed extended homologous sequences (Bhargava et al., 2016). A recent study in yeast shows that, while long-range resection is mechanistically dispensable for HR, it plays an important role in DNA damage checkpoint activation (Kimble et al., 2023). Together, these observations suggest that although LRR might be catalytically redundant for HR completion, it serves a key function in checkpoint signaling and may influence repair pathway choice.

1.2.3. Strand invasion

The product of resection is a long 3' single stranded DNA overhang, which is coated by RPA. Initiation of homology search requires RPA to be exchanged with the recombinase Rad51/RAD51, forming the presynaptic filament. Due to the high affinity of RPA for ssDNA, the efficient loading of Rad51/RAD51 requires additional recombination mediators, such as Rad52 in yeast (Sung, 1997a, Shinohara and Ogawa, 1998, New et

al., 998, San Filippo et al., 2008). In humans, RAD52 is largely dispensable for RAD51 loading, which is mainly mediated by the tumor suppressor BRCA2 (Yuan et al., 1999, Masson et al., 2001, Jasin, 2002, Fujimori et al., 2001, Belan et al., 2023). The filament is stabilized by the Rad51 paralogs, Rad55-Rad57 (RAD51B, RAD51C, RAD51D, XRCC2 and XRCC3 in humans) (Greenhough et al., 2026, Deveryshetty et al., 2025, Akita et al., 2024, Berti et al., 2020, Masson et al., 2001, Chun et al., 2013, Gaines et al., 2015) and the Shu complex, composed of Csm2-Psy3-Shu1-Shu2 in yeast and SWSAP1-SWS1 in humans (Carver and Zhang, 2021, Hengel et al., 2024, Abreu et al., 2018, Zhang et al., 2017). In yeast Rad52, Rad55-Rad57 and the Shu complex also counteract the anti-recombinase activity of Srs2 (Liu et al., 2011a, Bernstein et al., 2011, Ma et al., 2018). Another tumor suppressor, BRCA1, has also been implicated in promoting the template invasion step (Zhao et al., 2017).

Strand invasion occurs when the presynaptic filament engages a homologous template, resulting in the formation of a D-loop. This process is mediated by Rad54 (RAD54 in humans), which also promotes the dissociation of Rad51 from DNA after a successful strand exchange (Wright and Heyer, 2014, Tavares et al., 2019, Nimonkar et al., 2012, Mazin et al., 2003, Li et al., 2007). Rad51 removal is necessary for subsequent extension of the 3' end of the invading strand by Polδ in conjunction with RFC-PCNA (Li et al., 2013).

1.2.4. Processing of the double Holliday junction

The fate of the D-loop intermediate dictates the further repair steps. The intermediate can be dismantled by the motor activity of Srs2 or Sgs1/BLM, channeling repair through SDSA, as mentioned above (Wu and Hickson, 2003, Ira et al., 2003, Liu et al., 2017, Nassif et al., 1994). Alternatively, second-end capture can occur when the other resected end of the DSB anneals to the displaced DNA strand of the D-loop. Subsequent ligation generates a double Holliday junction intermediate (Szostak et al., 1983).

This intermediate can be "dissolved" through the action of the Sgs1-Top3-Rmi1 (STR) complex (BLM-TopoIIIα-RMI1-RMI2 or BTRR in humans) (Figure 4). Dissolution occurs through the motor activity of Sgs1/BLM combined with the topoisomerase activity of Top3/TopoIIIα, which release the torsional strain generated by the helicase as the junctions converge and eventually collapse. Dissolution generally leads to non-crossover outcomes (Xu et al., 2008, Wu and Hickson, 2003, Cejka et al., 2012, Plank et al., 2006, Cejka and Kowalczykowski, 2010).

dHJs that were not dissolved are processed by structure-specific nucleases, a mechanism known as "resolution". The enzymes responsible for this process are Yen1 (GEN1 is humans), Mus81-Mms4 or Slx1-Slx4 (MUS81-EME1-SLX1-SLX4 in humans). These factors act by cleaving the joint molecule at the junction point and, depending on the orientation, might generate crossovers (Wyatt et al., 2013, Rass et al., 2010, Garner et al., 2013, Gaillard et al., 2003, Ehmsen and Heyer, 2008, Castor et al., 2013, Ip et al.,

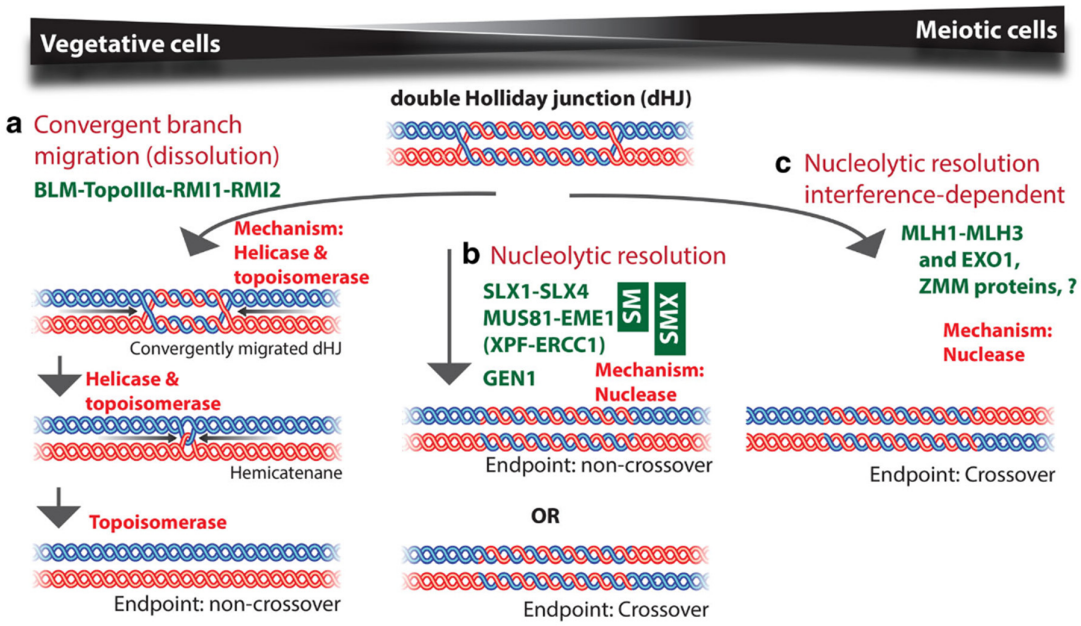

Figure 4: An overview of double Holliday junction processing mechanisms.

In vegetative cells, dHJs can be "dissolved" by the BTRR complex (Sgs1-Top3-Rmi1 in yeast), leading to non-crossover outcomes. Alternatively, dHJs can be "resolved" by structure-specific nucleases, such as MUS81-EME1-SLX1-SLX4 (Mus81-Mms4 or Slx1-Slx4 in yeast) or GEN1 (Yen1 in yeast). This resolution can lead to both crossover and non-crossover outcomes depending on the orientation of the cleavages. Alternatively, meiotic cells are highly biased towards crossovers, making dHJ resolution dependent on the action of the MLH1-MLH3 complex together with EXO1 and ZMM family proteins. From (Ranjha et al., 2018).

2008, Blanco et al., 2010). In meiotic cells, dHJ resolution is strongly biased towards crossovers to increase genetic variation. Therefore, mitotic dHJ resolution employs the Mlh1-Mlh3 or MutLγ nuclease (MLH1-MLH3 or MUTLγ in humans) (Zakharyevich et al., 2012). The long-range resection nuclease Exo1/EXO1 also plays a nuclease-independent role in this pathway by stimulating the nuclease activity of MutLγ/MUTLγ (Roy et al., 2025, Cannavo et al., 2020).

1.3. Regulation of homologous recombination

After a DSB occurs, the broken ends are initially recognized by Ku (KU and DNA-PKcs in humans) and by MRX/MRN, which bridges the two DNA ends. Beyond facilitating repair, the binding of MRX/MRN also triggers the DNA damage response (DDR) pathway by activating the kinase Tel1 (ATM in humans) (Keener et al., 2019, Carson et al., 2003, Uziel et al., 2003, Lee and Paull, 2005, Gobbini et al., 2013, Oh et al., 2018, Nakada et al., 2003). Among the downstream targets of Tel1 is Rad53 (CHK2 in humans), which contributes to the initiation of the DNA damage checkpoint and subsequent cell cycle arrest (Sanchez et al., 1996, Matsuoka et al., 1998, Sanchez et al., 1999). In resection, Tel1/ATM has dual and seemingly opposed roles: it promotes the recruitment of Rad9 (53BP1 in humans), an anti-resection factor that physically limits resection (Sweeney et al., 2005, Sun et al., 1998, Schwartz et al., 2002, Noordermeer et al., 2018, DiTullio et al., 2002, Callen et al., 2013), while also activating the resection (Mantiero et al., 2007, Galli

et al., 2024). In humans, the tumor suppressor BRCA1 provides another regulatory layer by counteracting 53BP1 (Escribano-Diaz et al., 2013, Cruz-Garcia et al., 2014, Yun and Hiom, 2009).

1.3.1. Kinase-mediated control of resection

Since HR is predominantly restricted to the S and G2 cell phases, resection is tightly regulated by cyclin-dependent kinase (CDK) (Figure 5). CDK phosphorylates and activates Sae2 at residue S267 (residue T847 in CtIP). This modification is required for the ability of Sae2/CtIP to stimulate both the endonuclease and exonuclease activities of MRX/MRN (Cannavo et al., 2018, Cannavo et al., 2019, Tamai et al., 2024, Huertas and Jackson, 2009, Huertas et al., 2008, Fu et al., 2014, Polato et al., 2014). Sae2 is also a substrate of Tel1, even though Tel1-mediated phosphorylation of Sae2 is seemingly catalytically dispensable for resection *in vitro* (Cannavo et al., 2018). A potential role for the interplay between Sae2 and Tel1 might be to dampen checkpoint hyperactivation by Tel1 by potentially outcompeting other substrates of the kinase (Yu et al., 2018, Yu et al., 2019, Liang et al., 2015, Colombo et al., 2019).

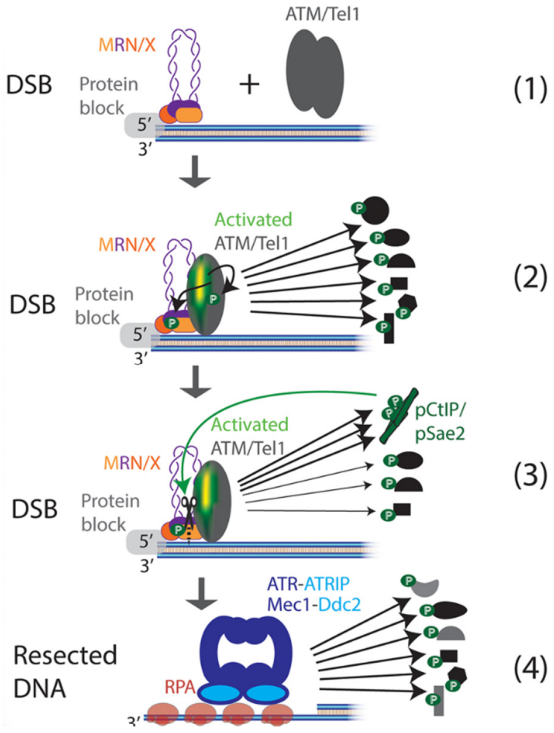

Figure 5: An overview of MRX/MRN function in DNA damage response and the subsequent kinase-mediated regulatory cascade.

MRN/MRX localizes at the broken DNA ends and recruits and activates ATM/Tel1. ATM/Tel1 phosphorylates a wide array of proteins involved in DSB repair regulation and cell cycle progression, including the resection factors CtIP/Sae2 and MRN/MRX. Phosphorylation of CtIP/Sae2 activates short-range resection and promotes HR. At the same time, CtIP/Sae2 likely attenuates checkpoint activation by competing for ATM/Tel1 substrates. Resected DNA is coated by RPA, which acts as a signal for the kinase ATR-ATRIP/Mec1-Ddc2 and further modulates checkpoint signaling. From (Reginato and Cejka, 2020)

In humans, CDK-mediated phosphorylation of CtIP at residue S327 is critical for the interaction with BRCA1 and for increased resection kinetics (Chen et al., 2008, Hoa et al., 2015, Cruz-Garcia et al., 2014). ATM and ATR-mediated phosphorylation of CtIP at residue T859 is also functionally important, as it modulates the association of CtIP with chromatin and promotes the MRN-mediated eviction of DNA-PK from DNA ends (Deshpande et al., 2020, Wang et al., 2013, Peterson et al., 2011). Phosphorylation of CtIP also modulates its stimulatory effect on the BLM helicase (Daley et al., 2017).

Lastly, the Xrs2/NBS1 subunit of MRX/MRN is a target of phosphorylation by Tel1/ATM. and these modifications contribute to the regulation of checkpoint signaling and DDR activation at sites of damage. However, their direct role in controlling short-range DNA end resection has not been fully defined (Zhou et al., 2017, Wu et al., 2000, Lim et al., 2000, Gatei et al., 2000, Huang et al., 2016, D'Amours and Jackson, 2001).

1.3.2. BRCA1-BARD1 and 53BP1

In higher eukaryotes, there is another level of regulation of DSB repair mediated by the antagonistic effect of 53BP1, a pro-NHEJ factor, and BRCA1, a pro-HR factor (Figure 6). Both proteins bind mutually exclusive domains with damaged chromatin (Chapman et al., 2012a, Escribano-Diaz et al., 2013, Bunting et al., 2010, Bouwman et al., 2010). BRCA1 is recruited to chromatin in the S/G2 phase through the action of its obligate binding partner, BARD1 (Nakamura et al., 2019).

53BP1 interacts with the Shieldin complex, a heterotetramer composed of SHLD1, SHLD2, SHLD3 and REV7, and with RIF1 (Ghezraoui et al., 2018, Noordermeer et al., 2018, Setiaputra et al., 2022). Shieldin has been shown to possess ssDNA binding activity (Gao et al., 2018) and might be recruited to short ssDNA overhangs by RIF1 and 53BP1 and restrict the activity of long-range resection enzymes (Xu et al., 2015, Gupta et al.,

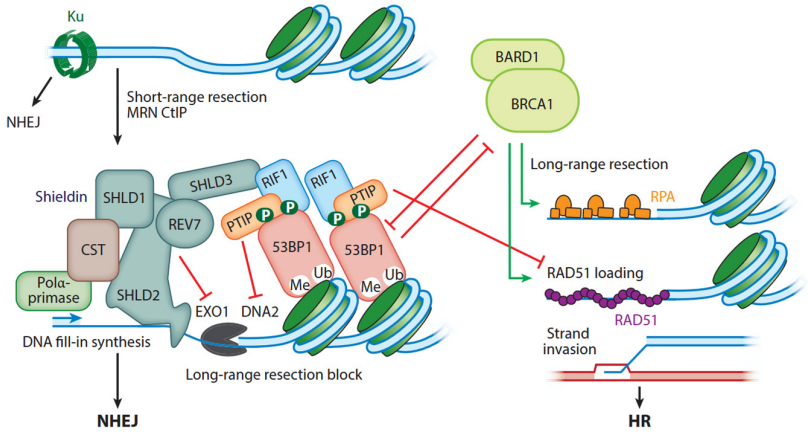

Figure 6: The antagonistic roles of 53BP1 and BRCA1 in regulating DSB repair pathway choice.

53BP1 binds damaged chromatin and recruits RIF1 and the Shieldin complex (REV7, SHLD1, SHLD2, and SHLD3), which in turn recruits the CST complex (CTC1-STN1-TEN1) and Polα-primase to initiate fill-in synthesis. This counteracts long-range resection by EXO1 and DNA2 and promotes NHEJ. In contrast, BRCA1-BARD1 binds chromatin at sites mutually exclusive to 53BP1and promotes end resection and RAD51 loading in S/G2-phase cells. From (Cejka and Symington, 2021).

2018, Ghezraoui et al., 2018, Dev et al., 2018, Sifri et al., 2023). Additionally, Shieldin can interact and recruit CST (CTC1-STN1-TEN1), an RPA-like ssDNA binding complex that promotes fill-in DNA synthesis at resected ends through recruitment of Polα-primase (King et al., 2025, Mirman et al., 2018).

Beyond antagonizing 53BP1, BRCA1-BARD1 also promotes long-range resection by directly stimulating the BLM and WRN helicase and the EXO1 exonuclease activities (Salunkhe et al., 2024, Ceppi et al., 2024). BRCA1 also interacts with CtIP and improves resection speed (Cruz-Garcia et al., 2014, Nakamura et al., 2010, Reczek et al., 2013, Polato et al., 2014).

1.3.3. The relationship between HR and NHEJ

Canonically, HR and NHEJ were thought to be two pathways in direct competition with each other, with the final choice resting at the level of protein complex recruitment at DNA ends (Shao et al., 2012, Lee et al., 1998). In this model, if Ku/DNA-PK binds to the DNA ends, the break undergoes NHEJ. Conversely, if MRX-pSae2/MRN-pCtIP-mediated resection is initiated, repair is committed to HR (Biehs et al., 2017, Shibata et al., 2014). There are several observations that support this model: Ku overexpression delays the onset of resection, while loss of Ku allows rapid resection (Mimitou and Symington, 2010, Clerici et al., 2008, Shao et al., 2012). However, kinetically, Ku recruitment to DNA ends outpaces resection (Wu et al., 2008, Lisby et al., 2004) and the short-range resection machinery can still initiate resection of Ku-bound DNA ends (Shim et al., 2010, Mimitou and Symington, 2010, Chanut et al., 2016) and, in some contexts, Ku can promote SRR (Reginato et al., 2017, Gnugge et al., 2023, Deshpande et al., 2020). Moreover, MRX/MRN is involved in the early steps of both HR and NHEJ (Moore and Haber, 1996, Lisby et al., 2004, Mimitou and Symington, 2010).

These new findings led to a revised model, where NHEJ and HR act sequentially. NHEJ is the early responder and attempts to repair the DSB. If ligation fails, end-joining factors can be displaced by resection factors (MRX-pSae2 in yeast) and repair is redirected towards HR (Paull, 2021). How the DNA is protected from resection while ligation occurs and how is Ku removed from DNA ends are still open questions that will be further detailed in this thesis.

Another revision to the model comes at the level of pathway commitment. It was generally thought that once resection occurs, NHEJ can no longer be performed (Biehs et al., 2017, Shibata et al., 2014). However, fill-in synthesis by Polα-primase may limit or reverse resection and shunt repair back to NHEJ (Mirman et al., 2018). All these findings reveal that NHEJ and HR are dynamically regulated and kinetically coupled processes that compete and transition depending on the state of the DNA end and cellular context.

1.3.4. Regulation of presynaptic filament stability

Rad51/RAD51 is a relatively small ATPase (400 amino acids in yeast and 339 in humans) and can bind both single-stranded and double-stranded DNA (Xu et al., 2017, Short et al., 2016, Namsaraev and Berg, 1998, Brouwer et al., 2018). The dsDNA binding activity is important in protecting stalled replicating forks from nuclease degradation (Taglialatela et al., 2017, Schlacher et al., 2012, Schlacher et al., 2011, Mijic et al., 2017, Kolinjivadi et al., 2017). The ssDNA binding activity is key for the recombinase activity of Rad51. Structural studies have shown that Rad51 binds ssDNA in a one protomer to three nucleotides ratio and explained the link between ATPase function of hRAD51 and filament stability and provided insights into homology search and strand invasion. Rad51-ssDNA filaments sample dsDNA tracts of at least 8 nucleotides. These results suggest a microhomology search model that can sample large parts of the genome before committing to strand exchange, which is carried out in discrete 3-nucleotide steps (Qi et al., 2015, Lee et al., 2015). The stability of the presynaptic filament is positively correlated with the length of homologous sequence and modulated by various proteins and protein complexes (Figure 7).

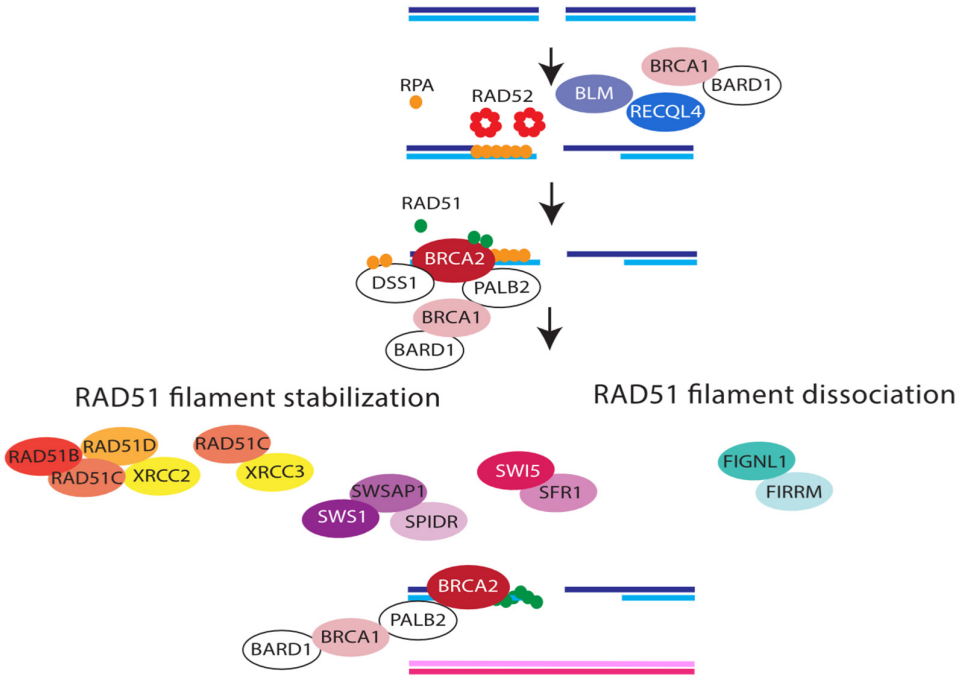

Figure 7: Positive and negative regulators of RAD51 presynaptic filament stability in somatic HR.

The BRCA2-PALB2 and BRCA1-BARD1 complexes together with DSS1 and RAD52 facilitate the replacement of RPA with RAD51. In yeast, Rad52 is the primary mediator of RPA-to-Rad51 exchange. The RAD51-ssDNA filaments are further stabilized by the RAD51 paralogs (RAD51B, RAD51C, RAD51D, XRCC2, XRCC3 in humans; Rad55-Rad57 in yeast), the Shu complex (SWSAP1-SWS1 in humans; Psy3, Csm2, Shu1 and Shu2 in yeast) and SWI5-SFR1 (Swi5-Mei5 in yeast). In humans, FIGNL1-FIRRM destabilizes and disrupts the RAD51 filaments, an activity antagonized by the Shu complex. In yeast, the major anti-recombinase is Srs2, whose activity is counteracted by the Shu complex, RAD51 paralogs, and Rad52. From (Ito et al., 2024).

In yeast, Rad52 is responsible for the initial stage of filament formation by assisting the exchange of RPA with Rad51 (Shinohara and Ogawa, 1998, Sung, 1997a, Song and Sung, 2000, New et al., 1998) and by protecting the filaments against the Srs2 anti-recombinase (Ma et al., 2018). In humans, RAD52 shares this function and is partially redundant with BRCA2 (Feng et al., 2011, Thorslund et al., 2010, Liu et al., 2010, Jensen et al., 2010). In both yeast and humans, Rad52 also has Rad51-independent functions in DNA repair, by promoting DNA annealing during SSA (Mortensen et al., 1996, Van Dyck et al., 2001). BRCA2 contains eight BRC repeats that can collectively bind to RAD51 (Shahid et al., 2014, Chen et al., 1998, Wong et al., 1997). These repeats have both faciliatory and disassembling effects on RAD51 filament formation. BRC repeats 1-4 have the highest affinity for RAD51 and can block filament formation by inhibiting DNA binding by the recombinase. In contrast, BRC repeats 5-8 bind RAD51-ssDNA filaments with high affinity and potentiate RAD51-mediated DNA strand pairing. Thus, differential roles for the BRC repeats have been speculated, with BRC1-4 acting on recruiting RAD51 and BRC5-8 stabilizing RAD51-ssDNA filaments (Chatterjee et al., 2016, Carreira and Kowalczykowski, 2011, Chen et al., 1998, Wong et al., 1997). PALB2 is a binding partner of BRCA2 and has been observed to promote RAD51 recruitment to DNA (Sy et al., 2009, Hartford et al., 2016, Dray et al., 2010). Furthermore, BRCA1-BARD1, which also interacts with PALB2 (Sy et al., 2009, Zhang et al., 2009), plays a role in strand exchange by directly binding and enhancing RAD51-mediated homologous DNA pairing (Zhao et al., 2017). Yeast Mms22 (MMS22L-TONSL in humans) has also been shown to promote RAD51-ssDNA filament formation at stalled or collapsed replication forks (Piwko et al., 2016, O'Donnell et al., 2010, Duro et al., 2008, Duro et al., 2010).

There are also factors that contribute to the stabilization of Rad51/RAD51-ssDNA filaments prior to homology search, such as Swi5-Mei5 (SWI5-SFR1 in humans), the Shu complex (composed of Psy3, Csm2, Shu1 and Shu2 in yeast and SWSAP1-SWS1 in humans), and the Rad51 paralogs (Rad55-Rad57 in yeast and RAD51B, RAD51C, RAD51D, XRCC2 and XRCC3 in humans) (Bernstein et al., 2011, Zhang et al., 2017, Yuan and Chen, 2011, Haruta et al., 2006, Abreu et al., 2018, Masson et al., 2001, Sung, 1997b, Gaines et al., 2015, Berti et al., 2020, Chun et al., 2013, Hengel et al., 2024, Greenhough et al., 2026, Deveryshetty et al., 2025, Belan et al., 2023, Akita et al., 2024).

To precisely control strand invasion and ensure its accuracy, further factors oversee the disassembly of the presynaptic filament. In yeast, Srs2, a 3’ to 5’ helicase-translocase is the primary anti-recombinase that can directly remove Rad51 from ssDNA (Veaute et al., 2003, Krejci et al., 2003). This interaction is dependent on the ATPase activity of both proteins (Qiu et al., 2013, Antony et al., 2009). Several Rad51 stabilizers also act to counteract Srs2-mediated filament disruption, such as Rad52, Rad55-57 and the Shu complex (Ma et al., 2018, Bernstein et al., 2011, Liu et al., 2011a). An exact human ortholog of Srs2 has not yet been identified, but there are several candidates with similar functions. FBH1, BLM and RECQL5 are all reported to be able to disrupt presynaptic

filaments (Hu et al., 2007, Chiolo et al., 2007, Bugreev et al., 2007). Although RTEL1 shares functional similarities with yeast Srs2, the two proteins have low sequence homology. RTEL1 has been shown to disrupt recombination intermediates; however, whether it can dissociate RAD51 from ssDNA remains controversial (Barber et al., 2008).

Another recently identified anti-recombinase, Fidgetin-like protein 1 (FIGNL1), has taken the center stage. It is part of the AAA+ (ATPase Associated with Diverse Cellular Activities) protein family, whose members typically operate as hexamers. FIGNL1 interacts with RAD51 through its FRBD domain, as well as through the pore-loop domain formed of the hexameric complex in a seemingly antagonistic manner to BRCA2. RAD51 removal from ssDNA by FIGNL1 is dependent on the ATPase activity of FIGNL1, but, unlike Srs2, is not affected by the RAD51 ATPase (Matsuzaki et al., 2024, Ito et al., 2023, Carver et al., 2025, Kuthethur et al., 2025). This disruptive activity can be inhibited by the Shu complex, particularly SWSAP1 (Matsuzaki et al., 2019). FIGNL1 is highly conserved across vertebrates and invertebrates. In *Arabidopsis* and rice plant cells, knocking out FIGL1, the ortholog of FIGNL1, leads to severe meiotic chromosome fragmentation (Fernandes et al., 2018, Emmenecker et al., 2024, Yang et al., 2022). FIGNL1 also interacts with FIRRM (FIGNL1-interacting regulator of recombination and meiosis). This interaction is proposed to stimulate the anti-recombinase activity of FIGNL1, although the exact mechanisms are still unknown (Zhou et al., 2023, Zainu et al., 2024, Stok et al., 2023, Pinedo-Carpio et al., 2023, Hu et al., 2017).

1.4. The MRX-(p)Sae2 complex

The conserved functional core of the MRX/MRN complex (Figure 8) is composed of the nuclease Mre11/MRE11 and the ATPase Rad50/RAD50 arranged as a dimer of dimers (M2R2) (Anderson et al., 2001, Usui et al., 1998, de Jager et al., 2001). The oligomerization of MR can be of higher order as well, as shown *in vivo* and *in vitro* (Lisby et al., 2004, de Jager et al., 2001, Kissling et al., 2022). The stoichiometry of the third subunit, Xrs2/NBS1, is less clear. In fission yeast, Nbs1 is thought to be 1:1 with Mre11, while in budding yeast, one Xrs2 binds one M2R2 core (Chen et al., 2001, Schiller et al., 2012).

Mre11/MRE11 on its own is a manganese-dependent 3’ to 5’ nuclease and ssDNA endonuclease (Usui et al., 1998, Paull and Gellert, 1998, Trujillo et al., 1998, Herdendorf et al., 2011). When complexed with Rad50/RAD50, it gains a magnesium/manganese/ATP-dependent dsDNA endonuclease activity (Deshpande et al., 2016, Cannavo and Cejka, 2014). Structurally, Mre11/MRE11 can be split into two domains: an N-terminal nuclease domain, with a catalytic site composed of five phosphoesterase motifs, and a C-terminal capping domain, with DNA binding activity and which controls the access of the DNA to the enzymatic core (Williams et al., 2008, Hopfner et al., 2001, Das et al., 2010). The C-terminal part of Mre11/MRE11 also interacts with Rad50/RAD50 (Lammens et al., 2011, Lafrance-Vanasse et al., 2015).

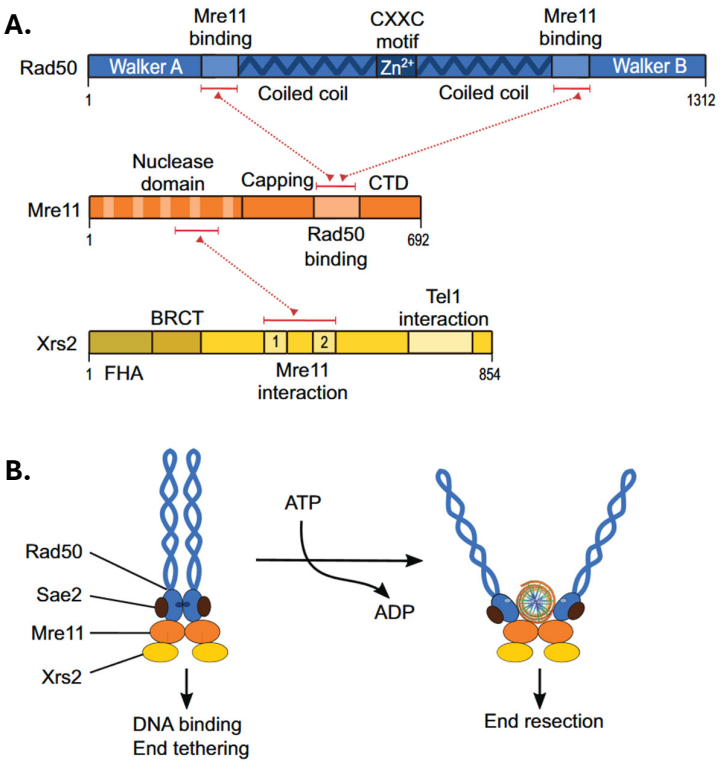

Figure 8: The domain architecture of the MRX complex and their association with Sae2.

A. *Domain organization of the MRX complex subunits and their principal interactions with one another and with the DNA damage response (DDR) regulator Tel1.*

B. *The proposed 3D structure of the M2R2 core together with Xrs2 and Sae2 illustrating ATP-dependent conformational changes. In the ATP-bound state, the catalytic nuclease domain of Mre11 is inaccessible to DNA. However, ATP hydrolysis by Rad50, causes a conformational change which exposes the nuclease domain of Mre11 to DNA. From (Yadav and Claeys Bouuaert, 2021).*

Rad50/RAD50 is an ABC (ATP-Binding Cassette) ATPase and part of the SMC family of proteins, together with cohesins and condensins (Hopfner et al., 2000, Herdendorf et al., 2011). Rad50/RAD50 contains two globular domains at each terminus of the protein connected by two long coiled-coil regions that fold into each other in an antiparallel fashion at the central region comprised by a Zinc hook (CXXC motif). The N-terminal globular domain contains the Walker A motif, whereas the Walker B motif rests at the C-terminal globular domain. Both domains interact with each other upon ATP binding to dimerize and form two complete ATPase catalytic sites (Lim et al., 2011, Lammens et al., 2011, Hopfner et al., 2001). After dimerization, the zinc hooks of the dimer can coordinate one Zn^{2+} ion, further mediating the inter- and intramolecular oligomerization (Hopfner et al., 2002). Mre11/MRE11 interacts with the base of the coiled-coil regions to form the M2R2 core (Lammens et al., 2011, Hopfner et al., 2001). These regions and the zinc hook are important for the functions of MRX/MRN in both end-tethering in NHEJ and resection in HR (Deshpande et al., 2014, Wiltzius et al., 2005, Nakai et al., 2011, Lobachev et al., 2004, He et al., 2012, de Jager et al., 2001). In yeast, Rad50 is also responsible for sensing the phosphorylation state of Sae2 (Cannavo et al., 2018, Nicolas et al., 2024).

The M2R2 core undergoes major conformational changes upon ATP binding and hydrolysis. Without ATP, M2R2 is an “open” conformation that allows the DNA access to the exonuclease catalytic site of Mre11/MRE11. When ATP is bound, Rad50/RAD50 dimerization occurs turning the nuclease site inaccessible. This “closed” state confers the complex higher affinity for DNA and higher oligomeric state. ATP hydrolysis causes another structural shift which could lead to the melting of the dsDNA and is necessary for the dsDNA endonuclease activity (Mockel et al., 2012, Majka et al., 2012, Deshpande et al., 2014, Lim et al., 2011, Hopfner et al., 2000, Lammens et al., 2011, Hopfner et al., 2001).

In yeast, Xrs2 per se is not required for the catalytic roles of MRX in resection (Reginato et al., 2017, Cannavo and Cejka, 2014, Wang et al., 2017, Oh et al., 2016) but is needed for the nuclear import of the complex *in vivo* (Tsukamoto et al., 2005), as well as for NHEJ and DDR signaling (Oh et al., 2016, Oh et al., 2018, Nakada et al., 2003). In fact, Xrs2 interacts with the NHEJ factor Lif1 (Chen et al., 2001) and with the DDR kinase Tel1 (Iwasaki et al., 2016, Hailemariam et al., 2019). In humans, NBS1 directly influences the nuclease functions of the MRN complex, as NBS1 is the main sensor of CtIP phosphorylation via its BRCT repeats (Anand et al., 2016, Anand et al., 2019, Deshpande et al., 2016). Moreover, Xrs2/NBS1 act as substrates for Tel1/ATM-mediated phosphorylation and contribute to the regulation of cellular responses to DSBs (Zhou et al., 2017, Wu et al., 2000, Lim et al., 2000, Gatei et al., 2000, Huang et al., 2016, D'Amours and Jackson, 2001).

Sae2/CtIP is the main cofactor of MRX/MRN in resection and capable of stimulating both the exonuclease and endonuclease activities of the short-range resection machinery (Anand et al., 2016, Tamai et al., 2024, Cannavo et al., 2019, Cannavo and Cejka, 2014). Sae2/CtIP is responsible for the cell-cycle dependent regulation of HR (Huertas and Jackson, 2009, Huertas et al., 2008). This cofactor is known to tetramerize via an N-terminal alpha-helical domain (Davies et al., 2015, Cannavo et al., 2018). Sae2 phosphorylation also determines its oligomeric state, with the unphosphorylated protein being present in higher order, but inactive multimers (Fu et al., 2014, Cannavo et al., 2018). While the N-terminal domain of Sae2 is partially dispensable for the endonuclease stimulation of MRX, it is required for promoting the exonuclease of the complex (Cannavo et al., 2019, Reginato et al., 2017). Sae2 and CtIP share a conserved C-terminal region involved in the stimulation of MRX/MRN (Cannavo et al., 2018, Anand et al., 2016, Sartori et al., 2007, Davies et al., 2015). Unlike in yeast, the intrinsically disordered region (IDR) of CtIP contains MRE11 and NBS1 interaction sites and further phosphorylation sites with regulatory functions (Wang et al., 2013, Sartori et al., 2007, Williams et al., 2009).

Due to its mode of action, the MRX-pSae2 resection machinery has a versatile and highly conserved capability of cleaving past proteins bound to DNA ends, ranging from the less-physiological streptavidin to proteins relevant *in vivo*, such as Spo11, Top2 and Ku (Hoa et al., 2016, Cannavo and Cejka, 2014, Reginato et al., 2017, Keeney and Kleckner, 1995,

Keeney et al., 1997, Neale et al., 2005, Deshpande et al., 2020, Anand et al., 2016, Deshpande et al., 2016, Myler et al., 2017). MRX-Sae2 can cleave DNA near oligonucleotide-bound nucleosomes, even though the complex was also seen to bypass nucleosomes while sliding (Wang et al., 2017). This function of MRX-Sae2 does not require direct interaction with the proteins bound to the ends, which is a key reason for its versatility (Wang et al., 2017, Reginato et al., 2017, Cannavo and Cejka, 2014). The Ku heterodimer with its ring-like structure deserves special attention due to its involvement in NHEJ, where it quickly engages with the DNA ends. MRX-Sae2 ensemble can cleave near Ku-bound DSBs, at ~30bp from the end (Reginato et al., 2017, Wang et al., 2017, Gnugge et al., 2023). *In vivo*, *mre11* nuclease-deficient cells are sensitive to DNA damage, which can be alleviated by the deletion of Ku, pointing that the Mre11 nuclease is required to remove Ku (Moreau et al., 1999, Foster et al., 2011, Mimitou and Symington, 2010). Conversely, the catalytic activity of Mre11 is not required for the processing of clean DSBs (Llorente and Symington, 2004, Mimitou and Symington, 2008, Mimitou and Symington, 2010).

1.5. Replication protein A and DNA repair

Replication protein A (RPA) is a highly conserved heterotrimeric complex and the main ssDNA-binding protein in eukaryotic cells. It functions in most processes related to DNA metabolism, ranging from DNA replication, transcription, DNA damage signaling and to various DNA repair pathways. Although, it is mostly employed as a protective factor to prevent excessive nucleolytic degradation of ssDNA, RPA interacts and can directly influence the activity of a wide array of enzymes (Wold, 1997, Nasheuer et al., 2024).

In DNA replication, RPA is essential for its ssDNA binding activity, which protects the unwound DNA from degradation, and for its protein recruitment function (Szambowska et al., 2017, Lavrik et al., 1998, Jones et al., 2021, Jones et al., 2023). At stalled replication forks, RPA is involved in the process of fork restart by interacting with Primpol (Wan et al., 2013) or by acting as a fidelity clamp for Polα to maintain its processivity (Maga et al., 2001, Braun et al., 1997). This indicates that RPA can collaborate in polymerase switching from primase to Polα. The contacts between RPA and RFC can later recruit Polδ (Yuzhakov et al., 1999). Additionally, RPA is employed in Okazaki fragment processing by binding the 5' flap ssDNA, generated by Polδ during displacement synthesis, and protect against FEN1 cleavage. RPA then recruits DNA2 which endonucleolytically removes the flap (Bae et al., 2001).

During DNA damage signaling, under environmental or cellular stress, the protein DOCK7 promotes the accumulation of RPA at chromatin and replication forks, where it again acts as a scaffold for other proteins (Gao et al., 2021, Wu et al., 2023). In this context, RPA is ubiquitinated and binds to ATRIP (ATR-interacting protein) to recruit ATR to the ssDNA stretches (Ball et al., 2005). Cyclin-dependent kinases (CDKs), ATR, ATM and DNA-PK phosphorylate eight serine and threonine residues the N-terminus of RPA32 in response

to genotoxic stress and this hyperphosphorylation is a marker for resection at DSB sites (Nuss et al., 2005, Borgstahl et al., 2014, Binz and Wold, 2008).

RPA also plays a role in DNA repair. In nucleotide excision repair, XPA and RPA stabilize the ssDNA and correctly position the ERCC1-XPF and XPG endonucleases (Saijo et al., 2011, Overmeer et al., 2011, Matsuda et al., 1995, Li et al., 1995). After ERCC1-XPF incises DNA at the 5' end, RPA assists in recruiting RFC to load PCNA and promote DNA synthesis by Polδ and/or ε (Yuzhakov et al., 1999).

1.5.1. The structure of RPA

RPA is a heterotrimeric protein composed of three subunits: Rfa1 (RPA70), Rfa2 (RPA32) and Rfa3 (RPA14). Each of these subunits contains one or more of the universally conserved oligonucleotide/oligosaccharide-binding (OB)-fold domains (Figure 9A), which are characterized by twisted β sheets and α-helix capped ends. These OB-fold domains allow RPA to bind ssDNA or act as protein-protein interaction sites (Bochkarev et al., 1997, Bochkarev et al., 1999, Bochkareva et al., 2002, Wold and Kelly, 1988, Wu et al., 2023).

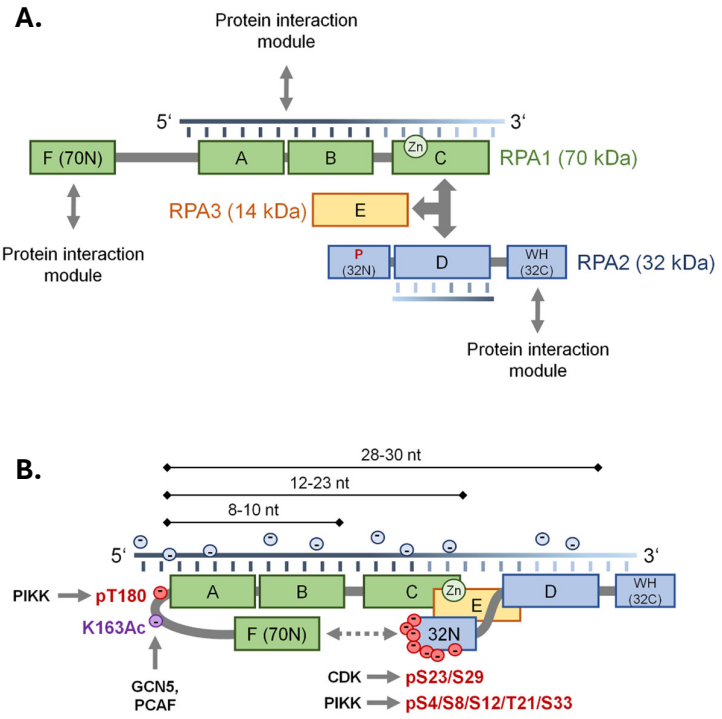

Figure 9: The domains of the RPA subunits and their interaction with ssDNA and cell kinases.

A. *Domain architecture of the RPA heterotrimer, highlighting the ssDNA-binding domains and the trimerization core of the complex. The Zinc-binding motif within DBD-C is also indicated.*

B. *The three proposed ssDNA-binding modes of RPA. RPA is a target of kinase-mediated phosphorylation and these post-translation modifications can alter the interactions between the OB-folds of the complex and modulate its DNA binding activity.*

From (Dueva and Iliakis, 2020).

Rfa1/RPA70 is the largest subunit (70 kDa in size) and contains four OB-folds, also called DNA-binding domains (DBD). The first one, DBD-F, is located at the N-terminus and has little to no DNA binding activity. Instead, this domain is a hub for protein-protein interactions. The interaction partners range from Mec1-Ddc2 (ATR-ATRIP in humans), Sgs1 (BLM and WRN in humans), Rad51/RAD51, Rad52/RAD52, RFC and Polα, to Dna2/DNA2 and Mre11/MRE11 (Acharya et al., 2021, Zhou et al., 2015, Shorrocks et al., 2021, Yates et al., 2023, Wu et al., 2023, Nasheuer et al., 2024). The next two domains of Rfa1, DBD-A and DBD-B, possess the highest affinity for ssDNA. They bind DNA with a groove composed by the loops L12 and L45 flanking the β strands β2 and β3 of the OB-fold and they each contain two highly conserved aromatic residues, that stack with DNA bases, and two conserved hydrophobic amino acids (Pestryakov et al., 2003, Fan and Pavletich, 2012, Bochkarev et al., 1997). The last OB-fold of Rfa1 is DBD-C, which also contributes to ssDNA binding. Unlike the other OB-folds, this domain contains zinc-binding motifs, with unknown cellular functions, but crucial for RPA structural stability and its DNA-binding capability (Fan and Pavletich, 2012, Bochkareva et al., 2000, Bochkareva et al., 2002). At the C-terminus of Rfa1 there is a trimerization core, composed of a hydrophobic α-helix which holds the complex together by interacting with the OB-fold domain of Rfa2 and with Rfa3 (Bochkareva et al., 2002).

Rfa2/RPA32 is the middle-sized member of the trimer (32 kDa) and contains only one OB-fold, DBD-D (Bochkareva et al., 1998). Although Rfa2 is known to be able to bind to ssDNA, its affinity is much lower compared to Rfa1 (Bochkarev et al., 1999, Bastin-Shanower and Brill, 2001). As mentioned above, the N-terminus of Rfa2 is a target of phosphorylation and highly relevant for protein interactions and cellular signaling and regulation (Nuss et al., 2005, Borgstahl et al., 2014). In addition, Rfa2 contains a C-terminal Winged Helix Domain (WHD), which is another protein interaction hub, binding to proteins such as Polα/primase and Rad52 (Dueva and Iliakis, 2020, Nasheuer et al., 2024).

Rfa3/RPA14 is the smallest subunit and contains only one domain, the OB-fold DBD-E (Bochkarev et al., 1999, Bochkareva et al., 2002). Although there is some evidence that Rfa3 also possesses DNA-binding activity, the subunit mostly appears to coordinate the association between Rfa1 and Rfa2 and modulate the binding modes of RPA, especially when needed to accommodate shorter DNA lengths (Salas et al., 2009). Accordingly, as for all other subunits, *rfa3* deletion in yeast is also lethal (Brill and Stillman, 1991).

Three ssDNA binding modes have been observed for the trimeric RPA (Figure 9B). Binding starts with 8-10 nt-binding mode, where the ssDNA is compactly engaged by the DBD-A and DBD-B domains of Rfa1. This is followed by the 12–23 nt-binding mode, where the DBD-C of Rfa1 is recruited on the DNA. Lastly, RPA can establish a 28-30 nt-binding mode, when the DBD-D of Rfa2 also interacts with the ssDNA (Fan and Pavletich, 2012, Cai et al., 2007, Bastin-Shanower and Brill, 2001). This flexibility of RPA suggests a

dynamic DNA binding, which is further influenced by the phosphorylation state of the N-terminus of Rfa2/RPA32 (Soniat et al., 2019, Kang et al., 2023, Binz et al., 2003).

Beyond its ability to bind ssDNA, RPA has been observed to possess a conserved, magnesium-dependent dsDNA melting activity when bound to the ssDNA-dsDNA boundaries. RPA uses a 'toehold'-like mechanism to trap small transient openings of the DNA helix with a microdomain, which are then expanded as the full protein wedges in to bind (Kemmerich et al., 2016).

1.5.2. The role of RPA in DSB repair

Although not involved in NHEJ, RPA is a critical factor in DSB repair, particularly HR. As mentioned earlier, RPA is an essential protective factor for ssDNA, and, in the context of HR, is reported to prevent aberrant nucleolytic degradation by Mre11 of the 3' ssDNA overhang created during resection (Chen et al., 2013, Niu et al., 2010). RPA binding to resected DNA also prevents repair by the mutagenic MMEJ pathways (Deng et al., 2015b, Deng et al., 2014, Deng et al., 2015a). However, its role extends far beyond protection. Upon DNA damage, RPA is ubiquitinated by the E3-ubiquitin ligase RING finger and WD repeat domain 3 (RFWD3) on the Rfa1 and Rfa2 subunits. This post-translationally modified RPA promotes HR through directly interacting with various repair factors (Liu et al., 2011b, Elia et al., 2015).

Although DNA stabilization by RPA is a necessary step in the repair process, the RPA-coated ssDNA is not compatible with strand invasion and RPA must be exchanged with Rad51/RAD51 (Ding et al., 2023). The mechanism and factors involved in this process have been addressed in previous sections. In yest, Rad52 interacts with the WHD of Rfa2 and changes the ssDNA-binding dynamics of DBD-D, leading to a reduction in the affinity of RPA to ssDNA. This allows the nucleation of Rad52-bound Rad51 on the RPA-bound ssDNA and further decreases the affinity of RPA to ssDNA, causing its complete replacement with Rad51 (Pokhrel et al., 2019, Davis and Symington, 2003).

RPA promotes long-range resection by removing secondary ssDNA structures (Chen et al., 2013) and binding and stimulating the DNA unwinding activity of Sgs1 (similarly with BLM in humans) and the 5' to 3' exonuclease activity of Dna2/DNA2, reinforcing its polarity (Cejka et al., 2010a, Niu et al., 2010, Nimonkar et al., 2011, Acharya et al., 2021, Zhou et al., 2015). In humans, RPA phosphorylation at the N-terminus of RPA32 is a signal to terminate resection by interrupting the BLM-RPA interactions (Soniat et al., 2019). Additionally, RPA can also stimulate the exonuclease activity of Exo1/EXO1, although a direct physical interaction between the two proteins has not been reported. The mechanisms of this interplay are still debated, but the data suggests that RPA promotes the displacement of Exo1/EXO1 from ssDNA and this, while limiting the processivity of the nuclease, also improves its turnover rate (Myler et al., 2016, Cannavo et al., 2013). Whether RPA also plays a role during short-range resection is not yet known. However, RPA does co-localize and interact with Mre11/MRE11 at stalled replication forks through

the DBD-F of Rfa1/RPA70 (Seeber et al., 2016, Robison et al., 2004). In humans, this interaction is modulated by the phosphorylation of RPA32 (Oakley et al., 2009). It is possible to speculate that, even though RPA binding to DNA is a downstream step of resection, RPA might influence the nuclease activity of MRX/MRN. This aspect will be further explored in this thesis.

2. Aim of the thesis

One mechanism regulating the balance between HR and NHEJ is the rapid recruitment of Ku to broken DNA ends and the ability of short-range resection machinery to process protein-blocked DNA ends. The individual stages of HR are also highly interconnected, although many of the underlying mechanistic details remain poorly understood. Regulation can additionally occur at the level of strand exchange and RAD51-ssDNA presynaptic filament stability, yet many of the factors involved have not been fully characterized. Addressing these questions could have important implications for the field of genome editing and may uncover previously unrecognized therapeutic targets.

The work presented in this thesis seeks to elucidate the following:

1) The mechanistic regulation of DSB repair pathway choice during the early stages of repair, particularly through Ku removal from DNA ends, and repair pathway commitment.
2) The role of the strand exchange factor BRCA1-BARD1 in end resection.
3) The interplay between the anti-recombinase FIGNL1 and RAD51, as well as the functional relationship between FIGNL1 and the strand exchange factor MMS22L-TONSL.

3. Results

3.1. NHEJ-mediated DNA synapsis and RPA-driven MRX exonuclease balance DNA end resection to control DSB repair pathway choice

Summary:

DNA double-strand breaks (DSBs) are critical lesions that must be repaired quickly and accurately, either through the fast but mutagenic non-homologous end-joining (NHEJ) pathway or the slower but more accurate homologous recombination (HR) pathway. NHEJ promotes repair by rapidly synapsing DNA ends and favoring direct ligation. In contrast, HR requires DNA end resection to generate single-stranded DNA, a process initiated in yeast by the short-range resection complex, MRX-pSae2, which produces RPA-coated ssDNA. The opposing activities of NHEJ-mediated end synapsis and MRX-pSae2-mediated short-range resection establish a balance that governs the extent of resection and thereby controls DSB repair pathway choice.

We found that, while end-joining factors per se do not affect short-range resection, synapsis of the DNA ends masks them and renders them inaccessible to nucleolytic degradation by MRX-pSae2. I observed that MRX-pSae2 can efficiently cleave Ku-bound DNA ends but is incapable of removing the Ku protein block through the sole action of its 3' to 5' exonuclease activity. I identified a novel role of RPA in stimulating the exonuclease activity of the short-range resection machinery and thus promoting Ku displacement from DNA ends. RPA acts *in cis* and interacts with both MRX and Sae2 via the DBD-F of Rfa1. Deletion of this domain in RPA abrogates its interaction with both resection factors but shows only a minor functional defect. In contrast, deletion of the whole Rfa3 subunit abrogated the stimulatory effect of RPA on MRX-pSae2 and its ability to remove Ku, suggesting that an additional transient interaction interface is located on the smallest subunit of the RPA trimer. Finally, end joining of partially resected DNA remains possible but is significantly inhibited by the presence of RPA.

My contribution:

I expressed and purified most of the recombinant protein used in this study. I designed and executed the biochemical assays investigating the role of RPA in MRX-pSae2-mediated Ku removal from DNA ends (Fig. 4, 5, 6, 7, 8b and Ext. Fig. 3, 4, 5, 6, 7, 8). I analyzed the data and wrote the manuscript together with P.C. with inputs from the other lab members.

This work was submitted to *Nature Communications* and is currently under review.

NHEJ-mediated DNA synapsis and RPA-driven MRX exonuclease balance DNA end resection to control DSB repair

Stefan Braunshier[1,§], Elda Cannavo[1,§], Vincent Morin[2,3], Sriram KK[4], Ananya Acharya[1,#], Giordano Reginato[1,##], Florian Morati[4], Virginie Ropars[2], Raphael Guerois[2], Jean-Baptiste Charbonnier[2], Fredrik Westerlund[4], Terence Strick[3] and Petr Cejka[1,*]

[1]Faculty of Biomedical Sciences, Institute for Research in Biomedicine, Università della Svizzera italiana (USI), Bellinzona, Switzerland.

[2]Institute for Integrative Biology of the Cell (I2BC), Institute Joliot, CEA, CNRS, Université Paris-Saclay, Gif-sur-Yvette, France.

[3]École normale supérieure, Institut de Biologie de l'École normale supérieure (IBENS), CNRS, INSERM, PSL Research University, 75005 Paris, France.

[4]Department of Life Sciences, Chalmers University of Technology, 412 96 Gothenburg, Sweden.

[§], These authors contributed equally.

[#], Current address: Division of Radiation and Genome Stability, Department of Radiation Oncology, Dana-Farber Cancer Institute, Harvard Medical School, Boston, MA, USA.

[##], Current address: Laboratory for Cell Biology and Genetics, The Rockefeller University, New York, USA.

*Correspondence: Petr Cejka, email: petr.cejka@irb.usi.ch

Summary

DNA double-strand breaks (DSBs) are repaired by Ku-dependent non-homologous end-joining (NHEJ) or DNA end resection-dependent homologous recombination (HR). Previously, it was shown that short-range resection by MRX-pSae2 can remove Ku from DSBs and initiate resection, showing flexibility in DSB repair pathway choice. However, which NHEJ intermediates can be disrupted by resection factors remains unknown. Using reconstituted reactions with purified *S. cerevisiae* proteins, we show here that short-range resection by MRX-pSae2 is not directly inhibited by any of the core NHEJ factors. Instead, we find that MRX-pSae2 is inhibited structurally. DNA synapsis, a dynamic NHEJ intermediate that bridges DSBs, strongly suppresses resection. Non-ligatable ends are refractory to MRX-pSae2 once synapsis formed, and NHEJ assemblies with catalytic mutants of DNA ligase IV that permit synapsis but do not allow ligation likewise inhibit resection. We further demonstrate that removal of Ku from DSBs requires RPA, which interacts with MRX and pSae2 to synergistically stimulate MRX 3'-5' exonuclease activity, generating free 3' overhangs. Our data support a model in which DNA synapsis temporarily prevents resection, allowing NHEJ to execute ligation. If ligation fails and synapsis dissociates, MRX-pSae2 and RPA promote resection that removes non-productive NHEJ assemblies and channels DSB repair toward HR. The data help explain the suppression of NHEJ by RPA observed in previous genetic experiments.

Introduction

DNA double-strand breaks (DSBs) are among the most cytotoxic forms of DNA damage. They are repaired primarily by either of two pathways: non-homologous end-joining (NHEJ) or homologous recombination (HR). Mechanistically, NHEJ involves little or no processing of DNA ends and functions throughout the cell cycle[1-5]. In *Saccharomyces cerevisiae*, DSBs are bound within seconds by the Yku70-Yku80 (Ku) heterodimer, which is followed by the recruitment of additional components, including the Mre11-Rad50-Xrs2 (MRX) complex, the accessory protein Nej1 and the DNA ligase IV (Dnl4-Lif1) complex. The NHEJ machinery first brings the two DNA ends of a DSB together and aligns them in a process known as synapsis. Synapsis allows limited DSB processing and is followed by ligation[6]. NHEJ does not rely on a template and can thus be highly mutagenic[1-5]. In contrast, HR uses a homologous DNA template, most often the sister chromatid, resulting in largely accurate repair. Consequently, HR is mostly restricted to the S and G2 phases of the cell cycle when sister chromatids are present[7]. HR is initiated by DNA end resection, which involves nucleolytic removal of the 5'-terminated strand at the DSB. This process generates a 3' single-stranded DNA (ssDNA) overhang that is essential for homology search and priming DNA synthesis during subsequent steps of HR[8]. DNA end resection therefore plays a pivotal role in DSB repair pathway choice: resected ends are directed into HR, whereas unresected ends can be joined by NHEJ[9,10]. A third pathway, microhomology-mediated end-joining (MMEJ), depends on limited resection, but represents a minor repair route in budding yeast[11].

DNA end resection is carried out by three nucleases, which are traditionally divided into short-range and long-range pathways. The Mre11 nuclease functions within the Mre11-Rad50-Xrs2 (MRX) complex in *Saccharomyces cerevisiae* (in humans, MRE11-RAD50-NBS1 or MRN) to catalyze short-range resection. Together with phosphorylated Sae2 (pSae2, or pCtIP in humans), MRX initiates resection by removing protein blocks or secondary DNA structures at break ends[12-16]. Specifically, MRX-pSae2 incises the 5'-terminated strand on the end-distal side of such obstacles through its endonuclease (i.e., nicking) activity, generating an entry point for long-range nucleases[12,17,18]. Subsequent 5'-3' resection is performed by Sgs1-Dna2 or Exo1, which can resect long DNA tracts but are often hindered by non-canonical DNA structures or bound proteins[19,20]. The single-stranded DNA (ssDNA) binding protein RPA does not affect DNA incision by the MRX-pSae2 complex[12], but whether it affects downstream steps in short-range resection remained unclear. RPA clearly regulates long-range resection[21-24]. Furthermore, while the ability of MRX-pSae2 to incise DNA endonucleolytically past protein blocks is well established[12], it is not clear whether its 3'-5' exonuclease activity, engaged subsequently to proceed back toward the DNA end, is sufficient to remove the protein block by itself or whether additional cofactors are

77 required. Since only a free 3' overhang can prime DNA synthesis upon strand invasion in HR, un-
78 derstanding how protein blocks are eliminated from DNA termini at DSBs remains critical for
79 gaining insight into how HR is executed.

80 Traditionally, DSB repair pathway choice has been viewed as a competition between end-binding
81 NHEJ factors, most prominently the Ku heterodimer, and DNA end resection. Consistent with this
82 view, cells lacking Ku show elevated levels of HR, suggesting that Ku restricts resection[25-29]. Ad-
83 ditional NHEJ proteins, such as yeast Nej1, have also been implicated in suppressing DNA end
84 resection[30,31]. However, interpreting these genetic results is challenging. In cells lacking NHEJ
85 factors, end-joining is unavailable, leaving resection and subsequent HR as the only major repair
86 route. Thus, it remains unclear whether NHEJ proteins actively inhibit resection, or whether the
87 increased HR observed in NHEJ-deficient cells merely reflects the engagement of the only re-
88 maining repair pathway. Subsequent studies, in both yeast and humans, have largely challenged
89 the notion of a simple competition model[18,32,33]. Ku is rapidly recruited to DSBs and most often
90 outcompetes pro-HR resection factors[32,34-36]. Furthermore, not all breaks are compatible with
91 end-to-end ligation, such as one-ended DSBs that may arise from collapsed replication forks[37,38],
92 indicating the need for flexibility in DSB repair pathway choice. Consequently, biochemical and
93 cell-based evidence indicates that Ku-bound DSBs can be resected by the MRX complex[14,25,26,33],
94 and, in some contexts, Ku even promotes short-range end resection[14,18]. These findings led to a
95 revised model: NHEJ factors typically assemble first and attempt ligation. If ligation fails, such as
96 due to incompatible or one-ended breaks, end-joining factors can be displaced by DNA end re-
97 section factors (MRX-pSae2 in yeast), allowing the break to be redirected to HR[32,39]. Still, it re-
98 mains unclear which end-joining assemblies can be removed by resection proteins, and whether
99 certain NHEJ intermediates prevent resection.

100 Using purified *S. cerevisiae* proteins, we reconstituted the competition between NHEJ and short-
101 range resection. Our assays recapitulate that NHEJ is a rapid process requiring low concentra-
102 tions of MRX. By contrast, resection is slower and requires higher MRX levels. We show that MRX-
103 pSae2 is not hindered by any of the NHEJ proteins *per se*. Instead, resection is strongly inhibited
104 by the synapsis of broken DNA ends. We also demonstrate that Ku removal from DSBs by MRX-
105 pSae2 is stimulated by the ssDNA-binding protein RPA. While RPA does not influence the initial
106 endonucleolytic incision by MRX-pSae2, it markedly enhances Ku removal by stimulating the
107 downstream MRX 3'-5' exonuclease activity in synergy with pSae2. Our assays illuminate the
108 mechanisms underlying the competition between the two main DSB repair pathways and define
109 how protein blocks are removed from DNA ends.

110

Results

Reconstituted end-joining acts more efficiently and faster than DNA end resection

To define the competition between NHEJ and DNA end resection, we first reconstituted these pathways individually. *S. cerevisiae* Yku70–Yku80 (Ku), Dnl4-Lif1, Nej1, as well as Mre11-Rad50-Xrs2 (MRX) and phosphorylated Sae2 (pSae2) proteins were expressed and purified (Fig. 1a; Supplementary Fig. 1a-e). Using a 2.5 kbp DNA substrate with 4-nucleotide (nt) overhangs, the recombinant end-joining machinery yielded ligated products, including circular DNA and various concatemers (Fig. 1b,c). Consistent with previous studies, the reconstituted end-joining reaction was absolutely dependent on the ligase complex (Dnl4-Lif1) and strongly stimulated by Ku, Nej1 and MRX (Fig. 1c,d)[3-5]. As expected, the Mre11-Rad50 complex lacking Xrs2 (Supplementary Fig. 1f) did not support NHEJ (Supplementary Fig. 2a)[3,40,41]. The MRX complex has been reported to play an important role in bridging DNA ends, in contrast to MR, which had a weaker effect[42-45]. Correspondingly, in our reactions, MRX was required for the formation of higher-order ligation products, while MR was functionally inactive (Supplementary Fig. 2a). However, DNA circularization still occurred even in the absence of MRX (Fig. 1c,d; Supplementary Fig. 2a). A kinetic analysis of the end-joining reaction showed that ligation is rapid, with most of the DNA substrate consumed within 4-8 minutes of incubation (Fig. 1e). Increasing the concentration of MRX had little effect on the overall rate of end-joining (Fig. 1e [ii]; Supplementary Fig. 2b), and very low MRX concentrations were sufficient to stimulate the reaction (Supplementary Fig. 2c).

In contrast, short-range DNA end resection by the MRX-pSae2 complex was significantly slower, not reaching saturation before 60 minutes. Similarly slow kinetics was observed when monitoring the removal of a terminal 5' fragment (Fig. 1f; Supplementary Fig. 2d) or resection at a distance of 50-70 bp from the DNA end upon annealing with a radioactive probe (Fig. 1g; Supplementary Fig. 2e). In addition to the lower rate, resection required ~ 5-10-fold higher MRX concentrations than end-joining (Fig. 1h; Supplementary Fig. 2f). Together, these results show that, *in vitro*, end-joining is faster than end resection, demonstrating that end-joining is kinetically favored and recapitulating relative rates consistent with conclusions based on cellular studies[15,34,36,46,47]. Considering the rapid recruitment of Ku to DSBs, previous work has indicated that short-range resection can remove Ku from DNA ends to channel repair toward HR[13,14,18,25,26,32]. It has also been suggested that some end-joining proteins inhibit resection[30,31,48], raising the question of which end-joining assemblies can be displaced from DNA ends by resection proteins.

End-joining factors *per se* do not inhibit short-range DNA end resection

Nej1 interacts with Sae2 and Dna2, and previous genetic work suggested that Nej1 inhibits DNA end resection[30,31,48]. End-joining-deficient cells can only repair DSBs by HR, so in a genetic system it is not straightforward to distinguish direct from indirect effects, as DSBs that would be normally joined by NHEJ must undergo resection. Using our recombinant proteins, we tested for inhibitory effects of end-joining components on short-range resection. Under conditions that are not permissive for end-joining, we observed that DSB-bound Ku affected the position of DNA incision by the MRX-pSae2 complex and moderately increased the efficacy of DNA incision (Fig. 1i, see also Supplementary Fig. 2f), in accord with previous data[13,14,18]. Other NHEJ complexes did not further affect the reaction, either in terms of efficacy or position of DNA incision sites (Fig. 1i). We next tested for a direct inhibitory effect of Nej1 on DNA end resection. High concentrations of Nej1 (0.5-1 μM) alone barely reduced the endonuclease activity of MRX-pSae2 (Supplementary Fig. 3a), much less efficiently than Rif2, a telomere protection factor and a known MRX inhibitor[26,49-54] (Supplementary Fig. 3a). In contrast, Nej1 promoted end-joining at very low concentrations (12 nM) (Fig. 1c,d). Considering that Nej1 binds dsDNA[55], it may non-specifically compete with MRX for DNA access, which could explain the modest inhibitory effect. Reciprocally, the addition of pSae2 also did not affect the efficiency of the end-joining reaction (Fig. 2a; Supplementary Fig. 3b). Overall, our results suggest that Nej1 may not be an efficient inhibitor of short-range resection by MRX-pSae2, but rather that its impact could be restricted to the suppression of Sae2-stimulated and Dna2-dependent long-range resection[30,31].

Synapsis of DNA ends is sufficient to inhibit resection

End-joining is expected to inhibit resection by ligating DNA ends before the resection machinery can process them. A potential role of DNA synapsis in masking DNA ends has not been investigated. To test whether DNA synapsis could inhibit DNA end resection, we prepared two sets of DNA substrates. The first substrate was 5'-phosphorylated and therefore ligatable (denoted 5'-P, Fig. 2b). The second substrate was not phosphorylated and thus non-ligatable (denoted 5'-OH, Fig. 2b). Non-phosphorylated ends, however, can still undergo synapsis[56]. As expected, the end-joining machinery could not ligate DNA molecules lacking 5' phosphorylation (Fig. 2c). Recruitment of the protein ensemble to DNA was not affected by the end modifications (Supplementary Fig. 3c), likely allowing non-ligatable DNA ends to synapse. Interestingly, whereas DNA ligation almost completely inhibited downstream resection, synapsis alone without ligation was sufficient to significantly reduce the nuclease activity of MRX-pSae2 (compare lanes 11 and 14 of

Fig. 2d,e). This effect was evident across a wide range of MRX protein concentrations (Fig. 2f; Supplementary Fig. 3d). Since we showed above that end-joining proteins by themselves do not affect resection, these experiments suggest that DNA synapsis likely masks DSBs and prevents their processing by MRX-pSae2.

Considering that MRX is known to bridge DNA ends[42,43], we next investigated whether the end bridging activity of MRX and/or the core NHEJ factors is responsible for the inhibition of DNA end resection. We observed that both MRX and the core NHEJ factors *per se* moderately inhibited resection (Fig. 2g; Supplementary Fig. 3e). The greatest effect was observed when both MRX and Ku/Dnl4-Lif1/Nej1 were combined, suggesting a synergistic interaction. In contrast, preincubation with MR had no effect on resection (Supplementary Fig. 3e), consistent with the need for Xrs2 to stimulate DNA end bridging by Mre11-Rad50[42,44].

Our data suggest that DNA synapsis inhibits DNA end resection. In order to directly validate that DNA synapsis forms with our purified proteins, we first used magnetic tweezers. The experiments monitor the lifetimes of synaptic events. We observed that the NHEJ core proteins (Ku, Nej1 and Dnl4-Lif1) generate synapsis (Fig. 2h,i; Supplementary Fig. 4a), in accord with previous data[57]. Under the assay conditions, these events were independent of DNA ligation, as there was no significant decrease in synaptic lifetime distribution when the catalytically inactive DNA ligase 4 (Dnl4) D284A mutant was used (Fig. 2h,i). Furthermore, the addition of MRX to the wild-type system stabilized DNA synapsis, as we observed a weak but not statistically significant increase in the duration of the synaptic events (Fig. 2i). Similar results were observed using single-molecule nanofluidics, which monitors the length of free DNA in solution (Supplementary Fig. 4b). Following the addition of recombinant proteins, we observed a cluster of DNA molecules of approximately twice the length of a single DNA molecule, suggesting dimer formation (Supplementary Fig. 4b [iii]). The same synaptic cluster was also identified at a similar level in experiments with the catalytically inactive Dnl4 D284A mutant (Supplementary Fig. 4b [iv]).

We next used an orthogonal method to validate the inhibitory effect of DNA synapsis on DNA end resection. Catalytic mutants in the active site of Dnl4 (K282R, D284A and K466A) were shown to eliminate or drastically reduce DNA ligation by preventing the auto-adenylation of Dnl4, while having minimal effect on DNA synapsis[34,58,59], in accord with the single-molecule data presented above (Fig. 2h,i; Supplementary Fig. 4a,b). We observed that NHEJ assemblies with the Dnl4-Lif1 variants that were either inefficient or inactive in end-joining (Fig. 3a,b) strongly inhibited DNA end resection by MRX-pSae2 (Fig. 3c), likely due to the DNA ends being synapsed.

Together, our data show that resection is only possible before synapsis is established. In a cellular context, the inhibition of resection by synapsis likely provides time for NHEJ to complete (Fig. 3d). Based on *in vitro* and cellular imaging experiments, DNA synapsis was observed to be quite dynamic and relatively short-lived, likely on the order of seconds or minutes[34,59-61] (see also Fig. 2i), suggesting that synapsis of incompatible ends is likely transient in cells. Disassembly of synapsed ends would again allow DNA end resection and thus channel the repair of non-ligatable ends toward resection-dependent HR or potentially MMEJ.

RPA promotes Ku removal from DNA ends

We next set out to determine whether the MRX-pSae2 complex removes Ku from DNA ends. The endonucleolytic incision of the 5'-terminated DNA strand on the internal side of a protein block by MRX-pSae2 is well documented[12-14,18]. It has also been shown that these incision sites serve as entry points for long-range resection, based on both *in vitro* and cellular experiments[13,14,18]. However, it remains unclear whether the MRX-pSae2 complex alone is sufficient to remove Ku, or whether it simply generates an internal gap near the broken end. In the latter case, additional components might be needed for Ku removal. Only complete displacement of the obstacle from the 5' end produces a free 3' overhang, which is essential for strand invasion and subsequent priming of DNA synthesis during HR.

To investigate the mechanism of Ku removal from DSBs, we used a blunt-ended 2.8 kbp dsDNA substrate labeled at the 5' end. Using electrophoretic mobility shift assays (Supplementary Fig. 5a), we first determined a Ku concentration that blocked all DNA ends without allowing additional Ku heterodimers to slide inward. MRX-pSae2 was able to resect Ku-blocked DNA, as indicated by general DNA degradation observed on native polyacrylamide gels (Fig. 4a, lanes 2 and 3). However, only a small fraction of the radioactive signal appeared at the bottom of the gel (Fig. 4a, lanes 2 and 3), suggesting that most of the terminal 5' segment carrying the label remained attached to the resected DNA. Heat denaturation of the same reaction products revealed a different pattern: the most prominent product migrated at the bottom of the gel (Fig. 4a, lanes 4 and 5), showing that the 5'-terminated strand was incised very efficiently. Running the same reaction products on a denaturing polyacrylamide gel revealed that the length of the prominent fragment was ~ 30 nt in length (see also Fig. 4b, lane 4), consistent with the combined footprint of Ku and MRX on dsDNA[2,14,62]. Because the 5'-terminal ~ 30 nt fragment was detectable only after heat denaturation (Fig. 4a, compare lanes 2–3 with 4–5), these data indicate that MRX-pSae2 efficiently (~ 80%) incised the 5'-terminated strand internally to Ku (Fig. 4c), but the terminal

fragment was not dissociated. Thus, MRX-pSae2 alone does not efficiently create a free 3' end, at least *in vitro*.

We next tested the effect of RPA, which regulates long-range DNA end resection pathways[21-23,63,64]. RPA coats the 3' overhang created by resection and prevents 3' strand loss and formation of secondary structures[65,66]. RPA interacts with MRX[67], and was proposed to recruit MRX to forks and DSBs[68]. Whether this interaction plays any functional role beyond recruitment has not been determined. Although RPA did not stimulate the MRX-pSae2 endonucleolytic activity (Fig. 4c; Supplementary Fig. 5b), in accord with previous data[12], RPA profoundly altered downstream processing of Ku-blocked DSBs (Fig. 4d,e). Already without heat denaturation, the predominant degradation product in the presence of RPA was a fragment <15 nt (Fig. 4a, lanes 7 and 8; Fig. 4b, lanes 7 and 8), showing that a significant fraction of the 5'-terminal segment was dissociated, generating a free 3' end. Such end architecture was also indicative of Ku removal. Upon heat denaturation (Fig. 4a, lanes 9 and 10), this short fragment remained the major product (~ 60%), although a smaller fraction of the larger fragment, consistent with Ku retention, was still observed, albeit as a minority fraction (Fig. 4a, lanes 9 and 10). Together, our data indicate that RPA strongly promotes Ku removal (Fig. 4d), leading to free 3' ends (Fig. 4e), created by MRX-pSae2. The observed effect was independent of Xrs2, as RPA stimulated Ku removal by the Mre11-Rad50 (MR) complex as well (Supplementary Fig. 5c). We also point out that RPA stabilized 3' ends from non-specific degradation by MRX (Supplementary Fig. 5d), in agreement with previous genetic work[65,66].

We next set out to independently validate the conclusion that RPA promotes resection of the 5'-terminal DNA segment at DSBs when Ku is present. To this end, we monitored the presence of resected DNA at specific locations by annealing radioactive ssDNA probes to the single-stranded DNA segments. DNA close to the end, which is bound by Ku (1-21 bp away from the end), remained largely double-stranded and led only to a small amount of probe being annealed. The addition of RPA stimulated resection 3-fold, corresponding to Ku being removed from the DNA end. In contrast, resection further away from the DNA end (39-60 bp away) was more efficient, and the effect of RPA was diminished (Fig. 4f), in accord with the data above (Fig. 4a-e) and our model, suggesting that RPA facilitates Ku removal from DNA ends (Fig. 4g). Finally, to directly monitor Ku displacement from DNA ends, we carried out the resection assay with Ku-blocked but unlabeled DNA and MRX-pSae2, with or without RPA. We next added a labeled dsDNA oligonucleotide as a trap for displaced Ku, and the Ku-DNA trap complex formation was monitored by electrophoretic mobility shift assays (Fig. 4h). RPA clearly promoted Ku removal from DSBs by MRX-pSae2 in a concentration-dependent manner (Fig. 4h; Supplementary Fig. 5e).

By contrast, RPA had no effect on processing of free DNA ends by MRX-pSae2 (i.e., without Ku, Supplementary Fig. 5f). With or without heat denaturation, the products were consistently <15 nt in length (Supplementary Fig. 5f, compare lanes 2–5 and 7–10). These data indicate that MRX-pSae2 alone is sufficient to generate free 3' overhangs from DSBs not bound by Ku, and RPA is not necessary (Supplementary Fig. 5g). Together, our findings demonstrate that RPA is a critical co-factor of MRX-pSae2 during the processing of Ku-blocked DSBs. RPA acts downstream of the MRX-pSae2 endonucleolytic incision and facilitates Ku removal from DNA ends, generating the free 3' overhangs required for subsequent HR steps (Fig. 4g).

RPA promotes Ku removal from DSBs in a species-specific manner

To better understand the displacement of Ku from DSBs by MRX-pSae2 and its stimulation by RPA, we next replaced yeast RPA with human RPA or human mitochondrial SSB (hmtSSB) (Supplementary Fig. 6a). All ssDNA-binding proteins had a similar affinity for ssDNA (Supplementary Fig. 1g-i; Supplementary Fig. 6b). As above, yeast RPA stimulated Ku removal by the cognate yeast MRX-pSae2 (Fig. 5a). In contrast, human RPA could stimulate the removal of yeast Ku by MRX-pSae2 only to a limited extent, and mtSSB was completely inefficient (Fig. 5a). Ku displacement and removal of the 5'-terminal DNA fragment was not dependent on the DNA melting activity of RPA, because human RPA has a much higher DNA melting capacity than the yeast counterpart (Supplementary Fig. 6c)[69], but it supported Ku displacement to a much lesser extent (Fig. 5a). Additionally, we observed that Ku and yeast RPA can bind simultaneously to overhanged DNA with a 31 bp-long dsDNA part, showing that RPA alone cannot displace Ku, without the engagement of the MRX-pSae2 complex (Supplementary Fig. 6d). Rather, the stimulatory effect of yeast RPA on the resection activity of MRX-pSae2 and Ku displacement suggested that it might be dependent on specific protein-protein interactions and on the stimulation of MRX activity. Indeed, MRX was previously described to interact with RPA[68]. In pulldown assays, we confirmed that yeast RPA directly binds MRX[68], and unexpectedly observed a robust interaction also with pSae2 (Fig. 5b).

Yeast RPA and pSae2 synergistically promote the exonuclease activity of MRX

We hypothesized that RPA assists Ku removal by stimulating the intrinsic 3'-5' exonuclease activity of the MRX complex. To test this, we used a gapped DNA plasmid devoid of DSBs to focus exclusively on the MRX exonuclease activity. 3'-5' DNA degradation was monitored by annealing of the reaction products with a radioactive ssDNA probe complementary to a region 127-147 bp away from the end of the DNA gap (Fig. 6a). While human RPA and mtSSB were either inactive or

inhibitory to DNA resection at higher concentrations, yeast RPA promoted the exonuclease activity of MRX-pSae2 nearly 4-fold (Fig. 6a). Yeast RPA instead inhibited ExoIII, a bacterial exonuclease with the same polarity as MRX (Supplementary Fig. 7a), further highlighting the species-specific nature of the functional interaction between MRX-pSae2 and RPA.

Next, we set out to identify which components of the MRX-pSae2 complex are necessary for the interplay with RPA (Fig. 6b,c). Previously, we showed that pSae2 can promote the exonuclease activity of MRX (or MR)[70]. We further observed that RPA and pSae2 enhance the activity of MRX synergistically, corresponding to ~ 80-fold stimulation compared to MRX alone (Fig. 6b), in line with their physical interaction (Fig. 5b). The stimulatory effect of RPA and pSae2 on MRX requires ATP and is independent of Xrs2 (Fig. 6b). In contrast, Mre11 alone (Supplementary Fig. 1j; Supplementary Fig. 7b) was not affected by pSae2 and was inhibited by RPA (Fig. 6c), showing the necessary involvement of the Rad50 subunit in the identified functional interaction.

We next gapped the plasmid DNA on the opposite strand and monitored the effect of RPA on the MRX-pSae2 exonuclease activity using two probes: one located close to the end of the gap (16-36 bp), and the other one at the equivalent distance as above, 127-147 bp away from the gap (Supplementary Fig. 7c). Very similar stimulatory effect of RPA was observed when we probed resection at the more distant site from the gap, similar to the experiment in Fig. 6a. Unexpectedly, when we used a probe complementary to a region much closer to the gap (16-36 bp), no stimulation by RPA was observed, and RPA was even moderately inhibitory (Supplementary Fig. 7c). These results suggested that RPA does not promote the recruitment of MRX-pSae2 to the DNA substrate and hence the initiation of the nuclease reaction. The moderate inhibition suggests that RPA and MRX-pSae2 may even compete for initial access to the gapped DNA. Rather, RPA promotes the extent of DNA degraded by MRX-pSae2, potentially through stimulating the processivity of the nuclease complex. Our experiments together demonstrate that RPA and pSae2 synergistically promote the 3'-5' exonuclease activity of the MRX complex. At DSBs, the enhanced exonuclease activity of MRX likely explains the facilitated removal of Ku.

The DNA binding activity of RPA is necessary to promote Ku removal by MRX-pSae2

To further define how RPA promotes Ku removal from DSBs by MRX-pSae2, we tested RPA variants carrying point mutations that reduce its affinity for DNA (Supplementary Fig. 8a). None of these mutants were able to stimulate the MRX-pSae2 exonuclease activity at limiting concentrations (Fig. 7a), indicating that the DNA-binding activity of RPA is needed for the stimulation. We next supplemented the plasmid-based exonuclease assays with either free RPA or RPA pre-bound to

short ssDNA. The stimulatory effect was markedly reduced when RPA was pre-sequestered (Fig. 7b), suggesting that RPA must engage ssDNA *in cis* to stimulate MRX-pSae2 (Fig. 7c). We next monitored the removal of Ku from DNA ends together with the RPA mutants. In agreement with the exonuclease assays above, DNA-binding-impaired RPA variants were less effective in facilitating Ku removal by MRX-pSae2 (Supplementary Fig. 8b). We note that the DNA-binding variants were prepared using a construct N-terminally tagged with 6xHis, employing a modified procedure including Ni-NTA affinity purification, and avoiding HiTrap Blue column that is used in the standard purification procedure. This modification was necessary because some RPA variants did not bind efficiently to HiTrap Blue. We observed that wild-type RPA prepared using the modified procedure was less efficient but still capable of removing Ku (Supplementary Fig. 8b, compared to Fig. 4a). This difference is not due to the Rfa1 N-terminal tag, as a T7 tag at the same position did not impair RPA's function, when the HiTrap Blue purification step was included. Nevertheless, even the His-tagged, affinity purified RPA clearly promoted Ku removal and the exonuclease activity of MRX-pSae2 (Supplementary Fig. 8b; Fig. 7a). We note that all RPA variants were consequently compared to the corresponding wild-type RPA, purified in the same way as the mutants. We conclude that RPA needs to bind ssDNA to stimulate Ku removal by MRX-pSae2 (Fig. 7c). During resection, MRX nicks at multiple positions along the 5'-terminated strand[70], leading to stretches of ssDNA, which permit RPA loading and license Ku displacement by MRX-pSae2.

The N-terminus of Rfa1 and the Rfa3 subunit are necessary to stimulate MRX-pSae2

RPA is a heterotrimer consisting of three subunits, which contain one or more OB-fold domains responsible for ssDNA-binding or protein-protein interactions. The largest subunit, Rfa1, contains four OB-fold domains, including OB-F, which serves as a protein interacting region, and OB-A, OB-B and OB-C, which mediate most of the ssDNA-binding activity of the RPA complex. Rfa2 and Rfa3 each contain one OB-fold domain, OB-D and OB-E, respectively, which modestly promote the ssDNA-binding capacity of RPA. Rfa2 also contains phosphorylation motifs at the N-terminus and a Winged-Helix domain (WHD) at the C-terminus, which serves as another protein interaction interface. Structural studies have shown that the RPA trimerization core consists of an alpha-helix situated at the very C-terminus of Rfa1, which interacts with OB-D of Rfa2 and OB-E of Rfa3 (schematic in Fig. 7d)[71]. We next tested which RPA subunits are necessary for MRX-pSae2 stimulation (Supplementary Fig. 8c). Interestingly, only the wild-type RPA trimer (Rfa1-Rfa2-Rfa3) could promote the exonuclease activity of MRX-pSae2 (Fig. 7d) or Ku removal from DSB ends (Supplementary Fig. 8d). We noted that the Rfa1 subunit alone had an inhibitory effect on the resection activity of MRX-pSae2 (Supplementary Fig. 8d). We hypothesized that this is due to the C-terminal

alpha-helix of Rfa1, which is highly hydrophobic, and is normally buried in the heterotrimer. We expressed and purified Rfa1ΔC-term (Rfa1 subunit alone, Δ601-621, Supplementary Fig. 8c) and observed that, while it no longer inhibited MRX-pSae2, it also could not assist in Ku removal (Supplementary Fig. 8e). These experiments suggested that the additional RPA subunits, Rfa2 or Rfa3, are necessary for the full stimulatory effect of RPA on MRX-pSae2.

Previously, the N-terminal OB-F domain of Rfa1 was described to bind MRX and promote its recruitment to DSBs and stalled replication forks[67,68]. We next set out to test whether removing OB-F impacts RPA's capacity to promote MRX-pSae2. To this end, we purified the truncated (RPAΔF) variant (Supplementary Fig. 9a). As expected, RPAΔF exhibited the same affinity for ssDNA as full-length RPA (Supplementary Fig. 9b). RPAΔF was strongly impaired in physical interaction with MRX (Fig. 7e). Unexpectedly, the OB-F domain truncation only modestly impaired RPA's capacity to promote the MRX-pSae2 exonuclease, which was nevertheless statistically significant (Fig. 7f), but Ku removal was largely unaffected (Supplementary Fig. 9c). Interestingly, the same OB-F domain of Rfa1 also mediated the interaction with pSae2 (Fig. 7g). The data showing that RPAΔF, albeit to a lesser degree, still stimulates MRX-pSae2 (Fig. 7f; Supplementary Fig. 9c), prompted us to test for a potential involvement of the WHD domain in Rfa2. RPAΔWHD activity was very comparable to WT RPA (Supplementary Fig. 9d,e), showing that the WHD domain of Rfa2 is dispensable. We next used RPA constructs lacking the OB-F of Rfa1 and the WHD of Rfa2, with or without Rfa3 (Supplementary Fig. 1k; Supplementary Fig. 9f). First, we confirmed that both constructs possess similar ssDNA-binding affinity as wild-type RPA (Supplementary Fig 9g). Interestingly, while RPAΔFΔWHD could stimulate the exonuclease activity of MRX-pSae2, the deletion of Rfa3 completely abolished this effect (Fig. 7h), suggesting that functional contacts between the Rfa3 subunit and the resection factors may be responsible for the stimulation of the MRX-pSae2 exonuclease activity. Correspondingly, loss of the Rfa3 subunit also negatively affected the ability of RPA to promote Ku removal from DNA ends by MRX-pSae2 (Fig. 7i; Supplementary Fig. 9h).

These results suggest that while the OB-F domain of RPA is needed for the bulk of physical interaction with MRX, its functional contribution to MRX-pSae2 stimulation is small, likely due to additional but more transient contact points between MRX and RPA, or pSae2 with RPA, or even RPA and Ku[72]. We propose that this additional interaction interface between RPA and the resection complex is located on the Rfa3 subunit and is essential for the stimulatory effects of RPA on short-range resection. We conclude that only the RPA trimer can effectively stimulate the exonuclease activity of MRX-pSae2 and Ku removal from DSBs.

RPA-dependent stimulation of Ku removal from DSB ends by MRX-pSae2 suppresses NHEJ

A failure to remove Spo11 from the ends of meiotic DSBs blocks HR repair and results in sterility[73,74]. The consequences of Ku remaining bound to DNA ends after incomplete resection are not understood. Our data presented above showed that RPA promotes Ku removal and helps generate free 3' ends, which are thought to inhibit NHEJ. Our hypothesis was that DSBs resected without RPA, which, as we hypothesize, retain Ku bound to a dsDNA stretch at the DNA end, can still undergo end-joining (Fig. 8a [i]). To test this model, we prebound DNA molecules with Ku and performed resection assays with MRX-pSae2 with or without RPA and subsequently performed end-joining assays on the DNA intermediates (Fig. 8a [ii]). The DNA substrate was phosphorylated at both ends, and therefore DNA circularization, tandem ligation and formation of higher-order ligation products is possible. Interestingly, RPA present during the preceding resection step significantly inhibited NHEJ (Fig. 8a [ii], compare lanes 4 and 9, and Fig. 8a [iii]). Moreover, we also observed a significant decrease in the formation of higher-order ligation products when resection was performed in the presence of RPA (Fig. 8a [iii]). RPA alone had no effect on end-joining efficiency (compare lanes 5 and 10 in Fig. 8a [ii]). These results suggest that, while resection is inhibitory to NHEJ, end-joining can still occur if Ku is not removed from the DNA ends. The addition of RPA during resection assists MRX-pSae2 in removing Ku and further inhibits NHEJ.

In a complementary experiment, we prebound a randomly labeled 1.5 kb-long DNA containing only one ligatable end with Ku and performed resection in the presence of yeast RPA or human mtSSB (to prevent aberrant degradation of the 3'-terminated strand by MRX). The reaction was also supplemented with excess yeast Rad50 (yRad50) to prevent degradation of ssDNA by the exonuclease activity of free Mre11 not complexed within MRX[70]. Subsequently, we elevated the salt concentration (up to 80 mM sodium chloride) to inhibit resection and monitored NHEJ that is not affected by the added salt (Fig. 8b). As above, the presence of RPA during resection reduced the extent of subsequent end-joining (Fig. 8b). Importantly, when analyzing the extent of resection, using a 5'-labeled version of the substrate, we observed that only around 50% of the DNA was incised by the resection complex during the same incubation time and conditions (Supplementary Fig. 10a). This implies that the effect of RPA on the suppression of NHEJ might be even greater than observed in Fig. 8a,b, as the unresected substrate will undergo end-joining. The data also imply that the NHEJ machinery can act on the partially resected gapped substrate. To directly confirm this point, we designed substrates containing either a 68 nt-long 3' overhang, mimicking the end-product of resection, or a 70 nt-long gap on the 5'-terminated strand, at a distance of 31 bp away from the end, mimicking the partially resected DNA when Ku is not removed (compare with data presented in Fig. 4). While the presence of the gap was slightly inhibitory for end-joining,

NHEJ of partially resected DNA was still possible, whereas fully resected overhanged DNA could not undergo NHEJ (Supplementary Fig. 10b). In summary, the RPA-dependent promotion of Ku removal from DNA ends during short-range resection could represent one of the mechanisms explaining the known suppression of NHEJ by RPA[65,66,75].

Discussion

The choice between the two major pathways of DSB repair, namely non-homologous end-joining (NHEJ) and homologous recombination (HR), has profound consequences for genetic outcomes, influencing the fidelity of repair and disease risk[9]. Elucidating how cells balance NHEJ and HR pathways is therefore fundamental to understanding genomic stability. Using recombinant proteins, we show that the resection activity of the *S. cerevisiae* MRX-pSae2 complex leading to HR is not intrinsically inhibited by NHEJ components. Instead, we find that DNA synapsis, i.e. an NHEJ intermediate in which the two broken DNA ends are bridged prior to ligation, strongly suppresses DNA end resection. This conclusion is supported by two sets of experiments. First, we compared the processing of DNA breaks either lacking or containing a 5' phosphate group, which is required for ligation. The presence of the phosphate group alone had no effect on MRX-pSae2-mediated resection. However, resection of these non-ligatable breaks was strongly inhibited when end-joining proteins assembled and likely established DNA synapsis. Second, we found that mutations in the catalytic site of DNA ligase IV (Dnl4) that block ligation but permit synapsis, as shown previously[34,58,59], suppress MRX-pSae2-mediated resection. The mechanism of how NHEJ limits resection is therefore largely structural, and not dependent on specific interactions with the NHEJ proteins. These findings are consistent with our previous observations that MRX-pSae2 fails to process Cas9-dependent DSBs, as long as they remain bridged[76]. A similar mechanism may restrict MRX-dependent activation of Tel1 on DSBs undergoing NHEJ, as Tel1 is inhibitory for NHEJ[77,78].

Our results support a sequential concept of DNA repair pathway choice[39]. In this model, NHEJ proteins rapidly assemble at DSBs and attempt ligation[34]. DNA end-resection factors are recruited with slower kinetics, and if ligation fails, the endonuclease activity of MRX-pSae2 then redirects repair toward resection-dependent HR. When synapsis occurs, DNA end resection is suppressed, giving NHEJ an opportunity to proceed. Previous work suggested that synapsis is short-lived: if ligation is possible, synapsis is quickly followed by ligation; if not, the synaptic complex is transient and undergoes repeated on–off cycles[6,59,60]. We suggest that resection is activated during the synapsis "off" cycles on non-ligatable DSBs. This model agrees with initial

observations showing that the recruitment of NHEJ proteins to DSBs is fast but transient, whereas HR factors are recruited later but then typically persist at the damage sites[79]. The model that DNA synapsis inhibits MRX-pSae2 is reminiscent of our previous observation that bridged DNA ends generated by the Cas9 nuclease are also refractory to resection, until Cas9 is displaced[76]. Therefore, while MRX-pSae2 can resect DSBs with any protein blocks, the short-range resection enzymes are inhibited by synapsed ends, or when the protein blocks cover longer lengths of DNA, such as at telomeres[80].

It has been proposed that Nej1 inhibits DNA end resection[31]. Nej1 binds Sae2 and was proposed to limit Sae2-stimulated long-range resection by Sgs1–Dna2[30,31]. However, whether Nej1 directly affects MRX-pSae2-dependent short-range has not been reported[31]. In our assays, recombinant Nej1 promoted NHEJ at very low protein levels but did not notably inhibit MRX-pSae2, even when used at much higher concentrations. Nej1 thus differs from the telomeric protein Rif2, a known MRX inhibitor[26,49,50,52,53]. Because Nej1 promotes DNA synapsis[4,48,55], the hyper-resection observed in *nej1* mutants may reflect an indirect effect caused by reduced synapsis and suppressed NHEJ, or its impact on long-range resection[30,31].

We observed that MRX-pSae2 can incise DNA next to a variety of NHEJ protein assemblies and intermediates, as long as the ends are not bridged. However, it has remained unclear whether the initial incision, followed by the 3'-5' exonuclease activity of MRX progressing back toward the DNA end, is sufficient to displace the protein block. We thus examined whether the short-range resection factor MRX-pSae2 can remove Ku from DNA ends, as Ku likely represents the most physiologically relevant protein block for MRX-pSae2 in vegetative cells. Our data reveal an unexpected requirement for RPA in this process, mediated through specific interactions with not only MRX[67,68], but also pSae2, or potentially even between RPA and Ku[72,81]. RPA does not influence the initial endonucleolytic incision by MRX-pSae2[12], likely because the incised DNA is double-stranded and lacks a binding site for RPA. Instead, RPA stimulates, *in cis*, the downstream step that depends on MRX's 3'-5' exonuclease activity by binding to the gap created by the stepwise resection of the DNA end by MRX-pSae2[70]. We previously showed that pSae2 promotes MRX exonuclease activity[70,82], and the data presented here demonstrate that RPA and pSae2 act synergistically to stimulate MRX. This enhanced 3'-5' exonuclease activity of MRX is sufficient to remove Ku from DNA ends and possibly contributes to the RPA-dependent suppression of NHEJ known from genetic experiments[65,66,75]. Indeed, Ku-blocked DNA resected without RPA still largely supports NHEJ.

In summary, our *in vitro* reconstitution of NHEJ and DNA end resection suggests that DSB repair pathway choice is governed not by direct inhibition of resection factors by NHEJ factors, but rather by the structural state of the DNA break. Formation of synapsed DSBs strongly limits the activity of MRX-pSae2 at DNA ends, giving time for NHEJ to complete the repair. Instead, we suggest that failed ligation events are followed by disassembly of the synaptic complex, which allows MRX-pSae2 to resect the break and redirect repair toward HR. Moreover, we describe a key role for RPA in promoting Ku removal by stimulating MRX exonuclease activity in concert with pSae2. The interaction is largely mediated by the OB-F domain of Rfa1, with more transient but functionally crucial interactions with the Rfa3 subunit. Together, our findings define the interplay of NHEJ and resection factors and provide insights into mechanisms governing the balance between NHEJ and HR pathway choice.

Methods

Cloning, expression and purification of recombinant proteins

Replication Protein A

The untagged *S. cerevisiae* RPA construct (p11d-sctRPA) was a kind gift from M. Wold, University of Iowa[83]. Untagged and T7-tagged RPA wild-type, ΔF, ΔWHD, F537E as well as the truncated Rfa1ΔC20 subunit of the trimer were purified using ÄKTA Pure (GE Healthcare) with HiTrap Blue HP, HiTrap Desalting and HiTrap Q HP chromatography columns (all Cytiva)[84]. Untagged RPA was used for the experiments in Fig. 4a-e, Supplementary Fig. 5 (except for the experiment in Supplementary Fig. 5e), Fig. 5a, Supplementary Fig. 6 (except for the experiment in Supplementary Fig. 6d), Fig. 6a-c, Fig. 8b and Supplementary Fig. 10a.

To prepare the construct for T7-tagged RPA, a sequence for the T7-tag was introduced at the N-terminus of Rfa1. This was achieved by PCR amplification of the p11d-sctRPA plasmid (primers: TGTACCATGGCTAGCATGACTGGTGGACAGCAAATGGGTCGGATCCAATGGGCAG-TGTTCAACTTTC and CAACTCTTGGTGTTTCGCTGGCCATGGATCATCTC)[83]. The PCR product was digested with NcoI (New England Biolabs) and cloned into the corresponding site in p11d-sctRPA plasmid, producing the p11d_T7_BamHI_yRPA WT plasmid. The RPA trimer lacking the N-terminus of Rfa1 (Δ1-180) was produced by PCR amplification (primers: TGTACCATGGCTAG-CATGACTGGTGGACAGCAAATGGGTACCAGACCAATTTTTGCCATC and AACTCTT-GGTGTTTCGCTGGCCATGGATCATCTC) and cloned into the corresponding site in p11d-sctRPA plasmid, to generate p11d_T7_yRPA deltaF. To produce the RPAΔWHD, the P184 amino acid of Rfa2 was mutagenized into a stop codon in the p11d_T7_BamHI_yRPA WT backbone with mutagenic primers (GCCAGTGGAATGATGAAACAATAATTGGAGAGTGCATCCAACAAC and GTTGTT-GGATGCACTCTCCAATTATTGTTTCATCATTCCACTGGC) and using the QuikChange II-XL site-directed mutagenesis kit (Agilent Technologies) according to manufacturer's recommendations, to generate expression vector p11d_T7_BamHI_yRPA_Rfa2dC90. The p11d_T7_yRPA deltaFdC90 construct was generated using the same procedure as above, but with the p11d_T7_yRPA deltaF vector as the starting template. The p11d_T7_yRPA deltaFdC90deltaRfa3 was generated by PCR amplification of the p11d_T7_yRPA deltaFdC90 plasmid (primers: CAGTCAC-TCGAGCGCTTTTATTCTTACCTTTATGTACTGTTGCCTCTATATG and GACTCACTCGAG-GATCCCCCGGGCTGCAGG). The PCR product was digested with XhoI (New England Biolabs)

and re-circularized using T4 DNA ligase (Thermo Fisher Scientific). The RPA F537E point mutant was cloned using the p11d_T7_BamHI_yRPA WT backbone, mutagenic primers (CCAATCAAC-TATGGCTCACTTTAGAAGACGACCAAGCTAAACAATTATTAG and CTAATAATTGTTTAGCTT-GGTCGTCTTCTAAAGTGAGCCATAGTTGATTGG) and the QuikChange II-XL site-directed mutagenesis kit to generate p11d_T7_BamHI_yRPA Rfa1F537E. The Rfa1 C-terminal truncation lacking the last 20 amino acids (Δ601-621) was cloned using the pET21b-T7-Rfa1-his backbone and the mutagenic primers (CCGTTGCTAACCTACACAGCTAAAATTACAGGGCTGAA-GCC and GGCTTCAGCCCTGTAATTTTAGCTGTGTAGGTTAGCAACGG) to generate pET21b-T7-Rfa1dC20-his.

All yeast recombinant trimeric untagged or T7-tagged wild-type RPA, truncations (ΔF, ΔWHD, ΔFΔWHD and ΔFΔWHDΔRfa3) and the RPA F537E mutant, as well as the Rfa1ΔC20 mutant were expressed in BL21-DE3 pLysS *E. coli* cells. Transformed cells were grown at 30 °C for 16 h without shaking. This pre-culture was inoculated into 4 l of LB medium, and the cells were grown at 37 °C (200 rpm) until OD600 reached ~0.6. Protein expression was induced with 0.4 mM isopropyl β-D-1-thiogalactopyranoside (IPTG) for 16 h at 18 °C. The bacterial pellet was obtained by centrifugation at 3,500 g for 15 min at 4 °C, the cells were washed once with SD Buffer (10 mM Tris-HCl pH 8.0, 150 mM sodium chloride [NaCl], 1 mM ethylenediaminetetraacetic acid [EDTA]), snap-frozen and stored at -80 °C.

Point mutants of RPA that disrupt its ssDNA-binding activity (Rfa1 K494E, Rfa1 C505A, C508A), recombinant Rfa1, Rfa2, and Rfa3 as well as Rfa1-ABC, and -C were purified using Ni-NTA affinity resin (Qiagen) and a HiTrap Q HP chromatography column. Recombinant Rfa1-F, Rfa1-AB and Rfa1-FAB constructs were purified using Ni-NTA and HiTrap Heparin column (Cytiva)[24].

Human RPA (hRPA) was expressed in *Sf*9 insect cells using pFB-RPA1, pFB-RPA2 and pFB-6xhis-RPA3 and purified using Ni-NTA resin, followed by HiTrap Blue HP, HiTrap Desalting and HiTrap Q HP chromatography columns[85].

Mitochondrial SSB

Human mitochondrial SSB (mtSSB) was expressed using the pMALT-P-mtSSB plasmid in BL21-DE3 pLysS *E. coli* cells using amylose affinity resin (New England Biolabs) and a HiTrap Blue column[86].

Yeast MRX

pRS305_His-yMre11coy-Gal1-10-yRad50coy_NOTAG was cloned from pRS305_Mcm6-Gal1-Mcm7 (a kind gift of John Diffley, The Francis Crick Institute, UK). pRS303_yXrs2coy-3XFLAG-Gal1-10-Gal4 was obtained by cloning yXrs2coy-3XFLAG into pRS303_Cdt1-Gal1-10-Gal4 (a kind gift of John Diffley, The Francis Crick Institute, UK). All the codon-optimized sequences were purchased from GenScript or Twist Bioscience.

The yMRnXf-tda1delta strain was obtained by sequential transformation of the yJF1 yeast strain (a kind gift of John Diffley, The Francis Crick Institute, UK) with the NheI-linearized pRS303_yXrs2coy-3XFLAG-Gal1-10-Gal4 plasmid, expressing FLAG-tagged codon optimized Xrs2, and the AflIII-linearized pRS305_His-yMre11coy-Gal1-10-yRad50coy_NOTAG, expressing His-tagged codon optimized Mre11 and untagged codon optimized Rad50. The Tda1 kinase was knocked out by HR-mediated insertion of a URA-3 cassette amplified from the pUG72 plasmid, using primers containing sequences upstream and downstream of the Tda1 gene according to the standard protocol.

Recombinant *S. cerevisiae* Mre11-Rad50-Xrs2 was purified from yMRnXf-tda1delta yeast cells. To produce the complex, yMRnXf-tda1delta cells were cultured in 50 ml of YPAR media (10 g/l yeast extract [Gibco] 20 g/l Bacto peptone [Gibco], 40 mg/ml adenine [Sigma], 2% raffinose [Apollo Scientific]) overnight. The next day, cells were inoculated in 4 l of YPAR media and cultured overnight at 30 °C (200 rpm). Once the cell density reached $2x10^7$ cells/ml, expression was induced with 20 g/l of galactose (Thermo Fisher Scientific) for 3 h. Cells were harvested by centrifugation at 3,000 g for 15 min, washed with a buffer containing 30 mM Tris-HCl pH 7.5 and 1 M sorbitol, and centrifuged again at 3,000 g for 15 min. The pellet was washed with lysis buffer (50 mM Tris-HCl pH 7.5, 10% glycerol, 300 mM NaCl) and centrifuged at 3,000 g for 15 min. The supernatant was removed, and pellet volume was measured. The pellet was resuspended with 0.4 volumes of lysis buffer and supplemented with protease inhibitors (1:400 [v/v] protease inhibitor cocktail [P8340, Sigma], 1 mM phenylmethylsulphonyl fluoride [PMSF], 30 mg/ml leupeptin) and 5 mM β-mercaptoethanol. The cells were then frozen dropwise in liquid nitrogen and lysed using a freezer mill (Sartorius) using the following program: 10 cycles of 2 min each at a crushing rate of 15 cycles per second with 1 min cooling time in-between. The resulting powder was stored at -80 °C until further processing.

The powder was resuspended with 3 volumes of buffer containing 50 mM Tris-HCl pH 7.5, 10% glycerol, 400 mM NaCl, 1:400 (v/v) protease inhibitor cocktail (P8340, Sigma), 1 mM PMSF, 30 mg/ml leupeptin, 5 mM β-mercaptoethanol, 20 mM imidazole and 0.1% NP40. The extract was

clarified by centrifugation at 51,000 g for 30 min at 4 °C. The clarified extract was incubated with 10 ml of pre-equilibrated Ni-NTA resin for 1 h in rotation. The resin was separated by centrifugation at 2,000 g for 2 min at 4 °C and washed once batchwise in wash buffer containing 30 mM Tris-HCl pH 7.5, 10% glycerol, 300 mM NaCl, 1 mM PMSF, 5 mM β-mercaptoethanol, 20 mM imidazole and 0.1% NP40. The resin was separated from the supernatant, transferred to a disposable 10 ml polypropylene column (Thermo Fisher Scientific) and washed extensively with wash buffer. The resin was then washed with buffer A (50 mM Tris-HCl pH 7.5, 10% glycerol, 100 mM NaCl and 5 mM β-mercaptoethanol) to reduce the salt concentration and remove the detergent, and MRX was eluted with buffer A supplemented with imidazole to a final concentration of 250 mM. The relevant elution fractions as determined by Bradford assay were pooled, diluted with 5 volumes of buffer A and loaded on a pre-equilibrated 1 ml HiTrap SP HP column (Cytiva) on an ÄKTA Pure system (GE Healthcare) at 0.8 ml/min. After loading, the resin was washed with buffer A, and the protein was eluted with an 8 ml gradient to 100% buffer B (buffer A with 1 M NaCl). Fractions were analyzed by SDS-PAGE and pooled accordingly.

Phosphorylated Sae2 (pSae2), Mre11-Rad50, Mre11, Yku70-Yku80 (Ku), Dnl4-Lif1, Nej1 and Xrs2

All proteins were expressed in *Sf*9 insect cells. pSae2 was expressed using the pFB-MBP-Sae2-his construct. Mre11 was expressed using the pFB-MBP-Mre11-his construct. To preserve the phosphorylation state of pSae2, the insect cells were treated with 100 nM Okadaic acid (Enzo) for 3 h before cell harvesting[87]. Both Mre11 and pSae2 proteins were purified by amylose and Ni-NTA affinity steps. The maltose-binding protein (MBP) tag was cleaved with PreScission Protease (PP) before the protein was bound to the Ni-NTA resin. The Mre11-Rad50 complex was expressed using the pFB-Rad50 plasmid and the pTP391 vector (a kind gift of Tanya Paull, University of Texas at Austin, Austin, TX), containing His-tagged Mre11. The complex was purified by Ni-NTA resin and then using the HiTrap SP HP, followed by the HiTrap Q HP columns[41]. The yeast Ku heterodimer was expressed using the pFB-MBP-Ku70-his and pFB-Ku80-FLAG plasmids and purified by amylose and FLAG affinity steps. The MBP tag was cleaved by PP before the FLAG step[18]. Dnl4-Lif1 was expressed using the pFB-MBP-Lif1, pFB-FLAG-Dnl4 constructs and purified in the same manner as the Ku complex. For the Dnl4 variants, point mutagenesis of the expression vectors was carried out using the QuikChange II-XL site-directed mutagenesis kit according to the standard procedures. The mutant proteins were then expressed and purified in the same way as the wild-type proteins. Recombinant Xrs2-FLAG was prepared using pTP694 vector (a gift from T. Paull, University of Texas at Austin, USA) and purified using FLAG affinity resin (Sigma)[70]. Nej1

was purified from *Sf21* cells by Ni-NTA affinity purification followed by ion-exchange chromatography (Resource Q column, Cytiva)[76].

E. coli ExoIII was purchased from New England Biolabs.

Preparation of oligonucleotide-based substrates

Oligonucleotides and ssDNA probes were labeled at the 5'-terminus with [γ-^{32}P]ATP (Hartmann Analytic) using T4 Polynucleotide Kinase (New England Biolabs), or at the 3'-terminus with [α-^{32}P]dCTP (Hartmann Analytic) using Terminal Transferase (New England Biolabs). Unincorporated nucleotides were removed using Micro Bio-Spin P-30 Gel Columns (Bio-Rad). Oligonucleotide annealing reactions were performed in annealing buffer (10 mM Tris-HCl pH 8, 10 mM magnesium chloride [$MgCl_2$], 50 mM NaCl) with a two-fold excess of unlabeled oligonucleotides (in molecules). The mixture was heated at 95 °C for 3 min and allowed to cool overnight. The oligonucleotides used for substrate preparation are listed in Supplementary Table 1.

Preparation of plasmid-based substrates

In order to create the bottom-gapped plasmid used in the exonuclease assays, 40 µg of pG68 plasmid[88] were digested with 16 units of Nb.BbvCI (New England Biolabs) for 2 h at 37 °C. Afterwards, the reaction was incubated at 80 °C for 20 min to inactivate the enzymes and melt the nicked DNA fragments. The reaction was split into four 10 µg reactions and purified using the QIAquick PCR purification kit (Qiagen) according to the manufacturer's instructions.

To produce the top-gapped substrate, the pG68 plasmid was mutagenized to remove the BspQI restriction site using mutagenic primers (GCGTATTGGGCGGTCTTCCGCTTCCTCGC and GCGAGGAAGCGGAAGACCGCCCAATACGC) and the QuikChange II-XL site-directed mutagenesis kit. Afterwards, the BspQI site was re-introduced upstream the gapping site creating the pG68v2 plasmid. The sequence of the pG68v2 plasmid is listed in Supplementary Table 2. The pG68v2 plasmid was top-gapped using the same procedure as above, with the exception that the Nt.BbvCI enzyme (New England Biolabs) was used instead.

The blunt-ended 2.8 kbp-long DNA substrates were prepared using pAttP-S vectors, the annealed oligonucleotides PC216 and PC209, and ΦC31 integrase[12,89]. For Ku capture assays, an unlabeled, blunt-ended 2.85 kbp-long DNA substrate was produced by linearization of the pG68v2 plasmid with ScaI (New England Biolabs), followed by purification using the QIAquick PCR purification kit according to the manufacturer's instructions.

The 1.5 kbp-long randomly labeled PCR was produced by PCR amplification of the pG68v2 plasmid with the primers GCGCCGCGCGCCGGCCGCGGCCCGGAGGCCATGGAGCTTCACTCAC-TCGAGCCTCTCGAC and CGGTGAGCGTGGGTCTCGCG. To produce the gapped substrate, the PCR product was digested with Nt.BbvCI (as above), followed by XhoI. To produce a 68 nt-long 3' overhang, the PCR product was cut with XhoI (New England Biolabs) and BspQI (New England Biolabs) and then gapped with Nt.BbvCI (New England Biolabs). The 4 nt-long 5' overhang was produced by digesting the PCR product with XhoI (New England Biolabs).

To label the 1.5 kbp-long PCR at the 5' end upstream the gapping site, the unlabeled PCR product was digested with XhoI (New England Biolabs) and NcoI (New England Biolabs) and dephosphorylated with Antarctic Phosphatase (New England Biolabs). The DNA was purified using the QIAquick PCR purification kit and labeled at the 5'-terminus with [γ-^{32}P]ATP using T4 Polynucleotide Kinase. Unincorporated nucleotides were removed using Micro Bio-Spin P-30 Gel Columns. The obtained product was digested with BsaI-HFv2 (New England Biolabs) to remove the label from the opposite end of the DNA. The DNA was again purified using the QIAquick PCR purification kit.

The randomly labeled 2.5 kbp-long substrate used for the *in vitro* end-joining assays was prepared by PCR supplemented with 10 µCi of [α-^{32}P]dCTP using as substrate pUC19 linearized with HindIII-HF (New England Biolabs) and primers NHEJ-FOR-NheI (CCTAGCTCGCTAGCCTG-CAGGTCGACTCTAGAGG) and NHEJ-REV-NheI (TGCAGTTCGCTAGCCAGCTG-CATTAATGAATCGG). The PCR product was purified with QIAquick PCR Purification Kit and digested with NheI-HF (New England Biolabs) for 1 h at 37 °C. The DNA was then loaded on a 1% agarose gel and the band corresponding to the desired product was purified by gel extraction and a MiniElute column (Qiagen).

To obtain the modified substrate with dephosphorylated ends, and therefore non-ligatable, the gel-purified PCR product was treated with Antarctic Phosphatase for 1 h at 37 °C. The enzyme was inactivated for 2 min at 80 °C and the reaction was purified by MiniElute column.

To prepare the 5'-labeled 2.5 kbp-long substrate used for resection reactions, the primer NHEJ-0dx_2.5kb_BbsI-rev (GATCTGAAGACACTGCATCACTCAAAGGCGGTAATACGG) was first labeled at the 5'-terminus with [γ-^{32}P]ATP using T4 Polynucleotide Kinase. Unincorporated nucleotides were removed using Micro Bio-Spin P-30 Gel Columns. The substrate was then prepared by PCR using the plasmid NHEJ 0x_dx as substrate and the labeled primer NHEJ-0dx_2.5kb_BbsI-rev, together with the unlabeled primer NHEJ-amp-rev (TATGACCATGATTACACCAAGCTT-GATGGGTCTCGCTAGC). The PCR product was run on a 1% agarose gel and the band corresponding to the desired product was purified by gel extraction and a MiniElute column.

End-joining assays

The *in vitro* end-joining assays on the 2.5 kbp-long randomly labeled dsDNA were performed in 15 µl final volume in a buffer containing 60 mM Tris-HCl pH 7.5, 5 mM dithiothreitol (DTT), 10 mM $MgCl_2$, 1 mM ATP, 0.25 mg/ml bovine serum albumin (BSA) (New England Biolabs) and 0.2 nM substrate (in molecules). Unless otherwise indicated, 4.5 nM of recombinant Ku protein complex was added, and the reactions were incubated on ice for 3 min. Additional proteins, as indicated, were added on ice and the reactions were then incubated at 25 °C for 1 h. Reactions were stopped with 5 µl of 2% stop solution (100 mM Tris-HCl pH 7.5, 150 mM EDTA, 2% sodium dodecyl sulfate [SDS], 30% glycerol, bromophenol blue) and 1 µl of Proteinase K (Roche, 18 mg/ml) and incubated for 1 h at 50 °C. Unless otherwise indicated, ligation products were separated on 1.5% agarose gels. The gels were dried on DE81 chromatography paper (Whatman), exposed to storage phosphor screens (GE Healthcare) and scanned with Typhoon FLA 9500 Phosphor Imager (GE Healthcare). All data were quantified using Fiji (ImageJ).

Resection assays with plasmid length substrates

DNA end resection assays using the blunt-ended 2.8 kbp-long DNA substrate were carried out in 15 µl volume of reaction buffer containing 25 mM Tris-acetate pH 7.5, 5 mM $MgCl_2$, 1 mM $MnCl_2$, 1 mM ATP, 1 mM DTT, 0.25 mg/ml BSA, 1 mM phosphoenolpyruvate (PEP), 80 U/ml pyruvate kinase (Sigma) and 1 nM substrate (in molecules). Recombinant proteins were added on ice. Ku was first preincubated with the DNA for 5 min at 30 °C. Afterwards, the rest of the proteins were added. Unless otherwise indicated, resection was conducted in the presence of 25 nM MRX and

200 nM pSae2 by incubating for 2 h at 30 °C. The reactions were then stopped by adding 1 µl Proteinase K (Roche, 18 mg/ml) and 5 µl of 0.2% stop solution (100 mM Tris-HCl pH 7.5, 150 mM EDTA, 0.2% SDS, 30% glycerol, bromophenol blue) and incubating at 37 °C for 15 min. Half of the volume of the samples (10 µl) was then loaded on a 10% polyacrylamide gel (ratio acrylamide:bisacrylamide 19:1, Bio-Rad) in TAE buffer (40 mM Tris, 20 mM acetic acid and 1 mM EDTA) and run at 100 V for 40 min using a PowerPac™ Basic Power Supply (Bio-Rad). For samples that were heat-denatured prior to running, they were heated to 95 °C for 3 min and loaded immediately on the gel and processed as above. The gels were dried on 17 CHR paper (Whatman) and analyzed as above. When the reactions were also run on denaturing gels, 10 µl of the sample was mixed with an equal volume of formamide dye (95% [v/v] formamide, 20 mM EDTA, bromophenol blue), heated at 95 °C for 4 min and the products were separated on 15% denaturing polyacrylamide gels in TBE buffer (89 mM Tris, 89 mM boric acid, 2 mM EDTA). The gels were fixed for 30 min with fixing solution (40% methanol, 10% acetic acid and 5% glycerol), dried on 3MM paper (Whatman) and analyzed as before.

For the assay in Supplementary Fig. 10a, resection was carried out in the same buffer as above, using as substrate the 5'-labeled 1.5 kbp-long dsDNA. The reactions were incubated for only 15 min at 30 °C and processed as above.

For the Ku capture assay in Fig. 4h and Supplementary Fig. 5e, resection of unlabeled blunt-ended 2.85-kbp-long DNA substrate was carried out in the same buffer as above, except that the substrate concentration was 5 nM (in molecules). The reactions were incubated the same as above. After the incubation with the resection complex, the reaction was supplemented with 0.5 nM of 3'-labeled 72 bp-long dsDNA (oligonucleotides CAG_X4_bottom_strand_biotin and Top strand oligo WT FRP), and the $MgCl_2$ and NaCl concentrations were increased to a final concentration of 10 and 130 mM, respectively. The reactions were incubated for 5 min at 30 °C and then mixed with 5 µl of EMSA loading dye (50% glycerol, bromophenol blue). The samples were loaded on a 4% polyacrylamide gel in TAE buffer and run on ice for 1 h at 100 V using a PowerPac™ Basic Power Supply. The gels were dried on 17 CHR paper and analyzed as above.

Resection assays with oligonucleotide-based substrates

Assays monitoring the endonuclease activity of MRX on oligonucleotide-based dsDNA (oligonucleotides PC210 and PC211 or WHDv2_197mer_bot and WHDv2_196mer_B_top)[12] were carried

out in 15 µl volume of reaction buffer containing 25 mM Tris-acetate pH 7.5, 5 mM $MgCl_2$, 1 mM $MnCl_2$, 1 mM ATP, 1 mM DTT, 0.25 mg/ml BSA, 1 mM PEP, 80 U/ml pyruvate kinase and 1 nM substrate (in molecules). If the ends were blocked by Ku, the reactions were preincubated for 5 min at 30 °C following the addition of the Ku complex. When the ends were blocked by monovalent streptavidin (mSTR, or S in the cartoons), the reactions were preincubated for 5 min at room temperature instead. The reactions were then moved back on ice where the other proteins were added. MRX was used at a concentration of 25 nM and pSae2 at 200 nM. The samples were incubated for 30 min at 30 °C. The reactions were stopped by adding 0.5 µl of 0.5 M EDTA and 1 µl Proteinase K and incubated for 30 min at 50 °C. An equal volume of formamide dye (95% [v/v] formamide, 20 mM EDTA, bromophenol blue) was added and the reactions were heated at 95 °C for 4 min and the products were separated on 15% denaturing polyacrylamide gels in TBE buffer. The gels were fixed for 30 min with fixing solution (40% methanol, 10% acetic acid and 5% glycerol), dried on 3MM paper and analyzed as before.

Resection assays monitored by annealing with ssDNA probes

The assays were performed in 15 µl reaction volume containing 25 mM Tris-acetate pH 7.5, 5 mM $MgCl_2$, 1 mM $MnCl_2$, 1 mM ATP, 1 mM DTT, 0.25 mg/ml BSA, 1 mM PEP, 80 U/ml pyruvate kinase and 1 nM substrate (in molecules). The proteins were mixed on ice. Unless otherwise indicated, resection was conducted in the presence of 25 nM MRX and 200 nM pSae2 by incubating for 30 min at 30 °C. In the case of the experiment from Fig. 7b, RPA was preincubated with the ssDNA oligonucleotide trap (PC1255) for 5 min at 30 °C before being added to the reaction. The reactions were stopped by adding 1 µl Proteinase K and 5 µl of 2% HA stop solution (100 mM Tris-HCl pH 7.5, 30 mM EDTA, 2% SDS, 30% glycerol, bromophenol blue) and incubating at 37 °C for 1 h. The reactions were then supplemented with $MgCl_2$ to a final concentration of 9.2 mM and with the respective labeled oligonucleotide probe to a final concentration of 2.7 nM. The samples were incubated at 60 °C for 3 min and allowed to cool down overnight. In the experiment in Fig. 4f, the samples were incubated with the resection complex for 2 h at 30 °C before stopping. The probe annealing temperature was also reduced to 55 °C from 60 °C to avoid the unintentional melting of the terminal fragment obtained when Ku is still bound to the DNA. The following day the products were separated on a 1% agarose gel in TAE buffer. The gels were dried on DE81 chromatography paper (Whatman) and analyzed as described above.

The resection assays in Fig. 1g, Fig. 2d, Fig. 2g, Fig. 3c, Supplementary Fig. 2e,f and Supplementary Fig. 3d,e were monitored by annealing of the probe 70BP-NHEJ-PUC19TN. The assays in Fig. 4f were monitored with the probes INT 5'-0 and INT 5'-40. The assays in Fig. 6a-c, Fig. 7a,b, Fig. 7d, Fig. 7f, Fig. 7h, Supplementary Fig. 7a and Supplementary Fig. 9e were monitored with the probe 3'-100. The assays in Supplementary Fig. 7c were monitored with the probes V2 3'-15 TOP and V2 3'-100 TOP.

Electrophoretic mobility shift assays (EMSA)

Reactions monitoring DNA binding to a 50mer ssDNA (PC1255) were carried out in 15 µl reaction buffer containing 25 mM Tris-acetate pH 7.5, 5 mM $MgCl_2$, 1 mM ATP, 1 mM DTT, 0.25 mg/ml BSA, and 1 nM substrate (in molecules). Proteins were added on ice, and the reactions were incubated at 30 °C for 30 min. Afterwards, 5 µl of EMSA loading dye (50% glycerol, bromophenol blue) were added and the samples were loaded on a 6% polyacrylamide gel in TAE buffer and run on ice for 1 h at 100 V using a PowerPac™ Basic Power Supply. The gels were dried on 17 CHR paper and analyzed as above. For the assays in Supplementary Fig. 6d, a 68 nt 5' overhang substrate (oligonucleotides X12-4SC and X12-3L) was used. Ku was added first on ice, the reactions were incubated at 30 °C for 5 min. Afterwards, RPA was added on ice, followed by another incubation for 30 min at 30 °C. The samples were loaded on a 4% polyacrylamide gel in TAE buffer and processed as above.

Reactions monitoring Ku binding to 2.8 kbp-long dsDNA were performed in 15 µl reactions containing 25 mM Tris-acetate pH 7.5, 5 mM $MgCl_2$, 1 mM $MnCl_2$, 1 mM ATP, 1 mM DTT, 0.25 mg/ml BSA, 1 mM PEP, and 1 nM substrate (in molecules). Proteins were added on ice, and the reactions were incubated at 30 °C for 5 min. After the incubation, 5 µl of EMSA loading dye were added and the samples were loaded on a 0.6% agarose gel in TAE buffer and run at 4 °C for 3 h at 100 V using a PowerPac™ Basic Power Supply. The gels were dried on DE81 chromatography paper and analyzed as above.

Reactions monitoring the binding of NHEJ proteins to the randomly labeled 2.5 kbp-long substrate were carried out in 15 µl of the same reaction buffer used for the end-joining reactions. Proteins were added on ice, and the reactions were incubated at 25 °C for 30 min. Afterwards, 5 µl of EMSA loading dye were added and the samples were loaded on a 0.6% agarose gel in TAE

buffer and run at 4 °C for 2 h at 180 V using a PowerPac™ Basic Power Supply. The gels were dried on DE81 chromatography paper and analyzed as before.

DNA melting assay

DNA melting assays on a 25 nt 3' overhang (oligonucleotides PC1253 and 314) were performed in 15 µl reactions in buffer containing 25 mM Tris-acetate pH 7.5, 5 mM $MgCl_2$, 1 mM ATP, 1 mM DTT, 0.25 mg/ml BSA, and 1 nM substrate (in molecules). Proteins were added on ice, and the reactions were incubated at 30 °C for 30 min. The reactions were stopped with 1 µl Proteinase K and 5 µl of 2% stop solution. To avoid reannealing of the substrate, the stop solution was supplemented with a 20-fold excess of the unlabeled oligonucleotide with the same sequence as the radioactively labeled one. The samples were incubated at 37 °C for 15 min and the products were separated on an 8% polyacrylamide gel in TBE buffer. The gels were dried on 17 CHR paper and analyzed as above.

Resection/end-joining coupled assay

For the resection/end-joining coupled assay in Fig. 8a, the reactions were carried out in 15 µl volume of reaction buffer containing 60 mM Tris-HCl pH 7.5, 5 mM DTT, 10 mM $MgCl_2$, 1 mM ATP, 0.25 mg/ml BSA and 0.2 nM substrate (in molecules, using the randomly labeled 2.5 kbp-long dsDNA), either with or without 200 nM of RPA. Ku was first preincubated with the DNA for 3 min on ice. Where indicated, MRX (40 nM) and pSae2 (200 nM) were added on ice and the reactions were incubated for 30 min at 30 °C. Afterwards, the rest of the proteins were added (up to 4.5 nM Ku, 12 nM Nej1, 6 nM Dnl4-Lif1), and the reactions were incubated for 30 min at 25 °C and then processed according to the end-joining protocol. The quantitation of the data was done by subtracting the products obtained by resection alone (lanes 2 and 7 of Fig. 8a [ii]) as background.

For the resection/end-joining coupled assay in Fig. 8b, the reactions were carried out in 15 µl volume of reaction buffer containing 25 mM Tris-acetate pH 7.5, 5 mM $MgCl_2$, 1 mM manganese chloride ($MnCl_2$), 1 mM ATP, 1 mM DTT, 0.25 mg/ml BSA, and 1 nM substrate (in molecules, using the randomly labeled 1.5 kbp-long PCR). Recombinant proteins were added on ice. Ku (30 nM) was first preincubated with the DNA for 5 min at 30 °C. Afterwards, the rest of the proteins were added (25 nM MRX, 200 nM pSae2) and the reactions were incubated for 15 min at 30 °C. The

reactions were then diluted five-fold so that the final end-joining reaction mixture (15 µl per reaction) contains 60 mM Tris-HCl pH 7.5, 5 mM Tris-acetate pH 7.5, 10 mM $MgCl_2$, 0.2 mM $MnCl_2$, 1 mM ATP, 5 mM DTT, 0.25 mg/ml BSA, 80 mM NaCl and 0.2 nM substrate (in molecules). The end-joining proteins were added on ice (4.5 nM Ku, 12 nM Nej1, 6 nM Dnl4-Lif1), and the reactions were incubated for 1 h at 25 °C and then processed according to the end-joining protocol.

Protein interaction assays

To test the interaction between RPA and Mre11 or pSae2, 1 µg of anti-T7 antibody (abcam, ab9115) was immobilized on 10 µl Protein G magnetic beads (Dynabeads, Invitrogen) by incubating with gentle rotation for 1 h at 4 °C in PBS-T (PBS with 0.1% Tween-20 [Sigma]). The beads were washed 3 times on a magnetic rack with PBS-T. The beads were then mixed with 8 µg of T7-tagged RPA (corresponding to 5 µg of the tagged Rfa1 subunit) in 60 µl of IP buffer (25 mM Tris-HCl pH 7.5, 1 mM DTT, 3 mM EDTA, 0.20 µg/µl BSA, 150 mM NaCl) and incubated at 4 °C for 1 h. The beads were washed 3 times with 150 µl of wash buffer (25 mM Tris-HCl pH 7.5, 1 mM DTT, 3 mM EDTA, 80 mM NaCl, 0.1% Triton-X [Sigma]) and then incubated at 4 °C for 1 h with 1 µg of pSae2 or 3 µg of Mre11-Rad50 (corresponding to 1 µg of the His-tagged Mre11 subunit) in IP buffer. The beads were once again washed 3 times with 150 µl of wash buffer. The proteins were eluted in 1xSDS buffer (50 mM Tris-HCl pH 6.8, 1.6% SDS, 100 mM DTT, 10% glycerol, 0.01% bromophenol blue) by boiling for 3 min at 95 °C. PreScission Protease was added to the final eluate to a concentration of 0.12 mg/ml as a stabilizer and the samples were run on a 10% SDS–PAGE gel. Proteins were detected by western blotting using anti-T7 antibody (abcam, ab9115 1:1,000), anti-His antibody (MBL, D291-3, 1:1,000) or anti-Rad50 antibody (Invitrogen, PA5-32176, 1:1,000). The final images were acquired with Fusion FX7 capture software (Vilber Imaging).

For the reverse pulldown, 1 µg of anti-His antibody (MBL, D291-3) was immobilized as above. Afterwards, the beads were mixed with 1 µg of pSae2 or 3 µg of Mre11-Rad50 (corresponding to 1 µg of the His-tagged Mre11 subunit) in 60 µl of IP buffer (25 mM Tris-HCl pH 7.5, 1 mM DTT, 3 mM EDTA, 0.20 µg/µl BSA, 50 mM NaCl) and incubated at 4 °C for 1 h. The beads were washed 3 times with 150 µl wash buffer and incubated at 4 °C for 1 h with 8 µg of RPA (corresponding to 5 µg of the T7-tagged Rfa1 subunit) in IP buffer. The beads were washed again 3 times with 150 µl wash buffer, eluted and processed by western blotting as above. In this case, the anti-His antibody used (Invitrogen, PA1-983B, 1:1,000) was produced from rabbit.

Mass photometry

Borosilicate microscope glass plate (No. 1.5 H thickness, 24 × 50 mm, VWR) were cleaned by sequential soaking in Milli-Q-water, isopropanol and Milli-Q-water followed by drying under a stream of clean nitrogen. Silicone gaskets (CultureWell Reusable Gasket, Grace Bio-Labs) were placed on the clean coverslip to create a well for sample delivery. All measurements were performed on a TwoMP mass photometer (Refeyn Ltd). To convert optical reflection-interference contrast into a molecular mass, a known protein size marker (NativeMark Unstained Protein Standard, Invitrogen) was measured on the same day. For mass measurements, gaskets were filled with 18 µl of measurement buffer (25 mM Tris-HCl pH 7.5, 50 mM NaCl) to allow focusing the microscope onto the coverslip surface. Subsequently, proteins were added to a final concentration of 50 nM (final volume, 20 µl) and sample binding to the coverslip surface was monitored for 60 seconds using the software AcquireMP (Refeyn Ltd). Data analysis was performed using DiscoverMP software (Refeyn Ltd).

Magnetic tweezers assays

The sequences of the azido-oligonucleotides and the DBCO-oligonucleotides (ATDBio) used for assembly of the DNA construct are listed in Supplementary Table 1. The assembly was done similarly to existing protocols[60], with the only difference being that the click reaction between the azido groups and DBCO groups was considered to be essentially completed. The click reaction products were used directly as primers during the PCR. As such, a purification step was omitted with no detectable change in the quality of the materials prepared.

All assays were conducted at 34 °C in a filtered reaction buffer containing 20 mM HEPES-KOH pH 7.8, 100 mM KCl, 5 mM $MgCl_2$, 1 mM DTT, 0.05% Tween-20 and 0.5 mg/ml BSA. To prepare bead-DNA constructs, an aliquot of the DNA construct (1 µl at 300 pM) was diluted using reaction buffer to obtain a 10 µl solution. In parallel, 7 µl of magnetic beads (Dynabeads™ MyOne™ Streptavidin C1 at 10 mg/ml, Invitrogen) were washed with 200 µl of reaction buffer, then resuspended in 25 µl of reaction buffer and mixed with the DNA solution. The 35 µl bead+DNA solution was then injected into the functionalized reaction chamber and incubated for 10 min at room

temperature. Beads that remained untethered to the surface after the incubation were washed out using 4 ml of reaction buffer. The slide was then placed under the magnetic trap.

Using the PicoJAI magnetic bead tracking software suite (PicoTwist S.A.R.L), 30-60 beads were picked and tracked over time under cycles of low (~ 0 pN) and high (4 pN) forces for 60 and 30 seconds, respectively (Supplementary Fig. 4a). The force cycle was stopped at 4 pN, and the proteins were injected as a 400 µl solution containing 1 nM Ku, 0.3 nM Dnl4-Lif1 variants, 50 nM Nej1 and 1 nM MRX. After 5 min, when flow through the reaction chamber has ceased and the magnetic beads have recovered their equilibrium positions, the force cycle was relaunched and events were measured.

The data were analyzed using a homemade Python script that detects events using the derivatives of the measured points. First, a blank measurement was performed using a bead stuck to the surface that was picked in the experiment. Then, manually, each event detected by the script can be visualized, added, erased, or modified if necessary. Three kinds of events can be considered: the first category groups events that start and end during the high force step; the second category includes events that start during the high force step and end during a later, distinct high force step with the maximum duration being 90 seconds; the third category corresponds to events in the first or second category but for which the synapsis breaks during the low-force portion of the cycle. In the latter case the endpoint of the event was manually annotated as the midpoint of the low force phase. An event was characterized by its duration (in seconds) and its amplitude (in nanometers). With the 670 bp bridge used for this construct, the distribution of amplitudes for specific events followed a Gaussian with a mean of ~180 nm (for a 4 pN extending force) and a standard deviation of about 10 nm. Only events displaying an amplitude between 130 and 250 nm were retained for analysis. The distinction between specific and non-specific synaptic events was performed as previously described[60]. Moreover, beads were analyzed only if they were tethered by a DNA molecule displaying a contour length between 0.7 and 1.3 µm (as measured at 4 pN extending force). Analysis of event distributions, survival curves, plots of DNA length were then performed using Excel or Python.

Nanofluidic assays

Reactions were carried out in 10 µl volume of 2X reaction buffer containing 50 mM Tris-HCl pH 7.74, 4 mM $MgCl_2$, 2 mM DTT, 0.5 mg/ml BSA and 2 mM ATP, and 0.2 nM substrate (in molecules,

using 20 kbp-long dsDNA with 4 nt-long overhangs). Lower $MgCl_2$ concentrations are used in this assay as Mg^{2+} ions can interfere with the fluorescent dye YOYO-1[90]. Ku was first preincubated with DNA for 3 min on ice. Afterwards, the rest of the proteins were added, and the reactions were incubated for 1 hour at 25 °C. For the control (DNA only) experiment, the proteins were replaced with equivalent volume of 1X reaction buffer. For the experiments where MRX was not added, an equivalent volume of 1X reaction buffer was used. After protein incubation, DNA was fluorescently labelled by incubating with 20 µM YOYO-1 dye at 1:5 dye: base-pair ratio for 30 min at 50 °C. Finally, 0.05X TBE buffer and 2% β-mercaptoethanol were added to make a 50 µl loading solution.

Experiments were performed using nanofluidic devices that consisted of two microfluidic channels, each connecting two loading reservoirs. 200 nanofluidic channels span the microfluidic channels. Each nanochannel is 150 nm in width, 100 nm in depth and 500 µm in length and the spacing between two consecutive nanofluidic channels is 800 nm[91]. Images were collected using an inverted fluorescence microscope (Axio Observer Z1, Carl Zeiss AG) illuminated with a Colibri 7 LED light source (Carl Zeiss AG) with 512 x 512 pixels, 16 μm^2 EMCCD camera (Photometrics evolve, Teledyne Photometrics). A FITC filter (470/20 nm excitation and 530/50 nm emission) was used. 20 frames (100 ms each) were collected for each DNA molecule. Image analysis and plotting were performed using home-written MATLAB code[92]. Briefly, the images obtained were converted from .CZI to .TIFF file format, followed by generation of kymographs from the 20-frame images of individual DNA molecules (Supplementary Fig. 4b [i]). Kymographs were checked for quality, and DNA molecules fragmenting during image acquisition were discarded. Remaining kymographs from intact DNA molecules were used to obtain the plots shown in Supplementary Fig. 4b (ii-iv), where DNA length (µm) is on the X-axis, and the intensity (arbitrary units) on the Y-axis.

For each experimental condition, two replicate datasets are presented where one dataset is represented by light gray filled circles and the other by black unfilled circles. Each dataset comprises 250 to 300 datapoints from single DNA molecules. In the DNA-only control experiment, most of the molecules are ~3 µm in length and clustered around intensity per pixel of ~160 to 190 units (Supplementary Fig. 4b [ii]). The shorter length molecules are likely from DNA fragmented during sample preparation and handling and the lower intensity molecules are likely from partially stained DNA. Both populations are small in comparison and are commonly observed in single-molecule nanofluidic experiments.

Statistical analysis and reproducibility

Sample size or number of technical (for biochemical assays) were chosen on the basis of what is common in the field and what was practical to do. All experiments were repeated at least three times, unless otherwise stated. Where indicated, one representative experiment from independent repeats with similar results is shown. Protein-interaction assays and Coomassie-stained protein gels were performed twice. Data quantitation was performed with ImageJ (NIH). Statistical analysis was performed with Prism 10 (GraphPad), using ordinary one-way ANOVA followed by Šídák's multiple comparisons test, as well as two-sided ANOVA followed by Šídák's multiple comparisons test (Fig. 6b) and paired, two-tailed *t* tests (Fig. 8a[iii], Fig. 8b[iii]).

Data availability

Source data for the biochemical assays displayed in both main and supplementary figures is available as excel files containing all the associated repeats. The raw data for mass photometry movies, magnetic tweezer assays and single-molecule nanofluidics are deposited in the Dryad database under the DOI: https://doi.org/10.5061/dryad.tqjq2bwfk. All the plasmids and recombinant proteins used in this study will be available upon request from P.C.

REFERENCES:

1. Emerson, C.H. & Bertuch, A.A. Consider the workhorse: Nonhomologous end-joining in budding yeast. *Biochem Cell Biol* **94**, 396-406 (2016).
2. Vogt, A. & He, Y. Structure and mechanism in non-homologous end joining. *DNA Repair (Amst)* **130**, 103547 (2023).
3. Chen, L., Trujillo, K., Ramos, W., Sung, P. & Tomkinson, A.E. Promotion of Dnl4-catalyzed DNA end-joining by the Rad50/Mre11/Xrs2 and Hdf1/Hdf2 complexes. *Mol Cell* **8**, 1105-15 (2001).
4. Chen, X. & Tomkinson, A.E. Yeast Nej1 is a key participant in the initial end binding and final ligation steps of nonhomologous end joining. *J Biol Chem* **286**, 4931-40 (2011).
5. Zhang, Y. et al. Role of Dnl4-Lif1 in nonhomologous end-joining repair complex assembly and suppression of homologous recombination. *Nat Struct Mol Biol* **14**, 639-46 (2007).
6. Loparo, J.J. Holding it together: DNA end synapsis during non-homologous end joining. *DNA Repair (Amst)* **130**, 103553 (2023).
7. Kawale, A.S. & Sung, P. Mechanism and significance of chromosome damage repair by homologous recombination. *Essays Biochem* **64**, 779-790 (2020).
8. Ceccaldi, R. & Cejka, P. Mechanisms and regulation of DNA end resection in the maintenance of genome stability. *Nat Rev Mol Cell Biol* **26**, 586-599 (2025).
9. Otarbayev, D. & Myung, K. Exploring factors influencing choice of DNA double-strand break repair pathways. *DNA Repair (Amst)* **140**, 103696 (2024).
10. Symington, L.S. & Gautier, J. Double-strand break end resection and repair pathway choice. *Annu Rev Genet* **45**, 247-71 (2011).
11. Sfeir, A., Tijsterman, M. & McVey, M. Microhomology-Mediated End-Joining Chronicles: Tracing the Evolutionary Footprints of Genome Protection. *Annu Rev Cell Dev Biol* **40**, 195-218 (2024).
12. Cannavo, E. & Cejka, P. Sae2 promotes dsDNA endonuclease activity within Mre11-Rad50-Xrs2 to resect DNA breaks. *Nature* **514**, 122-5 (2014).
13. Wang, W., Daley, J.M., Kwon, Y., Krasner, D.S. & Sung, P. Plasticity of the Mre11-Rad50-Xrs2-Sae2 nuclease ensemble in the processing of DNA-bound obstacles. *Genes Dev* **31**, 2331-2336 (2017).
14. Gnugge, R., Reginato, G., Cejka, P. & Symington, L.S. Sequence and chromatin features guide DNA double-strand break resection initiation. *Mol Cell* **83**, 1237-1250 e15 (2023).
15. Mimitou, E.P. & Symington, L.S. Sae2, Exo1 and Sgs1 collaborate in DNA double-strand break processing. *Nature* **455**, 770-4 (2008).
16. Lobachev, K.S., Gordenin, D.A. & Resnick, M.A. The Mre11 complex is required for repair of hairpin-capped double-strand breaks and prevention of chromosome rearrangements. *Cell* **108**, 183-93 (2002).
17. Wang, W. et al. A DNA nick at Ku-blocked double-strand break ends serves as an entry site for exonuclease 1 (Exo1) or Sgs1-Dna2 in long-range DNA end resection. *J Biol Chem* **293**, 17061-17069 (2018).
18. Reginato, G., Cannavo, E. & Cejka, P. Physiological protein blocks direct the Mre11-Rad50-Xrs2 and Sae2 nuclease complex to initiate DNA end resection. *Genes Dev* **31**, 2325-2330 (2017).
19. Adkins, N.L., Niu, H., Sung, P. & Peterson, C.L. Nucleosome dynamics regulates DNA processing. *Nat Struct Mol Biol* **20**, 836-42 (2013).
20. Daley, J.M. et al. Specificity of end resection pathways for double-strand break regions containing ribonucleotides and base lesions. *Nat Commun* **11**, 3088 (2020).
21. Niu, H. et al. Mechanism of the ATP-dependent DNA end-resection machinery from Saccharomyces cerevisiae. *Nature* **467**, 108-11 (2010).

22. Cannavo, E., Cejka, P. & Kowalczykowski, S.C. Relationship of DNA degradation by Saccharomyces cerevisiae exonuclease 1 and its stimulation by RPA and Mre11-Rad50-Xrs2 to DNA end resection. *Proc Natl Acad Sci U S A* **110**, E1661-8 (2013).
23. Soniat, M.M., Myler, L.R., Kuo, H.C., Paull, T.T. & Finkelstein, I.J. RPA Phosphorylation Inhibits DNA Resection. *Mol Cell* **75**, 145-153 e5 (2019).
24. Acharya, A. et al. Distinct RPA domains promote recruitment and the helicase-nuclease activities of Dna2. *Nat Commun* **12**, 6521 (2021).
25. Mimitou, E.P. & Symington, L.S. Ku prevents Exo1 and Sgs1-dependent resection of DNA ends in the absence of a functional MRX complex or Sae2. *EMBO J* **29**, 3358-69 (2010).
26. Bonetti, D., Clerici, M., Manfrini, N., Lucchini, G. & Longhese, M.P. The MRX complex plays multiple functions in resection of Yku- and Rif2-protected DNA ends. *PLoS One* **5**, e14142 (2010).
27. Lee, S.E. et al. Saccharomyces Ku70, mre11/rad50 and RPA proteins regulate adaptation to G2/M arrest after DNA damage. *Cell* **94**, 399-409 (1998).
28. Clerici, M., Mantiero, D., Guerini, I., Lucchini, G. & Longhese, M.P. The Yku70-Yku80 complex contributes to regulate double-strand break processing and checkpoint activation during the cell cycle. *EMBO Rep* **9**, 810-8 (2008).
29. Barlow, J.H., Lisby, M. & Rothstein, R. Differential regulation of the cellular response to DNA double-strand breaks in G1. *Mol Cell* **30**, 73-85 (2008).
30. Sorenson, K.S., Mahaney, B.L., Lees-Miller, S.P. & Cobb, J.A. The non-homologous end-joining factor Nej1 inhibits resection mediated by Dna2-Sgs1 nuclease-helicase at DNA double strand breaks. *J Biol Chem* **292**, 14576-14586 (2017).
31. Mojumdar, A., Adam, N. & Cobb, J.A. Nej1 interacts with Sae2 at DNA double-stranded breaks to inhibit DNA resection. *J Biol Chem* **298**, 101937 (2022).
32. Deshpande, R.A. et al. DNA-dependent protein kinase promotes DNA end processing by MRN and CtIP. *Sci Adv* **6**, eaay0922 (2020).
33. Chanut, P., Britton, S., Coates, J., Jackson, S.P. & Calsou, P. Coordinated nuclease activities counteract Ku at single-ended DNA double-strand breaks. *Nat Commun* **7**, 12889 (2016).
34. Mikhova, M. et al. Single-molecule imaging reveals the kinetics of non-homologous end-joining in living cells. *Nat Commun* **15**, 10159 (2024).
35. Britton, S., Coates, J. & Jackson, S.P. A new method for high-resolution imaging of Ku foci to decipher mechanisms of DNA double-strand break repair. *J Cell Biol* **202**, 579-95 (2013).
36. Kochan, J.A. et al. Meta-analysis of DNA double-strand break response kinetics. *Nucleic Acids Res* **45**, 12625-12637 (2017).
37. Pavani, R. et al. Structure and repair of replication-coupled DNA breaks. *Science* **385**, eado3867 (2024).
38. Kimble, M.T. et al. Repair of replication-dependent double-strand breaks differs between the leading and lagging strands. *Mol Cell* **85**, 61-77 e6 (2025).
39. Paull, T.T. Reconsidering pathway choice: a sequential model of mammalian DNA double-strand break pathway decisions. *Curr Opin Genet Dev* **71**, 55-62 (2021).
40. Matsuzaki, K., Shinohara, A. & Shinohara, M. Forkhead-associated domain of yeast Xrs2, a homolog of human Nbs1, promotes nonhomologous end joining through interaction with a ligase IV partner protein, Lif1. *Genetics* **179**, 213-25 (2008).
41. Oh, J., Al-Zain, A., Cannavo, E., Cejka, P. & Symington, L.S. Xrs2 Dependent and Independent Functions of the Mre11-Rad50 Complex. *Mol Cell* **64**, 405-415 (2016).
42. Moller, C. et al. Xrs2/NBS1 promote end-bridging activity of the MRE11-RAD50 complex. *Biochem Biophys Res Commun* **695**, 149464 (2024).
43. de Jager, M. et al. Human Rad50/Mre11 is a flexible complex that can tether DNA ends. *Mol Cell* **8**, 1129-35 (2001).

44. Oh, J., Lee, S.J., Rothstein, R. & Symington, L.S. Xrs2 and Tel1 Independently Contribute to MR-Mediated DNA Tethering and Replisome Stability. *Cell Rep* **25**, 1681-1692 e4 (2018).
45. Deshpande, R.A. et al. ATP-driven Rad50 conformations regulate DNA tethering, end resection, and ATM checkpoint signaling. *EMBO J* **33**, 482-500 (2014).
46. Mao, Z., Bozzella, M., Seluanov, A. & Gorbunova, V. Comparison of nonhomologous end joining and homologous recombination in human cells. *DNA Repair (Amst)* **7**, 1765-71 (2008).
47. Zhu, Z., Chung, W.H., Shim, E.Y., Lee, S.E. & Ira, G. Sgs1 helicase and two nucleases Dna2 and Exo1 resect DNA double-strand break ends. *Cell* **134**, 981-94 (2008).
48. Mojumdar, A. et al. Nej1 Interacts with Mre11 to Regulate Tethering and Dna2 Binding at DNA Double-Strand Breaks. *Cell Rep* **28**, 1564-1573 e3 (2019).
49. Marsella, A. et al. Sae2 and Rif2 regulate MRX endonuclease activity at DNA double-strand breaks in opposite manners. *Cell Rep* **34**, 108906 (2021).
50. Hailemariam, S. et al. The telomere-binding protein Rif2 and ATP-bound Rad50 have opposing roles in the activation of yeast Tel1(ATM) kinase. *J Biol Chem* **294**, 18846-18852 (2019).
51. Martina, M. et al. A balance between Tel1 and Rif2 activities regulates nucleolytic processing and elongation at telomeres. *Mol Cell Biol* **32**, 1604-17 (2012).
52. Khayat, F. et al. Inhibition of MRN activity by a telomere protein motif. *Nat Commun* **12**, 3856 (2021).
53. Roisne-Hamelin, F. et al. Mechanism of MRX inhibition by Rif2 at telomeres. *Nat Commun* **12**, 2763 (2021).
54. Khayat, F., Alshmery, M., Pal, M., Oliver, A.W. & Bianchi, A. Binding of the TRF2 iDDR motif to RAD50 highlights a convergent evolutionary strategy to inactivate MRN at telomeres. *Nucleic Acids Res* **52**, 7704-7719 (2024).
55. Sulek, M., Yarrington, R., McGibbon, G., Boeke, J.D. & Junop, M. A critical role for the C-terminus of Nej1 protein in Lif1p association, DNA binding and non-homologous end-joining. *DNA Repair (Amst)* **6**, 1805-18 (2007).
56. Stinson, B.M., Carney, S.M., Walter, J.C. & Loparo, J.J. Structural role for DNA Ligase IV in promoting the fidelity of non-homologous end joining. *Nat Commun* **15**, 1250 (2024).
57. Grob, P. et al. Electron microscopy visualization of DNA-protein complexes formed by Ku and DNA ligase IV. *DNA Repair (Amst)* **11**, 74-81 (2012).
58. Chiruvella, K.K., Liang, Z., Birkeland, S.R., Basrur, V. & Wilson, T.E. Saccharomyces cerevisiae DNA ligase IV supports imprecise end joining independently of its catalytic activity. *PLoS Genet* **9**, e1003599 (2013).
59. Graham, T.G., Walter, J.C. & Loparo, J.J. Two-Stage Synapsis of DNA Ends during Non-homologous End Joining. *Mol Cell* **61**, 850-8 (2016).
60. Wang, J.L. et al. Dissection of DNA double-strand-break repair using novel single-molecule forceps. *Nat Struct Mol Biol* **25**, 482-487 (2018).
61. De Braganca, S. et al. APLF and long non-coding RNA NIHCOLE promote stable DNA synapsis in non-homologous end joining. *Cell Rep* **42**, 111917 (2023).
62. Seifert, F.U., Lammens, K., Stoehr, G., Kessler, B. & Hopfner, K.P. Structural mechanism of ATP-dependent DNA binding and DNA end bridging by eukaryotic Rad50. *EMBO J* **35**, 759-72 (2016).
63. Cejka, P. et al. DNA end resection by Dna2-Sgs1-RPA and its stimulation by Top3-Rmi1 and Mre11-Rad50-Xrs2. *Nature* **467**, 112-6 (2010).
64. Myler, L.R. et al. Single-molecule imaging reveals the mechanism of Exo1 regulation by single-stranded DNA binding proteins. *Proc Natl Acad Sci U S A* **113**, E1170-9 (2016).
65. Chen, H., Lisby, M. & Symington, L.S. RPA coordinates DNA end resection and prevents formation of DNA hairpins. *Mol Cell* **50**, 589-600 (2013).

66. Deng, S.K., Yin, Y., Petes, T.D. & Symington, L.S. Mre11-Sae2 and RPA Collaborate to Prevent Palindromic Gene Amplification. *Mol Cell* **60**, 500-8 (2015).
67. Oakley, G.G. et al. Physical interaction between replication protein A (RPA) and MRN: involvement of RPA2 phosphorylation and the N-terminus of RPA1. *Biochemistry* **48**, 7473-81 (2009).
68. Seeber, A. et al. RPA Mediates Recruitment of MRX to Forks and Double-Strand Breaks to Hold Sister Chromatids Together. *Mol Cell* **64**, 951-966 (2016).
69. Kemmerich, F.E. et al. Force regulated dynamics of RPA on a DNA fork. *Nucleic Acids Res* **44**, 5837-48 (2016).
70. Cannavo, E., Reginato, G. & Cejka, P. Stepwise 5' DNA end-specific resection of DNA breaks by the Mre11-Rad50-Xrs2 and Sae2 nuclease ensemble. *Proc Natl Acad Sci U S A* **116**, 5505-5513 (2019).
71. Chen, R. & Wold, M.S. Replication protein A: single-stranded DNA's first responder: dynamic DNA-interactions allow replication protein A to direct single-strand DNA intermediates into different pathways for synthesis or repair. *Bioessays* **36**, 1156-61 (2014).
72. Luciano, P. et al. RPA facilitates telomerase activity at chromosome ends in budding and fission yeasts. *EMBO J* **31**, 2034-46 (2012).
73. Romanienko, P.J. & Camerini-Otero, R.D. The mouse Spo11 gene is required for meiotic chromosome synapsis. *Mol Cell* **6**, 975-87 (2000).
74. Keeney, S., Giroux, C.N. & Kleckner, N. Meiosis-specific DNA double-strand breaks are catalyzed by Spo11, a member of a widely conserved protein family. *Cell* **88**, 375-84 (1997).
75. Ahrabi, S. et al. A role for human homologous recombination factors in suppressing microhomology-mediated end joining. *Nucleic Acids Res* **44**, 5743-57 (2016).
76. Reginato, G. et al. HLTF disrupts Cas9-DNA post-cleavage complexes to allow DNA break processing. *Nat Commun* **15**, 5789 (2024).
77. Lee, K. & Lee, S.E. Saccharomyces cerevisiae Sae2- and Tel1-dependent single-strand DNA formation at DNA break promotes microhomology-mediated end joining. *Genetics* **176**, 2003-14 (2007).
78. Nakada, D., Matsumoto, K. & Sugimoto, K. ATM-related Tel1 associates with double-strand breaks through an Xrs2-dependent mechanism. *Genes Dev* **17**, 1957-62 (2003).
79. Kim, J.S. et al. Independent and sequential recruitment of NHEJ and HR factors to DNA damage sites in mammalian cells. *J Cell Biol* **170**, 341-7 (2005).
80. Mattarocci, S. et al. Rap1-mediated steric hindrance protects telomeres from MRX sensing. *Nat Struct Mol Biol* **33**, 915-927 (2026).
81. Teixeira-Silva, A. et al. The end-joining factor Ku acts in the end-resection of double strand break-free arrested replication forks. *Nat Commun* **8**, 1982 (2017).
82. Tamai, T. et al. Sae2 controls Mre11 endo- and exonuclease activities by different mechanisms. *Nat Commun* **15**, 7221 (2024).
83. Sibenaller, Z.A., Sorensen, B.R. & Wold, M.S. The 32- and 14-kilodalton subunits of replication protein A are responsible for species-specific interactions with single-stranded DNA. *Biochemistry* **37**, 12496-506 (1998).
84. Anand, R., Pinto, C. & Cejka, P. Methods to Study DNA End Resection I: Recombinant Protein Purification. *Methods Enzymol* **600**, 25-66 (2018).
85. Ceppi, I. et al. Mechanism of BRCA1-BARD1 function in DNA end resection and DNA protection. *Nature* **634**, 492-500 (2024).
86. Pinto, C., Kasaciunaite, K., Seidel, R. & Cejka, P. Human DNA2 possesses a cryptic DNA unwinding activity that functionally integrates with BLM or WRN helicases. *Elife* **5**(2016).
87. Cannavo, E. et al. Regulatory control of DNA end resection by Sae2 phosphorylation. *Nat Commun* **9**, 4016 (2018).

88. Ralf, C., Hickson, I.D. & Wu, L. The Bloom's syndrome helicase can promote the regression of a model replication fork. *J Biol Chem* **281**, 22839-46 (2006).
89. Pinto, C., Anand, R. & Cejka, P. Methods to Study DNA End Resection II: Biochemical Reconstitution Assays. *Methods Enzymol* **600**, 67-106 (2018).
90. Moller, C., Winter, D., Nambannor Kunnath, R., Kk, S. & Westerlund, F. Effects of Mg(2+) and ATP on YOYO-1 labeling of genomic DNA in single molecule experiments. *Biochem Biophys Rep* **44**, 102248 (2025).
91. Kk, S. et al. Fluorescence Microscopy of Nanochannel-Confined DNA. *Methods Mol Biol* **2694**, 175-202 (2024).
92. Dvirnas, A. et al. Facilitated sequence assembly using densely labeled optical DNA barcodes: A combinatorial auction approach. *PLoS One* **13**, e0193900 (2018).

End notes

Acknowledgements

We thank members of the Cejka laboratory for their critical comments on this manuscript. The Swiss National Science Foundation (SNSF) (Grants 310030_207588 and 320030-236167) and the European Research Council (ERC) (Grant 101018257) support the research in the Cejka laboratory. Work in the Strick laboratory is supported by the French National Institute of Health and Medical Research (AAP_Inserm_ITMO Cancer PCSI PETITENhej) and by the "Equipe labellisée" programme of the Ligue Nationale Contre le Cancer. Work in the Westerlund laboratory is supported by the ERC consolidator grant nanoDNArepair (866238) and the Swedish Research Council (2025-05124). The nanofluidic devices used in the nanofluidic assays were fabricated at Chalmers MyFab.

Author contributions

S.B., E.C. and P.C. designed the study. S.B. and E.C. prepared most of the recombinant proteins, carried out and analyzed all the biochemical experiments. V.M. and S.K.K. contributed equally to this study. V.M. performed the magnetic tweezers experiments under the supervision of T.S. S.K.K. and F.M. performed the nanofluidic assays under the supervision of F.W. A.A. purified the RPA K494E and RPA C505A, C508A mutants and Rfa1 fragments. G.R. prepared recombinant MR, untagged RPA and designed the yMRnXf-tda1delta strain. V.M. and V.R. purified recombinant Nej1 under the supervision of J.B.C. R.G. performed the modeling of the interactions between RPA, MR and Sae2 not included in this manuscript. S.B. and P.C. wrote the manuscript with contributions from all authors.

Competing interests

The authors declare no competing interests

Additional Information

Supplementary Information is available for this paper. Correspondence and requests for materials should be addressed to Petr Cejka (petr.cejka@irb.usi.ch).

Figure 1: Reconstituted NHEJ is faster than DNA end resection.

a, Recombinant proteins used in this study. The polyacrylamide gel was stained with Coomassie Brilliant Blue.

b, A schematic of the non-homologous end-joining (NHEJ) assay. Red asterisks (*) indicate the positions of the radioactive labels.

c, End-joining assays with the indicated proteins. A representative image of five independent experiments is shown.

d, Quantitation of DNA ligation from experiments of panel **c**. Averages shown; error bars, s.e.m.; n = 5 independent experiments.

e, End-joining kinetic assays. **(i)** A representative image of three independent experiments. **(ii)** Quantitation of DNA ligation from experiments shown in **(i)** and Supplementary Fig. 2b. Averages shown; error bars, s.e.m.; n = 3 independent experiments.

f, Assay monitoring the kinetics of MRX-pSae2-mediated resection. The products were separated on 15% denaturing polyacrylamide gels. **(i)** A schematic of a DNA end resection experiment. Red asterisks (*) represent the positions of the radioactive labels. **(ii)** A representative image of three independent experiments. **(iii)** Quantitation of DNA resection from experiments shown in **(ii)** and Supplementary Fig. 2d. Averages shown; error bars, s.e.m.; n = 3 independent experiments.

g, Oligonucleotide annealing assays in a kinetic experiment. **(i)** A schematic of the assay. The red asterisk (*) represents the position of the radioactive label. **(ii)** A representative image of three independent experiments. **(iii)** Quantitation of DNA resection from experiments shown in **(ii)** and Supplementary Fig. 2e. Values are normalized to lane 9 in **(ii)**. Averages shown; error bars, s.e.m.; n = 3 independent experiments.

h, Resection assays as in panel **g**, but with products separated on 15% denaturing polyacrylamide gels. Top, quantitation of DNA resection. Averages shown; error bars, s.e.m.; n = 3 independent experiments. Bottom, a representative image of three independent experiments.

i, A resection assay using a 5'-labeled 196 bp-long dsDNA as a substrate. The products were separated on 15% denaturing polyacrylamide gels. Due to the substrate concentration used (1 nM), the reaction was not permissive for end-joining. **(i)** A schematic of the assay. The red asterisk (*) represents the position of the radioactive label. **(ii)** A representative image of three independent experiments.

Figure 2: NHEJ assemblies on non-ligatable ends inhibit DNA end resection.

a, Phosphorylated Sae2 (pSae2) does not inhibit end-joining. Top, quantitation of DNA ligation. Averages shown; error bars, s.e.m.; n = 3 independent experiments. Bottom, end-joining assays in the presence or absence of pSae2. A representative image of three independent experiments is shown.

b, A schematic of end-joining assays conducted with either phosphorylated or dephosphorylated DNA ends.

c, End-joining assays with phosphorylated or dephosphorylated DNA ends. Top, quantitation of DNA ligation. Averages shown; bars, range; n = 2 independent experiments, except for lane 2, where n = 4. Bottom, a representative image of two independent experiments.

d, Impact of end-joining on DNA end resection. **(i)** A schematic of the oligonucleotide annealing assay. The red asterisk (*) represents the position of the radioactive label. **(ii)** A representative image of three independent experiments.

e, Quantitation of assays from experiments of panel **d**. Values are normalized to lane 7. Averages shown; error bars, s.e.m.; n = 3 independent experiments. Statistical analysis was performed using Šídák's multiple comparisons test.

f, Quantitation of assays such as shown in Supplementary Fig. 3d. Values are normalized to lane 15. Averages shown; error bars, s.e.m.; n = 3 independent experiments. Statistical analysis was performed using Šídák's multiple comparisons test.

g, Quantitation of assays performed with MRX such as shown in Supplementary Fig. 3e. Values are normalized to lane 2 of Supplementary Fig. 3e. Averages shown; error bars, s.e.m.; n = 6 independent experiments. Statistical analysis was performed using Šídák's multiple comparisons test.

h, Schematic model of the magnetic tweezers experiment. A force cycle is applied to the DNA construct by manipulating a magnetic bead that is alternately subjected to high and low force. When the force is high, the DNA is extended. When the force is low, the bead exhibits Brownian motion. Synapsis between the two DNA ends leads to a reduced bead extension during the high force phase.

i, Binned survival curves of synaptic events. Data are binned every 0.2 log(s). The NHEJ curve is composed of 1216 events, NHEJ (Dnl4 D284A) is composed of 829 events and NHEJ + MRX is composed of 672 events. Averages shown; error bars, s.d.; n = 4 independent experiments.

Figure 3: DNA synapsis inhibits DNA end resection.

a, End-joining assays with Dnl4-Lif1 catalytic mutants. Top, quantitation of DNA ligation assays. Averages shown; error bars, s.e.m.; n = 3 independent experiments. KR (K282R), DA (D284A) and KA (K466A) are substitutions in Dnl4, prepared as a heterodimer together with Lif1. Statistical analysis was performed using Šídák's multiple comparisons test. Bottom, a representative image of three independent experiments. The products were separated on 0.6% agarose gels in TAE.

b, Recombinant wild-type Dnl4-Lif1 and point mutants in the Dnl4 subunit used in this study. The polyacrylamide gel were stained with Coomassie Brilliant Blue.

c, Oligonucleotide annealing assay used to monitor resection after end-joining reactions with wild-type Dnl4-Lif1 and catalytic mutants. **(i)** A schematic of experiments carried out to determine the impact of DNA synapsis on DNA end resection. **(ii)** A representative image of four independent experiments. **(iii)** Quantitation of DNA resection from experiments shown in **(ii)**. Values were normalized to lane 2 in **(ii)**. Averages shown; error bars, s.e.m.; n = 4 independent experiments.

d, A schematic showing the impact of end-joining assemblies on short-range DNA end resection by MRX-pSae2. While the end-joining ensemble *per se* does not inhibit resection, synapsis, even in the absence of ligation, renders the DNA ends largely resistant to resection by MRX-pSae2.

Figure 4: RPA stimulates Ku removal from DSBs by MRX-pSae2 in short-range resection.

a, RPA promotes resection of Ku-blocked ends by MRX (25 nM)-pSae2 (200 nM). Top, a cartoon of the substrate used. The red asterisk (*) represents the position of the radioactive label. Bottom, a representative image of three independent experiments. Heat, denaturation.

b, Length analysis of end resection products. Top, a cartoon of the substrate used. The red asterisk (*) represents the position of the radioactive label. Bottom, a representative image of two independent experiments. The products were separated on 15% denaturing polyacrylamide gels.

c, Quantitation of DNA incision from experiments of panel **a**, based on substrate utilization in lanes 4, 5 and 9, 10. Averages shown; error bars, s.e.m.; n = 3 independent experiments. Statistical analysis was performed using Šídák's multiple comparisons test; ns, not significant.

d, Quantitation of Ku removal from experiments of panel **a**, calculated as the "Ku removed" band vs. the "Ku not removed" band (lanes 4, 5 and 9, 10). Averages shown; error bars, s.e.m.; n = 3 independent experiments. Statistical analysis was performed using Šídák's multiple comparisons test.

e, Quantitation of free 3' ends from experiments of panel **a**, calculated as the "Ku removed" band vs. the rest of the lane (lanes 2, 3 and 7, 8). Averages shown; error bars, s.e.m.; n = 3 independent experiments. Statistical analysis was performed using Šídák's multiple comparisons test.

f, MRX (25 nM)-pSae2 (200 nM)-dependent DNA resection at various distances from Ku-blocked ends. **(i)** A cartoon of the assay. The red asterisk (*) represents the position of the radioactive label. **(ii)** A representative image of four independent experiments. **(iii)** Quantitation of experiments shown in **(ii)**. Values were normalized to lane 2 in **(ii)**. Averages shown; error bars, s.e.m.; n = 4 independent experiments. Statistical analysis was performed using Šídák's multiple comparisons test.

g, A cartoon of Ku-bound DNA end processing by MRX-pSae2 with or without RPA.

h, Ku displacement from DNA ends. **(i)** A cartoon of the assay. **(ii)** Quantitation of experiments of Supplementary Fig. 5e. Values were normalized to lane 2 of Supplementary Fig. 5e. Averages shown; error bars, s.e.m.; n = 4 independent experiments. Statistical analysis was performed using Šídák's multiple comparisons test.

Figure 5: RPA promotes Ku removal from DSBs in a species-specific manner.

a, Ku removal from DSBs by MRX (25 nM)-pSae2 (200 nM) with yeast RPA (yRPA), human RPA (hRPA) or human mitochondrial SSB (hmtSSB). **(i)** A cartoon of the assay. The red asterisk (*) represents the position of the radioactive label. **(ii)** Top, quantitation of Ku removal. Values were normalized to lane 2. Averages shown; error bars, s.e.m.; n = 3 independent experiments. Statistical analysis was performed using Šídák's multiple comparisons test; ns, not significant. Bottom, a representative image of three independent experiments.

b, RPA interacts with both MR and pSae2. **(i)** A schematic of the protein pulldown assay. The T7-tag is present on Rfa1. **(ii)** A representative pulldown assay out of three independent experiments.

Figure 6: RPA and pSae2 synergistically stimulate the exonuclease activity of MR or MRX.

a, Yeast RPA promotes the exonuclease of MRX (25 nM)-pSae2 (200 nM). Top right, a schematic of the oligonucleotide annealing assay. Middle, quantitation of exonuclease assays. Values were normalized to lane 2. Averages shown; error bars, s.e.m.; n = 5 independent experiments. Statistical analysis was performed using Šídák's multiple comparisons test. Bottom, a representative image of five independent experiments. Yeast RPA (yRPA), human RPA (hRPA), human mitochondrial SSB (hmtSSB).

b, RPA and pSae2 synergistically stimulate the exonuclease of MRX in the presence of ATP, and Xrs2 is dispensable. Top, quantitation of exonuclease assays. Values were normalized to lane 2. Averages shown; error bars, s.e.m.; n = 3 independent experiments. Statistical analysis was performed by two-way ANOVA followed by Šídák's multiple comparisons test; ns, not significant. Bottom, a representative image of three independent experiments.

c, Oligonucleotide annealing assay as in panel **b**, but with Mre11. RPA does not stimulate the exonuclease of Mre11. **(i)** A representative image of three independent experiments. **(ii)** Quantitation of exonuclease assays shown in **(i)**. Values were normalized to lane 2. Averages shown; error bars, s.e.m.; n = 3 independent experiments.

Figure 7: To promote the exonuclease activity of MRX-pSae2, RPA acts as a trimer, requires Rfa3 and needs to bind DNA.

a, DNA-binding-deficient RPA variants mutated in Rfa1 do not promote MRX (25 nM)-pSae2 (200 nM). Top, quantitation of the exonuclease assays. Values were normalized to lane 2. Averages shown; error bars, s.e.m.; n = 3 independent experiments. Statistical analysis was performed using Šídák's multiple comparisons test; ns, not significant. Bottom, a representative image of three independent experiments.

b, RPA promotes MRX (25 nM)-pSae2 (200 nM) *in cis*. Top, quantitation of exonuclease assays. Values were normalized to lane 2. Averages shown; error bars, s.e.m.; n = 4 independent experiments. Statistical analysis was performed using Šídák's multiple comparisons test; ns, not significant. Bottom, a representative image of four independent experiments.

c, A model showing RPA stimulating the 3'-5' exonuclease activity of MRX-pSae2.

d, The RPA trimer is necessary to stimulate MRX (25 nM)-pSae2 (200 nM). **(i)** A schematic of the domain architecture of RPA. **(ii)** Top, quantitation of exonuclease assays. Values were normalized to lane 2. Averages shown; error bars, s.e.m.; n = 4 independent experiments. Bottom, a representative image of four independent experiments.

e, The MR-RPA interaction is impaired in RPAΔF. **(i)** A schematic of the protein pulldown assay. **(ii)** A representative image of two independent experiments.

f, The effect of the Rfa1 OB-F domain on MRX-pSae2. Top, quantitation of exonuclease assays. Values were normalized to lane 2. Averages shown; error bars, s.e.m.; n = 4 independent

experiments. Statistical analysis was performed using Šídák's multiple comparisons test. Bottom, a representative image of four independent experiments.

g, The pSae2-RPA interaction is impaired in RPAΔF. **(i)** A schematic of the protein pulldown assay. **(ii)** A representative image of two independent experiments.

h, Rfa3 is required for stimulating MRX-pSae2. **(i)** A representative image of three independent experiments. **(ii)** Quantitation of exonuclease assays. Values were normalized to lane 2. Averages shown; error bars, s.e.m.; n = 3 independent experiments. Statistical analysis was performed using Šídák's multiple comparisons test; ns, not significant.

i, Rfa3 is indispensable for promoting Ku removal. Quantitation of Ku removal from Supplementary Fig. 9h. Values were normalized to lane 2 of Supplementary Fig. 9h. Averages shown; error bars, s.e.m.; n = 3 independent experiments. Statistical analysis was performed using Šídák's multiple comparisons test.

Figure 8: RPA-stimulated Ku removal by MRX-pSae2 during short-range resection inhibits subsequent NHEJ.

a, RPA inhibits end-joining and the formation of higher-order ligation products by stimulating Ku removal. **(i)** A cartoon depicting the resection-ligation assay using the randomly labeled 2.5 kbp-long dsDNA. **(ii)** End-joining assay (up to 4.5 nM Ku, 12 nM Nej1, 6 nM Dnl4-Lif1) of a 2.5 kbp-long dsDNA resected by MRX (40 nM)-pSae2 (200 nM) in the presence or absence of Ku and RPA. The lower mobility product observed in lanes 2 and 7 (without end-joining proteins) is caused by ssDNA generated during extensive 5'-end resection, which can spontaneously anneal to other DNA molecules of the substrate. A representative image of three independent experiments is shown. **(iii)** Quantitation of DNA ligation from experiments shown in **(ii)**. Averages shown; error bars, s.e.m.; n = 3 independent experiments. Statistical analysis was performed using a paired, two-tailed *t* test.

b, End-joining of Ku-bound, partially ligatable dsDNA is inhibited by RPA. **(i)** A cartoon depicting the resection-ligation assay using a randomly labeled 1.5 kbp-long dsDNA. Ku binding and MRX-pSae2 processing of the non-ligatable end were omitted for simplicity. **(ii)** End-joining assay (4.5 nM Ku, 12 nM Nej1, 6 nM Dnl4-Lif1) of a Ku-bound 1.5 kbp-long PCR product resected by MRX (25 nM)-pSae2 (200 nM) in the presence of yeast RPA (yRPA) or human mtSSB (hmtSSB). A representative image of five independent experiments is shown. yRad50 was supplemented to avoid excessive nucleolytic processing by Mre11. **(iii)** Quantitation of DNA ligation from experiments shown in **(ii)**. Averages shown; error bars, s.e.m.; n = 5 independent experiments. Statistical analysis was performed using a paired, two-tailed *t* test.

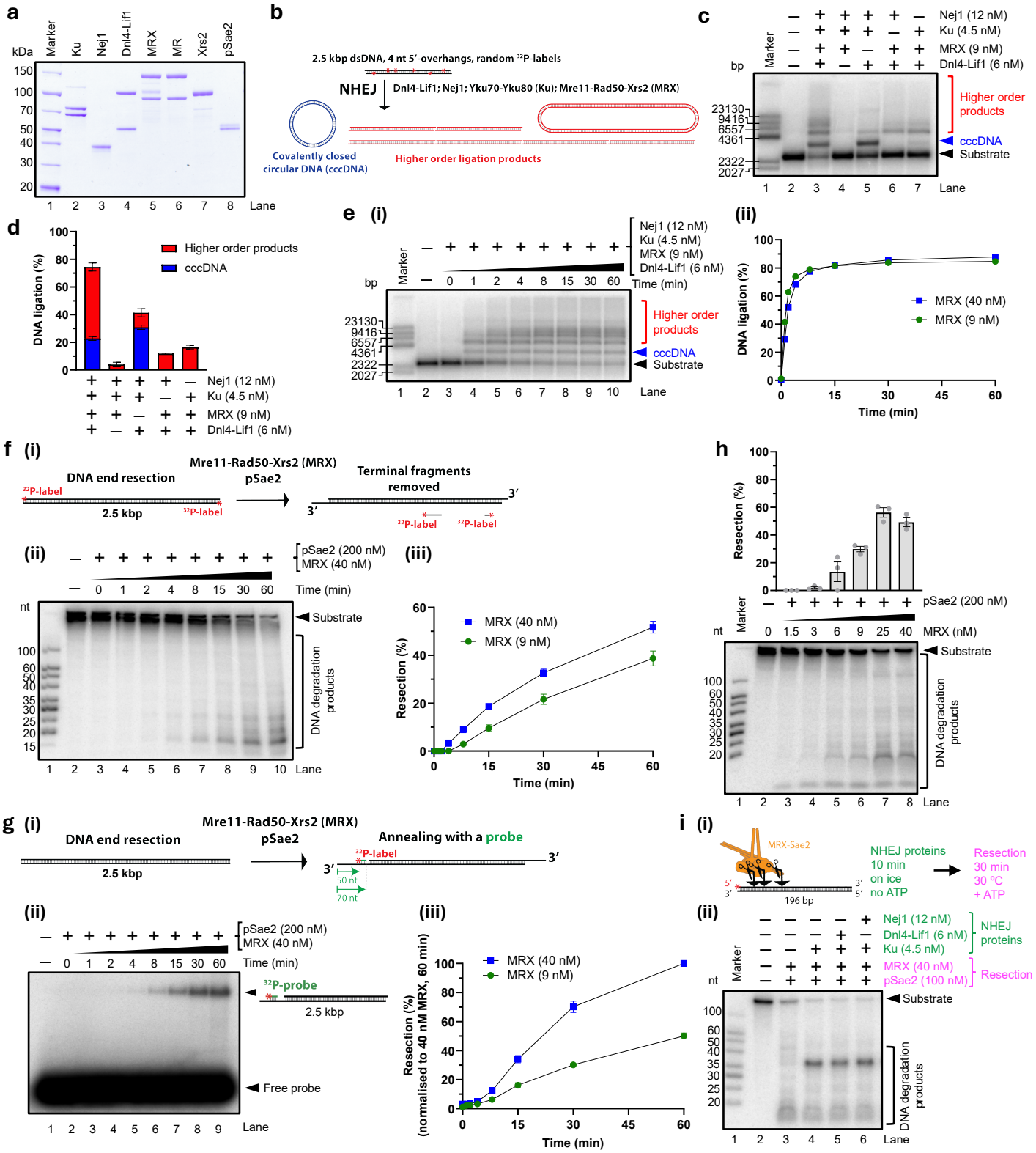
a
kDa
Marker
Ku
Nej1
Dnl4-Lif1
MRX
MR
Xrs2
pSae2
150
100
70
50
40
30
20
1 2 3 4 5 6 7 8 Lane
b
2.5 kbp dsDNA, 4 nt 5′-overhangs, random 32P-labels
NHEJ
Dnl4-Lif1; Nej1; Yku70-Yku80 (Ku); Mre11-Rad50-Xrs2 (MRX)
Covalently closed circular DNA (cccDNA)
Higher order ligation products
c
Nej1 (12 nM)
Ku (4.5 nM)
MRX (9 nM)
Dnl4-Lif1 (6 nM)
bp
Marker
23130
9416
6557
4361
2322
2027
Higher order products
cccDNA
Substrate
1 2 3 4 5 6 7 Lane
d
DNA ligation (%)
Higher order products
cccDNA
Nej1 (12 nM)
Ku (4.5 nM)
MRX (9 nM)
Dnl4-Lif1 (6 nM)
e (i)
Nej1 (12 nM)
Ku (4.5 nM)
MRX (9 nM)
Dnl4-Lif1 (6 nM)
Time (min)
0 1 2 4 8 15 30 60
Higher order products
cccDNA
Substrate
1 2 3 4 5 6 7 8 9 10 Lane
(ii)
DNA ligation (%)
MRX (40 nM)
MRX (9 nM)
Time (min)
f (i)
DNA end resection
Mre11-Rad50-Xrs2 (MRX)
pSae2
Terminal fragments removed
32P-label
2.5 kbp
3′
(ii)
pSae2 (200 nM)
MRX (40 nM)
Time (min)
0 1 2 4 8 15 30 60
nt
Substrate
DNA degradation products
1 2 3 4 5 6 7 8 9 10 Lane
(iii)
Resection (%)
MRX (40 nM)
MRX (9 nM)
Time (min)
h
Resection (%)
pSae2 (200 nM)
MRX (nM)
0 1.5 3 6 9 25 40
nt
Marker
Substrate
DNA degradation products
1 2 3 4 5 6 7 8 Lane
g (i)
DNA end resection
Mre11-Rad50-Xrs2 (MRX)
pSae2
Annealing with a probe
2.5 kbp
32P-label
50 nt
70 nt
(ii)
pSae2 (200 nM)
MRX (40 nM)
Time (min)
0 1 2 4 8 15 30 60
32P-probe
2.5 kbp
Free probe
1 2 3 4 5 6 7 8 9 Lane
(iii)
Resection (%) (normalised to 40 nM MRX, 60 min)
MRX (40 nM)
MRX (9 nM)
Time (min)
i (i)
MRX-Sae2
196 bp
NHEJ proteins 10 min on ice no ATP
Resection 30 min 30 °C + ATP
(ii)
Nej1 (12 nM)
Dnl4-Lif1 (6 nM)
Ku (4.5 nM)
MRX (40 nM)
pSae2 (100 nM)
NHEJ proteins
Resection
Marker
nt
Substrate
DNA degradation products
1 2 3 4 5 6 Lane

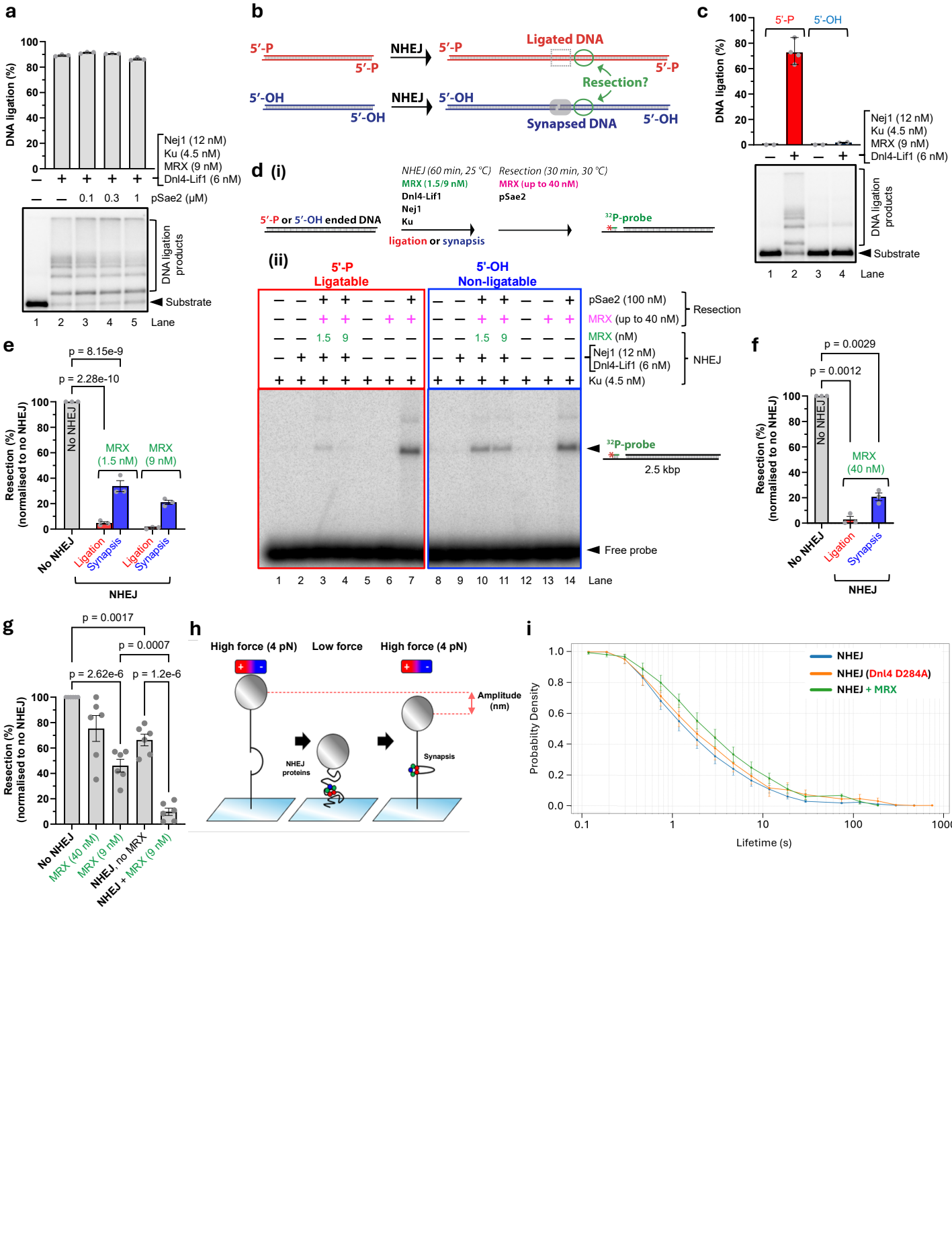
a
DNA ligation (%)
Nej1 (12 nM)
Ku (4.5 nM)
MRX (9 nM)
Dnl4-Lif1 (6 nM)
pSae2 (μM)
DNA ligation products
Substrate
Lane
b
5′-P
5′-OH
NHEJ
Ligated DNA
Resection?
Synapsed DNA
c
5′-P
5′-OH
DNA ligation (%)
Nej1 (12 nM)
Ku (4.5 nM)
MRX (9 nM)
Dnl4-Lif1 (6 nM)
DNA ligation products
Substrate
Lane
d (i)
NHEJ (60 min, 25 °C)
MRX (1.5/9 nM)
Dnl4-Lif1
Nej1
Ku
Resection (30 min, 30 °C)
MRX (up to 40 nM)
pSae2
5′-P or 5′-OH ended DNA
ligation or synapsis
32P-probe
(ii)
5′-P Ligatable
5′-OH Non-ligatable
pSae2 (100 nM)
MRX (up to 40 nM)
Resection
MRX (nM)
Nej1 (12 nM)
Dnl4-Lif1 (6 nM)
Ku (4.5 nM)
NHEJ
32P-probe
2.5 kbp
Free probe
Lane
e
p = 8.15e-9
p = 2.28e-10
Resection (%) (normalised to no NHEJ)
No NHEJ
MRX (1.5 nM)
MRX (9 nM)
Ligation
Synapsis
NHEJ
f
p = 0.0029
p = 0.0012
Resection (%) (normalised to no NHEJ)
No NHEJ
MRX (40 nM)
Ligation
Synapsis
NHEJ
g
p = 0.0017
p = 0.0007
p = 2.62e-6
p = 1.2e-6
Resection (%) (normalised to no NHEJ)
No NHEJ
MRX (40 nM)
MRX (9 nM)
NHEJ, no MRX
NHEJ + MRX (9 nM)
h
High force (4 pN)
Low force
High force (4 pN)
Amplitude (nm)
NHEJ proteins
Synapsis
i
Probability Density
Lifetime (s)
NHEJ
NHEJ (Dnl4 D284A)
NHEJ + MRX

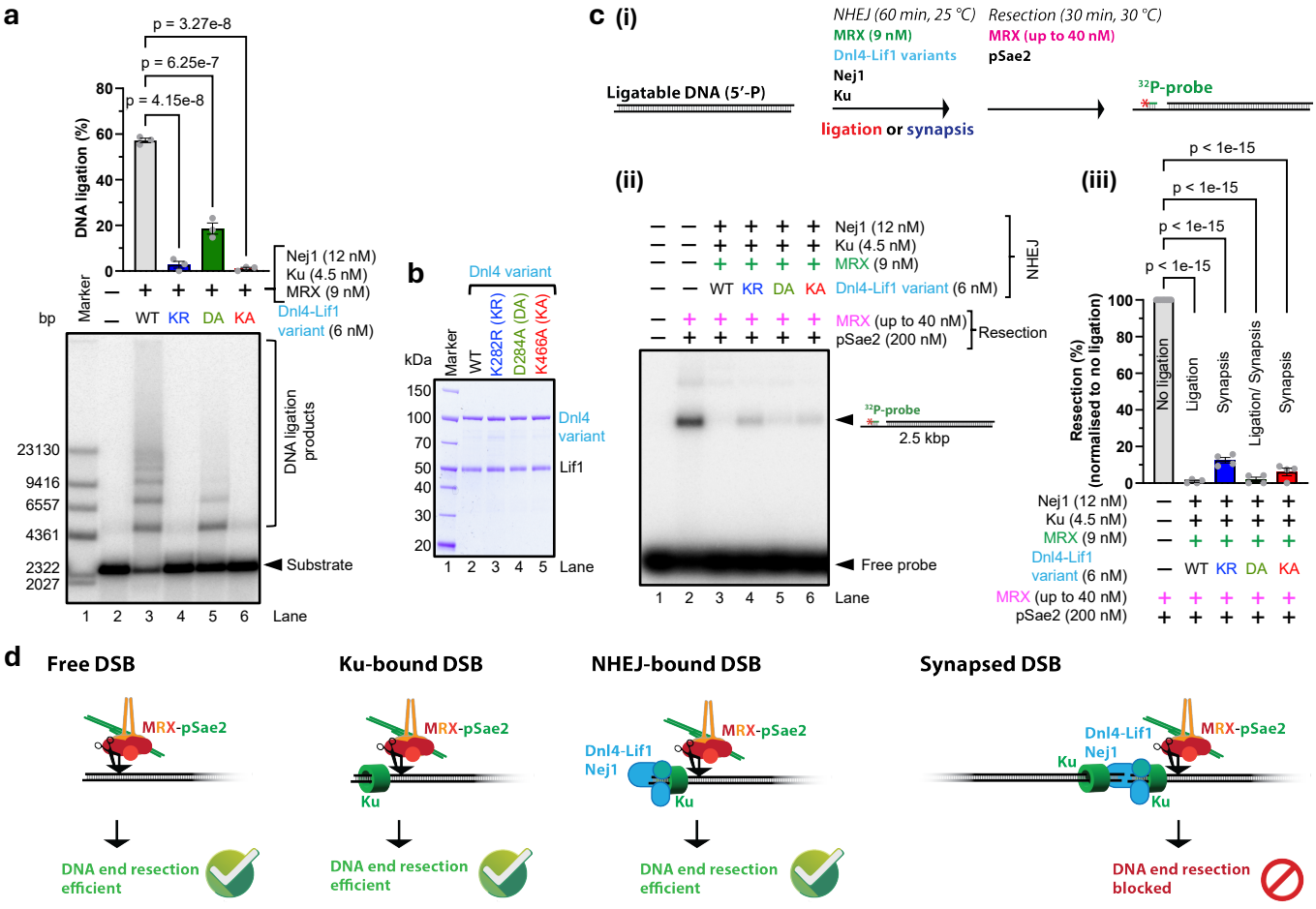
a
p = 3.27e-8
p = 6.25e-7
p = 4.15e-8
DNA ligation (%)
Marker
Nej1 (12 nM)
Ku (4.5 nM)
MRX (9 nM)
Dnl4-Lif1 variant (6 nM)
bp
WT KR DA KA
DNA ligation products
23130
9416
6557
4361
2322
2027
Substrate
1 2 3 4 5 6 Lane
b
Dnl4 variant
kDa
Marker
WT
K282R (KR)
D284A (DA)
K466A (KA)
150
100
70
50
40
30
20
Dnl4 variant
Lif1
1 2 3 4 5 Lane
c (i)
NHEJ (60 min, 25 °C)
MRX (9 nM)
Dnl4-Lif1 variants
Nej1
Ku
ligation or synapsis
Resection (30 min, 30 °C)
MRX (up to 40 nM)
pSae2
Ligatable DNA (5′-P)
32P-probe
(ii)
Nej1 (12 nM)
Ku (4.5 nM)
MRX (9 nM)
WT KR DA KA Dnl4-Lif1 variant (6 nM)
NHEJ
MRX (up to 40 nM)
pSae2 (200 nM)
Resection
32P-probe
2.5 kbp
Free probe
1 2 3 4 5 6 Lane
(iii)
p < 1e-15
p < 1e-15
p < 1e-15
p < 1e-15
Resection (%) (normalised to no ligation)
No ligation
Ligation
Synapsis
Ligation/ Synapsis
Synapsis
Nej1 (12 nM)
Ku (4.5 nM)
MRX (9 nM)
Dnl4-Lif1 variant (6 nM)
WT KR DA KA
MRX (up to 40 nM)
pSae2 (200 nM)
d
Free DSB
MRX-pSae2
DNA end resection efficient
Ku-bound DSB
MRX-pSae2
Ku
DNA end resection efficient
NHEJ-bound DSB
Dnl4-Lif1
Nej1
MRX-pSae2
Ku
DNA end resection efficient
Synapsed DSB
Dnl4-Lif1
Nej1
Ku
MRX-pSae2
Ku
DNA end resection blocked

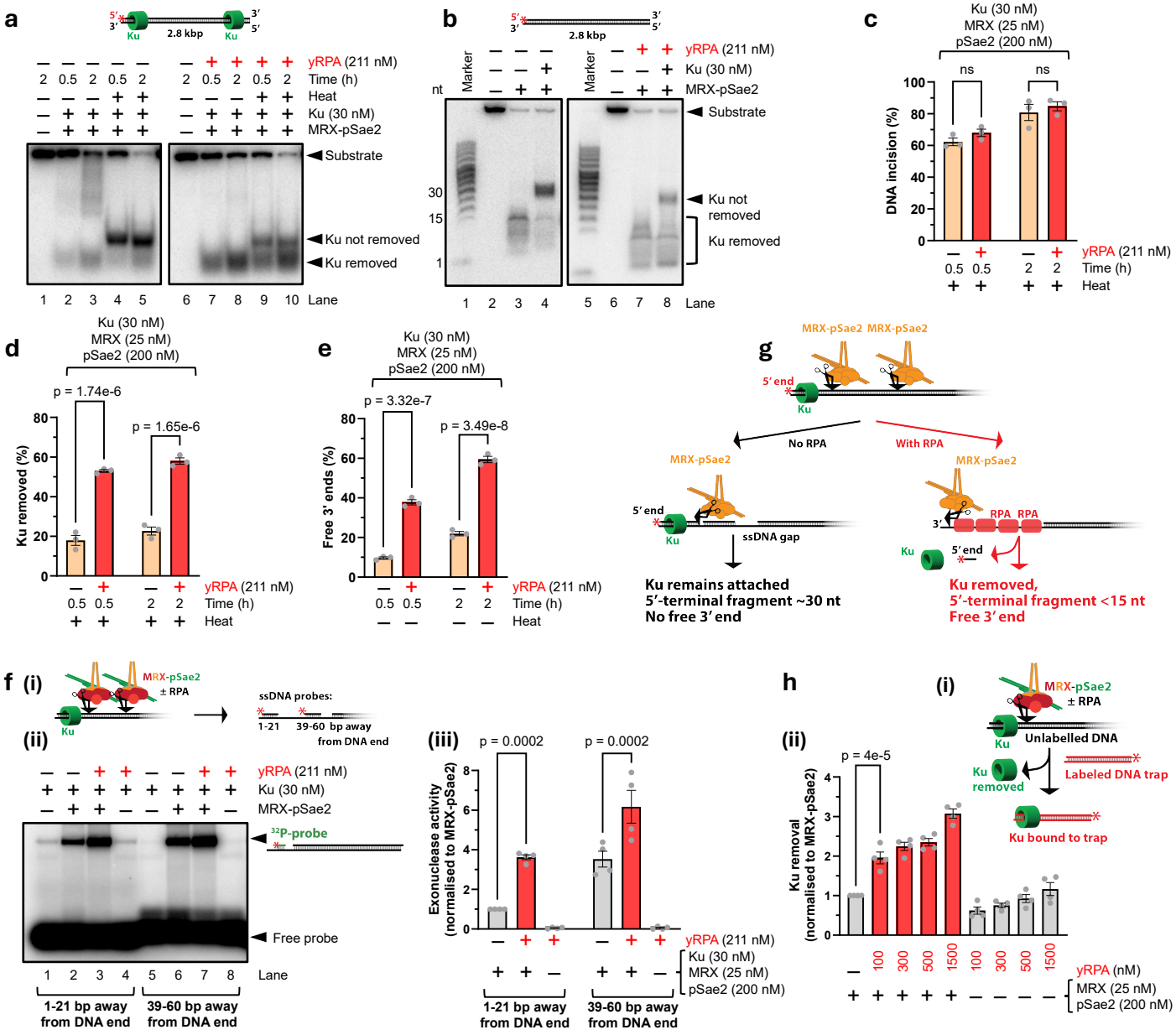
a
2.8 kbp
Ku
yRPA (211 nM)
Time (h)
Heat
Ku (30 nM)
MRX-pSae2
Substrate
Ku not removed
Ku removed
Lane
b
2.8 kbp
Marker
nt
30
15
1
yRPA (211 nM)
Ku (30 nM)
MRX-pSae2
Substrate
Ku not removed
Ku removed
Lane
c
Ku (30 nM)
MRX (25 nM)
pSae2 (200 nM)
ns
DNA incision (%)
yRPA (211 nM)
Time (h)
Heat
d
Ku (30 nM)
MRX (25 nM)
pSae2 (200 nM)
p = 1.74e-6
p = 1.65e-6
Ku removed (%)
yRPA (211 nM)
Time (h)
Heat
e
Ku (30 nM)
MRX (25 nM)
pSae2 (200 nM)
p = 3.32e-7
p = 3.49e-8
Free 3' ends (%)
yRPA (211 nM)
Time (h)
Heat
g
MRX-pSae2
5' end
Ku
No RPA
With RPA
ssDNA gap
RPA
Ku remains attached
5'-terminal fragment ~30 nt
No free 3' end
Ku removed,
5'-terminal fragment <15 nt
Free 3' end
f
(i)
MRX-pSae2
± RPA
Ku
ssDNA probes:
1-21
39-60 bp away
from DNA end
(ii)
yRPA (211 nM)
Ku (30 nM)
MRX-pSae2
32P-probe
Free probe
Lane
1-21 bp away
from DNA end
39-60 bp away
from DNA end
(iii)
p = 0.0002
p = 0.0002
Exonuclease activity
(normalised to MRX-pSae2)
yRPA (211 nM)
Ku (30 nM)
MRX (25 nM)
pSae2 (200 nM)
1-21 bp away
from DNA end
39-60 bp away
from DNA end
h
(i)
MRX-pSae2
± RPA
Ku
Unlabelled DNA
Ku
removed
Labeled DNA trap
Ku bound to trap
(ii)
p = 4e-5
Ku removal
(normalised to MRX-pSae2)
yRPA (nM)
MRX (25 nM)
pSae2 (200 nM)

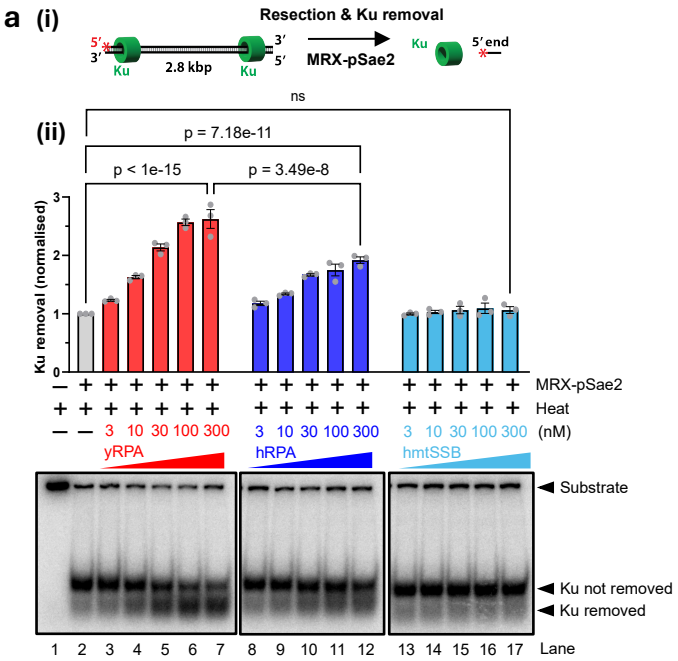
a (i)
Resection & Ku removal
5′
3′
Ku
2.8 kbp
Ku
3′
5′
MRX-pSae2
Ku
5′end
(ii)
ns
p = 7.18e-11
p < 1e-15
p = 3.49e-8
Ku removal (normalised)
0
1
2
3
MRX-pSae2
Heat
3 10 30 100 300
3 10 30 100 300
3 10 30 100 300
(nM)
yRPA
hRPA
hmtSSB
Substrate
Ku not removed
Ku removed
1 2 3 4 5 6 7 8 9 10 11 12 13 14 15 16 17
Lane

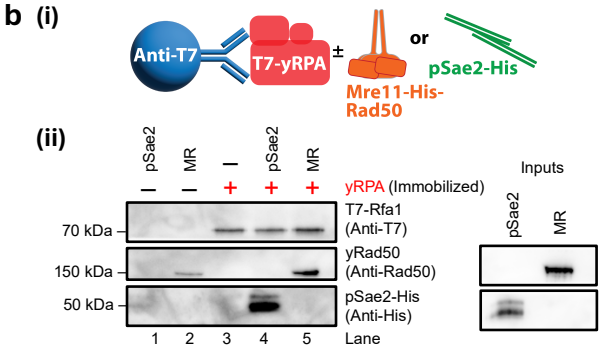
b (i)
Anti-T7
T7-yRPA
±
or
pSae2-His
Mre11-His-
Rad50
(ii)
pSae2
MR
pSae2
MR
Inputs
yRPA (Immobilized)
T7-Rfa1
(Anti-T7)
yRad50
(Anti-Rad50)
pSae2-His
(Anti-His)
70 kDa
150 kDa
50 kDa
pSae2
MR
1 2 3 4 5
Lane

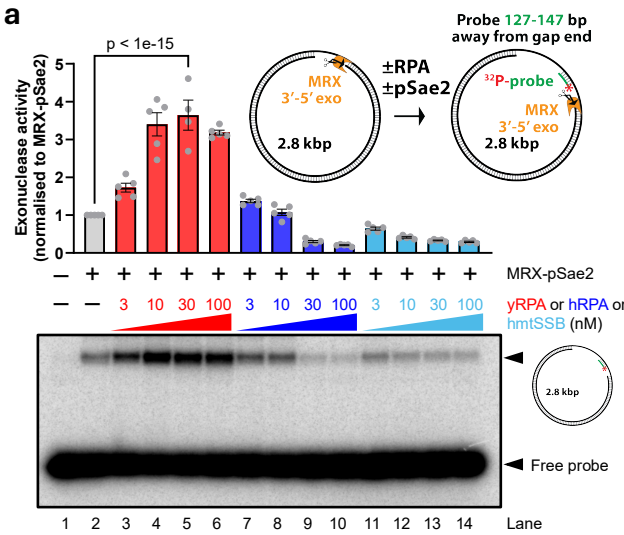
a
p < 1e-15
Exonuclease activity (normalised to MRX-pSae2)
MRX 3′-5′ exo
2.8 kbp
±RPA
±pSae2
Probe 127-147 bp away from gap end
32P-probe
MRX 3′-5′ exo
2.8 kbp
MRX-pSae2
yRPA or hRPA or hmtSSB (nM)
2.8 kbp
Free probe
1 2 3 4 5 6 7 8 9 10 11 12 13 14 Lane

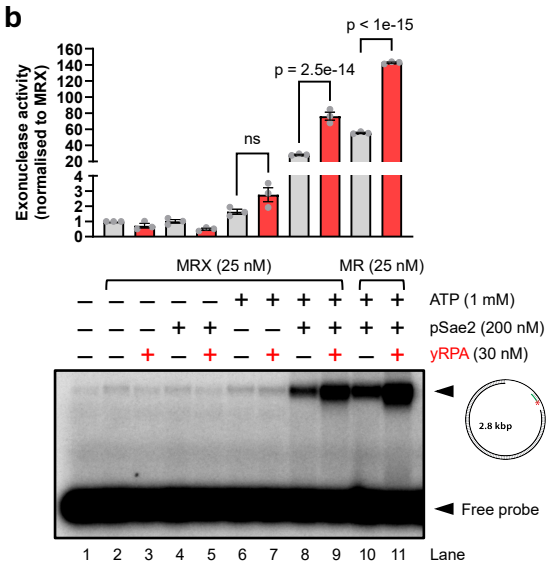
b
p < 1e-15
p = 2.5e-14
ns
Exonuclease activity (normalised to MRX)
MRX (25 nM)
MR (25 nM)
ATP (1 mM)
pSae2 (200 nM)
yRPA (30 nM)
2.8 kbp
Free probe
1 2 3 4 5 6 7 8 9 10 11 Lane

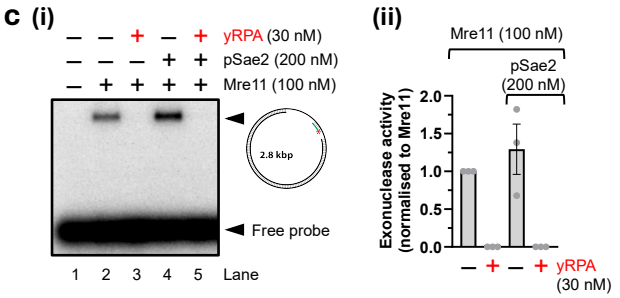
c (i)
yRPA (30 nM)
pSae2 (200 nM)
Mre11 (100 nM)
2.8 kbp
Free probe
1 2 3 4 5 Lane
(ii)
Mre11 (100 nM)
pSae2 (200 nM)
Exonuclease activity (normalised to Mre11)
yRPA (30 nM)

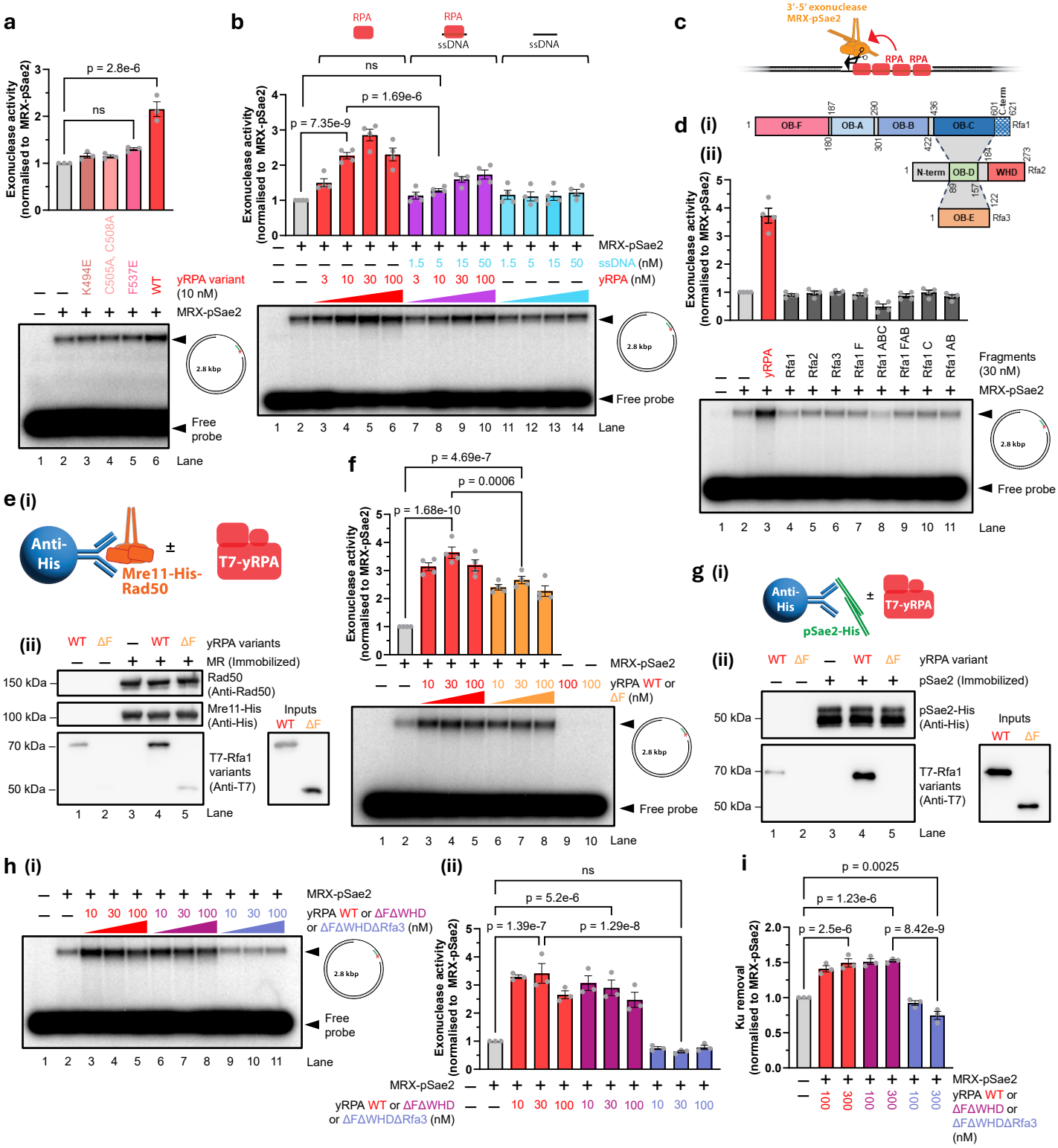
a
Exonuclease activity (normalised to MRX-pSae2)
p = 2.8e-6
ns
K494E
C505A, C508A
F537E
WT
yRPA variant (10 nM)
MRX-pSae2
2.8 kbp
Free probe
Lane
b
RPA
RPA
ssDNA
ssDNA
ns
p = 1.69e-6
p = 7.35e-9
MRX-pSae2
ssDNA (nM)
yRPA (nM)
Free probe
c
3′-5′ exonuclease
MRX-pSae2
RPA RPA
d (i)
OB-F
OB-A
OB-B
OB-C
Rfa1
N-term
OB-D
WHD
Rfa2
OB-E
Rfa3
(ii)
yRPA
Rfa1
Rfa2
Rfa3
Rfa1 F
Rfa1 ABC
Rfa1 FAB
Rfa1 C
Rfa1 AB
Fragments (30 nM)
MRX-pSae2
Free probe
e (i)
Anti-His
Mre11-His-Rad50
T7-yRPA
(ii)
yRPA variants
MR (Immobilized)
Rad50 (Anti-Rad50)
Mre11-His (Anti-His)
Inputs
T7-Rfa1 variants (Anti-T7)
150 kDa
100 kDa
70 kDa
50 kDa
f
p = 4.69e-7
p = 0.0006
p = 1.68e-10
MRX-pSae2
yRPA WT or ΔF (nM)
Free probe
g (i)
Anti-His
pSae2-His
T7-yRPA
(ii)
yRPA variant
pSae2 (Immobilized)
pSae2-His (Anti-His)
Inputs
T7-Rfa1 variants (Anti-T7)
h (i)
MRX-pSae2
yRPA WT or ΔFΔWHD or ΔFΔWHDΔRfa3 (nM)
Free probe
(ii)
ns
p = 5.2e-6
p = 1.39e-7
p = 1.29e-8
i
p = 0.0025
p = 1.23e-6
p = 2.5e-6
p = 8.42e-9
Ku removal (normalised to MRX-pSae2)
MRX-pSae2
yRPA WT or ΔFΔWHD or ΔFΔWHDΔRfa3 (nM)

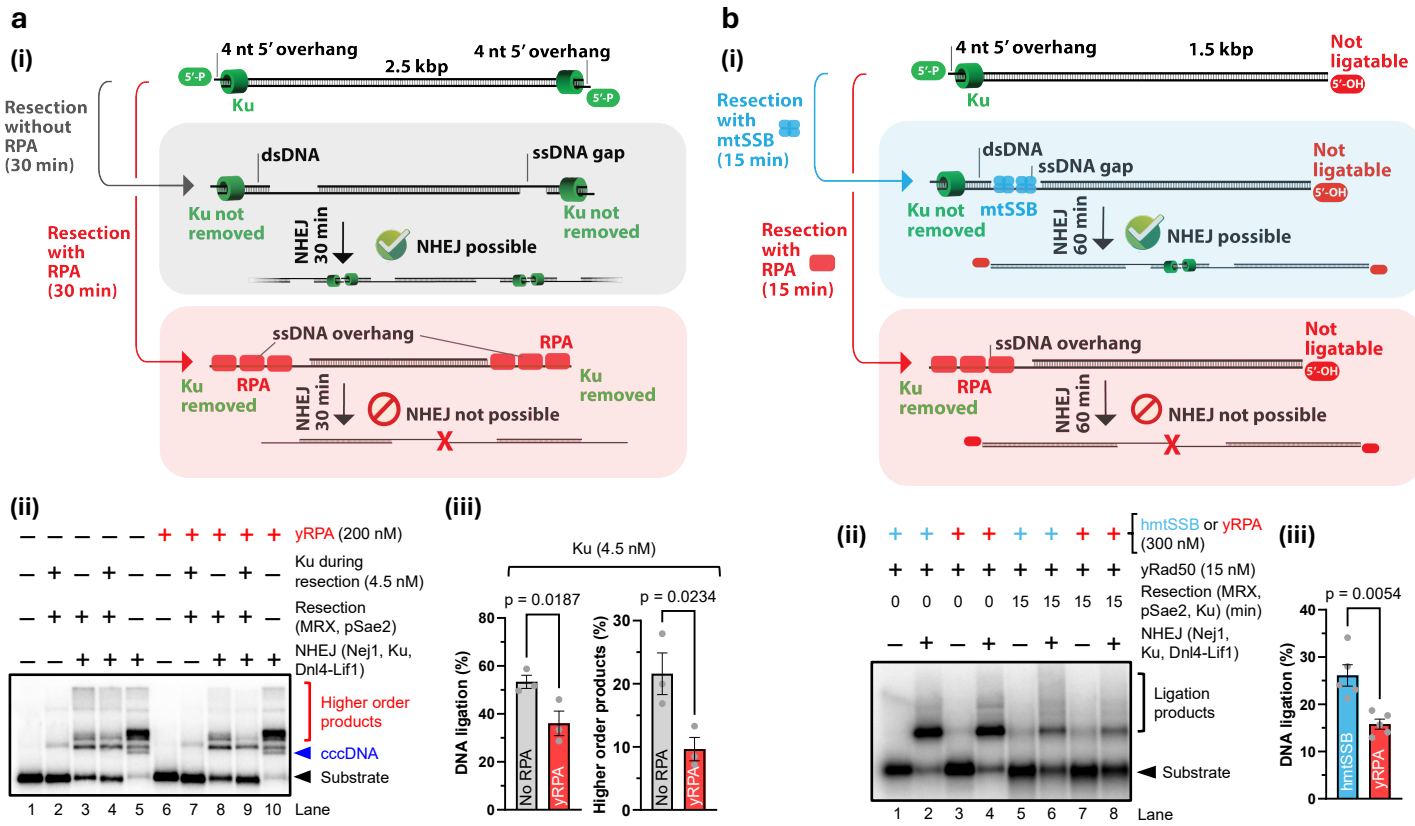
a
(i)
4 nt 5′ overhang
2.5 kbp
4 nt 5′ overhang
5′-P
Ku
5′-P
Resection without RPA (30 min)
dsDNA
ssDNA gap
Ku not removed
NHEJ 30 min
NHEJ possible
Ku not removed
Resection with RPA (30 min)
ssDNA overhang
RPA
Ku removed
RPA
NHEJ 30 min
NHEJ not possible
Ku removed
b
(i)
4 nt 5′ overhang
1.5 kbp
Not ligatable
5′-P
Ku
5′-OH
Resection with mtSSB (15 min)
dsDNA
ssDNA gap
Not ligatable
5′-OH
Ku not removed
mtSSB
NHEJ 60 min
NHEJ possible
Resection with RPA (15 min)
ssDNA overhang
Not ligatable
5′-OH
Ku removed
RPA
NHEJ 60 min
NHEJ not possible
(ii)
yRPA (200 nM)
Ku during resection (4.5 nM)
Resection (MRX, pSae2)
NHEJ (Nej1, Ku, Dnl4-Lif1)
Higher order products
cccDNA
Substrate
1 2 3 4 5 6 7 8 9 10 Lane
(iii)
Ku (4.5 nM)
p = 0.0187
p = 0.0234
DNA ligation (%)
Higher order products (%)
No RPA
yRPA
(ii)
hmtSSB or yRPA (300 nM)
yRad50 (15 nM)
Resection (MRX, pSae2, Ku) (min)
0 0 0 0 15 15 15 15
NHEJ (Nej1, Ku, Dnl4-Lif1)
Ligation products
Substrate
1 2 3 4 5 6 7 8 Lane
(iii)
p = 0.0054
DNA ligation (%)
hmtSSB
yRPA

Supplementary Information

NHEJ-mediated DNA synapsis and RPA-driven MRX exonuclease balance DNA end resection to control DSB repair

Stefan Braunshier, Elda Cannavo, Vincent Morin, Sriram K. Kesarimangalam, Ananya Acharya, Giordano Reginato, Florian Morati, Virginie Ropars, Raphael Guerois, Jean-Baptiste Charbonnier, Fredrik Westerlund, Terence Strick and Petr Cejka

This file contains:

- 10 Supplementary Figures with legends
- 2 Supplementary Data Tables

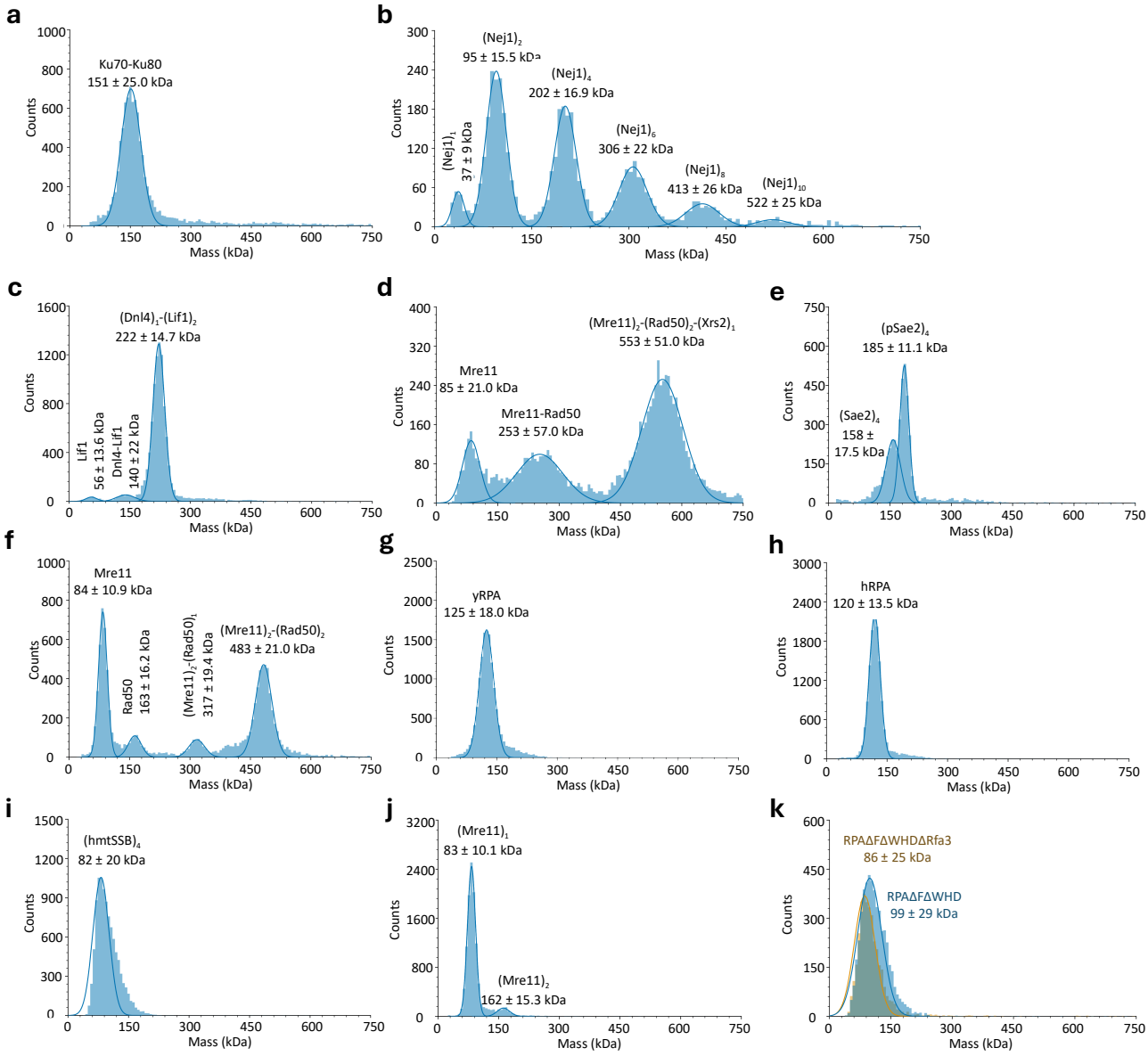

Supplementary Figure 1: Mass photometry analysis of the recombinant proteins used in this study.

a, yKu (25 nM), theoretical molecular weight: Ku70-Ku80, 142 kDa.

b, Nej1 (50 nM), theoretical molecular weights: $(Nej1)_1$, 40 kDa; $(Nej1)_2$, 80 kDa; $(Nej1)_4$, 160 kDa; $(Nej1)_6$, 240 kDa; $(Nej1)_8$, 320 kDa; $(Nej1)_{10}$, 400 kDa.

c, Dnl4-Lif1 (50 nM), theoretical molecular weights: Lif1, 49 kDa; $(Dnl4\text{-}Lif1)_1$, 158 kDa; $(Dnl4)_1\text{-}(Lif1)_2$, 207 kDa.

d, MRX (50 nM), theoretical molecular weights: Mre11, 79 kDa; Mre11-Rad50, 231 kDa; $(Mre11)_2\text{-}(Rad50)_2\text{-}(Xrs2)_1$, 561 kDa. MRX is known to oligomerize, and higher-order oligomers are not detectable by the mass photometer, possibly leading to an overestimation of the amount of uncomplexed Mre11.

e, Sae2 (50 nM), theoretical molecular weights: $(Sae2)_4$, 164 kDa; $(pSae2)_4$, 215 kDa.

f, MR (50 nM), theoretical molecular weights: Mre11, 79 kDa; Rad50, 152 kDa; $(Mre11)_2\text{-}(Rad50)_1$, 310 kDa; $(Mre11)_2\text{-}(Rad50)_2$, 462 kDa. As is the case with MRX, MR is also able to oligomerize. Therefore, due to limitations of the instrument, the amount of uncomplexed Mre11 might be overestimated.

g, yeast RPA (50 nM), theoretical molecular weight: yRPA, 116 kDa.

h, human RPA (50 nM), theoretical molecular weight: hRPA, 117 kDa.

i, human mitochondrial SSB (100 nM), theoretical molecular weight: $(hmtSSB)_4$, 63 kDa.

j, Mre11 (50 nM), theoretical molecular weights: Mre11, 79 kDa; $(Mre11)_2$, 158 kDa.

k, Comparison between RPAΔFΔWHD (50 nM, in blue, theoretical molecular weight 84 kDa) and RPAΔFΔWHDΔRfa3 (50 nM, in gold, theoretical molecular weight 70 kDa).

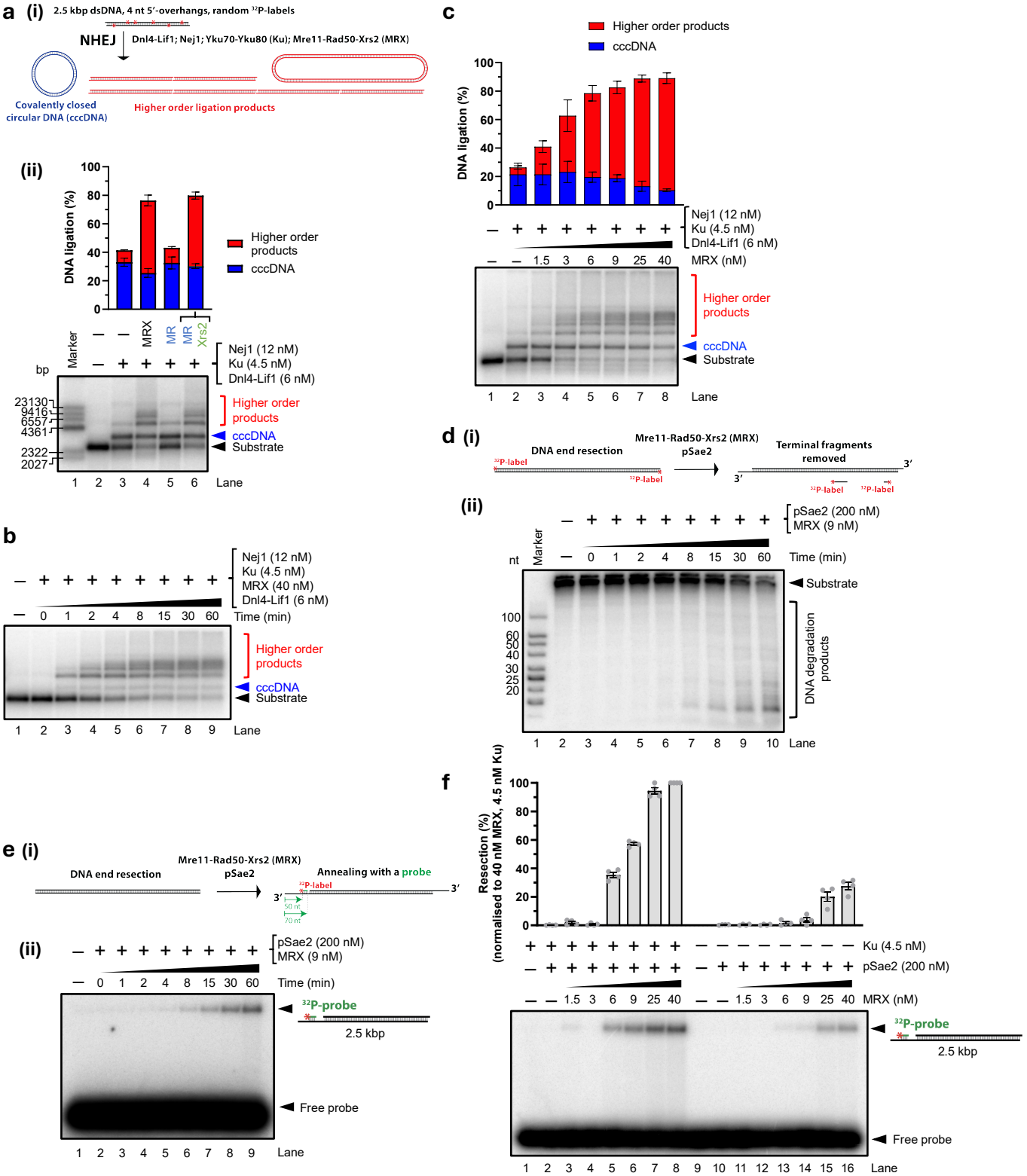

Supplementary Figure 2: Monitoring the efficacy of reconstituted NHEJ and DNA end resection assays.

a, Non-homologous end-joining assays with indicated proteins, and either MRX (9 nM), MR (9 nM) or MR (9 nM) added together with separately expressed Xrs2 (9 nM). **(i)** A schematic of the assay. Red asterisks (*) represent the random positions of the radioactive label. **(ii)** Top, quantitation of DNA ligation. Averages shown; error bars, s.e.m.; n = 4 independent experiments except for lanes 5 and 6, where n = 3. Bottom, a representative image of three independent experiments.

b, Non-homologous end-joining assay as a kinetic experiment. A representative image of three independent experiments is shown.

Continued on next page.

Continued from previous page.

Supplementary Figure 2: Monitoring the efficacy of reconstituted NHEJ and DNA end resection assays.

c, Non-homologous end-joining assay and its dependence on MRX concentration. Top, quantitation of DNA ligation. Averages shown; error bars, s.e.m.; n = 3 independent experiments. Bottom, a representative image of three independent experiments.

d, DNA end resection assays with 5'-terminally labeled DNA as a kinetic experiment. **(i)** A schematic of the assay. The red asterisk (*) represents the position of the radioactive label. **(ii)** A representative image of three independent experiments. The products were separated on 15% denaturing polyacrylamide gels.

e, DNA end resection assay, monitored by oligonucleotide annealing, as a kinetic experiment. **(i)** A schematic of the assay. The red asterisk (*) represents the position of the radioactive label. **(ii)** A representative image of three independent experiments.

f, DNA end resection assay, monitored by oligonucleotide annealing, as a function of MRX concentration, in the presence or absence of Ku. Top, quantitation of DNA resection. Values were normalized to lane 8. Averages shown; error bars, s.e.m.; n = 4 independent experiments. Bottom, a representative image of four independent experiments.

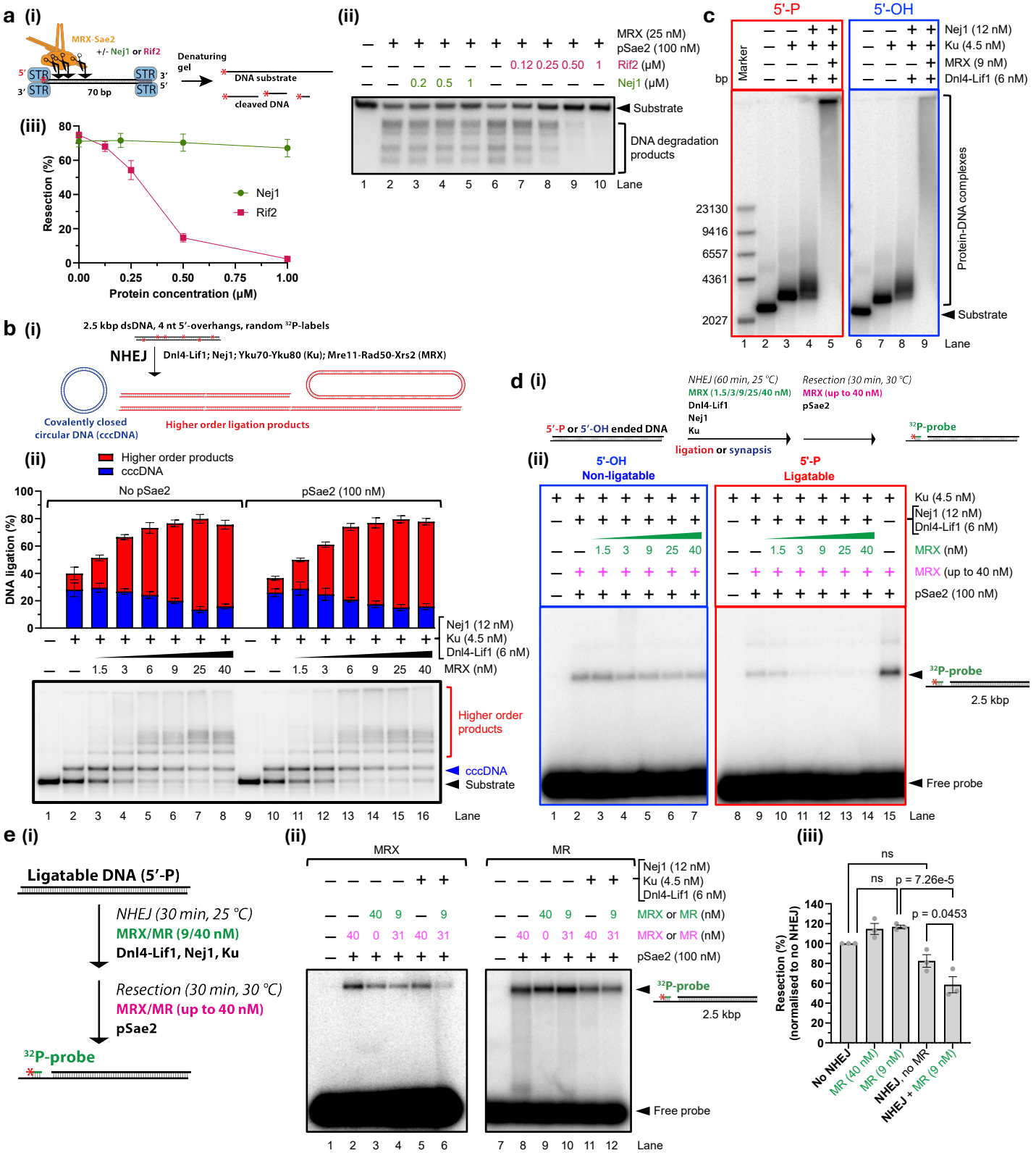

Supplementary Figure 3: Interplay of non-homologous end-joining and DNA end resection.

a, Endonuclease assays monitoring MRX-pSae2-mediated incision of end-blocked dsDNA in the presence or absence of Nej1 or Rif2. **(i)** A schematic of the endonuclease assay. The red asterisk (*) represents the position of the radioactive label. **(ii)** A representative image of three independent experiments. The products were separated on 15% denaturing polyacrylamide gels. **(iii)** Quantitation of DNA resection from experiments shown in **(ii)**. Averages shown; error bars, s.e.m.; n = 3 independent experiments.

Continued on next page.

Continued from previous page.

Supplementary Figure 3: Interplay of non-homologous end-joining and DNA end resection.

b, Phosphorylated Sae2 does not affect end-joining. **(i)** A schematic of the end-joining assay. Red asterisks (*) represent the random positions of the radioactive label. **(ii)** A representative image of three independent experiments.

c, Electrophoretic mobility shift assays (EMSA) with the indicated proteins and dsDNA containing either ligatable (5'-P) or non-ligatable (5'-OH) DNA ends. In the case of the 5'-OH substrate, the assay detects only DNA synapsis and protein-DNA binding. In contrast, the 5'-P DNA can be ligated as well, leading to a band of lower mobility (compare lanes 5 and 9). The products were separated on 0.6% agarose gels in TAE. A representative image of three independent experiments is shown.

d, Impact of NHEJ assembly on DNA end resection. **(i)** A schematic of the oligonucleotide annealing assay. **(ii)** A representative image of three independent experiments.

e, DNA synapsis by MRX and the core NHEJ factors synergistically inhibits short-range resection. **(i)** A schematic of the oligonucleotide annealing assay. The red asterisk (*) represents the position of the radioactive label. **(ii)** Left, a representative image of six independent experiments with MRX. Right, a representative image of three independent experiments with MR. **(iii)** Quantitation of assays performed with MR shown in **(ii)**. Values are normalized to lane 8 of **(ii)**. Averages shown; error bars, s.e.m.; n = 3 independent experiments. Statistical analysis was performed using Šídák's multiple comparisons test; ns, not significant.

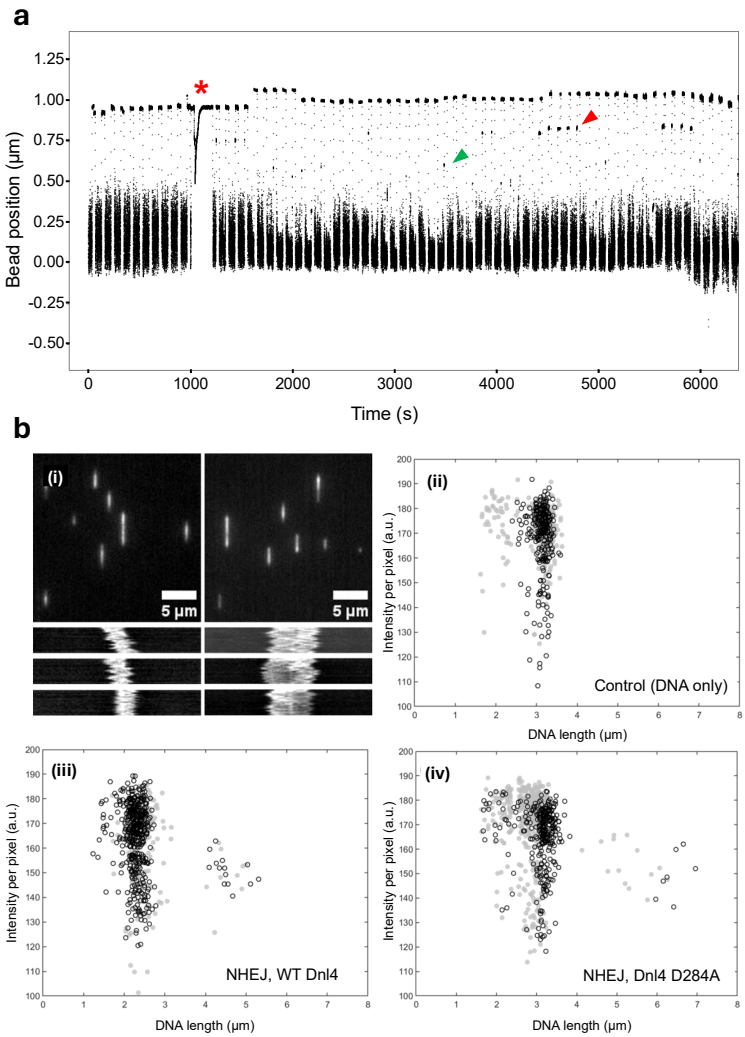

Supplementary Figure 4: Analysis of DNA end synapsis using single-molecule experiments.

a, A typical magnetic tweezer time-trace from one of the experimental conditions (1 nM yKu, 0.3 nM Dnl4-Lif1, 50 nM Nej1). Bead position is shown in black. The red asterisk denotes the moment proteins were injected into the flow cell. The red arrow highlights the DNA extension corresponding to specific synaptic events, the green arrow highlights the DNA extension corresponding to non-specific synaptic events.

b, Nanofluidic assay monitoring DNA end synapsis by the NHEJ ensemble. **(i)** Example snapshots of single-molecule images collected in nanochannels where both linear 20 kbp DNA molecules and synapsed dimers can be seen. Scale bar is 5 μm. Representative kymographs of both linear 20 kbp DNA and concatemers are shown below the snapshots. **(ii-iv)** DNA length (μm) vs. intensity (a.u.) plots for: DNA only **(ii)**, Ku + Dnl4(WT)-Lif1 + Nej1 + MRX **(iii)**, and Ku + Dnl4(D284A)-Lif1 + Nej1 + MRX **(iv)**. Each plot comprises two independent datasets, where dataset 1 is shown as light gray filled circles and dataset 2 is shown as black unfilled circles.

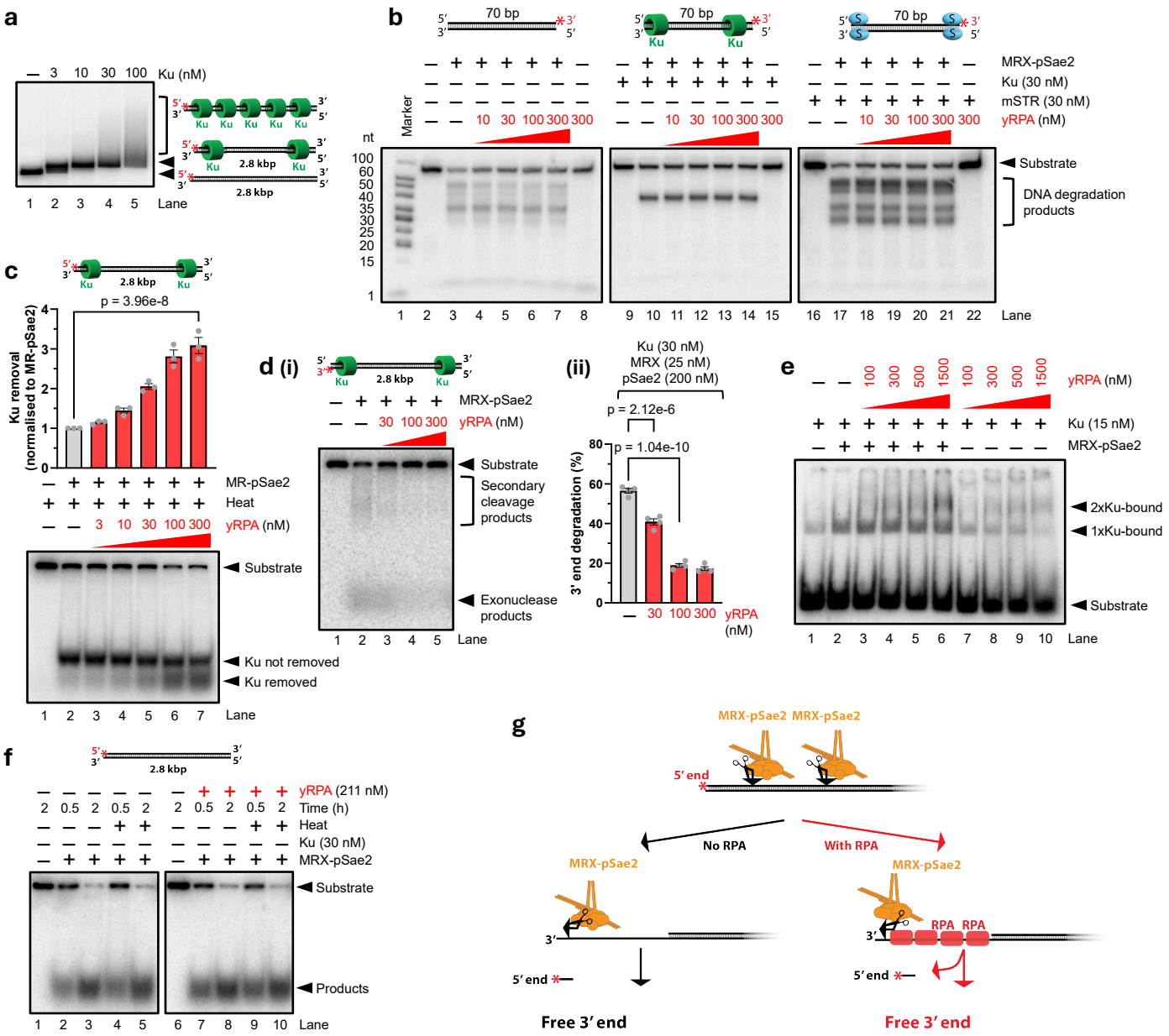

Supplementary Figure 5: Effect of RPA on the activities of the MR and MRX complexes.

a, DNA binding of Ku to dsDNA, monitored by EMSA. A representative image of two independent experiments. The products were separated on 0.6% agarose gels in TAE. The red asterisk (*) represents the position of the radioactive label.

b, RPA has no effect on the endonuclease of MRX (25 nM)-pSae2 (200 nM). Top, a cartoon of the substrates used. The position of monovalent streptavidin (mSTR) is marked with an S. The red asterisk (*) represents the position of the radioactive label. Bottom, a representative image of three independent experiments. The products were separated on 15% denaturing polyacrylamide gels.

c, The effect of RPA concentration on Ku removal by MR (25 nM)-pSae2 (200 nM). Top, a cartoon of the substrate used. The red asterisk (*) represents the position of the radioactive label. Middle, quantitation of Ku removal by MR-pSae2. Values were normalized to lane 2. Averages shown; error bars, s.e.m.; n = 3 independent experiments. Statistical analysis was performed using Šídák's multiple comparisons test. Bottom, a representative image of three independent experiments.

Continued on next page.

Continued from previous page.

Supplementary Figure 5: Effect of RPA on the activities of the MR and MRX complexes.

d, RPA protects the 3' end from degradation by MRX (25 nM)-pSae2 (200 nM). **(i)** Top, a cartoon of the substrate used. The red asterisk (*) represents the position of the radioactive label. Bottom, a representative image of three independent experiments. **(ii)** Quantitation of 3'-end degradation from experiments shown in **(i)**. Averages shown; error bars, s.e.m.; n = 4 independent experiments. Statistical analysis was performed using Šídák's multiple comparisons test.

e, Ku capture experiment showing Ku removal by MRX (25 nM)-pSae2 (200 nM). Ku displacement is monitored by binding to a radioactively labeled trap. A representative image of four independent experiments is shown. For quantitation and cartoon of the assay, see Fig. 4h.

f, RPA has no effect on the processing of DNA ends by MRX (25 nM)-pSae2 (200 nM) in the absence of Ku. Top, a cartoon of the substrate used. The red asterisk (*) represents the position of the radioactive label. Bottom, a representative image of three independent experiments.

g, A cartoon showing that MRX-pSae2 can efficiently process DNA ends without Ku, to produce free 3' ends.

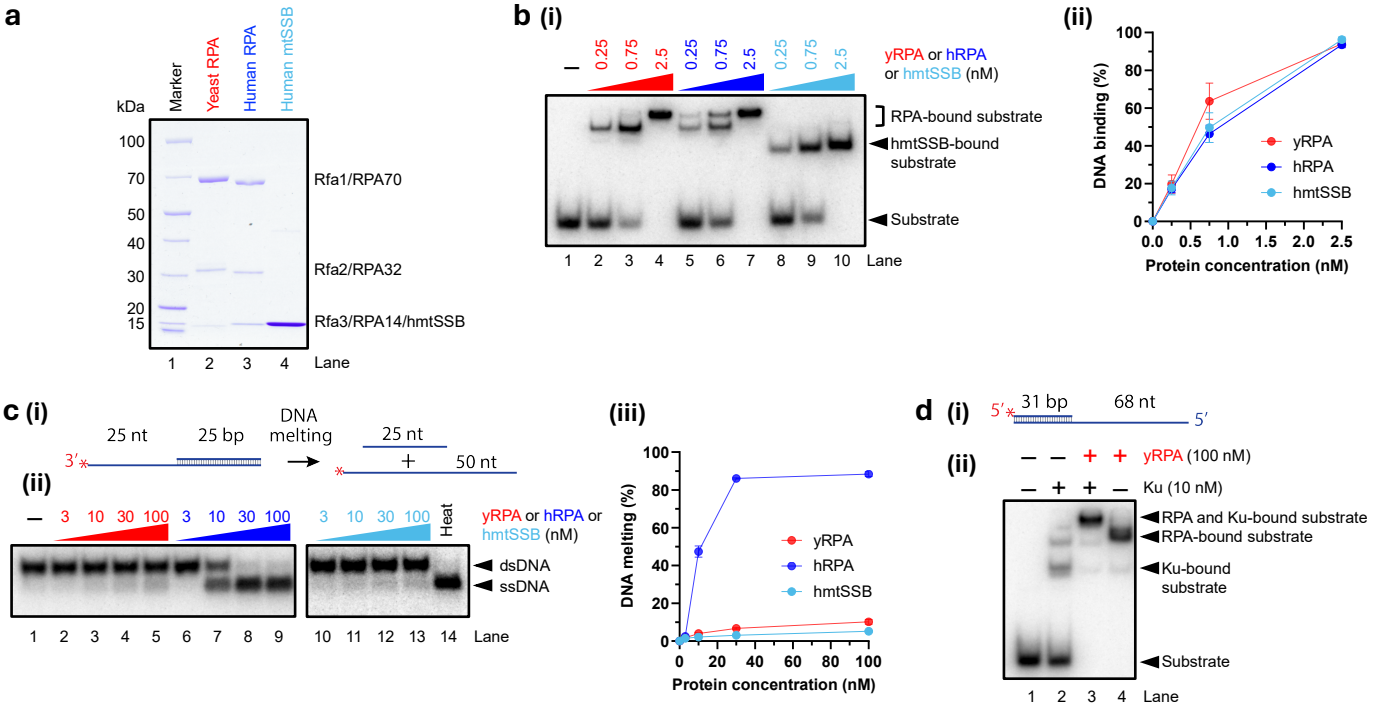

Supplementary Figure 6: Interplay of MRX-pSae2 with yeast RPA and non-cognate variants.

a, Recombinant yeast and human RPA proteins (yRPA, hRPA) and human mitochondrial SSB (hmtSSB) used in this study. The polyacrylamide gels were stained with Coomassie Brilliant Blue.

b, Electrophoretic mobility shift assays monitoring the binding of 50 nt-long ssDNA by yeast RPA (yRPA), human RPA (hRPA) and human mitochondrial SSB (hmtSSB). The products were separated on 6% native polyacrylamide gels in TAE. **(i)** A representative image of three independent experiments. **(ii)** Quantitation of ssDNA-binding by yRPA, hRPA and hmtSSB from experiments shown in **(i)**. Averages shown; error bars, s.e.m.; n = 3 independent experiments.

c, DNA melting by yRPA, hRPA and hmtSSB. **(i)** A cartoon of the substrate used. The red asterisk (*) represents the position of the radioactive label. **(ii)** A representative image of three independent experiments. The products were separated on 8% native polyacrylamide gels in TBE. **(iii)** Quantitation of DNA melting from experiments shown in **(ii)**. Averages shown; error bars, s.e.m.; n = 3 independent experiments.

d, RPA alone does not displace Ku from 5'-overhanged DNA. **(i)** A cartoon of the substrate used. The red asterisk (*) represents the position of the radioactive label. **(ii)** Electrophoretic mobility shift assays with yeast RPA and Ku and a 5'-overhanged substrate. The products were separated on 4% native polyacrylamide gels in TAE. A representative image of three independent experiments is shown. RPA and Ku can bind the DNA substrate simultaneously.

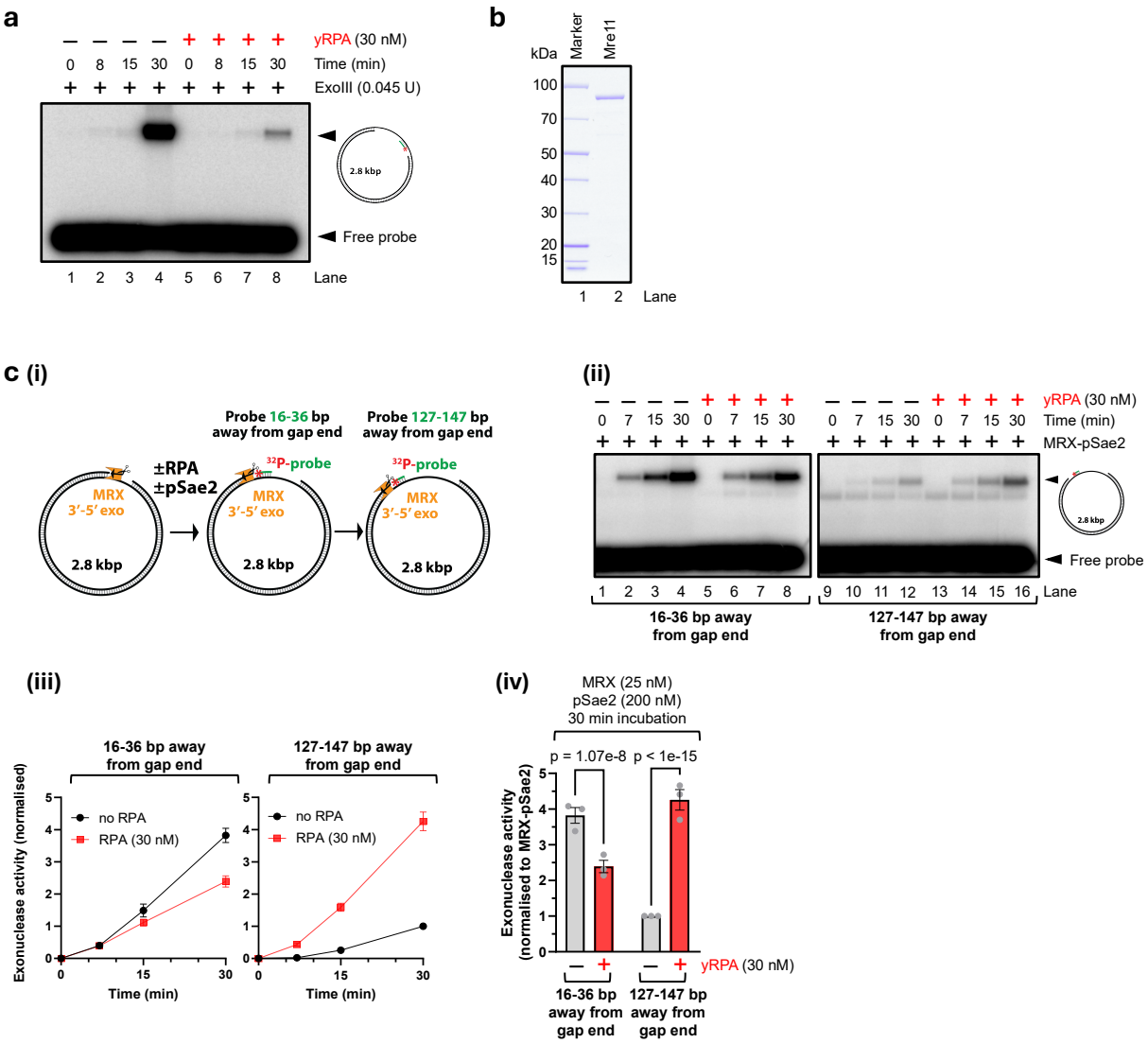

Supplementary Figure 7: RPA stimulates the processivity of the MRX-pSae2 exonuclease in a species-specific manner.

a, The exonuclease activity of ExoIII is inhibited by yeast RPA (yRPA). Oligonucleotide annealing assay used to monitor the 3'-5' exonuclease activity of *E. coli* ExoIII on a gapped plasmid. A representative image of three independent experiments is shown.

b, Recombinant yeast Mre11 used in this study. The polyacrylamide gels were stained with Coomassie Brilliant Blue.

c, Oligonucleotide annealing assay used to monitor the exonuclease activity of MRX (25 nM)-pSae2 (200 nM) on a gapped plasmid, probed either 16-36 or 127-147 bp away from the gap. **(i)** A schematic of the oligonucleotide annealing assays shown in **(ii)**. The exonuclease activity of MRX-pSae2, and the effect of RPA, was monitored in proximity to the gap (16-36 bp away) or further away from the gap (127-147 bp). **(ii)** A representative image of three independent experiments. **(iii)** Quantitation of exonuclease assays from experiments shown in **(ii)** as a function of time. Values were normalized to lane 12. Averages shown; error bars, s.e.m.; n = 3 independent experiments. **(iv)** Quantitation of exonuclease assays. Values were normalized to lane 12. Averages shown; error bars, s.e.m.; n = 3 independent experiments. Statistical analysis was performed using Šídák's multiple comparisons test.

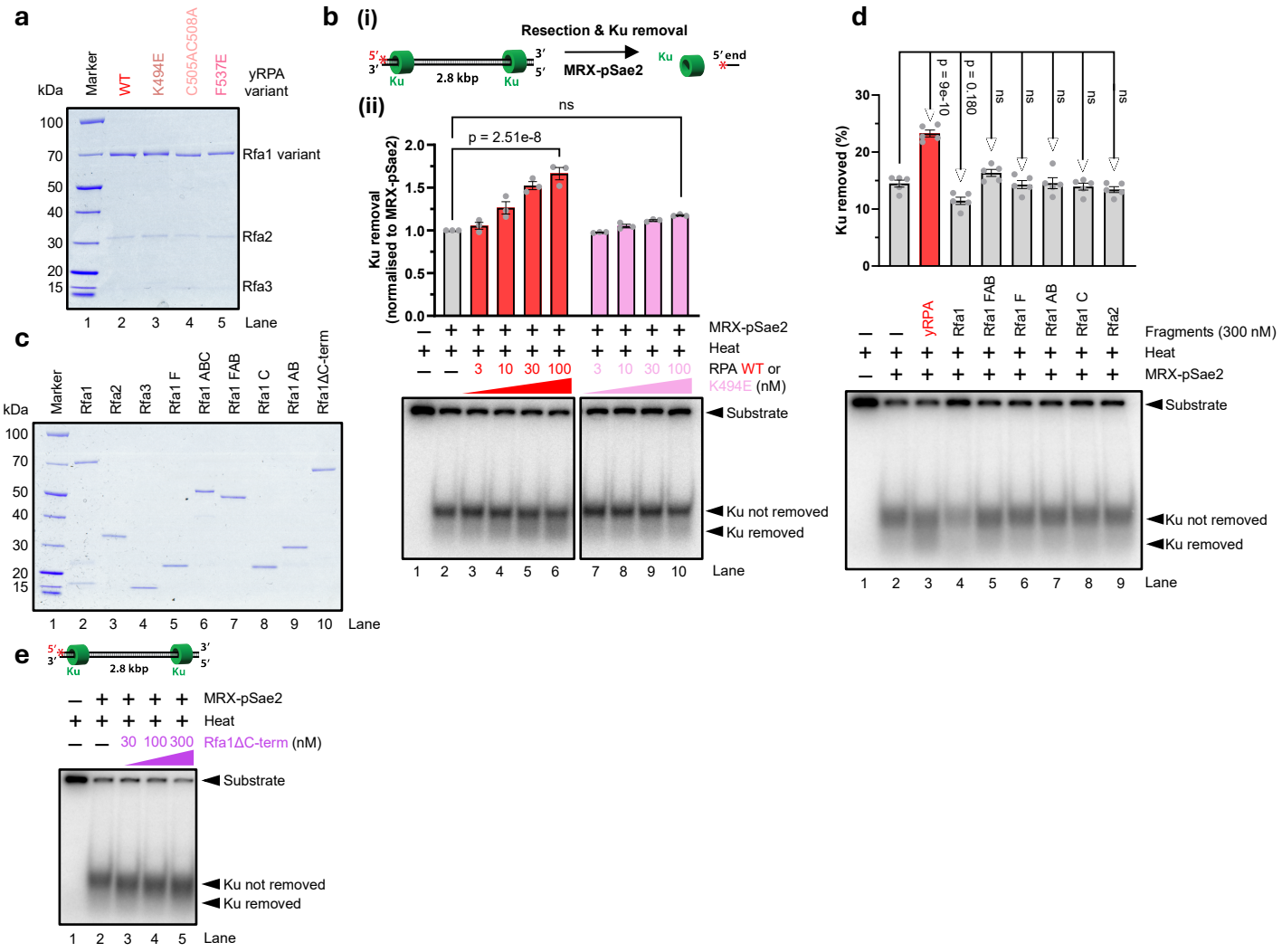

Supplementary Figure 8: Effect of various RPA mutants and fragments on MRX-pSae2-mediated Ku removal.

a, Yeast RPA point mutants used in this study. The polyacrylamide gels were stained with Coomassie Brilliant Blue.

b, DNA-binding-deficient RPA variant fails to assist MRX (25 nM)-pSae2 (200 nM) in removing Ku from DNA ends. **(i)** A cartoon of the assay. The red asterisk (*) represents the position of the radioactive label. **(ii)** Top, quantitation of Ku removal by MRX-pSae2 and its stimulation by wild-type RPA or RPA K494E (mutation in the OB-C domain of the Rfa1 subunit). Values were normalized to lane 2. Averages shown; error bars, s.e.m.; n = 3 independent experiments. Statistical analysis was performed using Šídák's multiple comparisons test; ns, not significant. Bottom, a representative image of three independent experiments.

c, Recombinant Rfa1 fragments used in this study. The polyacrylamide gels were stained with Coomassie Brilliant Blue.

d, Ku removal by MRX (25 nM)-pSae2 (200 nM) and its stimulation by RPA fragments. Assay as in panel **b**. Top, quantitation of Ku removal by MRX-pSae2, calculated as a fraction of the "Ku removed" band vs. the rest of the lane. Averages shown; error bars, s.e.m.; n = 5 independent experiments. Statistical analysis was performed using Šídák's multiple comparisons test; ns, not significant. Bottom, a representative image of five independent experiments.

e, The effect of the C-terminal domain of Rfa1 on Ku removal by MRX (25 nM)-pSae2 (200 nM). Top, a cartoon of the substrate used. The red asterisk (*) represents the position of the radioactive label. Bottom, a representative image of four independent experiments.

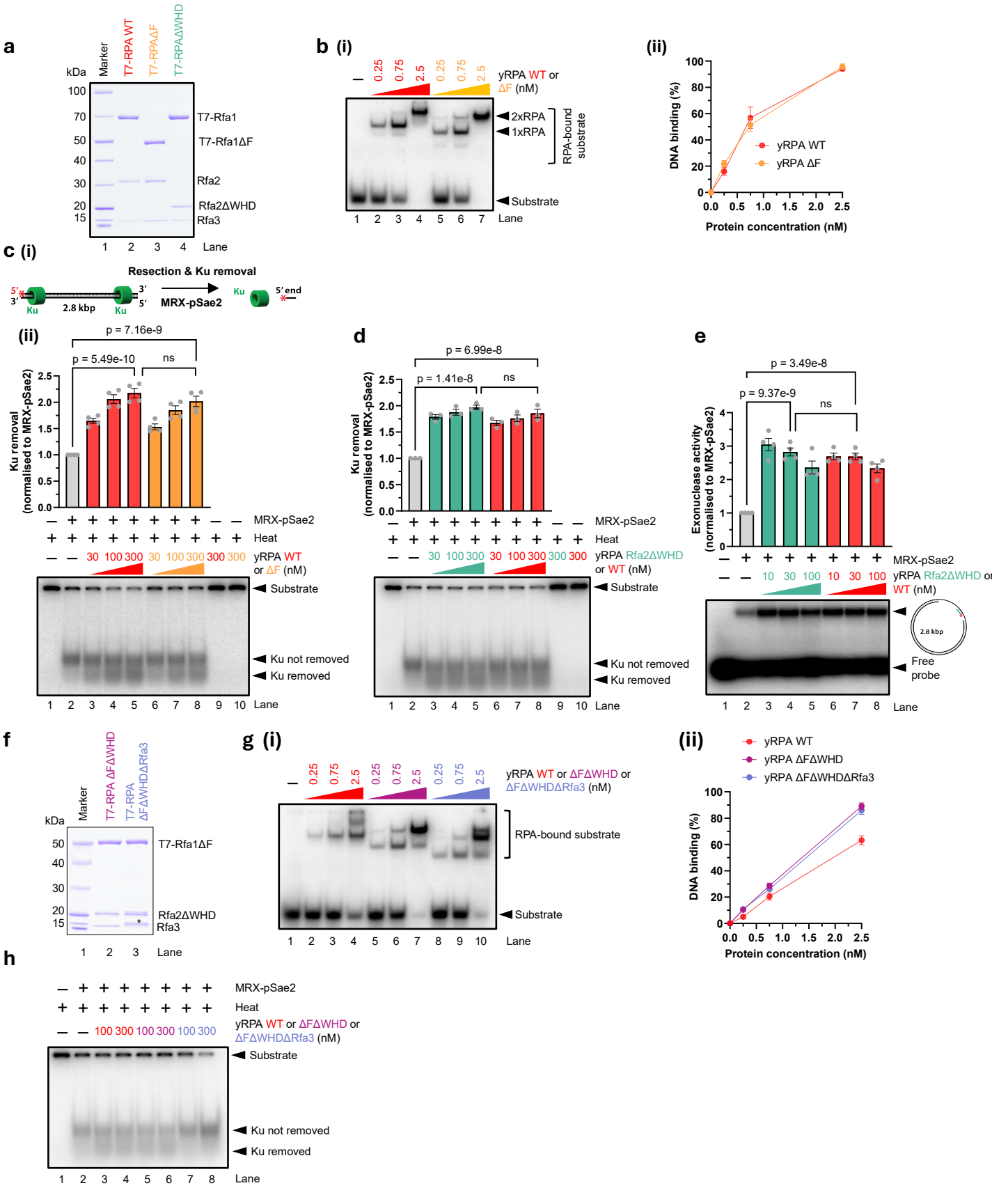

Figure legend on the next page.

Supplementary Figure 9: Effect of RPA truncations on Ku removal and exonuclease activity of MRX-pSae2.

a, RPA truncations used in this study. The polyacrylamide gels were stained with Coomassie Brilliant Blue.

b, Truncation of the Rfa1 OB-F does not affect ssDNA-binding affinity, as monitored by EMSA. **(i)** A representative image of three independent experiments. The products were separated on 6% native polyacrylamide gels in TAE. **(ii)** Quantitation of ssDNA-binding from experiments shown in **(i)**. Averages shown; error bars, s.e.m.; n = 3 independent experiments.

c, The Rfa1 OB-F domain is not essential for MRX (25 nM)-pSae2 (200 nM)-mediated Ku removal. **(i)** A cartoon of the assay. The red asterisk (*) represents the position of the radioactive label. **(ii)** Top, quantitation of Ku removal. Values were normalized to lane 2. Averages shown; error bars, s.e.m.; n = 4 independent experiments. Statistical analysis was performed using Šídák's multiple comparisons test; ns, not significant. Bottom, a representative image of four independent experiments.

d, The Rfa2 WHD domain is dispensable for MRX (25 nM)-pSae2 (200 nM)-mediated Ku removal. Top, quantitation of Ku removal. Values were normalized to lane 2. Averages shown; error bars, s.e.m.; n = 3 independent experiments. Statistical analysis was performed using Šídák's multiple comparisons test; ns, not significant. Bottom, a representative image of three independent experiments.

e, The Rfa2ΔWHD truncation of RPA does not affect the stimulation of the MRX (25 nM)-pSae2 (200 nM) exonuclease. Top, quantitation of exonuclease assays. Values were normalized to lane 2. Averages shown; error bars, s.e.m.; n = 4 independent experiments. Statistical analysis was performed using Šídák's multiple comparisons test; ns, not significant. Bottom, a representative image of four independent experiments.

f, RPA truncations used in this study. The polyacrylamide gels were stained with Coomassie Brilliant Blue. The asterisk (*) denotes a non-specific protein band.

g, Loss of Rfa3 does not affect the affinity of RPA for ssDNA, as monitored by EMSA. **(i)** A representative image of three independent experiments. The products were separated on 6% native polyacrylamide gels in TAE. **(ii)** Quantitation of ssDNA-binding from experiments shown in **(i)**. Averages shown; error bars, s.e.m.; n = 3 independent experiments.

h, Loss of Rfa3 abolishes RPA-mediated Ku removal by MRX-pSae2. A representative image of three independent experiments is shown.

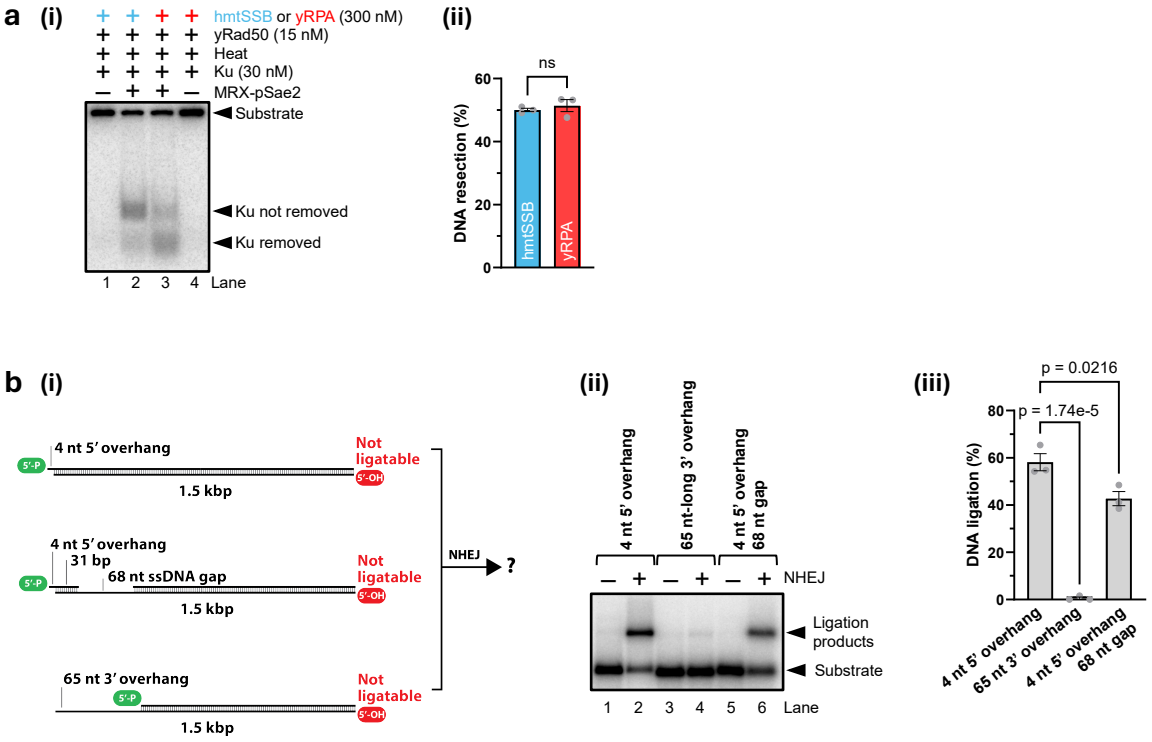

Supplementary Figure 10: Internal gaps at DSBs limit but do not eliminate NHEJ.

a, The efficiency of DNA end resection by MRX-pSae2 under assay conditions as in Fig. 8b. yRPA and hmtSSB do not affect DNA incision by MRX-pSae2. **(i)** MRX (25 nM) and pSae2 (200 nM)-mediated resection and Ku removal assay on a 5'-labeled 1.5 kbp-long PCR product. A representative image of three independent experiments is shown. **(ii)** Quantitation of DNA resection efficiency (calculated as substrate utilization) from experiments shown in **(i)**. Averages shown; error bars, s.e.m.; n = 3 independent experiments. Statistical analysis was performed using Šídák's multiple comparisons test; ns, not significant.

b, Internally gapped DNA is ligatable by NHEJ. **(i)** A cartoon of the substrates representing resection intermediates that were tested for end-joining. **(ii)** End-joining assay of resection intermediates. A representative image of three independent experiments is shown. **(iii)** Quantitation of DNA ligation efficiency from experiments shown in **(ii)**. Averages shown; error bars, s.e.m.; n = 3 independent experiments. Statistical analysis was performed using Šídák's multiple comparisons test.

Supplementary Table 1: Oligonucleotides used for substrate preparation in this study.

[B] and [TB] represent the positions of biotin modifications in the DNA. **Z** represents a thymine coupled to an azido group and **Y** represents a thymine coupled to a DBCO group.

Oligonucleotide name	DNA sequence
PC209	GATGCATGAGGTGGAGTACGCGCCCGGGGAGCCCAAGGGCAC-GCCCTGGCACCCGCACCGCGGCACT[TB]AC
PC210	G[TB]AAGTGCCGCGGTGCGGGTGCCAGGGCGTGCCCTT-GGGCTCCCCGGGCGCGTACTCCACCTCATGCA[TB]C
PC211	GA[TB]GCATGAGGTGGAGTACGCGCCCGGGGAGCCCAAGGGCAC-GCCCTGGCACCCGCACCGCGGCACT[TB]AC
PC216	GTAAGTGCCGCGGTGCGGGTGCCAGGGCGTGCCCTT-GGGCTCCCCGGGCGCGTACTCCACCTCATGCATC
PC1253	TGGGTCAACGTGGGCAAAGATGTCCTAGCAATGTAATCGTCTATGACGTT
PC1255	GTCGGATCCTCTAGACAGCTCCATGATCACTGGCACTGGTAGAATTCGGC
314	CATGGAGCTGTCTAGAGGATCCGAC
X12-4SC	GCGATAGTCTCTAGACAGCATGTCCTAGCAA
X12-3L	AACACCTACTATCCCACGAGCAGAGCTGATTCTTACAAATATGATTCGAGAC-GTCATAGACGATTACATTGCTAGGACATGCTGTCTAGAGACTATCGC
3'-100	GGCGGCTCGTATGTTGTGTGGA
INT 5'-0	GGGTAAGTGCCGCGGTGCGGGTG
INT 5'-40	GGTTCTCTCAGTTGGGGGCGTAG
V2 3'-100 TOP	GGGCTGCAAGGCGATTAAGTTG
V2 3'-15 TOP	GGACTGAGCCTCTCGACTTCAC
70BP-NHEJ-PUC19TN	GGCCGTCGTTTTACAACGT
CAG_X4_bot-tom_strand_biotin	[B]CGTATCTTACCGGGTTGGATTCAAGACGATAGTTAAGCAGTTGAAC-GACTGAGCGCAGCGACTCTGACGT[B]
Top strand oligo WT FRP	ACGTCAGAGTCGCTGCGCTCAGTCGTTCAACTGCTTAACTATCGTCTT-GAATCCAACCCGGTAAGATACG
WHDv2_197mer_bot	GCGAGTGGTCGGCAGATTGCGATAAACGGTCACATTAAATTTAACCTGAC-TATTCCACTG-CAACAACTGAACGGACTGGAAACACTGGTCATAATCATGGTGGCGAATAAG TACGCGTTCTTGCAAATCACCAGAAGGCGGTTCCTGAATGAATGGGAA-GCCTTCAAGAAGGTGATAAGCAGGAGAAACATACGAAG
WHDv2_196mer_B_top	[B]GCTTCGTATGTTTCTCCTGCTTATCACCTTCTT-GAAGGCTTCCCATTCATTCAGGAAC-CGCCTTCTGGTGATTTGCAAGAACGCGTACTTATTCGCCACCATGATTATGA CCAGTGTTTCCAGTCCGTTCAGTTGTTGCAGTGGAA-TAGTCAGGTTAAATTTAATGTGACCGTTTATCGCAATCTGCCGACCACTCG
Az-Charomid-3778-1	GAGAGAAGTGGCAAGTTTATAAATCCCGG-GAGCGAGG**Z**ATGTAGGCGGTGCTACAGAG
Az-Charomid-1456-1	GAGAGAGCTGGCCAGTTTATAACACCCGGGACGCCGC**Z**ATCG-CAAATGGTGCTATCC
DBCO-Hyb2	**Y**GAGCCAAGACGCCTCCATCCATGCA
DBCO-Hyb1	**Y**CCATGGGCATACTGATCGGTAGGG

Supplementary Table 2: The sequence of the pG68v2 plasmid

TCGCGCGTTTCGGTGATGACGGTGAAAACCTCTGACACATGCAGCTCCCGGAGAC-
GGTCACAGCTTGTCTGTAAGCGGATGCCGGGAGCAGACAAGCCCGTCAGGGCGCGTCAGCGGG
TGTTGGCGGGTGTCGGGGCTGGCTTAACTATGCGGCATCAGAGCAGATTGTACTGAGAGTG-
CACCATATGCGGTGTGAAATACCGCACAGATGCGTAAGGAGAAAATACCGCATCAGGCGCCATTC
GCCATTCAGGCTGCGCAACTGTTGGGAAGGGCGATCGGTGCGGGCCTCTTCGCTATTAC-
GCCAGCTGGCGAAAGGGGGATGTGCTGCAAGGCGATTAAGTTGGGTAACGCCAGGGTTTTCCCA
GTCACGACGTTGTAAAACGACGGCCAGTGCCAAGCTTAG-
TCTGCTGCCCTTAGGCCATGGAGCTTCACTCACTGAGCCTCTCGACTTCACAAGTAGCTGCTCTTC
CTCAGCACGTCCTCAGCTACACCTCAGCGATCCCTCAGCACTAGTCCTCAGCTAC-
GCCTCAGCGATTCCTCAGCATATCCATGAGCCTGTCACCCTAGGCGGCTGCCTGCGCATCCTGG
GATCCGGGAAGCCAGAGATGAGGCGAATTCG-
TAATCATGTCATAGCTGTTTCCTGTGTGAAATTGTTATCCGCTCACAATTCCACACAACATACGAGCCG
GAAGCATAAAGTGTAAAGCCTGGGGTGCCTAATGAGTGAGCTAACTCACATTAATTGCGTT-
GCGCTCACTGCCCGCTTTCCAGTCGGGAAACCTGTCGTGCCAGCTGCATTAATGAATCGGCCAAC
GCGCGGGGAGAGGCGGTTTGCGTATTGGGCGGTCTTCCGCTTCCTCGCTCAC-
TGACTCGCTGCGCTCGGTCGTTCGGCTGCGGCGAGCGGTATCAGCTCACTCAAAGGCGGTAATA
CGGTTATCCACAGAATCAGGGGATAACGCAGGAAAGAACATGTGAGCAAAAGGCCAG-
CAAAAGGCCAGGAACCGTAAAAAGGCCGCGTTGCTGGCGTTTTTCCATAGGCTCCGCCCCCCTG
ACGAGCATCACAAAAATCGACGCTCAAGTCAGAGGTGGCGAAACCCGACAGGACTATAAAGA-
TACCAGGCGTTTCCCCCTGGAAGCTCCCTCGTGCGCTCTCCTGTTCCGACCCTGCCGCTTACCG
GATACCTGTCCGCCTTTCTCCCTTCGGGAAGCGTGGCGCTTTCTCATAGCTCACGCTG-
TAGGTATCTCAGTTCGGTGTAGGTCGTTCGCTCCAAGCTGGGCTGTGTGCACGAACCCCCCGTTCA
GCCCGACCGCTGCGCCTTATCCGGTAACTATCGTCTTGAGTCCAACCCGGTAAGACAC-
GACTTATCGCCACTGGCAGCAGCCACTGGTAACAGGATTAGCAGAGCGAGGTATGTAGGCGGTGC
TACAGAGTTCTTGAAGTGGTGGCCTAACTACGGCTACACTAGAAGAACAGTATTTGG-
TATCTGCGCTCTGCTGAAGCCAGTTACCTTCGGAAAAAGAGTTGGTAGCTCTTGATCCGGCAAACAA
ACCACCGCTGGTAGCGGTGGTTTTTTTGTTTGCAAGCAGCAGATTACGCG-
CAGAAAAAAAGGATCTCAAGAAGATCCTTTGATCTTTTCTACGGGGTCTGACGCTCAGTGGAACGAA
AACTCACGTTAAGGGATTTTGGTCATGAGATTATCAAAAAGGATCTTCACCTA-
GATCCTTTTAAATTAAAAATGAAGTTTTAAATCAATCTAAAGTATATATGAGTAAACTTGGTCTGACAGTTA
CCAATGCTTAATCAGTGAGGCACCTATCTCAGCGATCTGTCTATTTCGTTCATCCATAGTT-
GCCTGACTCCCCGTCGTGTAGATAACTACGATACGGGAGGGCTTACCATCTGGCCCCAGTGCTGC
AATGATACCGCGAGACCCACGCTCACCGGCTCCAGATTTATCAGCAATAAACCAGCCAGCCG-
GAAGGGCCGAGCGCAGAAGTGGTCCTGCAACTTTATCCGCCTCCATCCAGTCTATTAATTGTTGCC
GGGAAGCTAGAGTAAGTAGTTCGCCAGTTAATAGTTTGCGCAACGTTGTTGCCATTGC-
TACAGGCATCGTGGTGTCACGCTCGTCGTTTGGTATGGCTTCATTCAGCTCCGGTTCCCAACGATCA
AGGCGAGTTACATGATCCCCCATGTTGTGCAAAAAA-
GCGGTTAGCTCCTTCGGTCCTCCGATCGTTGTCAGAAGTAAGTTGGCCGCAGTGTTATCACTCATGG
TTATGGCAGCACTGCATAATTCTCTTACTGTCATGCCATCCGTAA-
GATGCTTTTCTGTGACTGGTGAGTACTCAACCAAGTCATTCTGAGAATAGTGTATGCGGCGACCGAGT
TGCTCTTGCCCGGCGTCAATACGGGATAATAC-
CGCGCCACATAGCAGAACTTTAAAAGTGCTCATCATTGGAAAACGTTCTTCGGGGCGAAAACTCTC
AAGGATCTTACCGCTGTTGAGATCCAGTTCGATGTAACCCACTCGTG-
CACCCAACTGATCTTCAGCATCTTTTACTTTCACCAGCGTTTCTGGGTGAGCAAAAACAGGAAGGCA
AAATGCCGCAAAAAAGGGAATAAGGGCGACACGGAAATGTTGAATACTCAT-
ACTCTTCCTTTTTCAATATTATTGAAGCATTTATCAGGGTTATTGTCTCATGAGCGGATACATATTTGAAT
GTATTTAGAAAAATAAACAAATAGGGGTTCCGCGCACATTTCCCCGAAAAGTGCCACCTGAC-
GTCTAAGAAACCATTATTATCATGACATTAACCTATAAAAATAGGCGTATCACGAGGCCCTTTCGTC

3.2. Mechanism of BRCA1–BARD1 function in DNA end resection and DNA protection

Summary:

Ceppi and colleagues studied the role of the BRCA1-BARD1 complex in DNA end resection *in vitro* using recombinant proteins. They found that the BRCA1-C complex, consisting of BRCA1-BARD1, MRN and CtIP, significantly enhances DNA2-WRN-dependent long-range resection and that BRCA1-BARD1 stimulates the helicase activity of WRN. I investigated the effect of BRCA1-BARD1 on the EXO1-dependent branch of long-range resection and found that the BRCA1-BARD1 complex promotes the nuclease activity of EXO1. In contrast to DNA2-WRN, addition of MRN and CtIP did not provide further stimulation. Lastly, I showed that BRCA1-BARD1 does not appear to stimulate the exonuclease of MRE11-RAD50 in short-range resection.

My contribution:

I designed and executed the biochemical assays investigating the stimulatory effect of BRCA1-BARD1 on EXO1 (Fig. 5a, b, d and Ext. Fig. 8b-f and h) and on the exonuclease activity of MR (Ext. Fig. 1d).

Article

Mechanism of BRCA1–BARD1 function in DNA end resection and DNA protection

https://doi.org/10.1038/s41586-024-07909-9

Received: 20 November 2023

Accepted: 5 August 2024

Published online: 11 September 2024

Open access

Check for updates

Ilaria Ceppi[1,11], Maria Rosaria Dello Stritto[1,11], Martin Mütze[2], Stefan Braunshier[1], Valentina Mengoli[1], Giordano Reginato[1], Hồ Mỹ Phúc Võ[3,4], Sonia Jimeno[5,6], Ananya Acharya[1], Megha Roy[1], Aurore Sanchez[1,8], Swagata Halder[1,9], Sean Michael Howard[1,10], Raphaël Guérois[7], Pablo Huertas[5,6], Sylvie M. Noordermeer[3,4], Ralf Seidel[2] & Petr Cejka[1]✉

DNA double-strand break (DSB) repair by homologous recombination is initiated by DNA end resection, a process involving the controlled degradation of the 5′-terminated strands at DSB sites[1,2]. The breast cancer suppressor BRCA1–BARD1 not only promotes resection and homologous recombination, but it also protects DNA upon replication stress[1,3–9]. BRCA1–BARD1 counteracts the anti-resection and pro-non-homologous end-joining factor 53BP1, but whether it functions in resection directly has been unclear[10–16]. Using purified recombinant proteins, we show here that BRCA1–BARD1 directly promotes long-range DNA end resection pathways catalysed by the EXO1 or DNA2 nucleases. In the DNA2-dependent pathway, BRCA1–BARD1 stimulates DNA unwinding by the Werner or Bloom helicase. Together with MRE11–RAD50–NBS1 and phosphorylated CtIP, BRCA1–BARD1 forms the BRCA1–C complex[17,18], which stimulates resection synergistically to an even greater extent. A mutation in phosphorylated CtIP (S327A), which disrupts its binding to the BRCT repeats of BRCA1 and hence the integrity of the BRCA1–C complex[19–21], inhibits resection, showing that BRCA1–C is a functionally integrated ensemble. Whereas BRCA1–BARD1 stimulates resection in DSB repair, it paradoxically also protects replication forks from unscheduled degradation upon stress, which involves a homologous recombination-independent function of the recombinase RAD51 (refs. 4–6,8). We show that in the presence of RAD51, BRCA1–BARD1 instead inhibits DNA degradation. On the basis of our data, the presence and local concentration of RAD51 might determine the balance between the pronuclease and the DNA protection functions of BRCA1–BARD1 in various physiological contexts.

DNA end resection includes two mechanistically distinct steps. The initial short-range resection involves a nucleolytic function of the MRE11 nuclease acting within the MRE11–RAD50–NBS1 (MRN) complex, stimulated by phosphorylated CtIP (pCtIP)[1,22,23]. The subsequent long-range resection is carried out by either of two nucleases, EXO1 or DNA2 (refs. 1,22,24). Whereas EXO1 acts on double-stranded DNA (dsDNA), DNA2 nuclease is single-stranded DNA (ssDNA) specific and thus requires a RecQ family helicase partner, Bloom (BLM) or Werner (WRN), together with the ssDNA binding protein replication protein A (RPA)[1,25]. However, a significant crosstalk exists between the resection pathways[24,26–30]. BRCA1–BARD1 promotes resection, as well as the downstream steps in the homologous recombination pathway, including RAD51 loading and strand invasion, probably in complex with BRCA2 (refs. 3,8,9,30). The pro-resection and homologous recombination function of BRCA1 is diminished in cells lacking 53BP1 (refs. 10–12), showing that the primary function of BRCA1–BARD1 in resection is to counteract 53BP1 and its effectors. Whether BRCA1 functions directly to promote resection, or whether its effect is largely indirect has not been clear. BRCA1 binds the MRN complex and CtIP, forming the BRCA1–C complex[17,18,30]. Efficient BRCA1–CtIP interaction is cell-cycle regulated and depends on the CDK-dependent phosphorylation of CtIP at the S327 site[19–21]. Consequently, the non-phosphorylatable CtIP-S327A mutant has resection and recombination defects according to some reports[16,17,31,32], whereas other studies failed to observe a phenotype[10,33,34], suggesting that the contribution of the BRCA1–CtIP interaction to resection may be redundant with other pathways or subject to suppressor mutations. CtIP stimulates DNA end resection by promoting the nuclease of MRN[23], DNA unwinding by BLM[29] and the

[1]Institute for Research in Biomedicine, Università della Svizzera italiana (USI), Faculty of Biomedical Sciences, Bellinzona, Switzerland. [2]Peter Debye Institute for Soft Matter Physics, Universität Leipzig, Leipzig, Germany. [3]Leiden University Medical Center, Leiden, the Netherlands. [4]Oncode Institute, Utrecht, the Netherlands. [5]Departamento de Genética, Facultad de Biología, Universidad de Sevilla, Sevilla, Spain. [6]Centro Andaluz de Biología Molecular y Medicina Regenerativa-CABIMER, Universidad de Sevilla-CSIC-Universidad Pablo de Olavide, Sevilla, Spain. [7]Institute for Integrative Biology of the Cell (I2BC), Commissariat à l'Energie Atomique, CNRS, Université Paris-Sud, Université Paris-Saclay, Gif-sur-Yvette, France. [8]Present address: Institut Curie, Paris Sciences and Lettres University, Sorbonne Université, CNRS UMR 3244, Dynamics of Genetic Information, Paris, France. [9]Present address: Biological Systems Engineering, Plaksha University, Mohali, India. [10]Present address: Department of Mechanical and Biomedical Engineering, Boise State University, Boise, ID, USA. [11]These authors contributed equally: Ilaria Ceppi, Maria Rosaria Dello Stritto. ✉e-mail: petr.cejka@irb.usi.ch

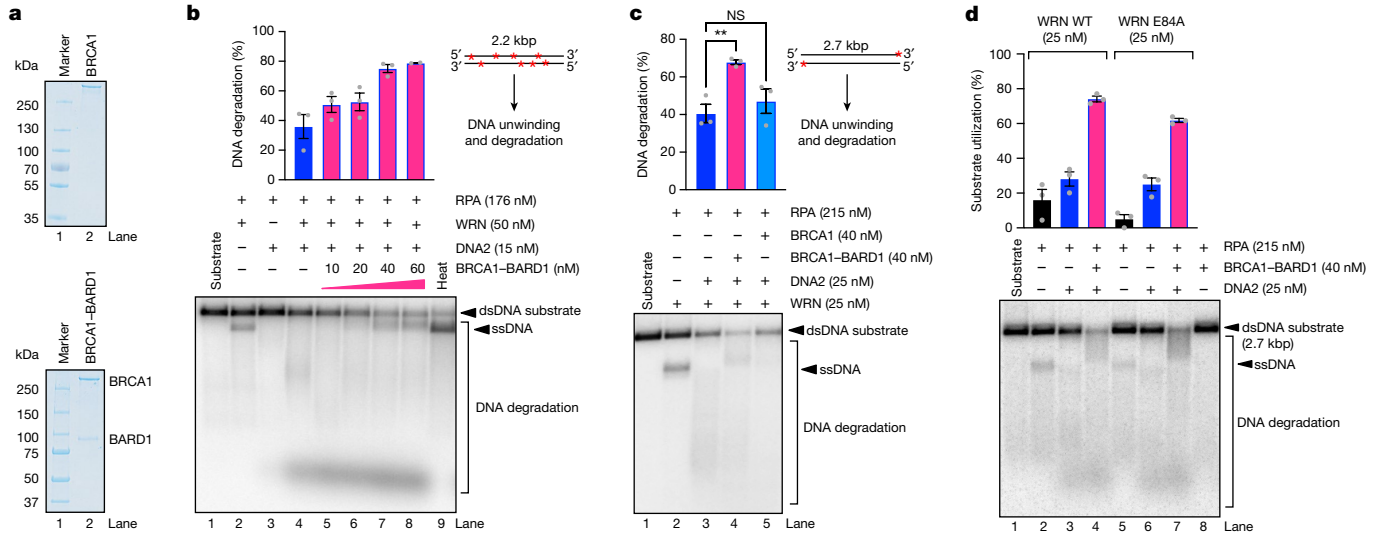

Fig. 1 | BRCA1–BARD1 directly promotes resection by WRN-DNA2-RPA. **a**, Recombinant BRCA1 (top) and the BRCA1–BARD1 (bottom) complex used in this study. The polyacrylamide gels were stained with Coomassie Brilliant Blue. **b**, Resection assays with WRN-DNA2-RPA, and its stimulation by BRCA1–BARD1. Top right, a schematic of the assay. Red asterisks (*) represent the position of the radioactive labels. Top, quantitation of DNA degradation. Averages shown; error bars, s.e.m. (lanes 4–7); $n = 2$ for the reaction containing 60 nM of BRCA1–BARD1 and $n = 3$ for all the other samples. Bottom, representative assays. **c**, Resection assays with WRN-DNA2-RPA, in the absence or presence of either BRCA1–BARD1 or BRCA1. Top right, a schematic of the assay. Red asterisks (*) represent the position of the radioactive labels. Top, quantitation of DNA degradation. Averages shown; error bars, s.e.m.; $n = 3$. $^{**}P = 0.0055$, two-tailed *t*-test. Bottom, representative assays. **d**, Resection assays with DNA2-RPA, and either wild-type (WT) WRN or exonuclease-dead WRN E84A, in the absence or presence of BRCA1–BARD1. Top, quantitation of the substrate utilization. Averages shown; error bars, s.e.m.; $n = 3$. Bottom, representative assays. Source data are provided in Supplementary Fig. 1. NS, not significant.

helicase-nuclease DNA2 (refs. 27,28). Whether any of these reactions is directly regulated by the BRCA1–BARD1 complex was not known.

BRCA1–BARD1 stimulates DNA end resection

To identify a potential direct function of BRCA1–BARD1 in DSB processing, we reconstituted DNA end resection reactions in vitro with purified recombinant proteins. BRCA1 was expressed in insect *Spodoptera frugiperda* 9 (*Sf*9) cells either on its own, or as a heterocomplex with BARD1, with approximate 1:1 stoichiometry (Fig. 1a). BRCA1, as well as BRCA1–BARD1, were largely mono- or heterodimeric (Extended Data Fig. 1a). BRCA1 was tagged with 2× maltose-binding protein (MBP) tag at the N terminus, which improved yield and solubility. We did not observe any effect of BRCA1–BARD1 on the endonuclease activity of MRN in conjunction with pCtIP, nor on the exonuclease activity of MRE11–RAD50, which function in the initial short-range resection (Extended Data Fig. 1b–d). However, BRCA1–BARD1 notably promoted long-range resection catalysed by WRN and DNA2 together with RPA (Fig. 1b and Extended Data Fig. 1b,e). The long-range resection by WRN-DNA2-RPA is dependent on DNA unwinding by WRN, which is thought to occur in a concerted manner with 5′–3′ ssDNA degradation by DNA2 (ref. 35). Both DNA unwinding and degradation are stimulated by RPA, which establishes the correct polarity of DNA end resection[1]. The accumulation of a partially resected DNA intermediate in Fig. 1b (lanes 7 and 8) suggested that BRCA1–BARD1 may promote DNA unwinding by WRN, resulting in accelerated DNA unwinding that was partially uncoupled from DNA degradation by DNA2. In accord, the intermediate was not visible at lower WRN concentrations, while the stimulatory effect of BRCA1–BARD1 remained apparent (Extended Data Fig. 1f). We note that the MBP tag on BRCA1 did not interfere with the stimulatory capacity of BRCA1–BARD1 on WRN-DNA2-RPA (Extended Data Fig. 1g,h). BRCA1 alone (without BARD1) did not significantly stimulate DNA end resection by WRN-DNA2-RPA, showing that the BRCA1–BARD1 heterodimer is necessary (Fig. 1c). Resection did not require the exonuclease activity of WRN (Fig. 1d and Extended Data Fig. 1i), whereas it was dependent on the WRN helicase activity and ATP hydrolysis (Extended Data Fig. 1i,j). The DNA degradation activity was entirely dependent on the nuclease active site of DNA2 (Extended Data Fig. 1i,j). BRCA1–BARD1 did not show any activity per se, showing that it is an accessory factor (Extended Data Fig. 1h,j). Together, we establish that the BRCA1–BARD1 heterodimer directly stimulates long-range DNA end resection by WRN-DNA2-RPA.

BRCA1–BARD1 promotes WRN helicase

To define how the BRCA1–BARD1 complex promotes DNA end resection by WRN-DNA2-RPA, we divided the resection reaction into its components. We observed that BRCA1–BARD1 promoted DNA unwinding by WRN-RPA on both short oligonucleotide-based and long dsDNA substrates, but not by nuclease-dead yeast Dna2 E675A (*Sc*Dna2 E675A) used as a non-cognate negative control[36] (Extended Data Fig. 2a–d). BRCA1–BARD1 also stimulated WRN ATPase activity (Extended Data Fig. 2e). To obtain more quantitative data, we turned to single-molecule magnetic tweezers. In our setup, 6.1 kilobase pair (kbp) long dsDNA with a 5′ ssDNA flap was on one side attached to a fixed surface, and on the other side to a mobile magnetic bead[37] (Fig. 2a). Owing to the length difference between ssDNA and dsDNA, DNA unwinding can be inferred from the relative bead position. BRCA1–BARD1 moderately stimulated both the processivity (160 versus 283 bp) and the rate (26 versus 34 bp per second) of DNA unwinding by WRN-RPA (Fig. 2b–g and Extended Data Fig. 2f,g). Moreover, with WRN-RPA alone, we observed both DNA unwinding and rewinding events (Fig. 2b,h and Extended Data Fig. 2f), probably resulting from frequent DNA strand switching by WRN, reminiscent of yeast Sgs1 (ref. 37). In the presence of BRCA1–BARD1, the rewinding events were strongly reduced (Fig. 2c,h and Extended Data Fig. 2g), which notably enhanced the extent of DNA being unwound (Fig. 2b,c). BRCA1–BARD1 and/or RPA showed no activity per se in the tweezer experiments (Extended Data Fig. 2h). In contrast to a strong direct effect on WRN, BRCA1–BARD1 did not notably stimulate the nuclease activity of DNA2-RPA, when

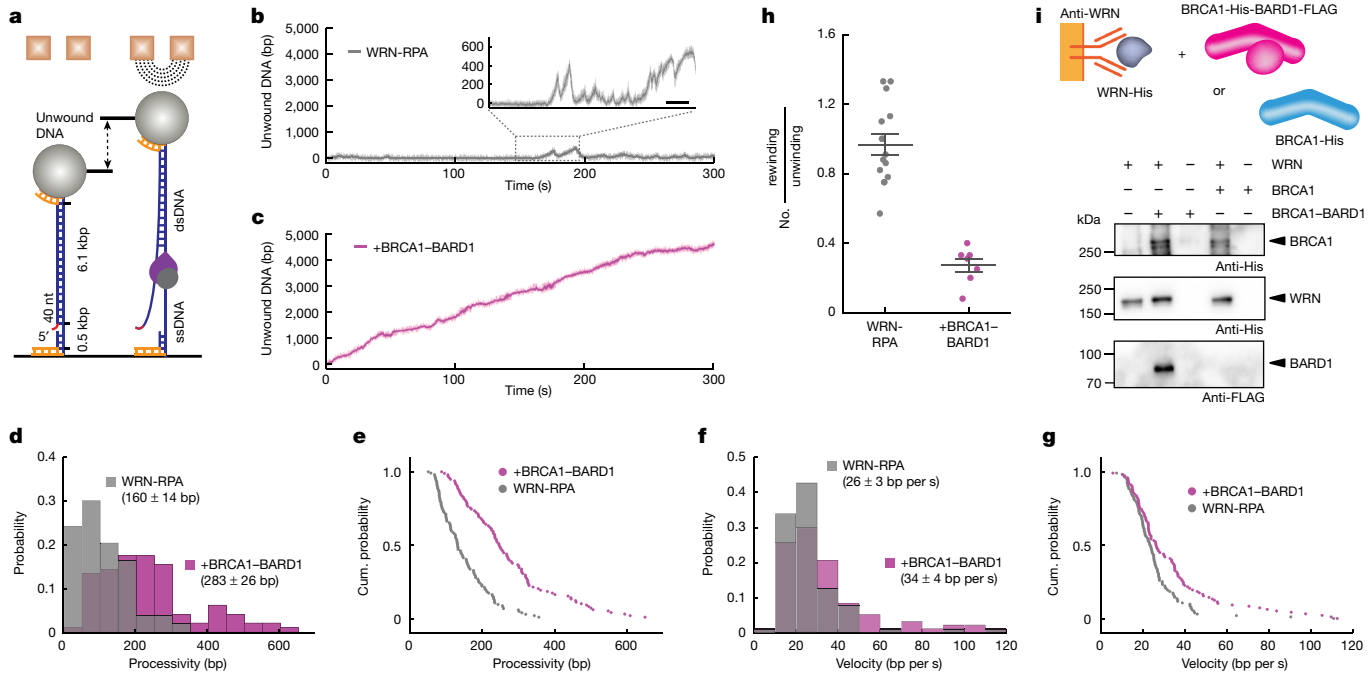

Fig. 2 | BRCA1–BARD1 promotes WRN-mediated DNA unwinding. **a**, A schematic of the single-molecule magnetic tweezers assay setup used and the DNA substrate. **b**, Representative trajectory of DNA unwinding events by WRN in the presence of RPA, both 25 nM. A zoomed-in view highlighting unwinding and rewinding events is shown in the dashed square. Scale bar, 10 s. **c**, Representative trajectory of DNA unwinding events by WRN (25 nM) in the presence of BRCA1–BARD1 (40 nM) and RPA (25 nM). **d**,**e**, Processivity histogram (**d**) and cumulative (Cum.) probability distribution (shown as survival probability) (**e**) of the observed DNA unwinding events by WRN-RPA, both 25 nM, in the absence (grey) or presence (pink) of BRCA1–BARD1 (40 nM), with mean values of 160 ± 14 bp (n = 104) and 283 ± 26 bp (n = 98), respectively. Error, 2 s.e.m. **f**,**g**, Velocity histogram (**f**) and cumulative probability distribution (shown as survival probability) (**g**) of the observed DNA unwinding events by WRN-RPA, both 25 nM, in the absence (grey) or presence (pink) of BRCA1–BARD1 (40 nM), with mean values of 26 ± 3 bp per second (n = 104) and 34 ± 4 bp per second (n = 98), respectively. Error, 2 s.e.m. **h**, Ratio of rewinding (DNA shortening) and unwinding (DNA extension) events by WRN-RPA, both 25 nM, in the absence (grey) or presence (pink) of BRCA1–BARD1 (40 nM). Averages shown; error bars, s.e.m.; n = 15 (in the absence of BRCA1–BARD1) and n = 7 (in the presence of BRCA1–BARD1). **i**, Representative protein-interaction assays. Top, a schematic of the assay. Source data are provided in Supplementary Fig. 1. nt, nucleotides; s, second.

ssDNA was used as a substrate (Extended Data Fig. 2i). DNA2, in addition to its essential nuclease function, has an ATPase-driven motor activity that acts as a ssDNA translocase in DNA end resection[1,27,28,38,39]. BRCA1–BARD1 did not efficiently stimulate the ATPase activity of wild-type DNA2 or nuclease-dead DNA2 D277A (Extended Data Fig. 2j). The stimulatory effect of BRCA1–BARD1 on the WRN helicase is underpinned by a direct physical interaction as observed in in vitro pull-down assays, which also showed that BARD1 is dispensable for the physical interaction with WRN (Fig. 2i), in agreement with experiments performed using cell extracts[36]. Together, we conclude that BRCA1–BARD1 stimulates the DNA2 nuclease-dependent branch of long-range DNA end resection by promoting the WRN helicase activity. Our single-molecule experiments determined that BRCA1–BARD1 supports WRN during the course of DNA unwinding, and it is not simply a recruitment factor[40].

BRCA1–BARD1 functions with CtIP

MRN and pCtIP together with BRCA1–BARD1 form the cell-cycle stage-dependent BRCA1–C complex that has been broadly implicated in DNA resection and homologous recombination[17,18,30], but the mechanism of its function remained unclear. It has been previously established that MRN and pCtIP, components of the short-range resection, have extra structural, nuclease-independent functions to stimulate long-range resection[24,26–29]. In this context, both MRN and pCtIP were shown to facilitate the recruitment and activity of BLM[24,29], but their interplay with WRN was not known. pCtIP also promotes the motor function of DNA2, which in turn enhances the rate of DNA degradation by the nuclease activity of DNA2 (refs. 28,40). We next set out to test for the effect of BRCA1–BARD1 on the WRN-DNA2-RPA-dependent resection when MRN and/or pCtIP were present. With pCtIP, the stimulation of WRN-DNA2-RPA by BRCA1–BARD1 was even more apparent (Extended Data Fig. 2k,l, compare with Extended Data Fig. 1e). These data agree with our previous observations that pCtIP promotes ssDNA degradation by DNA2 through the stimulation of its motor activity[28,41], and hence DNA2-CtIP can keep up with accelerated DNA unwinding by WRN-BRCA1–BARD1.

We next used λDNA/HindIII digest as a substrate to monitor DNA degradation of dsDNA fragments of various lengths up to 23 kbp (Extended Data Fig. 2m). In the absence of pCtIP (Fig. 3a, lanes 1–12 and Extended Data Fig. 2n), the stimulation by BRCA1–BARD1 was limited and restricted to the shorter dsDNA fragments. By contrast, with pCtIP, the stimulatory effect of BRCA1–BARD1 was notable, and very efficient degradation of long dsDNA substrates was observed (Fig. 3a, lanes 13–24 and Extended Data Fig. 2n). The DNA end resection activity of the BRCA1–BARD1-pCtIP-WRN-DNA2-RPA ensemble depends on the helicase activity of WRN, the nuclease activity of DNA2 and ATP (Extended Data Fig. 2o). Replacement of wild-type DNA2 with the helicase-dead DNA2 K654R variant within the ensemble also resulted in reduced resection (Extended Data Fig. 2o).

The BLM helicase functions in the DNA2 end resection pathway redundantly with WRN, depending on cell type and biological context[1]. We observed that BRCA1–BARD1 also promoted DNA unwinding by BLM (Fig. 3b, compare lanes 2 and 3), and BRCA1–BARD1 and pCtIP synergistically stimulated resection by BLM-DNA2-RPA (Fig. 3b). By contrast, BRCA1–BARD1 only moderately enhanced the nuclease

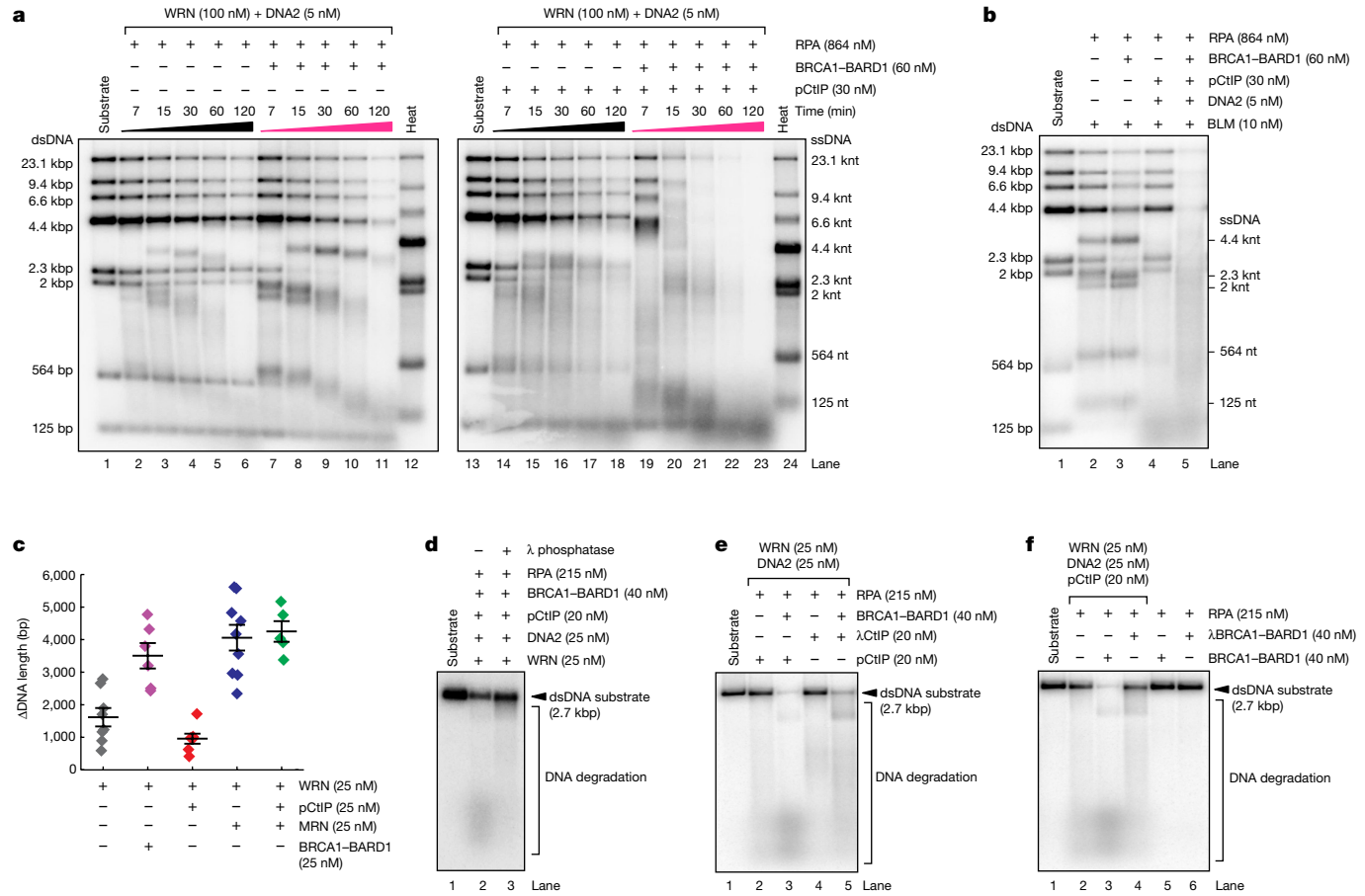

Fig. 3 | BRCA1–BARD1 together with CtIP and MRN promote resection by WRN-DNA2-RPA. a, Representative kinetic resection assays with WRN-DNA2-RPA, in the absence or presence of pCtIP and BRCA1–BARD1. **b**, Representative resection assays with BLM-DNA2-pCtIP-RPA, in the absence or presence of BRCA1–BARD1. **c**, DNA unwinding by the indicated proteins, at 25 nM, expressed as ΔDNA-length (Methods). Averages shown; error bars, s.e.m.; $n = 7$ (for WRN), $n = 6$ (for WRN-BRCA1–BARD1), $n = 7$ (for WRN-BRCA1–BARD1-pCtIP), $n = 9$ (for WRN-MRN-BRCA1–BARD1), $n = 5$ (for WRN-pCtIP-MRN). **d**, Representative resection assays with WRN-DNA2-pCtIP-BRCA1–BARD1-RPA, in the absence or presence of λ phosphatase (200 U). **e**, Representative resection assays with WRN-DNA2-RPA, in the presence of pCtIP or dephosphorylated CtIP (λCtIP) and in the absence or presence of BRCA1–BARD1. **f**, Representative resection assays with WRN-DNA2-pCtIP-RPA, in the absence or presence of either BRCA1–BARD1 (BRCA1–BARD1) or dephosphorylated BRCA1–BARD1 (λBRCA1–BARD1). Source data are provided in Supplementary Fig. 2. knt, kilonucleotides.

activity of DNA2 on ssDNA when pCtIP was also present and BLM and WRN were omitted (Extended Data Fig. 3a). BRCA1–BARD1 did not stimulate the processivity (264 versus 271 bp) nor the rate (57 versus 46 bp per s) of DNA unwinding by nuclease-dead DNA2 D277A in conjunction with RPA and pCtIP (Extended Data Fig. 3b–f).

When MRN was included in the ensemble reaction, resection was even more enhanced (Extended Data Fig. 3g). We observed that MRN promoted dsDNA unwinding by WRN in both ensemble (Extended Data Fig. 3h,i) and single-molecule experiments (Fig. 3c and Extended Data Fig. 3j). pCtIP, instead, had no effect on DNA unwinding by WRN (Fig. 3c and Extended Data Fig. 3j). Our data collectively demonstrate that BRCA1–BARD1, MRN and pCtIP stimulate long-range DNA end resection by WRN/BLM-DNA2-RPA. BRCA1–BARD1 and MRN primarily promote DNA unwinding by WRN/BLM and pCtIP activates DNA2.

Phosphorylation of BRCA1–C complex

We demonstrated that the BRCA1–C complex consisting of BRCA1–BARD1, pCtIP and MRN promotes DNA end resection by WRN-DNA2-RPA. The assembly of the BRCA1–C complex is cell-cycle regulated and it is dependent on protein phosphorylation[17,18,30]. We have observed a strong inhibition of DNA resection when the BRCA1–BARD1-pCtIP-WRN-DNA2-RPA reaction was supplemented with λ phosphatase (Fig. 3d). To determine which of the protein components need to be phosphorylated, we prepared separately BRCA1–BARD1, WRN and CtIP in the presence of λ phosphatase, which was then removed from the final protein pool (Extended Data Fig. 3k). We observed that phosphorylation of both CtIP and BRCA1–BARD1 was important (Fig. 3e,f), whereas λ phosphatase treatment did not affect the function of WRN (Extended Data Fig. 3l).

The binding of phosphorylated S327 of pCtIP by the C-terminal (BRCT) domains of BRCA1 is required for the assembly of the BRCA1–C complex[19–21]. To test whether the physical interaction between pCtIP and BRCA1–BARD1 within the BRCA1–C complex is required for the maximal stimulatory effect, we used the pCtIP S327A mutant known to be impaired in its interaction with BRCA1[19–21] (Fig. 4a,b and Extended Data Fig. 4a). As above, BRCA1–BARD1 strongly stimulated DNA end resection by WRN-DNA2-RPA in the presence of wild-type pCtIP, with or without MRN (Fig. 4b). When wild-type pCtIP was replaced with pCtIP S327A, that is, a variant with non-phosphorylatable S327, but otherwise prepared in the same way as the wild-type phosphorylated protein, BRCA1–BARD1 could not stimulate the reaction (Fig. 4a,b and Extended Data Fig. 4a).

In addition to pCtIP S327 mediating the interaction with BRCA1, the other CtIP region required for its function in the resection ensemble

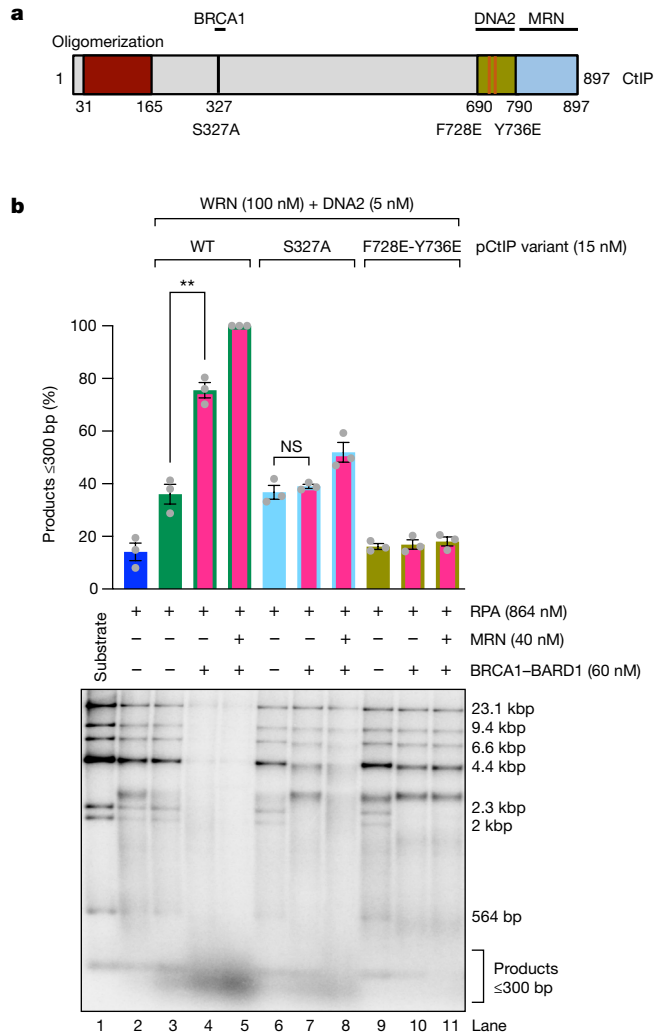

Fig. 4 | The integrity of the BRCA1–C complex is required to promote resection. a, Cartoon of the primary structure of the CtIP protein. Point mutants used in this study are highlighted. **b**, Resection assays with WRN-DNA2-RPA, in the absence or presence of the indicated pCtIP variant, MRN and BRCA1–BARD1. Top, quantitation of DNA degradation (based on the proportion of degradation products of ≤300 bp in length). Averages shown; error bars, s.e.m.; $n = 3$. $^{**}P = 0.0012$, two-tailed t-test. Bottom, representative assays. Source data are provided in Supplementary Fig. 3.

spans residues 690 and 740, including the F728 and Y736 residues (Fig. 4a,b and Extended Data Fig. 4a–c), required for interaction and stimulation of DNA2 (refs. 27,28). By contrast, the C-terminal domain of CtIP, which physically and functionally interacts with MRN in short-range resection[23], was largely dispensable (Extended Data Fig. 4a–c). Nevertheless, MRN further stimulated resection by the ensemble, with both wild-type as well as pCtIP S327A variants (Fig. 4b).

The pCtIP S327A mutant, although supporting DNA resection by WRN-DNA2-RPA in conjunction with BRCA1–BARD1 less efficiently compared to wild-type pCtIP (Fig. 4b), was in contrast not affected in its capacity to promote the nuclease activity of DNA2-RPA on ssDNA (without WRN and BRCA1–BARD1) (Extended Data Fig. 4d), nor in its ability to promote the endonuclease of MRN (Extended Data Fig. 4e). The pCtIP S327A mutant thus specifically disrupts the pCtIP function within the BRCA1–C complex in long-range resection[16]. The assembly of a functional pCtIP and BRCA1–BARD1 complex is therefore necessary for the maximal stimulatory effect in DNA end resection. As BRCA1–BARD1 promotes DNA unwinding by WRN, and pCtIP stimulates DNA degradation by DNA2, the data suggest that DNA unwinding and DNA degradation occur in a concerted manner.

Minimal BRCA1, BARD1 and WRN domains

The primary sequence of BRCA1 includes an N-terminal RING domain necessary for the interaction with BARD1, and C-terminal BRCT repeats that bind pCtIP[8] (Extended Data Fig. 5a). Consequently, the BRCA1(ΔRING)–BARD1 variant did not promote resection (Extended Data Figs. 4a and 5a,b), whereas BRCA1(ΔBRCT)–BARD1, which interacted with BARD1 (Extended Data Fig. 4a), was strongly impaired (Extended Data Fig. 5a,b), as expected. The coiled-coil region of BRCA1 is necessary for the interaction with PALB2-BRCA2, but dispensable for resection[8]. The central BRCA1 region encoded by exon 11 is largely unstructured, mediates many protein–protein interactions and is necessary for resection based on cellular assays[8,42]. To define a potential direct function of the central BRCA1 region in resection, we created a series of internal deletion mutants, which were copurified with BARD1 (Extended Data Figs. 4a and 5a). The BRCA1Δ1–BARD1 variant was impaired, whereas BRCA1Δ2–BARD1 (as well as BRCA1Δ3–BARD1 and BRCA1Δ4–BARD1) could promote resection of the ensemble almost as efficiently as wild-type BRCA1–BARD1 (Extended Data Figs. 4a and 5c,d). The BRCA1 region spanning residues 931 to 1171 is thus necessary for the stimulatory function of the resection ensemble. We found that BRCA1Δ2–BARD1, unlike BRCA1Δ1–BARD1, could promote DNA unwinding by WRN together with RPA (Extended Data Fig. 5e), showing that the identified BRCA1 region disrupts the interplay with WRN. The BRCA1 region between residues 931 and 1171 contains several conserved patches (Extended Data Fig. 5f), including phosphorylation sites necessary for resection but dispensable for BRCA1–C complex assembly[43]. We focused on two of these patches, creating BRCA1(V1035D-F1036D) and BRCA1(Y1127D-I1129D) substitutions within the full-length BRCA1–BARD1 heterodimer (Extended Data Figs. 4a and 5a). We noted that both variants were partially impaired in resection, particularly the BRCA1(V1035D-F1036D)–BARD1 mutant (Extended Data Fig. 5g).

BARD1 similarly contains the N-terminal RING domain mediating its interaction with BRCA1. This domain is followed by a largely unstructured region that was found to bind RAD51, followed by ankyrin repeats (ANK) and the BRCT domain, which mediate interactions with nucleosomes on nascent DNA (H4K20 mark) and poly(ADP-ribose), respectively[8] (Extended Data Fig. 6a). We could not purify BARD1 on its own, but we could prepare several BRCA1–BARD1 variants truncated at the C terminus of BARD1 (Extended Data Fig. 6a,b). Using more restrictive conditions that make resection entirely dependent on BARD1 (Extended Data Fig. 6c,d), we observed that the C-terminal two-thirds of BARD1 (beyond residue 261, including ankyrin and/or BRCT domains) was partially dispensable for resection (Extended Data Fig. 6e). Further truncation eliminating the BARD1 unstructured region completely abrogated resection (Extended Data Fig. 6e), but did not disrupt complex formation with BRCA1 (Extended Data Fig. 6b). Subsequently, we observed that internal deletion of the 123–261 region of BARD1 also entirely disrupted resection (Extended Data Fig. 6f,g). The BARD1 region between residues 123 and 261 contains four conserved patches (Extended Data Fig. 6f), the first of which interacts with SLX4 (MUSIC motif)[44]. We focused on the three subsequent ones (Extended Data Fig. 6a,b,f), and found that particularly the Y180E-F182E mutations in patch 2 (residues 175–190) and the deletion of patch 3 (BRCA1–BARD1Δ205–220) were disruptive for resection (Extended Data Fig. 6a,b,g).

The WRN protein contains an exonuclease domain, followed by a helicase domain, as well as RQC and HRDC domains, typical for members of the RecQ helicase family (Extended Data Fig. 6h,i). We have prepared six WRN truncation variants, and subjected them to DNA end resection assays together with DNA2, RPA and pCtIP, without or with

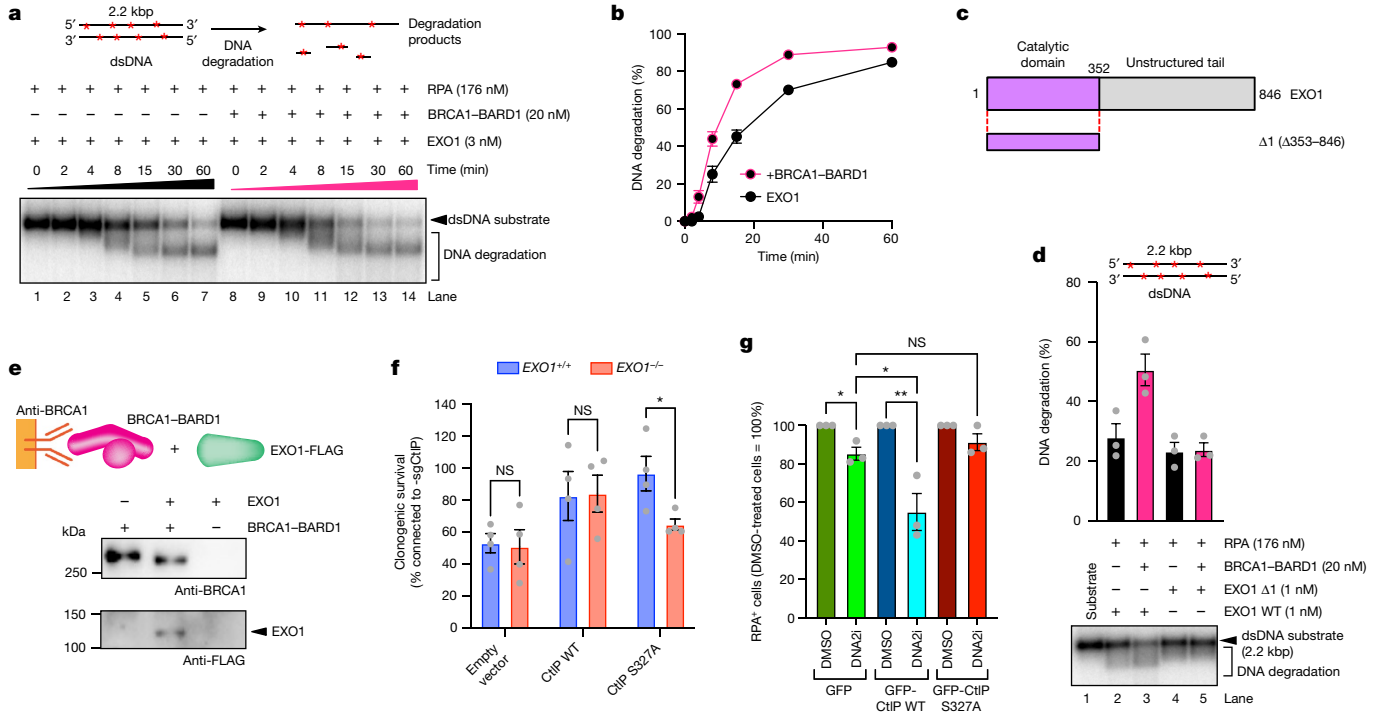

Fig. 5 | BRCA1–BARD1 promotes resection by EXO1 independently of CtIP. **a**, Representative kinetic resection assays with EXO1, RPA, in the absence or presence of BRCA1–BARD1. Top, a schematic of the assay. Red asterisks (*) represent the position of the radioactive labels. **b**, Quantitation of DNA degradation from assays such as shown in **a**. Averages shown; error bars, s.e.m.; $n = 3$. **c**, Cartoon of the primary structure of the EXO1 protein and the Δ1 variant used in the study. **d**, Resection assays with RPA, wild-type EXO1 or EXO1 Δ1, in the absence or presence of BRCA1–BARD1. Top, quantitation of DNA degradation. Averages shown; error bars, s.e.m.; $n = 3$. Bottom, representative assays. **e**, Representative protein-interaction assays. Top, a schematic of the assay. **f**, Quantitation of clonogenic cell survival of RPE1 cells *EXO1*$^{+/+}$ or *EXO1*$^{-/-}$ cells, which were lentivirally transduced with wild-type or S327A CtIP variants, and in which the endogenous CtIP was disrupted by Cas9–gRNA. Averages shown; error bars, s.e.m.; $n = 4$. *$P = 0.0274$, two-tailed *t*-test. **g**, Quantitation of RPA$^+$ cells from an experiment such as shown in Extended Data Fig. 8k. Values were normalized against the DMSO-treated cells. Averages shown; error bars, s.d.; $n = 3$. DMSO- versus DNA2i-treated GFP cells *$P = 0.012$, DMSO- versus DNA2i-treated GFP-CtIP-WT cells **$P = 0.0094$, DNA2i-treated GFP cells versus cells DNA2i-treated GFP-CtIP-WT *$P = 0.041$, two-tailed *t*-test. In all cases, at least 150 cells were studied per condition. Source data are provided in Supplementary Fig. 3.

BRCA1–BARD1 (Extended Data Fig. 6j,k). We observed that BRCA1–BARD1 stimulated resection in conjunction with all tested WRN variants, although to very different extents (Extended Data Fig. 6j,k). Similar data were obtained also without pCtIP (Extended Data Fig. 7a). The resection activity was not affected by the inactivation of the WRN exonuclease domain activity (Extended Data Fig. 7b,c). Single-molecule experiments revealed that the ability to promote resection largely corresponded to the DNA unwinding capacity of the respective WRN variants (Extended Data Fig. 7d,e). Nevertheless, BRCA1–BARD1 promoted DNA unwinding by even the WRN helicase core domain (Extended Data Fig. 7d,e). In accord, BRCA1, independently of BARD1, physically interacted with the WRN helicase core domain, and the interaction was enhanced when further WRN domains were included[36] (Extended Data Fig. 7f). We conclude that the BRCA1 subunit of BRCA1–BARD1 interacts with WRN through many contact points to promote its DNA unwinding activity, which is functionally coupled with DNA degradation by CtIP-DNA2 (Extended Data Fig. 7g).

BRCA1–BARD1 promotes EXO1

The 5′–3′ dsDNA specific EXO1 nuclease represents a second branch of eukaryotic DNA end resection, which functions with the DNA2 pathway in a redundant manner, depending on cellular background and biological context[1]. We observed a moderate stimulation of EXO1 by BRCA1–BARD1 (Fig. 5a,b and Extended Data Fig. 8a). As with the DNA2-dependent branch, the optimal stimulation was observed with the BRCA1–BARD1 heterodimer (as opposed to BRCA1 alone) (Extended Data Fig. 8b). Moreover, BRCA1Δ1–BARD1 was deficient, whereas BRCA1Δ2–BARD1 was proficient in EXO1 stimulation (Extended Data Fig. 8c). However, in contrast to the reactions with DNA2, pCtIP did not stimulate the EXO1 branch even in the presence of BRCA1–BARD1 (ref. 27) (Extended Data Fig. 8d–f). EXO1 contains an N-terminal structured nuclease core domain, followed by largely unstructured C-terminal tail (Fig. 5c). Truncated EXO1Δ1 (Δ353–846) shows a similar nuclease activity as full-length EXO1 (Extended Data Fig. 8g), but it fails to be stimulated by BRCA1–BARD1 (Fig. 5d). Hence, the C-terminal region of EXO1 contains residues that are necessary for the interplay with BRCA1–BARD1. Furthermore, we note that BRCA1–BARD1 instead moderately inhibited the *Escherichia coli* ExoIII nuclease used as a non-cognate negative control (Extended Data Fig. 8h), probably due to competition for DNA access, establishing thus a specificity for the BRCA1–BARD1 and human EXO1 interplay (Extended Data Fig. 8h,i). Accordingly, we found that BRCA1–BARD1 directly physically interacts with EXO1 (Fig. 5e).

CtIP–BRCA1 largely promotes DNA2 pathway

Recently, BRCA1 and EXO1 were found to show synthetic lethality[45,46]. Because our experiments suggested that CtIP promotes the DNA2-dependent pathway and not the EXO1 pathway, we proposed that the CtIP-S327A mutation might be more toxic in the EXO1-deficient background. To this point, we used RPE1 *EXO1*$^{+/+}$ or *EXO1*$^{-/-}$ cells, which were lentivirally transduced with wild-type or S327A CtIP variants, and in which the endogenous CtIP was disrupted by Cas9–gRNA (Extended

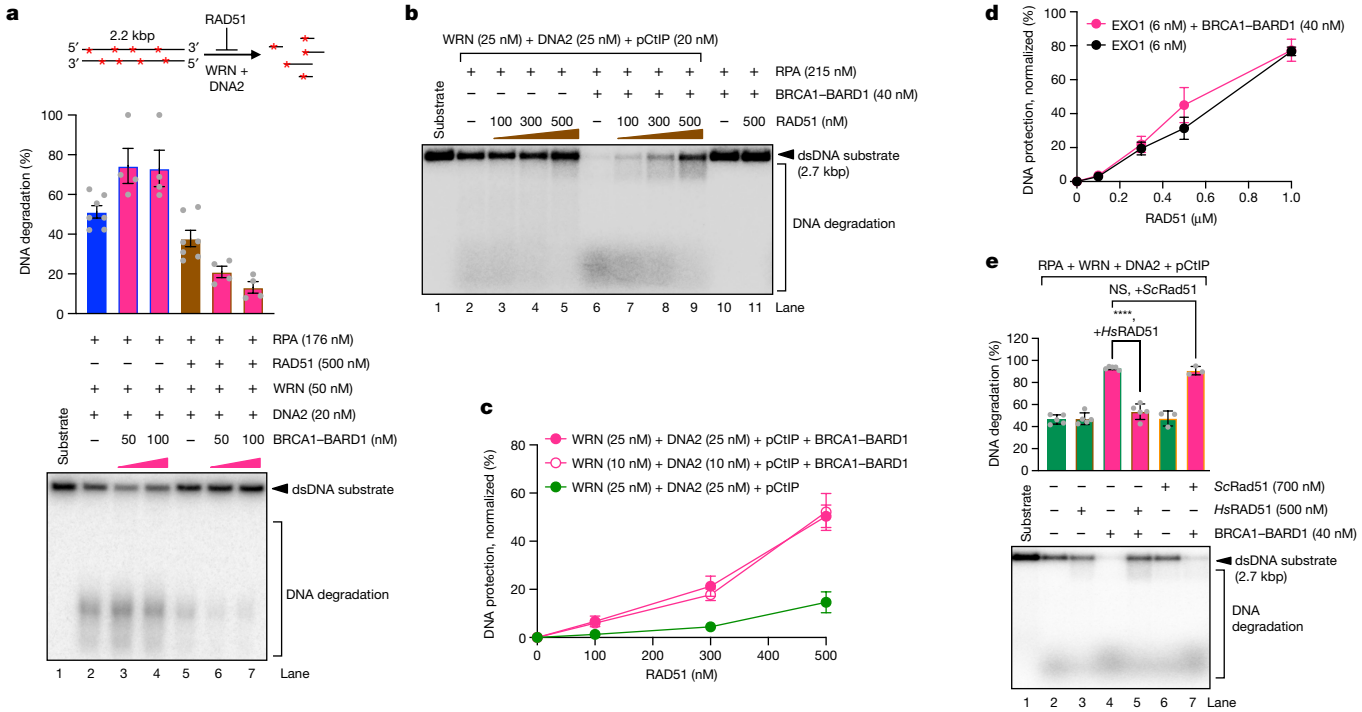

Fig. 6 | BRCA1–BARD1 enhances RAD51-mediated DNA protection. **a**, DNA protection assays with WRN-DNA2-RPA, in the absence or presence of BRCA1–BARD1 and RAD51, performed at 100 mM NaCl. Top, a schematic of the assay. Red asterisks (*) represent the position of the radioactive labels. Middle, quantitation of DNA degradation. Averages shown; error bars, s.e.m.; $n = 7$ (in the absence of BRCA1–BARD1) and $n = 4$ (in the presence of BRCA1–BARD1). Bottom, representative assays. **b**, Representative protection assays with WRN-DNA2-pCtIP-RPA, in the absence or presence of BRCA1–BARD1 and increasing concentration of RAD51. **c**, Quantitation of DNA protection assays such as shown in **b**. Averages shown; error bars, s.e.m.; $n = 4$. The data were normalized to the corresponding reaction without RAD51 (lane 2). Values without normalization are plotted in Extended Data Fig. 9g. Representative protection assays with WRN (10 nM) and DNA2 (10 nM), in presence of pCtIP and BRCA1–BARD1, not shown. **d**, Quantitation of DNA protection assays such as shown in Extended Data Fig. 9h. Averages shown; error bars, s.e.m.; $n = 3$. The data were normalized to the corresponding reaction without RAD51 (lane 2). Values without normalization are plotted in Extended Data Fig. 9i. **e**, Representative protection assays with WRN (25 nM), DNA2 (25 nM), pCtIP (20 nM) and RPA (215 nM), in the absence or presence of BRCA1–BARD1 and either human RAD51 (*Hs*RAD51) or yeast Rad51 (*Sc*Rad51). Top, quantitation of DNA degradation. Averages shown; error bars, s.e.m.; $n = 5$ for reactions containing *Hs*RAD51, in the presence or absence of BRCA1–BARD1 and $n = 3$ for reactions containing *Sc*RAD51, in the presence or absence of BRCA1–BARD1. ****$P \leq 0.0001$, two-tailed t-test. Source data are provided in Supplementary Fig. 3.

Data Fig. 8j). To overcome the lethality caused by CtIP loss, RPE1 *EXO1*$^{+/+}$ or *EXO1*$^{-/-}$ cells were also depleted for TP53. We then monitored cellular survival and observed that the CtIP-S327A mutant reduced the viability of EXO1-deficient but not EXO1-proficient cells (Fig. 5f). Furthermore, using U2OS-derived cells, we observed that C5-dependent inhibition of DNA2 reduced DNA end resection in CtIP wild-type cells but not in CtIP-S327A cells, as monitored by RPA-positive cells upon ionizing radiation (Fig. 5g and Extended Data Fig. 8k,l). We propose that wild-type CtIP channels the resection to the DNA2 pathway through the interactions with DNA2 and BRCA1, and DNA2 inhibition consequently impairs resection. By contrast, in CtIP-S327A cells, the resection primarily proceeds by means of the EXO1 pathway, and DNA2 inhibition is less consequential. These experiments support our conclusions that the CtIP–BRCA1 complex promotes resection primarily by the DNA2 pathway, in agreement with previous observations that CtIP and BRCA1 promote resection speed[16].

RAD51 and BRCA1–BARD1 protect DNA

Independently of their roles in recombination, BRCA1, BRCA2 and RAD51, the main eukaryotic recombinase, as well as many extra cofactors, were shown to prevent unscheduled nascent DNA degradation at challenged DNA replication forks, which may regulate the response of BRCA-deficient tumours to chemotherapy and poly(ADP-ribose) polymerase inhibitors[1,4–7]. Mechanistically, upon replication stress, RAD51 first facilitates replication fork reversal, which may involve its recombinase activity[47]. Subsequently, RAD51 protects nascent DNA[7], which is probably a structural, recombinase-independent function that depends on its ability to bind dsDNA to prevent nuclease access[48]. The involvement of BRCA1 in DNA protection has been puzzling due to its pro-resection function at DSBs, in particular because both processes involve the same nucleases[1]. We set out to test for the effect of RAD51 in the reconstituted DNA resection assays with BRCA1–BARD1 (Extended Data Fig. 9a). In the absence of RAD51, BRCA1–BARD1 promoted DNA end resection by WRN-DNA2-RPA (Fig. 6a). In the presence of RAD51, which partially inhibited resection per se[48], BRCA1–BARD1 enhanced this inhibitory effect (Fig. 6a). DNA protection by BRCA1–BARD1 and RAD51 was observed also with pCtIP (Fig. 6a and Extended Data Fig. 9b), and in kinetic experiments (Extended Data Fig. 9c). Inhibition of resection by RAD51 and BRCA1 was also found in the absence of BARD1 (Extended Data Fig. 9d,e). The inhibitory effect of RAD51 on DNA end resection was dependent on RAD51 capacity to bind DNA (Extended Data Fig. 9a,f). The RAD51 variant K133R, which forms more stable nucleoprotein filaments than wild-type RAD51, was more protective, whereas RAD51 variants K133A and T131P that are less efficient in DNA binding were correspondingly less protective (Extended Data Fig. 9a,f), in agreement with previous data[48].

Compared to the reactions in previous figures, the assays in Fig. 6a and related Extended Data figures were carried out with higher BRCA1–BARD1 concentrations and at higher ionic strength. Using conditions

resembling those used in Figs. 1–4, the stimulatory effect of BRCA1–BARD1 on DNA end resection, in reactions without RAD51, was more apparent (Fig. 6b,c and Extended Data Fig. 9g). RAD51 was inhibitory, and notably more so in the presence of BRCA1–BARD1, again arguing that BRCA1–BARD1 enhances the DNA protection effect of RAD51 (Fig. 6b,c and Extended Data Fig. 9g). By contrast, BRCA1–BARD1 did not affect the inhibitory effect of RAD51 on EXO1 (Fig. 6d and Extended Data Fig. 9h,i). BRCA1–BARD1 also did not affect the RAD51 capacity to protect ssDNA degradation by DNA2 (Extended Data Fig. 10a). Furthermore, whereas human RAD51 (*Hs*RAD51, at 500 nM) was inhibitory when used on top of BRCA1–BARD1-WRN-DNA2-pCtIP-RPA, yeast Rad51 (*Sc*Rad51, at 700 nM) did not inhibit resection (Fig. 6e). The reactions in Fig. 6e used equivalent specific activities of human RAD51 versus yeast Rad51, as determined by their ability to protect DNA against non-cognate endonucleases ScaI and SspI (Extended Data Fig. 10b–d). BRCA1–BARD1 also did not affect the capacity of yeast or human RAD51 to protect DNA from a non-cognate exonuclease ExoIII (Extended Data Fig. 10e). We thus conclude that RAD51 counteracts the nuclease-stimulatory effect of BRCA1–BARD1 and protects DNA in a partially species-specific manner (Extended Data Fig. 10f). It was reported that higher RAD51 concentrations are necessary for fork protection compared to fork reversal[49], highlighting the need for RAD51 cofactors, such as BRCA2, RADX and the RAD51 paralogues to control its levels on DNA to regulate DNA metabolism in various physiological contexts[2,3,6–8,49].

Discussion

We demonstrate that BRCA1–BARD1 directly promotes both DNA2 and EXO1-dependent long-range DNA end resection pathways (Extended Data Figs. 7g and 8i). In the DNA2 branch, BRCA1–BARD1 primarily activates the WRN or BLM helicase component. We found that the stimulatory effect of BRCA1–BARD1 on the DNA2 branch is most apparent when BRCA1–BARD1 is together with pCtIP and MRN, forming the BRCA1–C complex[17,20] (Extended Data Fig. 7g). Consequently, a mutation in pCtIP (S327A), which selectively disrupts the integrity of the BRCA1–C complex[19–21], strongly impairs the stimulation of WRN-DNA2-RPA. BRCA1–C is thus a functionally integrated multi-protein ensemble that directly stimulates resection by WRN/BLM-DNA2-RPA. We instead failed to find a role for the BRCA1 and CtIP interaction in the stimulation of EXO1- or MRN-dependent resection branches. We propose that the more efficient and faster DNA end resection in the presence of BRCA1–BARD1 is better capable to counteract the effectors of 53BP1, such as the Shieldin complex that may obstruct resection[13,15], or the CST complex/Polα-mediated fill-in synthesis at DNA ends[14,50]. BRCA1–BARD1 forms a super-complex together with BRCA2-DSS1, mediated by PALB2 (refs. 2,3,8). Having established that BRCA1 directly promotes DNA end resection, together with previous data demonstrating a role of BRCA1 and/or BRCA2 and cofactors in the activation of RAD51 loading and DNA strand exchange[3,8], it is tempting to speculate that the BRCA1–BRCA2 super-complex may comprehensively regulate and couple the individual initial steps of the homologous recombination pathway.

Online content

Any methods, additional references, Nature Portfolio reporting summaries, source data, extended data, supplementary information, acknowledgements, peer review information; details of author contributions and competing interests; and statements of data and code availability are available at https://doi.org/10.1038/s41586-024-07909-9.

1. Cejka, P. & Symington, L. S. DNA end resection: mechanism and control. *Annu. Rev. Genet.* **55**, 285–307 (2021).
2. Kawale, A. S. & Sung, P. Mechanism and significance of chromosome damage repair by homologous recombination. *Essays Biochem*. https://doi.org/10.1042/EBC20190093 (2020).
3. Prakash, R., Zhang, Y., Feng, W. & Jasin, M. Homologous recombination and human health: the roles of BRCA1, BRCA2, and associated proteins. *Cold Spring Harb. Perspect. Biol.* **7**, a016600 (2015).
4. Schlacher, K., Wu, H. & Jasin, M. A distinct replication fork protection pathway connects Fanconi anemia tumor suppressors to RAD51-BRCA1/2. *Cancer Cell* **22**, 106–116 (2012).
5. Schlacher, K. et al. Double-strand break repair-independent role for BRCA2 in blocking stalled replication fork degradation by MRE11. *Cell* **145**, 529–542 (2011).
6. Ray Chaudhuri, A. et al. Replication fork stability confers chemoresistance in BRCA-deficient cells. *Nature* **535**, 382–387 (2016).
7. Berti, M., Cortez, D. & Lopes, M. The plasticity of DNA replication forks in response to clinically relevant genotoxic stress. *Nat. Rev. Mol. Cell Biol.* **21**, 633–651 (2020).
8. Tarsounas, M. & Sung, P. The antitumorigenic roles of BRCA1-BARD1 in DNA repair and replication. *Nat. Rev. Mol. Cell Biol.* **21**, 284–299 (2020).
9. Stark, J. M., Pierce, A. J., Oh, J., Pastink, A. & Jasin, M. Genetic steps of mammalian homologous repair with distinct mutagenic consequences. *Mol. Cell. Biol.* **24**, 9305–9316 (2004).
10. Polato, F. et al. CtIP-mediated resection is essential for viability and can operate independently of BRCA1. *J. Exp. Med.* **211**, 1027–1036 (2014).
11. Bunting, S. F. et al. 53BP1 inhibits homologous recombination in Brca1-deficient cells by blocking resection of DNA breaks. *Cell* **141**, 243–254 (2010).
12. Bouwman, P. et al. 53BP1 loss rescues BRCA1 deficiency and is associated with triple-negative and BRCA-mutated breast cancers. *Nat. Struct. Mol. Biol.* **17**, 688–695 (2010).
13. Noordermeer, S. M. et al. The shieldin complex mediates 53BP1-dependent DNA repair. *Nature* **560**, 117–121 (2018).
14. Mirman, Z. et al. 53BP1-RIF1-shieldin counteracts DSB resection through CST- and Polalpha-dependent fill-in. *Nature* **560**, 112–116 (2018).
15. Dev, H. et al. Shieldin complex promotes DNA end-joining and counters homologous recombination in BRCA1-null cells. *Nat. Cell Biol.* **20**, 954–965 (2018).
16. Cruz-Garcia, A., Lopez-Saavedra, A. & Huertas, P. BRCA1 accelerates CtIP-mediated DNA-end resection. *Cell Rep.* **9**, 451–459 (2014).
17. Chen, L., Nievera, C. J., Lee, A. Y. & Wu, X. Cell cycle-dependent complex formation of BRCA1.CtIP.MRN is important for DNA double-strand break repair. *J. Biol. Chem.* **283**, 7713–7720 (2008).
18. Wang, B. BRCA1 tumor suppressor network: focusing on its tail. *Cell Biosci.* **2**, 6 (2012).
19. Wong, A. K. et al. Characterization of a carboxy-terminal BRCA1 interacting protein. *Oncogene* **17**, 2279–2285 (1998).
20. Yu, X., Wu, L. C., Bowcock, A. M., Aronheim, A. & Baer, R. The C-terminal (BRCT) domains of BRCA1 interact in vivo with CtIP, a protein implicated in the CtBP pathway of transcriptional repression. *J. Biol. Chem.* **273**, 25388–25392 (1998).
21. Yu, X. & Chen, J. DNA damage-induced cell cycle checkpoint control requires CtIP, a phosphorylation-dependent binding partner of BRCA1 C-terminal domains. *Mol. Cell. Biol.* **24**, 9478–9486 (2004).
22. Gravel, S., Chapman, J. R., Magill, C. & Jackson, S. P. DNA helicases Sgs1 and BLM promote DNA double-strand break resection. *Genes Dev.* **22**, 2767–2772 (2008).
23. Anand, R., Ranjha, L., Cannavo, E. & Cejka, P. Phosphorylated CtIP functions as a co-factor of the MRE11-RAD50-NBS1 endonuclease in DNA end resection. *Mol. Cell* **64**, 940–950 (2016).
24. Nimonkar, A. V. et al. BLM-DNA2-RPA-MRN and EXO1-BLM-RPA-MRN constitute two DNA end resection machineries for human DNA break repair. *Genes Dev.* **25**, 350–362 (2011).
25. Sturzenegger, A. et al. DNA2 cooperates with the WRN and BLM RecQ helicases to mediate long-range DNA end resection in human cells. *J. Biol. Chem.* **289**, 27314–27326 (2014).
26. Cannavo, E., Cejka, P. & Kowalczykowski, S. C. Relationship of DNA degradation by *Saccharomyces cerevisiae* exonuclease 1 and its stimulation by RPA and Mre11-Rad50-Xrs2 to DNA end resection. *Proc. Natl Acad. Sci. USA* **110**, E1661–E1668 (2013).
27. Ceppi, I. et al. CtIP promotes the motor activity of DNA2 to accelerate long-range DNA end resection. *Proc. Natl Acad. Sci. USA* **117**, 8859–8869 (2020).
28. Ceppi, I. et al. PLK1 regulates CtIP and DNA2 interplay in long-range DNA end resection. *Genes Dev.* **37**, 119–135 (2023).
29. Daley, J. M. et al. Enhancement of BLM-DNA2-mediated long-range DNA end resection by CtIP. *Cell Rep.* **21**, 324–332 (2017).
30. Whelan, D. R. & Rothenberg, E. Super-resolution mapping of cellular double-strand break resection complexes during homologous recombination. *Proc. Natl Acad. Sci. USA* https://doi.org/10.1073/pnas.2021963118 (2021).
31. Wang, H. et al. The interaction of CtIP and Nbs1 connects CDK and ATM to regulate HR-mediated double-strand break repair. *PLoS Genet.* **9**, e1003277 (2013).
32. Yun, M. H. & Hiom, K. CtIP-BRCA1 modulates the choice of DNA double-strand-break repair pathway throughout the cell cycle. *Nature* **459**, 460–463 (2009).
33. Nakamura, K. et al. Collaborative action of Brca1 and CtIP in elimination of covalent modifications from double-strand breaks to facilitate subsequent break repair. *PLoS Genet.* **6**, e1000828 (2010).
34. Reczek, C. R., Szabolcs, M., Stark, J. M., Ludwig, T. & Baer, R. The interaction between CtIP and BRCA1 is not essential for resection-mediated DNA repair or tumor suppression. *J. Cell Biol.* **201**, 693–707 (2013).
35. Pinto, C., Kasaciunaite, K., Seidel, R. & Cejka, P. Human DNA2 possesses a cryptic DNA unwinding activity that functionally integrates with BLM or WRN helicases. *eLife* https://doi.org/10.7554/eLife.18574 (2016).
36. Cheng, W. H. et al. Collaboration of Werner syndrome protein and BRCA1 in cellular responses to DNA interstrand cross-links. *Nucleic Acids Res.* **34**, 2751–2760 (2006).
37. Kasaciunaite, K. et al. Competing interaction partners modulate the activity of Sgs1 helicase during DNA end resection. *EMBO J.* **38**, e101516 (2019).
38. Levikova, M., Pinto, C. & Cejka, P. The motor activity of DNA2 functions as an ssDNA translocase to promote DNA end resection. *Genes Dev.* **31**, 493–502 (2017).
39. Miller, A. S. et al. A novel role of the Dna2 translocase function in DNA break resection. *Genes Dev.* **31**, 503–510 (2017).

40. Hoa, N. N. et al. BRCA1 and CtIP are both required to recruit Dna2 at double-strand breaks in homologous recombination. *PLoS ONE* **10**, e0124495 (2015).
41. Oz, R. et al. Phosphorylated CtIP bridges DNA to promote annealing of broken ends. *Proc. Natl Acad. Sci. USA* **117**, 21403–21412 (2020).
42. Zhao, W. et al. BRCA1-BARD1 promotes RAD51-mediated homologous DNA pairing. *Nature* **550**, 360–365 (2017).
43. Parameswaran, B. et al. Damage-induced BRCA1 phosphorylation by Chk2 contributes to the timing of end resection. *Cell Cycle* **14**, 437–448 (2015).
44. Tsukada, K. et al. BLM and BRCA1-BARD1 coordinate complementary mechanisms of joint DNA molecule resolution. *Mol. Cell* **84**, 640–658 e610 (2024).
45. van de Kooij, B. et al. EXO1 protects BRCA1-deficient cells against toxic DNA lesions. *Mol. Cell* **84**, 659–674 e657 (2024).
46. Garcia-Rodriguez, N., Dominguez-Garcia, I., Dominguez-Perez, M. D. C. & Huertas, P. EXO1 and DNA2-mediated ssDNA gap expansion is essential for ATR activation and to maintain viability in BRCA1-deficient cells. *Nucleic Acids Res*. https://doi.org/10.1093/nar/gkae317 (2024).
47. Liu, W. et al. RAD51 bypasses the CMG helicase to promote replication fork reversal. *Science* **380**, 382–387 (2023).
48. Halder, S. et al. Double-stranded DNA binding function of RAD51 in DNA protection and its regulation by BRCA2. *Mol. Cell* **82**, 3553–3565 e3555 (2022).
49. Bhat, K. P. et al. RADX modulates RAD51 activity to control replication fork protection. *Cell Rep.* **24**, 538–545 (2018).
50. Mirman, Z., Sasi, N. K., King, A., Chapman, J. R. & de Lange, T. 53BP1-shieldin-dependent DSB processing in BRCA1-deficient cells requires CST-Polalpha-primase fill-in synthesis. *Nat. Cell Biol.* **24**, 51–61 (2022).

Publisher's note Springer Nature remains neutral with regard to jurisdictional claims in published maps and institutional affiliations.

Open Access This article is licensed under a Creative Commons Attribution-NonCommercial-NoDerivatives 4.0 International License, which permits any non-commercial use, sharing, distribution and reproduction in any medium or format, as long as you give appropriate credit to the original author(s) and the source, provide a link to the Creative Commons licence, and indicate if you modified the licensed material. You do not have permission under this licence to share adapted material derived from this article or parts of it. The images or other third party material in this article are included in the article's Creative Commons licence, unless indicated otherwise in a credit line to the material. If material is not included in the article's Creative Commons licence and your intended use is not permitted by statutory regulation or exceeds the permitted use, you will need to obtain permission directly from the copyright holder. To view a copy of this licence, visit http://creativecommons.org/licenses/by-nc-nd/4.0/.

© The Author(s) 2024, corrected publication 2025

Methods

Cloning, expression and purification of recombinant proteins

Human wild-type DNA2, helicase-dead DNA2 K654R and nuclease-dead DNA2 D277A were expressed in *Sf*9 insect cells and purified by affinity chromatography taking advantage of the N-terminal 6×His tag and the C-terminal FLAG tag[35]. Yeast nuclease-dead Dna2 E675A was expressed in *S. cerevisiae* and purified using the N-terminal FLAG tag and the C-terminal 6×His tag[51]. Full-length wild-type WRN, helicase-dead WRN K577M, exonuclease-dead WRN E84A, WRN fragments, BLM, as well as wild-type CtIP and its variants were purified exploiting the MBP tag at the N terminus and 10×His tag at the C terminus[23,28,35,38,52,53]. The MBP tag was removed during purification by cleavage with PreScission protease. For the expression of phosphorylated wild-type CtIP (pCtIP) and its variants, *Sf*9 cells were treated with 50 nM Okadaic acid (APExBIO) 3 h before collection to preserve the phosphorylated state of the proteins, and 1 μM camptothecin (Sigma) 1 h before collection to increase the activation of the protein phosphorylation cascade. For the expression of dephosphorylated WRN (λWRN) and CtIP (λCtIP), proteins were incubated with λ phosphatase at room temperature for 30 min during purification. The MRN and MRE11–RAD50 complexes were obtained using the 6×His tag and 3×FLAG tag at the C termini of MRE11 and RAD50, respectively[23]. Human wild-type EXO1, as well as nuclease-dead EXO1 D173A, were purified using M2 anti-FLAG affinity resin (Sigma) and HiTrap SP HP cation exchange chromatography column (Cytiva)[26,54]. EXO1Δ1 (Δ353–846) fragment, along with a matched wild-type control, were purified omitting the HiTrap SP HP cation exchange chromatography step. *E. coli* ExoIII, ScaI and SspI were purchased from New England Biolabs. Wild-type human RAD51, as well as the indicated human RAD51 variants and yeast Rad51, were expressed in BL21 (DE3)pLysS *E. coli* cells and purified using amylose affinity chromatography followed by HiTrap Q chromatography (Cytiva)[48].

The *BRCA1* sequence was codon optimized for the expression in *Sf*9 cells (Biomatik) with flanked NheI and XmaI restriction sites. The full-length sequence is listed in Supplementary Table 1 provided in the Supplementary Information. The *BRCA1* gene was then cloned into pFB-2×MBP-CtIP-10×His[55] to generate pFB-2×MBP-BRCA1co-10×His. The cloning created a fusion construct with the 2×MBP tag at the N terminus and the 10×His tag at the C terminus. All BRCA1 variants were cloned from pFB-2×MBP-BRCA1co-10×His using the primers listed in Supplementary Table 3 provided in the Supplementary Information. Similarly, the *BARD1* sequence was codon optimized for the expression in *Sf*9 cells (Supplementary Table 2 provided in the Supplementary Information, Biomatik) with BamHI and XmaI restriction sites. The *BARD1* gene was then cloned into pFB-RAD50co-FLAG[23] to generate pFB-BARD1co-FLAG (BARD1 with C-terminal FLAG tag). All BARD1 variants were cloned from pFB-BARD1co-FLAG using the primers listed in Supplementary Table 3 provided in the Supplementary Information. The BRCA1–BARD1 complex, BRCA1 on its own and all variants were expressed in *Sf*9 cells using the SFX Insect serum-free medium (Hyclone) and the Bac-to-Bac expression system (Invitrogen), according to the manufacturer's recommendations. Frozen *Sf*9 pellets from 1 l of culture were resuspended in lysis buffer (50 mM Tris-HCl pH 7.5, 1 mM ethylenediaminetetraacetic (EDTA), 1:400 protease inhibitor cocktail (Sigma, P8340), 30 μg ml^{-1} leupeptin (Merck Millipore), 1 mM phenylmethylsulfonyl fluoride (PMSF), 1 mM dithiothreitol (DTT), 0.5% NP40) and incubated at 4 °C for 20 min. Glycerol was added to a final concentration of 25%, NaCl was added to a final concentration of 325 mM and the cell suspension was incubated at 4 °C for 20 min. The cell suspension was centrifuged at 55,000*g* at 4 °C for 30 min. The soluble extract was incubated with amylose resin (New England Biolabs) at 4 °C for 1 h. The resin was washed with amylose wash buffer (50 mM Tris-HCl pH 7.5, 2 mM β-mercaptoethanol, 300 mM NaCl, 10% glycerol, 1 mM PMSF). Proteins were eluted using amylose elution buffer (50 mM Tris-HCl pH 7.5, 2 mM β-mercaptoethanol, 300 mM NaCl, 10% glycerol, 1 mM PMSF, 10 mM maltose (Sigma), 20 mM imidazole (Sigma)). The solution was immediately loaded onto pre-equilibrated Ni-NTA agarose resin (Qiagen) at 4 °C, in flow. The resin was washed with Ni-NTA buffer 1 (50 mM Tris-HCl pH 7.5, 2 mM β-mercaptoethanol, 10% glycerol, 1 mM PMSF, 20 mM imidazole and 1 M NaCl for BRCA1 or 0.3 M NaCl for BRCA1–BARD1), and subsequently with Ni-NTA buffer 2 (50 mM Tris-HCl pH 7.5, 2 mM β-mercaptoethanol, 150 mM NaCl, 10% glycerol, 1 mM PMSF, 20 mM imidazole). Proteins were eluted with Ni-NTA elution buffer (50 mM Tris-HCl pH 7.5, 2 mM β-mercaptoethanol, 150 mM NaCl, 10% glycerol, 1 mM PMSF, 200 mM imidazole). Fractions containing high protein concentration as estimated by the Bradford assay were pooled, aliquoted, snap-frozen in liquid nitrogen and stored at −80 °C. The BRCA1–BARD1 mutants were purified in the same way. We note that attempts to cleave the MBP tag before Ni-NTA purification resulted in protein precipitation. We could obtain up to roughly 0.6 mg of BRCA1–BARD1 from 1 l of media (approximate stock concentration, 800 nM). For the expression of dephosphorylated BRCA1–BARD1 (λBRCA1–BARD1), the complex was incubated with λ phosphatase at room temperature for 30 min during purification, along with a matched control that was similarly incubated but without λ phosphatase.

Human *RPA* sequence was cloned from p11d–tRPA construct[56] using the primers listed in Supplementary Table 3 provided in the Supplementary Information. Whereas both RPA1 and RPA2 were flanked by the BamHI and NheI restriction sites, RPA3 was flanked by SalI and XbaI. These restriction enzymes were used to generate pFB-RPA1, pFB-RPA2 and pFB-6×His-RPA3 insect expression vectors used for the protein purification. RPA was expressed in *Sf*9 cells in SFX Insect serum-free medium (Hyclone) using the Bac-to-Bac expression system (Invitrogen), according to the manufacturer's recommendations. A frozen *Sf*9 pellet from 2 l of culture was resuspended in lysis buffer (50 mM Tris-HCl pH 7.5, 2 mM β-mercaptoethanol, 1:200 protease inhibitor cocktail, 60 μg ml^{-1} leupeptin, 1 mM PMSF, 20 mM imidazole, 0.1% NP40) and incubated at 4 °C for 20 min. Glycerol was added to a final concentration of 25%, KCl was added to a final concentration of 325 mM and the cell suspension was incubated at 4 °C for 30 min. The cell suspension was centrifuged at 55,000*g* at 4 °C for 30 min. The soluble extract was incubated with Ni-NTA affinity resin at 4 °C for 1 h. Ni-NTA resin was washed with wash buffer (50 mM Tris-HCl pH 7.5, 2 mM β-mercaptoethanol, 1 mM PMSF, 10% glycerol, 500 mM KCl, 20 mM imidazole, 0.1% NP40). Protein was eluted using wash buffer containing 300 mM imidazole. The eluate was diluted by adding 2 volumes of buffer A (30 mM HEPES pH 7.5, 1 mM DTT, 1 mM PMSF, 10% glycerol, 500 mM KCl, 0.25 mM EDTA, 0.01% NP40). The diluted fractions were purified on a HiTrap Blue HP column (Cytiva) followed by HiTrap desalting column (Cytiva) as described[57]. Peak desalted fractions were pooled, diluted with 1 volume of buffer B (30 mM HEPES pH 7.5, 1 mM DTT, 1 mM PMSF, 10% glycerol, 0.25 mM EDTA) and loaded onto two 5 ml HiTrap Heparin columns (Cytiva) connected in tandem. Proteins were eluted using a 30 ml gradient of 50 mM to 1 M KCl in 1 ml fractions. Peak fractions were pooled and diluted to a final concentration of roughly 100 mM KCl with buffer B. The diluted eluate was loaded and further purified on a HiTrap Q column (Cytiva) as previously described[57]. We could obtain roughly 45 mg of human RPA from 2 l insect cells. The sequences of all primers used for cloning in this study are listed in Supplementary Table 3 provided in the Supplementary Information. Purified recombinant proteins were analysed by using SDS–PAGE denaturing electrophoresis and stained with Coomassie Brilliant Blue (VWR). The final images were acquired with a photo scanner operated with Epson Scan v.3.9.4.0 US software and CanoScan 9000F Mark II scanner operated with ImageCapture v.6.6(525) software.

The sg*CtIP* (CTCCCGGATCTATACTCCAC) used for depletion of endogenous CtIP in RPE1 *EXO1*$^{+/+}$ and RPE1 *EXO1*$^{-/-}$ cells was cloned into pLentiCRISPR-v2 using BsmBI. The PAM-sequence of this guide RNA (gRNA) was mutated in the full-length pcDNA3.1 CtIP overexpressing constructs (pcDNA3.1_CtIP-WT-2×FLAG and

pcDNA3.1_CtIP-S327A-2×FLAG) using site-directed mutagenesis to render the exogenous CtIP expression insensitive to CRISPR-mediated depletion. Subsequently, the coding sequence was cloned into the Gateway entry vector pENTR_1A using KpnI and NotI before transferring it to the destination vector pCW57.1-Zeo using a Gateway LR reaction.

Sequence analysis of BRCA1 and BARD1 proteins

Alignment of the BRCA1 region 931–1171 and of the BARD1 region 123–261 were generated using the MAFFT method[58] and represented using Jalview[59].

Preparation of DNA substrates

The sequences of all oligonucleotides used for DNA substrate preparation are listed in Supplementary Table 4 provided in the Supplementary Information. The oligonucleotide-based Y-structured DNA substrate was prepared with the oligonucleotides X12-3HJ3 and X12-3TOPLbis[35]. The oligonucleotide-based 70 bp-long dsDNA substrate was prepared with the oligonucleotides PC210 and PC211. X12-3HJ3 and PC210 oligonucleotides were ^{32}P-labelled at the 3′ terminus with (α-^{32}P)dCTP (Hartmann Analytic) and terminal transferase (New England Biolabs) according to the manufacturer's instructions. The oligonucleotide-based 70 bp-long dsDNA biotinylated at the 5′ terminus was prepared using the oligonucleotides PC206 and PC217. PC206 oligonucleotide was ^{32}P-labelled at the 5′ terminus with (γ-^{32}P) ATP (Hartmann Analytic) and T4 PNK (New England Biolabs) according to the manufacturer's instructions. The randomly labelled 2.2 kbp-long substrate was prepared by amplifying the human *NBS1* gene by PCR reaction containing 66 nM (α-^{32}P)dCTP (Hartmann Analytic) with the standard dNTPs concentration (200 μM each)[27]. When randomly labelled ssDNA was required, the 2.2 kbp-long substrate was heated at 95 °C for 5 min before the experiments. The HindIII digest of λ DNA (New England Biolabs) was labelled by fill-in at the 3′ end with (α-^{32}P) dCTP (Hartmann Analytic), dGTP, dATP (0.25 mM each) and 5 U of the Klenow fragment of DNA polymerase I exo- (lacking the 3′–5′ and 5′–3′ exonuclease activities of DNA polymerase I) (New England Biolabs). Unincorporated nucleotides were removed with Micro Bio-Spin P-30 Tris chromatography columns (BioRad). When the heat-denatured substrate was needed, the substrate was incubated at 95 °C for 5 min to obtain ssDNA[27]. pUC19-based dsDNA substrate was prepared by digesting the pUC19 plasmid with HindIII-HF restriction enzyme (New England Biolabs) according to the manufacturer's instructions, and purified by phenol-chloroform extraction and ethanol precipitation. The resulting linear dsDNA was labelled by fill-in at the 3′ end with 0.25 mM of (α-^{32}P)dCTP (Hartmann Analytic), dGTP, dATP and 5 U of the Klenow fragment of DNA polymerase I exo- (New England Biolabs). Unincorporated nucleotides were removed using Micro Bio-Spin P-30 Tris chromatography columns (BioRad). For the ATPase assay with wild-type DNA2 and helicase-dead DNA2 D277A, the 10.3 kbp-long pFB-MBP-hMLH3 plasmid[60] was linearized with NheI (New England Biolabs) and purified with QIAquick PCR purification kit (Qiagen). The substrate was denatured at 95 °C for 5 min to obtain ssDNA. The overhanging substrate used for single-molecule magnetic tweezer experiments was prepared as previously described[61,62]. Briefly, the main 6.6 kbp-long fragment was prepared from pNLRep plasmid[63] using the restriction enzymes BamHI and BsrGI (New England Biolabs). Furthermore, a 63 nt-long ssDNA gap was introduced using the nicking enzyme Nt.BbvCI (New England Biolabs). The gap was then filled by hybridizing a 25 nt-long DNA oligomer carrying an extra 40 nt-long polythimidine tail at the 5′ end (overhang), followed by 3′ end ligation inside the gap. Subsequently, 600 bp-long DNA handles carrying either several digoxigenin or biotin modifications were attached at either end. The handles were produced by PCR using as a template the plasmids pBlueScript II SK+ (digoxigenin, Dig handle Forward and Dig handle Reverse primers) or pNLRep (biotin, Bio handle Forward and Bio handle Reverse primers), respectively, in the presence of digoxigenin and biotin-modified nucleotides and digested with BamHI or BsrGI (New England Biolabs), respectively. The final construct shows the 5′ overhang at roughly 0.5 kbp distance from the surface attachment handle.

DNA end resection and protection assays

DNA endonuclease assays with the MRN complex and pCtIP were performed in 15 μl volume in nuclease buffer containing 25 mM Tris-acetate pH 7.5, 5 mM magnesium acetate, 1 mM manganese acetate, 1 mM ATP, 1 mM DTT, 0.25 mg ml^{-1} bovine serum albumin (BSA) (New England Biolabs), 1 mM phosphoenolpyruvate (PEP), 80 U ml^{-1} pyruvate kinase (Sigma) and 1 nM substrate (in molecules). Biotinylated DNA ends were blocked by adding 15 nM monovalent streptavidin (a kind gift from M. Howarth, University of Oxford)[64] and by incubating the samples at room temperature for 5 min. Different from above, DNA exonuclease assays with recombinant MRE11–RAD50 were carried out in nuclease buffer containing 3 mM manganese acetate. Recombinant proteins were added on ice and the reactions were incubated at 37 °C for 2 h. Reactions were stopped by adding 0.5 μl of 0.5 M EDTA and 1 μl Proteinase K (Roche, 18 mg ml^{-1}), and incubated at 50 °C for 30 min. An equal amount of formamide dye (95% [v/v] formamide, 20 mM EDTA, bromophenol blue) was added, samples were heated at 95 °C for 4 min and separated on 15% denaturing polyacrylamide gels (ratio acrylamide:bisacrylamide 19:1, BioRad). After fixing in a solution containing 40% methanol, 10% acetic acid and 5% glycerol for 30 min, the gels were dried on 3MM paper (Whatman), exposed to storage phosphor screens (GE Healthcare) and scanned with Typhoon FLA 9500 Phosphor Imager (GE Healthcare).

DNA end-resection assays with PCR-based or pUC19-based dsDNA substrate were performed in a 15 μl volume in 25 mM Tris-acetate pH 7.5, 2 mM magnesium acetate, 1 mM ATP, 1 mM DTT, 0.1 mg ml^{-1} BSA, 1 mM PEP, 80 U ml^{-1} pyruvate kinase and 1 nM substrate (in molecules). NaCl was added to the reaction buffer to a final concentration of 50 mM (unless indicated otherwise) taking into account the salt coming from protein storage or dilution buffers. When randomly labelled ssDNA was used, 2 nM substrate (in molecules) was used. Where indicated, AMP-PNP (Toronto Research Chemicals) or ATP-γ-S (Cayman Chemical) were used instead of ATP. Human RPA was included to saturate all ssDNA, as indicated. Further recombinant proteins were then added on ice and the reactions were incubated at 37 °C for 30 min, unless indicated otherwise. Reactions were stopped by adding 5 μl of 2% stop solution (150 mM EDTA, 2% SDS, 30% glycerol, bromophenol blue) and 1 μl of Proteinase K (Roche, 18 mg ml^{-1}) and incubated at 37 °C for 15 min. Samples were analysed by 1% agarose gel electrophoresis. Gels were dried on DE81 chromatography paper (Whatman) and analysed as described above.

The nuclease assays with λ DNA/HindIII-based substrates were carried out similarly as described above with the following differences. DNA was used at 0.15 nM (in molecules), the reaction buffer contained 3 mM magnesium acetate, 30 mM NaCl and, unless indicated otherwise, reactions were incubated at 37 °C for 1 h. DNA protection assays with PCR-based dsDNA substrate were carried out as indicated above for the respective DNA end resection assays, except RAD51, BRCA1–BARD1 or BRCA1 were pre-incubated at 37 °C for 10 min before the addition of the other recombinant proteins. Protection reactions were stopped by adding 0.5 μl of 0.5 M EDTA and 1 μl of Proteinase K (Roche, 18 mg ml^{-1}), and incubated at 50 °C for 30 min. An equal amount of formamide dye (95% [v/v] formamide, 20 mM EDTA, bromophenol blue) was added, and samples were heated at 95 °C for 4 min and separated on 20% denaturing polyacrylamide gels (ratio acrylamide:bisacrylamide 19:1). After fixing in a solution containing 40% methanol, 10% acetic acid and 5% glycerol for 30 min, the gels were dried on 3MM paper (Whatman) and analysed as described above. Protection assays with pUC19-based dsDNA substrate were carried out as indicated above for the respective DNA end resection assays. Signals were quantified using ImageJ2 (National Institutes of Health, NIH) and plotted with Prism 10 (GraphPad).

Helicase assays

Helicase assays with the oligonucleotide-based Y-structured DNA substrate were performed in 15 µl volume in reaction buffer (25 mM Tris-acetate pH 7.5, 5 mM magnesium acetate, 1 mM ATP, 1 mM DTT, 0.1 mg ml^{-1} BSA, 1 mM PEP, 80 U ml^{-1} pyruvate kinase and 50 mM NaCl) with 0.1 nM DNA substrate (in molecules). Recombinant proteins were added as indicated. Reactions were incubated at 37 °C for 30 min and stopped by adding 5 µl of 2% stop solution (150 mM EDTA, 2% SDS, 30% glycerol, bromophenol blue) and 1 µl of Proteinase K (Roche, 18 mg ml^{-1}) and incubated at 37 °C for 10 min. To avoid re-annealing of the substrate, the 2% stop solution was supplemented with a 20-fold excess of the unlabelled oligonucleotide with the same sequence as the ^{32}P-labelled one. The products were separated by 10% polyacrylamide gel electrophoresis, dried on 17 CHR chromatography paper (Whatman) and analysed as described for resection assays. Helicase assays with PCR-based, pUC19-based dsDNA substrate or HindIII digest of λ DNA were performed as described for the respective DNA end resection assays. Signals were quantified using ImageJ2 (NIH) and plotted with Prism 10 (GraphPad).

ATPase assays

ATPase assays with recombinant WRN were performed in 25 mM Tris-acetate pH 7.5, 5 mM magnesium acetate, 1 mM DTT, 0.1 mg ml^{-1} BSA, 1 mM ATP, 100 mM NaCl, 1 nM of (γ-^{32}P)ATP (Hartmann Analytic) and 0.1 nM (in molecules) of the X12-3HJ3 oligonucleotide used to prepare the Y-structured DNA substrate used in the helicase assays. RPA and BRCA1–BARD1 or BRCA1 were added on ice and samples were pre-incubated at 37 °C for 10 min. WRN was then added and reactions were incubated at 37 °C for 30 min. ATPase assays with recombinant wild-type DNA2 and nuclease-dead DNA2 D277A were performed in 25 mM Tris-acetate pH 7.5, 3 mM magnesium acetate, 1 mM DTT, 0.1 mg ml^{-1} BSA, 1 mM ATP, 20 mM NaCl, 1 nM of (γ-^{32}P)ATP (Hartmann Analytic) and 0.32 nM (in molecules) of a heat-denatured 10.3 kbp-long dsDNA as a substrate. RPA and indicated proteins were added on ice and samples were incubated at 37 °C for 15 min. Reactions were stopped with 1.1 µl of 0.5 M EDTA, and separated using thin layer chromatography plates (Merck) with 0.3 M LiCl and 0.3 M formic acid as the mobile phase. Dried plates were exposed to storage phosphor screens (GE Healthcare) and scanned with Typhoon FLA 9500 Phosphor Imager (GE Healthcare). Signals were quantified using ImageJ2 (NIH) and plotted with Prism 10 (GraphPad).

Protein-interaction assays

To test the interaction between BRCA1–BARD1 and WRN or EXO1, 1 µg of anti-BRCA1 antibody (Santa Cruz Biotechnology, sc-6954) or anti-WRN antibody (Cell Signaling, 4666S) were captured on 10 µl Protein G magnetic beads (Dynabeads, Invitrogen) by incubating at 4 °C for 1 h with gentle rotation in 50 µl of PBS-T (PBS with 0.1% Tween-20, Sigma). The beads were washed twice on a magnetic rack with 150 µl of PBS-T. The beads were then mixed with 1 µg of the bait in 60 µl of immunoprecipitation buffer (25 mM Tris-HCl pH 7.5, 1 mM DTT, 3 mM EDTA, 0.20 µg $µl^{-1}$ BSA, 100 mM NaCl) and incubated at 4 °C for 1 h with gentle rotation. Beads were washed three times with 150 µl of wash buffer (25 mM Tris-HCl pH 7.5, 1 mM DTT, 3 mM EDTA, 80 mM NaCl, 0.05% Triton-X, Sigma). Then 1 µg of the prey was added to the beads in 60 µl of immunoprecipitation buffer (25 mM Tris-HCl pH 7.5, 1 mM DTT, 3 mM EDTA, 0.20 µg $µl^{-1}$ BSA, 100 mM NaCl) and incubated at 4 °C for 1 h with gentle rotation. Beads were again washed three times with 150 µl of wash buffer (25 mM Tris-HCl pH 7.5, 1 mM DTT, 3 mM EDTA, 80 mM NaCl, 0.05% Triton-X) and proteins were eluted by boiling the beads in SDS buffer (50 mM Tris-HCl pH 6.8, 1.6% SDS, 100 mM DTT, 10% glycerol, 0.01% bromophenol blue) at 95 °C for 3 min. Avidin (Sigma) was added to the eluate as a stabilizer. The eluate was separated on a 7.5% SDS–PAGE gel and proteins were detected by western blotting using anti-BRCA1 antibody (Santa Cruz Biotechnology, sc-6954, 1:1,000), anti-His antibody (Invitrogen PA1-983B, 1:1,000) or anti-FLAG antibody (Sigma, F3165, 1:1,000). The final images were acquired with Fusion FX7 capture software (Vilber Imaging).

Mass photometry characterization of protein complexes

Mass photometry measurements were performed on a TwoMP mass photometer (Refeyn Ltd). First, borosilicate microscope glass plate (No. 1.5 H thickness, 24 × 50 mm, VWR) were cleaned by sequential soaking in Milli-Q-water, isopropanol and Milli-Q-water followed by drying under a stream of clean nitrogen. Next, silicone gaskets (CultureWell Reusable Gasket, Grace Bio-Labs) were placed on the clean coverslip to create a defined well for sample delivery. To convert optical reflection-interference contrast into a molecular mass, a known protein size marker (NativeMark Unstained Protein Standard, Invitrogen) was measured on the same day. For mass measurements, gaskets were filled with 18 µl of measurement buffer (25 mM Tris-HCl pH 7.5, 1 mM ATP, 3 mM magnesium acetate) to allow focusing the microscope onto the coverslip surface. Subsequently, 40 nM of either BRCA1 or BRCA1–BARD1 were added into the well (final volume, 20 µl) and sample binding to the coverslip surface was monitored for 1 min using the software AcquireMP (Refeyn Ltd). Data analysis was performed using DiscoverMP software (Refeyn Ltd).

Single-molecule magnetic tweezer experiments

Single-molecule magnetic tweezer experiments were carried out in a custom-built magnetic tweezers setup and operated using a self-developed code in Labview (2016, National Instruments)[65]. The DNA constructs were linked at their biotinylated ends with streptavidin-coated magnetic beads (Dynabeads M280, Thermo Fisher Scientific) and flushed into the flow cell, where the bottom slide was coated with antidigoxigenin to ensure surface-specific binding. Moving the magnet closer to the flow cell resulted in the stretching of the DNA molecules that were attached to a magnetic bead. Tracking of the magnetic beads for all measurements was conducted at 300 Hz using video microscopy and real-time GPU-accelerated image analysis[66]. The magnetic forces were calibrated based on fluctuation analysis[67]. The measurements were performed in a reaction buffer (25 mM Tris-acetate pH 7.5, 2 mM magnesium acetate, 1 mM ATP, 1 mM DTT, 0.1 mg ml^{-1} BSA), with the indicated protein concentrations at a temperature of 37 °C and forces between 15 and 25 pN. The analysis of the recorded traces was conducted with a custom written MATLAB program[68]. We considered only traces from measurements in which the magnetic bead position was traceable for at least 300 s. The acquired processivity and velocity for the unwinding events were calculated by fitting linear segments to parts of the recorded traces with roughly constant velocity, which were used to construct the histograms and for statistical analysis. To quantify the ratio of rewinding/unwinding events, the total number of the two events, acquired as described above, was determined for a fixed period of 300 s for each recorded trace. To characterize the different protein combinations (Fig. 3c) and WRN variants (Extended Data Fig. 7e), the difference between the maximum value and the minimum value of DNA extension for a given molecule was calculated during the first 300 s and expressed as ΔDNA-length. Each dot represents one measured molecule.

Cell lines

The RPE1 hTERT were purchased from American Type Culture Collection (ATCC). The RPE1 hTERT *PAC*$^{-/-}$*TP53*$^{-/-}$ cell line (referred to as RPE1 *EXO1*$^{+/+}$ in this paper)[45] was used to generate RPE1 hTERT *PAC*$^{-/-}$*TP53*$^{-/-}$ *EXO1*$^{-/-}$ (referred to as RPE1 *EXO1*$^{-/-}$) cells by nucleofection of pLentiCRISPR_v2 containing the sg*EXO1* (GCGTGGGATTGGATTAGCAA) as described before[45]. After clonal selection, genotyping was performed to confirm indel formation using target locus PCR amplification and Sanger sequencing, followed by TIDE (tracking of indels by decomposition) analysis. RPE1 *EXO1*$^{+/+}$ and *EXO1*$^{-/-}$ cells inducibly expressing

exogenous CtIP-WT or CtIP-S327A were obtained by viral transduction with pCW57.1_Zeo-CtIP-WT-2×FLAG or pCW57.1_Zeo-CtIP-S327A-2×FLAG.

U2OS cells were originally bought from ATCC. U2OS-derived cells, carrying green fluorescent protein (GFP), GFP-CtIP-WT or GFP-CtIP-S327A mutant[16], were grown in DMEM medium (Sigma). Media were supplemented with 10% fetal bovine serum (Sigma), 2 mM L-glutamine (Sigma), 100 U ml^{-1} penicillin and 100 µg ml^{-1} streptomycin (Sigma). U2OS cells were last authenticated in June 2024 by the GenePrint 10 System (Promega) using short tandem repeat profiling, and data were analysed using genemapper id-x v.1.2 software (Applied Biosystems) at the genomic core facility of the Instituto de Investigaciones Biomedicas Sols-Morreale. All cell lines were routinely tested for mycoplasm contamination. All the experiments performed here used mycoplasm-free cell lines.

Viral transductions and transfections

Third-generation packaging vectors pMDLg/pRRE, pRSV-Rev, pMD2.g and a lentiviral expression vector (pLentiCRISPR-v2 or pCW57.1) were transfected to human embryonic kidney (HEK) 293T using jet-PEI (Polyplus Transfection) to produce lentiviral particles. The HEK 293T cell line was originally purchased from ATCC. The medium was refreshed 16 h post-transfection. Viral supernatants were harvested 48 h post-transfection, filtered with a 0.45 mm filter and transduced into cells at a multiplicity of infection of 1 in the presence of 4 µg ml^{-1} polybrene. Puromycin (2 µg ml^{-1}) and zeocin (400 µg ml^{-1}) were used for the selection of pLentiCRISPR- and pCW57.1- transduced RPE1 cells, respectively.

Clonogenic survival assays

RPE1 *EXO1*$^{+/+}$ or *EXO1*$^{-/-}$ cells transduced with CtIP-WT or CtIP-S327A were induced with doxycycline (2 µg ml^{-1}) to express CtIP protein exogenously. Cells were virally transduced with pLentiCRISPR-sg*CtIP* or empty vector to deplete endogenous CtIP 24 h post-doxycycline induction. After 48 h of puromycin selection to select for pLentiCRISPR transduced cells, 500 cells were seeded in 10-cm dishes for clonogenic growth. Medium containing doxycycline (2 µg ml^{-1}) was refreshed after 7 days. After 14 days, colonies were stained with crystal violet solution (0.4% [w/v], 20% methanol) and counted manually. Simultaneously with plating cells for clonogenic survival, cells were collected for immunoblotting analysis and lysed in RIPA lysis buffer (1% NP40, 50 mM Tris-HCl pH 7.5, 150 mM NaCl, 0.1% SDS, 3 mM $MgCl_2$, 0.5% sodium deoxycholate) supplemented with Complete Protease Inhibitor Cocktail (Sigma) and 100 U ml^{-1} Benzonase (Sigma). Western blots were stained with primary antibodies against CtIP (Millipore, MABE1060, 1:2,000), FLAG (Sigma, F1804-200UG, 1:2,000), EXO1 (Abcam, ab95068, 1:1,000) and α-Tubulin (Sigma, T6199, 1:5,000); and with HRP-conjugated secondary antibodies donkey anti-rabbit IgG-HRP (Thermo Scientific, 31458, 1:5,000) or goat anti-mouse IgG-HRP (Thermo Scientific, 31432, 1:5,000).

Immunofluorescence and microscopy

For RPA foci visualization, U2OS-derived cells were seeded on coverslips. For the experiment with DNA2 inhibitor C5 (MedChemExpress, catalogue no. HY128729), 20 µM of the inhibitor or the same amount of vehicle (dimethylsulfoxide, DMSO) were added to the plates 6 h before irradiation. Then 1 h after irradiation (10 Gy), coverslips were washed once with PBS followed by treatment with pre-extraction buffer (25 mM Tris-HCl pH 7.5, 50 mM NaCl, 1 mM EDTA, 3 mM $MgCl_2$, 300 mM sucrose and 0.2% Triton-X-100) for 5 min on ice. Cells were fixed with 4% paraformaldehyde [w/v] in PBS for 20 min. Following two washes with PBS, cells were blocked for 1 h with 5% fetal bovine serum in PBS, costained with the appropriate primary antibodies (RPA2, Abcam, ab2175, 1:500) in blocking solution overnight at 4 °C or for 2 h at room temperature, washed again with PBS and then co-immuno-stained with the appropriate secondary antibodies (Alexa Fluor 594 goat anti-mouse, Invitrogen, A11032, 1:500 and Alexa Fluor 488 goat anti-rabbit, Invitrogen, A11034, 1:500) in blocking buffer. After washing with PBS, coverslips were incubated sequentially in 70% and 100% ethanol to dehydrate them. Finally, they were air dried and mounted into glass slides using Vectashield mounting medium with 4,6-diamidino-2-phenylindole (Vector Laboratories). RPA foci immunofluorescence was analysed using a Leica DM6000B Fluorescence microscope (AF6000).

Cell-cycle analysis

Cells were trypsinized and fixed with cold 70% ethanol overnight, incubated with 250 µg ml^{-1} RNase A (Sigma) and 10 µg ml^{-1} propidium iodide (Fluka) at 37 °C for 30 min and analysed with a LSRFortessaTM Cell Analyzer (BD) Flow Cytometer. Cell-cycle distribution data were further analysed using ModFit LT v.5.0 software (Verity Software House Inc.).

Statistics and reproducibility

Sample size or number of technical (for biochemical assays) and biological (for cellular assays) replicates were chosen on the basis of what is common in the field and what was practical to do. A minimum of three independent replicates were performed for each biochemical experiment to add statistical analysis, when required. Where indicated, a representative experiment from independent repeats with similar results was shown. Coomassie-stained protein gels were repeated twice to confirm the quality and the concentration of the indicated recombinant proteins. Protein-interaction assays were performed twice.

Reporting summary

Further information on research design is available in the Nature Portfolio Reporting Summary linked to this article.

Data availability

All relevant data generated or analysed during this study are included in this published Article and its Supplementary Information. Videos underlying mass photometry analysis and single-molecule source data are uploaded to Dryad (https://doi.org/10.5061/dryad.gf1vhhmxc)[69]. Source data are provided with this paper.

51. Acharya, A. et al. Distinct RPA domains promote recruitment and the helicase-nuclease activities of Dna2. *Nat. Commun.* **12**, 6521 (2021).
52. Mengoli, V. et al. WRN helicase and mismatch repair complexes independently and synergistically disrupt cruciform DNA structures. *EMBO J.* **42**, e111998 (2023).
53. Cejka, P. & Kowalczykowski, S. C. The full-length *Saccharomyces cerevisiae* Sgs1 protein is a vigorous DNA helicase that preferentially unwinds holliday junctions. *J. Biol. Chem.* **285**, 8290–8301 (2010).
54. Cannavo, E. et al. Regulation of the MLH1-MLH3 endonuclease in meiosis. *Nature* **586**, 618–622 (2020).
55. Howard, S. M., Ceppi, I., Anand, R., Geiger, R. & Cejka, P. The internal region of CtIP negatively regulates DNA end resection. *Nucleic Acids Res.* **48**, 5485–5498 (2020).
56. Henricksen, L. A., Umbricht, C. B. & Wold, M. S. Recombinant replication protein A: expression, complex formation, and functional characterization. *J. Biol. Chem.* **269**, 11121–11132 (1994).
57. Anand, R., Pinto, C. & Cejka, P. Methods to study DNA end resection I: recombinant protein purification. *Methods Enzymol.* **600**, 25–66 (2018).
58. Katoh, K. & Standley, D. M. MAFFT multiple sequence alignment software version 7: improvements in performance and usability. *Mol. Biol. Evol.* **30**, 772–780 (2013).
59. Waterhouse, A. M., Procter, J. B., Martin, D. M., Clamp, M. & Barton, G. J. Jalview version 2–a multiple sequence alignment editor and analysis workbench. *Bioinformatics* **25**, 1189–1191 (2009).
60. Ranjha, L., Anand, R. & Cejka, P. The *Saccharomyces cerevisiae* Mlh1-Mlh3 heterodimer is an endonuclease that preferentially binds to Holliday junctions. *J. Biol. Chem.* **289**, 5674–5686 (2014).
61. Levikova, M., Klaue, D., Seidel, R. & Cejka, P. Nuclease activity of *Saccharomyces cerevisiae* Dna2 inhibits its potent DNA helicase activity. *Proc. Natl Acad. Sci. USA* **110**, E1992–E2001 (2013).
62. Grigaitis, R. et al. Phosphorylation of the RecQ helicase Sgs1/BLM controls its DNA unwinding activity during meiosis and mitosis. *Dev. Cell* **53**, 706–723 e705 (2020).
63. Luzzietti, N. et al. Efficient preparation of internally modified single-molecule constructs using nicking enzymes. *Nucleic Acids Res.* **39**, e15 (2011).
64. Howarth, M. et al. A monovalent streptavidin with a single femtomolar biotin binding site. *Nat. Methods* **3**, 267–273 (2006).
65. Klaue, D. & Seidel, R. Torsional stiffness of single superparamagnetic microspheres in an external magnetic field. *Phys. Rev. Lett.* **102**, 028302 (2009).

66. Huhle, A. et al. Camera-based three-dimensional real-time particle tracking at kHz rates and Angstrom accuracy. *Nat. Commun.* **6**, 5885 (2015).
67. Daldrop, P., Brutzer, H., Huhle, A., Kauert, D. J. & Seidel, R. Extending the range for force calibration in magnetic tweezers. *Biophys. J.* **108**, 2550–2561 (2015).
68. Kemmerich, F. E., Kasaciunaite, K. & Seidel, R. Modular magnetic tweezers for single-molecule characterizations of helicases. *Methods* **108**, 4–13 (2016).
69. Ceppi, I. et al. Mechanism of BRCA1-BARD1 function in DNA end resection and DNA protection. *Dryad* https://doi.org/10.5061/dryad.gf1vhhmxc (2024).

Acknowledgements We thank members of the Cejka laboratory for their critical comments on this paper. The Swiss National Science Foundation (grant nos. 310030_207588 and 310030_205199) and the European Research Council (grant no. 101018257) support the research in the Cejka laboratory. M.R.D.S. is a recipient of the EMBO Postdoctoral Fellowship (grant no. ALTF-710-2021). Work in the Huertas laboratory was supported by grant no. PID2022-136791NB-I00 funded by grant no. MICIU/AEI/10.13039/501100011033/FEDER/UE. This work is supported by Agence Nationale de la Recherche (grant no. ANR-21-CE44-0009) and by IDRIS (grant no. AD010314343R1) to R.G. Research in the Noordermeer laboratory is funded by the European Union through the MSCA doctoral network Replifate and by Oncode Institute. We thank the Sung laboratory for communicating data before publication.

Author contributions I.C., M.R.D.S. and P.C. designed the study. I.C. and M.R.D.S. prepared most of the recombinant proteins, carried out and analysed most of the experiments. M.M. carried out single-molecule magnetic tweezer experiments with the supervision of R.S. S.B. prepared human RPA and performed resection experiments with human EXO1 and bacterial ExoIII. M.M. and S.B. contributed equally. V.M. prepared some of the truncated WRN protein variants and carried out preliminary unwinding assays. G.R. carried out assays in Extended Data Figs. 1e and 2k,l. H.M.P.V. performed clonogenic survival experiments with the supervision of S.M.N. S.J. carried out immunofluorescence and microscopy analysis of RPA^+ cells with the supervision of P.H. A.A. cloned and contributed to the preparation of all the BRCA1 and BARD1 variants. M.R. purified EXO1 Δ1. A.S. optimized and carried out the preliminary protection assays with WRN, DNA2 and RAD51. S.H. and S.M.H. performed the first BRCA1 and BRCA1–BARD1 protein preparations. R.G. carried out protein alignments and contributed to the design of the BRCA1 and BARD1 variants. I.C., M.R.D.S. and P.C. wrote the paper with contributions from all authors.

Competing interests The authors declare no competing interests.

Additional information
Supplementary information The online version contains supplementary material available at https://doi.org/10.1038/s41586-024-07909-9.
Correspondence and requests for materials should be addressed to Petr Cejka.
Peer review information *Nature* thanks Maria Spies and the other, anonymous, reviewer(s) for their contribution to the peer review of this work. Peer reviewer reports are available.
Reprints and permissions information is available at http://www.nature.com/reprints.

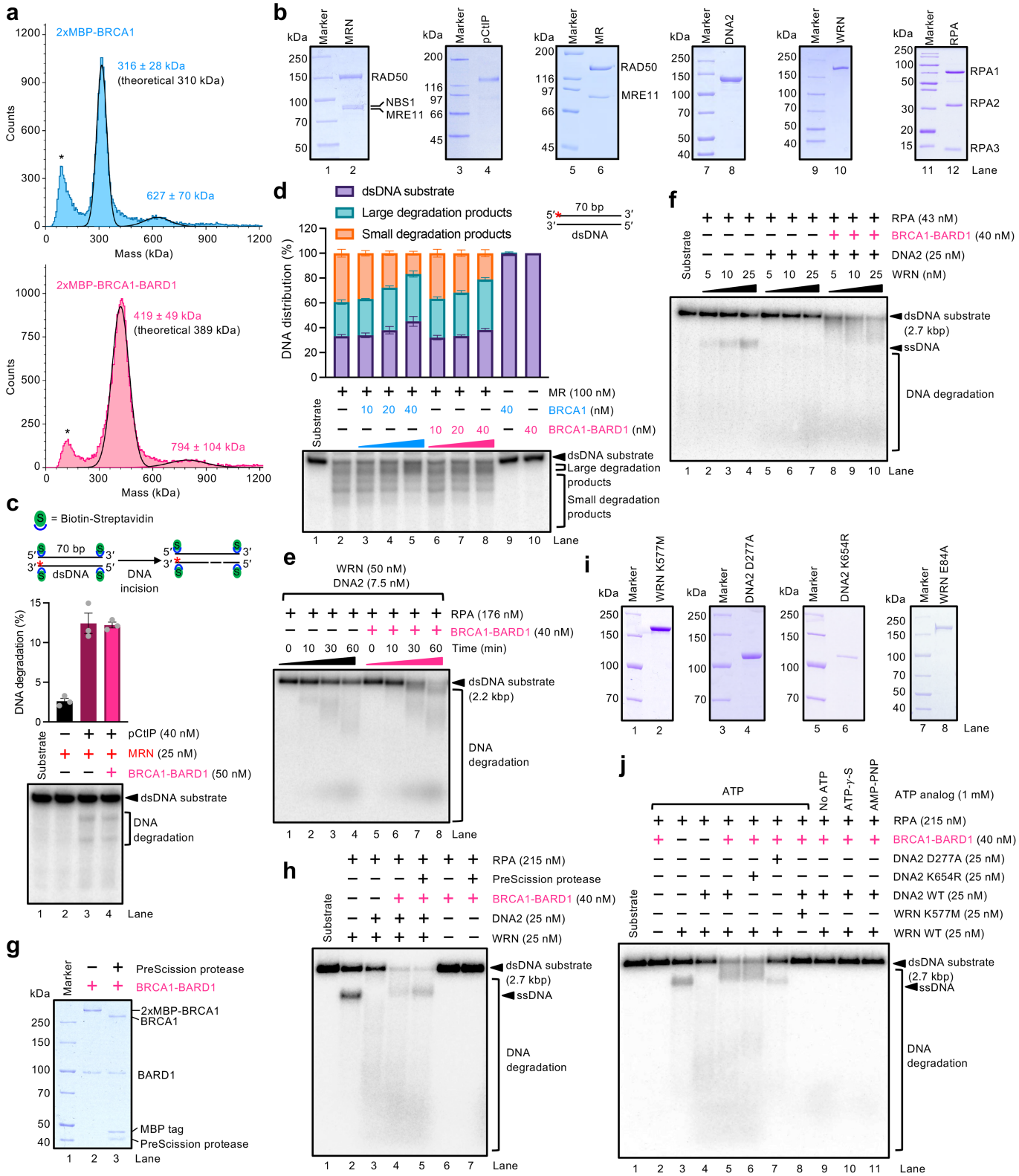

Extended Data Fig. 1 | See next page for caption.

Extended Data Fig. 1 | BRCA1–BARD1 stimulates long-range resection by WRN-DNA2-RPA. a, Molecular weight distributions of 2xMBP-tagged BRCA1 alone or in complex with BARD1 measured by mass photometry. Black asterisks (*) indicate background noise. **b**, Polyacrylamide gels of the indicated recombinant proteins stained with Coomassie Brilliant Blue. **c**, DNA endonuclease assays with MRN-pCtIP, in the absence or presence of BRCA1-BARD1. Top, a schematic of the assay. Red asterisk (*) represents the position of the radioactive label. Middle, quantitation of DNA degradation. Averages shown; error bars, SEM; n = 3. Bottom, representative assays. **d**, DNA exonuclease assays with MR, in the absence or presence of either BRCA1 or BRCA1-BARD1. Right, a schematic of the substrate. Red asterisk (*) represents the position of the radioactive label. Top left, quantitation of the different reaction intermediates. Averages shown; error bars, SEM; n = 3. Bottom, representative assays. **e**, Representative kinetic resection assays with WRN-DNA2-RPA, in the absence or presence of BRCA1-BARD1. **f**, Representative resection assays with RPA and the indicated concentrations of WRN in the absence or presence of BRCA1-BARD1 and DNA2. For this assay 0.2 nM of radioactively labeled substrate was used. **g**, 2xMBP-BRCA1-BARD1 either mock-treated or treated with PreScission protease (1:5 ratio, w:w) for 1 h at 4 °C. The polyacrylamide gel was stained with Coomassie Brilliant Blue. **h**, Representative resection assays on with WRN-DNA2-RPA, in the absence or presence of BRCA1-BARD1, either mock- or PreScission protease-treated. **i**, Polyacrylamide gels of the indicated recombinant WRN and DNA2 variants stained with Coomassie Brilliant Blue. **j**, Representative resection assays with wild type WRN or helicase-dead WRN K577M, wild type DNA2, helicase-dead DNA2 K654R or nuclease-dead DNA2 D277A, RPA, in the absence or presence of BRCA1-BARD1. ATP was omitted or substituted with non-hydrolysable ATP analogs (ATP-γ-S or AMP-PNP) as indicated. Source data are provided as Supplementary Information SI Fig. 4.

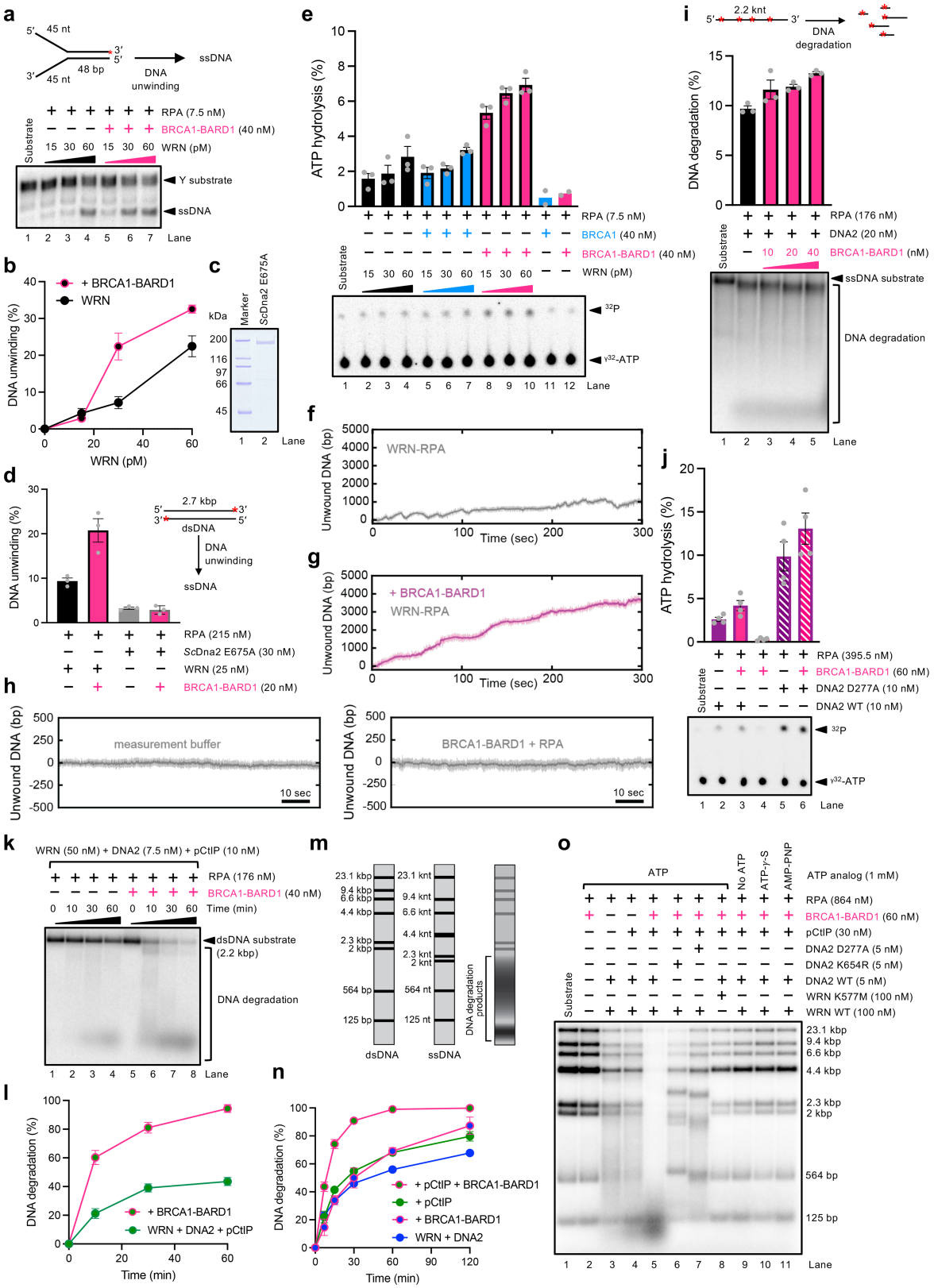

Extended Data Fig. 2 | See next page for caption.

Extended Data Fig. 2 | BRCA1-BARD1 stimulates ATP-dependent WRN helicase. a, Unwinding assays with WRN-RPA, in the absence or presence of BRCA1-BARD1. Top, a schematic of the assay. Red asterisk (*) represents the position of the radioactive label. Bottom, representative assays. **b**, Quantitation of DNA unwinding assays such as shown in a. Averages shown; error bars, SEM; n = 3. **c**, Recombinant nuclease-dead yeast Dna2 E675A used in this study. The polyacrylamide gel was stained with Coomassie Brilliant Blue. **d**, Quantitation of unwinding assays with WRN-RPA or nuclease-dead yeast Dna2 E675A and RPA, in the absence or presence of BRCA1-BARD1. Averages shown; error bars, SEM; n = 3. Top right, a schematic of the assay. Red asterisk (*) represents the position of the radioactive labels. **e**, ATPase assays with a 93 nt-long ssDNA, WRN and RPA, in the absence or presence of either BRCA1 or BRCA1-BARD1. Top, quantitation of ATP hydrolysis. Averages shown; error bars, SEM (lanes 2-10); n = 2 for BRCA1 and BRCA1-BARD1 alone controls and n = 3 for all the other samples. Bottom, representative assays. **f**, Representative trajectory of DNA unwinding events by WRN in the presence of RPA, both 25 nM. **g**, Representative trajectory of DNA unwinding events by WRN (25 nM) in the presence of BRCA1-BARD1 (40 nM) and RPA (25 nM). **h**, Representative trajectories with the reaction buffer (left) or BRCA1-BARD1 (40 nM) and RPA (25 nM) alone (right). **i**, Nuclease assays with DNA2-RPA, in the absence or presence of BRCA1-BARD1. Top, a schematic of the assay. Red asterisks (*) represent the position of the radioactive labels. Middle, quantitation of the DNA degradation products. Averages shown; error bars, SEM; n = 3. Bottom, representative assays. **j** ATPase assays in the presence of 10.3 knt-long ssDNA with wild type DNA2 or nuclease-dead DNA2 D277A and RPA, in the absence or presence of BRCA1-BARD1. Top, quantitation of ATP hydrolysis. Averages shown; error bars, SEM; n = 4. Bottom, representative assays. **k**, Representative kinetic assays with WRN-DNA2-RPA, phosphorylated CtIP (pCtIP), in the absence or presence of BRCA1-BARD1. **l**, Quantitation of DNA degradation products from assays such as shown in k. Averages shown; error bars, SEM; n = 3. **m**, A schematic of the λ DNA/HindIII-based substrate employed for the DNA end resection assays. Shown is the distribution of the DNA fragments in their double-stranded (left) or single-stranded (middle) forms. The right lane shows an example of a pattern upon partial DNA degradation. **n**, Quantitation of DNA degradation products (based on disappearance of DNA fragments of ≥4.3 kbp in length) from assays such as shown in Fig. 3a. Averages shown; error bars, SEM; n = 3. **o**, Representative resection assays with wild type WRN or helicase-dead WRN K577M, wild type DNA2, or helicase-dead DNA2 K654R or nuclease-dead DNA2 D277A, pCtIP and RPA, in the absence or presence of BRCA1-BARD1. ATP was omitted or substituted with non-hydrolysable ATP analogs (ATP-γ-S or AMP-PNP) as indicated. Source data are provided as Supplementary Information SI Fig. 5.

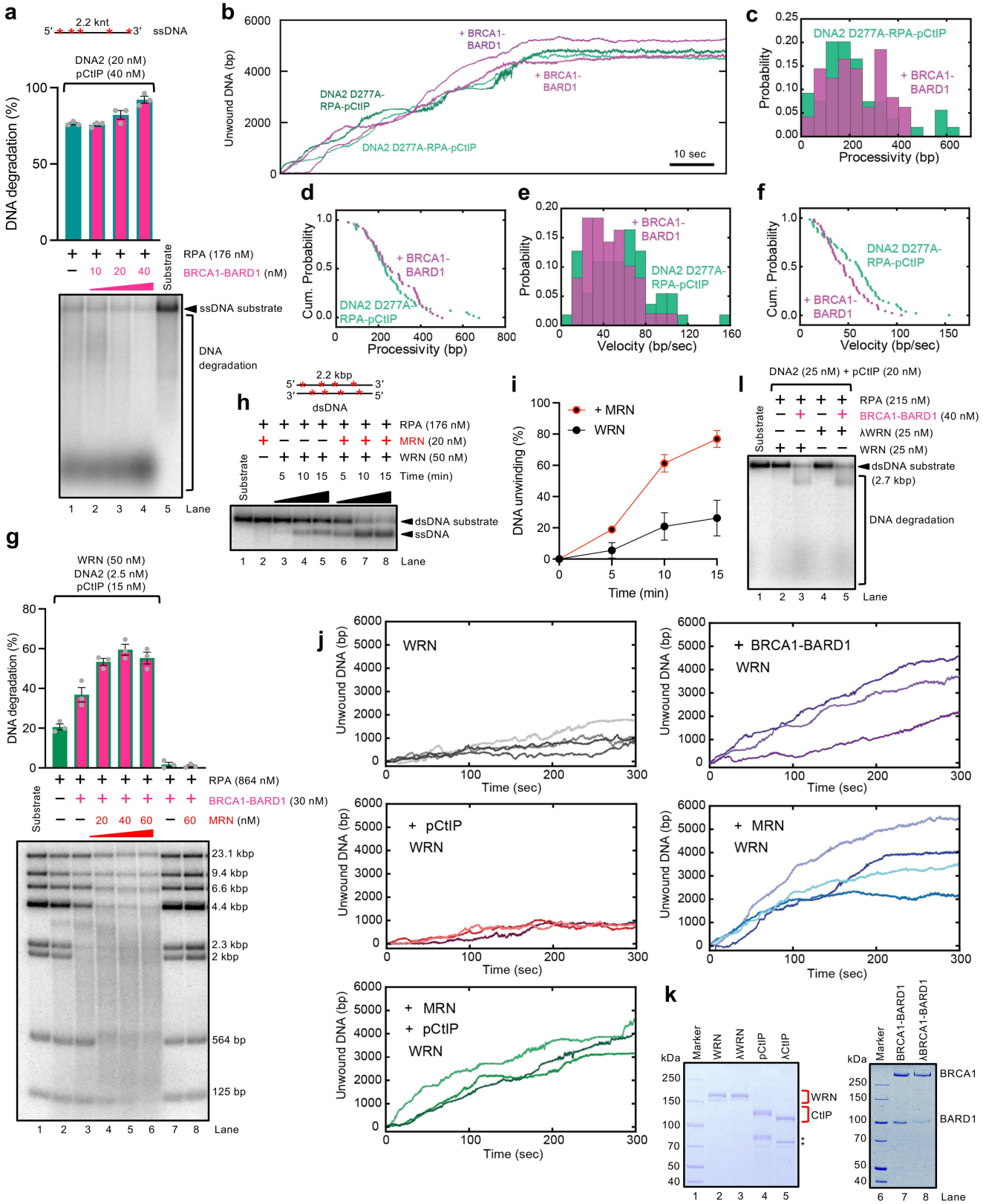

Extended Data Fig. 3 | See next page for caption.

Extended Data Fig. 3 | The BRCA1-C complex stimulates resection by WRN-DNA2-RPA. a, Nuclease assays with DNA2-pCtIP-RPA, in the absence or presence of BRCA1-BARD1. Top, a schematic of the substrate. Middle, quantitation of DNA degradation. Averages shown; error bars, SEM; n = 3. Bottom, representative assays. **b**, Representative trajectories of DNA unwinding events by nuclease-dead DNA2 D277A (10 nM) with pCtIP (10 nM) and RPA (25 nM), in the absence (green) or presence (pink) of BRCA1-BARD1 (25 nM). **c**, **d**, Processivity histogram and cumulative probability distribution (shown as survival probability) of the observed DNA unwinding events by nuclease-dead DNA2 D277A-pCtIP-RPA, in the absence (green) or presence (pink) of BRCA1-BARD1, with mean values of 264 ± 38 bp (n = 55) and 271 ± 32 bp (n = 49), respectively. Error, 2SEM. **e**, **f**, Velocity histogram and cumulative probability distribution (shown as survival probability) of the observed DNA unwinding events by nuclease-dead DNA2 D277A-pCtIP-RPA, in the absence (green) or presence (pink) of BRCA1-BARD1, with mean values of 57 ± 8 bp/sec (n = 55) and 46 ± 6 bp/sec (n = 49), respectively. Error, 2SEM. **g**, Representative resection assays with WRN-DNA2-pCtIP-RPA, BRCA1-BARD1, and the indicated concentration of MRN. Top, quantitation of DNA degradation products (based on disappearance of DNA fragments of ≥4.3 kbp in length). Averages shown; error bars, SEM; n = 3. **h**, Representative kinetic resection assays with WRN-RPA, in the absence or presence of MRN. **i**, Quantitation of DNA unwinding assays such as shown in h. Averages shown; error bars, SEM; n = 3. **j**, Representative trajectories of DNA unwinding events by WRN, in the absence or presence of the indicated proteins, all at 25 nM. **k**, Polyacrylamide gels of the indicated recombinant proteins stained with Coomassie Brilliant Blue (relevant proteins indicated with red brackets). Black asterisks (*) represent truncations of the indicated proteins (lanes 4 and 5). **l**, Representative resection assays with DNA2-pCtIP-RPA, in the presence of WRN (WRN) or de-phosphorylated WRN (λWRN), and in the absence or presence of BRCA1-BARD1. Source data are provided as Supplementary Information SI Fig. 6.

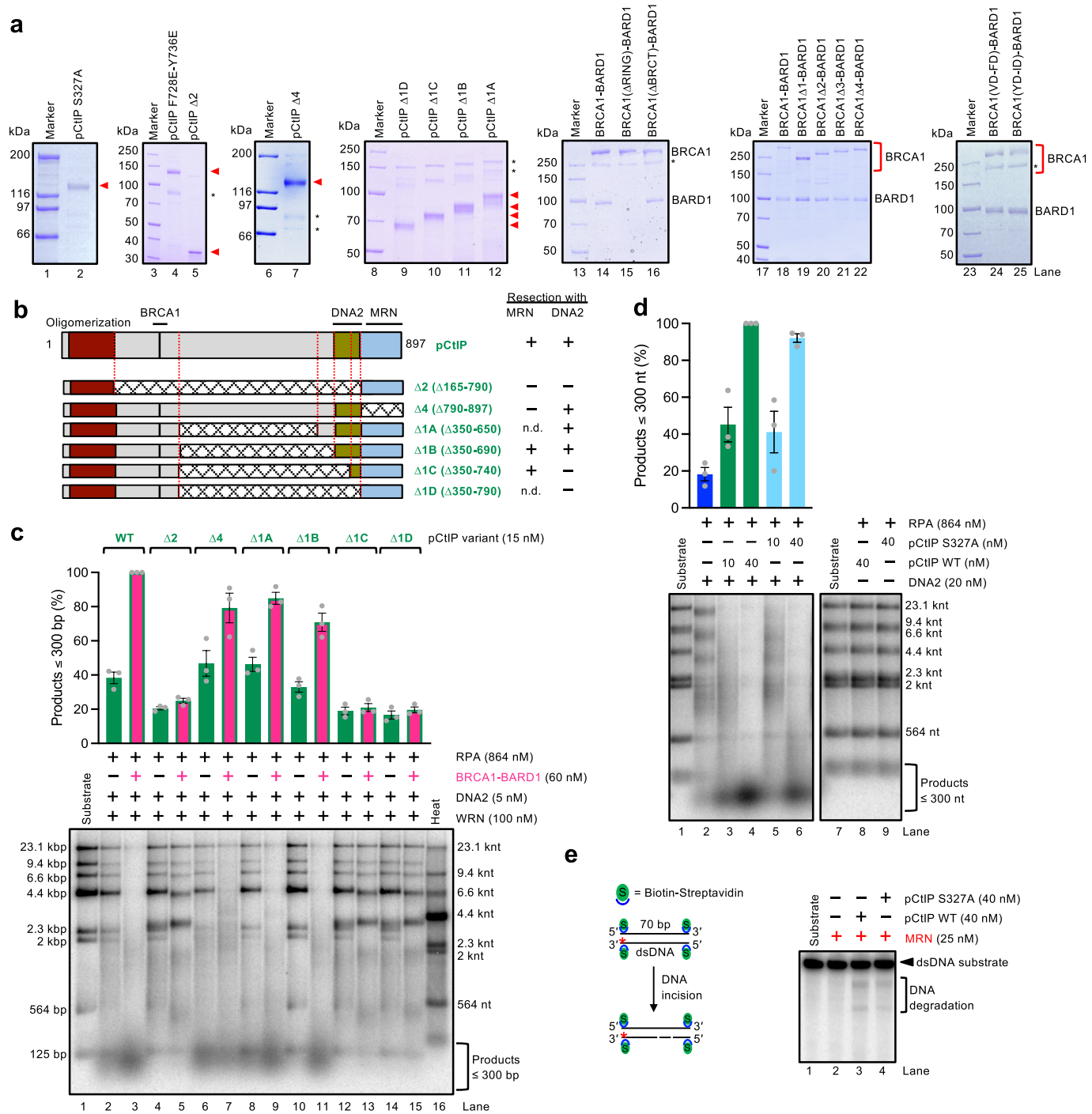

Extended Data Fig. 4 | CtIP interaction with BRCA1 and DNA2 is required for its function in the long-range DNA end resection ensemble. **a**, Polyacrylamide gels of the indicated recombinant proteins stained with Coomassie Brilliant Blue (relevant proteins indicated with red arrows or red brackets). Black asterisks (*) represent truncations of the indicated proteins (lanes 5, 7), proteins with uncleaved MBP-tag (lanes 9-12) or proteins with some spontaneous cleavage of the MBP-tag (lanes 14-16 and 25). BRCA1 VD-FD, V1035D-F1036D (lane 24). BRCA1 YD-ID, Y1127D-I1129D (lane 25). **b**, Cartoon of the primary structure of the phosphorylated CtIP (pCtIP) variants used in this study. Deleted portions of the protein are indicated with a diamond grid pattern. The capacity of each variant to stimulate MRN and/or DNA2-mediated resection, as reported from previous studies, is indicated on the right. n.d., not determined. **c**, Resection assays with WRN-DNA2-RPA, in the absence or presence of BRCA1-BARD1 and the indicated pCtIP variant (see panel b). Top, quantitation of DNA degradation products of ≤300 bp in length. Averages shown; error bars, SEM; n = 3. Bottom, representative assays. **d**, Resection assays showing the substrate degradation by DNA2-RPA, in the presence of either wild type pCtIP or pCtIP S327A variant. Top, quantitation of DNA degradation products of ≤300 bp in length. Averages shown; error bars, SEM; n = 3. Bottom, representative assays. **e**, Nuclease assays with MRN, in the presence of either wild type pCtIP or pCtIP S327A variants. Left, a schematic of the assay. Red asterisk (*) represents the position of the radioactive label. Right, representative assays. Source data are provided as Supplementary Information SI Fig. 7.

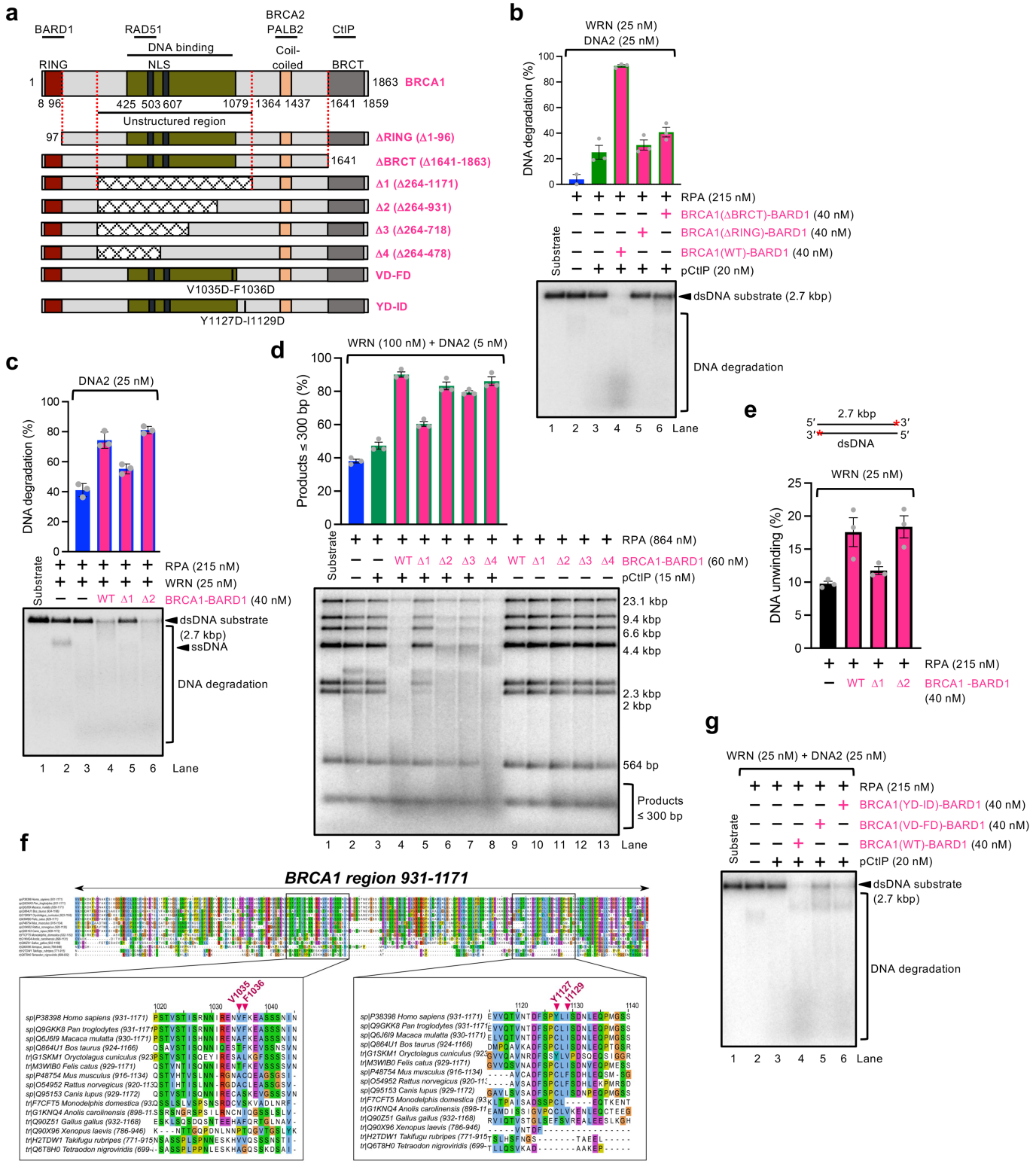

Extended Data Fig. 5 | Identification of BRCA1 regions necessary for DNA end resection. a, Cartoon of the primary structure of the BRCA1 protein including all variants used in this study. Deleted segments of the proteins are indicated with diamond grid pattern. **b**, Resection assays with WRN-DNA2-pCtIP-RPA, in the absence or presence of the indicated BRCA1 variants in complex with BARD1. Top, quantitation of DNA degradation. Averages shown; error bars, SEM; n = 3. Bottom, representative assays. **c**, Resection assays with WRN-DNA2-RPA, in the absence or presence of the indicated BRCA1 variants in complex with BARD1. Top, quantitation of DNA degradation. Averages shown; error bars, SEM; n = 3. Bottom, representative assays. **d**, Resection assays with WRN-DNA2-RPA, in absence or presence of pCtIP and the indicated BRCA1-BARD1 variants. Top, quantitation of DNA degradation products of ≤300 bp in length. Averages shown; error bars, SEM; n = 3. Bottom, representative assays. **e**, Unwinding assays with WRN-RPA, in the absence or presence of the indicated BRCA1-BARD1 variants. Averages shown; error bars, SEM; n = 3. Top, a schematic of the substrate. Red asterisk (*) represents the position of the radioactive label. **f**, Alignment of BRCA1 region 931-1171. Selected residues mutated in this study are highlighted by pink triangles. Insertions in the orthologs of human BRCA1 are not shown. **g**, Representative resection assays with WRN-DNA2-pCtIP-RPA, in the absence or presence of the indicated BRCA1 variants in complex with BARD1. Source data are provided as Supplementary Information SI Fig. 8.

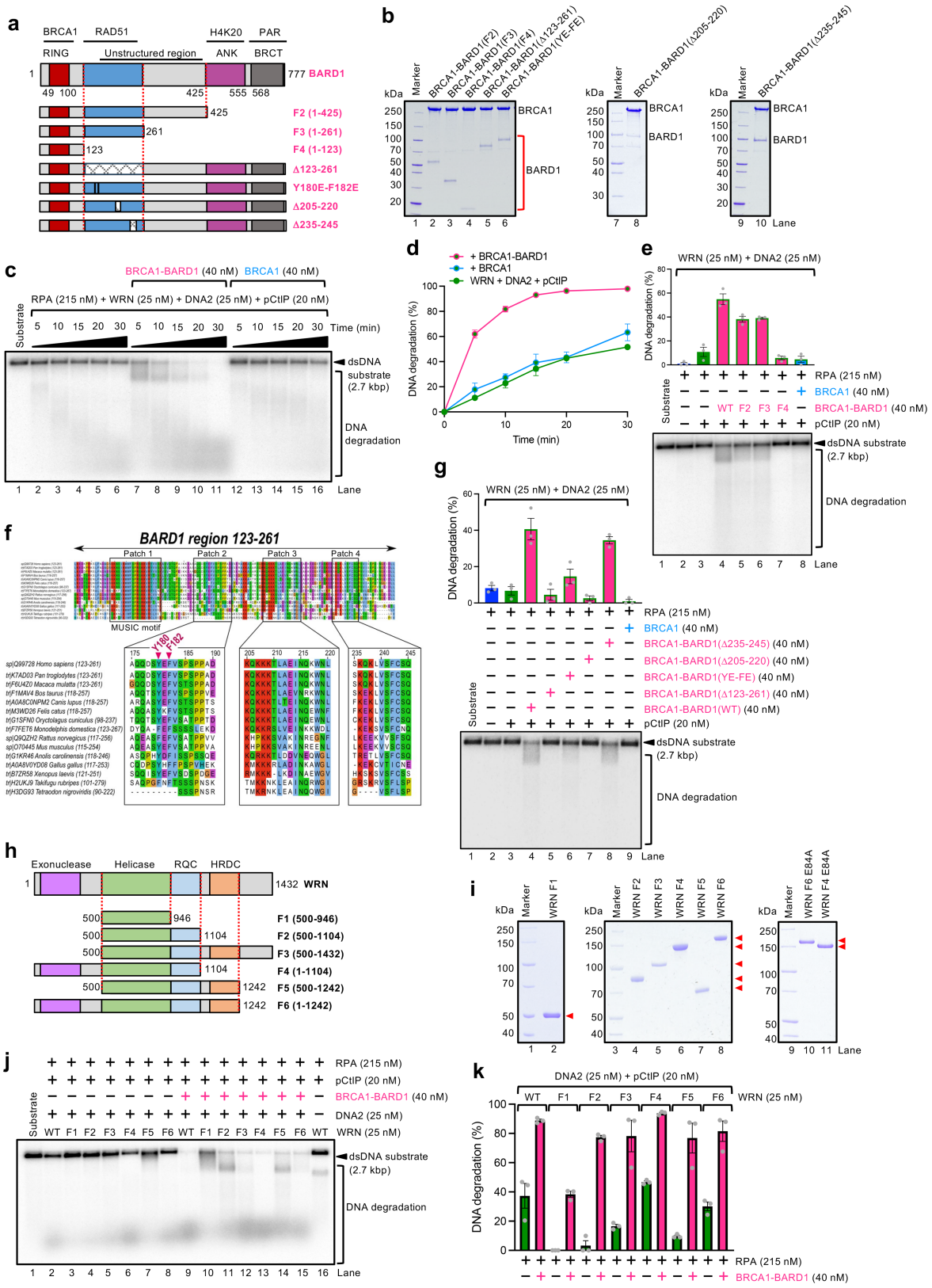

Extended Data Fig. 6 | See next page for caption.

Extended Data Fig. 6 | Identification of BARD1 and WRN regions necessary for DNA end resection. a, Cartoon of the primary structure of BARD1 and the truncated variants used in this study. **b**, Polyacrylamide gels of the indicated BARD1 variants stained with Coomassie Brilliant Blue. **c**, Representative kinetic resection assays with WRN-DNA2-pCtIP-RPA, in the absence or presence of either BRCA1-BARD1 or BRCA1. **d**, Quantitation of DNA degradation from assays such as shown in c. Averages shown; error bars, SEM; n = 3. **e**, Resection assays with WRN-DNA2-pCtIP-RPA, in the absence or presence of the indicated BARD1 variants in complex with BRCA1. Top, quantitation of DNA degradation. Averages shown; error bars, SEM; n = 3. Bottom, representative assays. **f**, Alignment of the BARD1 region 123-261. Selected patches and residues mutated in this study are highlighted. Insertions in the orthologs of human BARD1 are not shown. **g**, Resection assays with WRN-DNA2-pCtIP-RPA, in the absence or presence of the indicated BARD1 variant, expressed as BRCA1-BARD1. Top, quantitation of DNA degradation. Averages shown; error bars, SEM; n = 3. Bottom, representative assays. **h**, Cartoon of the primary structure of the WRN protein and the truncated variants used in this study. **i**, Polyacrylamide gels of the indicated recombinant proteins stained with Coomassie Brilliant Blue (relevant proteins indicated with red arrows). **j**, Representative resection assays with DNA2-pCtIP-RPA and the indicated WRN variant, in the absence or presence of BRCA1-BARD1. **k**, Quantitation of DNA degradation product from resection assays such as shown in i. Averages shown; error bars, SEM; n = 3. Source data are provided as Supplementary Information SI Fig. 8.

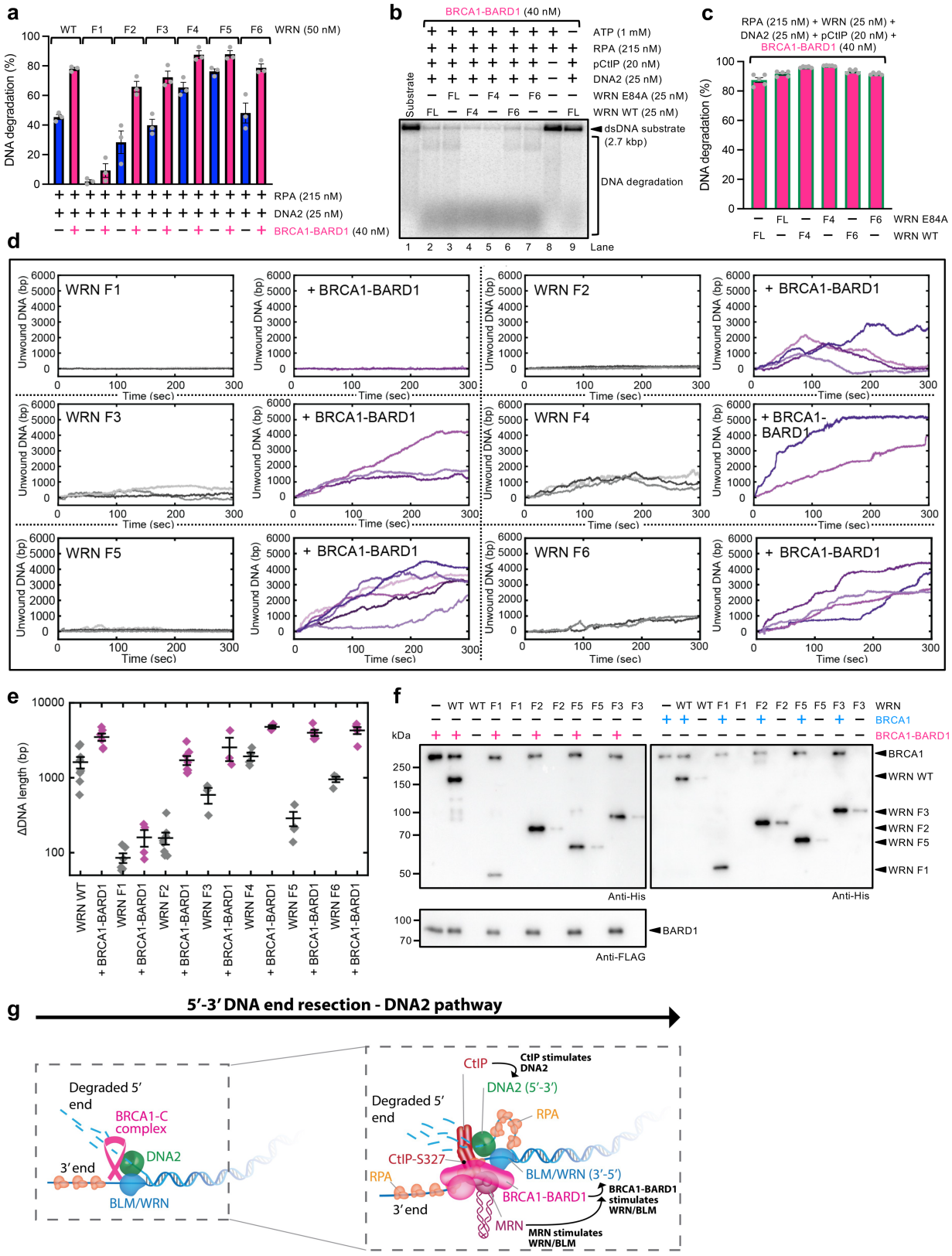

Extended Data Fig. 7 | See next page for caption.

Extended Data Fig. 7 | BRCA1 interacts with WRN through multiple contact points. a, Quantitation of DNA degradation products from resection assays with DNA2- RPA, in the absence or presence of BRCA1-BARD1 and the indicated WRN variant. Averages shown; error bars, SEM; n = 3. **b**, Representative resection assays with DNA2-pCtIP-RPA, the indicated WRN variant and BRCA1-BARD1. FL, full-length WRN protein. **c**, Quantitation of DNA degradation from assays such as shown in b. Averages shown; error bars, SEM; n = 5. **d**, Representative trajectories of DNA unwinding events by the indicated WRN variant, in the absence or presence of BRCA1-BARD1, all at 25 nM. FL, full-length WRN protein. **e**, ΔDNA-length analysis of the indicated WRN variants, in the absence or presence of BRCA1-BARD1, at 25 nM. Averages shown; error bars, SEM; n = 8 (for WRN WT, WRN F2, WRN F2 + BRCA1-BARD1), n = 6 (for WRN WT + BRCA1-BARD1, WRN F1), n = 5 (for WRN F5, WRN F5 + BRCA1-BARD1, WRN F6 + BRCA1-BARD1), n = 2 (for WRN F1 + BRCA1-BARD1, WRN F4, WRN F4 + BRCA1-BARD1, WRN F6), n = 3 (WRN F3, WRN F3 + BRCA1-BARD1). **f**, Representative protein interaction assays. **g**, A model of DNA2-dependent DNA end resection pathway and its stimulation by the BRCA1-C complex. Source data are provided as Supplementary Information SI Fig. 9.

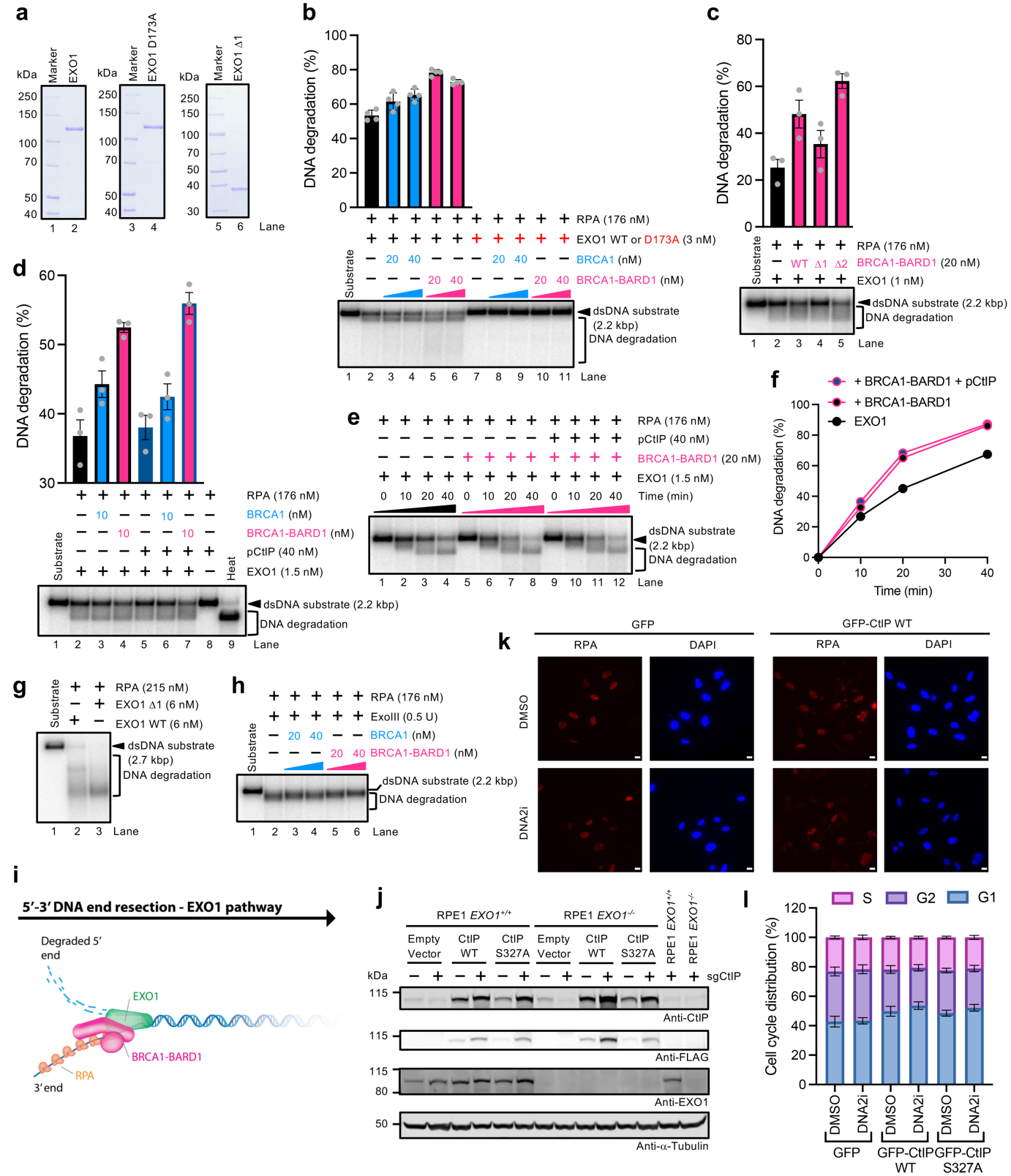

Extended Data Fig. 8 | See next page for caption.

Extended Data Fig. 8 | Stimulation of EXO1-dependent long-range DNA end resection by BRCA1-BARD1. a, Polyacrylamide gels of the indicated recombinant EXO1 variants stained with Coomassie Brilliant Blue. **b**, Resection assays with the indicated EXO1 variant and RPA, in the absence or presence of either BRCA1 or BRCA1-BARD1. Top, quantitation of DNA degradation. Averages shown; error bars, SEM; n = 4. Bottom, representative assays. **c**, Resection assays with EXO1, in the absence or presence of the indicated BRCA1-BARD1 variant. Top, quantitation of DNA degradation. Averages shown; error bars, SEM; n = 3. Bottom, representative assays. **d**, Resection assays with EXO1 and RPA, in the absence or presence of either BRCA1 or BRCA1-BARD1 and pCtIP. Top, quantitation of DNA degradation. Averages shown; error bars, SEM; n = 3. Bottom, representative assays. **e**, Representative kinetic resection assays with a randomly labeled 2.2 kbp-long dsDNA, EXO1 and RPA, in the absence or presence of BRCA1-BARD1 and pCtIP. **f**, Quantitation of DNA resection assays such as shown in e. Averages shown; error bars, SEM; n = 3. **g**, Representative assays with the indicated EXO1 variant and RPA. **h**, Representative resection assays with *E. coli* ExoIII and RPA, in the absence or presence of either BRCA1 or BRCA1-BARD1. **i**, A model of EXO1-dependent DNA end resection pathway and the involvement of BRCA1-BARD1. **j**, Western Blot analysis showing expression of lentivirally transduced FLAG-tagged CtIP WT or S327A in RPE1 *EXO1*$^{+/+}$ or *EXO1*$^{-/-}$ cells. **k**, Representative microscopy images of indicated U2OS-derived cell lines untreated (DMSO) or treated (DNA2i) with the DNA2 inhibitor C5, stained for RPA (red) or DAPI (blue). Scale bar, 10 µm. **l**, Quantitation of the cell cycle distribution of the indicated cell lines untreated (DMSO) or treated (DNA2i) with the DNA2 inhibitor C5. Source data are provided as Supplementary Information SI Figs. 9 and 10.

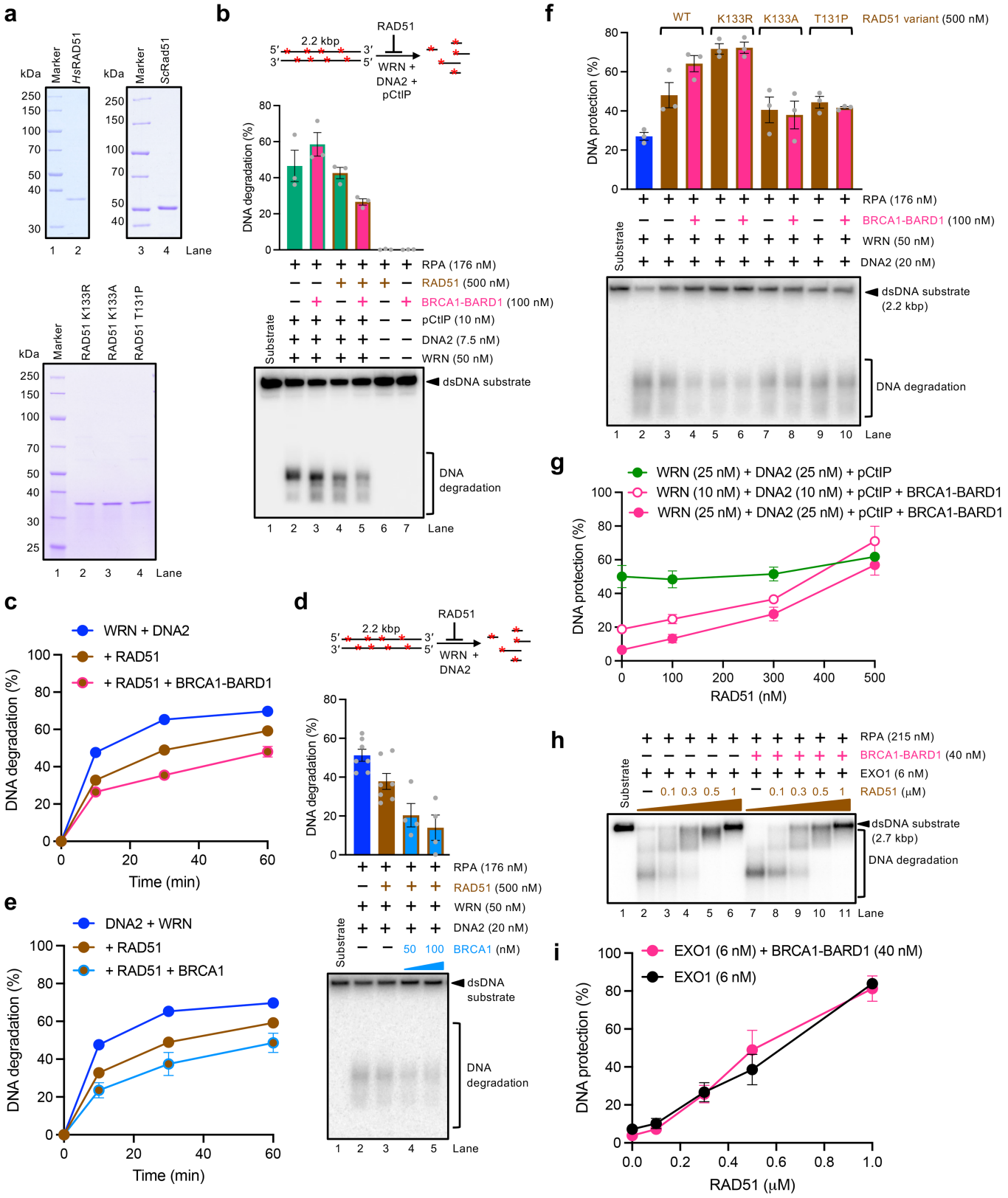

Extended Data Fig. 9 | See next page for caption.

Extended Data Fig. 9 | DNA protection by RAD51-BRCA1-BARD1 ensemble. **a**, Polyacrylamide gels of the indicated recombinant RAD51 variants stained with Coomassie Brilliant Blue. **b**, DNA protection assays with WRN-DNA2-pCtIP-RPA, in the absence or presence of BRCA1-BARD1 and RAD51, performed at 100 mM NaCl. Top, a schematic of the assay. Red asterisks (*) represent the position of the radioactive labels. Middle, quantitation of DNA degradation. Averages shown; error bars, SEM; n = 3. Bottom, representative assays. **c**, Quantitation of kinetic protection assays with WRN-DNA2-RPA, in the absence or presence of BRCA1-BARD1 and RAD51, performed at 100 mM NaCl. Averages shown; error bars, SEM; n = 2 (for DNA2-WRN), n = 7 (in the absence of BRCA1-BARD1) and n = 4 (in the presence of BRCA1). **d**, Protection assays with WRN-DNA2-RPA, in the absence or presence of BRCA1 and RAD51, performed at 100 mM NaCl. Top, a schematic of the assay. Red asterisks (*) represent the position of the radioactive labels. Middle, quantitation of DNA degradation. Averages shown; error bars, SEM; n = 7 (in the absence of BRCA1) and n = 4 (in the presence of BRCA1). Bottom, representative assays. **e**, Quantitation of kinetic protection assays with WRN-DNA2-RPA, in the absence or presence of BRCA1 and RAD51, performed at 100 mM NaCl. Quantitation of DNA degradation by WRN-DNA2, in the absence or presence of RAD51, such as shown in b is included as a reference. Averages shown; error bars, SEM; n = 2 (for DNA2-WRN), n = 7 (in the absence of BRCA1-BARD1) and n = 4 (in the presence of BRCA1). **f**, Protection assays with WRN-DNA2-RPA, in the absence or presence of BRCA1-BARD1 and the indicated RAD51 variant, performed at 100 mM NaCl. KR, K133R, defective in ATP hydrolysis; KA, K133A, defective in ATP binding; TP, T131P, impaired in DNA binding. Top, quantitation of DNA protection. Averages shown; error bars, SEM; n = 3. Bottom, representative assays. **g**, Quantitation of assays such as shown in Fig. 6b. Averages shown; error bars, SEM; n = 3. The quantitation was not normalized. Representative assays with WRN (10 nM) and DNA2 (10 nM), in presence of pCtIP and BRCA1-BARD1, not shown. **h**, Representative protection assays with EXO1-RPA, in the absence or presence of BRCA1-BARD1 and increasing concentration of RAD51. **i**, Quantitation of assays such as shown in h. Averages shown; error bars, SEM; n = 3. The quantitation was not normalized. Source data are provided as Supplementary Information SI Fig. 11.

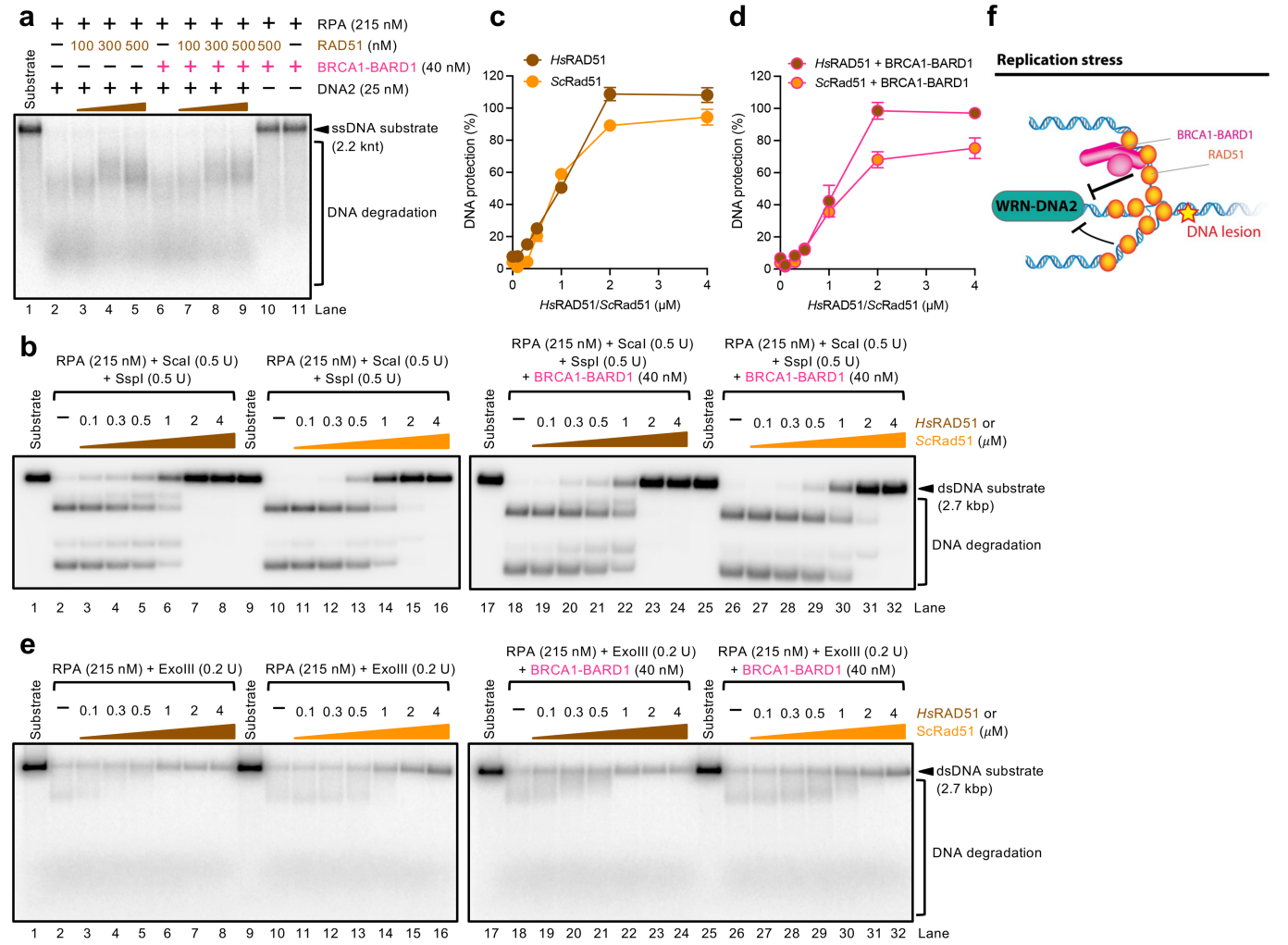

Extended Data Fig. 10 | BRCA1-BARD1 does not affect DNA degradation by non-cognate nucleases. a, Representative protection assays with DNA2-RPA, in the absence or presence of BRCA1-BARD1 and increasing concentration of RAD51. **b**, Representative protection assays with the endonucleases ScaI and SspI, with RPA and increasing concentration of human RAD51 (*Hs*RAD51) or yeast Rad51 (*Sc*Rad51) in the absence or presence of BRCA1-BARD1 **c**, Quantitation of assays such as shown in b (left). Averages shown; error bars, SEM; n = 3. **d**, Quantitation of assays such as shown in b (right). Averages shown; error bars, SEM; n = 3. **e**, Representative protection assays with *E. coli* ExoIII, with RPA and increasing concentrations of human RAD51 (*Hs*RAD51) or yeast Rad51 (*Sc*Rad51) in the absence or presence of BRCA1-BARD1. **f**, A model for DNA protection function of BRCA1-BARD1 in the presence of RAD51 upon replication stress. RAD51 inhibits DNA degradation by nucleases in an unspecific manner via its binding to dsDNA. Additionally, as shown here, RAD51, together with BRCA1-BARD1, inhibits specifically DNA2-dependent long-range resection. Source data are provided as Supplementary Information SI Fig. 11.

Supplementary Tables

Supplementary Table 1. Full-length sequence of *BRCA1* gene (in black) codon optimized for the expression in *Sf*9 cells. NheI and XmaI sites at the N- and C-terminus of the *BRCA1* gene, respectively, are highlighted in bold. The 2x MBP-tag and the 10x his-tag at the N- and C-terminus, respectively, are underlined.

ATGAAAATCGAAGAAGGTAAACTGGTAATCTGGATTAACGGCGATAAAGGCTATAACGGTCTCGCTGAAGTCGGTAAG
AAATTCGAGAAAGATACCGGAATTAAAGTCACCGTTGAGCATCCGGATAAACTGGAAGAGAAATTCCCACAGGTTGCG
GCAACTGGCGATGGCCCTGACATTATCTTCTGGGCACACGACCGCTTTGGTGGCTACGCTCAATCTGGCCTGTTGGCTG
AAATCACCCCGGACAAAGCGTTCCAGGACAAGCTGTATCCGTTTACCTGGGATGCCGTACGTTACAACGGCAAGCTGA
TTGCTTACCCGATCGCTGTTGAAGCGTTATCGCTGATTTATAACAAAGATCTGCTGCCGAACCCGCCAAAAACCTGGGA
AGAGATCCCGGCGCTGGATAAAGAACTGAAAGCGAAAGGTAAGAGCGCGCTGATGTTCAACCTGCAAGAACCGTACT
TCACCTGGCCGCTGATTGCTGCTGACGGGGGTTATGCGTTCAAGTATGAAAACGGCAAGTACGACATTAAAGACGTGG
GCGTGGATAACGCTGGCGCGAAAGCGGGTCTGACCTTCCTGGTTGACCTGATTAAAAACAAACACATGAATGCAGACA
CCGATTACTCCATCGCAGAAGCTGCCTTTAATAAAGGCGAAACAGCGATGACCATCAACGGCCCGTGGGCATGGTCCA
ACATCGACACCAGCAAAGTGAATTATGGTGTAACGGTACTGCCGACCTTCAAGGGTCAACCATCCAAACCGTTCGTTGG
CGTGCTGAGCGCAGGTATTAACGCCGCCAGTCCGAACAAAGAGCTGGCAAAAGAGTTCCTCGAAAACTATCTGCTGAC
TGATGAAGGTCTGGAAGCGGTTAATAAAGACAAACCGCTGGGTGCCGTAGCGCTGAAGTCTTACGAGGAAGAGTTGG
CGAAAGATCCACGTATTGCCGCCACTATGGAAAACGCCCAGAAAGGTGAAATCATGCCGAACATCCCGCAGATGTCCG
CTTTCTGGTATGCCGTGCGTACTGCGGTGATCAACGCCGCCAGCGGTCGTCAGACTGTCGATGAAGCCCTGAAAGACG
CGCAGACTAATTCGAGCTCGAACAACAACAACAATAACAATAACAACAACCTCGGGATCGAGGGAAGGCTGGAAGTTC
TGTTCCAGGGGCCCGCTAGAATGAAAATCGAAGAAGGTAAACTGGTAATCTGGATTAACGGCGATAAAGGCTATAACG
GTCTCGCTGAAGTCGGTAAGAAATTCGAGAAAGATACCGGAATTAAAGTCACCGTTGAGCATCCGGATAAACTGGAAG
AGAAATTCCCACAGGTTGCGGCAACTGGCGATGGCCCTGACATTATCTTCTGGGCACACGACCGCTTTGGTGGCTACGC
TCAATCTGGCCTGTTGGCTGAAATCACCCCGGACAAAGCGTTCCAGGACAAGCTGTATCCGTTTACCTGGGATGCCGTA
CGTTACAACGGCAAGCTGATTGCTTACCCGATCGCTGTTGAAGCGTTATCGCTGATTTATAACAAAGATCTGCTGCCGA
ACCCGCCAAAAACCTGGGAAGAGATCCCGGCGCTGGATAAAGAACTGAAAGCGAAAGGTAAGAGCGCGCTGATGTTC
AACCTGCAAGAACCGTACTTCACCTGGCCGCTGATTGCTGCTGACGGGGGTTATGCGTTCAAGTATGAAAACGGCAAG
TACGACATTAAAGACGTGGGCGTGGATAACGCTGGCGCGAAAGCGGGTCTGACCTTCCTGGTTGACCTGATTAAAAAC
AAACACATGAATGCAGACACCGATTACTCCATCGCAGAAGCTGCCTTTAATAAAGGCGAAACAGCGATGACCATCAAC
GGCCCGTGGGCATGGTCCAACATCGACACCAGCAAAGTGAATTATGGTGTAACGGTACTGCCGACCTTCAAGGGTCAA
CCATCCAAACCGTTCGTTGGCGTGCTGAGCGCAGGTATTAACGCCGCCAGTCCGAACAAAGAGCTGGCAAAAGAGTTC
CTCGAAAACTATCTGCTGACTGATGAAGGTCTGGAAGCGGTTAATAAAGACAAACCGCTGGGTGCCGTAGCGCTGAAG
TCTTACGAGGAAGAGTTGGCGAAAGATCCACGTATTGCCGCCACTATGGAAAACGCCCAGAAAGGTGAAATCATGCCG
AACATCCCGCAGATGTCCGCTTTCTGGTATGCCGTGCGTACTGCGGTGATCAACGCCGCCAGCGGTCGTCAGACTGTCG
ATGAAGCCCTGAAAGACGCGCAGACTAATTCGAGCTCGAACAACAACAACAATAACAATAACAACAACCTCGGGATCG
AGGGAAGGCTGGAAGTTCTGTTCCAGGGGCCC**GCTAGC**ATGGACCTGTCCGCTCTGCGCGTGGAGGAGGTGCAGAAC
GTGATCAACGCTATGCAGAAGATCCTGGAGTGCCCTATCTGCCTGGAGCTGATCAAGGAGCCTGTGTCCACCAAGTGC
GACCACATCTTCTGCAAGTTCTGCATGCTGAAGCTGCTGAACCAGAAGAAGGGTCCTTCCCAGTGCCCTCTGTGCAAGA
ACGACATCACCAAGCGCTCCCTGCAGGAGTCCACCCGCTTCTCCCAGCTGGTGGAGGAGCTGCTGAAGATCATCTGCG
CTTTCCAGCTGGACACCGGTCTGGAGTACGCTAACTCCTACAACTTCGCTAAGAAGGAGAACAACTCCCCTGAGCACCT
GAAGGACGAGGTGTCCATCATCCAGTCCATGGGTTACCGCAACCGCGCTAAGCGCCTGCTGCAGTCCGAGCCTGAGAA
CCCTTCCCTGCAGGAGACCTCCCTGTCCGTGCAGCTGTCCAACCTGGGTACCGTGCGCACCCTGCGCACCAAGCAGCGC
ATCCAGCCTCAGAAGACCTCCGTGTACATCGAGCTGGGTTCCGACTCCTCCGAGGACACCGTGAACAAGGCTACCTACT
GCTCCGTGGGTGACCAGGAGCTGCTGCAGATCACCCCTCAGGGTACCCGCGACGAGATCTCCCTGGACTCCGCTAAGA
AGGCTGCTTGCGAGTTCTCCGAGACCGACGTGACCAACACCGAGCACCACCAGCCTTCCAACAACGACCTGAACACCAC
CGAGAAGCGCGCTGCTGAGCGCCACCCTGAGAAGTACCAGGGTTCCTCCGTGTCCAACCTGCACGTGGAGCCTTGCGG
TACCAACACCCACGCTTCCTCCCTGCAGCACGAGAACTCCTCCCTGCTGCTGACCAAGGACCGCATGAACGTGGAGAAG
GCTGAGTTCTGCAACAAGTCCAAGCAGCCTGGTCTGGCTCGCTCCCAGCACAACCGCTGGGCTGGTTCCAAGGAGACC
TGCAACGACCGCCGCACCCCTTCCACCGAGAAGAAGGTGGACCTGAACGCTGACCCTCTGTGCGAGCGCAAGGAGTG
GAACAAGCAGAAGCTGCCTTGCTCCGAGAACCCTCGCGACACCGAGGACGTGCCTTGGATCACCCTGAACTCCTCCATC
CAGAAGGTGAACGAGTGGTTCTCCCGCTCCGACGAGCTGCTGGGTTCCGACGACTCCCACGACGGTGAGTCCGAGTCC
AACGCTAAGGTGGCTGACGTGCTGGACGTGCTGAACGAGGTGGACGAGTACTCCGGTTCCTCCGAGAAGATCGACCT
GCTGGCTTCCGACCCTCACGAGGCTCTGATCTGCAAGTCCGAGCGCGTGCACTCCAAGTCCGTGGAGTCCAACATCGA

GGACAAGATCTTCGGTAAGACCTACCGCAAGAAGGCTTCCCTGCCTAACCTGTCCCACGTGACCGAGAACCTGATCATC
GGTGCTTTCGTGACCGAGCCTCAGATCATCCAGGAGCGCCCTCTGACCAACAAGCTGAAGCGCAAGCGCCGCCCTACC
TCCGGTCTGCACCCTGAGGACTTCATCAAGAAGGCTGACCTGGCTGTGCAGAAGACCCCTGAGATGATCAACCAGGGT
ACCAACCAGACCGAGCAGAACGGTCAGGTGATGAACATCACCAACTCCGGTCACGAGAACAAGACCAAGGGTGACTC
CATCCAGAACGAGAAGAACCCTAACCCTATCGAGTCCCTGGAGAAGGAGTCCGCTTTCAAGACCAAGGCTGAGCCTAT
CTCCTCCTCCATCTCCAACATGGAGCTGGAGCTGAACATCCACAACTCCAAGGCTCCTAAGAAGAACCGCCTGCGCCGC
AAGTCCTCCACCCGCCACATCCACGCTCTGGAGCTGGTGGTGTCCCGCAACCTGTCCCCTCCTAACTGCACCGAGCTGC
AGATCGACTCCTGCTCCTCCTCCGAGGAGATCAAGAAGAAGAAGTACAACCAGATGCCTGTGCGCCACTCCCGCAACCT
GCAGCTGATGGAGGGTAAGGAGCCTGCTACCGGTGCTAAGAAGTCCAACAAGCCTAACGAGCAGACCTCCAAGCGCC
ACGACTCCGACACCTTCCCTGAGCTGAAGCTGACCAACGCTCCTGGTTCCTTCACCAAGTGCTCCAACACCTCCGAGCTG
AAGGAGTTCGTGAACCCTTCCCTGCCTCGCGAGGAGAAGGAGGAGAAGCTGGAGACCGTGAAGGTGTCCAACAACGC
TGAGGACCCTAAGGACCTGATGCTGTCCGGTGAGCGCGTGCTGCAGACCGAGCGCTCCGTGGAGTCCTCCTCCATCTC
CCTGGTGCCTGGTACCGACTACGGTACCCAGGAGTCCATCTCCCTGCTGGAGGTGTCCACCCTGGGTAAGGCTAAGAC
CGAGCCTAACAAGTGCGTGTCCCAGTGCGCTGCTTTCGAGAACCCTAAGGGTCTGATCCACGGTTGCTCCAAGGACAA
CCGCAACGACACCGAGGGTTTCAAGTACCCTCTGGGTCACGAGGTGAACCACTCCCGCGAGACCTCCATCGAGATGGA
GGAGTCCGAGCTGGACGCTCAGTACCTGCAGAACACCTTCAAGGTGTCCAAGCGCCAGTCCTTCGCTCCTTTCTCCAAC
CCTGGTAACGCTGAGGAGGAGTGCGCTACCTTCTCCGCTCACTCCGGTTCCCTGAAGAAGCAGTCCCCTAAGGTGACCT
TCGAGTGCGAGCAGAAGGAGGAGAACCAGGGTAAGAACGAGTCCAACATCAAGCCTGTGCAGACCGTGAACATCACC
GCTGGTTTCCCTGTGGTGGGTCAGAAGGACAAGCCTGTGGACAACGCTAAGTGCTCCATCAAGGGTGGTTCCCGCTTC
TGCCTGTCCTCCCAGTTCCGCGGTAACGAGACCGGTCTGATCACCCCTAACAAGCACGGTCTGCTGCAGAACCCTTACC
GCATCCCTCCTCTGTTCCCTATCAAGTCCTTCGTGAAGACCAAGTGCAAGAAGAACCTGCTGGAGGAGAACTTCGAGGA
GCACTCCATGTCCCCTGAGCGCGAGATGGGTAACGAGAACATCCCTTCCACCGTGTCCACCATCTCCCGCAACAACATC
CGCGAGAACGTGTTCAAGGAGGCTTCCTCCTCCAACATCAACGAGGTGGGTTCCTCCACCAACGAGGTGGGTTCCTCCA
TCAACGAGATCGGTTCCTCCGACGAGAACATCCAGGCTGAGCTGGGTCGCAACCGCGGTCCTAAGCTGAACGCTATGC
TGCGCCTGGGTGTGCTGCAGCCTGAGGTGTACAAGCAGTCCCTGCCTGGTTCCAACTGCAAGCACCCTGAGATCAAGA
AGCAGGAGTACGAGGAGGTGGTGCAGACCGTGAACACCGACTTCTCCCCTTACCTGATCTCCGACAACCTGGAGCAGC
CTATGGGTTCCTCCCACGCTTCCCAGGTGTGCTCCGAGACCCCTGACGACCTGCTGGACGACGGTGAGATCAAGGAGG
ACACCTCCTTCGCTGAGAACGACATCAAGGAGTCCTCCGCTGTGTTCTCCAAGTCCGTGCAGAAGGGTGAGCTGTCCCG
CTCCCCTTCCCCTTTCACCCACACCCACCTGGCTCAGGGTTACCGCCGCGGTGCTAAGAAGCTGGAGTCCTCCGAGGAG
AACCTGTCCTCCGAGGACGAGGAGCTGCCTTGCTTCCAGCACCTGCTGTTCGGTAAGGTGAACAACATCCCTTCCCAGT
CCACCCGCCACTCCACCGTGGCTACCGAGTGCCTGTCCAAGAACACCGAGGAGAACCTGCTGTCCCTGAAGAACTCCCT
GAACGACTGCTCCAACCAGGTGATCCTGGCTAAGGCTTCCCAGGAGCACCACCTGTCCGAGGAGACCAAGTGCTCCGC
TTCCCTGTTCTCCTCCCAGTGCTCCGAGCTGGAGGACCTGACCGCTAACACCAACACCCAGGACCCTTTCCTGATCGGTT
CCTCCAAGCAGATGCGCCACCAGTCCGAGTCCCAGGGTGTGGGTCTGTCCGACAAGGAGCTGGTGTCCGACGACGAG
GAGCGCGGTACCGGTCTGGAGGAGAACAACCAGGAGGAGCAGTCCATGGACTCCAACCTGGGTGAGGCTGCTTCCGG
TTGCGAGTCCGAGACCTCCGTGTCCGAGGACTGCTCCGGTCTGTCCTCCCAGTCCGACATCCTGACCACCCAGCAGCGC
GACACCATGCAGCACAACCTGATCAAGCTGCAGCAGGAGATGGCTGAGCTGGAGGCTGTGCTGGAGCAGCACGGTTC
CCAGCCTTCCAACTCCTACCCTTCCATCATCTCCGACTCCTCCGCTCTGGAGGACCTGCGCAACCCTGAGCAGTCCACCTC
CGAGAAGGCTGTGCTGACCTCCCAGAAGTCCTCCGAGTACCCTATCTCCCAGAACCCTGAGGGTCTGTCCGCTGACAAG
TTCGAGGTGTCCGCTGACTCCTCCACCTCCAAGAACAAGGAGCCTGGTGTGGAGCGCTCCTCCCCTTCCAAGTGCCCTT
CCCTGGACGACCGCTGGTACATGCACTCCTGCTCCGGTTCCCTGCAGAACCGCAACTACCCTTCCCAGGAGGAGCTGAT
CAAGGTGGTGGACGTGGAGGAGCAGCAGCTGGAGGAGTCCGGTCCTCACGACCTGACCGAGACCTCCTACCTGCCTC
GCCAGGACCTGGAGGGTACCCCTTACCTGGAGTCCGGTATCTCCCTGTTCTCCGACGACCCTGAGTCCGACCCTTCCGA
GGACCGCGCTCCTGAGTCCGCTCGCGTGGGTAACATCCCTTCCTCCACCTCCGCTCTGAAGGTGCCTCAGCTGAAGGTG
GCTGAGTCCGCTCAGTCCCCTGCTGCTGCTCACACCACCGACACCGCTGGTTACAACGCTATGGAGGAGTCCGTGTCCC
GCGAGAAGCCTGAGCTGACCGCTTCCACCGAGCGCGTGAACAAGCGCATGTCCATGGTGGTGTCCGGTCTGACCCCTG
AGGAGTTCATGCTGGTGTACAAGTTCGCTCGCAAGCACCACATCACCCTGACCAACCTGATCACCGAGGAGACCACCCA
CGTGGTGATGAAGACCGACGCTGAGTTCGTGTGCGAGCGCACCCTGAAGTACTTCCTGGGTATCGCTGGTGGTAAGTG
GGTGGTGTCCTACTTCTGGGTGACCCAGTCCATCAAGGAGCGCAAGATGCTGAACGAGCACGACTTCGAGGTGCGCG
GTGACGTGGTGAACGGTCGCAACCACCAGGGTCCTAAGCGCGCTCGCGAGTCCCAGGACCGCAAGATCTTCCGCGGTC
TGGAGATCTGCTGCTACGGTCCTTTCACCAACATGCCTACCGACCAGCTGGAGTGGATGGTGCAGCTGTGCGGTGCTTC
CGTGGTGAAGGAGCTGTCCTCCTTCACCCTGGGTACCGGTGTGCACCCTATCGTGGTGGTGCAGCCTGACGCTTGGAC
CGAGGACAACGGTTTCCACGCTATCGGTCAGATGTGCGAGGCTCCTGTGGTGACCCGCGAGTGGGTGCTGGACTCCGT
GGCTCTGTACCAGTGCCAGGAGCTGGACACCTACCTGATCCCTCAGATCCCTCACTCCCACTAC**CCCGGG**CTCGAG<u>CAC
CATCACCATCACCATCACCATCACCATT</u>GA

Supplementary Table 2. Full-length sequence of the *BARD1* gene codon optimized for the expression in *Sf*9 cells. BamHI and XmaI sites at the N- and C-terminus of the *BARD1* gene, respectively, are highlighted in bold. The FLAG-tag at the C-terminus is underlined.

GGATCCACCATGCCTGACAACCGCCAGCCTCGCAACCGCCAGCCTCGCATCCGCTCCGGTAACGAGCCTCGCTCCGCTC
CTGCTATGGAGCCTGACGGTCGCGGTGCTTGGGCTCACTCCCGCGCTGCTCTGGACCGCCTGGAGAAGCTGCTGCGCT
GCTCCCGCTGCACCAACATCCTGCGCGAGCCTGTGTGCCTGGGTGGTTGCGAGCACATCTTCTGCTCCAACTGCGTGTC
CGACTGCATCGGTACCGGTTGCCCTGTGTGCTACACCCCTGCTTGGATTCAAGACCTGAAGATCAACCGCCAGCTGGAC
TCCATGATCCAGCTGTGCTCCAAGCTGCGCAACCTGCTGCACGACAACGAGCTGTCCGACCTGAAGGAGGACAAGCCT
CGCAAGTCCCTGTTCAACGACGCTGGTAACAAGAAGAACTCCATCAAGATGTGGTTCTCCCCTCGCTCCAAGAAGGTGC
GCTACGTGGTGTCCAAGGCTTCCGTGCAGACCCAGCCTGCTATCAAGAAGGACGCTTCCGCTCAGCAGGACTCCTACG
AGTTCGTGTCCCCTTCCCCTCCTGCTGACGTGTCCGAGCGCGCTAAGAAGGCTTCCGCTCGCTCCGGTAAGAAGCAGAA
GAAGAAGACCCTGGCTGAGATCAACCAGAAGTGGAACCTGGAGGCTGAGAAGGAGGACGGTGAGTTCGACTCCAAG
GAGGAGTCCAAGCAGAAGCTGGTGTCCTTCTGCTCCCAGCCTTCCGTGATCTCCTCCCCTCAGATCAACGGTGAGATCG
ACCTGCTGGCTTCCGGTTCCCTGACCGAGTCCGAGTGCTTCGGTTCCCTGACCGAGGTGTCCCTGCCTCTGGCTGAGCA
GATCGAGTCCCCTGACACCAAGTCCCGCAACGAGGTGGTGACCCCTGAGAAGGTGTGCAAGAACTACCTGACCTCCAA
GAAGTCCCTGCCTCTGGAGAACAACGGTAAGCGCGGTCACCACAACCGCCTGTCCTCCCCTATCTCCAAGCGCTGCCGC
ACCTCCATCCTGTCCACCTCCGGTGACTTCGTGAAGCAGACCGTGCCTTCCGAGAACATCCCTCTGCCTGAGTGCTCCTC
CCCTCCTTCCTGCAAGCGCAAGGTGGGTGGTACCTCCGGTCGCAAGAACTCCAACATGTCCGACGAGTTCATCTCCCTG
TCCCCTGGTACCCCTCCTTCCACCCTGTCCTCCTCCTCCTACCGCCGCGTGATGTCCTCCCCTTCCGCTATGAAGCTGCTG
CCTAACATGGCTGTGAAGCGCAACCACCGCGGTGAGACCCTGCTGCACATCGCTTCCATCAAGGGTGACATCCCTTCCG
TGGAGTACCTGCTGCAGAACGGTTCCGACCCTAACGTGAAGGACCACGCTGGTTGGACCCCTCTGCACGAGGCTTGCA
ACCACGGTCACCTGAAGGTGGTGGAGCTGCTGCTGCAGCACAAGGCTCTGGTGAACACCACCGGTTACCAGAACGACT
CCCCTCTGCACGACGCTGCTAAGAACGGTCACGTGGACATCGTGAAGCTGCTGCTGTCCTACGGTGCTTCCCGCAACGC
TGTGAACATCTTCGGTCTGCGCCCTGTGGACTACACCGACGACGAGTCCATGAAGTCCCTGCTGCTGCTGCCTGAGAAG
AACGAGTCCTCCTCCGCTTCCCACTGCTCCGTGATGAACACCGGTCAGCGCCGCGACGGTCCTCTGGTGCTGATCGGTT
CCGGTCTGTCCTCCGAGCAGCAGAAGATGCTGTCCGAGCTGGCTGTGATCCTGAAGGCTAAGAAGTACACCGAGTTCG
ACTCCACCGTGACCCACGTGGTGGTGCCTGGTGACGCTGTGCAGTCCACCCTGAAGTGCATGCTGGGTATCCTGAACG
GTTGCTGGATCTTGAAGTTCGAGTGGGTGAAGGCTTGCCTGCGCCGCAAGGTGTGCGAGCAGGAGGAGAAGTACGAG
ATCCCTGAGGGTCCTCGCCGCTCCCGCCTGAACCGTGAGCAGCTGCTGCCTAAGCTGTTCGACGGTTGCTACTTCTACCT
GTGGGGTACCTTCAAGCACCACCCTAAGGACAACCTGATCAAGCTGGTGACCGCTGGTGGTGGTCAGATCCTGTCCCG
CAAGCCTAAGCCTGACTCCGACGTGACCCAGACCATCAACACCGTGGCTTACCACGCTCGCCCTGACTCCGACCAGCGC
TTCTGCACCCAGTACATCATCTACGAGGACCTGTGCAACTACCACCCTGAGCGCGTGCGCCAGGGTAAGGTGTGGAAG
GCTCCTTCCTCCTGGTTCATCGACTGCGTGATGTCCTTCGAGCTGCTGCCTCTGGACTCCGATTACAAGGATGACGACGA
TAAGTGA**CCCGGG**

Supplementary Table 3. List of oligonucleotides for cloning and site-directed mutagenesis used in this study.

Name	Sequence (5′ to 3′)
fw_WRN_ATPase domain_NheI	TAGGAAGCTAGCAATCTGGGTCTTCCTACTAAAGAAG
rev_WRN_ATPase-Helicase_core_XhoI	TAGGAACTCGAGGCAATGATCCAATCTGGACCTGCAA
rev_WRN_RQC domain_XhoI	TAGGAACTCGAGAGACTTCTTCTCTGTACTTAATTCA
rev_WRN_HRDC_XhoI	TAGGAACTCGAGCTGTTCTTCTTGAGGTTTTG
PforWRN_E84A_forward	GTGGGATTTGACATGGcGTGGCCACCATTATAC
PrevWRN_E84A_reverse	GTATAATGGTGGCCACGCCATGTCAAATCCCAC
Pforward_WRN	TAGGAAGCTAGCGGATCCATGAGTGAAAAAAAATTGGAAACAA
Prevers_WRN	TAGGAACTCGAGCCCGGGACTAAAAAGACCTCCCCTTTT
PforWRN_K577M	GCAACTGGATATGGAATGAGTTTGTGCTTCCAGTATCC
PrevWRN_K577M	GGATACTGGAAGCACAAACTCATTCCATATCCAGTTGC
hDNA2c_D277A_for	GGCCTGAAGGGAAAGATCGCTGTCACAGTTGGAGTGAAG
hDNA2c_D277A_rev	CTTCACTCCAACTGTGACAGCGATCTTTCCCTTCAGGCC
DNA2_K654R_F	GGCATGCCGGGAACTGGCAGGACAACCACTATCTGCACA
DNA2_K654R_R	TGTGCAGATAGTGGTTGTCCTGCCAGTTCCCGGCATGCC
CtIP_S327A_F	AATTACCTACTCGAGTGTCAGCTCCTGTATTTGGAGCTACCTC
CtIP_S327A_R	GAGGTAGCTCCAAATACAGGAGCTGACACTCGAGTAGGTAATT
CtIP_F728E_For	AATGATAGCTTGGAAGATATGGAAGATCGGACAACACATGAAGAG
CtIP_F728E_Rev	CTCTTCATGTGTTGTCCGATCTTCCATATCTTCCAAGCTATCATT
CtIP_Y736E_For	GATCGGACAACACATGAAGAGGAAGAATCCTGTTTGGCAGACAG
CtIP_Y736E_Rev	CTGTCTGCCAAACAGGATTCTTCCTCTTCATGTGTTGTCCGATC
AS86_EXO1_DA_For	CCATAATTACAGAGGACTCGGATCTCCTAGCTTTTGGCTGTAAAAAGG
AS87_EXO1_DA_Rev	CCTTTTTACAGCCAAAAGCTAGGAGATCCGAGTCCTCTGTAATTATGG
Fw_BamH1-EXO1_Δ1	atgcatGGATCCATGGGGATACAGGGATTGCTACAAT
Rev_Xma1-FLAG-EXO1_ Δ1	ctcgagCCCGGGCTACTTGTCGTCATCGT
Human_RPA1_FP	CCTGCCGGATCCATGGTCGGCCAGCTGAGCGAGG
Human_RPA1_RP	CCTGCCGCTAGCTCACATCAATGCACTTCTCCTG
Human_RPA2_FP	CCTGCCGGATCCATGTGGAACAGTGGATTCG
Human_RPA2_RP	CCTGCCGCTAGCTTATTCTGCATCTGTGGATTTAAAATG
Human_RPA3_FP	CCTGCCGTCGACGTGGACATGATGGACTTGCCCAGG
Human_RPA3_RP	CCTGCCTCTAGATCAATCATGTTGCACAATCCC
BRCA1-(c)_rev	ATCCCTCACTCCCACTACCACCATCACCATCACCATTAACCCGGGCTGCAGCCTGCT
BRCA1-(N)_Fwd	CCTGCTGCTAGCATGGACCTGTCCGCTCTGCGCG
BRCA1-(263)-Rev	AGCAGGCCCGGGTAGCTGACGCGTACCCTGGTACTTCTCAGG
BRCA1-Rev	AGCAGGCCCGGGGTAGTGGGAGTGAGGGAT
BRCA1-(1172)-Fwd	CCTGCTACGCGTGAGTCCTCCGCTGTGTTCTCCA
BRCA1-(932)-Fwd	CCTGCTACGCGTGTGGGTCAGAAGGACAAGCCTG
BRCA1-(719)-Fwd	CCTGCTACGCGT AAGGAGTTCGTGAACCCTTCCC
BRCA1-(479)-Fwd	CCTGCTACGCGT GAGAACCTGATCATCGGTGCTT
BRCA1-Delta Ring_fw	CCTGCTGGATCCGCTAGCACCGGTCTGGAGTACG
BRCA1-Delta BRCT_rev	GCTTCCACCGAGCGCGTGCACCATCACCATCACCATTAACCCGGGCTGCAGCCTGCT
BRCA1 V1035D F1036D F	CAACATCCGCGAGAACGACGACAAGGAGGCTTCCTCCTCC
BRCA1 V1035D F1036D R	GGAGGAGGAAGCCTCCTTGTCGTCGTTCTCGCGGATGTTG
BRCA1 Y1127D I1129D F	GAACACCGACTTCTCCCCTGACCTGGACTCCGACAACCTGGAGC
BRCA1 Y1127D I1129D R	GCTCCAGGTTGTCGGAGTCCAGGTCAGGGGAGAAGTCGGTGTTC
BARD1-F2_RP	CCTGCCCCCGGGTCACTTATCGTCGTCATCCTTGTAATCGTTGCGCTTCACAGCCATG
BARD1-F3_RP	CCTGCCCCCGGGTCACTTATCGTCGTCATCCTTGTAATCCAGCAGGTCGATCTCACCG

BARD1-F4_RP	CCTGCCCCCGGGTCACTTATCGTCGTCATCCTTGTAATCCAGGTCGGACAGCTCGTTGTC
BARD1-F_FP	CCTGCCGGATCCACCATGCCTGACAACCG
BARD1_Deletion_(123-261) FP	ACCTCACCTGCGTACGCTTCCGGTTCCCTGACCGAGTCCGAG
BARD1_Deletion_(123-261) RP	AGGTCACCTGCCCTGAAGCGTCGGACAGCCGTTGTCG
BARD1-Y180E+F182E_FP	GCTCAGCAGGACTCCGAAGAGGAAGTGTCCCCTTCCCCTC
BARD1-Y180E+F182E_RP	GCTCAGCAGGACTCCGAAGAGGAAGTGTCCCCTTCCCCTC
BARD1-Deletion_(205-220)_FP	ACCTCACCTGCGTACGAGGCTGAGAAGGAGGAC
BARD1-Deletion_(205-220)_RP	AGGTCACCTGCCCTGCCTCCTTACCGGAGCGAGCGGAAGCC
BARD1-Deletion_(235-245)_FP	ACCTCACCTGCGTACCCTTCCGTGATCTCCTCCC
BARD1-Deletion_(235-245)_RP	AGGTCACCTGCCCTGAAGGCTCCTCCTTGGAGTCGAACTCACC

Supplementary Table 4. List of oligonucleotides for substrate preparation used in this study. The bold **T** represents the site of the biotin modification.

Name	**Sequence (5′ to 3′)**
X12-3HJ3	GAGATCTATCTGGTGCCTTCTGACAGTGAATGGGTAACGAATCGTAATAGTCTCTAGAC AGCATGTCCTAGCAATGTAATCGTCTATGACGTC
X12-3TOPLbis	GACGTCATAGACGATTACATTGCTAGGACATGCTGTCTAGAGACTATCGCGACTTACGT TCCATCGCTAGGTTATTTTTTTTTTTTTTTTTTT
PC210	G**T**AAGTGCCGCGGTGCGGGTGCCAGGGCGTGCCCTTGGGCTCCCCGGGCGCGTACTCC ACCTCATGCA**T**C
PC211	GA**T**GCATGAGGTGGAGTACGCGCCCGGGGAGCCCAAGGGCACGCCCTGGCACCCGCAC CGCGGCACT**T**AC
PC206	G**T**AAGTGCCGCGGTGCGGGTGCCAGGGCGTGCCCTTGGGCTCCCCGGGCGCGTACTCC ACCTCATGCATC
PC217	GATGCATGAGGTGGAGTACGCGCCCGGGGAGCCCAAGGGCACGCCCTGGCACCCGCA CCGCGGCACTTAC
NBS1_F	GGCTAGATGGATCCTCTAGAGCTAGCATGTGGAAACTGCTGCCCGC
NBS1_R	GATTTGCGCTCGAGTTACCCGGGTCTTCTCCTTTTTAAATAAG
Main fragment Forward	CATTATGGGGATCCTCAACTGTGAGGAG
Main fragment Reverse	GTCATTCGCCCTCCTAAGAGACGGGATTTA
Dig handle Forward	GACCGAGATAGGGTTGAGTG
Dig handle Reverse	CAGGGTCGGAACAGGAGAGC
Bio handle Forward	ATGACGGACCACGACAGGCCCGCAGTTATC
Bio handle Reverse	GCCGGGCGCGGTTGCGGTATGAGCCGGGTC
Overhang	TTTTTTTTTTTTTTTTTTTTTTTTTTTTTTTTTTTTTTTTCAGCTAGCCTCAGCCTACAATCACC

3.3. FIGNL1 inhibits homologous recombination in BRCA2 deficient cells by dissociating RAD51 filaments

Summary:

Raviprasad and colleagues observed that genetic knockout of the anti-recombinase FIGNL1 can rescue HR defects and reduce the lethality associated with BRCA2 deficiency by preventing the aberrant removal of RAD51 from DNA. Our group was contacted to provide a biochemical characterization of the interplay between FIGNL1, RAD51, and BRCA2. Using recombinant proteins, we showed that FIGNL1 removes RAD51 from ssDNA and inhibits strand exchange. I purified FIGNL1 variants and showed that the interaction between FIGNL1 and RAD51 is primarily mediated by the FRBD domain of FIGNL1. Under our experimental conditions, this interaction occurred predominantly between monomers, although interactions between FIGNL1 oligomers and RAD51 monomers were also detected. I also found that the ATPase activity of FIGNL1 is essential for its inhibitory effect. Furthermore, our data suggest that MMS22L-TONSL can support RAD51 function during HR in the absence of both BRCA2 and FIGNL1. Using pull-down assays, I investigated the interaction between MMS22L-TONSL and FIGNL1 and demonstrated that it is likewise dependent on the FRBD domain of the anti-recombinase. I observed that RAD51 and MMS22L-TONSL compete for the same binding site on FIGNL1, with RAD51 being able to displace MMS22L-TONSL from FIGNL1.

My contribution:

I expressed and purified the FIGNL1-dNLS variants used in this study. I designed and performed the biochemical assays to characterize these variants *in vitro* (Fig. 3C, D, Fig. 5G and Fig. S3C, E, Fig. S8A, Fig. S9, Fig. S12J and Fig. S17B).

Check for updates

RESEARCH ARTICLE SUMMARY

MOLECULAR BIOLOGY

FIGNL1 inhibits homologous recombination in BRCA2 deficient cells by dissociating RAD51 filaments

Raviprasad Kuthethur *et al.*

Full article and list of author affiliations: https://doi.org/10.1126/science.adt1210

INTRODUCTION: Homologous recombination (HR) is essential for DNA double-strand break (DSB) repair, and Breast Cancer Gene 2 (BRCA2) facilitates RAD51 nucleofilament formation crucial for strand exchange in DSB repair. Cells lacking BRCA2 show defects in RAD51 loading, leading to impaired HR and genomic instability and predisposing them to cell death, drug sensitivity, and tumorigenesis. RAD51 loading requires stringent regulation as excessive RAD51 on chromatin causes genome instability. This regulation occurs through RAD51 dissociation from DNA, mediated by helicases during HR, suggesting a balance between RAD51 loading and removal.

RATIONALE: Pathogenic BRCA2 mutations are viable chemotherapy targets through synthetic lethal strategies targeting HR deficiency. However, some BRCA2-deficient patients develop resistance through unknown HR restoration mechanisms. We hypothesized that HR restoration might result from inactivating mechanisms dissociating RAD51 from DSBs. We investigated the role of the AAA+ ATPase Fidgetin Like 1 (FIGNL1) in facilitating the dissociation of RAD51 and assessed its impact on the restoration of homologous recombination in the context of BRCA2 deficiency.

RESULTS: Our findings demonstrate that the loading of RAD51 at DSBs in BRCA2-deficient cells can be restored through the loss of the anti-recombinase FIGNL1. The genetic knockout of FIGNL1 in both mouse and human BRCA2-deficient cells reverses HR defects and mitigates genome instability, which correlates with increased chemoresistance to PARPi and platinum-based drugs. Additionally, the loss of FIGNL1 results in the synthetic viability of BRCA2-deficient mouse embryonic stem cells, with restored RAD51 loading at DSBs. These findings suggest that HR defects in BRCA2-deficient cells arise from the unregulated removal of RAD51 by FIGNL1, rather than from defective RAD51 loading.

We also show that FIGNL1 can dissociate RAD51 when assembled into a hexameric form, with initial interaction facilitated by FIGNL1's RAD51 binding domain (FRBD). The hexameric interactions between RAD51 and FIGNL1 are crucial for RAD51 removal from DSBs. We identified the MMS22L-TONSL complex as responsible for loading RAD51 in cells deficient in BRCA2 and FIGNL1. MMS22L-TONSL and RAD51 compete for the same binding site on FIGNL1's FRBD region. FIGNL1 loss results in increased MMS22L loading at DSBs, suggesting that FIGNL1 facilitates removal of RAD51 loaded by MMS22L-TONSL. The absence of MMS22L-TONSL in BRCA2/FIGNL1 double-deficient cells leads to HR defects, genome instability, and re-sensitization to chemotherapeutic agents.

CONCLUSION: Our findings define a pathway for modulating RAD51 levels during homologous recombination (HR), thereby refining the prevailing notion that HR defects in BRCA2-deficient cells are primarily attributable to RAD51 loading deficiencies. Our data suggest that the removal of RAD51 by FIGNL1 is responsible for HR defects in BRCA2-deficient cells. Furthermore, the identification of the MMS22L-TONSL complex as a potential mediator of RAD51 loading holds implications for understanding chemoresistance in BRCA2-deficient tumors and for developing strategies to re-sensitize these tumors to chemotherapy. □

*Corresponding author. Email: petr.cejka@irb.usi.ch (P.C.); a.raychaudhuri@erasmusmc.nl (A.R.C.) Cite this article as R. Kuthethur *et al.*, *Science* **390**, eadt1210 (2025). DOI: 10.1126/science.adt1210

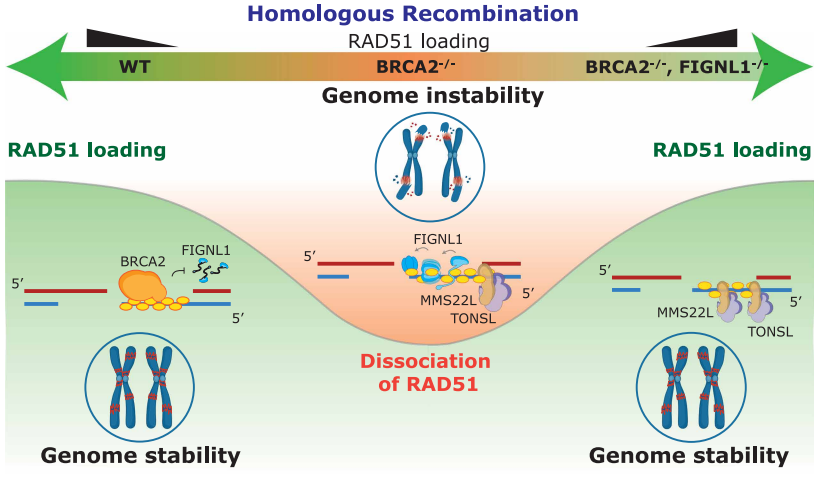

Modulating regulation of RAD51 during homologous recombination. BRCA2 facilitates the loading and stabilization of RAD51 and suppresses the anti-recombinase function of FIGNL1. In cells lacking BRCA2, FIGNL1 dissociates RAD51 from double-strand breaks (DSBs), leading to a deficiency in homologous recombination and resulting in genomic instability. In BRCA2-deficient cells, the absence of FIGNL1 can restore RAD51 loading through the MMS22L-TONSL complex, thereby re-establishing homologous recombination and genomic stability.

Downloaded from https://www.science.org at Biblioteca Universitaria Di Lugano on July 21, 2026

MOLECULAR BIOLOGY

FIGNL1 inhibits homologous recombination in BRCA2 deficient cells by dissociating RAD51 filaments

Raviprasad Kuthethur[1,2], Safa Nasrin VZ[3]†, Satheesh Kumar Sengodan[4]†, Carmen Fonseca[1]†, Stefan Braunshier[3]†, Nupur Nagar[5]†, Ananya Acharya[3]†‡, Xingde Wang[1], Arjan F. Theil[1], Oluwakemi Ibini[1], Eleni-Maria Manolika[1], Kelly de Koning[1,2], Julien Dessapt[6,7]§, Amélie Fradet-Turcotte[6,7], Joyce H. G. Lebbink[1,2,8], Roland Kanaar[1,2], Krishna Mohan Poluri[5], Shyam K. Sharan[4], Petr Cejka[3]*, Arnab Ray Chaudhuri[1]*

Homologous recombination (HR) deficiency upon Breast Cancer Gene 2 (BRCA2) loss arises from defects in the formation of RAD51 nucleoprotein filaments. We demonstrate that loss of the anti-recombinase Fidgetin Like 1 (FIGNL1) retains RAD51 loading at DNA double-stranded breaks (DSBs) in BRCA2-deficient cells, leading to genome stability, HR proficiency, and viability of BRCA2-deficient mouse embryonic stem cells. Mechanistically, we demonstrate that strand invasion and subsequent HR defects upon BRCA2 loss primarily arise from the unrestricted removal of RAD51 from DSB sites by FIGNL1, rather than from defective RAD51 loading. Furthermore, we identify that the MMS22L-TONSL complex interacts with FIGNL1 and is critical for HR in BRCA2/FIGNL1 double-deficient cells. These findings identify a pathway for tightly regulating RAD51 activity to promote efficient HR, offering insights into mechanisms of chemoresistance in BRCA2-deficient tumors.

The homologous recombination (HR) pathway is essential for accurate repair of DNA double-stranded breaks (DSBs) (*1*). BRCA2 is essential for the HR process and interacts with RAD51, mediating nucleation of RAD51 nucleoprotein filaments on single-stranded DNA (ssDNA) by displacing RPA (*2*–*4*). This step is crucial for the strand invasion and DNA synthesis steps in HR. BRCA2 loss restricts RAD51 accumulation at DSBs, disrupting HR and leading to genome instability (*5*–*11*). Tumor cells with BRCA2 mutations show RAD51 loading and HR deficiencies (*12*–*15*), which are targets for chemotherapeutics such as poly(adenosine-diphosphate-ribose) polymerase inhibitors (PARPi) and DNA crosslinking agents (*15*–*17*). Although these treatments have shown success, some tumors develop resistance through compensatory mechanisms (*13*, *18*, *19*). No compensatory mechanisms of RAD51 loading and HR have been identified upon BRCA2 loss, highlighting its crucial role in HR.

The MMS22L-TONSL heterodimeric complex regulates HR by controlling RAD51 dynamics at replication-induced DSBs (*20*–*22*). This heterodimer interacts with RPA and contains a RAD51 interaction motif, facilitating RAD51-mediated strand invasion (*22*). TONSL interacts with ASF1 and CAF1 and recognizes H4K20me0 at DSBs, enabling MMS22L-mediated RAD51 loading on nascent DNA at DSBs (*21*, *23*, *24*). Loss of MMS22L-TONSL does not affect BRCA2 localization to DSBs, suggesting that it either functions downstream or separately in RAD51-mediated HR (*21*). Nevertheless, the relationship between BRCA2 and MMS22L-TONSL-dependent pathways in HR remains poorly understood.

The regulation of RAD51 loading and stabilization is critical as excessive accumulation of RAD51 on chromatin is associated with genome instability and cell death (*25*, *26*). This regulation is achieved through dissociation of RAD51 from DNA or by disruption of recombination intermediates through various helicases and translocases, including the RECQ family helicases, PARI, RTEL1, and FBH1 (*27*–*32*). FIGNL1 (fidgetin-like 1), a member of the AAA+ ATPase family, plays a major role in maintaining genome stability (*33*). Depletion of FIGNL1 results in accumulation of RAD51 and genome instability characterized by persistent ultrafine chromosome bridges (*33*). The interaction between FIGNL1 and FIRRM/FLIP is crucial for DNA crosslink repair and homologous recombination (*34*–*39*). FIGNL1 is also crucial for meiotic recombination, as its absence results in impaired spermatogenesis due to RAD51 hyperaccumulation (*40*, *41*). Mutations in the *Arabidopsis* BRCA2 paralog can also suppress the meiotic phenotypes associated with loss of FIGL1, underscoring the importance of FIGNL1 in HR (*42*). Nevertheless, the underlying mechanisms governing RAD51 loading and dissociation, as well as their effects on HR fidelity and genomic stability, remain to be elucidated.

Results

FIGNL1 loss restores RAD51 loading at DSBs upon BRCA2 deficiency

Loss of FIGNL1 increases chromatin association of RAD51 and is not compatible with cellular viability (*40*, *43*). Therefore, we genetically inactivated FIGNL1 using CRISPR-Cas9 in RPE1 hTERT $p53^{-/-}$ cells with doxycycline (Dox)-inducible shRNA against BRCA2 (wild type (WT) or shBRCA2) (*44*) (fig. S1, A and B). FIGNL1 inactivation was also performed in the *Brca2*$^{-/-}$*; Trp53*$^{-/-}$ mouse mammary tumor cell line KB2P1.21 (*Brca2*$^{-/-}$) and the KB2P1.21 reconstituted with wild type *Brca2* (WT/KB2PR) derived from *K14cre; Trp53*$^{F/F}$*;Brca2*$^{F/F}$ mouse tumor model (*45*) (fig. S1, C and D). Inactivation of FIGNL1 in a p53-deficient background yielded viable cells without substantial changes in cell cycle profiles, indicating that genome instability from FIGNL1 loss is tolerated upon p53 deficiency (fig. S1, E and F). We then assessed RAD51 accumulation with or without DSBs upon FIGNL1 loss in BRCA2-proficient or deficient conditions. Upon treatment with ionizing radiation (IR) to induce DSBs, we analyzed chromatin-bound RAD51 foci using quantitative immunofluorescence-based cytometry (QIBC) (*46*, *47*). FIGNL1 loss in both cell lines resulted in significantly higher RAD51 accumulation on chromatin, apparent under untreated conditions and enhanced by IR, correlating with increased H2AX colocalization (Fig. 1A and fig. S2, A and B). BRCA2 loss resulted in defective RAD51 accumulation as expected (Fig. 1A and fig. S2, A and B). Loss of FIGNL1 in BRCA2-deficient cells considerably rescued the RAD51 focus formation defect upon IR induced DSB induction (Fig. 1A, fig. S2, A and B). Next, to test whether FIGNL1 loss increases RAD51 focus formation upon site-specific DSBs, we expressed the AsiSI restriction enzyme in mouse mammary tumor lines, in which DSBs can be induced by Dox and 4-hydroxytamoxifen (4-OHT) treatment (Fig. 1B and fig. S2C) (*48*). AsiSI induction resulted

[1]Department of Molecular Genetics, Erasmus MC Cancer Institute, Erasmus University Medical Center, Rotterdam, the Netherlands. [2]Oncode Institute, Erasmus University Medical Center, Rotterdam, the Netherlands. [3]Institute for Research in Biomedicine, Università della Svizzera italiana (USI), Faculty of Biomedical Sciences, Bellinzona, Switzerland. [4]Mouse Cancer Genetics Program, Center for Cancer Research, National Cancer Institute at Frederick, Frederick, MD, USA. [5]Department of Biosciences and Bioengineering, Indian Institute of Technology Roorkee, Uttarakhand, India. [6]Department of Molecular Biology, Medical Biochemistry and Pathology, Université Laval, Québec, Canada. [7]CHU de Québec Research Center-Université Laval, Laval University Cancer Research Center, Québec, Canada. [8]Department of Radiotherapy, Erasmus MC Cancer Institute, Erasmus University Medical Center, Rotterdam, the Netherlands. ***Corresponding author. Email: petr.cejka@irb.usi.ch (P.C.); a.raychaudhuri@erasmusmc.nl (A.R.C.)** †These authors contributed equally to this work. ‡Present address: Division of Radiation and Genome Stability, Department of Radiation Oncology, Dana-Farber Cancer Institute, Harvard Medical School, Boston, MA, USA. §Present address: Centre for Molecular and Systems Biology, Lunenfeld-Tanenbaum Research Institute, Mount Sinai Hospital, Toronto, ON, Canada.

Downloaded from https://www.science.org at Biblioteca Universitaria Di Lugano on July 21, 2026

in similar levels of DSBs across the tested cell lines, measured by 53BP1 foci using QIBC (fig. S2C). Site-specific DSBs showed substantially higher RAD51 foci upon FIGNL1 loss compared with WT cells. BRCA2 abrogated RAD51 focus formation, which was restored to WT levels upon concomitant FIGNL1 loss (Fig. 1B). Furthermore, we also confirmed this effect in U2OS-DIvA cells by downregulating BRCA2, FIGNL1, or both with 4-OHT treatment (*49*). FIGNL1 loss in BRCA2-deficient U2OS cells rescued RAD51 focus formation defects (fig. S2D). These data suggest that RAD51 accumulation defects from BRCA2 loss could at least in part result from RAD51 removal by FIGNL1, and not defective RAD51 loading.

FIGNL1 interacts with FIRRM/FLIP and disassembles RAD51 nucleoprotein filaments (*35*–*39*). To test whether DNA binding of FIGNL1 is required, we purified an N-terminal–truncated fragment of FIGNL1 (FIGNL1-dNLS) lacking 1 to 120 residues, which disrupts FIRRM/FLIP binding but remains functional (fig. S3A) (*35*). FIGNL1-dNLS showed weak binding to both ssDNA and double-stranded DNA (dsDNA), with binding observed only at high concentrations (fig. S3, B and C). Although saturating RPA did not recruit FIGNL1 to ssDNA, at low RPA concentrations FIGNL1 enhanced RPA binding to ssDNA but not mitochondrial SSB (fig. S3, D and E). These data suggest that FIGNL1 disrupts RAD51 nucleofilaments through direct interaction with the RAD51 protein. FIGNL1 interacts with RAD51 (*38*). In line, our in vitro assays using recombinant FIGNL1-dNLS and RAD51 and pulldown assays with reconstituted FIGNL1 from cells demonstrated robust FIGNL1-RAD51 interaction (fig. S3, F to H).

Next, to assess whether FIGNL1 disassembles RAD51 from ssDNA, we performed nuclease protection assays. Without RAD51, DNA2 nuclease considerably degraded DNA. The presence of RAD51 protected DNA, indicative of RAD51 binding. Addition of FIGNL1-dNLS to RAD51-bound ssDNA resulted in decreased protection of ssDNA in a concentration-dependent manner (fig. S4A), indicative of RAD51 dissociation from ssDNA. We then tested whether the dissociation of RAD51 from ssDNA by FIGNL1-dNLS also affected its DNA strand exchange activity. RAD51 catalyzes the exchange of a 3′-tailed oligonucleotide-based substrate with a radiolabeled dsDNA donor (Fig. 1C) (*5*). Increasing FIGNL1-dNLS concentrations inhibited the formation of the strand exchange product, indicating that RAD51 filament disruption results in DNA strand exchange defects (Fig. 1C and fig. S4B). Furthermore, in D-loop assays (*50*), FIGNL1-dNLS inhibited D-loop formation catalyzed by RAD51 and RAD54 (fig. S4, C and D). The addition of AMP-PNP to the strand exchange reaction ablated the ability of FIGNL1-dNLS to inhibit the RAD51-mediated strand exchange reaction, indicating the critical role of the FIGNL1-dNLS ATPase domain in dissociating RAD51 (fig. S4E). Next, we tested whether ATP hydrolysis by RAD51 was required for its removal by FIGNL1-dNLS. We employed RAD51-K133R, a mutant defective in ATP hydrolysis (*51*, *52*). FIGNL1-dNLS inhibited DNA strand exchange to an extent similar to that of wild-type RAD51, indicating that FIGNL1-dNLS does not dissociate RAD51 by stimulating its ATP hydrolytic activity (Fig. 1D and fig. S4F). Our immunofluorescence data suggest that BRCA2 could prevent FIGNL1-mediated RAD51 dissociation (Fig. 1, A and B, and fig. S2, A to D). We next reconstituted DNA strand exchange with RPA and mini-BRCA2 (miBRCA2), containing the BRC1 and BRC2 motifs, DNA-binding, and C-terminal domains of BRCA2 (*53*) (fig. S5, A and B). miBRCA2 stimulated strand exchange in the presence of RAD51 and/or RPA (Fig. 1E and fig. S5C) (*5*, *6*, *54*, *55*). The presence of BRCA2 in the reaction prevented the inhibition of DNA strand exchange by FIGNL1-dNLS compared with RAD51 alone (Fig. 1E and fig. S5C), suggesting that BRCA2 counteracts FIGNL1-mediated RAD51 dissociation for efficient HR.

Finally, we tested whether the loss of FIGNL1 restores functional HR in BRCA2-deficient cells. We performed siRNA-mediated downregulation of BRCA2, FIGNL1, and BRCA2/FIGNL1 in U2OS DR-GFP cells (*56*). I-SceI endonuclease expression in FIGNL1-deficient cells showed a slight but notable increase in HR efficiency (Fig. 1F). BRCA2 down-regulation decreased HR efficiency as expected. However, FIGNL1 deficiency significantly rescued HR defects observed in BRCA2-deficient cells. Our data suggest that the HR defects upon BRCA2 loss result from unrestricted dissociation of RAD51 from DNA by FIGNL1 rather than through RAD51 nucleofilament loading and stabilization defects.

Loss of FIGNL1 rescues lethality of BRCA2 deficient ESC and resistance to chemotherapeutic drugs

Genetic knockout of either *Brca2* or *Fignl1* in mouse embryonic stem cells (mESCs) are incompatible with survival, possibly due to defects in the tight control of HR (*9*, *40*, *43*, *57*). Because loss of FIGNL1 in BRCA2-deficient cells rescues HR (Fig. 1F), we tested whether FIGNL1 deficiency rescues the lethality of BRCA2 deficient mESCs. We generated FIGNL1-deficient PL2F7 mESCs with one null and one conditional allele of *Brca2* (*Brca2*$^{f/-}$) (*58*) by targeting with short hairpin RNAs (shRNAs) and selecting colonies with residual levels of FIGNL1 (Fig. 2A and fig. S6A). Upon transfection of *Brca2*$^{f/-}$ mESCs with Cre-recombinase and HAT selection, no *Brca2*-null colonies were obtained, confirming BRCA2's essential role (Fig. 2B). However, targeting FIGNL1 with two separate shRNAs yielded 37.1 and 53.2% HAT-resistant *Brca2*-null colonies (Fig. 2B and fig. S6B). Additionally, IR-induced RAD51 focus formation was substantially rescued in *Brca2/Fignl1* double-deficient mESCs when compared with HR-defective *Brca2* hypomorphic mutant ESCs (R2336H) (*59*) (Fig. 2C), suggesting that the double deficient cells were competent for HR.

Because the loss of FIGNL1 upon BRCA2 deficiency resulted in the restoration of HR (Fig. 1F), we next assessed the levels of genome instability by analyzing metaphase spreads after PARPi (olaparib) and cisplatin treatment in mouse mammary tumors and RPE1 cells. BRCA2/FIGNL1 double deficiency significantly reduced chromosomal aberrations compared to BRCA2 loss alone (Fig. 2, D to E, and fig. S7A). Similar data were also observed in mESCs, which displayed restoration of genome stability upon PARPi treatment in *Brca2*$^{-/-}$ *shFignl1* double-deficient cells compared to *Brca2*^{R2336H} hypomorphic cells (fig. S7B). Finally, clonogenic survival assays in mouse mammary tumors and mESCs showed that FIGNL1 loss in BRCA2-deficient cells rescued cellular sensitivity to PARPi and platinum drugs (Fig. 2, F to G, and fig. S7, C to F). These data suggest that restored HR in BRCA2-deficient cells upon FIGNL1 loss restores RAD51 loading, driving synthetic viability and chemoresistance.

FIGNL1 interaction with RAD51 is critical for its regulation

To gain further insights into the molecular interactions involving FIGNL1, we performed mass photometry experiments with FIGNL1-dNLS, which revealed the existence of various forms including monomer and hexameric species of FIGNL1 (fig. S8, A and B) consistent with recent reports (*35*, *43*). AlphaFold3-predicted hexameric structure of full-length FIGNL1 revealed that the N-terminal region is likely to be unstructured as indicated by predicted local distance difference test (pLDDT) < 50 and that oligomerization likely occurs between the C-terminal domains (pLDDT > 70) in the presence of Mg^{2+} and ATP (fig. S8, C and D, and table S1). Our mass photometry and pulldown experiments revealed predominantly a monomer-monomer RAD51-FIGNL1 interaction and possibly a FIGNL1 hexamer-RAD51 monomer interaction (fig. S9, A to D), aligning with recent evidence (*35*, *43*). The data indicate that the interaction between the RAD51 monomer and the FIGNL1 hexamer may be transient. We further modeled the interaction between FIGNL1 hexamer and RAD51 using AlphaFold3. The predicted structure indicated that RAD51 is embedded into the hexameric pore of FIGNL1 (a hallmark of many AAA+ ATPases) through the N-terminal end of RAD51 (fig. S10, A and B, and table S2). The model revealed three FIGNL1 regions, including FIGNL1-RAD51 binding domain (FRBD), Pore loop 1 and Pore loop 2 contributing to the

Downloaded from https://www.science.org at Biblioteca Universitaria Di Lugano on July 21, 2026

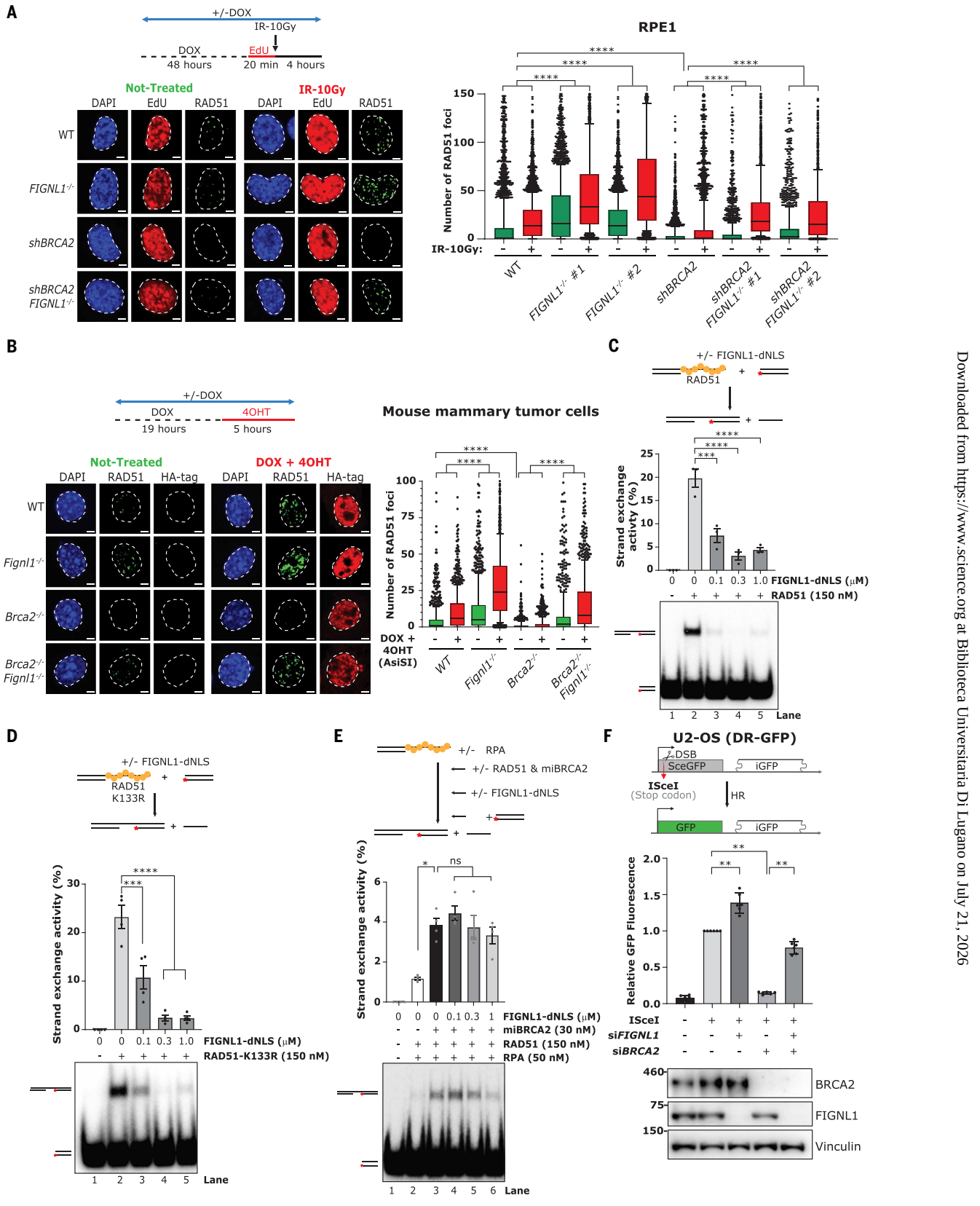

Fig. 1. Loss of FIGNL1 in BRCA2 deficient cells rescues RAD51 mediated HR. (**A**) (Top) Schematics showing the experimental setup for the high-content, automated RAD51 immunofluorescence (IF) in human RPE1 cells. 2 μg/ml of doxycycline for 48 hours to induce the knock-down of BRCA2, followed by EdU labelling and induction of DSB via 10 Gy of x-ray treatment. (Left) Representative IF images showing EdU and RAD51 foci in not-treated and ionizing radiation treated cells; scale bar, 5 μm. (Right) Automated Quantitative Image Based Cytometry (QIBC) plot of the RAD51 foci per nucleus; scatter box plot showing the foci distribution between the 10 to 90th percentiles from 2000 cells (experiment was repeated three times). *P*-values from Mann-Whitney test (two-tailed) comparing between respective not-treated or IR-treated groups (****: <0.0001).

Downloaded from https://www.science.org at Biblioteca Universitaria Di Lugano on July 21, 2026

(**B**) (Top) Schematics showing the experimental setup for RAD51-IF in mouse mammary tumor cells expressing AsiSI with HA-tag. 24 hours of doxycycline treatment to induce AsiSI-HA expression with last 5 hours to translocate it to the nucleus by 400 nM 4-hydroxytamoxifen (4OHT). (Left) Representative IF images of the RAD51 and HA-tag in not-treated and DOX+4OHT cells; scale bar, 5 μm. (Right) Automated QIBC plots of the RAD51 foci per nucleus; scatter box plot showing the foci distribution between the 10 to 90th percentiles from 1500 cells (experiment was repeated three times). *P*-values from Mann-Whitney test (two-tailed) comparing between respective not-treated or DOX+4OHT treated groups (****: <0.0001). (**C**) (Top) Schematics of the DNA strand exchange assays. The assays were performed by adding 150 nM purified RAD51 to the DNA substrates in the presence of increasing concentrations of purified FIGNL1-dNLS. The red asterisk indicates the position of the radioactive label. (Bottom) Quantification of the absolute DNA strand exchange activity showing the band intensity of the exchanged DNA; error bars are indicative of mean ± SEM from three independent experiments ($n = 3$). *P*-values from Dunnett's multiple comparison one-way ANOVA comparing between indicated groups (***: <0.001; ****: <0.0001). (**D**) (Top) Schematics of the DNA strand exchange assays. The assays were performed by adding 150 nM purified RAD51-K133R to the DNA substrates in the presence of increasing concentrations of purified FIGNL1-dNLS. The red asterisk indicates the position of the radioactive label. (Bottom) Quantification of the absolute DNA strand exchange activity showing the band intensity of the exchanged DNA; error bars are indicative of mean ± SEM from four independent experiments ($n = 4$). *P*-values from Dunnett's multiple comparison one-way ANOVA comparing between indicated groups (***: <0.001; ****: <0.0001). (**E**) (Top) Schematics of the DNA strand exchange assays. The assays were performed by adding 150 nM RAD51 and 30 nM miBRCA2 to the DNA substrates pre-incubated with 50 nM RPA. The reactions were then supplemented with the increasing concentrations of purified FIGNL1-dNLS and labelled donor oligos. The red asterisk indicates the position of the radioactive label. (Bottom) Quantification of the absolute DNA strand exchange activity showing the band intensity of the exchanged DNA; error bars are indicative of mean ± SEM from 4 independent experiments ($n = 4$). *P*-values from Dunnett's multiple comparison one-way ANOVA comparing between indicated groups (*: <0.05). (**F**) (Top) Schematics of DR-GFP assay showing the strategy behind the experiment. Mutant Sce-GFP containing ISceI recognition site and stop codon is repaired by the downstream iGFP to restore the GFP fluorescence in the cells. (Center) U2-OS cells with a stable integrated DR-GFP system were transfected for 72 hours with the indicated siRNAs and underwent 48 hours of ISceI treatment to measure the levels of GFP fluorescence relative to the WT cells undergoing ISceI treatment. Error bars are representative of the mean ± SD from three independent experiments ($n = 3$). *P*-values from unpaired *t*-test comparing between indicated groups (**: <0.01). (Bottom) Western blot analysis showing the levels of FIGNL1 and BRCA2 from the corresponding cells used for FACS analysis.

FIGNL1-RAD51 complex. Both Pore loops interact with RAD51's N-terminal region (table S2), as reported recently (*43*). The FRBD region was predicted to interact with two loops between Walker A and Walker B of the RAD51 ATPase domain with low confidence (pLDDT < 50) owing to the N-terminal region of FIGNL1 being unstructured. All five models generated, however, consistently predicted the interaction of RAD51 to the FRBD and the Pore loop regions with favorable binding energy (fig. S10, A and B, and table S2). Additionally, since the FRBD domain appears to be the primary RAD51 binding region on FIGNL1 (*38*), we used AlphaFold2 multimer to model RAD51 binding to the FRBD region. AlphaFold2 multimer prediction revealed a FIGNL1 FRBD-RAD51 dimer complex in which FRBD interacted with both RAD51 monomers (fig. S11, A and B, and table S3). These predictions suggest that although FRBD domain of FIGNL1 can bind to a RAD51 dimer, only one RAD51 molecule can interact with the pore loops of FIGNL1 in its hexameric form.

To validate AlphaFold3 predictions of the FIGNL1-RAD51 interactions, we generated mutants targeting conserved residues at interfaces. For in vitro reactions, mutants were generated in the FIGNL1-dNLS construct including dFRBD (lacking residues 295 to 344), FxxA mutation (F295E), Pore loop 1+2 mutations (K473E+W474A+H514A), dPore loop (lacking residues 461 to 562) predicted to affect RAD51 interaction (fig. S12, A to I). To evaluate the function of the catalytic domain of the FIGNL1- and RAD51-interacting region, we engineered several mutants by combining segments of the ATPase and RAD51 interaction domains. These include ATPase mutations (K447A+D500A), ATPase + Pore loop 1+2 mutations, F295E + ATPase + Pore loop 1+2 mutations, and dFRBD + ATPase + Pore loop 1+2 mutations (fig. S12, A to I). Testing these mutants revealed that FRBD deletion in FIGNL1-dNLS abolished RAD51 binding, whereas the other mutants retained the interaction with RAD51 in vitro under physiological salt conditions (Fig. 3A). This suggests multiple points of interaction between RAD51 and FIGNL1-dNLS, consistent with AlphaFold3 predictions. Notably, the ATPase and dPore loop mutants showed increased DNA binding compared to FIGNL1-dNLS (fig. S12J), though the implications remain unclear. Our data demonstrate that RAD51 interacts through multiple contacts with FIGNL1-dNLS, primarily in its FRBD domain.

To assess the modeled interactions in cells, we reconstituted eGFP-tagged full-length (FL) FIGNL1, dFRBD, FxxA mutant, dNLS, ATPase, Pore loop 1+2 mutations, ATPase + Pore loop 1+2 mutations, and dPore loop in *FIGNL1*$^{-/-}$ RPE1 cells (fig. S13, A and B) and conducted immunoprecipitation (IP) experiments. All reconstituted FIGNL1 mutants exhibited reduced RAD51 interaction compared with full-length FIGNL1. The dNLS mutation, which disrupts the interaction of FIGNL1 with FIRRM, demonstrated the lowest reduction whereas the dFRBD and F295E mutations showed the highest reduction among the mutants (Fig. 3B). This confirmed FRBD as the most critical domain for RAD51 binding (*38*), though FIGNL1's interaction with partners like FIRRM remains essential for optimal RAD51 interaction within protein complexes.

Subsequently, we evaluated the FIGNL1-RAD51 interaction mutants (fig. S12, A to I) in disassembling RAD51 from ssDNA through nuclease protection assays. As previously demonstrated (fig. S4A), FIGNL1-dNLS led to reduced protection of ssDNA through RAD51 filament disassembly (Fig. 3C). All generated RAD51 interaction mutants exhibited significant impairment in the removal of RAD51 from ssDNA compared to FIGNL1-dNLS (Fig. 3C). The ssDNA deprotection impairment by FIGNL1-dNLS mutants was associated with reduced ATP hydrolysis activity in mutants targeting conserved ATPase motifs (Fig. 3D). These findings indicate that the AlphaFold3 predicted interfaces between hexameric FIGNL1 and RAD51 are essential for FIGNL1 function in the dissociation of RAD51 filaments from DNA.

FIGNL1 association with RAD51 is essential for its removal and restricting strand exchange

Based on our in vitro biochemical data and cellular reconstitution experiments of FIGNL1-RAD51 interface mutants, we assessed the impact of these mutants in RAD51 focus accumulation after IR treatments. The reconstitution of FIGNL1-FL led to *FIGNL1*$^{-/-}$ and shBRCA2 *FIGNL1*$^{-/-}$ cells exhibiting reduced levels of RAD51 foci, akin to the conditions observed in WT or BRCA2-deficient cells, respectively. (Fig. 4, A and B). Reconstitution with all the mutants tested (fig. S13, A and B) failed to reduce the number of RAD51 foci in *FIGNL1*$^{-/-}$ or shBRCA2 *FIGNL1*$^{-/-}$ cells (Fig. 4, A and B). To test whether the mutants' failure to reduce RAD51 focus levels correlated with genome stability in shBRCA2 *FIGNL1*$^{-/-}$ cells, we measured chromosomal aberrations upon PARPi or cisplatin treatment. Reconstitution with FIGNL1-FL and treatment with either PARPi or cisplatin increased chromosomal aberrations in the BRCA2/FIGNL1 double-deficient cells (fig. S13C), in contrast to the FIGNL1 mutants (fig. S13C). Finally, we evaluated whether the RAD51 interaction mutants of FIGNL1-dNLS could impede RAD51-mediated DNA strand exchange products in our biochemical assay. Consistent with ssDNA protection data (Fig. 3C), each mutant showed impairment in disrupting DNA strand exchange reaction catalyzed by RAD51 (Fig. 4C). These data indicate that stabilization of FIGNL1 by FIRRM/FLIP and the interaction of RAD51 with FRBD, ATPase and Pore loop regions of FIGNL1 are critical for RAD51 dissociation from resected DSBs.

Downloaded from https://www.science.org at Biblioteca Universitaria Di Lugano on July 21, 2026

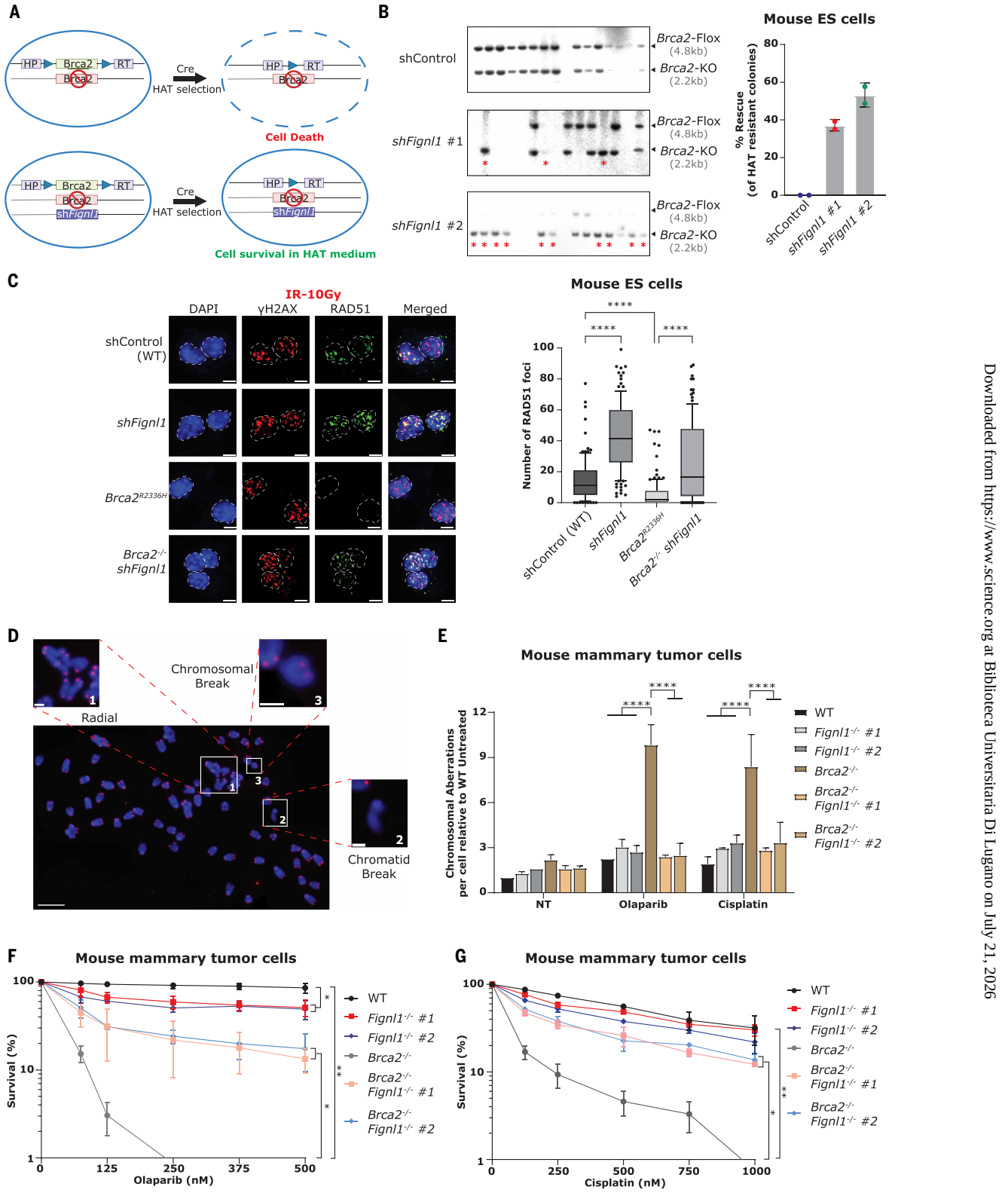

Fig. 2. FIGNL1 loss results in synthetic viability of BRCA2 null ESCs and confers resistance to chemotherapeutic drugs. (**A**) Schematic representation of strategy behind deletion of BRCA2 in mouse embryonic stem cells. (**B**) (Left) Representative southern blot images showing the 4.8 kb conditional knock-out allele (upper band) and 2.2 kb deleted allele (lower band) of *Brca2*. Stars in the shFIGNL1 clones represents the rescued clones in the absence of BRCA2. (Right) Percentage quantification of rescued clones. (**C**) (Left) Representative RAD51-IF images in mouse embryonic stem cells (scale bar: 20 μm). *Brca2*^{R2336H} a *Brca2* mutant ES cell line that expressed a hypomorphic allele (p.Arg2336His) of BRCA2 that is defective in HR. (Right) Semi-automated QIBC plots of the RAD51 foci per nucleus in WT and FIGNL1 knock down clones; scatter box plot showing the foci distribution between 10-90th percentile ($n = 150$). *P*-values from Mann-Whitney test (two-tailed) comparing between indicated groups (****: <0.0001). (**D**) Representative metaphase spread image showing different aberrations analyzed for genomic instability. Scale bar (whole metaphase): 5 μm; scale bar (individual aberrations): 1 μm.

Downloaded from https://www.science.org at Biblioteca Universitaria Di Lugano on July 21, 2026

(**E**) Quantification of chromosomal aberrations in mouse mammary tumor cells in response to Olaparib and cisplatin from three independent experiments in which 50 individual metaphases were analyzed for each sample per experiment. *P* values from ordinary two-way ANOVA (****: <0.0001). (**F**) Percentage survivability of mouse mammary tumor cells in response to Olaparib; quantification was performed by normalization to non-treated cells. *P*-values from Dunnett's multiple comparison one-way ANOVA comparing between indicated groups (*: <0.05, **: <0.01). (**G**) Percentage survivability of mouse mammary tumor cells in response to cisplatin; quantification was performed by normalization to non-treated cells. *P*-values from Dunnett's multiple comparison one-way ANOVA comparing between indicated groups (*: <0.05, **: <0.01).

FIGNL1 interacts with MMS22L-TONSL complex in the absence of RAD51

Functional RAD51 loading and HR in BRCA2/FIGNL1 double-deficient cells (Fig. 1, A, B, and F) indicated that other factors could mediate RAD51 loading and stimulate HR without BRCA2. To identify factors that could stimulate HR and be regulated by FIGNL1, we investigated protein-protein interactions (PPIs) of FIGNL1 using the PREDICTOMES classifier database (https://predictomes.org/view/ddr) (*60*). Our search revealed FIRRM, RAD51, and DMC1 as top potential interactors of FIGNL1 based on pLDDT scores (fig. S14A and table S4). FIGNL1 was predicted to interact with high confidence with both MMS22L and TONSL, which exists as a complex mediating HR though RAD51 interaction (fig. S14A and table S4) (*20*–*22*). Using AlphaFold3, we predicted interactions between monomeric FIGNL1 and MMS22L-TONSL complex. The modeled architecture showed FIGNL1 monomer wrapping around MMS22L, with NLS, FRBD, and Pore loops interacting with different MMS22L regions (Fig. 5A, fig. S15, A and B, and table S5). Although unstructured regions showed low confidence interactions, all models predicted favorable binding energy (table S5). To test the predicted PPI between FIGNL1 and MMS22L-TONSL complexes, we performed an in vitro interaction assay with purified FIGNL1-dNLS and MMS22L-TONSL (figs. S3A and S15C). The addition of MMS22L-TONSL complex to immobilized FIGNL1-dNLS revealed a direct physical interaction (Fig. 5B). To validate this in cells, we performed IP experiments using eGFP-tagged FIGNL1 in *FIGNL1*$^{-/-}$ RPE1 cells. Pulldowns of FIGNL1 contained MMS22L-TONSL complex, confirming our prediction and the in vitro data (Fig. 5C).

Since both the MMS22L-TONSL complex and FIGNL1 modulate RAD51 activity in HR, we modeled the FIGNL1-MMS22L-TONSL ternary complex with RAD51. The predicted quaternary complex suggests that with RAD51, FIGNL1 dissociates from the MMS22L-TONSL and interacts with RAD51 via the FRBD region (Fig. 5D, fig. S16, A and B, and table S6). To test this model, we performed interaction assays with purified FIGNL1-dNLS and MMS22L-TONSL complex with or without RAD51 and ssDNA-bound RAD51. RAD51-K133R (*51*, *52*) was used to ensure stronger ssDNA binding (fig. S4F). Supporting our structural prediction, RAD51-K133R reduced MMS22L-TONSL and FIGNL1 interaction without affecting RAD51 binding, with no changes observed when adding ssDNA-bound RAD51 compared to RAD51 alone (Fig. 5E and S16C).

BRCA2 has been proposed to sequester cellular RAD51 to prevent inappropriate DNA interactions (*61*). We hypothesized that RAD51 availability for the MMS22L-TONSL-FIGNL1 complex in cells could be constrained by BRCA2. Pull-down experiments of FIGNL1 showed that BRCA2 deficiency resulted in the dissociation between FIGNL1 and the MMS22L-TONSL complex compared with WT cells (Fig. 5F), potentially due to increased RAD51 availability. AlphaFold3 predictions of the FIGNL1-MMS22L-TONSL ternary complex and FIGNL1-MMS22L-TONSL-RAD51 quaternary complex indicated that FIGNL1 could interact with both RAD51 and MMS22L-TONSL through the FRBD domain, suggesting competitive interaction (Fig. 5, A and D, figs. S15, A and B, and S16, A and B, and tables S5 and S6). Our in vitro experiments showed that RAD51 interaction with FIGNL1-dNLS was lost following FRBD region deletion (Fig. 3A). Additional experiments confirmed that the absence of FRBD resulted in a loss of interaction with both RAD51 and MMS22L-TONSL, supporting that they compete for the same binding region on FIGNL1, with RAD51's primary interaction being with FIGNL1 (Fig. 5G). Subsequently, cellular pulldowns validated that FRBD loss disrupted both FIGNL1-MMS22L and FIGNL1-RAD51 interactions (Fig. 5H). BRCA2 loss, which would increase the availability of RAD51, only disrupted interaction between full-length FIGNL1 and MMS22L, whereas FRBD loss upon BRCA2 depletion disrupted both RAD51 and MMS22L interactions, further suggesting that MMS22L and RAD51 compete for the same binding site on FIGNL1 (Fig. 5H). These data suggest that the MMS22L-TONSL-FIGNL1 interaction may be critical for controlling FIGNL1 activity and limiting unwanted RAD51 removal during HR.

MMS22L-TONSL promotes RAD51 accumulation and facilitates HR in BRCA2/FIGNL1 double-deficient cells

Our data suggest that the interaction between MMS22L-TONSL and FIGNL1 regulates RAD51 dynamics upon DSB induction. We therefore assessed MMS22L localization to DSBs with or without BRCA2 and/or FIGNL1 in RPE1 and mouse mammary tumor cells. Upon IR treatments, WT cells showed increased MMS22L localization compared to untreated cells (Fig. 6A and fig. S17A). FIGNL1 loss in two clones significantly increased MMS22L foci compared with WT cells. BRCA2 loss caused a slight increase in MMS22L foci, further enhanced in BRCA2/FIGNL1 double-deficient cells (Fig. 6A and fig. S17A). The increased MMS22L upon loss of FIGNL1 was correlated with increased RAD51 localization upon IR exposure (Fig. 1A and fig. S2, A and B). These data suggest that FIGNL1 primarily dissociates RAD51 loaded by the MMS22L-TONSL complex. To validate, we conducted in vitro ssDNA protection assay with purified RAD51, the MMS22L-TONSL complex, and FIGNL1-dNLS. MMS22L-TONSL addition to RAD51-bound ssDNA in the presence of FIGNL1 did not protect against nuclease degradation (fig. S17B). Furthermore, in DNA strand exchange reactions, MMS22L-TONSL complex enhanced RAD51-mediated strand exchange (*22*) but FIGNL1-dNLS addition inhibited the reaction in a concentration-dependent manner (Fig. 6B). This indicates that the MMS22L-TONSL complex cannot counteract FIGNL1-mediated RAD51 dissociation, thus inhibiting HR.

Given the enhanced MMS22L localization in BRCA2/FIGNL1 double-deficient cells (Fig. 6A and fig. S17A), we investigated whether the MMS22L-TONSL complex facilitates RAD51 loading at DSBs. We down-regulated MMS22L, TONSL, or both in WT, *FIGNL1*$^{-/-}$ and shBRCA2 *FIGNL1*$^{-/-}$ RPE1 cells (fig. S17, C and E) and probed for RAD51 accumulation upon DSB induction. Loss of the MMS22L-TONSL complex reduced RAD51 foci in WT cells, though to a lesser extent than BRCA2 deficiency (fig. S17D). Down-regulation of the MMS22L-TONSL complex decreased RAD51 focus accumulation in *FIGNL1*$^{-/-}$ cells to nearly WT levels, supporting that FIGNL1 primarily dissociates RAD51 accumulation mediated by MMS22L-TONSL (Fig. 6C). Loss of the MMS22L-TONSL complex in BRCA2/FIGNL1 double-deficient cells almost completely abrogated RAD51 focus accumulation (Fig. 6C), suggesting that MMS22L-TONSL is essential for RAD51 accumulation in BRCA2/FIGNL1 double-deficient cells (Fig. 6C). Additionally, DR-GFP reporter assays (*56*) showed that loss of MMS22L-TONSL in BRCA2/FIGNL1 double-deficient cells significantly reduced HR efficiency (Fig. 6D and fig. S17F). These results confirm the critical role of MMS22L-TONSL in mediating HR upon the loss of BRCA2 and FIGNL1 expression. We then tested whether MMS22L-TONSL loss in BRCA2/FIGNL1 double-deficient cells affects genomic stability upon DSB-inducing treatments. Metaphase spread analysis revealed increased chromosomal aberrations upon MMS22L-TONSL complex down-regulation in sh*BRCA2 FIGNL1*$^{-/-}$ cells treated with PARPi and cisplatin (Fig. 6E). Finally, in line with the genomic instability data, clonogenic survival assays with PARPi treatment in *Brca2*$^{-/-}$ *Fignl1*$^{-/-}$ mouse mammary tumor cells showed that MMS22L loss resulted in significant cellular sensitivity compared with *Brca2*$^{-/-}$ *Fignl1*$^{-/-}$ cells

Downloaded from https://www.science.org at Biblioteca Universitaria Di Lugano on July 21, 2026

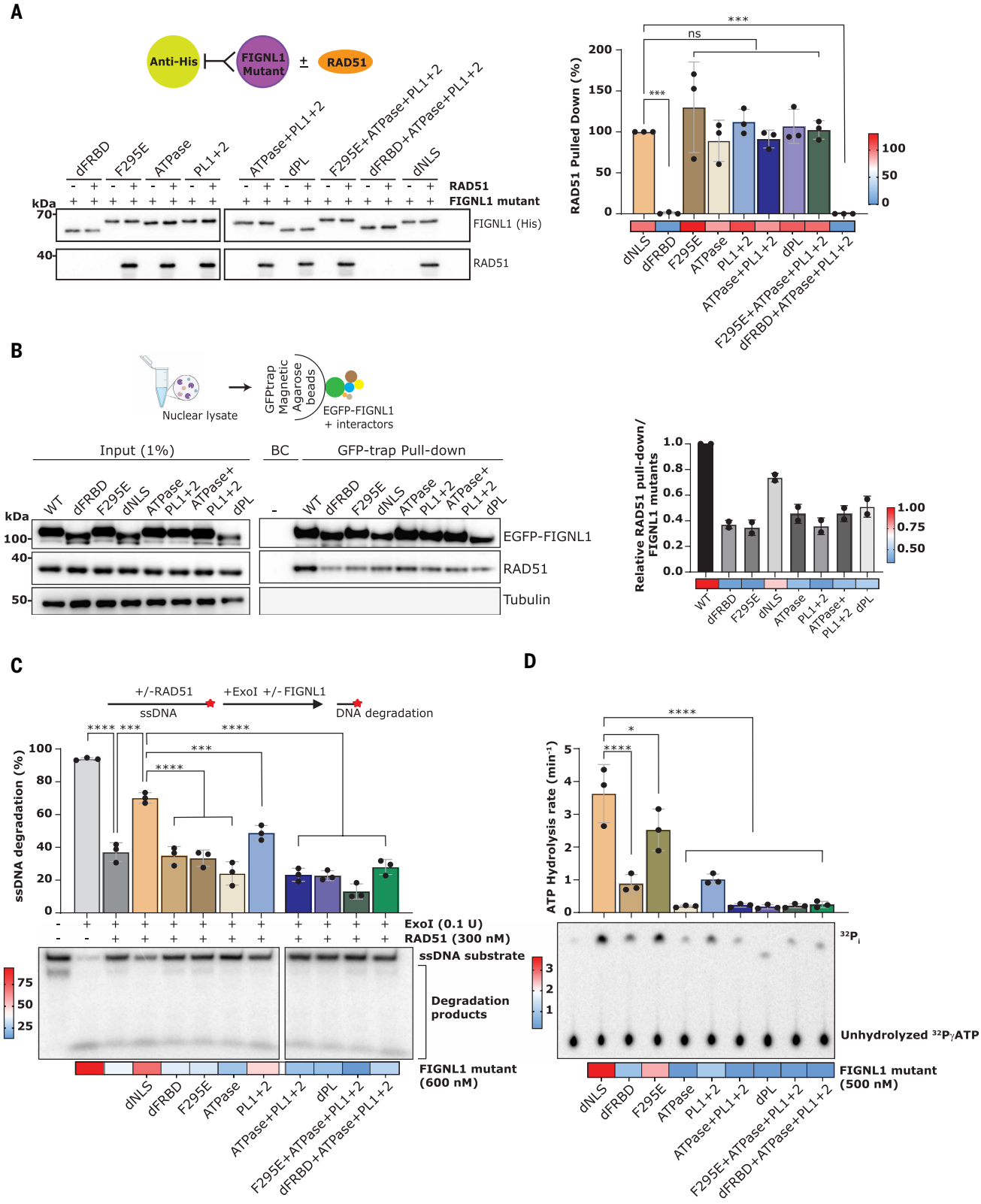

Fig. 3. FRBD and ATPase domain of FIGNL1 are important for its interaction with RAD51. (**A**) (Top) Schematics of the in vitro pull-down assay. (Left) Western blot showing the RAD51 pulled down by the different FIGNL1 mutants. (Right) Quantification of the percentage of RAD51 pulled down by the FIGNL1 mutants normalized to the dNLS mutant; error bars are indicative of mean ± SEM from three independent experiments ($n = 3$). *P*-values from Dunnett's multiple comparison one-way ANOVA comparing between indicated groups (***: <0.001). Heatmap also showing the percentage pull-down of RAD51 by the FIGNL1 mutants. (**B**) (Top) Schematics of the GFP-trap pull-down for the FIGNL1 mutants and RAD51 from the nuclear extracts. (Left) Western blot results indicative of the interaction between the FIGNL1 mutants and RAD51. (Right) Quantification of the relative RAD51 pull-down efficiency normalized for respective FIGNL1 mutants from 2 independent experiments ($n = 2$). Heatmap also showing the relative pull-down efficiency of RAD51 by the FIGNL1 mutants. (**C**) (Top) Schematics of the ssDNA protection assay showing the protection efficiency of 300 nM RAD51 against degradation by 0.1 U

Downloaded from https://www.science.org at Biblioteca Universitaria Di Lugano on July 21, 2026

ExoI nuclease in the presence or absence of 600 nM FIGNL1 mutants. The red asterisk indicates the position of the radioactive label. (Bottom) Quantification of the absolute ssDNA degradation; error bars are indicative of mean ± SEM from three independent experiments ($n = 3$). *P*-values from Dunnett's multiple comparison one-way ANOVA comparing between indicated groups (***: <0.001; ****: <0.0001). Heatmap also showing the percentage of ssDNA degradation in the presence of FIGNL1 mutants. (**D**) ATP hydrolysis rate measured in the presence of 500 nM FIGNL1 mutants. (Top) Quantification of the ATP hydrolysis rate per minute; error bars are indicative of mean ± SEM from three independent experiments ($n = 3$). *P*-values from Dunnett's multiple comparison one-way ANOVA comparing between indicated groups (*: <0.05; ****: <0.0001). Heatmap also showing the ATP hydrolysis rate in the presence of FIGNL1 mutants.

alone (Fig. 6F and fig. S17G). These data underscore the essential role of MMS22L-TONSL mediated stimulation of HR to maintain genome stability in BRCA2- and FIGNL1-deficient cells.

Discussion

BRCA2 deficiency impairs HR primarily by preventing RAD51 nucleation and filament stabilization (*5*–*11*). We show that loss of the AAA+ ATPase FIGNL1 restores RAD51 loading and HR activity, thereby conferring synthetic viability in BRCA2-deficient mESCs and resistance to PARPi inhibitors and cisplatin. We show that HR defects in BRCA2-deficient cells result from excessive RAD51 dissociation mediated by FIGNL1 (fig. S18). These findings underscore the importance of finely tuned RAD51 dynamics—both loading and dissociation—for genome maintenance and cell viability (*9*, *40*, *43*, *57*).

FIGNL1 can directly displace RAD51 from ssDNA and thus inhibit strand invasion and HR to balance the activity of BRCA2. FIGNL1 may also dissociate RAD51 from dsDNA, a process potentially relevant to reversed replication forks, in which RAD51 loading onto dsDNA is facilitated by BRCA2's C-terminal TR2 binding site for fork protection (*19*, *62*–*65*). The inability to stabilize RAD51 through TR2 interactions at reversed forks in BRCA2-deficient cells is likely attributable to unopposed FIGNL1 activity, which may result in fork degradation and genomic instability.

In BRCA2/FIGNL1-deficient cells, the MMS22L-TONSL complex emerges as the principal pathway mediating RAD51 loading and HR. Loss of this complex abrogates RAD51 accumulation and HR and increases genomic instability and drug sensitivity. The association of TONSL with H4K20me0, along with its interaction with ASF1 and CAF1, may mediate the recruitment of MMS22L-bound RAD51 to sites of DSBs on newly replicated DNA, thereby facilitating RAD51 loading in BRCA2/FIGNL1–deficient cells (*23*, *24*). The process of loading and stabilizing RAD51 in this context may also involve the interaction with other RAD51-associated proteins, including the RAD51 paralogs, which can facilitate nucleation and extension of RAD51 filaments (*66*–*68*).

Collectively, our findings reveal that inhibition of RAD51 dissociation by FIGNL1 restores HR in BRCA2-deficient cells, driving synthetic viability and drug resistance. These results have major implications for understanding mechanisms of chemoresistance in BRCA2-mutant tumors, which could restore RAD51 loading and HR without reversion mutations in the BRCA2 gene during therapy (*13*, *18*, *69*). Notably, reduced FIGNL1 expression correlates with acquired resistance to PARPi inhibitors in BRCA2-deficient mouse tumors (*70*). Targeting alternative RAD51-loading pathways, such as MMS22L-TONSL, may provide new therapeutic avenues to overcome resistance and highlights the necessity of dissecting RAD51 regulation in HR and replication stress responses.

Materials and methods

Cell Culture

Human RPE1-hTERT *TP53*$^{-/-}$*; shBRCA2* cells were cultured in DMEM/F12+GlutaMAX^{TM} (GIBCO) media containing 10% FBS (Capricorn) and 1% penicillin-streptomycin (PS) (GIBCO) at 37°C and 5% CO_2 in a humidified incubator. Mouse mammary tumor cells KB2PR and KB2P cells [previously described (*71*)], were cultured in DMEM (Gibco) media supplemented with 10% FBS, 1% PS, 5 μg/ml insulin (Merck), 5 ng/ml murine epidermal growth factor (Merck) and 5 ng/ml cholera toxin and grown under low oxygen conditions (3% O_2, 5% CO_2 at 37°C). HEK293T, BOSC and U2-OS [both DIvA (*49*) and DR-GFP (*72*)] cells were cultured in DMEM supplemented with 10% FBS, 1% PS, 1x Non-Essential Amino Acids Solution (Gibco) and 1% Glutamax^{TM} (Gibco) at 37°C and 5% CO_2 in a humidified incubator. All the cell lines were authenticated by short tandem repeat profiling and routinely tested for mycoplasma contamination.

Cloning and generation of stable cell line models

Human *FIGNL1* sgRNAs (oligonucleotides table below) were cloned into pDG458 (Addgene #100900) plasmid at BbsI sites on the Cas9 expression plasmid. Mouse *Fignl1* sgRNA start and stop sequences (oligonucleotides table below) were cloned into pSpCas9(BB)-2A-GFP (pX458) (Addgene #48138) at BbsI site. To generate FIGNL1 knock-out models in both human RPE1 and mouse mammary tumor cells, sgRNA cloned plasmids were transfected and FACS sorted for GFP positive cells. Sorted GFP positive cells were then seeded as single cell per well in 96 well plate. Clones grown from single cells were then genotyped and analyzed by Western blot to confirm homozygous knockouts.

FIGNL1 mutant constructs: full-length FIGNL1, RAD51 interaction mutants dFRBD (Δ295-344) and FxxA point mutant (F295E); FIRRM/FLIP interaction mutant: dNLS (Δ1-120); and ATPase point mutant (K447A+D500A) cloned in entry clones were used for LR reaction to generate expression clones using Gateway cloning (*35*). PL1+2 and dPL mutants were created by site-directed mutagenesis using the full-length WT constructs. Gateway clonase LR enzyme mix II (Invitrogen) was used to clone FIGNL1 mutants into destination vector pCW57.1-eGFP vector (pCW57.1-eGFPnls for dNLS mutant). To create vector backbones for FIGNL1 mutants, Tetracycline-Responsive promoter from pCW57.1-TRE-eGFP/eGFPnls vector was replaced with CMV promoter to create pCW57.1-CMV-eGFP/eGFPnls backbone using NEBuilder® HiFi DNA Assembly Master Mix. Finally, FIGNL1 mutant constructs were co-transfected into HEK293T cells with 3rd generation lentiviral packaging and envelop vectors to create viral particles and transduced into RPE1 FIGNL1 knock-out cells. Transduced RPE1 FIGNL1-KO cells were then sorted using GFP FACS and analyzed for eGFP fused FIGNL1 fusion protein using Western blot analysis.

KB2P-AsiSI cells were generated by transfecting doxycycline-inducible AsiSI-YFP plasmid pTRE3G-HA-ER-AsiSI-PGK-GFPVenus-IRES-rtTA3 (a kind gift from Andres Canela, Kyoto University, Japan) into BOSC cells along with pCL-Eco retro-viral packaging vector. Retro-viral particles were collected after 48 hours and transduced into KB2P cells. Transduced cells were then FACS sorted for YFP and clones were selected with equal number of AsiSI induced damage marked by 53BP1 foci levels.

For recombinant FIGNL1-dNLS protein purification, cDNA sequence of FIGNL1-dNLS was cloned into pFB-1xMBP-10xHis Baculovirus backbone or pGEX-2T backbone using NEBuilder® HiFi DNA Assembly Master Mix. FIGNL1 mutants for insect *Sf9* cell expression were created by transferring the mutant construct from pCW57.1-CMV backbone to pFB-1xMBP-10xHis Baculoviral construct using NEBuilder® HiFi DNA Assembly Master Mix.

The miBRCA2 construct was PCR amplified from the plasmid pCAGGS_Mini_BRCA2-1xFlag (*53*) (kind gift from Maria Jasin) without the Nuclear Localization Signal (NLS) using the primers Mini_BRCA2_F

Downloaded from https://www.science.org at Biblioteca Universitaria Di Lugano on July 21, 2026

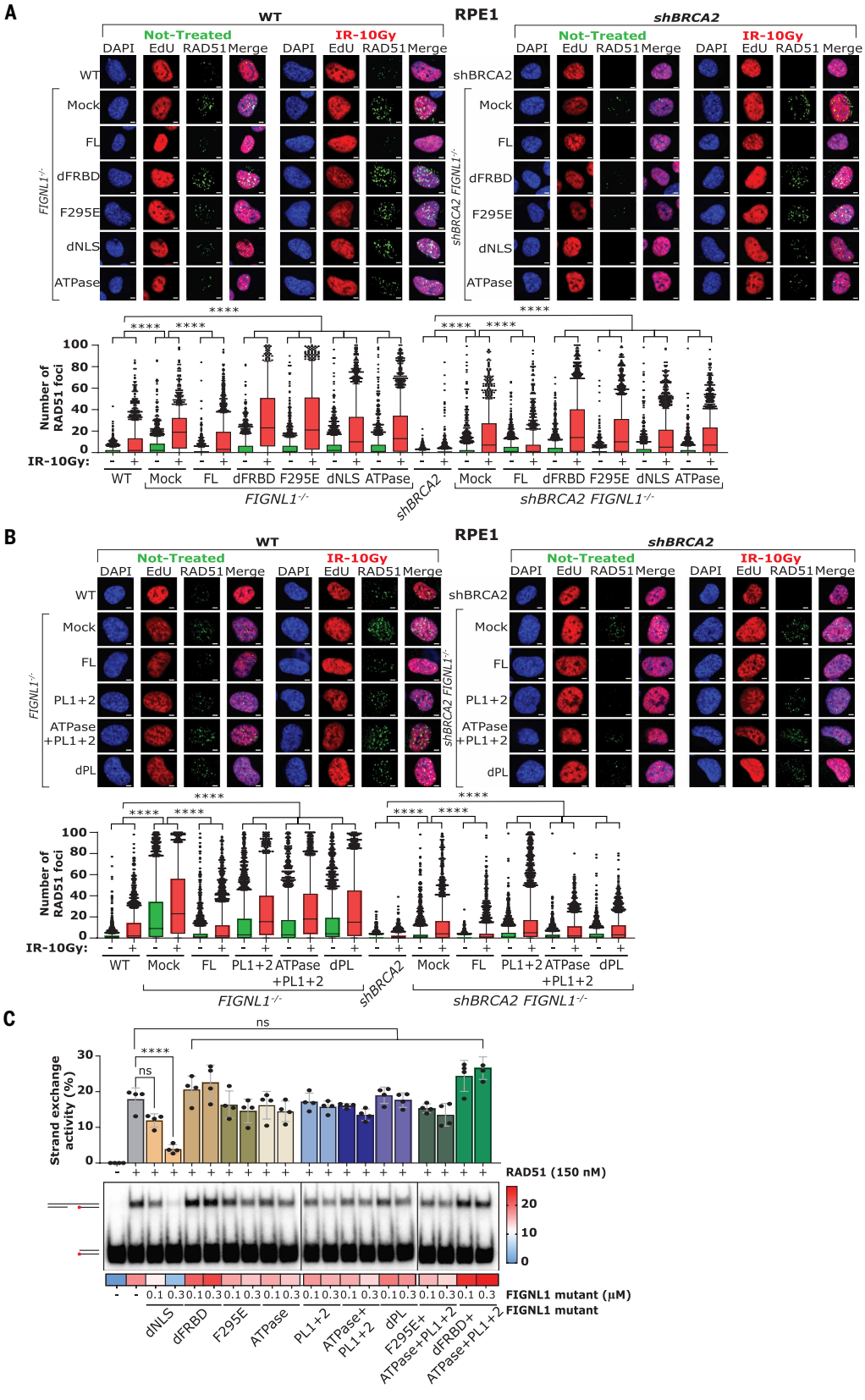

Fig. 4. FIGNL1 association with RAD51 is critical for function. (**A**) (Top) Representative images of high-content, automated RAD51-IF images showing the EdU and RAD51 foci in not-treated and ionizing radiation treated human RPE1 cells; scale bar: 5 μm. (Bottom) Automated QIBC plots of the RAD51 foci per nucleus; scatter box plot showing the foci distribution between 10-90th percentile from 1500 cells (experiment was repeated 3 times). *P*-values from Mann-Whitney test (two-tailed) comparing between respective not-treated or IR treated groups (****: <0.0001). (**B**) (Top) Representative images of high-content, automated RAD51-IF images showing the EdU and RAD51 foci in not-treated and ionizing radiation treated human RPE1 cells; scale bar: 5 μm. (Bottom) Automated QIBC plots of the RAD51 foci per nucleus; scatter box plot showing the

Downloaded from https://www.science.org at Biblioteca Universitaria Di Lugano on July 21, 2026

foci distribution between 10-90th percentile from 1500 cells (experiment was repeated 3 times). *P*-values from Mann-Whitney test (two-tailed) comparing between respective not-treated or IR treated groups (****: <0.0001). (**C**) Quantification of the absolute DNA strand exchange activity showing the band intensity of the exchanged DNA; error bars are indicative of mean ± SEM from 4 independent experiments ($n = 4$). The red asterisk indicates the position of the radioactive label. *P*-values from Dunnett's multiple comparison one-way ANOVA comparing between indicated groups (****:<0.0001). Heatmap also showing the percentage strand exchange activity of RAD51 in the presence of FIGNL1 mutants.

and Midi1_BRCA2_BRC1-2_NotI_R with introducing NheI and NotI site at the ends. The product was then cloned into the vector pFastBac-2XMBP-HLTFco-His (*73*) between the NheI and NotI sites to generate the final plasmid pFB-2xMBP-Mini_BRCA2-FLAG-His.

Transfection and infection

All the plasmid DNA transfections were performed using X-tremeGENE 9 DNA Transfection Reagent (Merck) and siRNAs were transfected using Lipofectamine RNAiMAX Transfection Reagent (Invitrogen) according to manufacturer's instructions. For viral infections, 48-hour viral soups collected from HEK293T (lenti-viral) and BOSC (retro-viral) cells were transduced into target cell lines with 8 μg/ml polybrene (Sigma-Aldrich). Viral titers were assessed by qPCR Lenti/Retrovirus Titer Kits (ABM, Canada).

ES cell culture and generation of stable lines

PL2F7 mouse embryonic stem cells (mESCs) used in the study were generated from AB2.2 mESC line by knocking out one copy of *Brca2* and flanking the other allele with two *loxP* sites along with 5′ and 3′ human *HPRT minigene* (*58*). mESCs were cultured on mitotically inactive SNL feeder cells in M15 (knockout DMEM) media (Life technologies) as described previously (*58*).

For generation of stable *Fignl1* knockdown in PL2F7 mESC, two different shRNAs against *Fignl1* and one control shRNA were cloned into PLKO lentiviral vector. Sh*Fignl1* lentiviral particles were generated by co-transfecting HEK293T cells with PLKO_sh*Fignl1* plasmid and packaging plasmid for 48 hours. PL2F7-A10 (PL2F7 clone lacking puromycin resistance gene) mESCs were transduced with PLKO_sh*Fignl1* or PLKO_Control lentiviral particles on feeder free gelatinized plate. After 48 hours, cells were trypsinized and 10^4 cells were seeded on a 10 cm plate containing SNL feeder cells. Cells were selected with puromycin (3 ug/ml) for 5 days. Visible colonies were picked and the stable knockdown of sh*Fignl1* were confirmed by Western blot.

Deletion of Brca2 cko allele and confirmation of shFignl1 Brca2$^{ko/ko}$ mESCs by Southern blot

sh*Fignl1* expressing PL2F7-A10 stable clones were used for deletion of *Brca2 cko* allele. Ten million mESCs were electroporated with 25 ug of *Pgk-Cre* plasmid. After 36 hours of electroporation, recombinant clones were selected in HAT media for 5 days followed by HT selection for 2 days. Cells were then maintained in M15 media, and mESC colonies were picked into 96 well plate for expansion and genomic DNA isolation using mESCs lysis buffer containing 10 mg/ml of proteinase K as described previously (*58*). Genomic DNA was digested with *EcoRV* at 37°C overnight and the digested DNA was electrophoresed on 1% agarose gel in 1X TBE buffer, transferred to Hybond-N+ nylon membrane. DNA probe was labelled with [α^{32}P]-dCTP, hybridized overnight, washed and imaged using Amersham Typhoon image scanner (Cytiva) as described previously (*58*). The PCR based genotyping was performed as described previously (*19*) to detect the *Brca2 cko* and *Brca2 ko* alleles, using the primers listed in the table below.

Western blot

Cells for Western blot were harvested and lysed in lysis buffer [50 mM Tris-HCl (pH 7.5), 150 mM NaCl, 0.1% Triton X-100, 0.5% sodium deoxycholate, 0.1% SDS, 2 mM EDTA and protease inhibitor cocktail (PIC)]. The protein concentration was determined using the Pierce BCA protein Assay kit. Proteins were loaded and run on a 4 to 12% Bis-Tris pre-cast gel or a 3 to 8% Tris-Acetate pre-cast gel (Invitrogen) and were electrophoretically transferred to a PVDF membrane (Millipore). After transfer, the membranes were blocked in 5% milk for 1 hour and incubated overnight in primary antibodies. Membranes were then washed four times in 0.1% TBST and probed with horseradish peroxidase-conjugated secondary antibodies (Cytiva). Finally, the ECL Prime Western Blotting Detection Reagent kit (GE Healthcare) was used to develop the blot.

Flow-cytometry analysis of cell cycle

For flow-cytometry analysis of the cell cycle, the cells were labeled with EdU for 30 min followed by fixation in 4% formaldehyde/PBS and permeabilization in 1% saponin buffer in 1% BSA/PBS. The Click-It reaction was performed using Fluor Azide 594 according to the manufacturer's instructions (Invitrogen) to label the EdU. The cells were treated with DAPI as a nuclear stain. The samples were measured in BD LSR Fortessa and analyzed by FlowJo software v10.5.0.

High content microscopy

Immunofluorescence staining was performed as described previously (*46*). Briefly, the RPE1 and mouse mammary tumor cells were seed in 96- or 364-well plates. 48 hours (RPE1 cells) or 24 hours (mouse mammary tumor cells) after seeding the cells were treated with EdU for 20 min before irradiation with 10 Gy of x-ray. Cells were maintained at 37°C for 4 hours before the cells were pre-extracted with ice-cold CSK buffer [10 mM PIPES (pH 6.8), 100 mM NaCl, 300 mM sucrose, 1 mM EGTA, 1 mM $MgCl_2$, 1 mM DTT and PIC], fixed with 4% formaldehyde and permeabilized with 0,1% Triton X-100. The cells were blocked in 5% BSA/PBS before they underwent the Click-IT reaction with Alexa Fluor 488 (Invitrogen) according to the manufacturer's instruction. The cells were washed and then incubated with corresponding primary antibodies for 1 hour 30 min at room temperature. Next, they were incubated with Alexa Fluor-conjugated secondary antibodies (Invitrogen) for 1 hour at room temperature, after which the cells were treated with DAPI as a nuclear stain. The images were captured with the Opera Phenix High-Content spinning disc confocal microscope and analyzed using CellProfiler.

For AsiSI induced DSB-IF in KB2P-AsiSI cells, HA-tagged AsiSI was expressed by adding 2 μg/ml of doxycycline for 24 hours with last 5 hours of 400 nM 4OHT for nuclear translocation. While DivA-AsiSI cells with constitutive AsiSI expression were treated with 400 nM 4OHT after 24 hours of seeding. Cells were then processed similarly as mentioned above.

mESCs were seeded on a 24-well plate and after 24 hours, cells were irradiated at 10Gy. Cells were maintained at 37°C for 4 hours in fresh M15 media before it was fixed and stained for RAD51. Imaging was performed using Confocal spinning Disk microscopy (Opera Phenix) at 40x magnification and maximum intensity projection were used to count RAD51 foci. DAPI was used as a nuclear stain.

Automated image analysis

Z-stack images (3 stacks of 1 μm height) of individual channels from high throughput microscopy images were merged to create maximum intensity projection and subjected to CellProfiler analysis (*74*). Briefly, after the illumination correction, nuclei were identified using the DAPI channel and used as mask to identify and measure the intensities of other corresponding channels. Foci detection was performed from masked nuclear regions in the corresponding channels to automatically

Downloaded from https://www.science.org at Biblioteca Universitaria Di Lugano on July 21, 2026

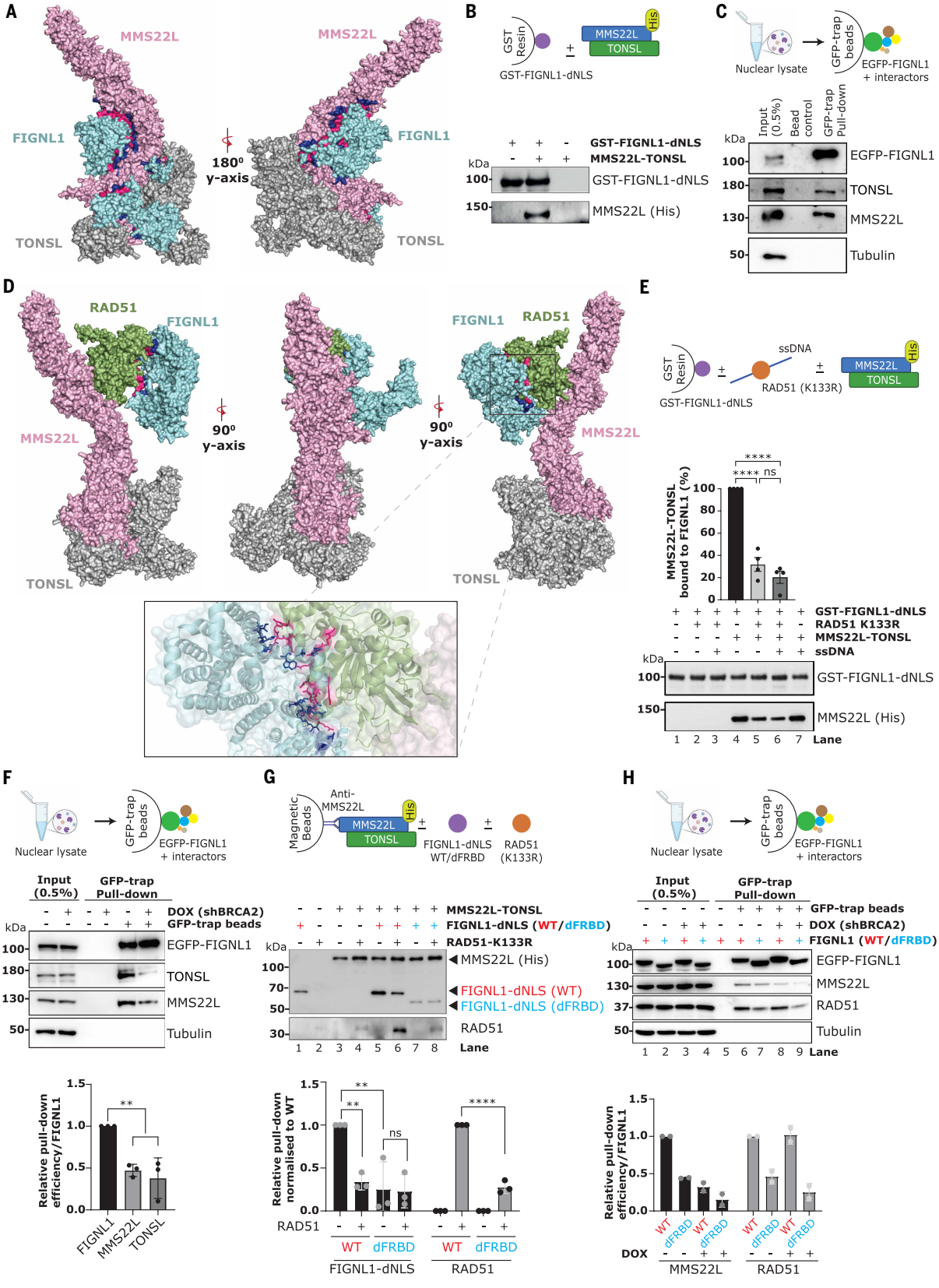

Fig. 5. RAD51 availability determines FIGNL1 interaction with MMS22L-TONSL complex via FRBD domain. (**A**) Surface representation of FIGNL1-MMS22L-TONSL ternary complex model shown in two different orientations [FIGNL1 (cyan), MMS22L (light pink), and TONSL (gray)]. The binding interface of FIGNL1 and MMS22L are depicted by pink and dark blue colors, respectively. (**B**) (Top) Schematics of the in vitro interaction assay between recombinant FIGNL1-dNLS (immobilized) and MMS22L-TONSL. (Bottom) Western blot results show that FIGNL1-dNLS interacts with MMS22L-TONSL in the in vitro interaction assay. (**C**) (Top) Schematics of the GFP-trap pull-down of the eGFP-FIGNL1 and MMS22L-TONSL from nuclear extracts. eGFP-FIGNL1 stably overexpressing cells in FIGNL1 knock-out RPE1 cells were used for nuclear fractionation and GFP-trap pulled

Downloaded from https://www.science.org at Biblioteca Universitaria Di Lugano on July 21, 2026

down. (Bottom) Western blot results indicative of the interaction between FIGNL1 and MMS22L-TONSL. (**D**) Surface representation of FIGNL1-RAD51-MMS22L-TONSL quaternary complex shown in three different orientations [FIGNL1 (cyan), RAD51 (green), MMS22L (light pink), and TONSL (gray)]. The inset shows a zoom-in view of the FIGNL1 and RAD51 interacting surface in dark blue (FIGNL1) and pink (RAD51). (**E**) (Top) Schematics of the in vitro interaction assay between recombinant FIGNL1-dNLS (immobilized), MMS22L-TONSL and RAD51-K133R in the presence or absence of ssDNA. (Bottom) Percentage quantifications showing the band intensity of the bound MMS22L-TONSL to FIGNL1-dNLS; error bars are indicative of mean ± SEM from four independent experiments ($n = 4$). *P*-values from ordinary one-way ANOVA comparing between indicated groups (****: <0.0001). Western blot results indicate the interactions between the proteins involved. (**F**) (Top) Schematics of the GFP-trap pulldown of the eGFP-FIGNL1 and its interactors from nuclear extracts. eGFP-FIGNL1 stably over-expressing cells in FIGNL1 knock-out RPE1 cells were used for nuclear fractionation and GFP-trap pulled down. (Middle) Western blot results indicative of the interaction between FIGNL1 and MMS22L-TONSL. (Bottom) Quantification showing the relative fold change of the MMS22L or TONSL binding to FIGNL1 in the presence or absence of BRCA2; error bars are indicative of mean ± SD from three independent experiments ($n = 3$). *P*-values from ordinary one-way ANOVA comparing between indicated groups (**: <0.01). (**G**) (Top) Schematics of the in vitro interaction assay between MMS22L-TONSL complex (immobilized), FIGNL1-dNLS (WT or dFRBD) and RAD51. (Middle) Western blot results indicative of the interaction between the proteins involved. (Bottom) Quantification showing the relative fold change of the FIGNL1-dNLS (WT or dFRBD) interacting with MMS22L in the presence or absence of RAD51; error bars are indicative of mean ± SEM from three independent experiments ($n = 3$). *P*-values from ordinary one-way ANOVA comparing between indicated groups (**: <0.01; ****: <0.0001). (**H**) (Top) Schematics of the GFP-trap pull-down of the eGFP-FIGNL1 and its interactors from nuclear extracts. eGFP-FIGNL1 (WT or dFRBD) stably over-expressing cells in FIGNL1 knock-out RPE1 cells were used for nuclear fractionation and GFP-trap pulled down. (Middle) Western blot results indicative of the interaction between FIGNL1, MMS22L, and RAD51. (Bottom) Quantification showing the relative fold change of the MMS22L or RAD51 interacting with FIGNL1 (WT or dFRBD), normalized to FIGNL1-WT in the presence or absence of BRCA2; error bars are indicative of mean ± SD from 2 independent experiments ($n = 2$).

calculate the intensity threshold to robustly and accurately classify the foci's local intensity maxima as foreground and separate it from the background. For unbiased detection of foci, a single threshold was set for all the groups in each experiment. For colocalization analysis between RAD51 and γH2AX, identified RAD51 foci were used as a parental object to mask on the γH2AX children object and classify the masked foci as a new group to measure the percentage colocalization. Finally, the data output was exported to TIBCO Spotfire software/Graphpad Prism for visualization.

Structural modelling of FIGNL1 molecular complexes

The full-length amino acid sequences for FIGNL1 (Q6PIW4), RAD51 (Q06609), MMS22L (Q6ZRQ5), and TONSL (Q96HA7) were obtained from UniProt. Structural models of FIGNL1 hexamer and its complexes with RAD51 in the presence of Mg^{2+}/ATP, and FIGNL1 monomer complexes with MMS22L-TONSL (ternary), and RAD51-MMSS22L/TONSL (quaternary) were generated by AlphaFold3 (*75*). Further, the FIGNL1 FRBD-RAD51 dimer structure model was generated using AlphaFold2-Multimer, ColabFold version 1.5.5. For AlphaFold2-Multimer, a single query sequence consisting of the RAD51 dimer and the FIGNL1 FRBD (295-344) amino acid sequence was provided as input using the Amber refinement model with default settings (*76*). The interacting domains and binding energies of hexameric FIGNL1 and its complex with RAD51, and monomeric FIGNL1 ternary (FIGNL1-MMS22L/TONSL), and quaternary (FIGNL1-RAD51-MMS22L/TONSL) complexes were evaluated with the help of PRODIGY (*77*). The PAE matrices and pLDDT colored structures for each predicted model were prepared using PAE viewer (*78*). All the molecular interactions were analyzed and visualized with PyMol 2.2.3 visualization software (https://legacy.ccp4.ac.uk/).

Protein purification

Human MMS22L-TONSL (*22*), FIGNL1-dNLS, miBRCA2 and RPA (*73*) were expressed in *Spodoptera frugiperda* 9 (*Sf*9) insect cells in SFX Insect serum-free medium (Hyclone) using the Bac-to-Bac expression system (Invitrogen), according to manufacturer's recommendations. MMS22L and TONSL proteins were co-expressed to prepare MMS22L-TONSL protein complex using pFB-MBP-MMS22L-His and pFB-GST-TONSL plasmids. The protein was extracted from *Sf*9 cell pellets with 325 mM NaCl as described previously (*22*). The protein was then bound to amylose resin (New England Biolabs) via the MBP tag on the MMS22L subunit. The amylose resin with bound protein was washed with Amylose Wash Buffer (50 mM Tris–HCl [pH 7.5], 2 mM β-mercaptoethanol, 200 mM NaCl, 10% glycerol, and 1 mM phenylmethanesulfonyl fluoride [PMSF]) and eluted using Amylose Wash Buffer supplemented with 10 mM maltose. Both MBP and GST tags were then cleaved by PreScission protease. The GST-tag was not used during the purification. The final protein complex was obtained by affinity purification on NiNTA agarose (Qiagen) via a 10x-His-tag on the C-terminus of MMS22L. The NiNTA resin bound protein was washed with NiNTA wash buffer (50 mM Tris–HCl [pH 7.5], 2 mM β-mercaptoethanol, 150 mM NaCl, 10% glycerol, 1 mM PMSF and 40 mM imidazole) and eluted using NiNTA wash buffer supplemented with 400 mM imidazole. The complex was then dialyzed in dialysis buffer (50 mM Tris–HCl [pH 7.5], 2 mM β-mercaptoethanol, 100 mM NaCl, 10% glycerol, 1 mM PMSF). FIGNL1-dNLS and its mutants were purified from pFB-MBP-FIGNL1-dNLS-His plasmids using identical procedures as MMS22L-TONSL, except that the Amylose wash buffer contained 1 M NaCl, but the PreScission protease digestion was done at 300 mM NaCl. FIGNL1-dNLS used for mass photometry experiments were supplemented with or without 1 mM ATP and 5 mM $CaCl_2$ in all the buffers during the purification. The miBRCA2 proteins were purified from pFB-2xMBP-Mini_BRCA2-FLAG-His plasmids using similar protocols as the MMS22L-TONSL with 1 M NaCl during the MBP washing steps, but the PreScission protease digestion was done at 300 mM NaCl. The NiNTA resin with bound miBRCA2 was washed with the NiNTA Wash Buffer containing 58 mM imidazole and eluted using NiNTA Wash Buffer supplemented with 300 mM imidazole. The final protein sample was dialyzed against storage buffer (50 mM Tris–HCl [pH 7.5], 5 mM β-mercaptoethanol, 150 mM NaCl, 10% glycerol, and 0.5 mM PMSF) (amino acid sequence of miBRCA2 is provided in the oligonucleotide table below).

Human RPA1, RPA2, and RPA3 were co-expressed to produce RPA heterotrimer using pFB-RPA1, pFB-RPA2 and pFB-6xHis-RPA3 constructs. Trimeric RPA was purified by exploiting the His-tag on RPA3 using NiNTA affinity chromatography, followed by HiTrap Blue HP, HiTrap Desalting and HiTrap Q HP chromatography columns (all GE Healthcare) using ÄKTA pure (GE Healthcare) (*73*). Wild type RAD51, as well as the RAD51-K133R variant, were expressed from pMALT-P-RAD51 and pMALT-P-RAD51-K133R plasmids in BL21(DE3)pLysS *E. coli* cells and purified using amylose affinity chromatography (New England Biolabs) followed by Hitrap Q HP chromatography (Cytiva) (*22*). The MBP tag was cleaved during the purification of all RAD51 variants. Human DNA2 was expressed from the pFB-His-DNA2-FLAG plasmid in *Sf*9 insect cells and purified by affinity chromatography taking advantage of the N-terminal 6x His-tag and the C-terminal FLAG-tag (*79*). For purification of human RAD54, *Sf*9 cells were infected with virus produced with the pFB_MBP-TEV-hRAD54co-FLAG vector, and the protein was purified by amylose and FLAG affinity purification as described before (*80*).

For purification of human mitochondrial single-stranded DNA binding protein (mtSSB), pMALT-P-mtSSB vector was transformed into in *E. coli* BL21 cells and mtSSB was purified with amylose affinity purification

Downloaded from https://www.science.org at Biblioteca Universitaria Di Lugano on July 21, 2026

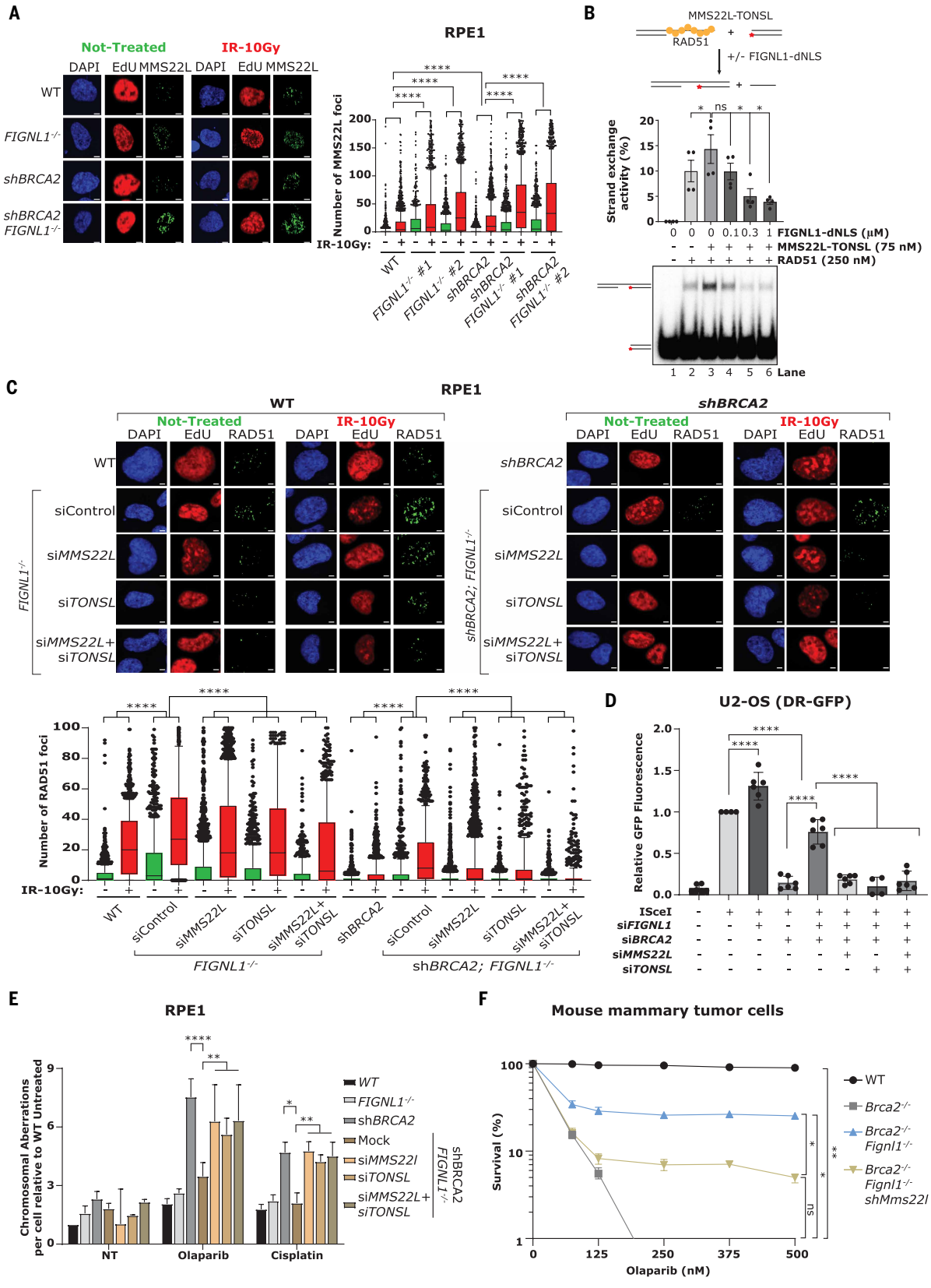

Fig. 6. MMS22L-TONSL complex loads RAD51 in the BRCA2-FIGNL1–deficient cells to recue HR and confer chemoresistance. (**A**) (Left) Representative high-content, automated IF images showing EdU and MMS22L foci in not-treated and ionizing radiation treated cells; scale bar, 5 μm. (Right) Automated QIBC plots of the MMS22L foci per nucleus; scatter box plot showing the foci distribution between 10th and 90th percentiles from 2,000 cells (experiment was repeated three times). *P*-values from Mann-Whitney test (two-tailed) comparing between respective not-treated or ionizing radiation treated groups (****: <0.0001). (**B**) (Top) Schematics of the DNA strand exchange assay. The strand exchange assays were performed by adding 250 nM purified RAD51 and 75 nM MMS22L-TONSL to the DNA substrate. The assay was then supplemented by increasing

Downloaded from https://www.science.org at Biblioteca Universitaria Di Lugano on July 21, 2026

concentrations of purified FIGNL1-dNLS. The red asterisk indicates the position of the radioactive label. (Bottom) Quantification of the absolute DNA strand exchange activity showing the band intensity of the exchanged DNA; error bars are indicative of mean ± SEM from four independent experiments ($n = 4$). *P*-values from ordinary one-way ANOVA comparing between indicated groups (*: <0.05). (**C**) (Top) Representative high-content, automated IF images showing EdU and RAD51 foci in not-treated and ionizing radiation treated human RPE1 cells; scale bar, 5 μm. (Bottom) Automated QIBC plots of the RAD51 foci per nucleus; scatter box plot showing the foci distribution between 10th and 90th percentiles from 1,500 cells (experiment was repeated three times). *P*-values from Mann-Whitney test (two-tailed) comparing between indicated groups (****: <0.0001). (**D**) DR-GFP system stably integrated U2-OS cells transfected for 72 hours with indicated siRNAs and 48 hours of ISceI to measure the relative levels of GFP fluorescence to the WT cells. Error bars are representative of the mean ± SD from three independent experiments ($n = 3$). *P*-values from unpaired *t*-test comparing between indicated groups (****: <0.0001). (**E**) Quantification of chromosomal aberrations in RPE1 FIGNL1 knockout clones with siRNAs against MMS22L and TONSL in response to Olaparib and cisplatin from three independent experiments in which 50 individual metaphases were analyzed for each sample per experiment. *P*-values from ordinary two-way ANOVA (*: <0.05; **: <0.01; ****: <0.0001). (**F**) Percentage survivability of mouse mammary tumor cells in response to Olaparib; quantification was performed by normalization to non-treated cells. *P*-values from Dunnett's multiple comparison one-way ANOVA comparing between indicated groups (*: <0.05, **: <0.01).

followed by HiTrap Blue column (GE Healthcare) as previously described (*79*).

DNA substrate preparation

For DNA strand exchange assays (*22*), the 3′-tailed DNA was prepared by annealing oligonucleotides RJ-167-mer and RJ-PHIX-42-1 in 1:1 ratio with the annealing buffer (100 mM Tris-HCl [pH 8.0], 500 mM NaCl and 100 mM $MgCl_2$). The dsDNA was generated by radio-labeling RJ-Oligo1 with ^{32}P at the 3′-end and annealing it to RJ-Oligo2 in 1:2 ratio. DNA protection assays were performed using PC1253 as ssDNA oligonucleotide. DNA binding assays were performed using PC1253 ssDNA oligonucleotide annealed with PC1253c complementary oligonucleotide to form the dsDNA. All oligonucleotides were ^{32}P-labeled at the 3′ terminus with [α-^{32}P] dCTP (Hartmann Analytic) and terminal transferase (New England Biolabs) according to the manufacturer's instructions. Sequences of all the oligonucleotide substrates used in the study are listed in the table below.

DNA binding assay

Binding reactions (15 μl volume) were carried out in binding buffer (25 mM Tris- acetate [pH 7.5], 3 mM EDTA, 1 mM dithiothreitol [DTT], and 100 μg/ml bovine serum albumin [BSA]), and indicated DNA substrate (1 nM, in molecules). 3 mM EDTA was replaced with 1 mM ATP (Sigma, A7699) and 2 mM magnesium acetate, where indicated. Proteins were added and incubated for 15 min on ice. Loading dye (5 μl; 50% glycerol [w/vol] and bromophenol blue) was added to the reactions and the products were separated on 6% polyacrylamide gels (ratio acrylamide:bisacrylamide 19:1, Bio-Rad) in TAE (40 mM Tris, 20 mM acetic acid and 1 mM EDTA) buffer at 4°C. The gels were dried on 17 CHR paper (Whatman), exposed to a storage phosphor screen (GE Healthcare) and scanned by a Typhoon Phosphor Imager (FLA9500, GE Healthcare). Signals were quantified using ImageJ and plotted with GraphPad Prism. The binding assays for the FIGNL1-dNLS mutants were carried out similarly, with the exception that the ssDNA substrate was used at a concentration of 0.5 nM in molecules.

DNA strand exchange assay

2 nM (in molecules) cold 3′ tailed DNA substrate was incubated with the indicated concentration of RAD51 for 5 min in a buffer (25 mM Tris Acetate [pH 7.5] 1 mM DTT, 1 mM $MgCl_2$, 2 mM ATP/AMP-PNP, 2 mM $CaCl_2$, and 0.1 mg/ml Recombinant Albumin [NEB]) in a total reaction volume of 15 μl. FIGNL1-dNLS was titrated on top and incubated at 37°C for another 5 min. This was followed by adding 2 nM ^{32}P-radiolabeled dsDNA (in molecules) and incubation for 30 min at 37°C. The reaction was stopped with 5 μl of stop solution (150 mM EDTA, 0.2% sodium dodecyl sulfate, 30% glycerol and bromophenol blue) and 1 μl Proteinase K (Roche, 18 mg/ml) supplemented with 10-fold excess of cold RJ oligo 1 for another 10 min at 37°C. Reaction products were separated by running 6% PAGE gel in 1X TAE buffer for 55 min at 8 V/cm. For reactions with RPA, 50 nM RPA was preincubated with the cold substrate for 5 min at 37°C before adding RAD51. For reactions with miBRCA2, 30 nM of miBRCA2 was incubated with RAD51 for 5 min at 37°C. Where indicated, MMS22L-TONSL was incubated after adding RAD51 for 5 min at 37°C before adding FIGNL1-dNLS. Where proteins were omitted, protein dilution buffer was (25 mM Tris- HCl [pH 7.5] and 100 mM NaCl) used instead. The gels were dried on 17 CHR paper (Whatman), exposed to a storage phosphor screen (GE Healthcare) and scanned by a Typhoon Phosphor Imager (FLA9500, GE Healthcare). Signals were quantified using ImageJ and plotted with GraphPad Prism.

DNA protection assays

DNA2 and Exonuclease I (*E. coli,* New England Biolabs)-catalyzed nuclease assays were performed in a 15 μl volume reaction buffer (25 mM Tris-acetate [pH 7.5], 2 mM magnesium acetate, 1 mM ATP, 1 mM DTT, 0.1 mg/ml BSA, 1 mM phosphoenolpyruvate [PEP], and 80 U/ml pyruvate kinase [Sigma]), and 7.5 nM DNA substrate (in molecules). RAD51-WT (as indicated in the figure) was preincubated with the substrates for 15 min at 37°C in the reaction buffer, which was then supplemented with the indicated amounts of DNA2 or Exonuclease I, FIGNL1-dNLS and MMS22L-TONSL and the reaction was continued for 30 min at 37°C. Reactions were stopped by adding 0.5 μl of 0.5 M EDTA and 1 μl Proteinase K (Roche, 18 mg/ml), and incubated at 50°C for 30 min. An equal amount of formamide dye (95% [v/v] formamide, 20 mM EDTA, bromophenol blue) was added, samples were heated at 95°C for 4 min and separated on 15% denaturing polyacrylamide gels (ratio acrylamide:bis acrylamide 19:1 [Biorad]). After fixing in a solution (40% methanol, 10% acetic acid and 5% glycerol) for 30 min, the gels were dried on 3MM paper (Whatman), exposed to storage phosphor screens (GE Healthcare) and scanned with a Typhoon Phosphor Imager (FLA9500).

DR-GFP assay

U2-OS cells with stable integration of DR-GFP were transfected with respective siRNAs for 24 hours followed by ISceI expressing pCBASceI transfection for further 48 hours. Cells were then harvested, washed with PBS+10% FBS and filtered through 40 μm cell strainer to prepare single cells suspension. Samples were then measured for GFP in BD LSR Fortessa and analyzed by FlowJo software v10.5.0. Remaining samples were then lysed and analyzed by Western blotting for respective protein knockdowns.

D-loop assay

26.6 nM of labelled 89-mer ssDNA (D-loop-89) was incubated with 800 nM of RAD51 for 15 minutes at 37°C in reaction buffer (25 mM Tris Acetate [pH 7.5], 1 mM DTT, 3 mM $MgCl_2$, 2 mM ATP, 2 mM $CaCl_2$, 2 mM PEP, 80 U/ml pyruvate kinase, and 0.1 mg/ml Recombinant Albumin [NEB]) in a total volume of 15 μl. FIGNL1-dNLS was titrated on top and incubated for another 5 min at 37°C. This was followed by addition of 25 nM of pUC19 plasmid (*81*) and 150 nM of RAD54 and incubated for another 20 min at 37°C. The reaction was stopped with 5 μl of stop solution (150 mM EDTA, 2% sodium dodecyl sulfate, 30%

Downloaded from https://www.science.org at Biblioteca Universitaria Di Lugano on July 21, 2026

glycerol and bromophenol blue) and 1 µl Proteinase K (Roche) for another 15 min at 37°C. Reaction products were separated on 1% agarose gel in 1x TAE buffer for 75 min. The gel was dried on DE81 paper, exposed to storage phosphor screens (GE Healthcare) and scanned with a Typhoon Phosphor Imager (FLA9500). Signals were quantified using ImageJ and plotted with GraphPad Prism.

Genome stability assay

The genome stability assay was carried out according to the standard protocol described previously (*82*). Cells were treated with 500 nM Olaparib for 24 hours or 750 nM cisplatin for 6 hours. Cells that were treated with Olaparib were exposed to colcemid containing media 12 hours after the start of the treatment and continued the Olaparib and colcemid treatment for the next 12 hours. For the cells that were treated with cisplatin, the drug treated media was washed off and the cells were exposed to colcemid containing media for the next 12 hours. Metaphase spreads were prepared by conventional methods. Metaphase slides were washed with 2x SSC, PBS and $MgCl_2$ in PBS, denatured at 80°C after which telomere probes were hybridized onto the metaphase spreads. After hybridization, the slides were washed with 50% formamide in 2x SSC, 0,1X SSC and 4x SSC containing 0,1% Tween-20. The metaphase spreads were stained with DAPI and mounted with MOWIOL. A minimum of 50 metaphase images were captured using Metafer5 and analyzed with Adobe Photoshop for chromosomal aberrations.

Survival assay

For the mESCs, 10,000 cells were seeded per well in a gelatinized 96-well plate. After 24 hours, cells were treated with varying concentrations of Olaparib or cisplatin for 72 hours. After 72 hours, cells were rinsed with PBS and incubated with 1 mg/ml of XTT (2,3-bis(2-methoxy-4-nitro-5-sulfophenyl)-5-[(phenylamino)carbonyl]-2H-tetrazolium hydroxide), 2 mM phenazine methosulfate (PMS) at 37°C for 60 min. Plates were read in iMark Microplate reader (Bio-Rad) at 455 nm.

1×10^3 mouse mammary tumor cells were seeded in a 6-well plate and 24 hours later cells were treated with indicated concentrations or Olaparib or cisplatin. Cells treated with Olaparib were refreshed with fresh Olaparib every 48 hours for 7 days, while cells treated with cisplatin were refreshed after 12 hours and incubated in fresh media without cisplatin for 7 days. After 7 days, survivability was quantified with CellTiter-Blue® Cell Viability Assay (Promega) as per manufacturer's instructions and plates were fixed and stained with Brilliant Blue G (Sigma Aldrich).

Interaction assays

To examine the interaction between the purified FIGNL1 mutants with RAD51, 1 µg of anti-HIS mouse antibody (MBL, D291-39, mouse) was immobilized on 10 µl protein G magnetic beads (Dynabeads, Invitrogen). The antibodies were incubated in 50 µl PBS-T (PBS containing 0.1% Tween-20) for 1 hour at 4°C with continuous rotation. After incubation, the beads were washed three times with 150 µl of wash buffer (50 mM Tris-HCl [pH 7.5], 3 mM EDTA, 1 mM DTT, 100 mM NaCl, 0.05% Triton X-100 [Sigma]). The beads were then mixed with 1 µg of each FIGNL1 mutant proteins in 60 µl of binding buffer (25 mM Tris-HCl [pH 7.5], 3 mM EDTA, 1 mM DTT, 0.2 µg/µl BSA, 100 mM NaCl) and incubated at 4°C with continuous rotation for 1 hour. Beads were again washed 3 times with 150 µl of wash buffer and incubated with 1 µg of RAD51 followed by incubation for another 1 hour at 4°C in continuous rotation. Beads were again washed 3 times with 200 µl of wash buffer and the proteins were eluted by boiling the beads in SDS buffer (50 mM Tris-HCl [pH 6.8], 1.6% sodium dodecyl sulfate, 1 mM DTT, 10% glycerol, 0.01% bromophenol blue) for 3 min at 95°C. The eluate was separated on a 7.5% SDS-PAGE gel, and the proteins were detected by Western blot using Anti-HIS (rabbit) and anti-RAD51 (rabbit) for FIGNL1 mutants and RAD51 respectively.

To study the interaction between FIGNL1-dNLS and MMS22L-TONSL in the presence of RAD51-K133R mutant, soluble extracts of GST-FIGNL1-dNLS prepared from pGEX-2T-FIGNL1-dNLS plasmid in Rosetta (DE3) pLysS *E. coli* cells were used. Each culture was supplemented with 0.2% glucose, induced with 0.5 mM IPTG and grown overnight at 18°C. The cells were then pelleted at 2500 g for 15 min at 4°C, washed once with STE buffer (10 mM Tris-HCl [pH 8], 500 mM NaCl, 1 mM EDTA), snap-frozen and kept at -80°C until use. The soluble extract containing GST-FIGNL1-dNLS was prepared by resuspending the bacterial pellets in GST-buffer (50 mM Tris HCl [pH 7.5], 5 mM $MgCl_2$, 2 mM ATP, 1 mM PMSF, 2 mM β-mercaptoethanol, 150 mM NaCl, 10% glycerol, 1 mM EDTA) followed by sonication and centrifugation for 30 min at 48,000 g. The supernatant was immobilized on GST resin (GE Healthcare) upon incubation for 1 hour at 4°C with continuous rotation. The resin was washed 3 times with GST-buffer post incubation. Next, either 50 µl binding buffer (50 mM Tris–HCl, [pH 7.5], 2 mM β-mercaptoethanol, 3 mM EDTA, 100 mM NaCl, 0.2 µg/ml bovine serum albumin [BSA], 1 mM PMSF) alone or additionally supplemented with 0.5 µg of RAD51-K133R or RAD51-K133R (pre-bound with ssDNA [PC1253]) was added to the immobilized GST-FIGNL1-dNLS for 1 hour at 4°C with continuous rotation. Where indicated, ssDNA was pre-bound for 1 hour to RAD51-K133R at 37°C. Next, the resin was washed once with GST buffer and MMS22L-TONSL was added to the appropriate samples and incubated again for 1 hour, followed by three washes and elution using GST buffer supplemented with 10 mM reduced glutathione (Sigma). The eluates were separated on a 10% SDS-PAGE gel and proteins were detected by Western blotting.

For the interaction between FIGNL1-dNLS WT and dFRBD with MMS22L-TONSL, 0.1 µg of anti- MMS22L antibody was immobilized on 10 µl protein G magnetic beads (Dynabeads, Invitrogen). The antibodies were incubated in 50 µl PBS-T (PBS containing 0.1% Tween-20) for 1 hour at 4°C with continuous rotation. After incubation, the beads were washed 3 times with 150 µl of PBS-T. The beads were then mixed with 1 µg of MMS22L-TONSL in 60 µl of binding buffer (25 mM Tris-HCl [pH 7.5], 3 mM EDTA, 1 mM DTT, 0.2 µg/µl BSA, 100 mM NaCl, 2 mM ATP, 5 mM $MgCl_2$) and incubated at 4°C with continuous rotation for 1 hour. Beads were washed 3 times with 150 µl of wash buffer (50 mM Tris-HCl [pH 7.5], 3 mM EDTA, 1 mM DTT, 150 mM NaCl, 0.05% Triton X-100 [Sigma], 2 mM ATP, 5 mM $MgCl_2$) and incubated with 1 µg of FIGNL1-dNLS WT or equimolar amount of the dFRBD mutant, followed by incubation for another 1 hour at 4°C in continuous rotation. Beads were again washed 2 times with 150 µl of Wash Buffer. The beads were then again incubated with 1 µg of RAD51-K133R for another 1 hour at 4°C. Lastly, the beads were washed 3 times with 150 µl of wash buffer and the proteins were eluted by boiling the beads in SDS buffer (50 mM Tris-HCl [pH 6.8], 1.6% sodium dodecyl sulfate, 1 mM DTT, 10% glycerol, 0.01% bromophenol blue) for 3 min at 95°C. The eluate was separated on a AccuPAGE Tris-Glycine Precast PAGE Gel 4-20% (Bio Bench) gel, and the proteins were detected by Western blot.

Silver staining determination of stoichiometry

To determine the FIGNL1-RAD51 stoichiometry, an interaction assay between FIGNL1 and RAD51 at various molar ratios was performed as described above for the FIGNL1 mutants. The samples were run on a 7.5% SDS-PAGE gel and analyzed by silver staining using standard procedure.

Mass photometry

Borosilicate microscope glass plate (No. 1.5 H thickness, 24 × 50 mm, VWR) were washed by soaking in Milli-Q-water, followed by isopropanol and, lastly, Milli-Q-water again. The slides were dried under a stream of clean nitrogen. Silicone gaskets (CultureWell Reusable Gasket, Grace Bio-Labs) were placed on the clean coverslip to create a well for sample delivery. For calibration and determination of molecular weights, a protein size marker (NativeMark Unstained Protein Standard, Invitrogen) was measured on the same day. All experiments were carried out with a

Downloaded from https://www.science.org at Biblioteca Universitaria Di Lugano on July 21, 2026

Oligonucleotides used in the study

Sl. No.	Name	Sequence	Organism	Purpose
1	sgRNA1	TGGCATATGTACCGGACCGA	Human	CRISPR-KO
2	sgRNA2	TCGGCCACAAGAAATTGATG	Human	CRISPR-KO
3	sgRNA-Start	CTAAAATGCAGACCTCCAGC	Mouse	CRISPR-KO
4	sgRNA-Stop	TTTGGTTGTGGAAAGTAAGT	Mouse	CRISPR-KO
5	shFignl1 #1 (mESCs)	CTTGACTACTGACTGATATAT	Mouse	shRNA
6	shFignl1 #2 (mESCs)	GTTCGACCAATAGCTTATATT	Mouse	shRNA
7	hFIGNL1-GT-For	GTCCAGTGTCCCTTCCTTCA	Human	Genotyping
8	hFIGNL1-GT-Rev	ACACATCCCCAACTTTCTATGC	Human	Genotyping
9	mFignl1-GT-For	GCATCACATTTCCCAAGTCCT	Mouse	Genotyping
10	mFignl1-GT-Rev	GAACCTCAAAGGCGGTGGG	Mouse	Genotyping
11	Brca2-KO-For	GCCACCTCTGCCTGATTCTA	Mouse	Genotyping
12	Brca2-KO-Rev	AAAGAACCAGCTGGGGCTCGAG	Mouse	Genotyping
13	Brca2-flox-For	TGAAGTGGACCCTGTAACCC	Mouse	Genotyping
14	Brca2-flox-Rev	AGTTCTCTCCTTTCAGCCTTCT	Mouse	Genotyping
15	CMV_EGFP_Frag.FOR	TTTGGCCGCGAATCGATATGCGTTACATAACT	Human	Gibson assembly
16	CMV_EGFP_Frag.REV	CATGgctagCCAATTCTCCAAGCTCTGCTTATATAGACCTCCCAC	Human	Gibson assembly
17	CMV_EGFP_Vector.FOR	AGGTCTATATAAGCAGAGCTTGGAGAATTGGctagcCATGG	Human	Gibson assembly
18	CMV_EGFP_Vector.REV	TTACCGTAAGTTATGTAACGCATATCGATTCGCGGCCAAAGT	Human	Gibson assembly
19	pFB-FIGNL1_Frag.FOR	aagttctgttccaggggcccTCCATGGCTGGCAAAAAAT	Human	Gibson assembly
20	pFB-FIGNL1_Frag.REV	tgatggtgctcgagcccgggCTTTCCACAACCAAAAGTTTTGTTCCAG	Human	Gibson assembly
21	pFB-FIGNL1-Vector.FOR	AAACTTTTGGTTGTGGAAAGcccgggctcgagcac	Human	Gibson assembly
22	pFB-FIGNL1-Vector.REV	AATTTTTTGCCAGCCATGGAgggcccctggaacagaacttccagc	Human	Gibson assembly
23	FIGNL1-dNLS_pGEX-For	atctggttccgcgtggatccTCCATGGCTGGCAAAAAATTCAAAG	Human	Gibson assembly
24	FIGNL1-dNLS_pGEX-Rev	gtcagtcacgatgaattctaTTACTTTCCACAACCAAAAGTTTTGTTCC	Human	Gibson assembly
25	Vector_FIGNL1-pGEX-For	CTTTTGGTTGTGGAAAGTAAtagaattcatcgtgactgactgacga	Human	Gibson assembly
26	Vector_FIGNL1-pGEX-Rev	AATTTTTTGCCAGCCATGGAggatccacgcggaaccag	Human	Gibson assembly

TwoMP mass photometer (Refeyn Ltd). Reactions containing FIGNL1-dNLS with or without RAD51 were prepared in reaction buffer containing 30 mM HEPES-KOH (pH 7.5), 100 mM KCl, 20 mM NaCl, 3.5 mM $MgCl_2$, 5% glycerol and 0.8 mM ATPγS (BIOLOG Life Science Institute). The protein concentrations for initial binding were 1 μM to allow for protein complex formation. The samples were incubated for 10 min at 37°C, followed by 1 hour at room temperature. The samples were then diluted for measurement to 100 nM using a dilution buffer containing 25 mM Tris-HCl (pH 7.5) and 100 mM NaCl in a final volume of 20 μl. Movies were recorded for 120 s using AcquireMP (Refeyn Ltd) and processed and analyzed using DiscoverMP (Refeyn ltd).

ATPase assay

ATPase assays with wild-type and mutant FIGNL1-dNLS were performed in reaction buffer (25 mM Tris-acetate [pH 7.5], 1 mM magnesium acetate, 1 mM DTT, 0.1 mg/ml BSA, 0.1 mM ATP, 1 nM of [γ-32P] ATP [Hartmann-Analytic]) in 10 μl reaction volume. Recombinant proteins were added as indicated. The samples were mixed on ice and incubated at 37°C for 30 min. Reactions were stopped with 1.25 μl of 0.5 M EDTA and separated using thin-layer chromatography plates (Merck) with 0.3 M LiCl and 0.3 M formic acid as the mobile phase. Dried plates were exposed to storage phosphor screens (GE Healthcare) and scanned by a Typhoon Phosphor Imager (FLA9500). Signals were quantified using ImageJ software. Spontaneous ATP hydrolysis signal from no protein lanes was removed as a background during quantitation. The rate of ATP hydrolysis was obtained as a measure of the amount of hydrolyzed ATP per molecule of FIGNL1-dNLS per min.

GFPtrap pull down

$10x10^6$ eGFP-FIGNL1 over expressing RPE1 cells were harvested and subjected to nuclear fractionation. Briefly, cells were lysed with cytoplasmic extraction buffer [10 mM HEPES (pH-8.0), 1.5 mM $MgCl_2$, 10 mM KCl, 0.5 mM DTT, 0.05% NP40 supplemented with protease inhibitor cocktail (PIC)] and incubated on ice for 10 min. separated by centrifugation at then separated by centrifugation at 1400 g for 5 min. Nuclear fraction at the pellet was then separated and lysed with immunoprecipitation buffer (50 mM Tris-HCl [pH 7.4], 150 mM NaCl, 10% glycerol, 1% Triton X-100, 0.5 mM EDTA, 0.5 mM EGTA, and Protease Inhibitor cocktail) supplemented with 50 U/ml Benzonase, on ice for 30 min. Finally, the lysed nuclear fraction was collected by centrifugation at 17,000 g for 10 min. Cleared nuclear fraction was quantified by BCA method (Pierce, Invitrogen) and used for overnight GFPtrap magnetic agarose bead pull-down (Proteintech) after separating 5% lysate as input. After overnight GFPtrap pull down, beads were washed 5 times with wash buffer (10 mM Tris-HCl [pH 7.4], 150 mM NaCl, 0.05% NP40 Substitute, 0.5 mM EDTA supplemented with PIC). Pull down eluates were separated by heating with NuPAGE™ LDS sample buffer (Invitrogen) + 4x DTT at 95°C for 15 min and analyzed by western blotting.

REFERENCES AND NOTES

1. R. Prakash, Y. Zhang, W. Feng, M. Jasin, Homologous recombination and human health: The roles of BRCA1, BRCA2, and associated proteins. *Cold Spring Harb. Perspect. Biol.* **7**, a016600 (2015). doi: 10.1101/cshperspect.a016600; pmid: 25833843
2. O. Belan *et al.*, Visualization of direct and diffusion-assisted RAD51 nucleation by full-length human BRCA2 protein. *Mol. Cell* **83**, 2925–2940.e8 (2023). doi: 10.1016/j.molcel.2023.06.031; pmid: 37499663

Downloaded from https://www.science.org at Biblioteca Universitaria Di Lugano on July 21, 2026

3. J. C. Bell, C. C. Dombrowski, J. L. Plank, R. B. Jensen, S. C. Kowalczykowski, BRCA2 chaperones RAD51 to single molecules of RPA-coated ssDNA. *Proc. Natl. Acad. Sci. U.S.A.* **120**, e2221971120 (2023). doi: 10.1073/pnas.2221971120; pmid: 36976771
4. A. A. Davies *et al.*, Role of BRCA2 in control of the RAD51 recombination and DNA repair protein. *Mol. Cell* **7**, 273–282 (2001). doi: 10.1016/S1097-2765(01)00175-7; pmid: 11239456
5. R. B. Jensen, A. Carreira, S. C. Kowalczykowski, Purified human BRCA2 stimulates RAD51-mediated recombination. *Nature* **467**, 678–683 (2010). doi: 10.1038/nature09399; pmid: 20729832
6. J. Liu, T. Doty, B. Gibson, W. D. Heyer, Human BRCA2 protein promotes RAD51 filament formation on RPA-covered single-stranded DNA. *Nat. Struct. Mol. Biol.* **17**, 1260–1262 (2010). doi: 10.1038/nsmb.1904; pmid: 20729859
7. L. Y. Marmorstein, T. Ouchi, S. A. Aaronson, The BRCA2 gene product functionally interacts with p53 and RAD51. *Proc. Natl. Acad. Sci. U.S.A.* **95**, 13869–13874 (1998). doi: 10.1073/pnas.95.23.13869; pmid: 9811893
8. M. E. Moynahan, A. J. Pierce, M. Jasin, BRCA2 is required for homology-directed repair of chromosomal breaks. *Mol. Cell* **7**, 263–272 (2001). doi: 10.1016/S1097-2765(01)00174-5; pmid: 11239455
9. S. K. Sharan *et al.*, Embryonic lethality and radiation hypersensitivity mediated by Rad51 in mice lacking Brca2. *Nature* **386**, 804–810 (1997). doi: 10.1038/386804a0; pmid: 9126738
10. F. Xia *et al.*, Deficiency of human BRCA2 leads to impaired homologous recombination but maintains normal nonhomologous end joining. *Proc. Natl. Acad. Sci. U.S.A.* **98**, 8644–8649 (2001). doi: 10.1073/pnas.151253498; pmid: 11447276
11. V. P. Yu *et al.*, Gross chromosomal rearrangements and genetic exchange between nonhomologous chromosomes following BRCA2 inactivation. *Genes Dev.* **14**, 1400–1406 (2000). doi: 10.1101/gad.14.11.1400; pmid: 10837032
12. M. Castroviejo-Bermejo *et al.*, A RAD51 assay feasible in routine tumor samples calls PARP inhibitor response beyond BRCA mutation. *EMBO Mol. Med.* **10**, e9172 (2018). doi: 10.15252/emmm.201809172; pmid: 30377213
13. C. Cruz *et al.*, RAD51 foci as a functional biomarker of homologous recombination repair and PARP inhibitor resistance in germline BRCA-mutated breast cancer. *Ann. Oncol.* **29**, 1203–1210 (2018). doi: 10.1093/annonc/mdy099; pmid: 29635390
14. K. A. Naipal *et al.*, Functional ex vivo assay to select homologous recombination-deficient breast tumors for PARP inhibitor treatment. *Clin. Cancer Res.* **20**, 4816–4826 (2014). doi: 10.1158/1078-0432.CCR-14-0571; pmid: 24963051
15. S. S. Yuan *et al.*, BRCA2 is required for ionizing radiation-induced assembly of Rad51 complex in vivo. *Cancer Res.* **59**, 3547–3551 (1999). pmid: 10446958
16. H. E. Bryant *et al.*, Specific killing of BRCA2-deficient tumours with inhibitors of poly(ADP-ribose) polymerase. *Nature* **434**, 913–917 (2005). doi: 10.1038/nature03443; pmid: 15829966
17. H. Farmer *et al.*, Targeting the DNA repair defect in BRCA mutant cells as a therapeutic strategy. *Nature* **434**, 917–921 (2005). doi: 10.1038/nature03445; pmid: 15829967
18. E. Harvey-Jones *et al.*, Longitudinal profiling identifies co-occurring BRCA1/2 reversions, TP53BP1, RIF1 and PAXIP1 mutations in PARP inhibitor-resistant advanced breast cancer. *Ann. Oncol.* **35**, 364–380 (2024). doi: 10.1016/j.annonc.2024.01.003; pmid: 38244928
19. A. Ray Chaudhuri *et al.*, Replication fork stability confers chemoresistance in BRCA-deficient cells. *Nature* **535**, 382–387 (2016). doi: 10.1038/nature18325; pmid: 27443740
20. E. Duro *et al.*, Identification of the MMS22L-TONSL complex that promotes homologous recombination. *Mol. Cell* **40**, 632–644 (2010). doi: 10.1016/j.molcel.2010.10.023; pmid: 21055984
21. L. O'Donnell *et al.*, The MMS22L-TONSL complex mediates recovery from replication stress and homologous recombination. *Mol. Cell* **40**, 619–631 (2010). doi: 10.1016/j.molcel.2010.10.024; pmid: 21055983
22. W. Piwko *et al.*, The MMS22L–TONSL heterodimer directly promotes RAD51-dependent recombination upon replication stress. *The EMBO Journal* **35**, 2584–2601 (2016). doi: 10.1016/j.molcel.2018.01.031; pmid: 29478807
23. T. H. Huang *et al.*, The Histone Chaperones ASF1 and CAF-1 Promote MMS22L-TONSL-Mediated Rad51 Loading onto ssDNA during Homologous Recombination in Human Cells. *Mol. Cell* **69**, 879–892.e5 (2018). doi: 10.1016/j.molcel.2018.01.031; pmid: 29478807
24. G. Saredi *et al.*, H4K20me0 marks post-replicative chromatin and recruits the TONSL–MMS22L DNA repair complex. *Nature* **534**, 714–718 (2016). doi: 10.1038/nature18312; pmid: 27338793
25. J. Flygare *et al.*, Effects of HsRad51 overexpression on cell proliferation, cell cycle progression, and apoptosis. *Exp. Cell Res.* **268**, 61–69 (2001). doi: 10.1006/excr.2001.5265; pmid: 11461118
26. C. Richardson, J. M. Stark, M. Ommundsen, M. Jasin, Rad51 overexpression promotes alternative double-strand break repair pathways and genome instability. *Oncogene* **23**, 546–553 (2004). doi: 10.1038/sj.onc.1207098; pmid: 14724582
27. L. J. Barber *et al.*, RTEL1 maintains genomic stability by suppressing homologous recombination. *Cell* **135**, 261–271 (2008). doi: 10.1016/j.cell.2008.08.016; pmid: 18957201
28. Y. Hu *et al.*, RECQL5/Recql5 helicase regulates homologous recombination and suppresses tumor formation via disruption of Rad51 presynaptic filaments. *Genes Dev.* **21**, 3073–3084 (2007). doi: 10.1101/gad.1609107; pmid: 18003859
29. G.-L. Moldovan *et al.*, Inhibition of homologous recombination by the PCNA-interacting protein PARI. *Mol. Cell* **45**, 75–86 (2012). doi: 10.1016/j.molcel.2011.11.010; pmid: 22153967
30. D. S. Patel, S. M. Misenko, J. Her, S. F. Bunting, BLM helicase regulates DNA repair by counteracting RAD51 loading at DNA double-strand break sites. *J. Cell Biol.* **216**, 3521–3534 (2017). doi: 10.1083/jcb.201703144; pmid: 28912125
31. J. Simandlova *et al.*, FBH1 helicase disrupts RAD51 filaments in vitro and modulates homologous recombination in mammalian cells. *J. Biol. Chem.* **288**, 34168–34180 (2013). doi: 10.1074/jbc.M113.484493; pmid: 24108124
32. J. A. Sommers *et al.*, FANCJ uses its motor ATPase to destabilize protein-DNA complexes, unwind triplexes, and inhibit RAD51 strand exchange. *J. Biol. Chem.* **284**, 7505–7517 (2009). doi: 10.1074/jbc.M809019200; pmid: 19150983
33. K. Matsuzaki, A. Shinohara, M. Shinohara, Human AAA+ ATPase FIGNL1 suppresses RAD51-mediated ultra-fine bridge formation. *Nucleic Acids Res.* **52**, 5774–5791 (2024). doi: 10.1093/nar/gkae263; pmid: 38597669
34. K. Matsuzaki, S. Kondo, T. Ishikawa, A. Shinohara, Human RAD51 paralogue SWSAP1 fosters RAD51 filament by regulating the anti-recombinase FIGNL1 AAA+ ATPase. *Nat. Commun.* **10**, 1407 (2019). doi: 10.1038/s41467-019-09190-1; pmid: 30926776
35. E. Pinedo-Carpio *et al.*, FIRRM cooperates with FIGNL1 to promote RAD51 disassembly during DNA repair. *Sci. Adv.* **9**, eadf4082 (2023). doi: 10.1126/sciadv.adf4082; pmid: 37556550
36. C. Stok *et al.*, FIRRM/C1orf112 is synthetic lethal with PICH and mediates RAD51 dynamics. *Cell Rep.* **42**, 112668 (2023). doi: 10.1016/j.celrep.2023.112668; pmid: 37347663
37. J. D. Tischler *et al.*, FLIP(C1orf112)-FIGNL1 complex regulates RAD51 chromatin association to promote viability after replication stress. *Nat. Commun.* **15**, 866 (2024). doi: 10.1038/s41467-024-45139-9; pmid: 38286805
38. J. Yuan, J. Chen, FIGNL1-containing protein complex is required for efficient homologous recombination repair. *Proc. Natl. Acad. Sci. U.S.A.* **110**, 10640–10645 (2013). doi: 10.1073/pnas.1220662110; pmid: 23754376
39. Z. Zhou *et al.*, C1orf112 teams up with FIGNL1 to facilitate RAD51 filament disassembly and DNA interstrand cross-link repair. *Cell Rep.* **42**, 112907 (2023). doi: 10.1016/j.celrep.2023.112907; pmid: 37515771
40. M. Ito *et al.*, FIGNL1 AAA+ ATPase remodels RAD51 and DMC1 filaments in pre-meiotic DNA replication and meiotic recombination. *Nat. Commun.* **14**, 6857 (2023). doi: 10.1038/s41467-023-42576-w; pmid: 37891173
41. A. Zainu *et al.*, FIGNL1-FIRRM is essential for meiotic recombination and prevents DNA damage-independent RAD51 and DMC1 loading. *Nat. Commun.* **15**, 7015 (2024). doi: 10.1038/s41467-024-51458-8; pmid: 39147779
42. R. Kumar, M. Duhamel, E. Coutant, E. Ben-Nahia, R. Mercier, Antagonism between BRCA2 and FIGL1 regulates homologous recombination. *Nucleic Acids Res.* **47**, 5170–5180 (2019). doi: 10.1093/nar/gkz225; pmid: 30941419
43. A. Carver *et al.*, Molecular basis of FIGNL1 in dissociating RAD51 from DNA and chromatin. *Science* **387**, 426–431 (2025). doi: 10.1126/science.adr7920; pmid: 39636933
44. A. M. Heijink *et al.*, Sister chromatid exchanges induced by perturbed replication can form independently of BRCA1, BRCA2 and RAD51. *Nat. Commun.* **13**, 6722 (2022). doi: 10.1038/s41467-022-34519-8; pmid: 36344511
45. B. Evers *et al.*, A high-throughput pharmaceutical screen identifies compounds with specific toxicity against BRCA2-deficient tumors. *Clin. Cancer Res.* **16**, 99–108 (2010). doi: 10.1158/1078-0432.CCR-09-2434; pmid: 20008842
46. C. S. Y. Lo, N. Taneja, A. Ray Chaudhuri, Enhancing quantitative imaging to study DNA damage response: A guide to automated liquid handling and imaging. *DNA Repair* **144**, 103769 (2024). doi: 10.1016/j.dnarep.2024.103769; pmid: 39395383
47. L. I. Toledo *et al.*, ATR prohibits replication catastrophe by preventing global exhaustion of RPA. *Cell* **155**, 1088–1103 (2013). doi: 10.1016/j.cell.2013.10.043; pmid: 24267891
48. A. Canela *et al.*, DNA Breaks and End Resection Measured Genome-wide by End Sequencing. *Mol. Cell* **63**, 898–911 (2016). doi: 10.1016/j.molcel.2016.06.034; pmid: 27477910
49. J. S. Iacovoni *et al.*, High-resolution profiling of gammaH2AX around DNA double strand breaks in the mammalian genome. *EMBO J.* **29**, 1446–1457 (2010). doi: 10.1038/emboj.2010.38; pmid: 20360682
50. S. Raynard, P. Sung, Assay for human Rad51-mediated DNA displacement loop formation. *Cold Spring Harb Protoc.* **4**, pdb.prot5120 (2009). doi: 10.1038/emboj.2010.38; pmid: 20360682
51. P. Chi, S. Van Komen, M. G. Sehorn, S. Sigurdsson, P. Sung, Roles of ATP binding and ATP hydrolysis in human Rad51 recombinase function. *DNA Repair* **5**, 381–391 (2006). doi: 10.1016/j.dnarep.2005.11.005; pmid: 16388992
52. J. M. Stark *et al.*, ATP hydrolysis by mammalian RAD51 has a key role during homology-directed DNA repair. *J. Biol. Chem.* **277**, 20185–20194 (2002). doi: 10.1074/jbc.M112132200; pmid: 11923292
53. N. Siaud *et al.*, Plasticity of BRCA2 function in homologous recombination: Genetic interactions of the PALB2 and DNA binding domains. *PLOS Genet.* **7**, e1002409 (2011). doi: 10.1371/journal.pgen.1002409; pmid: 22194698
54. Y. Kwon *et al.*, DNA binding and RAD51 engagement by the BRCA2 C-terminus orchestrate DNA repair and replication fork preservation. *Nat. Commun.* **14**, 432 (2023). doi: 10.1038/s41467-023-36211-x; pmid: 36702902

Downloaded from https://www.science.org at Biblioteca Universitaria Di Lugano on July 21, 2026

55. T. Thorslund *et al.*, The breast cancer tumor suppressor BRCA2 promotes the specific targeting of RAD51 to single-stranded DNA. *Nat. Struct. Mol. Biol.* **17**, 1263–1265 (2010). doi: 10.1038/nsmb.1905; pmid: 20729858
56. K. Nakanishi, F. Cavallo, E. Brunet, M. Jasin, in *DNA Recombination: Methods and Protocols*, H. Tsubouchi, Ed. (Humana Press, 2011), pp. 283–291.doi: 10.1007/978-1-61779-129-1_16
57. A. Suzuki *et al.*, Brca2 is required for embryonic cellular proliferation in the mouse. *Genes Dev.* **11**, 1242–1252 (1997). doi: 10.1101/gad.11.10.1242; pmid: 9171369
58. S. G. Kuznetsov, P. Liu, S. K. Sharan, Mouse embryonic stem cell-based functional assay to evaluate mutations in BRCA2. *Nat. Med.* **14**, 875–881 (2008). doi: 10.1038/nm.1719; pmid: 18607349
59. K. Biswas *et al.*, A comprehensive functional characterization of BRCA2 variants associated with Fanconi anemia using mouse ES cell-based assay. *Blood* **118**, 2430–2442 (2011). doi: 10.1182/blood-2010-12-324541; pmid: 21719596
60. E. W. Schmid, J. C. Walter, Predictomes, a classifier-curated database of AlphaFold-modeled protein-protein interactions. *Mol. Cell* **85**, 1216–1232.e5 (2025). doi: 10.1016/j.molcel.2025.01.034; pmid: 40015271
61. M. Reuter *et al.*, BRCA2 diffuses as oligomeric clusters with RAD51 and changes mobility after DNA damage in live cells. *J. Cell Biol.* **207**, 599–613 (2014). doi: 10.1083/jcb.201405014; pmid: 25488918
62. S. Halder *et al.*, Double-stranded DNA binding function of RAD51 in DNA protection and its regulation by BRCA2. *Mol. Cell* **82**, 3553–3565.e5 (2022). doi: 10.1016/j.molcel.2022.08.014; pmid: 36070766
63. M. A. Longo *et al.*, BRCA2 C-terminal clamp restructures RAD51 dimers to bind B-DNA for replication fork stability. *Mol. Cell* **85**, 2080–2096.e6 (2025). doi: 10.1016/j.molcel.2025.05.010; pmid: 40441151
64. S. Mijic *et al.*, Replication fork reversal triggers fork degradation in BRCA2-defective cells. *Nat. Commun.* **8**, 859 (2017). doi: 10.1038/s41467-017-01164-5; pmid: 29038466
65. K. Schlacher *et al.*, Double-strand break repair-independent role for BRCA2 in blocking stalled replication fork degradation by MRE11. *Cell* **145**, 529–542 (2011). doi: 10.1016/j.cell.2011.03.041; pmid: 21565612
66. L. A. Greenhough *et al.*, Structure and function of the RAD51B-RAD51C-RAD51D-XRCC2 tumour suppressor. *Nature* **619**, 650–657 (2023). doi: 10.1038/s41586-023-06179-1; pmid: 37344587
67. M. A. Longo *et al.*, RAD51C-XRCC3 structure and cancer patient mutations define DNA replication roles. *Nat. Commun.* **14**, 4445 (2023). doi: 10.1038/s41467-023-40096-1; pmid: 37488098
68. Y. Rawal *et al.*, Structural insights into BCDX2 complex function in homologous recombination. *Nature* **619**, 640–649 (2023). doi: 10.1038/s41586-023-06219-w; pmid: 37344589
69. T. G. Meijer *et al.*, Direct Ex Vivo Observation of Homologous Recombination Defect Reversal After DNA-Damaging Chemotherapy in Patients With Metastatic Breast Cancer. *JCO Precis. Oncol.* **3**, 1–12 (2019). doi: 10.1200/PO.18.00268; pmid: 35100677
70. J. Bhin *et al.*, Multi-omics analysis reveals distinct non-reversion mechanisms of PARPi resistance in BRCA1- versus BRCA2-deficient mammary tumors. *Cell Rep.* **42**, 112538 (2023). doi: 10.1016/j.celrep.2023.112538; pmid: 37209095
71. J. Jonkers *et al.*, Synergistic tumor suppressor activity of BRCA2 and p53 in a conditional mouse model for breast cancer. *Nat. Genet.* **29**, 418–425 (2001). doi: 10.1038/ng747; pmid: 11694875
72. K. Nakanishi, F. Cavallo, E. Brunet, M. Jasin, Homologous recombination assay for interstrand cross-link repair. *Methods Mol. Biol.* **745**, 283–291 (2011). doi: 10.1007/978-1-61779-129-1_16; pmid: 21660700
73. I. Ceppi *et al.*, Mechanism of BRCA1-BARD1 function in DNA end resection and DNA protection. *Nature* **634**, 492–500 (2024). doi: 10.1038/s41586-024-07909-9; pmid: 39261728
74. D. R. Stirling *et al.*, CellProfiler 4: Improvements in speed, utility and usability. *BMC Bioinformatics* **22**, 433 (2021). doi: 10.1186/s12859-021-04344-9; pmid: 34507520
75. J. Abramson *et al.*, Accurate structure prediction of biomolecular interactions with AlphaFold 3. *Nature* **630**, 493–500 (2024). doi: 10.1038/s41586-024-07487-w; pmid: 38718835
76. G. Kim *et al.*, Easy and accurate protein structure prediction using ColabFold. *Nat. Protoc.* **20**, 620–642 (2025). doi: 10.1038/s41596-024-01060-5; pmid: 39402428
77. L. C. Xue, J. P. Rodrigues, P. L. Kastritis, A. M. Bonvin, A. Vangone, PRODIGY: A web server for predicting the binding affinity of protein-protein complexes. *Bioinformatics* **32**, 3676–3678 (2016). doi: 10.1093/bioinformatics/btw514; pmid: 27503228
78. C. Elfmann, J. Stülke, PAE viewer: A webserver for the interactive visualization of the predicted aligned error for multimer structure predictions and crosslinks. *Nucleic Acids Res.* **51**, W404–W410 (2023). doi: 10.1093/nar/gkad350; pmid: 37140053
79. C. Pinto, K. Kasaciunaite, R. Seidel, P. Cejka, Human DNA2 possesses a cryptic DNA unwinding activity that functionally integrates with BLM or WRN helicases. *eLife* **5**, e18574 (2016). doi: 10.7554/eLife.18574; pmid: 27612385
80. G. Reginato *et al.*, HLTF disrupts Cas9-DNA post-cleavage complexes to allow DNA break processing. *Nat. Commun.* **15**, 5789 (2024). doi: 10.1038/s41467-024-50080-y; pmid: 38987539
81. A. V. Mazin, E. Zaitseva, P. Sung, S. C. Kowalczykowski, Tailed duplex DNA is the preferred substrate for Rad51 protein-mediated homologous pairing. *EMBO J.* **19**, 1148–1156 (2000). doi: 10.1093/emboj/19.5.1148; pmid: 10698955
82. C. Mukherjee *et al.*, RIF1 promotes replication fork protection and efficient restart to maintain genome stability. *Nat. Commun.* **10**, 3287 (2019). doi: 10.1038/s41467-019-11246-1; pmid: 31337767
83. A. R. Chaudhuri, R. Kuthethur, FIGNL1 inhibits homologous recombination in BRCA2 deficient cells by dissociating RAD51 filaments. Zenodo (2025); https://zenodo.org/records/15462520.
84. A. R. Chaudhuri, K. M. Poluri, R. Kuthethur, N. Nagar, FIGNL1 inhibits homologous recombination in BRCA2 deficient cells by dissociating RAD51 filaments (Version 1). Zenodo (2025); https://zenodo.org/records/15454978

ACKNOWLEDGMENTS

The authors thank Optical Imaging Centre of the Erasmus MC for assistance and microscope access for the study. The authors thank M. Jasin for the miBRCA2 expression construct, I. Ceppi and M.R.D. Sritto for cloning the miBRCA2 construct, and W. Vermeulen for critical reading of the manuscript and discussions. **Funding:** This work was funded by the following: NWO (Dutch research Council) VIDI award (Vidi.193.131) (to A.R.C.); Ammodo Science Award (to A.R.C., R.Ka., and J.H.G.L.); and Josephine Nefkens Cancer Program (to A.R.C., R.Ka., and J.H.G.L.); R.Ka. is also funded by the Oncode Institute, which is partly financed by the Dutch Cancer Society (to K.W.F.); Canadian Institutes of Health Research Grants (PDT_180310) to A.F.T. A.F.T. holds a Canada Research Chair in Molecular Virology and Genomic Instability (Tier 2) and the Foundation J.-Louis Lévesque also supports her lab work. This work was also funded by SERB-INDIA (Science and Engineering Research Board) research grants STR/2022/000008 and CRG/2022/003028 to KMP; research in the PC laboratory is funded by the Swiss National Science Foundation (SNSF) (grants 310030_207588 and 310030_205199) and the European Research Council (ERC) (grant 101018257). The S.K. Sharan lab is funded by Intramural Research Program, Center for Cancer Research, National Cancer Institute, US National Institutes of Health. **Author contributions:** Conceptualization: A.R.C. and R.Ku. Methodology: R.Ku., A.A., S.K.Se., C.F., N.N., S.B., and J.D. Investigation: R.Ku., A.A., S.K.Se., C.F., N.N., O.I., S.N., S.B., E.-M.M., K.dK., A.T., and X.W. Funding acquisition: A.R.C., P.C., S.K.Sha., K.M.P., J.H.G.L., R.Ka., and A.F.T. Project administration A.R.C. Supervision: A.R.C., P.C., S.K.Sha., K.M.P., J.H.G.L., and R.Ka. Writing-original draft: A.R.C. with contributions from R.Ku. and C.F. Writing-review & editing: P.C., S.K.Sha., K.M.P., J.H.G.L., and R.Ka. and all other authors. **Competing interests:** The authors declare that they have no competing interests. **Data and materials availability:** CellProfiler pipeline templates used for foci detection and colocalization analysis are deposited in the zenodo repository (*83*). All the relevant materials used for AlphaFold structural data analysis are deposited in the Zenodo repository (*84*). Cell lines and plasmids created in this study are available upon request from A.R.C. under materials transfer agreement with Erasmus University Medical Centre, Rotterdam, NL. Transfer of cell lines and plasmids may be subject to third party obligations. All other data are available in the main text or the supplementary materials. **License information:** Copyright © 2025 the authors, some rights reserved; exclusive licensee American Association for the Advancement of Science. No claim to original US gover nMent works. https://www.science.org/content/page/science-licenses-journal-article-reuse

SUPPLEMENTARY MATERIALS

science.org/doi/10.1126/science.adt1210
Figs. S1 to S18; Tables S1 to S6; MDAR Reproducibility Checklist

Submitted 13 September 2024; accepted 24 July 2025

10.1126/science.adt1210

Downloaded from https://www.science.org at Biblioteca Universitaria Di Lugano on July 21, 2026

Science
AAAS

Supplementary Materials for

FIGNL1 inhibits homologous recombination in BRCA2 deficient cells by dissociating RAD51 filaments

Raviprasad Kuthethur *et al*.

Corresponding authors: Petr Cejka, petr.cejka@irb.usi.ch; Arnab Ray Chaudhuri, a.raychaudhuri@erasmusmc.nl

Science **390**, eadt1210 (2025)
DOI: 10.1126/science.adt1210

The PDF file includes:

Figs. S1 to S18
Tables S1 to S6

Other Supplementary Material for this manuscript includes the following:

MDAR Reproducibility Checklist

fig. S1

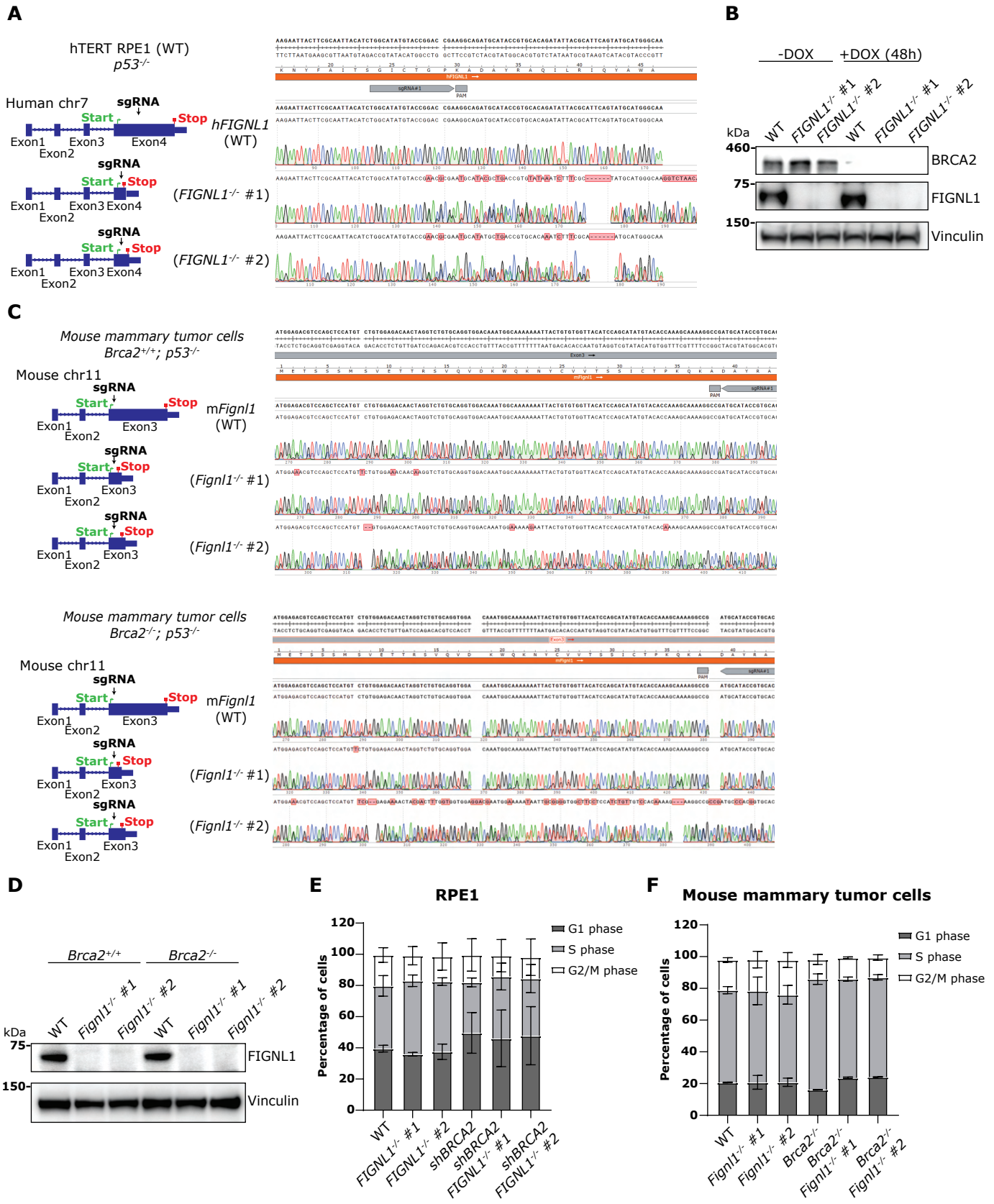
A
hTERT RPE1 (WT)
p53-/-
Human chr7
sgRNA
Start
Stop
Exon1
Exon2
Exon3
Exon4
hFIGNL1
(WT)
(FIGNL1-/- #1)
(FIGNL1-/- #2)
B
-DOX
+DOX (48h)
kDa
WT
FIGNL1-/- #1
FIGNL1-/- #2
460
75
150
BRCA2
FIGNL1
Vinculin
C
Mouse mammary tumor cells
Brca2+/+; p53-/-
Mouse chr11
mFignl1
(WT)
(Fignl1-/- #1)
(Fignl1-/- #2)
Mouse mammary tumor cells
Brca2-/-; p53-/-
D
Brca2+/+
Brca2-/-
FIGNL1
Vinculin
E
RPE1
Percentage of cells
G1 phase
S phase
G2/M phase
shBRCA2
F
Mouse mammary tumor cells

fig. S1: Validation of FIGNL1 knock-out cells in human RPE1 and mouse mammary tumor cells

(A) Left: Schematics of the results of knocking-out *FIGNL1* in RPE1-WT cells. Right: Genotyping results from RPE1-WT and 2 different knock-out clones of *FIGNL1*. Electropherogram representative figure showing the alignment of the *FIGNL1* genomic DNA region at the indicated binding site of sgRNA followed by its PAM sequence.

(B) Western blot analysis of BRCA2 with doxycycline induced knock-down and FIGNL1 levels upon CRISPR-Cas9 mediated knock-out in RPE1 cells.

(C) Left: Schematics of the results of knocking-out *Fignl1* in *Brca2* proficient (top) and deficient (bottom) mouse mammary tumor cells. Right: Genotyping results from *Brca2* proficient (top) and deficient (bottom) mouse mammary tumor cells with 2 different clones of *Fignl1* knock-outs each. Electropherogram representative figure showing the alignment of *Fignl1* genomic DNA region at the indicated binding site of sgRNA followed by its PAM sequence.

(D) Western blot analysis of FIGNL1 levels from each clone upon CRISPR-Cas9 mediated knock-out in mouse mammary tumor cells.

(E) The percentage of cells in the different phases of the cell cycle profile of RPE1 and RPE1 *FIGNL1*-KO cells. Error bars are indicative of mean±SD from 2 independent flow cytometry experiments.

(F) The percentage of cells in the different phases of the cell cycle profile of mouse mammary tumor cells with *Fignl1*-KO. Error bars are indicative of mean±SD from 2 independent flow cytometry experiments.

fig. S2

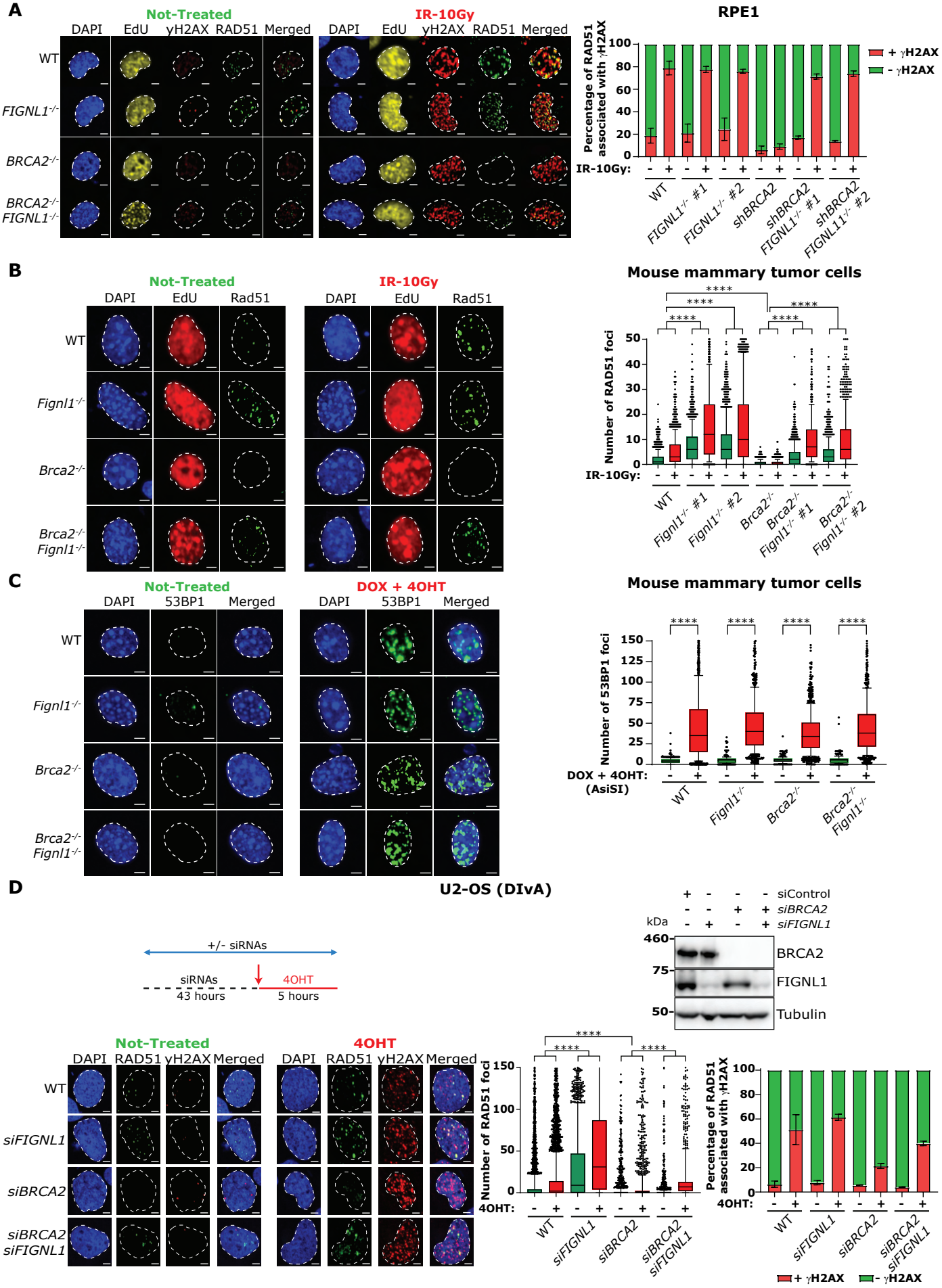
A
Not-Treated
IR-10Gy
DAPI EdU γH2AX RAD51 Merged
WT
FIGNL1-/-
BRCA2-/-
BRCA2-/- FIGNL1-/-
RPE1
Percentage of RAD51 associated with γH2AX
+ γH2AX
- γH2AX
IR-10Gy:
WT
FIGNL1-/- #1
FIGNL1-/- #2
shBRCA2
shBRCA2 FIGNL1-/- #1
shBRCA2 FIGNL11-/- #2
B
Not-Treated
IR-10Gy
DAPI EdU Rad51
Fignl1-/-
Brca2-/-
Brca2-/- Fignl1-/-
Mouse mammary tumor cells
Number of RAD51 foci
IR-10Gy:
Brca2-/- Fignl1-/- #1
Brca2-/- Fignl1-/- #2
C
Not-Treated
DOX + 4OHT
DAPI 53BP1 Merged
Mouse mammary tumor cells
Number of 53BP1 foci
DOX + 4OHT: (AsiSI)
D
U2-OS (DIvA)
+/- siRNAs
siRNAs 43 hours
4OHT 5 hours
siControl
siBRCA2
siFIGNL1
kDa
460
75
50
BRCA2
FIGNL1
Tubulin
Not-Treated
4OHT
DAPI RAD51 γH2AX Merged
siFIGNL1
siBRCA2
siBRCA2 siFIGNL1
Number of RAD51 foci
Percentage of RAD51 associated with γH2AX
4OHT:
WT
siFIGNL1
siBRCA2
siBRCA2 siFIGNL1
+ γH2AX
- γH2AX

fig. S2: Validation of RAD51 rescue in BRCA2-FIGNL1 deficient cells in mouse mammary tumor cells and human U2-OS cells

(A) Left: representative images of high-content, automated RAD51-IF images showing the EdU, H2AX and RAD51 foci in not-treated and ionizing radiation treated RPE1 cells; scale bar: 5 m. Right Percentage of RAD51 foci associated with H2AX. Error bars are indicative of mean±SD from 3 independent experiments.

(B) Left: representative images of high-content, automated RAD51-IF images showing the EdU and RAD51 foci in not-treated and ionizing radiation treated mouse mammary tumor cells; scale bar: 5 µm. Right: Automated QIBC plots of the RAD51 foci per nucleus; scatter box plot showing the foci distribution between 10-90th percentile from 1,500 cells (experiment was repeated 3 times). P-values from Mann-Whitney test (two-tailed) comparing between indicated groups (****: <0.0001).

(C) Left: representative images of 53BP1-IF images showing the 53BP1 foci in not-treated and AsiSI induced mouse mammary tumor cells; scale bar: 5 µm. Right: Automated QIBC plots of the 53BP1 foci per nucleus; scatter box plot showing the foci distribution between 10-90th percentile from 1,500 cells (experiment was repeated 3 times). P-values from Mann-Whitney test (two-tailed) comparing between indicated groups (****: <0.0001).

(D) Top Left: Schematics showing the experimental setup for RAD51-IF in U2-OS AsiSI (DIvA) cells. 48 hours of siRNA transfection to knock-down BRCA2 and FIGNL1 with last 5 hours to translocate constitutively expressing cytoplasmic AsiSI to the nucleus by 400 nM 4-hydroxytamoxifen (4-OHT). Top right: Western blot analysis showing the levels of BRCA2 and FIGNL1 upon siRNA mediated knock-down in DIvA cells. Bottom left: representative images of high-content, automated RAD51-IF images showing the RAD51 and H2AX foci in not-treated and AsiSI induced DIvA cells; scale bar: 5 m. Bottom middle Automated QIBC plots of the RAD51 foci per nucleus; scatter box plot showing the foci distribution between 10-90th percentile from 1,500 cells (experiment was repeated 3 times). P-values from Mann-Whitney test (two-tailed) comparing between indicated groups (****: <0.0001). Bottom right: Percentage of RAD51 foci associated with H2AX. Error bars are indicative of mean SD from 2 independent experiments.

fig. S3

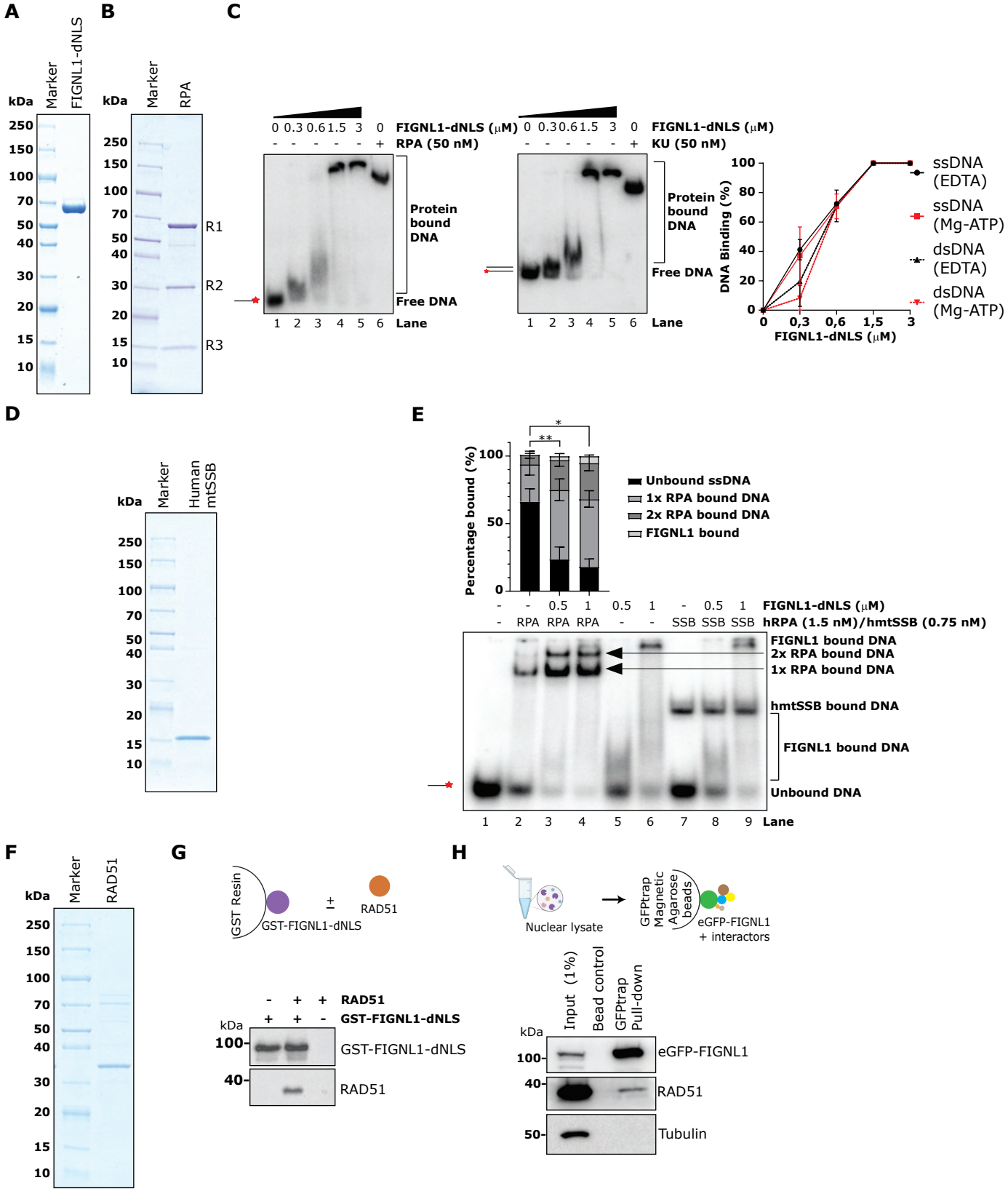
A
Marker
FIGNL1-dNLS
kDa
250
150
100
70
50
40
30
20
15
10
B
Marker
RPA
R1
R2
R3
C
FIGNL1-dNLS (μM)
RPA (50 nM)
KU (50 nM)
Protein bound DNA
Free DNA
Lane
DNA Binding (%)
ssDNA (EDTA)
ssDNA (Mg-ATP)
dsDNA (EDTA)
dsDNA (Mg-ATP)
D
Human mtSSB
E
Percentage bound (%)
Unbound ssDNA
1x RPA bound DNA
2x RPA bound DNA
FIGNL1 bound
hRPA (1.5 nM)/hmtSSB (0.75 nM)
FIGNL1 bound DNA
hmtSSB bound DNA
Unbound DNA
F
RAD51
G
GST Resin
GST-FIGNL1-dNLS
RAD51
GST-FIGNL1-dNLS
H
Nuclear lysate
GFPtrap Magnetic Agarose beads
eGFP-FIGNL1 + interactors
Input (1%)
Bead control
GFPtrap Pull-down
eGFP-FIGNL1
RAD51
Tubulin

fig. S3: FIGNL1 interacts with RAD51

(A) Recombinant FIGNL1-dNLS protein purified from baculovirus infected insect *Sf*9 cells. The purified protein was separated on a polyacrylamide gel and stained with Coomassie blue.

(B) Recombinant RPA protein purified from baculovirus infected insect *Sf*9 cells. The purified protein was separated on a polyacrylamide gel and stained with Coomassie blue. R1: RPA1, R2: RPA2 and R3: RPA3.

(C) Representative images of electrophoretic mobility shift assay showing the concentration dependent binding of FIGNL1 to ssDNA (left) or dsDNA (middle); RPA was used as a control for ssDNA binding and yeast Ku as a control for dsDNA binding. The red asterisk indicates the position of the radioactive label. Right: quantification of binding efficiency with ssDNA and dsDNA in the presence or absence of Mg^{2+} and ATP; error bars are indicative of mean±SEM.

(D) Recombinant human mtSSB protein purified from BL21-(DE3) pLysS *E. coli* cells. The purified protein was separated on a polyacrylamide gel and stained with Coomassie blue.

(E) Top: Percentage quantification of DNA binding efficiency; error bars are indicative of mean±SEM. P-values from One-Way ANOVA comparing between indicated groups (*: <0.05; **: <0.01). Bottom: Electrophoretic mobility shift assay showing the concentration dependent binding of RPA and human mtSSB to ssDNA.

(F) Recombinant RAD51 protein purified from BL21-(DE3) pLysS *E. coli* cells. The purified protein was separated on a polyacrylamide gel and stained with Coomassie blue.

(G) Top: Schematics of the *in vitro* interaction assay between FIGNL1-dNLS (immobilized) and RAD51. Bottom: Western blot results indicative of the interaction between FIGNL1 and RAD51 in the *in vitro* interaction assay.

(H) Top: Schematics of the GFP-trap pull-down of the eGFP-FIGNL1 and RAD51 from nuclear extracts. eGFP-FIGNL1 stably over-expressing cells in FIGNL1 knock-out cells were used for nuclear fractionation and GFP-trap pull-down. Bottom: Western blot results indicative of the interaction between FIGNL1 and RAD51.

fig. S4

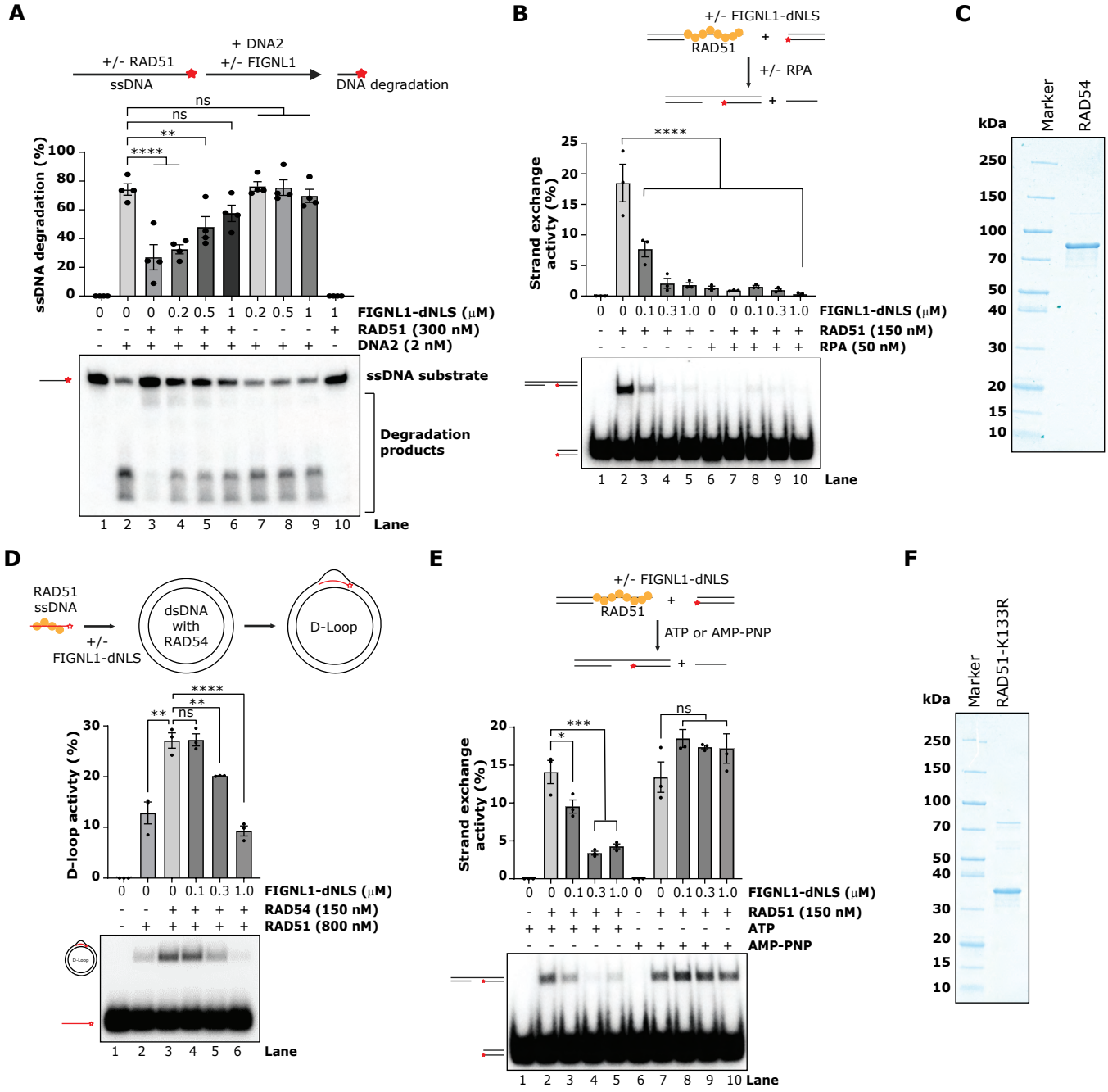
A
+/- RAD51
ssDNA
+ DNA2
+/- FIGNL1
DNA degradation
ssDNA degradation (%)
FIGNL1-dNLS (μM)
RAD51 (300 nM)
DNA2 (2 nM)
ssDNA substrate
Degradation products
Lane
B
+/- FIGNL1-dNLS
RAD51
+/- RPA
Strand exchange activty (%)
FIGNL1-dNLS (μM)
RAD51 (150 nM)
RPA (50 nM)
Lane
C
kDa
Marker
RAD54
D
RAD51 ssDNA
+/- FIGNL1-dNLS
dsDNA with RAD54
D-Loop
D-loop activty (%)
FIGNL1-dNLS (μM)
RAD54 (150 nM)
RAD51 (800 nM)
Lane
E
+/- FIGNL1-dNLS
RAD51
ATP or AMP-PNP
Strand exchange activty (%)
FIGNL1-dNLS (μM)
RAD51 (150 nM)
ATP
AMP-PNP
Lane
F
kDa
Marker
RAD51-K133R

fig. S4: FIGNL1 mediated RAD51 dissociation leads to the inhibition of strand protection and exchange

(A) Top: Schematics of the ssDNA protection assay showing the protection efficiency of RAD51 against degradation by the DNA2 nuclease in the presence of increasing concentrations of FIGNL1-dNLS. Bottom: Quantification of the ssDNA degradation; error bars are indicative of mean±SEM from 4 independent experiments (n=4). P-values from Ordinary One-Way ANOVA comparing between indicated groups (**: <0.01; ****: <0.0001). The red asterisk indicates the position of the radioactive label.

(B) Top: Schematic of the DNA strand exchange assays. The assays were performed by adding 150nM purified RAD51 to the DNA substrates in the presence or absence of 50 nM RPA and in the presence of increasing concentrations of purified FIGNL1-dNLS. The red asterisk indicates the position of the radioactive label. Bottom: Quantification of the absolute DNA strand exchange activity showing the band intensity of the exchanged DNA; error bars are indicative of mean±SEM from 3 independent experiments (n=3). P-values from Ordinary One-Way ANOVA comparing between indicated groups (****: <0.0001).

(C) Recombinant human RAD54 protein purified from baculovirus infected insect *Sf*9 cells. The purified protein was separated on a polyacrylamide gel and stained with Coomassie blue.

(D) Top: Schematics of the D-loop assay. The assays were performed by adding 800 nM purified RAD51 to the ssDNA and 150 nM purified RAD54 to the dsDNA in the presence of increasing concentration of purified FIGNL1-dNLS. The red asterisk indicates the position of the radioactive label. Bottom: Quantification of the absolute D-loop formation activity showing the band intensity of the exchanged DNA; error bars are indicative of mean±SEM from 3 independent experiments (n=3). P-values from Ordinary One-Way ANOVA comparing between indicated groups (**: <0.01; ****: <0.0001).

(E) Top: Schematics of the DNA strand exchange assay. The assays were performed by adding 150 nM purified RAD51 to the DNA substrates in the presence or absence of ATP or AMP-PNP and in the presence of increasing concentrations of purified FIGNL1-dNLS. The red asterisk indicates the position of the radioactive label. Bottom: Quantification of the absolute DNA strand exchange activity showing the band intensity of the exchanged DNA; error bars

are indicative of mean±SEM from 3 independent experiments (n=3). P-values from Ordinary One-Way ANOVA comparing between indicated groups (*: <0.05; ***:<0.001).

(F) Recombinant RAD51-K133R protein purified from BL21-(DE3) pLysS *E. coli* cells. The purified protein was separated on a polyacrylamide gel and stained with Coomassie blue.

fig. S5

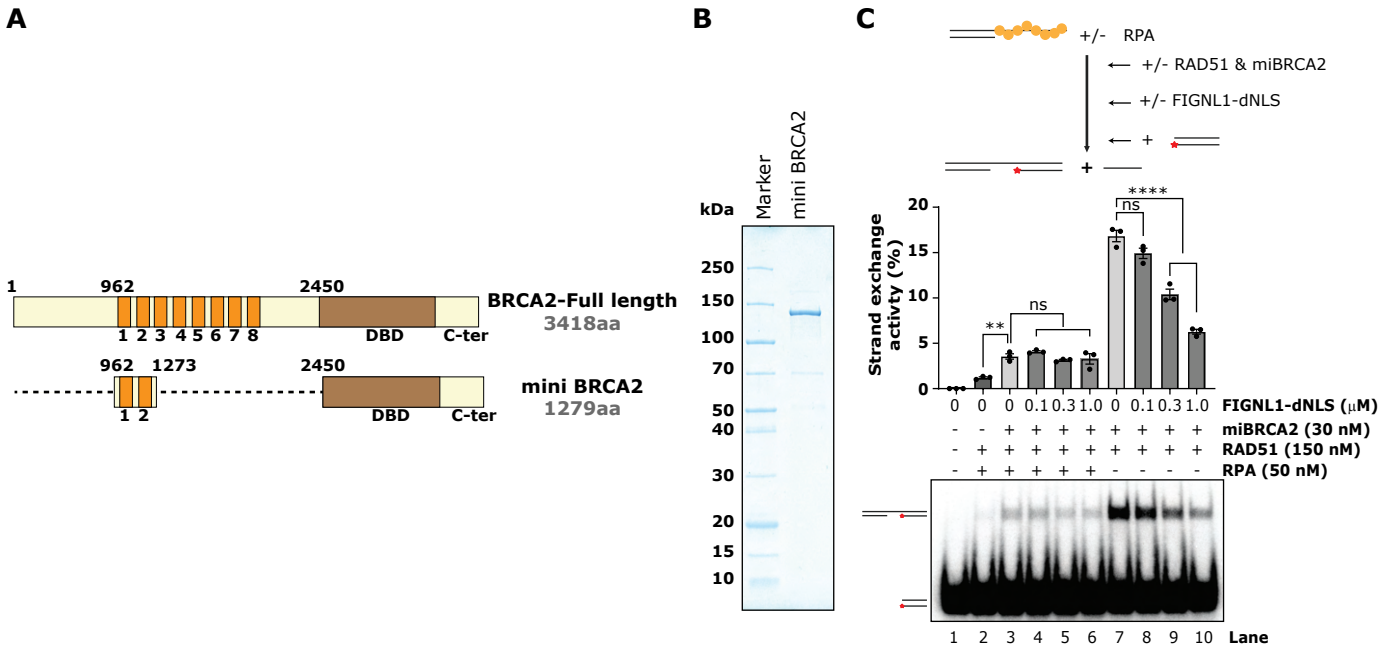
A
1
962
2450
1 2 3 4 5 6 7 8
DBD
C-ter
BRCA2-Full length
3418aa
962 1273
2450
1 2
DBD
C-ter
mini BRCA2
1279aa
B
kDa
Marker
mini BRCA2
250
150
100
70
50
40
30
20
15
10
C
+/- RPA
+/- RAD51 & miBRCA2
+/- FIGNL1-dNLS
+
Strand exchange activity (%)
20
15
10
5
0
****
ns
ns
**
0 0 0 0.1 0.3 1.0 0 0.1 0.3 1.0
FIGNL1-dNLS (μM)
miBRCA2 (30 nM)
RAD51 (150 nM)
RPA (50 nM)
1 2 3 4 5 6 7 8 9 10
Lane

fig. S5: BRCA2 promotes RAD51 mediated strand exchange by inhibiting FIGNL1

(A) Schematics of miBRCA2 constructed with BRC repeats BRC1 & 2, DNA binding domain (DBD) and C-terminal domain (C-ter) compared to the full-length BRCA2.

(B) Recombinant miBRCA2 protein purified from baculovirus infected insect *Sf*9 cells. The purified protein was separated on a polyacrylamide gel and stained with Coomassie blue.

(C) Top: Schematic of the DNA strand exchange assays. The assays were performed by adding 150 nM RAD51 and 30 nM miBRCA2 to the DNA substrates pre-incubated with 50 nM RPA. The reactions were then supplemented with the increasing concentrations of purified FIGNL1-dNLS and labelled donor oligos. The red asterisk indicates the position of the radioactive label. Bottom: Quantification of the absolute strand exchange activity showing the band intensity of the exchanged DNA; error bars are indicative of mean±SEM from 3 independent experiments (n=3). P-values from Ordinary One-Way ANOVA comparing between indicated groups (**: <0.01; ****: <0.0001).

fig. S6

A

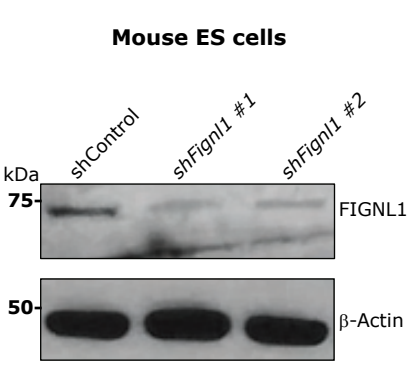
Mouse ES cells
kDa
shControl
shFignl1 #1
shFignl1 #2
75
FIGNL1
50
β-Actin

B

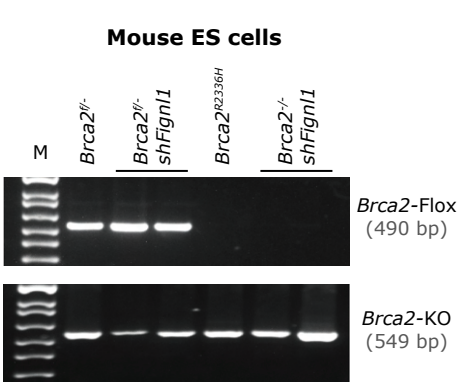
Mouse ES cells
M
Brca2f/-
Brca2f/- shFignl1
Brca2R2336H
Brca2-/- shFignl1
Brca2-Flox
(490 bp)
Brca2-KO
(549 bp)

fig. S6: Validation of FIGNL1 knock-down in mouse ES cells

(A) Representative western blot images showing the FIGNL1 knock-down in mouse embryonic stem cells.

(B) Representative PCR genotyping images of mouse embryonic stem cells with conditional knock-out of BRCA2. Upper lane for floxed allele of BRCA2 and lower lane for the deleted allele of BRCA2.

fig. S7

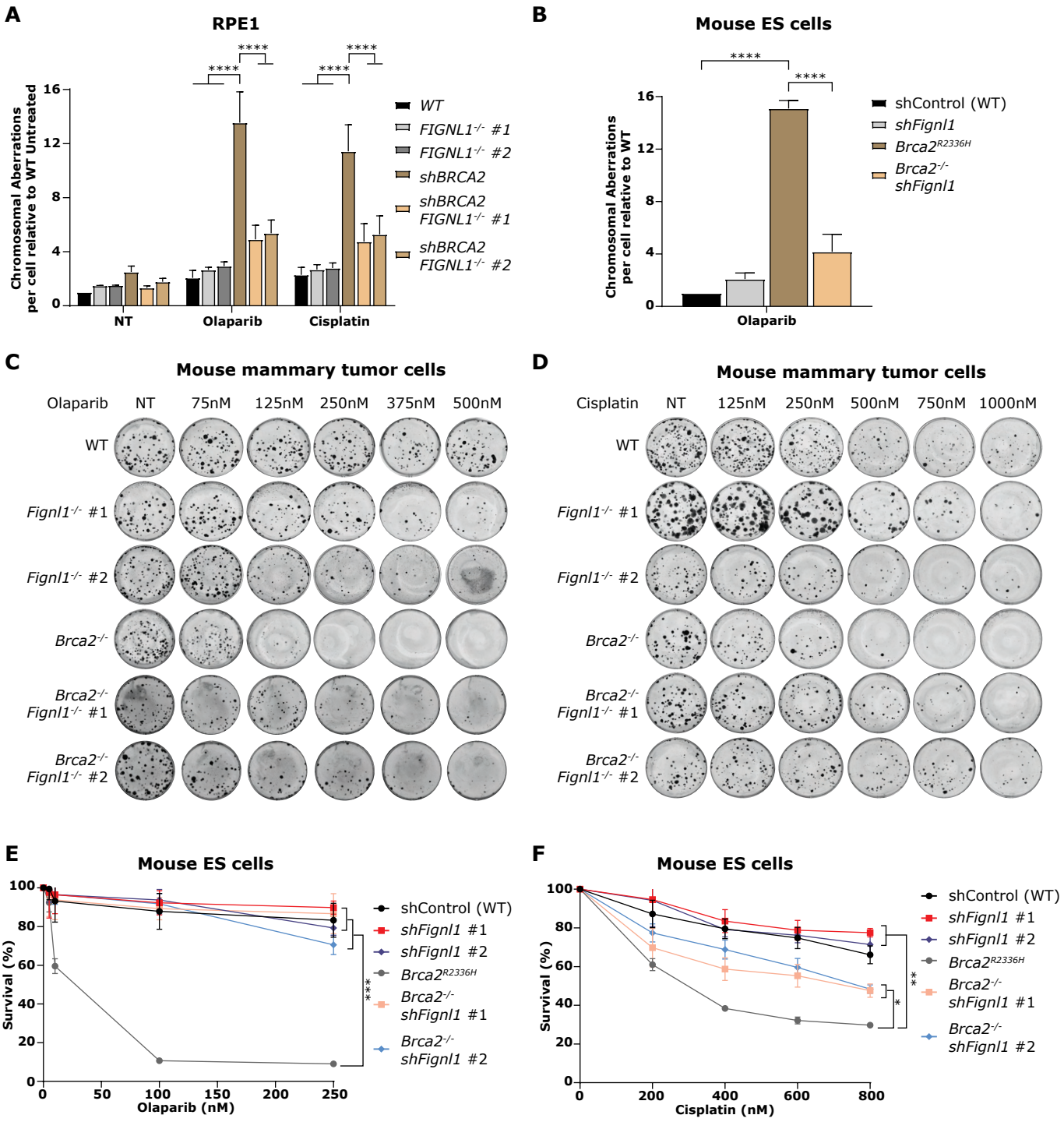
A
RPE1
Chromosomal Aberrations per cell relative to WT Untreated
WT
FIGNL1-/- #1
FIGNL1-/- #2
shBRCA2
shBRCA2 FIGNL1-/- #1
shBRCA2 FIGNL1-/- #2
NT
Olaparib
Cisplatin
B
Mouse ES cells
Chromosomal Aberrations per cell relative to WT
shControl (WT)
shFignl1
Brca2R2336H
Brca2-/- shFignl1
Olaparib
C
Mouse mammary tumor cells
Olaparib
NT
75nM
125nM
250nM
375nM
500nM
WT
Fignl1-/- #1
Fignl1-/- #2
Brca2-/-
Brca2-/- Fignl1-/- #1
Brca2-/- Fignl1-/- #2
D
Mouse mammary tumor cells
Cisplatin
NT
125nM
250nM
500nM
750nM
1000nM
E
Mouse ES cells
Survival (%)
Olaparib (nM)
shControl (WT)
shFignl1 #1
shFignl1 #2
Brca2R2336H
Brca2-/- shFignl1 #1
Brca2-/- shFignl1 #2
F
Mouse ES cells
Survival (%)
Cisplatin (nM)

fig. S7: Loss of FIGNL1 in BRCA2 deficient cells reverses genome instability and confers chemoresistance

(A) Quantification of chromosomal aberrations in RPE1 FIGNL1 knock-out clones in response to Olaparib and cisplatin from 3 independent experiments in which 50 individual metaphases were analyzed for each sample per experiment. P-values from Ordinary two-way ANOVA (****: <0.0001)

(B) Quantification of chromosomal aberrations in mouse embryonic stem cells with FIGNL1 knock down clones in response to Olaparib from 3 independent experiments in which 50 individual metaphases were analyzed for each sample per experiment. P-values from Ordinary two-way ANOVA (****: <0.0001)

(C) Representative clonogenic images of mouse mammary tumor cells in response to Olaparib.

(D) Representative clonogenic images of mouse mammary tumor cells in response to cisplatin.

(E) Percentage survivability of mouse embryonic stem cells in response to Olaparib; quantification was performed by normalization to non-treated cells. P-values from Dunnett's multiple comparison One-way ANOVA comparing between indicated groups (***: <0.001).

(F) Percentage survivability of mouse embryonic stem cells in response to cisplatin; quantification was performed by normalization to non-treated cells. P-values from Dunnett's multiple comparison One-way ANOVA comparing between indicated groups (*: <0.05, **: <0.01).

fig. S8

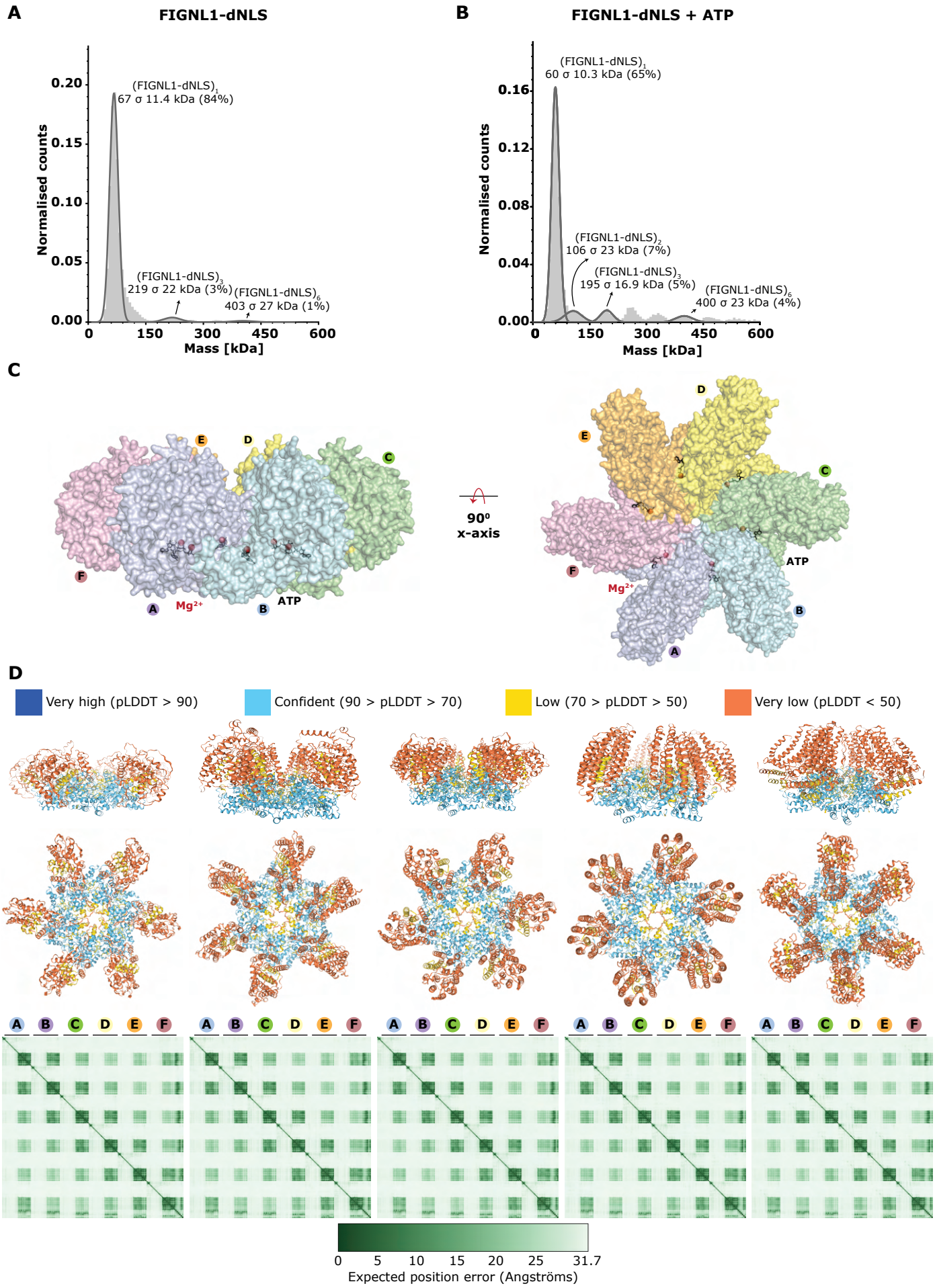
A
FIGNL1-dNLS
(FIGNL1-dNLS)1
67 σ 11.4 kDa (84%)
(FIGNL1-dNLS)3
219 σ 22 kDa (3%)
(FIGNL1-dNLS)6
403 σ 27 kDa (1%)
Normalised counts
Mass [kDa]
B
FIGNL1-dNLS + ATP
(FIGNL1-dNLS)1
60 σ 10.3 kDa (65%)
(FIGNL1-dNLS)2
106 σ 23 kDa (7%)
(FIGNL1-dNLS)3
195 σ 16.9 kDa (5%)
(FIGNL1-dNLS)6
400 σ 23 kDa (4%)
C
90º
x-axis
ATP
Mg2+
D
Very high (pLDDT > 90)
Confident (90 > pLDDT > 70)
Low (70 > pLDDT > 50)
Very low (pLDDT < 50)
Expected position error (Angströms)

fig. S8: FIGNL1 majorly forms monomers including hexamers

(A) Mass photometry analysis of FIGNL1-dNLS purified in the absence of ATP. Observed masses of each complex are shown with percentage of population that make up each population in bracket.

(B) Mass photometry analysis of FIGNL1-dNLS purified in the presence of ATP. Observed masses of each complex are shown with percentage of population that make up each population in bracket.

(C) The side and top view of the predicted FIGNL1 hexamer-Mg^{2+}/ATP complex. The monomers are shown as surface representation (Chain A: Light blue; Chain B: Pale cyan; Chain C: Pale green; Chain D: Light yellow; Chain E: Light Orange; Chain F: Light pink). The Mg^{2+} and ATP molecules are shown as sphere and stick representations (Mg^{2+}: Red; ATP: Black) respectively. K447 of ATPase domain of FIGNL1 is involved in the binding of ATP to FIGNL1.

(D) Top: The side and top view of five predicted models of FIGNL1 hexamer in the presence of Mg^{2+}/ATP colored by pLDDT values, which measures the confidence of atomic positions relative to its neighboring atoms. Bottom: The predicted aligned error (PAE) plots, displaying long-range relationships, for the five models generated using AF3 for the FIGNL1 hexamer-Mg^{2+}/ATP complex. Subunits are indicated above plots with color coding as in panel C.

fig. S9

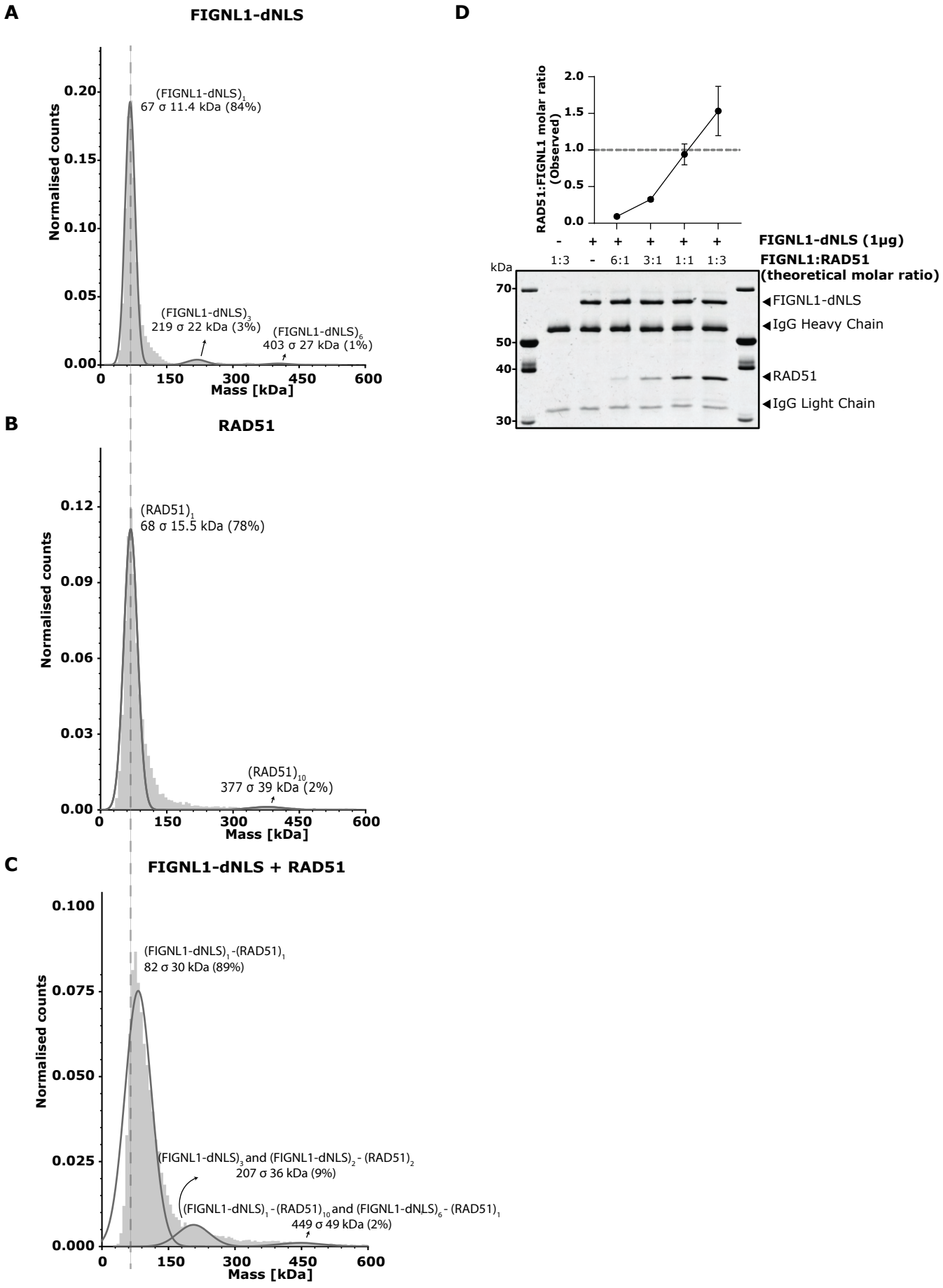
A
FIGNL1-dNLS
Normalised counts
(FIGNL1-dNLS)1
67 σ 11.4 kDa (84%)
(FIGNL1-dNLS)3
219 σ 22 kDa (3%)
(FIGNL1-dNLS)6
403 σ 27 kDa (1%)
Mass [kDa]
B
RAD51
(RAD51)1
68 σ 15.5 kDa (78%)
(RAD51)10
377 σ 39 kDa (2%)
C
FIGNL1-dNLS + RAD51
(FIGNL1-dNLS)1-(RAD51)1
82 σ 30 kDa (89%)
(FIGNL1-dNLS)3 and (FIGNL1-dNLS)2 - (RAD51)2
207 σ 36 kDa (9%)
(FIGNL1-dNLS)1 - (RAD51)10 and (FIGNL1-dNLS)6 - (RAD51)1
449 σ 49 kDa (2%)
D
RAD51:FIGNL1 molar ratio (Observed)
FIGNL1-dNLS (1µg)
FIGNL1:RAD51 (theoretical molar ratio)
1:3
6:1
3:1
1:1
1:3
kDa
FIGNL1-dNLS
IgG Heavy Chain
RAD51
IgG Light Chain

fig. S9: FIGNL1 hexamer transiently interacts with RAD51

(A) Mass photometry analysis of FIGNL1-dNLS purified in the absence of ATP. Observed masses of each complex are shown with percentage of population that make up each population in bracket.

(B) Mass photometry analysis of RAD51 purified in the absence of ATP. Observed masses of each complex are shown with percentage of population that make up each population in bracket.

(C) Mass photometry analysis of FIGNL1-dNLS+RAD51 purified in the absence of ATP. Observed masses of each complex are shown with percentage of population that make up each population in bracket. Dashed line across each mass analysis (A-C) shows the shift in the monomeric FIGNL1-dNLS population in the presence of RAD51.

(D) Top: Quantitative analysis of FIGNL1-dNLS and RAD51. Error bars are representative of mean±SEM from 4 independent experiments (n=4). Bottom: Silver-stained gel of the FIGNL1-dNLS and RAD51 interaction assay. RAD51 concentration was calculated based on the indicated theoretical molar ratios to the immobilized FIGNL1-dNLS and loaded on a polyacrylamide gel.

fig. S10

A

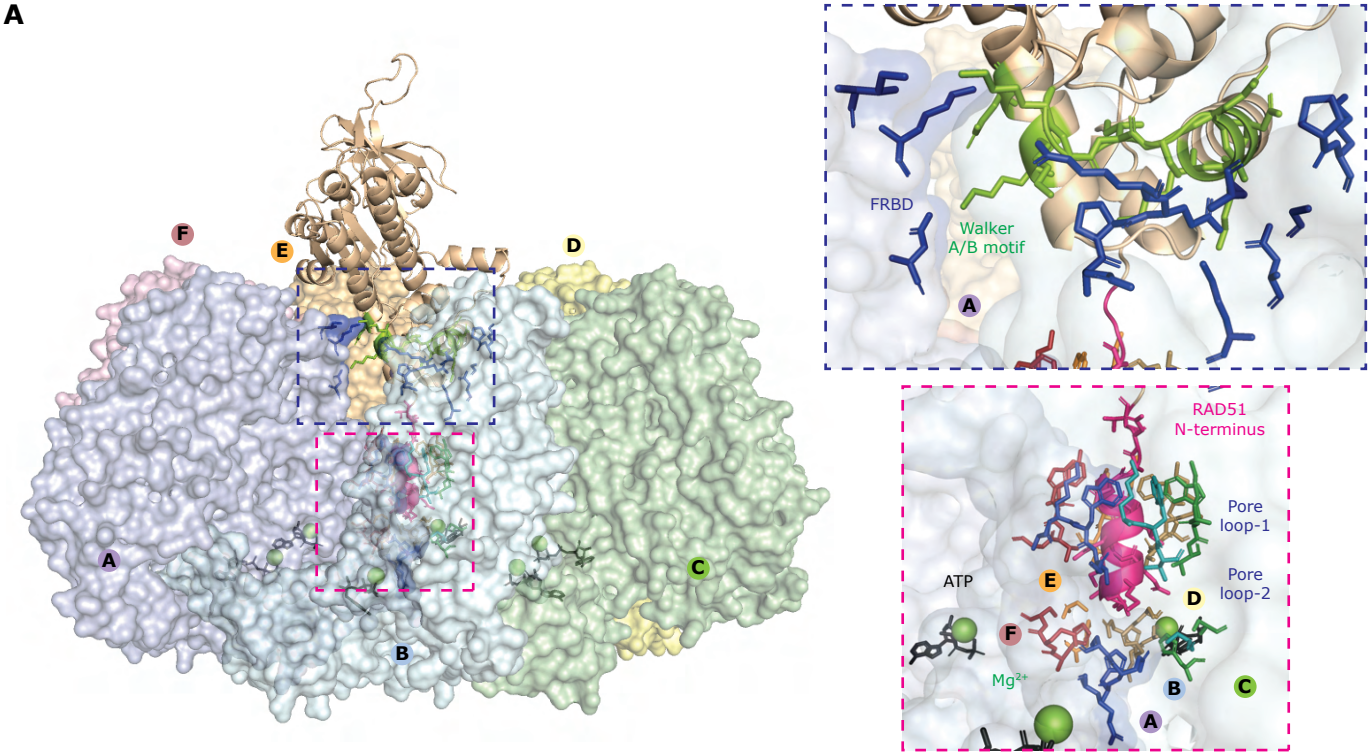
F
E
D
A
C
B
FRBD
Walker
A/B motif
A
RAD51
N-terminus
Pore
loop-1
ATP
E
Pore
loop-2
D
F
Mg2+
B
C
A

B

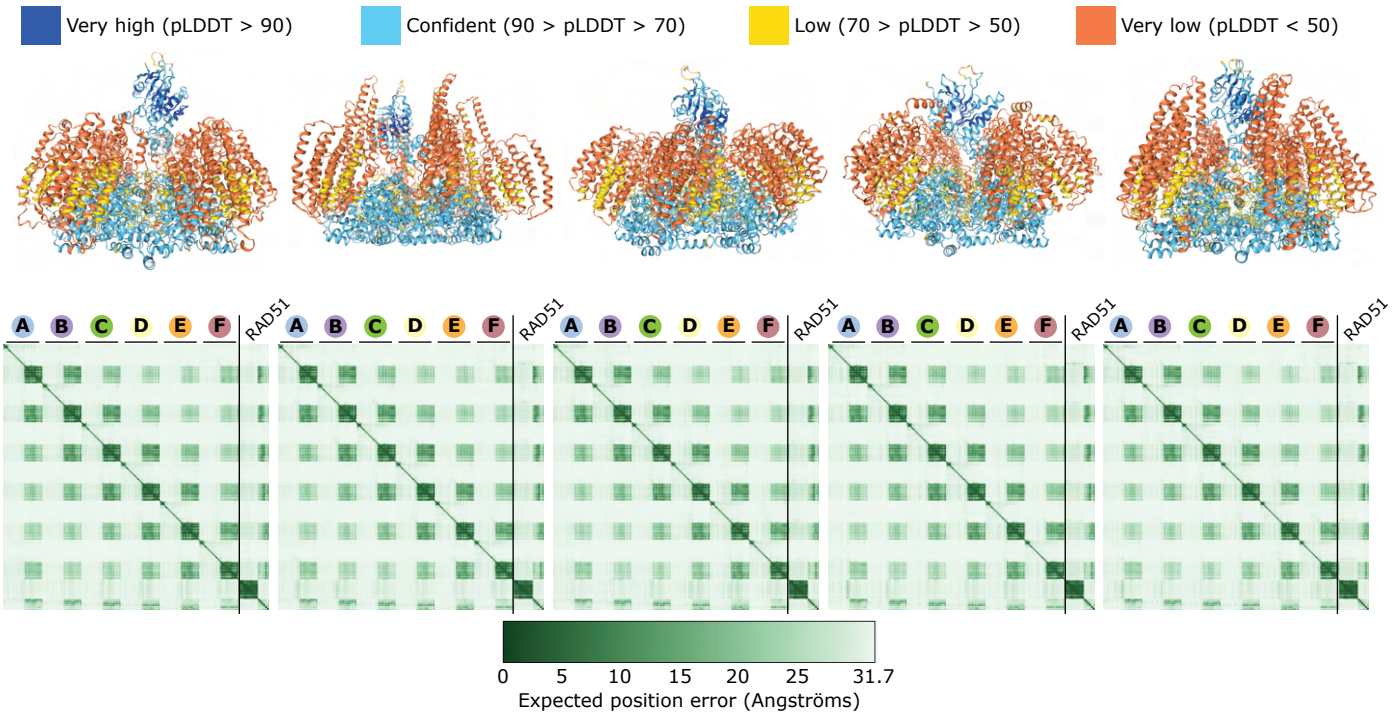
Very high (pLDDT > 90)
Confident (90 > pLDDT > 70)
Low (70 > pLDDT > 50)
Very low (pLDDT < 50)
A B C D E F RAD51
0 5 10 15 20 25 31.7
Expected position error (Angströms)

fig. S10: Hexameric FIGNL1 interacts with RAD51

(A) The side and zoom-in view of the hexameric FIGNL1-RAD51- Mg^{2+}/ATP complex. The FIGNL1 monomers are shown as surface representation (Chain A: Light blue; Chain B: Pale cyan; Chain C: Pale green; Chain D: Light yellow; Chain E: Light Orange; Chain F: Light pink) while RAD51 (beige) is shown in cartoon representation. Note that despite the prediction depicting the N-terminal regions of FIGNL1 (top part of the hexameric dome) as folded α-helical domains, these regions have low confidence scores (see panel B) and are expected to be unstructured. The zoom-in views represent the interacting region of FIGNL1 and RAD51. The blue inset represents the interaction between FIGNL1 FRBD (dark blue) and RAD51 loops present between Walker A/B motifs (green). Despite low confidence scores (panel B), reflecting the unstructured nature of the FRBD region, FRBD is interacting with RAD51 in all predictions. The pink inset represents the interaction between two FIGNL1 Pore Loops present in the ATPase region (the residues are shown as stick and colored according to the FIGNL1 chains) and RAD51 N-terminal domain (pink). The Mg^{2+} and ATP molecules are shown as sphere and stick representation (Mg^{2+}: Green; ATP: Black), respectively.

(B) Top: The five predicted models of FIGNL1 hexamer-RAD51 complex in presence of Mg^{2+}/ATP colored by pLDDT values, which measures the confidence of atomic positions relative to its neighboring atoms. Bottom: The predicted aligned error (PAE) plots, displaying long-range relationships, for the five models generated using AF3 for the FIGNL1 hexamer-RAD51 in the presence of Mg^{2+}/ATP complex. FIGNL1 subunits are indicated above plots with color coding as in panel A.

fig. S11

A

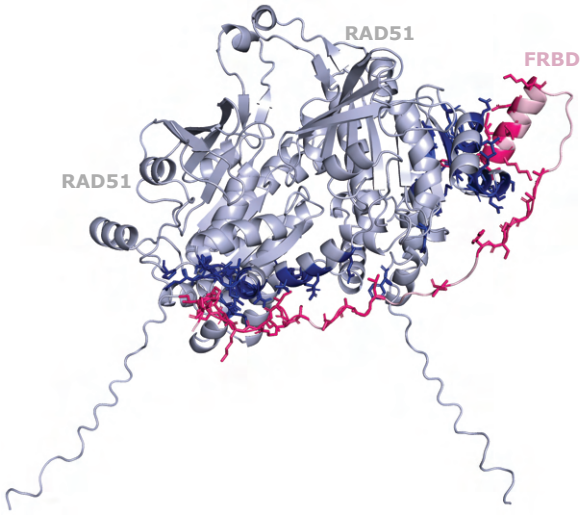
RAD51
FRBD
RAD51

B

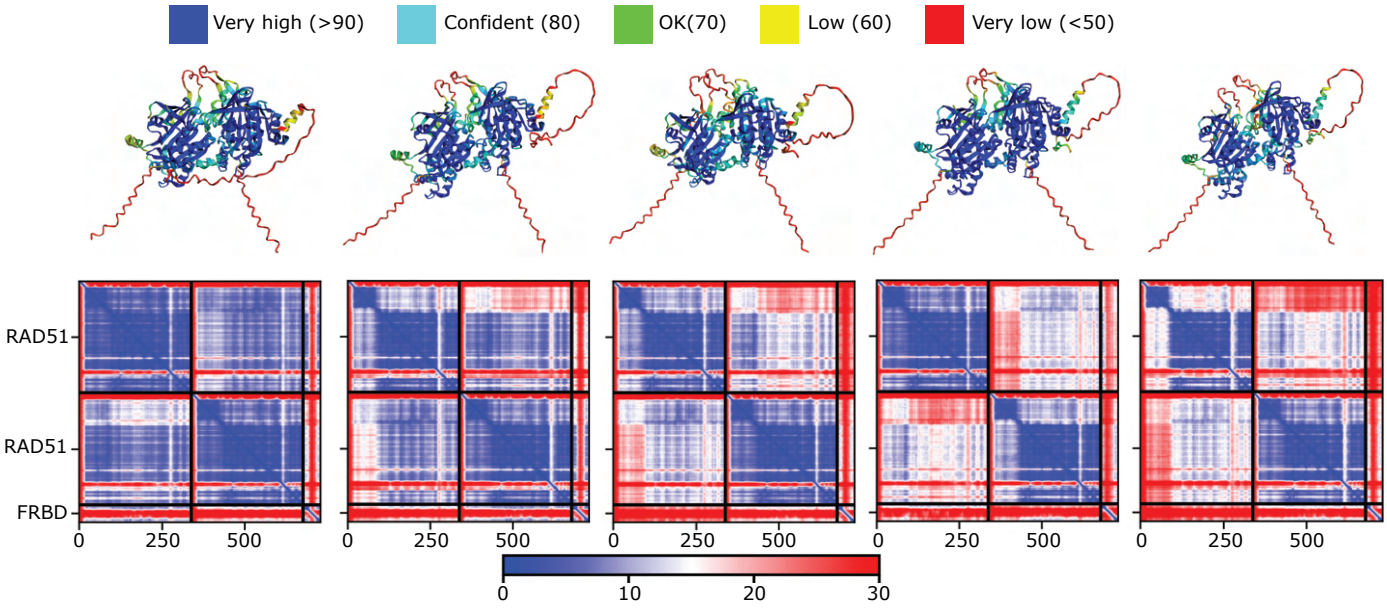
Very high (>90)
Confident (80)
OK(70)
Low (60)
Very low (<50)
RAD51
RAD51
FRBD
0
250
500
0
10
20
30

fig. S11: FIGNL1 FRBD region can accommodate 2 RAD51 molecules

(A) The cartoon representation of RAD51 dimer - FIGNL1 FRBD complex. (RAD51 dimer: Light blue; FIGNL1 FRBD: Light pink). The interacting regions of RAD51 dimer and FIGNL1 FRBD are colored in dark blue and pink respectively.

(B) Top: The five predicted models of RAD51 dimer-FIGNL1 FRBD complex colored by pLDDT values, which measures the confidence of atomic positions relative to its neighboring atoms. Bottom: The predicted aligned error (PAE) plots, displaying long-range relationships, for the five models generated using AF2-Multimer for the RAD51 dimer-FIGNL1 FRBD complex.

fig. S12

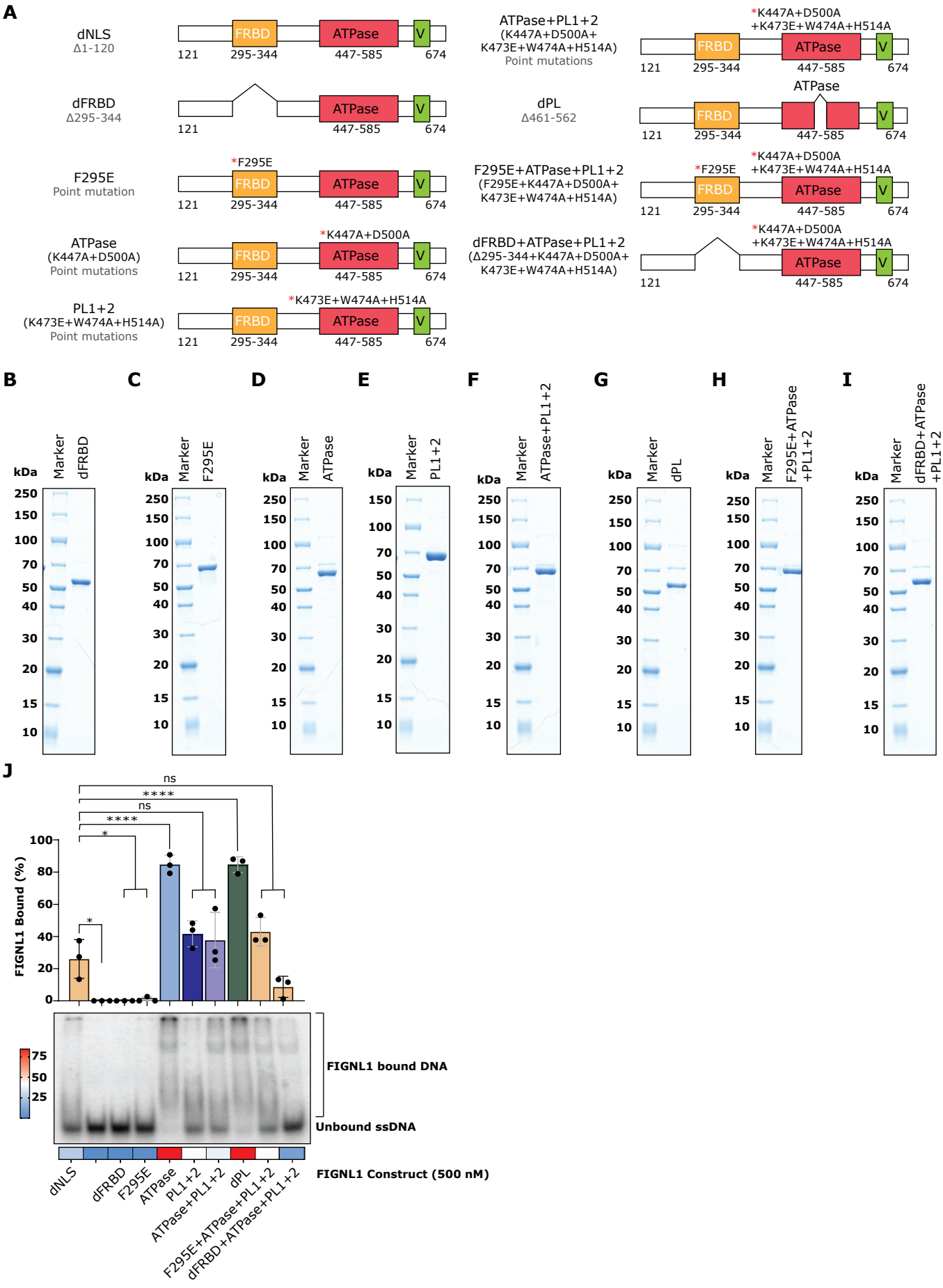
A
dNLS
Δ1-120
dFRBD
Δ295-344
F295E
Point mutation
ATPase
(K447A+D500A)
Point mutations
PL1+2
(K473E+W474A+H514A)
Point mutations
ATPase+PL1+2
(K447A+D500A+
K473E+W474A+H514A)
Point mutations
dPL
Δ461-562
F295E+ATPase+PL1+2
(F295E+K447A+D500A+
K473E+W474A+H514A)
dFRBD+ATPase+PL1+2
(Δ295-344+K447A+D500A+
K473E+W474A+H514A)
FRBD
ATPase
V
121
295-344
447-585
674
*F295E
*K447A+D500A
*K473E+W474A+H514A
*K447A+D500A
+K473E+W474A+H514A
B
C
D
E
F
G
H
I
kDa
Marker
dFRBD
F295E
ATPase
PL1+2
ATPase+PL1+2
dPL
F295E+ATPase
+PL1+2
dFRBD+ATPase
+PL1+2
J
FIGNL1 Bound (%)
ns
****
*
FIGNL1 bound DNA
Unbound ssDNA
FIGNL1 Construct (500 nM)
dNLS
dFRBD
F295E
ATPase
PL1+2
ATPase+PL1+2
dPL
F295E+ATPase+PL1+2
dFRBD+ATPase+PL1+2

fig. S12: FIGNL1 mutants used for *in vitro* studies

(A) Schematics of the FIGNL1 mutant proteins

(B) Recombinant FIGNL1 dFRBD mutant protein purified from baculovirus infected insect *Sf*9 cells. The purified protein was separated on a polyacrylamide gel and stained with Coomassie blue.

(C) Recombinant FIGNL1 F295E mutant protein purified from baculovirus infected insect *Sf*9 cells. The purified protein was separated on a polyacrylamide gel and stained with Coomassie blue.

(D) Recombinant FIGNL1 ATPase mutant protein purified from baculovirus infected insect *Sf*9 cells. The purified protein was separated on a polyacrylamide gel and stained with Coomassie blue.

(E) Recombinant FIGNL1 PL1+2 mutant protein purified from baculovirus infected insect *Sf*9 cells. The purified protein was separated on a polyacrylamide gel and stained with Coomassie blue.

(F) Recombinant FIGNL1 ATPase+PL1+2 mutant protein purified from baculovirus infected insect *Sf*9 cells. The purified protein was separated on a polyacrylamide gel and stained with Coomassie blue.

(G) Recombinant FIGNL1 PL mutant protein purified from baculovirus infected insect *Sf*9 cells. The purified protein was separated on a polyacrylamide gel and stained with Coomassie blue.

(H) Recombinant FIGNL1 F295E+ATPase+PL1+2 mutant protein purified from baculovirus infected insect *Sf*9 cells. The purified protein was separated on a polyacrylamide gel and stained with Coomassie blue.

(I) Recombinant FIGNL1 dFRBD+ATPase+PL1+2 mutant protein purified from baculovirus infected insect *Sf*9 cells. The purified protein was separated on a polyacrylamide gel and stained with Coomassie blue.

(J) Top: Percentage quantification of the DNA binding efficiency of the FIGNL1 mutants; error bars are indicative of mean±SEM from 3 independent experiments (n=3). P-values from One-Way ANOVA comparing between indicated groups (*: <0.05; ****: <0.0001). Bottom: Electrophoretic mobility shift assay showing the concentration dependent binding of the FIGNL1 mutants to ssDNA. Heatmap also showing the percentage of FIGNL1 bound to ssDNA.

fig. S13

A

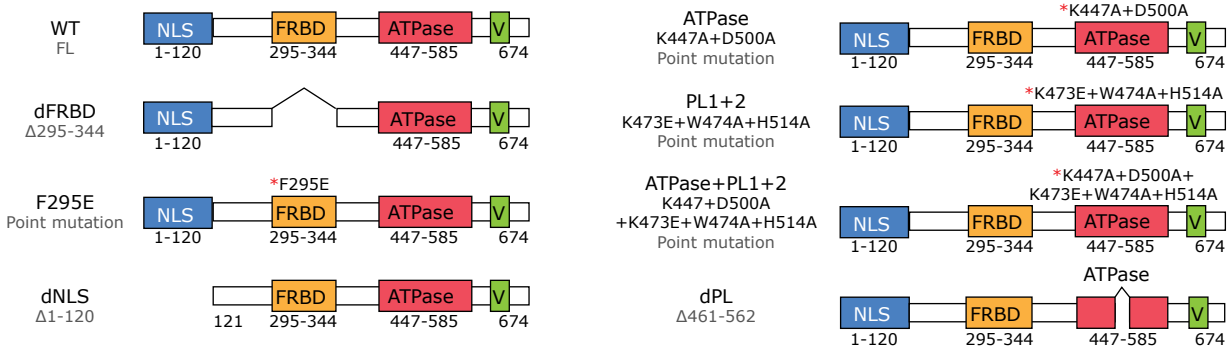
WT
FL
NLS
FRBD
ATPase
V
1-120
295-344
447-585
674
dFRBD
Δ295-344
F295E
Point mutation
*F295E
dNLS
Δ1-120
121
ATPase
K447A+D500A
Point mutation
*K447A+D500A
PL1+2
K473E+W474A+H514A
Point mutation
*K473E+W474A+H514A
ATPase+PL1+2
K447+D500A
+K473E+W474A+H514A
Point mutation
*K447A+D500A+
K473E+W474A+H514A
dPL
Δ461-562

B

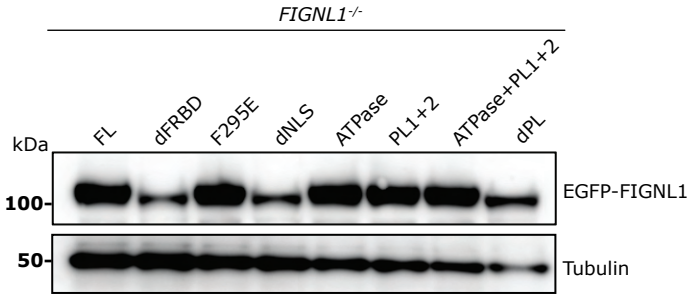
FIGNL1-/-
kDa
FL
dFRBD
F295E
dNLS
ATPase
PL1+2
ATPase+PL1+2
dPL
100
50
EGFP-FIGNL1
Tubulin

C

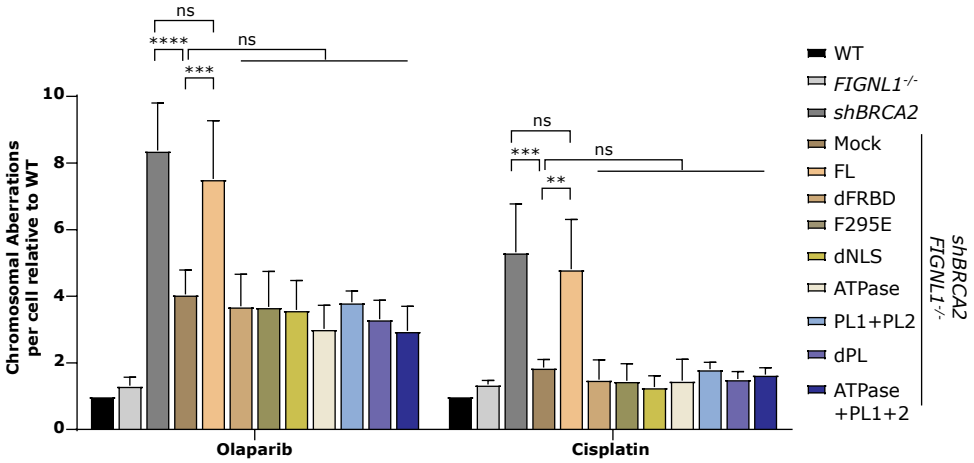
Chromosomal Aberrations per cell relative to WT
0
2
4
6
8
10
ns
****
ns
***
ns
***
ns
**
Olaparib
Cisplatin
WT
FIGNL1-/-
shBRCA2
Mock
FL
dFRBD
F295E
dNLS
ATPase
PL1+PL2
dPL
ATPase +PL1+2
shBRCA2 FIGNL1-/-

fig. S13: FIGNL1-RAD51 interaction is essential for genome stability

(A) Schematics of the FIGNL1 mutant proteins.

(B) Western blot analysis of N-terminal eGFP fused FIGNL1 mutants expressed in FIGNL1$^{-/-}$ RPE1 cells.

(C) Quantification of chromosomal aberrations in RPE1 FIGNL1 knock-out clones reconstituted with FIGNL1 mutants in response to Olaparib and cisplatin from 3 independent experiments in which 50 individual metaphases were analyzed for each sample per experiment. P values from Ordinary two-way ANOVA (**: <0.01; ***: <0.001; ****: <0.0001).

fig. S14
A

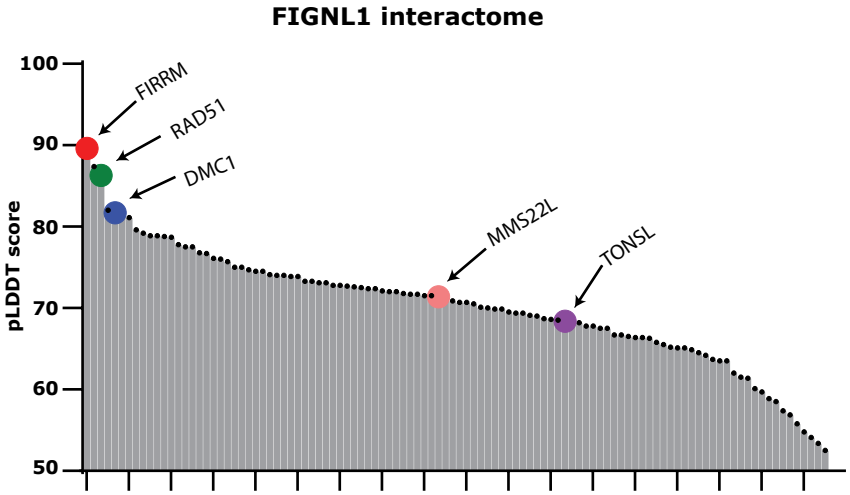
FIGNL1 interactome
pLDDT score
100
90
80
70
60
50
FIRRM
RAD51
DMC1
MMS22L
TONSL

fig. S14: Identification of MMS22L-TONSL complex as FIGNL1 interacting partners

(A) Predictome analysis showing the FIGNL1 interacting partners involved in genome maintenance.

fig. S15

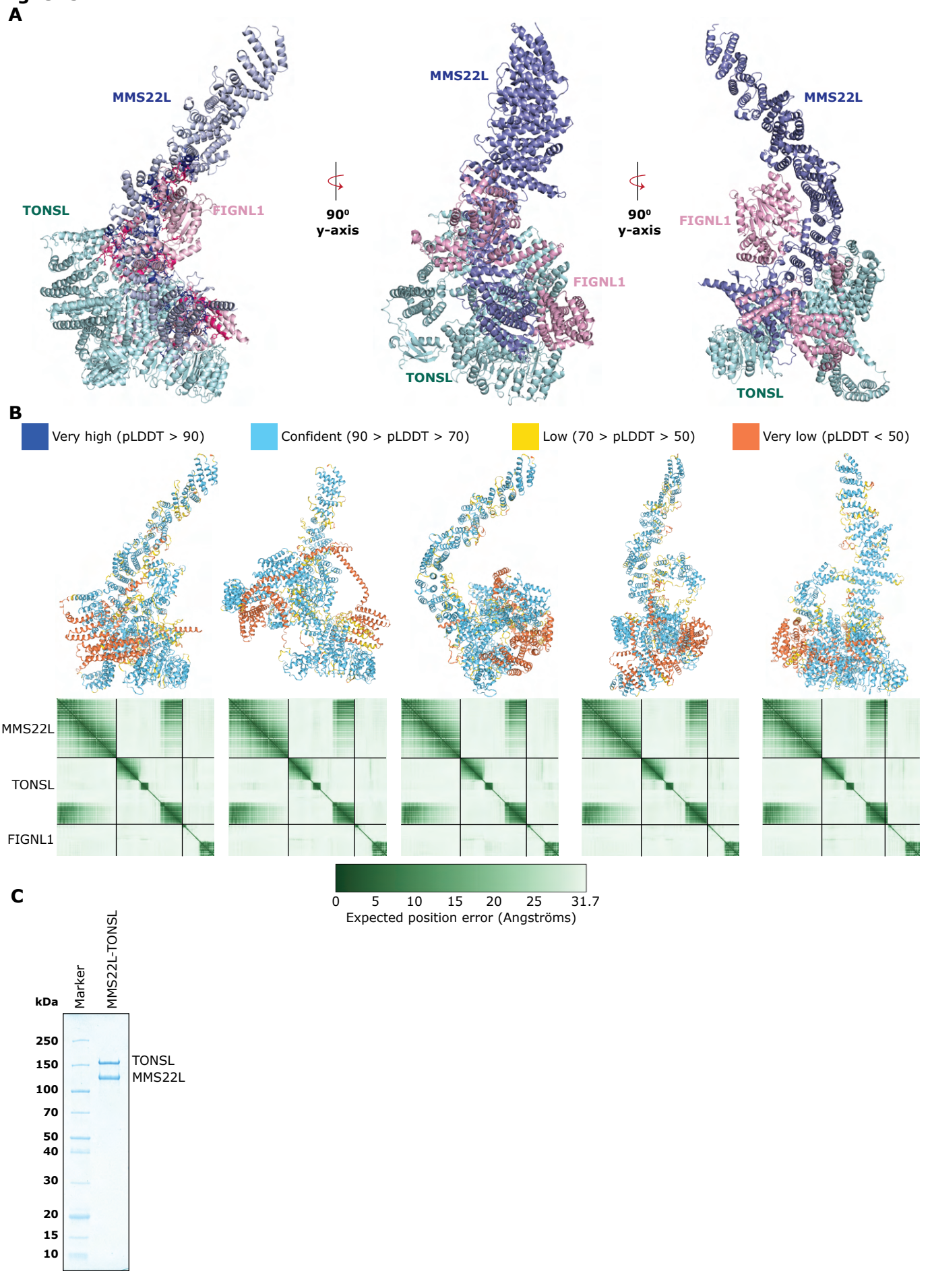
A
MMS22L
TONSL
FIGNL1
90⁰
y-axis
MMS22L
FIGNL1
TONSL
90⁰
y-axis
MMS22L
FIGNL1
TONSL
B
Very high (pLDDT > 90)
Confident (90 > pLDDT > 70)
Low (70 > pLDDT > 50)
Very low (pLDDT < 50)
MMS22L
TONSL
FIGNL1
0
5
10
15
20
25
31.7
Expected position error (Angströms)
C
kDa
Marker
MMS22L-TONSL
250
150
100
70
50
40
30
20
15
10
TONSL
MMS22L

fig. S15: FIGNL1 monomer predicted interaction with the MMS22L-TONSL heterodimer

(A) Cartoon representation of FIGNL1-MMS22L-TONSL ternary complex shown in three different orientations [FIGNL1 (Light Pink), MMS22L (Slate), and TONSL (Cyan)].

(B) Top: The five predicted models of FIGNL1-MMS22L-TONSL complex colored by pLDDT values, which measures the confidence of atomic positions relative to its neighboring atoms. Bottom: The Predicted aligned error (PAE) plots, displaying long-range interactions, for the five models generated using AF3 for the FIGNL1-MMS22L-TONSL complex.

(C) Recombinant MMS22L and TONSL heterodimer purified from baculovirus infected insect *Sf*9 cells. Purified proteins were separated on a polyacrylamide gel and stained with Coomassie blue.

fig. S16

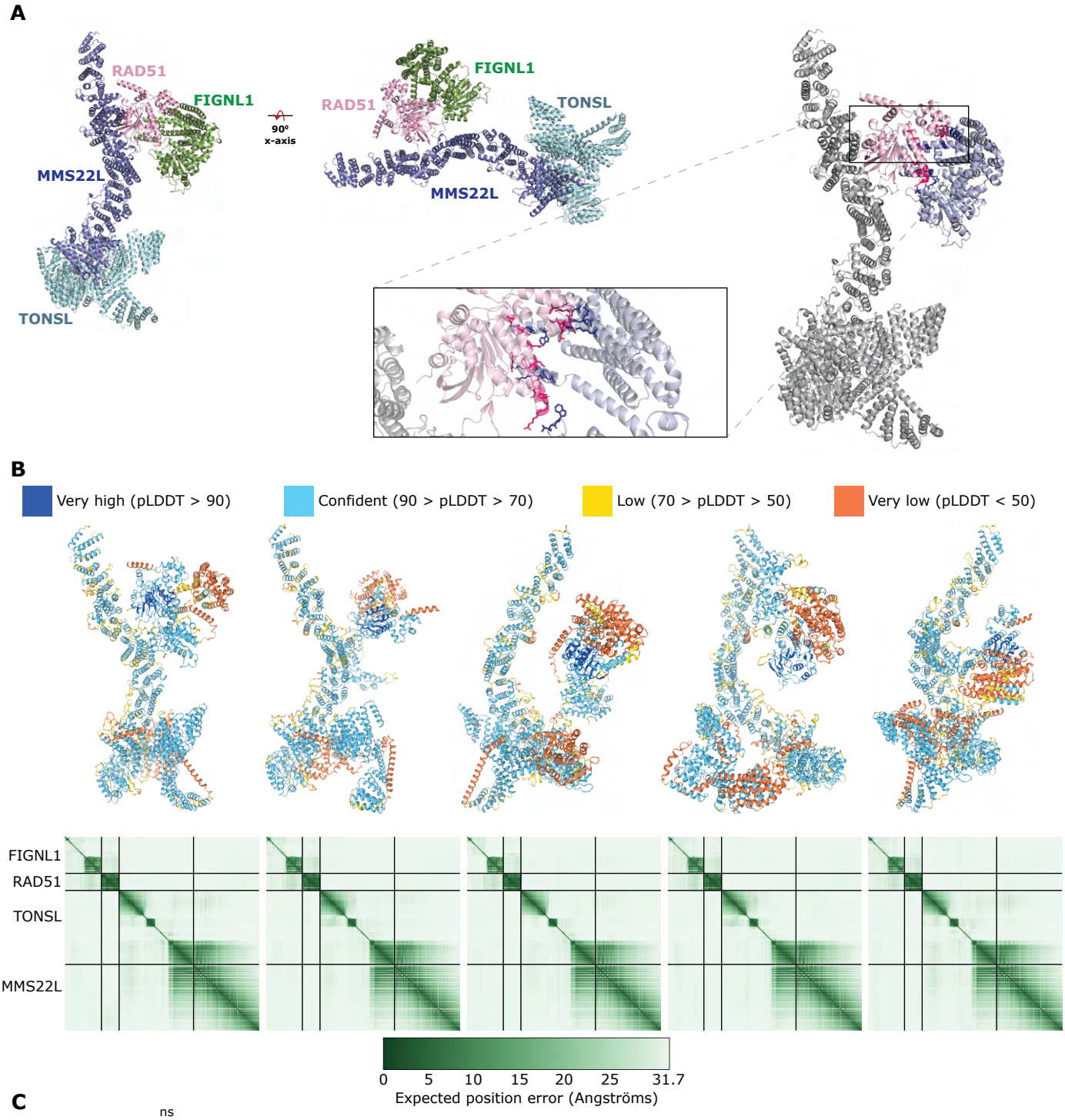
A
RAD51
FIGNL1
MMS22L
TONSL
90°
x-axis
B
Very high (pLDDT > 90)
Confident (90 > pLDDT > 70)
Low (70 > pLDDT > 50)
Very low (pLDDT < 50)
FIGNL1
RAD51
TONSL
MMS22L
0
5
10
15
20
25
31.7
Expected position error (Angströms)
C
ns
RAD51 bound to FIGNL1
2.5
2.0
1.5
1.0
0.5
0.0
GST-FIGNL1-dNLS
RAD51 K133R
MMS22L-TONSL
ssDNA
kDa
100
40
150
GST-FIGNL1-dNLS
RAD51 K133R
MMS22L (His)

fig. S16: FIGNL1 monomer predicted interaction with the MMS22L-TONSL heterodimer and RAD51

(A) Cartoon representation of FIGNL1/RAD51/MMS22L-TONSL quaternary complex shown in two different orientations [FIGNL1 (Green), RAD51 (Light Pink), MMS22L (Slate), and TONSL (Cyan)]. The inset shows the interacting surface of FIGNL1 and RAD51 colored in Dark blue and Pink respectively, with the non-interacting MMS22L/TONSL shown in grey.

(B) Top: The five predicted models of FIGNL1/RAD51/MMS22L-TONSL complex colored by pLDDT values, which measures the confidence of atomic positions relative to its neighboring atoms. Bottom: The Predicted aligned error (PAE) plots, displaying long-range interactions, for the five models generated using AF3 for the FIGNL1-MMS22L-TONSL-RAD51 complex.

(C) Percentage quantification showing the band intensity of the bound RAD51-K133R to FIGNL1-dNLS in the presence or absence of MMS22L and ssDNA; error bars are indicative of mean±SEM from 8 independent experiments (n=8). P-values from Ordinary One-Way ANOVA comparing between indicated groups. Western blot results indicate the interactions between the proteins involved.

fig. S17

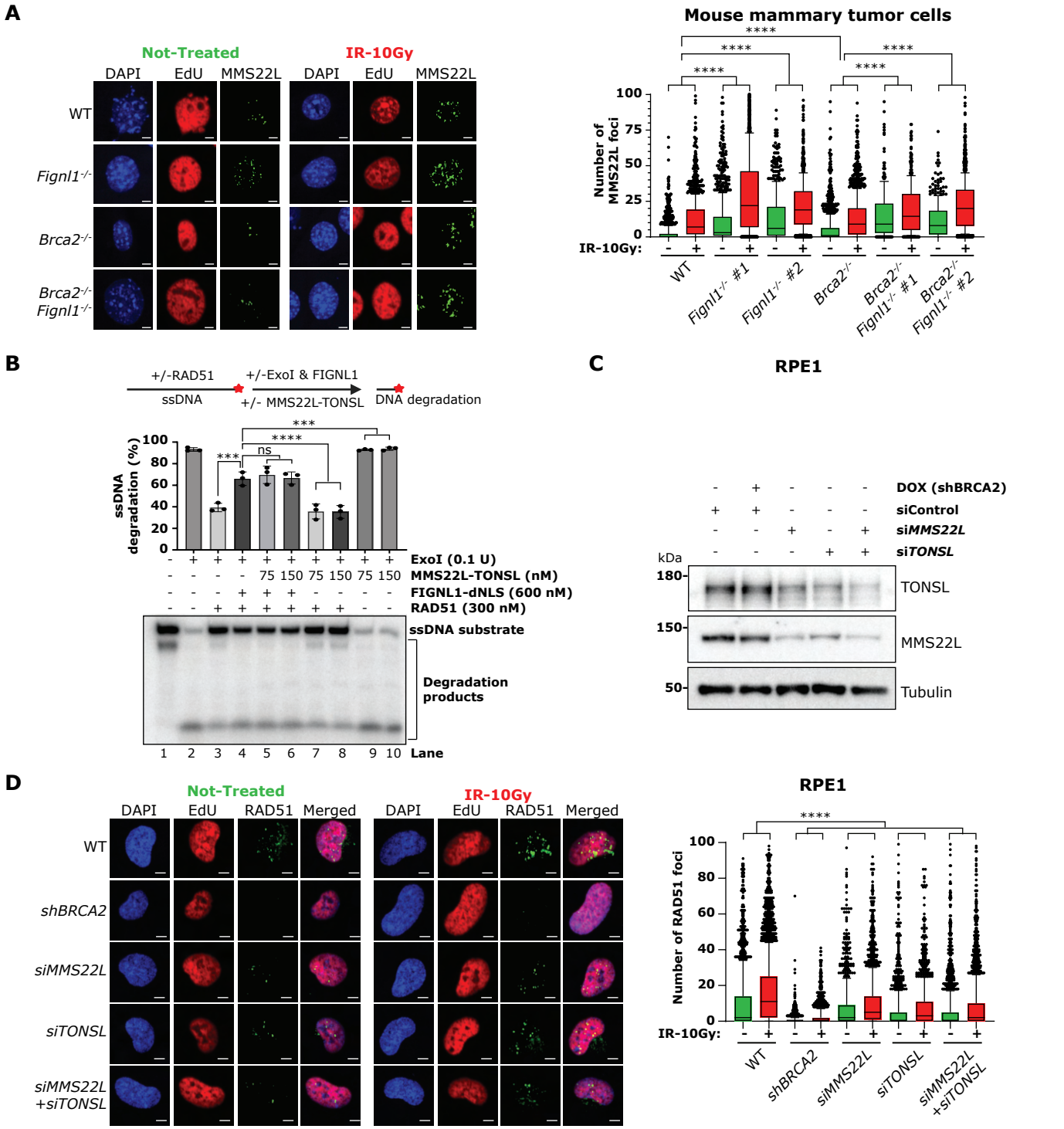
A
Not-Treated
IR-10Gy
DAPI
EdU
MMS22L
WT
Fignl1-/-
Brca2-/-
Brca2-/- Fignl1-/-
Mouse mammary tumor cells
Number of MMS22L foci
IR-10Gy:
WT
Fignl1-/- #1
Fignl1-/- #2
Brca2-/-
Brca2-/- Fignl1-/- #1
Brca2-/- Fignl1-/- #2
B
+/-RAD51
ssDNA
+/-ExoI & FIGNL1
+/- MMS22L-TONSL
DNA degradation
ssDNA degradation (%)
ExoI (0.1 U)
MMS22L-TONSL (nM)
FIGNL1-dNLS (600 nM)
RAD51 (300 nM)
ssDNA substrate
Degradation products
Lane
C
RPE1
DOX (shBRCA2)
siControl
siMMS22L
siTONSL
kDa
TONSL
MMS22L
Tubulin
D
Not-Treated
IR-10Gy
DAPI
EdU
RAD51
Merged
WT
shBRCA2
siMMS22L
siTONSL
siMMS22L +siTONSL
RPE1
Number of RAD51 foci
IR-10Gy:
E
RPE1
WT
FIGNL1-/-
DOX (shBRCA2)
siControl
siMMS22L
siTONSL
TONSL
MMS22L
FIGNL1
Tubulin
F
U2-OS (DR-GFP)
siControl
siBRCA2
siFIGNL1
siMMS22L
siTONSL
ISceI
BRCA2
TONSL
MMS22L
FIGNL1
Tubulin
G
Mouse mammary tumor cells
WT
Brca2-/-
Brca2-/- Fignl1-/-
Brca2-/- Fignl1-/- +shMms22l
MMS22L
Tubulin

fig. S17: Validation of MMS22L-TONSL levels in the presence or absence of BRCA2 and FIGNL1

(A) Left: Representative high-content, automated IF images showing EdU and MMS22L foci in not-treated and ionizing radiation treated cells; scale bar: 5 µm. Right: Automated QIBC plots of the MMS22L foci per nucleus; scatter box plot showing the foci distribution between 10-90th percentile from 1,500 cells (experiment was repeated 3 times). P-values from Mann-Whitney test (two-tailed) comparing between indicated groups (****: <0.0001).

(B) Top: Schematics of the ssDNA protection assay showing the protection efficiency of 300 nM RAD51 against degradation by ExoI nuclease in the presence of 600 nM FIGNL1 and increasing concentrations of MMS22L-TONSL. Bottom: Quantification of the ssDNA degradation; error bars are indicative of mean±SEM from 3 independent experiments (n=3). P-values from Ordinary One-Way ANOVA comparing between indicated groups (***: <0.001; ****: <0.0001). The red asterisk indicates the position of the radioactive label.

(C) Representative western blot analysis showing the levels of MMS22L and TONSL in human RPE1 cells used for RAD51-IF.

(D) Left: Representative high-content, automated IF images showing EdU and RAD51 foci in not-treated and ionizing radiation treated cells; scale bar: 5 µm. Right: Automated QIBC plots of the RAD51 foci per nucleus; scatter box plot showing the foci distribution between 10-90th percentile from 1,500 cells (experiment was repeated 3 times). P-values from Mann-Whitney test (two-tailed) comparing between indicated groups (****: <0.0001).

(E) Representative western blot analysis showing the levels of MMS22L, TONSL and FIGNL1 in human RPE1 cells used for RAD51-IF and genomic stability assay.

(F) Western blot analysis showing the levels of FIGNL1, BRCA2, MMS22L and TONSL from the corresponding cells used for HR assay.

(G) Western blot analysis showing the levels of MMS22L from the corresponding cells used for clonogenic assay in Figure 6F in mouse mammary tumor cells.

fig. S18

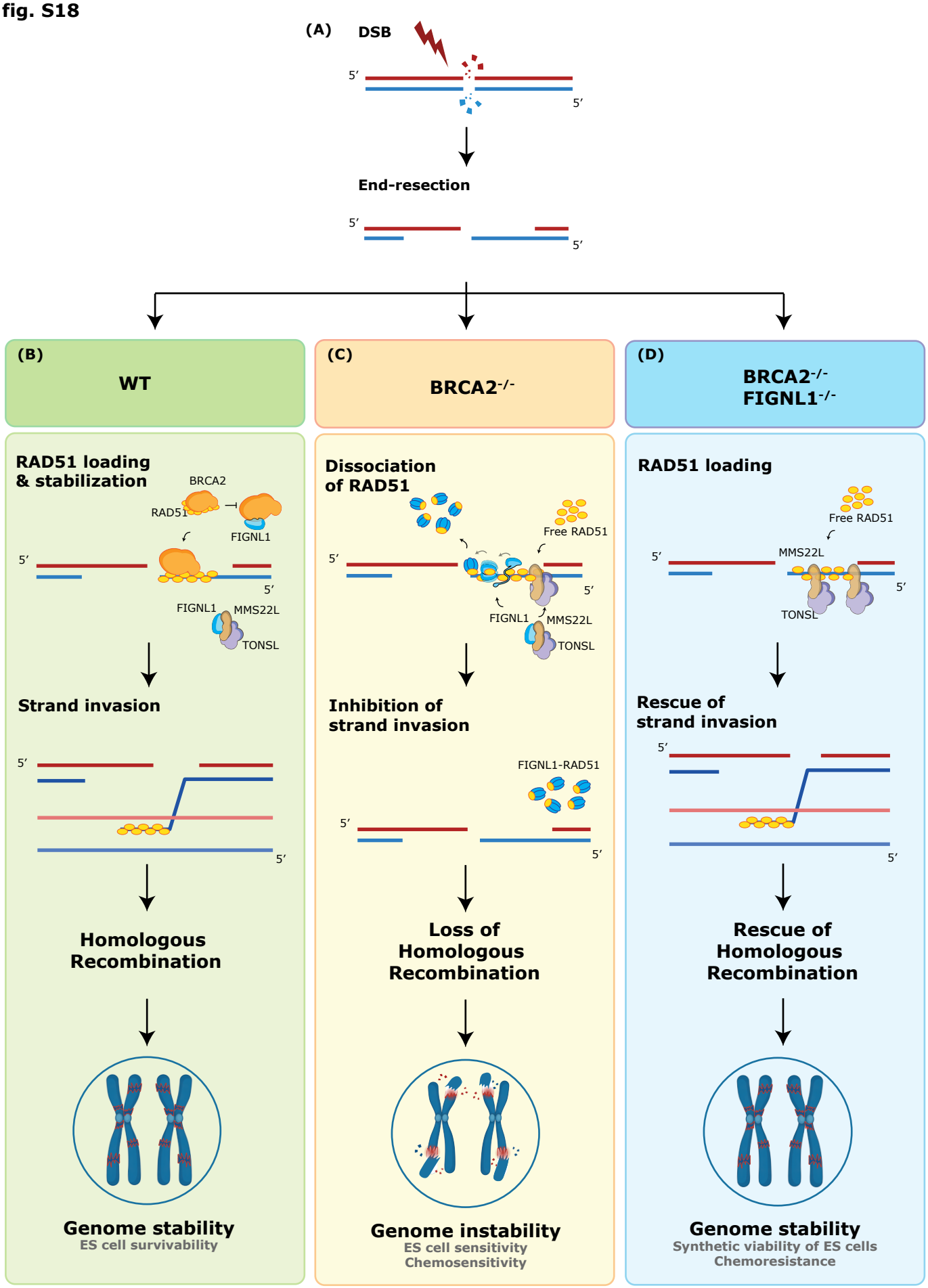
(A)
DSB
5′
5′
End-resection
5′
5′
(B)
WT
RAD51 loading
& stabilization
BRCA2
RAD51
FIGNL1
5′
5′
FIGNL1
MMS22L
TONSL
Strand invasion
5′
5′
Homologous
Recombination
Genome stability
ES cell survivability
(C)
BRCA2-/-
Dissociation
of RAD51
Free RAD51
5′
5′
FIGNL1
MMS22L
TONSL
Inhibition of
strand invasion
FIGNL1-RAD51
5′
5′
Loss of
Homologous
Recombination
Genome instability
ES cell sensitivity
Chemosensitivity
(D)
BRCA2-/-
FIGNL1-/-
RAD51 loading
Free RAD51
5′
MMS22L
5′
TONSL
Rescue of
strand invasion
5′
5′
Rescue of
Homologous
Recombination
Genome stability
Synthetic viability of ES cells
Chemoresistance

fig. S18: Proposed model of the interplay between FIGNL1, BRCA2 and MMS22L-TONSL

(A) Upon induction of DSBs, the break ends are resected in the 5'to 3' direction, exposing a 3'ssDNA overhang.

(B) BRCA2 plays a key role by loading and stabilizing RAD51 on the resected single-stranded ssDNA, facilitating RAD51-mediated strand invasion. Besides facilitating RAD51 loading, BRCA2 is crucial for maintaining RAD51 filament stability by preventing its premature dissociation caused by the anti-recombinase FIGNL1. In the presence of BRCA2, the limited availability of free RAD51 allows the monomeric FIGNL1 to interact with the MMS22L-TONSL complex. This interaction ensures that RAD51 levels are finely regulated during HR in wild-type cells.

(C) However, in the absence of BRCA2, the elevated concentration of free RAD51 results in the dissociation of the FIGNL1-MMS22L-TONSL complex. FIGNL1 in its monomeric form interacts with RAD51 via its FRBD region. This allows the FIGNL1 to transiently form hexameric structure, which dissociates RAD51 from the ssDNA. This could lead to dynamic cycles of RAD51 loading and dissociation between the MMS22L-TONSL complex and FIGNL1, ultimately causing RAD51 loading defect and increased genome instability.

(D) The loss of FIGNL1 in BRCA2-deficient cells restores productive RAD51 loading by the MMS22L-TONSL complex and potentially other associated factors, rescuing HR efficiency, which in turn restores the genome instability observed upon loss of BRCA2.

table S1: Intermolecular interactions between FIGNL1 monomers in the presence of Mg^{2+}/ATP complex modelled using AlphaFold3.

Complex	**Interacting domains**		
FIGNL1 hexamer-Mg^{2+}/ATP complex.	**FIGNL1 Chain A**	**FIGNL1 Chain B/F**	**Mg^{2+}/ATP**
	NLS	Loop before/after FRBD; ATPase; V domain	
	FRBD	----	
	Loop before/after FRBD	NLS; ATPase; V domain	
	ATPase	NLS; Loop before/after FRBD; ATPase; V domain	ATPase
	V domain	NLS; Loop before/after FRBD; ATPase	

table S2. Summary of the details of interacting domains/residues for FIGNL1 hexamer-RAD51 complex in the presence of $Mg2^{+}$/ATP modelled using AlphaFold3.

Complex	**Binding energy (kcal/mol)**	**Interacting domains**	
		FIGNL1	**RAD51**
FIGNL1-RAD51	-15.9	FRBD region (321-349);	N-terminal α-helix (29-47, 63-73); Loops between Walker motifs (202-211) -
		Pore loop 1 (471-476); Pore loop 2 (514-516)	N-terminal (1-11)

table S3. Summary of the details of interacting domains/residues for FIGNL1 FRBD- RAD51 dimer complex modelled using AlphaFold2 multimer.

Complex	**Binding energy (kcal/mol)**	**Interacting domains**		
FIGNL1 FRBD-RAD51 Dimer	-10.2	**FRBD**	**RAD51 CHAIN A**	**RAD51 CHAIN B**
		FRBD N-terminal (294-324)	N-terminal flexible linker (86-98); Loops between Walker motifs (157-211)	---
		FRBD C-terminal (328-345)	---	Loops between Walker motifs (146-216)

table S4: Predictome interacting partners of FIGNL1 involved in genome maintenance

Sl. No.	Name	pLDDT	Sl. No.	Name	pLDDT	Sl. No.	Name	pLDDT
1	FIRRM	89.6	37	RMI2	72.8	73	REV1	67.8
2	POLD3	87.4	38	TIMELESS	72.7	74	RAD18	67.5
3	RAD51	86.3	39	RECQL	72.6	75	PALB2	67.5
4	CCNA2	82	40	DDB1	72.5	76	FANCI	66.7
5	DMC1	81.7	41	DNA2	72.4	77	MCMBP	66.7
6	PCNA	81.3	42	NEIL1	72.4	78	SLF1	66.5
7	RAD51B	81.1	43	FANCL	72.1	79	MAD2L2	66.4
8	FANCC	79.6	44	HELQ	72	80	MUS81	66.4
9	RAD51C	79.2	45	AFG2A	72	81	POLD1	66.3
10	XRCC3	78.9	46	STAG2	71.8	82	RPA3	65.8
11	POLL	78.9	47	FANCD2	71.7	83	BARD1	65.5
12	FIGNL1	78.8	48	PRIM2	71.7	84	ETAA1	65.2
13	CTC1	78.7	49	AFG2B	71.5	85	TP53BP1	65.1
14	ABRAXAS1	77.8	50	PDS5B	71.5	86	SSRP1	65.1
15	GINS3	77.5	51	ERCC3	71.4	87	MCM6	64.9
16	ESCO1	77.5	52	SMC5	71	88	RNASEH2C	64.5
17	CHTF8	76.8	53	RAD52	70.9	89	PDS5A	64.2
18	RFC2	76.7	54	MMS22L	70.7	90	PRIMPOL	63.7
19	ORC5	76.1	55	TOP1	70.7	91	RFC3	63.5
20	POLA2	76	56	UBE2T	70.5	92	XPC	63.5
21	EXO5	75.7	57	MCM9	70.1	93	WAPL	62
22	RAD51D	75	58	SUPT16H	70	94	ATR	61.5
23	SHLD3	75	59	GINS1	69.9	95	MCM7	61.4
24	TERF1	74.7	60	UBE2B	69.9	96	MSH6	60.1
25	DTL	74.5	61	CDK2	69.5	97	DCLRE1A	59.7
26	WRAP53	74.5	62	CDT1	69.4	98	EME1	58.9
27	STN1	74.1	63	SETMAR	69.4	99	GMNN	58.5
28	GINS2	74	64	ERCC4	69.1	100	TICRR	57.4
29	MAU2	74	65	RECQL4	69	101	SLX4	56.9
30	ORC6	73.9	66	FAAP100	68.7	102	MLH3	55.8
31	ORC1	73.9	67	RFC1	68.6	103	FAAP20	54.8
32	BLM	73.3	68	TDP2	68.5	104	FAN1	54.1
33	TIPIN	73.3	69	TONSL	68.4	105	TTF2	53.4
34	CHTF18	73.1	70	DBF4B	68.3	106	RNASEH2B	52.5
35	TERF2	73.1	71	MSH3	68.2			
36	CHAF1B	72.8	72	POLE	67.8			

table S5. Summary of the details of interacting domains/residues for monomeric FIGNL1-MMS22L/TONSL complex modelled using AlphaFold3.

Complex	**Binding energy (kcal/mol)**	**Interacting domains**		
FIGNL1-MMS22L-TONSL	-23.0	**FIGNL1**	**MMS22L**	**TONSL**
		NLS (35-59, 64-100)	N-terminal (51-68, 230-233)	---
		FRBD (296-351)	Mid Region (497-526)	---
		ATPase (Pore loops) (473-475, 513-515)	C-terminal (625-738, 840-851)	---

table S6. Summary of the binding energy and the details of interacting domains/residues for monomeric FIGNL1-RAD51-MMS22L/TONSL complex modelled using AlphaFold3.

Complex	**Binding energy (kcal/mol)**	**Interacting domains**		
FIGNL1-RAD51-MMS22L-TONSL	-7.5	**FIGNL1**	**RAD51**	**MMS22L/TONSL**
		NLS (106-117)	N-terminal α-helix (61-66)	---
		FRBD (296-339)	Loops between Walker motifs (193-210); Loop 2 present after Walker B motif (231-232)	----
		ATPase (Pore loops) (474-475, 513-519)	Loop 2 present after Walker B motif (235-239)	----

4. Discussion and outlook

DNA damage is an unavoidable consequence of cellular metabolism. However, cells have evolved complex DNA repair pathways that maintain genomic integrity and cellular viability. Double-strand breaks are among the most deleterious types of DNA damage and are clinically relevant in fields such as oncology and genome editing. In oncology, targeted therapies aim to disrupt DNA repair pathways on which cancer cells depend, whereas genome editing requires DNA repair to be directed toward a desired pathway. The ability to manipulate DSB repair relies heavily on understanding the balance between the two main pathways, NHEJ and HR, and their underlying molecular mechanisms. Our data shed light on DSB repair pathway choice and uncover the processes and factors involved in pathway commitment. Although HR proceeds through distinct stages, these steps are mechanistically interconnected. In this thesis, we also investigated how the 53BP1 antagonist and strand exchange factor BRCA1-BARD1 modulates DNA end resection. Lastly, we examined the anti-recombinases that regulate strand invasion and their interplay with pro-HR factors. Our results suggest that FIGNL1 plays a significant role in inhibiting strand exchange and acts antagonistically to BRCA2.

4.1. The sequential model of NHEJ and HR

DNA end resection stands at the crossroads between the two main DSB repair pathways: HR and NHEJ. Canonically, it was thought that once MRX-pSae2/MRN-pCtIP-mediated resection occurs, NHEJ is inhibited and repair is committed to HR. Conversely, if end-joining is allowed to begin following the rapid recruitment of Ku to DNA ends, resection is prevented and repair is directed toward the more error-prone NHEJ (Biehs et al., 2017, Shibata et al., 2014). Recent findings have challenged this model, revealing that the early stages of each process exist in a delicate balance. For instance, CST-mediated fill-in synthesis by Polα can slow down and potentially reverse resection, allowing NHEJ a second chance (Mirman et al., 2018, King et al., 2025). Furthermore, short-range resection can still process Ku-bound ends, indicating that the recruitment of the end-joining ensemble at the ends is not sufficient to block HR (Wang et al., 2017, Reginato et al., 2017). The rapid kinetics of NHEJ and the ability of MRX-pSae2 to process Ku-blocked DNA ends suggest that repair pathway choice and commitment are not solely determined by competition between the initial steps of each pathway.

We performed *in vitro* reconstitution assays with recombinant proteins to gain mechanistic insight into how MRX-pSae2 removes Ku from DNA ends. Our observations are consistent with a sequential model of repair pathway choice. In this model, the NHEJ machinery is rapidly recruited to DSBs, and first attempts repair by synapsing the DNA ends. We showed that, while none of the end-joining factors directly inhibit short-range resection by MRX-pSae2, synapsis masks the DNA ends and renders them inaccessible to resection, similarly to Cas9- or Rap1-bound DNA ends (Mattarocci et al., 2026, Reginato et al., 2024). This provides a window of opportunity for ligation to occur and,

therefore, for NHEJ to be completed if the ends are compatible. Synapsis is short-lived, and the synaptic complex is transient, undergoing repeated on–off cycles (Wang et al., 2018, Graham et al., 2016). We propose that resection is activated during the "off" phase at DNA ends that are incompatible with ligation, thereby directing DSB repair to HR.

Previous work revealed that MRX-pSae2 can process a wide range of protein-bound DNA ends. The endonucleolytic cleavage by MRX-pSae2 internal to the protein block is well established both *in vitro* and in high–resolution resection assays *in vivo* (Reginato et al., 2017, Cannavo and Cejka, 2014, Gnugge et al., 2023, Wang et al., 2017). The subsequent 3' to 5' exonuclease activity of the complex has also been characterized and was thought to play a key role in the removal of protein blocks, including Ku, from DNA ends, although direct evidence for this role is currently lacking (Gobbini et al., 2018, Mimitou and Symington, 2010, Langerak et al., 2011, Myler et al., 2017, Deshpande et al., 2023, Deshpande et al., 2020).

We showed that while the initial endonucleolytic activity of MRX-pSae2 is highly efficient, the complex alone is insufficient to displace Ku. We identified RPA as a co-factor of SRR by stimulating the exonuclease activity of MRX-pSae2. RPA acts *in cis* by binding to the ssDNA generated during short-range resection. Accordingly, we demonstrate that the ssDNA-binding activity of RPA is important for its stimulatory effect on SRR.

We found that MRX interacts with RPA through the DBD-F of Rfa1, as previously reported (Seeber et al., 2016, Robison et al., 2004, Oakley et al., 2009), and propose that this interaction plays a recruitment role during resection by maintaining MRX at DNA ends. Our data reveal that pSae2 is indispensable for the stimulatory effect of RPA on MRX and that pSae2 also interacts with the DBD-F domain of RPA. Deletion of the DBD-F in Rfa1 did not affect the affinity of RPA for ssDNA but significantly reduced the interaction between RPA and the short-range resection factors. Unexpectedly, the truncated form of RPA was only mildly impaired in stimulating the exonuclease of MRX-pSae2. Unlike in the case of Dna2, the Rfa1 subunit was not sufficient to activate the MRX exonuclease, suggesting that the integrity of the RPA trimer is necessary for its effect on Ku removal. Interestingly, deletion of Rfa3 abrogated the stimulatory effect of RPA on MRX-pSae2, suggesting that the transient functional interaction lies in this smallest subunit of RPA.

We propose that the DBD-F domain has a scaffolding function by allowing MRX and pSae2 to co-localize at the DNA end but is functionally dispensable, as observed with Dna2 (Acharya et al., 2021). The functionally relevant contacts between RPA and MRX-pSae2 are likely located on Rfa3 and transient to allow the resection machinery to easily translocate towards the Ku-bound DNA end as RPA is progressively loaded on the resected DNA.

Lastly, we noted that Ku-blocked DNA resected in the absence of RPA can still largely undergo NHEJ. This novel role of RPA in Ku removal might contribute to the RPA-dependent suppression of NHEJ observed in genetic experiments in yeast. Together,

these findings support a model in which pathway choice is not governed by a single irreversible decision but instead emerges from a dynamic competition between end protection by synapsis and RPA-mediated Ku removal during short-range resection.

Despite the biochemical evidence provided, this study lacks cellular data. Deletion of any RPA subunit is lethal in yeast and, as such, makes the RPA-degron system the only possibility for studying this interplay *in vivo*. Furthermore, to isolate the impact of RPA on short-range resection, the strains used would need to lack long-range resection (exo1Δsgs1Δ). The synthetic sickness of this genetic combination makes such experiments difficult. Moreover, *in silico* modelling of the interaction between RPA and Sae2 or RPA and MRX did not yield any relevant interaction points. This could be due to the phosphorylation and oligomeric state of Sae2, which makes analysis difficult. Structural analysis of the full-length MRX complex is also not available, further complicating *in silico* mapping and modelling. Additionally, the truncations of RPA characterized in this study could not be expanded due to the need for maintaining the ssDNA-binding activity of the complex. Lastly, we identify Rfa3 as the subunit required for the functional interaction between RPA and the short-range resection machinery, making it a potential target for AlphaFold modelling and *in vivo* characterization, especially in the context of Ku overexpression in yeast.

Several additional aspects remain unexplored. Synapsis requires the presence of MRX at DNA ends (Zhang and Paull, 2005, Schiestl et al., 1993, Moore and Haber, 1996, Chen et al., 2001, Chen et al., 2005). Since MRX is also a resection factor, an important question is how its nuclease activity is restrained in this context. Phosphorylation of Sae2 is an important cell-cycle regulatory mechanism of HR (Yu et al., 2019, Fu et al., 2014, Huertas et al., 2008) and its co-localization with MRX may mark the transition from synapsis to resection initiation. One open question is whether a failure in ligation could signal the recruitment of Sae2. Additionally, Xrs2 is functionally dispensable for resection (Reginato et al., 2017, Cannavo and Cejka, 2014, Wang et al., 2017, Oh et al., 2016), while critically important for NHEJ (Matsuzaki et al., 2008, Palmbos et al., 2005). As Xrs2 is also subject to phosphorylation (Huang et al., 2016, D'Amours and Jackson, 2001), post-translational modification could modulate its role in end-joining and regulate synapsis stability, allowing synapsis to be disengaged when DNA ends are not ligatable.

RPA also undergoes several post-translational modifications, with the N-terminus of Rfa2 representing an important target for multiple kinases (Binz et al., 2003, Yates et al., 2023, Nuss et al., 2005). A role for RPA phosphorylation in modulating resection has been proposed (Soniat et al., 2019), but the molecular mechanism behind it has not been thoroughly investigated. The interaction between RPA and Sae2 could indicate an additional level of coordination between short-range and long-range resection. In humans, CtIP stimulates the recruitment and function of DNA2 (Hoa et al., 2015, Daley et al., 2017, Ceppi et al., 2020). While, in yeast, Sae2 can activate Exo1 and Dna2-mediated resection, a direct interaction has not been observed (Daley et al., 2017,

Nicolette et al., 2010). This raises the possibility that RPA facilitates the handover of Sae2 from the short-range resection machinery to Dna2-mediated long-range resection.

In humans, an additional layer of complexity is provided by the presence of DNA-PKcs. Preliminary experiments show that, although RPA can stimulate the exonuclease of MRN-pCtIP *in vitro*, the observed effect is weaker than in yeast and may not be a major driver of KU-DNA-PKcs removal. However, the nuclease activity of MRE11 was reported to be required for this process (Myler et al., 2017). A speculative model is that MRN-pCtIP first nicks the DNA ends past the DNA-PK complex, thereby providing an entry point for WRN. Subsequently, KU stimulates the 3' to 5' exonuclease activity of WRN (Zahid et al., 2026), leading to DNA-PK displacement from DNA.

4.2. The role of BRCA1-BARD1 in long-range resection

Early observations that BRCA1 interacts and colocalizes with RAD51 at ionizing radiation-induced nuclear foci provided the first evidence linking BRCA1 to HR (Scully et al., 1997). Furthermore, ablation of either the *BRCA1* or the *BARD1* gene in mouse and human cells decreases the formation of DNA damage-induced RAD51 foci and impairs HR, suggesting that the complex contributes to RAD51 loading onto resected DNA (Zhao et al., 2017, McCarthy et al., 2003, Huber et al., 2001, Bhattacharyya et al., 2000). Among the BRCA1–BARD1 interaction partners are MRN and CtIP, two factors involved in DNA end resection, implicating the complex in the initial stages of HR (Whelan and Rothenberg, 2021, Chen et al., 2008, Wang, 2012, Zhong et al., 1999).

Our data, generated using reconstitution assays with recombinant proteins, provide the first *in vitro* evidence that BRCA1-BARD1 directly stimulates long-range resection. We showed that BRCA1-BARD1 stimulates the DNA2-dependent branch of LRR by interacting with WRN and promoting its helicase activity. Reconstitution of the BRCA1-C complex, which includes MRN and CtIP, further enhanced resection by DNA2-WRN, consistent with the effect of CtIP on DNA2 (Ceppi et al., 2020, Daley et al., 2017). Disruption of either the CtIP-interacting BRCT domain or BARD1-interacting RING domain of BRCA1 abolished this synergistic effect of the BRCA1-C complex.

In silico modelling revealed that the BRCA1 region spanning residues 931-1171 is required for its stimulatory activity, while the minimal functional BARD1 comprises residues 1-261, encompassing the N-terminal RING domain and the adjacent RAD51-interacting region. In contrast, only the helicase core domain of WRN is required for BRCA1–BARD1-mediated stimulation of its unwinding activity.

The assembly of the BRCA1-C complex is tightly regulated during the cell cycle and several of its components are targets of cell-cycle-dependent phosphorylation (Chen et al., 2008, Wang et al., 2013, Huertas and Jackson, 2009, Peterson et al., 2011). We

demonstrated that the phosphorylation state of both CtIP and BRCA1-BARD1 are crucial for the functional integrity of the BRCA1-C complex.

I investigated the effect of BRCA1-BARD1 on the EXO1-dependent branch of LRR. Our data indicate that BRCA1-BARD1 stimulates EXO1 and requires BRCA1 residues 931-1171 and the C-terminal unstructured region of EXO1. Unlike the DNA2-WRN pathway, this stimulatory effect was not further augmented by MRN or CtIP. Lastly, BRCA1-BARD1 does not appear to be involved in short-range resection, as it did not stimulate the MRN-pCtIP nuclease activity.

We propose that the BRCA1-C complex contributes to counteracting the 53BP1-mediated inhibition of end resection. Since BRCA1-BARD1 also forms a complex with BRCA2-PALB2 (Zhang et al., 2009, Sy et al., 2009), we speculate that this supercomplex might be involved in regulating and coupling the initial stages of HR. This model is consistent with previous work showing that BRCA2 is important for the early recruitment of EXO1 during DNA end resection (Zhang et al., 2015) .

The work done in this study relies heavily on reconstituted biochemical systems. Although the conclusions of this study benefit from cellular validation, further *in vivo* exploration of disease-associated BRCA1-BARD1 variants is required. The study also employs naked DNA and therefore does not address the interaction between BRCA1-BARD1 and nucleosomes in promoting long-range resection.

An open question is how the phosphorylation of BRCA1-BARD1 regulates its role in HR. Preliminary data reveal that several residues in both BRCA1 and BARD1 are kinase targets, and that hyperphosphorylation and dephosphorylation of BRCA1–BARD1 abrogate its stimulatory effect on DNA2-WRN. This observation suggests that BRCA1-BARD1 function may depend on a specific phosphorylation pattern rather than phosphorylation per se. Furthermore, a direct effect of BRCA1-BARD1 on MRN-pCtIP-mediated short-range resection cannot be fully ruled out and might also be phosphorylation-dependent. Moreover, the role of the BRCA1 complex in fork protection is unclear. A study shows that BRCA1 phosphorylation at S114 and PIN1-mediated isomerization of BRCA1-BARD1 are required for fork protection (Daza-Martin et al., 2019). How these post-translational modifications alter the balance between RAD51 loading and stimulation of DNA2-WRN requires further biochemical investigation.

4.3. The role of the FIGNL1 anti-recombinase in RAD51 filament dynamics

BRCA2-deficient cells are defective in RAD51 loading and show increased genomic instability. However, excessive loading of RAD51 on chromatin is also deleterious as it can lead to unlicensed recombination events (Richardson et al., 2004). Therefore, cells

need to strike a delicate balance at the level of RAD51 loading and RAD51-ssDNA filament dynamics. This regulation involves the action of anti-recombinases, including FIGNL1, which dissociate RAD51 from DNA and thereby counteract the activity of BRCA2 (Carver and Zhang, 2021).

Data from our collaborators indicate that loss of FIGNL1 in BRCA2-deficient cells restores viability and genomic stability and confers resistance to PARP inhibitors and cisplatin. This suggests that FIGNL1 is a major contributor to RAD51 homeostasis through filament disassembly. This observation led our collaborators to contact our group for *in vitro* biochemical characterization of the effect of FIGNL1 in RAD51 filament stability.

FIGNL1 directly displaces RAD51 from both single-stranded and double-stranded DNA (Ito et al., 2023). We show that this mechanism underlies FIGNL1-mediated inhibition of strand exchange. Our experiments suggest that FIGNL1 does not act by modulating the ATPase activity of RAD51, which is crucial for nucleoprotein filament stability, but instead may physically strip RAD51 from ssDNA via its translocase activity.

FIGNL1 interacts with RAD51 through its FRBD domain (Yuan and Chen, 2013). As a member of the AAA+ ATPase family, FIGNL1 oligomerizes and is functionally active as a hexamer (Carver et al., 2025). Our experiments revealed the RAD51-FIGNL1 interaction to be predominantly monomer-to-monomer with transient associations between the FIGNL1 hexamer and RAD51 monomers. Disrupting either the RAD51-binding interfaces or the ATPase activity of FIGNL1 abolished its dissociation activity and its inhibitory effect on RAD51-ssDNA filament stability and strand exchange.

In the absence of both BRCA2 and FIGNL1, strand exchange becomes reliant on MMS22L-TONSL. Further loss of this complex impairs DNA damage-induced RAD51 foci formation and results in genomic instability. We showed that FIGNL1 can directly interact with MMS22L-TONSL through the FRBD domain. However, structural modelling and pull-down experiments revealed that RAD51 outcompetes MMS22L-TONSL for binding to FIGNL1.

We speculate that in BRCA2-proficient cells, MMS22L-TONSL interacts with and regulates FIGNL1 activity. However, in BRCA2-deficient cells, MMS22L-TONSL is unable to efficiently antagonize the anti-recombinase activity of FIGNL1, which disrupts RAD51-ssDNA filaments and severely impairs HR. In the absence of both BRCA2 and FIGNL1, MMS22L-TNOSL acts as a back-up mechanism to ensure RAD51 loading and enable successful HR. This work has potential implications for oncology, identifying MMS22L-TONSL as a compensatory pathway in BRCA2- and FIGNL1-deficient cancer cells and suggesting it as a possible therapeutic target.

All the biochemical assays were performed in this study using a truncated version of FIGNL1, which lacks the N-terminus, containing the nuclear localization signal (FIGNL1-

dNLS). This truncation had the advantage of being very well expressed in the *Sf*9 insect cell system employed for recombinant protein purification, while being enzymatically active. However, it is not clear how the deletion of such a large portion of the protein affects its oligomerization state, and therefore catalytic activity, or its interaction with other cellular partners. Although this limitation is partially addressed *in vivo*, where full-length FIGNL1 was used, the cellular data shows that FIGNL1-dNLS interacts significantly less with RAD51 compared to wild-type FIGNL1. Further biochemical analysis of the full-length construct is necessary for the conclusions to be more relevant in cells.

In humans, FIGNL1 forms a complex with FIRRM (Zhou et al., 2023, Zainu et al., 2024, Stok et al., 2023, Pinedo-Carpio et al., 2023). This interaction partner has been reported to stimulate the RAD51 filament disassembly activity of FIGNL1, although the molecular details of this interaction remain unclear. Furthermore, FIGNL1 can also remove RAD51 from dsDNA (Carver et al., 2025). This function might be especially relevant for replication fork stability, where BRCA2-PALB2 and BRCA1-BARD1 also play a role. Interestingly, in plants, FIGL1, the FIGNL1 ortholog is counteracted by the RAD51 paralog XRCC2 (Emmenecker et al., 2024) and a similar interplay in humans has not been described yet. Another open question is whether the FIGNL1-FIRRM complex contributes to dissociating RAD51 from dsDNA after strand invasion, for example during meiosis or heteroduplex rejection, to prevent aberrant recombination events. This idea is supported by the fact that FIGNL1 loss in plants leads to aberrant recombination intermediates and chromosome associations (Fernandes et al., 2018, Emmenecker et al., 2024, Yang et al., 2022, Hu et al., 2017) and that the FIGNL1-FIRRM complex can dissociate DMC1, a meiosis-specific recombinase closely related to RAD51 (Zainu et al., 2024, Ito et al., 2023).

5. References

ABREU, C. M., PRAKASH, R., ROMANIENKO, P. J., ROIG, I., KEENEY, S. & JASIN, M. 2018. Shu complex SWS1-SWSAP1 promotes early steps in mouse meiotic recombination. *Nat Commun,* 9**,** 3961.

ACHARYA, A., KASACIUNAITE, K., GOSE, M., KISSLING, V., GUEROIS, R., SEIDEL, R. & CEJKA, P. 2021. Distinct RPA domains promote recruitment and the helicase-nuclease activities of Dna2. *Nat Commun,* 12**,** 6521.

AKITA, M., GIRVAN, P., SPIREK, M., NOVACEK, J., RUEDA, D., PROKOP, Z. & KREJCI, L. 2024. Mechanism of BCDX2-mediated RAD51 nucleation on short ssDNA stretches and fork DNA. *Nucleic Acids Res,* 52**,** 11738-11752.

ANAND, R., JASROTIA, A., BUNDSCHUH, D., HOWARD, S. M., RANJHA, L., STUCKI, M. & CEJKA, P. 2019. NBS1 promotes the endonuclease activity of the MRE11-RAD50 complex by sensing CtIP phosphorylation. *EMBO J,* 38.

ANAND, R., RANJHA, L., CANNAVO, E. & CEJKA, P. 2016. Phosphorylated CtIP Functions as a Co-factor of the MRE11-RAD50-NBS1 Endonuclease in DNA End Resection. *Mol Cell,* 64**,** 940-950.

ANDERSON, D. E., TRUJILLO, K. M., SUNG, P. & ERICKSON, H. P. 2001. Structure of the Rad50 x Mre11 DNA repair complex from Saccharomyces cerevisiae by electron microscopy. *J Biol Chem,* 276**,** 37027-33.

ANTONY, E., TOMKO, E. J., XIAO, Q., KREJCI, L., LOHMAN, T. M. & ELLENBERGER, T. 2009. Srs2 disassembles Rad51 filaments by a protein-protein interaction triggering ATP turnover and dissociation of Rad51 from DNA. *Mol Cell,* 35**,** 105-15.

BAE, S. H., BAE, K. H., KIM, J. A. & SEO, Y. S. 2001. RPA governs endonuclease switching during processing of Okazaki fragments in eukaryotes. *Nature,* 412**,** 456-61.

BAE, S. H., CHOI, E., LEE, K. H., PARK, J. S., LEE, S. H. & SEO, Y. S. 1998. Dna2 of Saccharomyces cerevisiae possesses a single-stranded DNA-specific endonuclease activity that is able to act on double-stranded DNA in the presence of ATP. *J Biol Chem,* 273**,** 26880-90.

BALL, H. L., MYERS, J. S. & CORTEZ, D. 2005. ATRIP binding to replication protein A-single-stranded DNA promotes ATR-ATRIP localization but is dispensable for Chk1 phosphorylation. *Mol Biol Cell,* 16**,** 2372-81.

BARBER, L. J., YOUDS, J. L., WARD, J. D., MCILWRAITH, M. J., O'NEIL, N. J., PETALCORIN, M. I., MARTIN, J. S., COLLIS, S. J., CANTOR, S. B., AUCLAIR, M., TISSENBAUM, H., WEST, S. C., ROSE, A. M. & BOULTON, S. J. 2008. RTEL1 maintains genomic stability by suppressing homologous recombination. *Cell,* 135**,** 261-71.

BARTEL, D. P., SZOSTAK, J. W. & NEW COLLECTIVE, A. 1993. Isolation of new ribozymes from a large pool of random sequences [see comment]. *Science,* 261**,** 1411-8.

BASTIN-SHANOWER, S. A. & BRILL, S. J. 2001. Functional analysis of the four DNA binding domains of replication protein A. The role of RPA2 in ssDNA binding. *J Biol Chem,* 276**,** 36446-53.

BEBENEK, K., GARCIA-DIAZ, M., PATISHALL, S. R. & KUNKEL, T. A. 2005. Biochemical properties of Saccharomyces cerevisiae DNA polymerase IV. *J Biol Chem,* 280**,** 20051-8.

BECK, M., SCHMIDT, A., MALMSTROEM, J., CLAASSEN, M., ORI, A., SZYMBORSKA, A., HERZOG, F., RINNER, O., ELLENBERG, J. & AEBERSOLD, R. 2011. The quantitative proteome of a human cell line. *Mol Syst Biol,* 7**,** 549.

BELAN, O., GREENHOUGH, L., KUHLEN, L., ANAND, R., KACZMARCZYK, A., GRUSZKA, D. T., YARDIMCI, H., ZHANG, X., RUEDA, D. S., WEST, S. C. & BOULTON, S. J. 2023. Visualization of direct and diffusion-assisted RAD51 nucleation by full-length human BRCA2 protein. *Mol Cell,* 83**,** 2925-2940 e8.

BENNETT, R. J., SHARP, J. A. & WANG, J. C. 1998. Purification and characterization of the Sgs1 DNA helicase activity of Saccharomyces cerevisiae. *J Biol Chem,* 273**,** 9644-50.

BERNSTEIN, K. A., REID, R. J., SUNJEVARIC, I., DEMUTH, K., BURGESS, R. C. & ROTHSTEIN, R. 2011. The Shu complex, which contains Rad51 paralogues, promotes DNA repair through inhibition of the Srs2 anti-recombinase. *Mol Biol Cell,* 22**,** 1599-607.

BERTI, M., TELONI, F., MIJIC, S., URSICH, S., FUCHS, J., PALUMBIERI, M. D., KRIETSCH, J., SCHMID, J. A., GARCIN, E. B., GON, S., MODESTI, M., ALTMEYER, M. & LOPES, M. 2020. Sequential role of RAD51 paralog complexes in replication fork remodeling and restart. *Nat Commun,* 11**,** 3531.

BHARGAVA, R., CARSON, C. R., LEE, G. & STARK, J. M. 2017. Contribution of canonical nonhomologous end joining to chromosomal rearrangements is enhanced by ATM kinase deficiency. *Proc Natl Acad Sci U S A,* 114**,** 728-733.

BHARGAVA, R., ONYANGO, D. O. & STARK, J. M. 2016. Regulation of Single-Strand Annealing and its Role in Genome Maintenance. *Trends Genet,* 32**,** 566-575.

BHATTACHARYYA, A., EAR, U. S., KOLLER, B. H., WEICHSELBAUM, R. R. & BISHOP, D. K. 2000. The breast cancer susceptibility gene BRCA1 is required for subnuclear assembly of Rad51 and survival following treatment with the DNA cross-linking agent cisplatin. *J Biol Chem,* 275**,** 23899-903.

BIEHS, R., STEINLAGE, M., BARTON, O., JUHASZ, S., KUNZEL, J., SPIES, J., SHIBATA, A., JEGGO, P. A. & LOBRICH, M. 2017. DNA Double-Strand Break Resection Occurs during Non-homologous End Joining in G1 but Is Distinct from Resection during Homologous Recombination. *Mol Cell,* 65**,** 671-684 e5.

BINZ, S. K., LAO, Y., LOWRY, D. F. & WOLD, M. S. 2003. The phosphorylation domain of the 32-kDa subunit of replication protein A (RPA) modulates RPA-DNA interactions. Evidence for an intersubunit interaction. *J Biol Chem,* 278**,** 35584-91.

BINZ, S. K. & WOLD, M. S. 2008. Regulatory functions of the N-terminal domain of the 70-kDa subunit of replication protein A (RPA). *J Biol Chem,* 283**,** 21559-70.

BLANCO, M. G., MATOS, J., RASS, U., IP, S. C. & WEST, S. C. 2010. Functional overlap between the structure-specific nucleases Yen1 and Mus81-Mms4 for DNA-damage repair in S. cerevisiae. *DNA Repair (Amst),* 9**,** 394-402.

BLATTNER, F. R., PLUNKETT, G., 3RD, BLOCH, C. A., PERNA, N. T., BURLAND, V., RILEY, M., COLLADO-VIDES, J., GLASNER, J. D., RODE, C. K., MAYHEW, G. F., GREGOR, J., DAVIS, N. W., KIRKPATRICK, H. A., GOEDEN, M. A., ROSE, D. J., MAU, B. & SHAO, Y. 1997. The complete genome sequence of Escherichia coli K-12. *Science,* 277**,** 1453-62.

BLIER, P. R., GRIFFITH, A. J., CRAFT, J. & HARDIN, J. A. 1993. Binding of Ku protein to DNA. Measurement of affinity for ends and demonstration of binding to nicks. *J Biol Chem,* 268**,** 7594-601.

BOCHKAREV, A., BOCHKAREVA, E., FRAPPIER, L. & EDWARDS, A. M. 1999. The crystal structure of the complex of replication protein A subunits RPA32 and RPA14 reveals a mechanism for single-stranded DNA binding. *EMBO J,* 18**,** 4498-504.

BOCHKAREV, A., PFUETZNER, R. A., EDWARDS, A. M. & FRAPPIER, L. 1997. Structure of the single-stranded-DNA-binding domain of replication protein A bound to DNA. *Nature,* 385**,** 176-81.

BOCHKAREVA, E., FRAPPIER, L., EDWARDS, A. M. & BOCHKAREV, A. 1998. The RPA32 subunit of human replication protein A contains a single-stranded DNA-binding domain. *J Biol Chem,* 273**,** 3932-6.

BOCHKAREVA, E., KOROLEV, S. & BOCHKAREV, A. 2000. The role for zinc in replication protein A. *J Biol Chem,* 275**,** 27332-8.

BOCHKAREVA, E., KOROLEV, S., LEES-MILLER, S. P. & BOCHKAREV, A. 2002. Structure of the RPA trimerization core and its role in the multistep DNA-binding mechanism of RPA. *EMBO J,* 21**,** 1855-63.

BORDE, V. & DE MASSY, B. 2013. Programmed induction of DNA double strand breaks during meiosis: setting up communication between DNA and the chromosome structure. *Curr Opin Genet Dev,* 23**,** 147-55.

BORGSTAHL, G. E., BRADER, K., MOSEL, A., LIU, S., KREMMER, E., GOETTSCH, K. A., KOLAR, C., NASHEUER, H. P. & OAKLEY, G. G. 2014. Interplay of DNA damage and cell cycle signaling at the level of human replication protein A. *DNA Repair (Amst),* 21**,** 12-23.

BOUWMAN, P., ALY, A., ESCANDELL, J. M., PIETERSE, M., BARTKOVA, J., VAN DER GULDEN, H., HIDDINGH, S., THANASOULA, M., KULKARNI, A., YANG, Q., HAFFTY, B. G., TOMMISKA, J., BLOMQVIST, C., DRAPKIN, R., ADAMS, D. J., NEVANLINNA, H., BARTEK, J., TARSOUNAS, M., GANESAN, S. & JONKERS, J. 2010. 53BP1 loss rescues BRCA1 deficiency and is associated with triple-negative and BRCA-mutated breast cancers. *Nat Struct Mol Biol,* 17**,** 688-95.

BRAUN, K. A., LAO, Y., HE, Z., INGLES, C. J. & WOLD, M. S. 1997. Role of protein-protein interactions in the function of replication protein A (RPA): RPA modulates the activity of DNA polymerase alpha by multiple mechanisms. *Biochemistry,* 36**,** 8443-54.

BRILL, S. J. & STILLMAN, B. 1991. Replication factor-A from Saccharomyces cerevisiae is encoded by three essential genes coordinately expressed at S phase. *Genes Dev,* 5**,** 1589-600.

BROUWER, I., MOSCHETTI, T., CANDELLI, A., GARCIN, E. B., MODESTI, M., PELLEGRINI, L., WUITE, G. J. & PETERMAN, E. J. 2018. Two distinct conformational states define the interaction of human RAD51-ATP with single-stranded DNA. *EMBO J,* 37.

BUGREEV, D. V., YU, X., EGELMAN, E. H. & MAZIN, A. V. 2007. Novel pro- and anti-recombination activities of the Bloom's syndrome helicase. *Genes Dev,* 21**,** 3085-94.

BUNTING, S. F., CALLEN, E., WONG, N., CHEN, H. T., POLATO, F., GUNN, A., BOTHMER, A., FELDHAHN, N., FERNANDEZ-CAPETILLO, O., CAO, L., XU, X., DENG, C. X., FINKEL, T., NUSSENZWEIG, M., STARK, J. M. & NUSSENZWEIG, A. 2010. 53BP1 inhibits homologous recombination in Brca1-deficient cells by blocking resection of DNA breaks. *Cell,* 141**,** 243-54.

CAI, L., ROGINSKAYA, M., QU, Y., YANG, Z., XU, Y. & ZOU, Y. 2007. Structural characterization of human RPA sequential binding to single-stranded DNA using ssDNA as a molecular ruler. *Biochemistry,* 46**,** 8226-33.

CALLEN, E., DI VIRGILIO, M., KRUHLAK, M. J., NIETO-SOLER, M., WONG, N., CHEN, H. T., FARYABI, R. B., POLATO, F., SANTOS, M., STARNES, L. M., WESEMANN, D. R., LEE,

J. E., TUBBS, A., SLECKMAN, B. P., DANIEL, J. A., GE, K., ALT, F. W., FERNANDEZ-CAPETILLO, O., NUSSENZWEIG, M. C. & NUSSENZWEIG, A. 2013. 53BP1 mediates productive and mutagenic DNA repair through distinct phosphoprotein interactions. *Cell,* 153**,** 1266-80.

CANNAVO, E. & CEJKA, P. 2014. Sae2 promotes dsDNA endonuclease activity within Mre11-Rad50-Xrs2 to resect DNA breaks. *Nature,* 514**,** 122-5.

CANNAVO, E., CEJKA, P. & KOWALCZYKOWSKI, S. C. 2013. Relationship of DNA degradation by Saccharomyces cerevisiae exonuclease 1 and its stimulation by RPA and Mre11-Rad50-Xrs2 to DNA end resection. *Proc Natl Acad Sci U S A,* 110**,** E1661-8.

CANNAVO, E., JOHNSON, D., ANDRES, S. N., KISSLING, V. M., REINERT, J. K., GARCIA, V., ERIE, D. A., HESS, D., THOMA, N. H., ENCHEV, R. I., PETER, M., WILLIAMS, R. S., NEALE, M. J. & CEJKA, P. 2018. Regulatory control of DNA end resection by Sae2 phosphorylation. *Nat Commun,* 9**,** 4016.

CANNAVO, E., REGINATO, G. & CEJKA, P. 2019. Stepwise 5' DNA end-specific resection of DNA breaks by the Mre11-Rad50-Xrs2 and Sae2 nuclease ensemble. *Proc Natl Acad Sci U S A,* 116**,** 5505-5513.

CANNAVO, E., SANCHEZ, A., ANAND, R., RANJHA, L., HUGENER, J., ADAM, C., ACHARYA, A., WEYLAND, N., ARAN-GUIU, X., CHARBONNIER, J. B., HOFFMANN, E. R., BORDE, V., MATOS, J. & CEJKA, P. 2020. Regulation of the MLH1-MLH3 endonuclease in meiosis. *Nature,* 586**,** 618-622.

CARREIRA, A. & KOWALCZYKOWSKI, S. C. 2011. Two classes of BRC repeats in BRCA2 promote RAD51 nucleoprotein filament function by distinct mechanisms. *Proc Natl Acad Sci U S A,* 108**,** 10448-53.

CARSON, C. T., SCHWARTZ, R. A., STRACKER, T. H., LILLEY, C. E., LEE, D. V. & WEITZMAN, M. D. 2003. The Mre11 complex is required for ATM activation and the G2/M checkpoint. *EMBO J,* 22**,** 6610-20.

CARVER, A., YU, T. Y., YATES, L. A., WHITE, T., WANG, R., LISTER, K., JASIN, M. & ZHANG, X. 2025. Molecular basis of FIGNL1 in dissociating RAD51 from DNA and chromatin. *Science,* 387**,** 426-431.

CARVER, A. & ZHANG, X. 2021. Rad51 filament dynamics and its antagonistic modulators. *Semin Cell Dev Biol,* 113**,** 3-13.

CASTOR, D., NAIR, N., DECLAIS, A. C., LACHAUD, C., TOTH, R., MACARTNEY, T. J., LILLEY, D. M., ARTHUR, J. S. & ROUSE, J. 2013. Cooperative control of holliday junction resolution and DNA repair by the SLX1 and MUS81-EME1 nucleases. *Mol Cell,* 52**,** 221-33.

CECCALDI, R., LIU, J. C., AMUNUGAMA, R., HAJDU, I., PRIMACK, B., PETALCORIN, M. I., O'CONNOR, K. W., KONSTANTINOPOULOS, P. A., ELLEDGE, S. J., BOULTON, S. J., YUSUFZAI, T. & D'ANDREA, A. D. 2015. Homologous-recombination-deficient tumours are dependent on Poltheta-mediated repair. *Nature,* 518**,** 258-62.

CECCALDI, R., RONDINELLI, B. & D'ANDREA, A. D. 2016. Repair Pathway Choices and Consequences at the Double-Strand Break. *Trends Cell Biol,* 26**,** 52-64.

CEJKA, P. 2015. DNA End Resection: Nucleases Team Up with the Right Partners to Initiate Homologous Recombination. *J Biol Chem,* 290**,** 22931-8.

CEJKA, P., CANNAVO, E., POLACZEK, P., MASUDA-SASA, T., POKHAREL, S., CAMPBELL, J. L. & KOWALCZYKOWSKI, S. C. 2010a. DNA end resection by Dna2-Sgs1-RPA and its stimulation by Top3-Rmi1 and Mre11-Rad50-Xrs2. *Nature,* 467**,** 112-6.

CEJKA, P. & KOWALCZYKOWSKI, S. C. 2010. The full-length Saccharomyces cerevisiae Sgs1 protein is a vigorous DNA helicase that preferentially unwinds holliday junctions. *J Biol Chem,* 285**,** 8290-301.

CEJKA, P., PLANK, J. L., BACHRATI, C. Z., HICKSON, I. D. & KOWALCZYKOWSKI, S. C. 2010b. Rmi1 stimulates decatenation of double Holliday junctions during dissolution by Sgs1-Top3. *Nat Struct Mol Biol,* 17**,** 1377-82.

CEJKA, P., PLANK, J. L., DOMBROWSKI, C. C. & KOWALCZYKOWSKI, S. C. 2012. Decatenation of DNA by the S. cerevisiae Sgs1-Top3-Rmi1 and RPA complex: a mechanism for disentangling chromosomes. *Mol Cell,* 47**,** 886-96.

CEJKA, P. & SYMINGTON, L. S. 2021. DNA End Resection: Mechanism and Control. *Annu Rev Genet,* 55**,** 285-307.

CEPPI, I., DELLO STRITTO, M. R., MUTZE, M., BRAUNSHIER, S., MENGOLI, V., REGINATO, G., VO, H. M. P., JIMENO, S., ACHARYA, A., ROY, M., SANCHEZ, A., HALDER, S., HOWARD, S. M., GUEROIS, R., HUERTAS, P., NOORDERMEER, S. M., SEIDEL, R. & CEJKA, P. 2024. Mechanism of BRCA1-BARD1 function in DNA end resection and DNA protection. *Nature,* 634**,** 492-500.

CEPPI, I., HOWARD, S. M., KASACIUNAITE, K., PINTO, C., ANAND, R., SEIDEL, R. & CEJKA, P. 2020. CtIP promotes the motor activity of DNA2 to accelerate long-range DNA end resection. *Proc Natl Acad Sci U S A,* 117**,** 8859-8869.

CHANUT, P., BRITTON, S., COATES, J., JACKSON, S. P. & CALSOU, P. 2016. Coordinated nuclease activities counteract Ku at single-ended DNA double-strand breaks. *Nat Commun,* 7**,** 12889.

CHAPMAN, J. R., SOSSICK, A. J., BOULTON, S. J. & JACKSON, S. P. 2012a. BRCA1-associated exclusion of 53BP1 from DNA damage sites underlies temporal control of DNA repair. *J Cell Sci,* 125**,** 3529-34.

CHAPMAN, J. R., TAYLOR, M. R. & BOULTON, S. J. 2012b. Playing the end game: DNA double-strand break repair pathway choice. *Mol Cell,* 47**,** 497-510.

CHATTERJEE, G., JIMENEZ-SAINZ, J., PRESTI, T., NGUYEN, T. & JENSEN, R. B. 2016. Distinct binding of BRCA2 BRC repeats to RAD51 generates differential DNA damage sensitivity. *Nucleic Acids Res,* 44**,** 5256-70.

CHATTERJEE, N. & WALKER, G. C. 2017. Mechanisms of DNA damage, repair, and mutagenesis. *Environ Mol Mutagen,* 58**,** 235-263.

CHEN, H., LISBY, M. & SYMINGTON, L. S. 2013. RPA coordinates DNA end resection and prevents formation of DNA hairpins. *Mol Cell,* 50**,** 589-600.

CHEN, J., POTLAPALLI, R., QUAN, H., CHEN, L., XIE, Y., POURIYEH, S., SAKIB, N., LIU, L. & XIE, Y. 2024. Exploring DNA Damage and Repair Mechanisms: A Review with Computational Insights. *BioTech (Basel),* 13.

CHEN, L., NIEVERA, C. J., LEE, A. Y. & WU, X. 2008. Cell cycle-dependent complex formation of BRCA1.CtIP.MRN is important for DNA double-strand break repair. *J Biol Chem,* 283**,** 7713-20.

CHEN, L., TRUJILLO, K., RAMOS, W., SUNG, P. & TOMKINSON, A. E. 2001. Promotion of Dnl4-catalyzed DNA end-joining by the Rad50/Mre11/Xrs2 and Hdf1/Hdf2 complexes. *Mol Cell,* 8**,** 1105-15.

CHEN, L., TRUJILLO, K. M., VAN KOMEN, S., ROH, D. H., KREJCI, L., LEWIS, L. K., RESNICK, M. A., SUNG, P. & TOMKINSON, A. E. 2005. Effect of amino acid substitutions in the rad50 ATP binding domain on DNA double strand break repair in yeast. *J Biol Chem,* 280**,** 2620-7.

CHEN, P. L., CHEN, C. F., CHEN, Y., XIAO, J., SHARP, Z. D. & LEE, W. H. 1998. The BRC repeats in BRCA2 are critical for RAD51 binding and resistance to methyl methanesulfonate treatment. *Proc Natl Acad Sci U S A,* 95**,** 5287-92.

CHEN, X. & TOMKINSON, A. E. 2011. Yeast Nej1 is a key participant in the initial end binding and final ligation steps of nonhomologous end joining. *J Biol Chem,* 286**,** 4931-40.

CHIARLE, R., ZHANG, Y., FROCK, R. L., LEWIS, S. M., MOLINIE, B., HO, Y. J., MYERS, D. R., CHOI, V. W., COMPAGNO, M., MALKIN, D. J., NEUBERG, D., MONTI, S., GIALLOURAKIS, C. C., GOSTISSA, M. & ALT, F. W. 2011. Genome-wide translocation sequencing reveals mechanisms of chromosome breaks and rearrangements in B cells. *Cell,* 147**,** 107-19.

CHIOLO, I., SAPONARO, M., BARYSHNIKOVA, A., KIM, J. H., SEO, Y. S. & LIBERI, G. 2007. The human F-Box DNA helicase FBH1 faces Saccharomyces cerevisiae Srs2 and postreplication repair pathway roles. *Mol Cell Biol,* 27**,** 7439-50.

CHIRUVELLA, K. K., RENARD, B. M., BIRKELAND, S. R., SUNDER, S., LIANG, Z. & WILSON, T. E. 2014. Yeast DNA ligase IV mutations reveal a nonhomologous end joining function of BRCT1 distinct from XRCC4/Lif1 binding. *DNA Repair (Amst),* 24**,** 37-45.

CHUN, J., BUECHELMAIER, E. S. & POWELL, S. N. 2013. Rad51 paralog complexes BCDX2 and CX3 act at different stages in the BRCA1-BRCA2-dependent homologous recombination pathway. *Mol Cell Biol,* 33**,** 387-95.

CICCIA, A. & ELLEDGE, S. J. 2010. The DNA damage response: making it safe to play with knives. *Mol Cell,* 40**,** 179-204.

CLERICI, M., MANTIERO, D., GUERINI, I., LUCCHINI, G. & LONGHESE, M. P. 2008. The Yku70-Yku80 complex contributes to regulate double-strand break processing and checkpoint activation during the cell cycle. *EMBO Rep,* 9**,** 810-8.

COLOMBO, C. V., MENIN, L., RANIERI, R., BONETTI, D., CLERICI, M. & LONGHESE, M. P. 2019. Uncoupling Sae2 Functions in Downregulation of Tel1 and Rad53 Signaling Activities. *Genetics,* 211**,** 515-530.

CRUZ-GARCIA, A., LOPEZ-SAAVEDRA, A. & HUERTAS, P. 2014. BRCA1 accelerates CtIP-mediated DNA-end resection. *Cell Rep,* 9**,** 451-9.

D'AMOURS, D. & JACKSON, S. P. 2001. The yeast Xrs2 complex functions in S phase checkpoint regulation. *Genes Dev,* 15**,** 2238-49.

D'AMOURS, D. & JACKSON, S. P. 2002. The Mre11 complex: at the crossroads of dna repair and checkpoint signalling. *Nat Rev Mol Cell Biol,* 3**,** 317-27.

DALEY, J. M., JIMENEZ-SAINZ, J., WANG, W., MILLER, A. S., XUE, X., NGUYEN, K. A., JENSEN, R. B. & SUNG, P. 2017. Enhancement of BLM-DNA2-Mediated Long-Range DNA End Resection by CtIP. *Cell Rep,* 21**,** 324-332.

DAS, D., MOIANI, D., AXELROD, H. L., MILLER, M. D., MCMULLAN, D., JIN, K. K., ABDUBEK, P., ASTAKHOVA, T., BURRA, P., CARLTON, D., CHIU, H. J., CLAYTON, T., DELLER, M. C., DUAN, L., ERNST, D., FEUERHELM, J., GRANT, J. C., GRZECHNIK, A., GRZECHNIK, S. K., HAN, G. W., JAROSZEWSKI, L., KLOCK, H. E., KNUTH, M. W., KOZBIAL, P., KRISHNA, S. S., KUMAR, A., MARCIANO, D., MORSE, A. T., NIGOGHOSSIAN, E., OKACH, L., PAULSEN, J., REYES, R., RIFE, C. L., SEFCOVIC, N., TIEN, H. J., TRAME, C. B., VAN DEN BEDEM, H., WEEKES, D., XU, Q., HODGSON, K. O., WOOLEY, J., ELSLIGER, M. A., DEACON, A. M., GODZIK, A., LESLEY, S. A., TAINER, J. A. & WILSON, I. A. 2010. Crystal structure of the first

eubacterial Mre11 nuclease reveals novel features that may discriminate substrates during DNA repair. *J Mol Biol,* 397**,** 647-63.

DAVIES, O. R., FORMENT, J. V., SUN, M., BELOTSERKOVSKAYA, R., COATES, J., GALANTY, Y., DEMIR, M., MORTON, C. R., RZECHORZEK, N. J., JACKSON, S. P. & PELLEGRINI, L. 2015. CtIP tetramer assembly is required for DNA-end resection and repair. *Nat Struct Mol Biol,* 22**,** 150-157.

DAVIS, A. P. & SYMINGTON, L. S. 2003. The Rad52-Rad59 complex interacts with Rad51 and replication protein A. *DNA Repair (Amst),* 2**,** 1127-34.

DAZA-MARTIN, M., STAROWICZ, K., JAMSHAD, M., TYE, S., RONSON, G. E., MACKAY, H. L., CHAUHAN, A. S., WALKER, A. K., STONE, H. R., BEESLEY, J. F. J., COLES, J. L., GARVIN, A. J., STEWART, G. S., MCCORVIE, T. J., ZHANG, X., DENSHAM, R. M. & MORRIS, J. R. 2019. Isomerization of BRCA1-BARD1 promotes replication fork protection. *Nature,* 571**,** 521-527.

DE JAGER, M., VAN NOORT, J., VAN GENT, D. C., DEKKER, C., KANAAR, R. & WYMAN, C. 2001. Human Rad50/Mre11 is a flexible complex that can tether DNA ends. *Mol Cell,* 8**,** 1129-35.

DENG, S. K., CHEN, H. & SYMINGTON, L. S. 2015a. Replication protein A prevents promiscuous annealing between short sequence homologies: Implications for genome integrity. *Bioessays,* 37**,** 305-13.

DENG, S. K., GIBB, B., DE ALMEIDA, M. J., GREENE, E. C. & SYMINGTON, L. S. 2014. RPA antagonizes microhomology-mediated repair of DNA double-strand breaks. *Nat Struct Mol Biol,* 21**,** 405-12.

DENG, S. K., YIN, Y., PETES, T. D. & SYMINGTON, L. S. 2015b. Mre11-Sae2 and RPA Collaborate to Prevent Palindromic Gene Amplification. *Mol Cell,* 60**,** 500-8.

DESHPANDE, R. A., LEE, J. H., ARORA, S. & PAULL, T. T. 2016. Nbs1 Converts the Human Mre11/Rad50 Nuclease Complex into an Endo/Exonuclease Machine Specific for Protein-DNA Adducts. *Mol Cell,* 64**,** 593-606.

DESHPANDE, R. A., MARIN-GONZALEZ, A., BARNES, H. K., WOOLLEY, P. R., HA, T. & PAULL, T. T. 2023. Genome-wide analysis of DNA-PK-bound MRN cleavage products supports a sequential model of DSB repair pathway choice. *Nat Commun,* 14**,** 5759.

DESHPANDE, R. A., MYLER, L. R., SONIAT, M. M., MAKHARASHVILI, N., LEE, L., LEES-MILLER, S. P., FINKELSTEIN, I. J. & PAULL, T. T. 2020. DNA-dependent protein kinase promotes DNA end processing by MRN and CtIP. *Sci Adv,* 6**,** eaay0922.

DESHPANDE, R. A., WILLIAMS, G. J., LIMBO, O., WILLIAMS, R. S., KUHNLEIN, J., LEE, J. H., CLASSEN, S., GUENTHER, G., RUSSELL, P., TAINER, J. A. & PAULL, T. T. 2014. ATP-driven Rad50 conformations regulate DNA tethering, end resection, and ATM checkpoint signaling. *EMBO J,* 33**,** 482-500.

DESHPANDE, R. A. & WILSON, T. E. 2007. Modes of interaction among yeast Nej1, Lif1 and Dnl4 proteins and comparison to human XLF, XRCC4 and Lig4. *DNA Repair (Amst),* 6**,** 1507-16.

DEV, H., CHIANG, T. W., LESCALE, C., DE KRIJGER, I., MARTIN, A. G., PILGER, D., COATES, J., SCZANIECKA-CLIFT, M., WEI, W., OSTERMAIER, M., HERZOG, M., LAM, J., SHEA, A., DEMIR, M., WU, Q., YANG, F., FU, B., LAI, Z., BALMUS, G., BELOTSERKOVSKAYA, R., SERRA, V., O'CONNOR, M. J., BRUNA, A., BELI, P., PELLEGRINI, L., CALDAS, C., DERIANO, L., JACOBS, J. J. L., GALANTY, Y. &

JACKSON, S. P. 2018. Shieldin complex promotes DNA end-joining and counters homologous recombination in BRCA1-null cells. *Nat Cell Biol,* 20**,** 954-965.

DEVERYSHETTY, J., MISTRY, A., PANGENI, S., GHONEIM, M., TOKMINA-LUKASZEWSKA, M., GORE, S. K., LIU, J., KAUSHIK, V., KARUNAKARAN, S., TADDEI, A., HEYER, W. D., HA, T., BOTHNER, B. & ANTONY, E. 2025. Mechanism of Rad51 filament formation by Rad52 and Rad55-Rad57 in homologous recombination. *Nat Commun,* 16**,** 6685.

DING, J., LI, X., SHEN, J., ZHAO, Y., ZHONG, S., LAI, L., NIU, H. & QI, Z. 2023. ssDNA accessibility of Rad51 is regulated by orchestrating multiple RPA dynamics. *Nat Commun,* 14**,** 3864.

DITULLIO, R. A., JR., MOCHAN, T. A., VENERE, M., BARTKOVA, J., SEHESTED, M., BARTEK, J. & HALAZONETIS, T. D. 2002. 53BP1 functions in an ATM-dependent checkpoint pathway that is constitutively activated in human cancer. *Nat Cell Biol,* 4**,** 998-1002.

DRAY, E., ETCHIN, J., WIESE, C., SARO, D., WILLIAMS, G. J., HAMMEL, M., YU, X., GALKIN, V. E., LIU, D., TSAI, M. S., SY, S. M., SCHILD, D., EGELMAN, E., CHEN, J. & SUNG, P. 2010. Enhancement of RAD51 recombinase activity by the tumor suppressor PALB2. *Nat Struct Mol Biol,* 17**,** 1255-9.

DUEVA, R. & ILIAKIS, G. 2020. Replication protein A: a multifunctional protein with roles in DNA replication, repair and beyond. *NAR Cancer,* 2**,** zcaa022.

DURO, E., LUNDIN, C., ASK, K., SANCHEZ-PULIDO, L., MACARTNEY, T. J., TOTH, R., PONTING, C. P., GROTH, A., HELLEDAY, T. & ROUSE, J. 2010. Identification of the MMS22L-TONSL complex that promotes homologous recombination. *Mol Cell,* 40**,** 632-44.

DURO, E., VAISICA, J. A., BROWN, G. W. & ROUSE, J. 2008. Budding yeast Mms22 and Mms1 regulate homologous recombination induced by replisome blockage. *DNA Repair (Amst),* 7**,** 811-8.

EHMSEN, K. T. & HEYER, W. D. 2008. Saccharomyces cerevisiae Mus81-Mms4 is a catalytic, DNA structure-selective endonuclease. *Nucleic Acids Res,* 36**,** 2182-95.

ELIA, A. E., WANG, D. C., WILLIS, N. A., BOARDMAN, A. P., HAJDU, I., ADEYEMI, R. O., LOWRY, E., GYGI, S. P., SCULLY, R. & ELLEDGE, S. J. 2015. RFWD3-Dependent Ubiquitination of RPA Regulates Repair at Stalled Replication Forks. *Mol Cell,* 60**,** 280-93.

ELLENBERGER, T. & TOMKINSON, A. E. 2008. Eukaryotic DNA ligases: structural and functional insights. *Annu Rev Biochem,* 77**,** 313-38.

EMERSON, C. H. & BERTUCH, A. A. 2016. Consider the workhorse: Nonhomologous end-joining in budding yeast. *Biochem Cell Biol,* 94**,** 396-406.

EMMENECKER, C., PAKZAD, S., TURE, F., GUERIN, J., HUREL, A., CHAMBON, A., GIRARD, C., MERCIER, R. & KUMAR, R. 2024. FIGL1 attenuates meiotic interhomolog repair and is counteracted by the RAD51 paralog XRCC2 and the chromosome axis protein ASY1 during meiosis. *New Phytol,* 244**,** 2442-2457.

ESCRIBANO-DIAZ, C., ORTHWEIN, A., FRADET-TURCOTTE, A., XING, M., YOUNG, J. T., TKAC, J., COOK, M. A., ROSEBROCK, A. P., MUNRO, M., CANNY, M. D., XU, D. & DUROCHER, D. 2013. A cell cycle-dependent regulatory circuit composed of 53BP1-RIF1 and BRCA1-CtIP controls DNA repair pathway choice. *Mol Cell,* 49**,** 872-83.

FAN, J. & PAVLETICH, N. P. 2012. Structure and conformational change of a replication protein A heterotrimer bound to ssDNA. *Genes Dev,* 26**,** 2337-47.

FASCHING, C. L., CEJKA, P., KOWALCZYKOWSKI, S. C. & HEYER, W. D. 2015. Top3-Rmi1 dissolve Rad51-mediated D loops by a topoisomerase-based mechanism. *Mol Cell,* 57**,** 595-606.

FENG, Z., SCOTT, S. P., BUSSEN, W., SHARMA, G. G., GUO, G., PANDITA, T. K. & POWELL, S. N. 2011. Rad52 inactivation is synthetically lethal with BRCA2 deficiency. *Proc Natl Acad Sci U S A,* 108**,** 686-91.

FERNANDES, J. B., DUHAMEL, M., SEGUELA-ARNAUD, M., FROGER, N., GIRARD, C., CHOINARD, S., SOLIER, V., DE WINNE, N., DE JAEGER, G., GEVAERT, K., ANDREY, P., GRELON, M., GUEROIS, R., KUMAR, R. & MERCIER, R. 2018. FIGL1 and its novel partner FLIP form a conserved complex that regulates homologous recombination. *PLoS Genet,* 14**,** e1007317.

FONTANA, G. A., REINERT, J. K., THOMA, N. H. & RASS, U. 2018. Shepherding DNA ends: Rif1 protects telomeres and chromosome breaks. *Microb Cell,* 5**,** 327-343.

FOSTER, S. S., BALESTRINI, A. & PETRINI, J. H. 2011. Functional interplay of the Mre11 nuclease and Ku in the response to replication-associated DNA damage. *Mol Cell Biol,* 31**,** 4379-89.

FRANK-VAILLANT, M. & MARCAND, S. 2001. NHEJ regulation by mating type is exercised through a novel protein, Lif2p, essential to the ligase IV pathway. *Genes Dev,* 15**,** 3005-12.

FU, Q., CHOW, J., BERNSTEIN, K. A., MAKHARASHVILI, N., ARORA, S., LEE, C. F., PERSON, M. D., ROTHSTEIN, R. & PAULL, T. T. 2014. Phosphorylation-regulated transitions in an oligomeric state control the activity of the Sae2 DNA repair enzyme. *Mol Cell Biol,* 34**,** 778-93.

FUJIMORI, A., TACHIIRI, S., SONODA, E., THOMPSON, L. H., DHAR, P. K., HIRAOKA, M., TAKEDA, S., ZHANG, Y., RETH, M. & TAKATA, M. 2001. Rad52 partially substitutes for the Rad51 paralog XRCC3 in maintaining chromosomal integrity in vertebrate cells. *EMBO J,* 20**,** 5513-20.

GAILLARD, P. H. L., NOGUCHI, E., SHANAHAN, P. & RUSSELL, P. 2003. The endogenous Mus81-Eme1 complex resolves Holliday junctions by a nick and counternick mechanism. *Mol Cell,* 12**,** 747-59.

GAINES, W. A., GODIN, S. K., KABBINAVAR, F. F., RAO, T., VANDEMARK, A. P., SUNG, P. & BERNSTEIN, K. A. 2015. Promotion of presynaptic filament assembly by the ensemble of S. cerevisiae Rad51 paralogues with Rad52. *Nat Commun,* 6**,** 7834.

GALLI, M., FRIGERIO, C., COLOMBO, C. V., CASARI, E., LONGHESE, M. P. & CLERICI, M. 2024. Exo1 cooperates with Tel1/ATM in promoting recombination events at DNA replication forks. *iScience,* 27**,** 110410.

GAO, M., GUO, G., HUANG, J., HOU, X., HAM, H., KIM, W., ZHAO, F., TU, X., ZHOU, Q., ZHANG, C., ZHU, Q., LIU, J., YAN, Y., XU, Z., YIN, P., LUO, K., WEROHA, J., DENG, M., BILLADEAU, D. D. & LOU, Z. 2021. DOCK7 protects against replication stress by promoting RPA stability on chromatin. *Nucleic Acids Res,* 49**,** 3322-3337.

GAO, S., FENG, S., NING, S., LIU, J., ZHAO, H., XU, Y., SHANG, J., LI, K., LI, Q., GUO, R. & XU, D. 2018. An OB-fold complex controls the repair pathways for DNA double-strand breaks. *Nat Commun,* 9**,** 3925.

GARCIA, V., PHELPS, S. E., GRAY, S. & NEALE, M. J. 2011. Bidirectional resection of DNA double-strand breaks by Mre11 and Exo1. *Nature,* 479**,** 241-4.

GARNER, E., KIM, Y., LACH, F. P., KOTTEMANN, M. C. & SMOGORZEWSKA, A. 2013. Human GEN1 and the SLX4-associated nucleases MUS81 and SLX1 are essential for the resolution of replication-induced Holliday junctions. *Cell Rep,* 5**,** 207-15.

GATEI, M., YOUNG, D., CEROSALETTI, K. M., DESAI-MEHTA, A., SPRING, K., KOZLOV, S., LAVIN, M. F., GATTI, R. A., CONCANNON, P. & KHANNA, K. 2000. ATM-dependent phosphorylation of nibrin in response to radiation exposure. *Nat Genet,* 25**,** 115-9.

GHEZRAOUI, H., OLIVEIRA, C., BECKER, J. R., BILHAM, K., MORALLI, D., ANZILOTTI, C., FISCHER, R., DEOBAGKAR-LELE, M., SANCHIZ-CALVO, M., FUEYO-MARCOS, E., BONHAM, S., KESSLER, B. M., ROTTENBERG, S., CORNALL, R. J., GREEN, C. M. & CHAPMAN, J. R. 2018. 53BP1 cooperation with the REV7-shieldin complex underpins DNA structure-specific NHEJ. *Nature,* 560**,** 122-127.

GNUGGE, R., REGINATO, G., CEJKA, P. & SYMINGTON, L. S. 2023. Sequence and chromatin features guide DNA double-strand break resection initiation. *Mol Cell,* 83**,** 1237-1250 e15.

GOBBINI, E., CASSANI, C., VERTEMARA, J., WANG, W., MAMBRETTI, F., CASARI, E., SUNG, P., TISI, R., ZAMPELLA, G. & LONGHESE, M. P. 2018. The MRX complex regulates Exo1 resection activity by altering DNA end structure. *EMBO J,* 37.

GOBBINI, E., CESENA, D., GALBIATI, A., LOCKHART, A. & LONGHESE, M. P. 2013. Interplays between ATM/Tel1 and ATR/Mec1 in sensing and signaling DNA double-strand breaks. *DNA Repair (Amst),* 12**,** 791-9.

GOFFEAU, A., BARRELL, B. G., BUSSEY, H., DAVIS, R. W., DUJON, B., FELDMANN, H., GALIBERT, F., HOHEISEL, J. D., JACQ, C., JOHNSTON, M., LOUIS, E. J., MEWES, H. W., MURAKAMI, Y., PHILIPPSEN, P., TETTELIN, H. & OLIVER, S. G. 1996. Life with 6000 genes. *Science,* 274**,** 546, 563-7.

GRAHAM, T. G., WALTER, J. C. & LOPARO, J. J. 2016. Two-Stage Synapsis of DNA Ends during Non-homologous End Joining. *Mol Cell,* 61**,** 850-8.

GRAVEL, S., CHAPMAN, J. R., MAGILL, C. & JACKSON, S. P. 2008. DNA helicases Sgs1 and BLM promote DNA double-strand break resection. *Genes Dev,* 22**,** 2767-72.

GREENHOUGH, L. A., GALANTI, L., LIANG, C. C., BOULTON, S. J. & WEST, S. C. 2026. Cryo-electron microscopic visualization of RAD51 filament assembly and end-capping by XRCC3-RAD51C-RAD51D-XRCC2. *Science,* 391**,** eaea1546.

GROB, P., ZHANG, T. T., HANNAH, R., YANG, H., HEFFERIN, M. L., TOMKINSON, A. E. & NOGALES, E. 2012. Electron microscopy visualization of DNA-protein complexes formed by Ku and DNA ligase IV. *DNA Repair (Amst),* 11**,** 74-81.

GUPTA, R., SOMYAJIT, K., NARITA, T., MASKEY, E., STANLIE, A., KREMER, M., TYPAS, D., LAMMERS, M., MAILAND, N., NUSSENZWEIG, A., LUKAS, J. & CHOUDHARY, C. 2018. DNA Repair Network Analysis Reveals Shieldin as a Key Regulator of NHEJ and PARP Inhibitor Sensitivity. *Cell,* 173**,** 972-988 e23.

HAILEMARIAM, S., KUMAR, S. & BURGERS, P. M. 2019. Activation of Tel1(ATM) kinase requires Rad50 ATPase and long nucleosome-free DNA but no DNA ends. *J Biol Chem,* 294**,** 10120-10130.

HANAHAN, D. & WEINBERG, R. A. 2011. Hallmarks of cancer: the next generation. *Cell,* 144**,** 646-74.

HARTFORD, S. A., CHITTELA, R., DING, X., VYAS, A., MARTIN, B., BURKETT, S., HAINES, D. C., SOUTHON, E., TESSAROLLO, L. & SHARAN, S. K. 2016. Interaction with PALB2 Is Essential for Maintenance of Genomic Integrity by BRCA2. *PLoS Genet,* 12**,** e1006236.

HARTSUIKER, E., NEALE, M. J. & CARR, A. M. 2009. Distinct requirements for the Rad32(Mre11) nuclease and Ctp1(CtIP) in the removal of covalently bound topoisomerase I and II from DNA. *Mol Cell,* 33**,** 117-23.

HARUTA, N., KUROKAWA, Y., MURAYAMA, Y., AKAMATSU, Y., UNZAI, S., TSUTSUI, Y. & IWASAKI, H. 2006. The Swi5-Sfr1 complex stimulates Rhp51/Rad51- and Dmc1-mediated DNA strand exchange in vitro. *Nat Struct Mol Biol,* 13**,** 823-30.

HE, J., SHI, L. Z., TRUONG, L. N., LU, C. S., RAZAVIAN, N., LI, Y., NEGRETE, A., SHILOACH, J., BERNS, M. W. & WU, X. 2012. Rad50 zinc hook is important for the Mre11 complex to bind chromosomal DNA double-stranded breaks and initiate various DNA damage responses. *J Biol Chem,* 287**,** 31747-56.

HENGEL, S. R., OPPENHEIMER, K. G., SMITH, C. M., SCHAICH, M. A., REIN, H. L., MARTINO, J., DARRAH, K. E., WITHAM, M., EZEKWENNA, O. C., BURTON, K. R., VAN HOUTEN, B., SPIES, M. & BERNSTEIN, K. A. 2024. The human Shu complex promotes RAD51 activity by modulating RPA dynamics on ssDNA. *Nat Commun,* 15**,** 7197.

HERDENDORF, T. J., ALBRECHT, D. W., BENKOVIC, S. J. & NELSON, S. W. 2011. Biochemical characterization of bacteriophage T4 Mre11-Rad50 complex. *J Biol Chem,* 286**,** 2382-92.

HERRMANN, G., LINDAHL, T. & SCHAR, P. 1998. Saccharomyces cerevisiae LIF1: a function involved in DNA double-strand break repair related to mammalian XRCC4. *EMBO J,* 17**,** 4188-98.

HOA, N. N., KOBAYASHI, J., OMURA, M., HIRAKAWA, M., YANG, S. H., KOMATSU, K., PAULL, T. T., TAKEDA, S. & SASANUMA, H. 2015. BRCA1 and CtIP Are Both Required to Recruit Dna2 at Double-Strand Breaks in Homologous Recombination. *PLoS One,* 10**,** e0124495.

HOA, N. N., SHIMIZU, T., ZHOU, Z. W., WANG, Z. Q., DESHPANDE, R. A., PAULL, T. T., AKTER, S., TSUDA, M., FURUTA, R., TSUTSUI, K., TAKEDA, S. & SASANUMA, H. 2016. Mre11 Is Essential for the Removal of Lethal Topoisomerase 2 Covalent Cleavage Complexes. *Mol Cell,* 64**,** 580-592.

HOPFNER, K. P., CRAIG, L., MONCALIAN, G., ZINKEL, R. A., USUI, T., OWEN, B. A., KARCHER, A., HENDERSON, B., BODMER, J. L., MCMURRAY, C. T., CARNEY, J. P., PETRINI, J. H. & TAINER, J. A. 2002. The Rad50 zinc-hook is a structure joining Mre11 complexes in DNA recombination and repair. *Nature,* 418**,** 562-6.

HOPFNER, K. P., KARCHER, A., CRAIG, L., WOO, T. T., CARNEY, J. P. & TAINER, J. A. 2001. Structural biochemistry and interaction architecture of the DNA double-strand break repair Mre11 nuclease and Rad50-ATPase. *Cell,* 105**,** 473-85.

HOPFNER, K. P., KARCHER, A., SHIN, D. S., CRAIG, L., ARTHUR, L. M., CARNEY, J. P. & TAINER, J. A. 2000. Structural biology of Rad50 ATPase: ATP-driven conformational control in DNA double-strand break repair and the ABC-ATPase superfamily. *Cell,* 101**,** 789-800.

HU, Q., LI, Y., WANG, H., SHEN, Y., ZHANG, C., DU, G., TANG, D. & CHENG, Z. 2017. Meiotic Chromosome Association 1 Interacts with TOP3alpha and Regulates Meiotic Recombination in Rice. *Plant Cell,* 29**,** 1697-1708.

HU, Y., RAYNARD, S., SEHORN, M. G., LU, X., BUSSEN, W., ZHENG, L., STARK, J. M., BARNES, E. L., CHI, P., JANSCAK, P., JASIN, M., VOGEL, H., SUNG, P. & LUO, G. 2007. RECQL5/Recql5 helicase regulates homologous recombination and

suppresses tumor formation via disruption of Rad51 presynaptic filaments. *Genes Dev,* 21**,** 3073-84.

HUANG, D., PIENING, B. D., KENNEDY, J. J., LIN, C., JONES-WEINERT, C. W., YAN, P. & PAULOVICH, A. G. 2016. DNA Replication Stress Phosphoproteome Profiles Reveal Novel Functional Phosphorylation Sites on Xrs2 in Saccharomyces cerevisiae. *Genetics,* 203**,** 353-68.

HUANG, S., LI, B., GRAY, M. D., OSHIMA, J., MIAN, I. S. & CAMPISI, J. 1998. The premature ageing syndrome protein, WRN, is a 3'-->5' exonuclease. *Nat Genet,* 20**,** 114-6.

HUBER, L. J., YANG, T. W., SARKISIAN, C. J., MASTER, S. R., DENG, C. X. & CHODOSH, L. A. 2001. Impaired DNA damage response in cells expressing an exon 11-deleted murine Brca1 variant that localizes to nuclear foci. *Mol Cell Biol,* 21**,** 4005-15.

HUERTAS, P., CORTES-LEDESMA, F., SARTORI, A. A., AGUILERA, A. & JACKSON, S. P. 2008. CDK targets Sae2 to control DNA-end resection and homologous recombination. *Nature,* 455**,** 689-92.

HUERTAS, P. & JACKSON, S. P. 2009. Human CtIP mediates cell cycle control of DNA end resection and double strand break repair. *J Biol Chem,* 284**,** 9558-65.

IP, S. C., RASS, U., BLANCO, M. G., FLYNN, H. R., SKEHEL, J. M. & WEST, S. C. 2008. Identification of Holliday junction resolvases from humans and yeast. *Nature,* 456**,** 357-61.

IRA, G., MALKOVA, A., LIBERI, G., FOIANI, M. & HABER, J. E. 2003. Srs2 and Sgs1-Top3 suppress crossovers during double-strand break repair in yeast. *Cell,* 115**,** 401-11.

ITO, M., FUJITA, Y. & SHINOHARA, A. 2024. Positive and negative regulators of RAD51/DMC1 in homologous recombination and DNA replication. *DNA Repair (Amst),* 134**,** 103613.

ITO, M., FURUKOHRI, A., MATSUZAKI, K., FUJITA, Y., TOYODA, A. & SHINOHARA, A. 2023. FIGNL1 AAA+ ATPase remodels RAD51 and DMC1 filaments in pre-meiotic DNA replication and meiotic recombination. *Nat Commun,* 14**,** 6857.

IWASAKI, D., HAYASHIHARA, K., SHIMA, H., HIGASHIDE, M., TERASAWA, M., GASSER, S. M. & SHINOHARA, M. 2016. The MRX Complex Ensures NHEJ Fidelity through Multiple Pathways Including Xrs2-FHA-Dependent Tel1 Activation. *PLoS Genet,* 12**,** e1005942.

JACKSON, S. P. & BARTEK, J. 2009. The DNA-damage response in human biology and disease. *Nature,* 461**,** 1071-8.

JAENISCH, R. & BIRD, A. 2003. Epigenetic regulation of gene expression: how the genome integrates intrinsic and environmental signals. *Nat Genet,* 33 Suppl**,** 245-54.

JASIN, M. 2002. Homologous repair of DNA damage and tumorigenesis: the BRCA connection. *Oncogene,* 21**,** 8981-93.

JASIN, M. & ROTHSTEIN, R. 2013. Repair of strand breaks by homologous recombination. *Cold Spring Harb Perspect Biol,* 5**,** a012740.

JEGGO, P. A., GEUTING, V. & LOBRICH, M. 2011. The role of homologous recombination in radiation-induced double-strand break repair. *Radiother Oncol,* 101**,** 7-12.

JENSEN, R. B., CARREIRA, A. & KOWALCZYKOWSKI, S. C. 2010. Purified human BRCA2 stimulates RAD51-mediated recombination. *Nature,* 467**,** 678-83.

JONES, M. L., ARIA, V., BARIS, Y. & YEELES, J. T. P. 2023. How Pol alpha-primase is targeted to replisomes to prime eukaryotic DNA replication. *Mol Cell,* 83**,** 2911-2924 e16.

JONES, M. L., BARIS, Y., TAYLOR, M. R. G. & YEELES, J. T. P. 2021. Structure of a human replisome shows the organisation and interactions of a DNA replication machine. *EMBO J,* 40**,** e108819.

KANG, Y., HAN, Y. G., KHIM, K. W., CHOI, W. G., JU, M. K., PARK, K., SHIN, K. J., CHAE, Y. C., CHOI, J. H., KIM, H. & LEE, J. Y. 2023. Alteration of replication protein A binding mode on single-stranded DNA by NSMF potentiates RPA phosphorylation by ATR kinase. *Nucleic Acids Res,* 51**,** 7936-7950.

KAO, H. I., VEERARAGHAVAN, J., POLACZEK, P., CAMPBELL, J. L. & BAMBARA, R. A. 2004. On the roles of Saccharomyces cerevisiae Dna2p and Flap endonuclease 1 in Okazaki fragment processing. *J Biol Chem,* 279**,** 15014-24.

KAWALE, A. S. & SUNG, P. 2020. Mechanism and significance of chromosome damage repair by homologous recombination. *Essays Biochem,* 64**,** 779-790.

KEENER, R., CONNELLY, C. J. & GREIDER, C. W. 2019. Tel1 Activation by the MRX Complex Is Sufficient for Telomere Length Regulation but Not for the DNA Damage Response in Saccharomyces cerevisiae. *Genetics,* 213**,** 1271-1288.

KEENEY, S., GIROUX, C. N. & KLECKNER, N. 1997. Meiosis-specific DNA double-strand breaks are catalyzed by Spo11, a member of a widely conserved protein family. *Cell,* 88**,** 375-84.

KEENEY, S. & KLECKNER, N. 1995. Covalent protein-DNA complexes at the 5' strand termini of meiosis-specific double-strand breaks in yeast. *Proc Natl Acad Sci U S A,* 92**,** 11274-8.

KEGEL, A., SJOSTRAND, J. O. & ASTROM, S. U. 2001. Nej1p, a cell type-specific regulator of nonhomologous end joining in yeast. *Curr Biol,* 11**,** 1611-7.

KEMMERICH, F. E., DALDROP, P., PINTO, C., LEVIKOVA, M., CEJKA, P. & SEIDEL, R. 2016. Force regulated dynamics of RPA on a DNA fork. *Nucleic Acids Res,* 44**,** 5837-48.

KENT, T., CHANDRAMOULY, G., MCDEVITT, S. M., OZDEMIR, A. Y. & POMERANTZ, R. T. 2015. Mechanism of microhomology-mediated end-joining promoted by human DNA polymerase theta. *Nat Struct Mol Biol,* 22**,** 230-7.

KIMBLE, M. T., JOHNSON, M. J., NESTER, M. R. & SYMINGTON, L. S. 2023. Long-range DNA end resection supports homologous recombination by checkpoint activation rather than extensive homology generation. *Elife,* 12.

KING, A., REICHL, P. I., METSON, J. S., PARKER, R., MUNRO, D., OLIVEIRA, C., SOMMEROVA, L., BECKER, J. R., BIGGS, D., PREECE, C., DAVIES, B. & CHAPMAN, J. R. 2025. Shieldin and CST co-orchestrate DNA polymerase-dependent tailed-end joining reactions independently of 53BP1-governed repair pathway choice. *Nat Struct Mol Biol,* 32**,** 86-97.

KISSLING, V. M., REGINATO, G., BIANCO, E., KASACIUNAITE, K., TILMA, J., CEREGHETTI, G., SCHINDLER, N., LEE, S. S., GUEROIS, R., LUKE, B., SEIDEL, R., CEJKA, P. & PETER, M. 2022. Mre11-Rad50 oligomerization promotes DNA double-strand break repair. *Nat Commun,* 13**,** 2374.

KOLINJIVADI, A. M., SANNINO, V., DE ANTONI, A., ZADOROZHNY, K., KILKENNY, M., TECHER, H., BALDI, G., SHEN, R., CICCIA, A., PELLEGRINI, L., KREJCI, L. & COSTANZO, V. 2017. Smarcal1-Mediated Fork Reversal Triggers Mre11-Dependent Degradation of Nascent DNA in the Absence of Brca2 and Stable Rad51 Nucleofilaments. *Mol Cell,* 67**,** 867-881 e7.

KOWALCZYKOWSKI, S. C. 2015. An Overview of the Molecular Mechanisms of Recombinational DNA Repair. *Cold Spring Harb Perspect Biol,* 7.

KREJCI, L., VAN KOMEN, S., LI, Y., VILLEMAIN, J., REDDY, M. S., KLEIN, H., ELLENBERGER, T. & SUNG, P. 2003. DNA helicase Srs2 disrupts the Rad51 presynaptic filament. *Nature,* 423**,** 305-9.

KROGH, B. O. & SYMINGTON, L. S. 2004. Recombination proteins in yeast. *Annu Rev Genet,* 38**,** 233-71.

KUTHETHUR, R., VZ, S. N., SENGODAN, S. K., FONSECA, C., BRAUNSHIER, S., NAGAR, N., ACHARYA, A., WANG, X., THEIL, A. F., IBINI, O., MANOLIKA, E. M., DE KONING, K., DESSAPT, J., FRADET-TURCOTTE, A., LEBBINK, J. H. G., KANAAR, R., POLURI, K. M., SHARAN, S. K., CEJKA, P. & RAY CHAUDHURI, A. 2025. FIGNL1 inhibits homologous recombination in BRCA2 deficient cells by dissociating RAD51 filaments. *Science,* 390**,** eadt1210.

LAFRANCE-VANASSE, J., WILLIAMS, G. J. & TAINER, J. A. 2015. Envisioning the dynamics and flexibility of Mre11-Rad50-Nbs1 complex to decipher its roles in DNA replication and repair. *Prog Biophys Mol Biol,* 117**,** 182-193.

LAM, I. & KEENEY, S. 2014. Mechanism and regulation of meiotic recombination initiation. *Cold Spring Harb Perspect Biol,* 7**,** a016634.

LAMMENS, K., BEMELEIT, D. J., MOCKEL, C., CLAUSING, E., SCHELE, A., HARTUNG, S., SCHILLER, C. B., LUCAS, M., ANGERMULLER, C., SODING, J., STRASSER, K. & HOPFNER, K. P. 2011. The Mre11:Rad50 structure shows an ATP-dependent molecular clamp in DNA double-strand break repair. *Cell,* 145**,** 54-66.

LANDER, E. S., LINTON, L. M., BIRREN, B., NUSBAUM, C., ZODY, M. C., BALDWIN, J., DEVON, K., DEWAR, K., DOYLE, M., FITZHUGH, W., FUNKE, R., GAGE, D., HARRIS, K., HEAFORD, A., HOWLAND, J., KANN, L., LEHOCZKY, J., LEVINE, R., MCEWAN, P., MCKERNAN, K., MELDRIM, J., MESIROV, J. P., MIRANDA, C., MORRIS, W., NAYLOR, J., RAYMOND, C., ROSETTI, M., SANTOS, R., SHERIDAN, A., SOUGNEZ, C., STANGE-THOMANN, Y., STOJANOVIC, N., SUBRAMANIAN, A., WYMAN, D., ROGERS, J., SULSTON, J., AINSCOUGH, R., BECK, S., BENTLEY, D., BURTON, J., CLEE, C., CARTER, N., COULSON, A., DEADMAN, R., DELOUKAS, P., DUNHAM, A., DUNHAM, I., DURBIN, R., FRENCH, L., GRAFHAM, D., GREGORY, S., HUBBARD, T., HUMPHRAY, S., HUNT, A., JONES, M., LLOYD, C., MCMURRAY, A., MATTHEWS, L., MERCER, S., MILNE, S., MULLIKIN, J. C., MUNGALL, A., PLUMB, R., ROSS, M., SHOWNKEEN, R., SIMS, S., WATERSTON, R. H., WILSON, R. K., HILLIER, L. W., MCPHERSON, J. D., MARRA, M. A., MARDIS, E. R., FULTON, L. A., CHINWALLA, A. T., PEPIN, K. H., GISH, W. R., CHISSOE, S. L., WENDL, M. C., DELEHAUNTY, K. D., MINER, T. L., DELEHAUNTY, A., KRAMER, J. B., COOK, L. L., FULTON, R. S., JOHNSON, D. L., MINX, P. J., CLIFTON, S. W., HAWKINS, T., BRANSCOMB, E., PREDKI, P., RICHARDSON, P., WENNING, S., SLEZAK, T., DOGGETT, N., CHENG, J. F., OLSEN, A., LUCAS, S., ELKIN, C., UBERBACHER, E., FRAZIER, M., et al. 2001. Initial sequencing and analysis of the human genome. *Nature,* 409**,** 860-921.

LANGERAK, P., MEJIA-RAMIREZ, E., LIMBO, O. & RUSSELL, P. 2011. Release of Ku and MRN from DNA ends by Mre11 nuclease activity and Ctp1 is required for homologous recombination repair of double-strand breaks. *PLoS Genet,* 7**,** e1002271.

LAVRIK, O. I., KOLPASHCHIKOV, D. M., NASHEUER, H. P., WEISSHART, K. & FAVRE, A. 1998. Alternative conformations of human replication protein A are detected by crosslinks with primers carrying a photoreactive group at the 3'-end. *FEBS Lett,* 441**,** 186-90.

LEE BI, B. I., NGUYEN, L. H., BARSKY, D., FERNANDES, M. & WILSON, D. M., 3RD 2002. Molecular interactions of human Exo1 with DNA. *Nucleic Acids Res,* 30**,** 942-9.
LEE, J. H. & PAULL, T. T. 2005. ATM activation by DNA double-strand breaks through the Mre11-Rad50-Nbs1 complex. *Science,* 308**,** 551-4.
LEE, J. Y., TERAKAWA, T., QI, Z., STEINFELD, J. B., REDDING, S., KWON, Y., GAINES, W. A., ZHAO, W., SUNG, P. & GREENE, E. C. 2015. DNA RECOMBINATION. Base triplet stepping by the Rad51/RecA family of recombinases. *Science,* 349**,** 977-81.
LEE, K. & LEE, S. E. 2007. Saccharomyces cerevisiae Sae2- and Tel1-dependent single-strand DNA formation at DNA break promotes microhomology-mediated end joining. *Genetics,* 176**,** 2003-14.
LEE, S. E., MOORE, J. K., HOLMES, A., UMEZU, K., KOLODNER, R. D. & HABER, J. E. 1998. Saccharomyces Ku70, mre11/rad50 and RPA proteins regulate adaptation to G2/M arrest after DNA damage. *Cell,* 94**,** 399-409.
LEVIKOVA, M., KLAUE, D., SEIDEL, R. & CEJKA, P. 2013. Nuclease activity of Saccharomyces cerevisiae Dna2 inhibits its potent DNA helicase activity. *Proc Natl Acad Sci U S A,* 110**,** E1992-2001.
LI, J., HOLZSCHU, D. L. & SUGIYAMA, T. 2013. PCNA is efficiently loaded on the DNA recombination intermediate to modulate polymerase delta, eta, and zeta activities. *Proc Natl Acad Sci U S A,* 110**,** 7672-7.
LI, L., LU, X., PETERSON, C. A. & LEGERSKI, R. J. 1995. An interaction between the DNA repair factor XPA and replication protein A appears essential for nucleotide excision repair. *Mol Cell Biol,* 15**,** 5396-402.
LI, X., ZHANG, X. P., SOLINGER, J. A., KIIANITSA, K., YU, X., EGELMAN, E. H. & HEYER, W. D. 2007. Rad51 and Rad54 ATPase activities are both required to modulate Rad51-dsDNA filament dynamics. *Nucleic Acids Res,* 35**,** 4124-40.
LIANG, J., SUHANDYNATA, R. T. & ZHOU, H. 2015. Phosphorylation of Sae2 Mediates Forkhead-associated (FHA) Domain-specific Interaction and Regulates Its DNA Repair Function. *J Biol Chem,* 290**,** 10751-63.
LIEBER, M. R. 2010. The mechanism of double-strand DNA break repair by the nonhomologous DNA end-joining pathway. *Annu Rev Biochem,* 79**,** 181-211.
LIM, D. S., KIM, S. T., XU, B., MASER, R. S., LIN, J., PETRINI, J. H. & KASTAN, M. B. 2000. ATM phosphorylates p95/nbs1 in an S-phase checkpoint pathway. *Nature,* 404**,** 613-7.
LIM, H. S., KIM, J. S., PARK, Y. B., GWON, G. H. & CHO, Y. 2011. Crystal structure of the Mre11-Rad50-ATPgammaS complex: understanding the interplay between Mre11 and Rad50. *Genes Dev,* 25**,** 1091-104.
LINDAHL, T. 1993. Instability and decay of the primary structure of DNA. *Nature,* 362**,** 709-15.
LISBY, M., BARLOW, J. H., BURGESS, R. C. & ROTHSTEIN, R. 2004. Choreography of the DNA damage response: spatiotemporal relationships among checkpoint and repair proteins. *Cell,* 118**,** 699-713.
LIU, J., DOTY, T., GIBSON, B. & HEYER, W. D. 2010. Human BRCA2 protein promotes RAD51 filament formation on RPA-covered single-stranded DNA. *Nat Struct Mol Biol,* 17**,** 1260-2.
LIU, J., EDE, C., WRIGHT, W. D., GORE, S. K., JENKINS, S. S., FREUDENTHAL, B. D., TODD WASHINGTON, M., VEAUTE, X. & HEYER, W. D. 2017. Srs2 promotes synthesis-

dependent strand annealing by disrupting DNA polymerase delta-extending D-loops. *Elife,* 6.

LIU, J., RENAULT, L., VEAUTE, X., FABRE, F., STAHLBERG, H. & HEYER, W. D. 2011a. Rad51 paralogues Rad55-Rad57 balance the antirecombinase Srs2 in Rad51 filament formation. *Nature,* 479**,** 245-8.

LIU, S., CHU, J., YUCER, N., LENG, M., WANG, S. Y., CHEN, B. P., HITTELMAN, W. N. & WANG, Y. 2011b. RING finger and WD repeat domain 3 (RFWD3) associates with replication protein A (RPA) and facilitates RPA-mediated DNA damage response. *J Biol Chem,* 286**,** 22314-22.

LLORENTE, B. & SYMINGTON, L. S. 2004. The Mre11 nuclease is not required for 5' to 3' resection at multiple HO-induced double-strand breaks. *Mol Cell Biol,* 24**,** 9682-94.

LOBACHEV, K., VITRIOL, E., STEMPLE, J., RESNICK, M. A. & BLOOM, K. 2004. Chromosome fragmentation after induction of a double-strand break is an active process prevented by the RMX repair complex. *Curr Biol,* 14**,** 2107-12.

LODISH, H. F., LODISH, H. F. & LODISH, H. F. 2004. *Molecular cell biology,* New York, W.H. Freeman and Co.

LYNCH, M. 2007. *The origins of genome architecture,* Sunderland, Mass, Sinauer Associates.

MA, E., DUPAIGNE, P., MALOISEL, L., GUEROIS, R., LE CAM, E. & COIC, E. 2018. Rad52-Rad51 association is essential to protect Rad51 filaments against Srs2, but facultative for filament formation. *Elife,* 7.

MA, J. L., KIM, E. M., HABER, J. E. & LEE, S. E. 2003. Yeast Mre11 and Rad1 proteins define a Ku-independent mechanism to repair double-strand breaks lacking overlapping end sequences. *Mol Cell Biol,* 23**,** 8820-8.

MA, Y., PANNICKE, U., SCHWARZ, K. & LIEBER, M. R. 2002. Hairpin opening and overhang processing by an Artemis/DNA-dependent protein kinase complex in nonhomologous end joining and V(D)J recombination. *Cell,* 108**,** 781-94.

MAGA, G., FROUIN, I., SPADARI, S. & HUBSCHER, U. 2001. Replication protein A as a "fidelity clamp" for DNA polymerase alpha. *J Biol Chem,* 276**,** 18235-42.

MAHANEY, B. L., LEES-MILLER, S. P. & COBB, J. A. 2014. The C-terminus of Nej1 is critical for nuclear localization and non-homologous end-joining. *DNA Repair (Amst),* 14**,** 9-16.

MAJKA, J., ALFORD, B., AUSIO, J., FINN, R. M. & MCMURRAY, C. T. 2012. ATP hydrolysis by RAD50 protein switches MRE11 enzyme from endonuclease to exonuclease. *J Biol Chem,* 287**,** 2328-41.

MANTIERO, D., CLERICI, M., LUCCHINI, G. & LONGHESE, M. P. 2007. Dual role for Saccharomyces cerevisiae Tel1 in the checkpoint response to double-strand breaks. *EMBO Rep,* 8**,** 380-7.

MAO, Z., BOZZELLA, M., SELUANOV, A. & GORBUNOVA, V. 2008. Comparison of nonhomologous end joining and homologous recombination in human cells. *DNA Repair (Amst),* 7**,** 1765-71.

MASSON, J. Y., TARSOUNAS, M. C., STASIAK, A. Z., STASIAK, A., SHAH, R., MCILWRAITH, M. J., BENSON, F. E. & WEST, S. C. 2001. Identification and purification of two distinct complexes containing the five RAD51 paralogs. *Genes Dev,* 15**,** 3296-307.

MASUDA-SASA, T., IMAMURA, O. & CAMPBELL, J. L. 2006. Biochemical analysis of human Dna2. *Nucleic Acids Res,* 34**,** 1865-75.

MATOS, J., BLANCO, M. G., MASLEN, S., SKEHEL, J. M. & WEST, S. C. 2011. Regulatory control of the resolution of DNA recombination intermediates during meiosis and mitosis. *Cell,* 147**,** 158-72.

MATSUDA, T., SAIJO, M., KURAOKA, I., KOBAYASHI, T., NAKATSU, Y., NAGAI, A., ENJOJI, T., MASUTANI, C., SUGASAWA, K., HANAOKA, F. & ET AL. 1995. DNA repair protein XPA binds replication protein A (RPA). *J Biol Chem,* 270**,** 4152-7.

MATSUOKA, S., HUANG, M. & ELLEDGE, S. J. 1998. Linkage of ATM to cell cycle regulation by the Chk2 protein kinase. *Science,* 282**,** 1893-7.

MATSUZAKI, K., KONDO, S., ISHIKAWA, T. & SHINOHARA, A. 2019. Human RAD51 paralogue SWSAP1 fosters RAD51 filament by regulating the anti-recombinase FIGNL1 AAA+ ATPase. *Nat Commun,* 10**,** 1407.

MATSUZAKI, K., SHINOHARA, A. & SHINOHARA, M. 2008. Forkhead-associated domain of yeast Xrs2, a homolog of human Nbs1, promotes nonhomologous end joining through interaction with a ligase IV partner protein, Lif1. *Genetics,* 179**,** 213-25.

MATSUZAKI, K., SHINOHARA, A. & SHINOHARA, M. 2024. Human AAA+ ATPase FIGNL1 suppresses RAD51-mediated ultra-fine bridge formation. *Nucleic Acids Res,* 52**,** 5774-5791.

MATTAROCCI, S., REGINATO, G., CANNAVO, E., ROISNE-HAMELIN, F., GNUGGE, R., DESHAYES, A., POBIEGA, S., ALIBERT, O., MORIN, V., ROPARS, V., MEHRINGER, J., GELI, V., CUNIASSE, P., CHARBONNIER, J. B., SYMINGTON, L. S., CEJKA, P. & MARCAND, S. 2026. Rap1-mediated steric hindrance protects telomeres from MRX sensing. *Nat Struct Mol Biol*.

MAZIN, A. V., ALEXEEV, A. A. & KOWALCZYKOWSKI, S. C. 2003. A novel function of Rad54 protein. Stabilization of the Rad51 nucleoprotein filament. *J Biol Chem,* 278**,** 14029-36.

MCCARTHY, E. E., CELEBI, J. T., BAER, R. & LUDWIG, T. 2003. Loss of Bard1, the heterodimeric partner of the Brca1 tumor suppressor, results in early embryonic lethality and chromosomal instability. *Mol Cell Biol,* 23**,** 5056-63.

MCVEY, M. & LEE, S. E. 2008. MMEJ repair of double-strand breaks (director's cut): deleted sequences and alternative endings. *Trends Genet,* 24**,** 529-38.

MIJIC, S., ZELLWEGER, R., CHAPPIDI, N., BERTI, M., JACOBS, K., MUTREJA, K., URSICH, S., RAY CHAUDHURI, A., NUSSENZWEIG, A., JANSCAK, P. & LOPES, M. 2017. Replication fork reversal triggers fork degradation in BRCA2-defective cells. *Nat Commun,* 8**,** 859.

MILLER, A. S., DALEY, J. M., PHAM, N. T., NIU, H., XUE, X., IRA, G. & SUNG, P. 2017. A novel role of the Dna2 translocase function in DNA break resection. *Genes Dev,* 31**,** 503-510.

MIMITOU, E. P. & SYMINGTON, L. S. 2008. Sae2, Exo1 and Sgs1 collaborate in DNA double-strand break processing. *Nature,* 455**,** 770-4.

MIMITOU, E. P. & SYMINGTON, L. S. 2009. DNA end resection: many nucleases make light work. *DNA Repair (Amst),* 8**,** 983-95.

MIMITOU, E. P. & SYMINGTON, L. S. 2010. Ku prevents Exo1 and Sgs1-dependent resection of DNA ends in the absence of a functional MRX complex or Sae2. *EMBO J,* 29**,** 3358-69.

MIRMAN, Z., LOTTERSBERGER, F., TAKAI, H., KIBE, T., GONG, Y., TAKAI, K., BIANCHI, A., ZIMMERMANN, M., DUROCHER, D. & DE LANGE, T. 2018. 53BP1-RIF1-shieldin

counteracts DSB resection through CST- and Polalpha-dependent fill-in. *Nature,* 560**,** 112-116.

MITCHEL, K., ZHANG, H., WELZ-VOEGELE, C. & JINKS-ROBERTSON, S. 2010. Molecular structures of crossover and noncrossover intermediates during gap repair in yeast: implications for recombination. *Mol Cell,* 38**,** 211-22.

MOCKEL, C., LAMMENS, K., SCHELE, A. & HOPFNER, K. P. 2012. ATP driven structural changes of the bacterial Mre11:Rad50 catalytic head complex. *Nucleic Acids Res,* 40**,** 914-27.

MOJUMDAR, A., ADAM, N. & COBB, J. A. 2022. Nej1 interacts with Sae2 at DNA double-stranded breaks to inhibit DNA resection. *J Biol Chem,* 298**,** 101937.

MOORE, J. K. & HABER, J. E. 1996. Cell cycle and genetic requirements of two pathways of nonhomologous end-joining repair of double-strand breaks in Saccharomyces cerevisiae. *Mol Cell Biol,* 16**,** 2164-73.

MOREAU, S., FERGUSON, J. R. & SYMINGTON, L. S. 1999. The nuclease activity of Mre11 is required for meiosis but not for mating type switching, end joining, or telomere maintenance. *Mol Cell Biol,* 19**,** 556-66.

MORTENSEN, U. H., BENDIXEN, C., SUNJEVARIC, I. & ROTHSTEIN, R. 1996. DNA strand annealing is promoted by the yeast Rad52 protein. *Proc Natl Acad Sci U S A,* 93**,** 10729-34.

MYLER, L. R., GALLARDO, I. F., SONIAT, M. M., DESHPANDE, R. A., GONZALEZ, X. B., KIM, Y., PAULL, T. T. & FINKELSTEIN, I. J. 2017. Single-Molecule Imaging Reveals How Mre11-Rad50-Nbs1 Initiates DNA Break Repair. *Mol Cell,* 67**,** 891-898 e4.

MYLER, L. R., GALLARDO, I. F., ZHOU, Y., GONG, F., YANG, S. H., WOLD, M. S., MILLER, K. M., PAULL, T. T. & FINKELSTEIN, I. J. 2016. Single-molecule imaging reveals the mechanism of Exo1 regulation by single-stranded DNA binding proteins. *Proc Natl Acad Sci U S A,* 113**,** E1170-9.

MYUNG, K., DATTA, A., CHEN, C. & KOLODNER, R. D. 2001. SGS1, the Saccharomyces cerevisiae homologue of BLM and WRN, suppresses genome instability and homeologous recombination. *Nat Genet,* 27**,** 113-6.

NAKADA, D., MATSUMOTO, K. & SUGIMOTO, K. 2003. ATM-related Tel1 associates with double-strand breaks through an Xrs2-dependent mechanism. *Genes Dev,* 17**,** 1957-62.

NAKAI, W., WESTMORELAND, J., YEH, E., BLOOM, K. & RESNICK, M. A. 2011. Chromosome integrity at a double-strand break requires exonuclease 1 and MRX. *DNA Repair (Amst),* 10**,** 102-10.

NAKAMURA, K., KOGAME, T., OSHIUMI, H., SHINOHARA, A., SUMITOMO, Y., AGAMA, K., POMMIER, Y., TSUTSUI, K. M., TSUTSUI, K., HARTSUIKER, E., OGI, T., TAKEDA, S. & TANIGUCHI, Y. 2010. Collaborative action of Brca1 and CtIP in elimination of covalent modifications from double-strand breaks to facilitate subsequent break repair. *PLoS Genet,* 6**,** e1000828.

NAKAMURA, K., SAREDI, G., BECKER, J. R., FOSTER, B. M., NGUYEN, N. V., BEYER, T. E., CESA, L. C., FAULL, P. A., LUKAUSKAS, S., FRIMURER, T., CHAPMAN, J. R., BARTKE, T. & GROTH, A. 2019. H4K20me0 recognition by BRCA1-BARD1 directs homologous recombination to sister chromatids. *Nat Cell Biol,* 21**,** 311-318.

NAMSARAEV, E. A. & BERG, P. 1998. Branch migration during Rad51-promoted strand exchange proceeds in either direction. *Proc Natl Acad Sci U S A,* 95**,** 10477-81.

NASHEUER, H. P., MEANEY, A. M., HULSHOFF, T., THIELE, I. & ONWUBIKO, N. O. 2024. Replication Protein A, the Main Eukaryotic Single-Stranded DNA Binding Protein, a Focal Point in Cellular DNA Metabolism. *Int J Mol Sci,* 25.

NASSIF, N., PENNEY, J., PAL, S., ENGELS, W. R. & GLOOR, G. B. 1994. Efficient copying of nonhomologous sequences from ectopic sites via P-element-induced gap repair. *Mol Cell Biol,* 14**,** 1613-25.

NEALE, M. J., PAN, J. & KEENEY, S. 2005. Endonucleolytic processing of covalent protein-linked DNA double-strand breaks. *Nature,* 436**,** 1053-7.

NEGRINI, S., GORGOULIS, V. G. & HALAZONETIS, T. D. 2010. Genomic instability--an evolving hallmark of cancer. *Nat Rev Mol Cell Biol,* 11**,** 220-8.

NEW, J. H., SUGIYAMA, T., ZAITSEVA, E. & KOWALCZYKOWSKI, S. C. 1998. Rad52 protein stimulates DNA strand exchange by Rad51 and replication protein A. *Nature,* 391**,** 407-10.

NICOLAS, Y., BRET, H., CANNAVO, E., ACHARYA, A., CEJKA, P., BORDE, V. & GUEROIS, R. 2024. Molecular insights into the activation of Mre11-Rad50 endonuclease activity by Sae2/CtIP. *Mol Cell,* 84**,** 2223-2237 e4.

NICOLETTE, M. L., LEE, K., GUO, Z., RANI, M., CHOW, J. M., LEE, S. E. & PAULL, T. T. 2010. Mre11-Rad50-Xrs2 and Sae2 promote 5' strand resection of DNA double-strand breaks. *Nat Struct Mol Biol,* 17**,** 1478-85.

NIMONKAR, A. V., DOMBROWSKI, C. C., SIINO, J. S., STASIAK, A. Z., STASIAK, A. & KOWALCZYKOWSKI, S. C. 2012. Saccharomyces cerevisiae Dmc1 and Rad51 proteins preferentially function with Tid1 and Rad54 proteins, respectively, to promote DNA strand invasion during genetic recombination. *J Biol Chem,* 287**,** 28727-37.

NIMONKAR, A. V., GENSCHEL, J., KINOSHITA, E., POLACZEK, P., CAMPBELL, J. L., WYMAN, C., MODRICH, P. & KOWALCZYKOWSKI, S. C. 2011. BLM-DNA2-RPA-MRN and EXO1-BLM-RPA-MRN constitute two DNA end resection machineries for human DNA break repair. *Genes Dev,* 25**,** 350-62.

NIMONKAR, A. V., OZSOY, A. Z., GENSCHEL, J., MODRICH, P. & KOWALCZYKOWSKI, S. C. 2008. Human exonuclease 1 and BLM helicase interact to resect DNA and initiate DNA repair. *Proc Natl Acad Sci U S A,* 105**,** 16906-11.

NIU, H., CHUNG, W. H., ZHU, Z., KWON, Y., ZHAO, W., CHI, P., PRAKASH, R., SEONG, C., LIU, D., LU, L., IRA, G. & SUNG, P. 2010. Mechanism of the ATP-dependent DNA end-resection machinery from Saccharomyces cerevisiae. *Nature,* 467**,** 108-11.

NOORDERMEER, S. M., ADAM, S., SETIAPUTRA, D., BARAZAS, M., PETTITT, S. J., LING, A. K., OLIVIERI, M., ALVAREZ-QUILON, A., MOATTI, N., ZIMMERMANN, M., ANNUNZIATO, S., KRASTEV, D. B., SONG, F., BRANDSMA, I., FRANKUM, J., BROUGH, R., SHERKER, A., LANDRY, S., SZILARD, R. K., MUNRO, M. M., MCEWAN, A., GOULLET DE RUGY, T., LIN, Z. Y., HART, T., MOFFAT, J., GINGRAS, A. C., MARTIN, A., VAN ATTIKUM, H., JONKERS, J., LORD, C. J., ROTTENBERG, S. & DUROCHER, D. 2018. The shieldin complex mediates 53BP1-dependent DNA repair. *Nature,* 560**,** 117-121.

NUSS, J. E., PATRICK, S. M., OAKLEY, G. G., ALTER, G. M., ROBISON, J. G., DIXON, K. & TURCHI, J. J. 2005. DNA damage induced hyperphosphorylation of replication protein A. 1. Identification of novel sites of phosphorylation in response to DNA damage. *Biochemistry,* 44**,** 8428-37.

O'DONNELL, L., PANIER, S., WILDENHAIN, J., TKACH, J. M., AL-HAKIM, A., LANDRY, M. C., ESCRIBANO-DIAZ, C., SZILARD, R. K., YOUNG, J. T., MUNRO, M., CANNY, M. D., KOLAS, N. K., ZHANG, W., HARDING, S. M., YLANKO, J., MENDEZ, M., MULLIN, M., SUN, T., HABERMANN, B., DATTI, A., BRISTOW, R. G., GINGRAS, A. C., TYERS, M. D., BROWN, G. W. & DUROCHER, D. 2010. The MMS22L-TONSL complex mediates recovery from replication stress and homologous recombination. *Mol Cell,* 40**,** 619-31.

OAKLEY, G. G., TILLISON, K., OPIYO, S. A., GLANZER, J. G., HORN, J. M. & PATRICK, S. M. 2009. Physical interaction between replication protein A (RPA) and MRN: involvement of RPA2 phosphorylation and the N-terminus of RPA1. *Biochemistry,* 48**,** 7473-81.

OH, J., AL-ZAIN, A., CANNAVO, E., CEJKA, P. & SYMINGTON, L. S. 2016. Xrs2 Dependent and Independent Functions of the Mre11-Rad50 Complex. *Mol Cell,* 64**,** 405-415.

OH, J., LEE, S. J., ROTHSTEIN, R. & SYMINGTON, L. S. 2018. Xrs2 and Tel1 Independently Contribute to MR-Mediated DNA Tethering and Replisome Stability. *Cell Rep,* 25**,** 1681-1692 e4.

OLIVE, P. L., BANATH, J. P. & DURAND, R. E. 1990. Heterogeneity in radiation-induced DNA damage and repair in tumor and normal cells measured using the "comet" assay. *Radiat Res,* 122**,** 86-94.

OOI, S. L., SHOEMAKER, D. D. & BOEKE, J. D. 2001. A DNA microarray-based genetic screen for nonhomologous end-joining mutants in Saccharomyces cerevisiae. *Science,* 294**,** 2552-6.

OVERMEER, R. M., MOSER, J., VOLKER, M., KOOL, H., TOMKINSON, A. E., VAN ZEELAND, A. A., MULLENDERS, L. H. & FOUSTERI, M. 2011. Replication protein A safeguards genome integrity by controlling NER incision events. *J Cell Biol,* 192**,** 401-15.

PALMBOS, P. L., DALEY, J. M. & WILSON, T. E. 2005. Mutations of the Yku80 C terminus and Xrs2 FHA domain specifically block yeast nonhomologous end joining. *Mol Cell Biol,* 25**,** 10782-90.

PALMBOS, P. L., WU, D., DALEY, J. M. & WILSON, T. E. 2008. Recruitment of Saccharomyces cerevisiae Dnl4-Lif1 complex to a double-strand break requires interactions with Yku80 and the Xrs2 FHA domain. *Genetics,* 180**,** 1809-19.

PAULL, T. T. 2021. Reconsidering pathway choice: a sequential model of mammalian DNA double-strand break pathway decisions. *Curr Opin Genet Dev,* 71**,** 55-62.

PAULL, T. T. & GELLERT, M. 1998. The 3' to 5' exonuclease activity of Mre 11 facilitates repair of DNA double-strand breaks. *Mol Cell,* 1**,** 969-79.

PESTRYAKOV, P. E., WEISSHART, K., SCHLOTT, B., KHODYREVA, S. N., KREMMER, E., GROSSE, F., LAVRIK, O. I. & NASHEUER, H. P. 2003. Human replication protein A. The C-terminal RPA70 and the central RPA32 domains are involved in the interactions with the 3'-end of a primer-template DNA. *J Biol Chem,* 278**,** 17515-24.

PETERSON, S. E., LI, Y., CHAIT, B. T., GOTTESMAN, M. E., BAER, R. & GAUTIER, J. 2011. Cdk1 uncouples CtIP-dependent resection and Rad51 filament formation during M-phase double-strand break repair. *J Cell Biol,* 194**,** 705-20.

PILIE, P. G., TANG, C., MILLS, G. B. & YAP, T. A. 2019. State-of-the-art strategies for targeting the DNA damage response in cancer. *Nat Rev Clin Oncol,* 16**,** 81-104.

PINEDO-CARPIO, E., DESSAPT, J., BENEYTON, A., SACRE, L., BERUBE, M. A., VILLOT, R., LAVOIE, E. G., COULOMBE, Y., BLONDEAU, A., BOULAIS, J., MALINA, A., LUO, V.

M., LAZARATOS, A. M., COTE, J. F., MALLETTE, F. A., GUARNE, A., MASSON, J. Y., FRADET-TURCOTTE, A. & ORTHWEIN, A. 2023. FIRRM cooperates with FIGNL1 to promote RAD51 disassembly during DNA repair. *Sci Adv,* 9**,** eadf4082.

PIWKO, W., MLEJNKOVA, L. J., MUTREJA, K., RANJHA, L., STAFA, D., SMIRNOV, A., BRODERSEN, M. M., ZELLWEGER, R., STURZENEGGER, A., JANSCAK, P., LOPES, M., PETER, M. & CEJKA, P. 2016. The MMS22L-TONSL heterodimer directly promotes RAD51-dependent recombination upon replication stress. *EMBO J,* 35**,** 2584-2601.

PLANK, J. L., WU, J. & HSIEH, T. S. 2006. Topoisomerase IIIalpha and Bloom's helicase can resolve a mobile double Holliday junction substrate through convergent branch migration. *Proc Natl Acad Sci U S A,* 103**,** 11118-23.

POKHREL, N., CALDWELL, C. C., CORLESS, E. I., TILLISON, E. A., TIBBS, J., JOCIC, N., TABEI, S. M. A., WOLD, M. S., SPIES, M. & ANTONY, E. 2019. Dynamics and selective remodeling of the DNA-binding domains of RPA. *Nat Struct Mol Biol,* 26**,** 129-136.

POLATO, F., CALLEN, E., WONG, N., FARYABI, R., BUNTING, S., CHEN, H. T., KOZAK, M., KRUHLAK, M. J., RECZEK, C. R., LEE, W. H., LUDWIG, T., BAER, R., FEIGENBAUM, L., JACKSON, S. & NUSSENZWEIG, A. 2014. CtIP-mediated resection is essential for viability and can operate independently of BRCA1. *J Exp Med,* 211**,** 1027-36.

QI, Z., REDDING, S., LEE, J. Y., GIBB, B., KWON, Y., NIU, H., GAINES, W. A., SUNG, P. & GREENE, E. C. 2015. DNA sequence alignment by microhomology sampling during homologous recombination. *Cell,* 160**,** 856-869.

QIU, Y., ANTONY, E., DOGANAY, S., KOH, H. R., LOHMAN, T. M. & MYONG, S. 2013. Srs2 prevents Rad51 filament formation by repetitive motion on DNA. *Nat Commun,* 4**,** 2281.

RANJHA, L., HOWARD, S. M. & CEJKA, P. 2018. Main steps in DNA double-strand break repair: an introduction to homologous recombination and related processes. *Chromosoma,* 127**,** 187-214.

RASS, U., COMPTON, S. A., MATOS, J., SINGLETON, M. R., IP, S. C., BLANCO, M. G., GRIFFITH, J. D. & WEST, S. C. 2010. Mechanism of Holliday junction resolution by the human GEN1 protein. *Genes Dev,* 24**,** 1559-69.

RECZEK, C. R., SZABOLCS, M., STARK, J. M., LUDWIG, T. & BAER, R. 2013. The interaction between CtIP and BRCA1 is not essential for resection-mediated DNA repair or tumor suppression. *J Cell Biol,* 201**,** 693-707.

REGINATO, G., CANNAVO, E. & CEJKA, P. 2017. Physiological protein blocks direct the Mre11-Rad50-Xrs2 and Sae2 nuclease complex to initiate DNA end resection. *Genes Dev,* 31**,** 2325-2330.

REGINATO, G. & CEJKA, P. 2020. The MRE11 complex: A versatile toolkit for the repair of broken DNA. *DNA Repair (Amst),* 91-92**,** 102869.

REGINATO, G., DELLO STRITTO, M. R., WANG, Y., HAO, J., PAVANI, R., SCHMITZ, M., HALDER, S., MORIN, V., CANNAVO, E., CEPPI, I., BRAUNSHIER, S., ACHARYA, A., ROPARS, V., CHARBONNIER, J. B., JINEK, M., NUSSENZWEIG, A., HA, T. & CEJKA, P. 2024. HLTF disrupts Cas9-DNA post-cleavage complexes to allow DNA break processing. *Nat Commun,* 15**,** 5789.

RENKAWITZ, J., LADEMANN, C. A. & JENTSCH, S. 2014. Mechanisms and principles of homology search during recombination. *Nat Rev Mol Cell Biol,* 15**,** 369-83.

RIBES-ZAMORA, A., INDIVIGLIO, S. M., MIHALEK, I., WILLIAMS, C. L. & BERTUCH, A. A. 2013. TRF2 interaction with Ku heterotetramerization interface gives insight into c-NHEJ prevention at human telomeres. *Cell Rep,* 5**,** 194-206.

RIBES-ZAMORA, A., MIHALEK, I., LICHTARGE, O. & BERTUCH, A. A. 2007. Distinct faces of the Ku heterodimer mediate DNA repair and telomeric functions. *Nat Struct Mol Biol,* 14**,** 301-7.

RICHARDSON, C., STARK, J. M., OMMUNDSEN, M. & JASIN, M. 2004. Rad51 overexpression promotes alternative double-strand break repair pathways and genome instability. *Oncogene,* 23**,** 546-53.

ROBERTSON, M. P. & JOYCE, G. F. 2012. The origins of the RNA world. *Cold Spring Harb Perspect Biol,* 4.

ROBISON, J. G., ELLIOTT, J., DIXON, K. & OAKLEY, G. G. 2004. Replication protein A and the Mre11.Rad50.Nbs1 complex co-localize and interact at sites of stalled replication forks. *J Biol Chem,* 279**,** 34802-10.

ROY, M., SANCHEZ, A., GUEROIS, R., SENOUSSI, I., CERANA, A., SGRIGNANI, J., CAVALLI, A., RINALDI, A. & CEJKA, P. 2025. EXO1 promotes the meiotic MLH1-MLH3 endonuclease through conserved interactions with MLH1, MSH4 and DNA. *Nat Commun,* 16**,** 4141.

SAIJO, M., TAKEDACHI, A. & TANAKA, K. 2011. Nucleotide excision repair by mutant xeroderma pigmentosum group A (XPA) proteins with deficiency in interaction with RPA. *J Biol Chem,* 286**,** 5476-83.

SALAS, T. R., PETRUSEVA, I., LAVRIK, O. & SAINTOME, C. 2009. Evidence for direct contact between the RPA3 subunit of the human replication protein A and single-stranded DNA. *Nucleic Acids Res,* 37**,** 38-46.

SALUNKHE, S., DALEY, J. M., KAUR, H., TOMIMATSU, N., XUE, C., RAINA, V. B., JASPER, A. M., ROGERS, C. M., LI, W., ZHOU, S., MOJIDRA, R., KWON, Y., FANG, Q., JI, J. H., BADAMCHI SHABESTARI, A., FITZGERALD, O., DINH, H., MUKHERJEE, B., HABIB, A. A., HROMAS, R., MAZIN, A. V., WASMUTH, E. V., OLSEN, S. K., LIBICH, D. S., ZHOU, D., ZHAO, W., GREENE, E. C., BURMA, S. & SUNG, P. 2024. Promotion of DNA end resection by BRCA1-BARD1 in homologous recombination. *Nature,* 634**,** 482-491.

SAN FILIPPO, J., SUNG, P. & KLEIN, H. 2008. Mechanism of eukaryotic homologous recombination. *Annu Rev Biochem,* 77**,** 229-57.

SANCHEZ, Y., BACHANT, J., WANG, H., HU, F., LIU, D., TETZLAFF, M. & ELLEDGE, S. J. 1999. Control of the DNA damage checkpoint by chk1 and rad53 protein kinases through distinct mechanisms. *Science,* 286**,** 1166-71.

SANCHEZ, Y., DESANY, B. A., JONES, W. J., LIU, Q., WANG, B. & ELLEDGE, S. J. 1996. Regulation of RAD53 by the ATM-like kinases MEC1 and TEL1 in yeast cell cycle checkpoint pathways. *Science,* 271**,** 357-60.

SARTORI, A. A., LUKAS, C., COATES, J., MISTRIK, M., FU, S., BARTEK, J., BAER, R., LUKAS, J. & JACKSON, S. P. 2007. Human CtIP promotes DNA end resection. *Nature,* 450**,** 509-14.

SCHIESTL, R. H., DOMINSKA, M. & PETES, T. D. 1993. Transformation of Saccharomyces cerevisiae with nonhomologous DNA: illegitimate integration of transforming DNA into yeast chromosomes and in vivo ligation of transforming DNA to mitochondrial DNA sequences. *Mol Cell Biol,* 13**,** 2697-705.

SCHILLER, C. B., LAMMENS, K., GUERINI, I., COORDES, B., FELDMANN, H., SCHLAUDERER, F., MOCKEL, C., SCHELE, A., STRASSER, K., JACKSON, S. P. & HOPFNER, K. P. 2012. Structure of Mre11-Nbs1 complex yields insights into ataxia-telangiectasia-like disease mutations and DNA damage signaling. *Nat Struct Mol Biol,* 19**,** 693-700.

SCHLACHER, K., CHRIST, N., SIAUD, N., EGASHIRA, A., WU, H. & JASIN, M. 2011. Double-strand break repair-independent role for BRCA2 in blocking stalled replication fork degradation by MRE11. *Cell,* 145**,** 529-42.

SCHLACHER, K., WU, H. & JASIN, M. 2012. A distinct replication fork protection pathway connects Fanconi anemia tumor suppressors to RAD51-BRCA1/2. *Cancer Cell,* 22**,** 106-16.

SCHWARTZ, M. F., DUONG, J. K., SUN, Z., MORROW, J. S., PRADHAN, D. & STERN, D. F. 2002. Rad9 phosphorylation sites couple Rad53 to the Saccharomyces cerevisiae DNA damage checkpoint. *Mol Cell,* 9**,** 1055-65.

SCULLY, R., CHEN, J., PLUG, A., XIAO, Y., WEAVER, D., FEUNTEUN, J., ASHLEY, T. & LIVINGSTON, D. M. 1997. Association of BRCA1 with Rad51 in mitotic and meiotic cells. *Cell,* 88**,** 265-75.

SCULLY, R., WALTER, J. C. & NUSSENZWEIG, A. 2024. One-ended and two-ended breaks at nickase-broken replication forks. *DNA Repair (Amst),* 144**,** 103783.

SEEBER, A., HEGNAUER, A. M., HUSTEDT, N., DESHPANDE, I., POLI, J., EGLINGER, J., PASERO, P., GUT, H., SHINOHARA, M., HOPFNER, K. P., SHIMADA, K. & GASSER, S. M. 2016. RPA Mediates Recruitment of MRX to Forks and Double-Strand Breaks to Hold Sister Chromatids Together. *Mol Cell,* 64**,** 951-966.

SETIAPUTRA, D., ESCRIBANO-DIAZ, C., REINERT, J. K., SADANA, P., ZONG, D., CALLEN, E., SIFRI, C., SEEBACHER, J., NUSSENZWEIG, A., THOMA, N. H. & DUROCHER, D. 2022. RIF1 acts in DNA repair through phosphopeptide recognition of 53BP1. *Mol Cell,* 82**,** 1359-1371 e9.

SFEIR, A. & SYMINGTON, L. S. 2015. Microhomology-Mediated End Joining: A Back-up Survival Mechanism or Dedicated Pathway? *Trends Biochem Sci,* 40**,** 701-714.

SHAHID, T., SOROKA, J., KONG, E., MALIVERT, L., MCILWRAITH, M. J., PAPE, T., WEST, S. C. & ZHANG, X. 2014. Structure and mechanism of action of the BRCA2 breast cancer tumor suppressor. *Nat Struct Mol Biol,* 21**,** 962-968.

SHAO, Z., DAVIS, A. J., FATTAH, K. R., SO, S., SUN, J., LEE, K. J., HARRISON, L., YANG, J. & CHEN, D. J. 2012. Persistently bound Ku at DNA ends attenuates DNA end resection and homologous recombination. *DNA Repair (Amst),* 11**,** 310-6.

SHIBATA, A., MOIANI, D., ARVAI, A. S., PERRY, J., HARDING, S. M., GENOIS, M. M., MAITY, R., VAN ROSSUM-FIKKERT, S., KERTOKALIO, A., ROMOLI, F., ISMAIL, A., ISMALAJ, E., PETRICCI, E., NEALE, M. J., BRISTOW, R. G., MASSON, J. Y., WYMAN, C., JEGGO, P. A. & TAINER, J. A. 2014. DNA double-strand break repair pathway choice is directed by distinct MRE11 nuclease activities. *Mol Cell,* 53**,** 7-18.

SHIM, E. Y., CHUNG, W. H., NICOLETTE, M. L., ZHANG, Y., DAVIS, M., ZHU, Z., PAULL, T. T., IRA, G. & LEE, S. E. 2010. Saccharomyces cerevisiae Mre11/Rad50/Xrs2 and Ku proteins regulate association of Exo1 and Dna2 with DNA breaks. *EMBO J,* 29**,** 3370-80.

SHINOHARA, A. & OGAWA, T. 1998. Stimulation by Rad52 of yeast Rad51-mediated recombination. *Nature,* 391**,** 404-7.

SHORROCKS, A. K., JONES, S. E., TSUKADA, K., MORROW, C. A., BELBLIDIA, Z., SHEN, J., VENDRELL, I., FISCHER, R., KESSLER, B. M. & BLACKFORD, A. N. 2021. The Bloom syndrome complex senses RPA-coated single-stranded DNA to restart stalled replication forks. *Nat Commun,* 12**,** 585.

SHORT, J. M., LIU, Y., CHEN, S., SONI, N., MADHUSUDHAN, M. S., SHIVJI, M. K. & VENKITARAMAN, A. R. 2016. High-resolution structure of the presynaptic RAD51 filament on single-stranded DNA by electron cryo-microscopy. *Nucleic Acids Res,* 44**,** 9017-9030.

SIFRI, C., HOEG, L., DUROCHER, D. & SETIAPUTRA, D. 2023. An AlphaFold2 map of the 53BP1 pathway identifies a direct SHLD3-RIF1 interaction critical for shieldin activity. *EMBO Rep,* 24**,** e56834.

SIMSEK, D., BRUNET, E., WONG, S. Y., KATYAL, S., GAO, Y., MCKINNON, P. J., LOU, J., ZHANG, L., LI, J., REBAR, E. J., GREGORY, P. D., HOLMES, M. C. & JASIN, M. 2011. DNA ligase III promotes alternative nonhomologous end-joining during chromosomal translocation formation. *PLoS Genet,* 7**,** e1002080.

SINHA, S., VILLARREAL, D., SHIM, E. Y. & LEE, S. E. 2016. Risky business: Microhomology-mediated end joining. *Mutat Res,* 788**,** 17-24.

SONG, B. & SUNG, P. 2000. Functional interactions among yeast Rad51 recombinase, Rad52 mediator, and replication protein A in DNA strand exchange. *J Biol Chem,* 275**,** 15895-904.

SONIAT, M. M., MYLER, L. R., KUO, H. C., PAULL, T. T. & FINKELSTEIN, I. J. 2019. RPA Phosphorylation Inhibits DNA Resection. *Mol Cell,* 75**,** 145-153 e5.

SORENSON, K. S., MAHANEY, B. L., LEES-MILLER, S. P. & COBB, J. A. 2017. The non-homologous end-joining factor Nej1 inhibits resection mediated by Dna2-Sgs1 nuclease-helicase at DNA double strand breaks. *J Biol Chem,* 292**,** 14576-14586.

SOUTOGLOU, E., DORN, J. F., SENGUPTA, K., JASIN, M., NUSSENZWEIG, A., RIED, T., DANUSER, G. & MISTELI, T. 2007. Positional stability of single double-strand breaks in mammalian cells. *Nat Cell Biol,* 9**,** 675-82.

STOK, C., TSARIDOU, S., VAN DEN TEMPEL, N., EVERTS, M., WIERENGA, E., BAKKER, F. J., KOK, Y., ALVES, I. T., JAE, L. T., RAAS, M. W. D., HUIS IN 'T VELD, P. J., DE BOER, H. R., BHATTACHARYA, A., KARANIKA, E., WARNER, H., CHEN, M., VAN DE KOOIJ, B., DESSAPT, J., TER MORSCHE, L., PEREPELKINA, P., FRADET-TURCOTTE, A., GURYEV, V., TROMER, E. C., CHAN, K. L., FEHRMANN, R. S. N. & VAN VUGT, M. 2023. FIRRM/C1orf112 is synthetic lethal with PICH and mediates RAD51 dynamics. *Cell Rep,* 42**,** 112668.

STURZENEGGER, A., BURDOVA, K., KANAGARAJ, R., LEVIKOVA, M., PINTO, C., CEJKA, P. & JANSCAK, P. 2014. DNA2 cooperates with the WRN and BLM RecQ helicases to mediate long-range DNA end resection in human cells. *J Biol Chem,* 289**,** 27314-27326.

SULEK, M., YARRINGTON, R., MCGIBBON, G., BOEKE, J. D. & JUNOP, M. 2007. A critical role for the C-terminus of Nej1 protein in Lif1p association, DNA binding and non-homologous end-joining. *DNA Repair (Amst),* 6**,** 1805-18.

SUN, Z., HSIAO, J., FAY, D. S. & STERN, D. F. 1998. Rad53 FHA domain associated with phosphorylated Rad9 in the DNA damage checkpoint. *Science,* 281**,** 272-4.

SUNG, P. 1997a. Function of yeast Rad52 protein as a mediator between replication protein A and the Rad51 recombinase. *J Biol Chem,* 272**,** 28194-7.

SUNG, P. 1997b. Yeast Rad55 and Rad57 proteins form a heterodimer that functions with replication protein A to promote DNA strand exchange by Rad51 recombinase. *Genes Dev,* 11**,** 1111-21.

SWEENEY, F. D., YANG, F., CHI, A., SHABANOWITZ, J., HUNT, D. F. & DUROCHER, D. 2005. Saccharomyces cerevisiae Rad9 acts as a Mec1 adaptor to allow Rad53 activation. *Curr Biol,* 15**,** 1364-75.

SY, S. M., HUEN, M. S. & CHEN, J. 2009. PALB2 is an integral component of the BRCA complex required for homologous recombination repair. *Proc Natl Acad Sci U S A,* 106**,** 7155-60.

SYMINGTON, L. S. 2014. End resection at double-strand breaks: mechanism and regulation. *Cold Spring Harb Perspect Biol,* 6.

SZAMBOWSKA, A., TESSMER, I., PRUS, P., SCHLOTT, B., POSPIECH, H. & GROSSE, F. 2017. Cdc45-induced loading of human RPA onto single-stranded DNA. *Nucleic Acids Res,* 45**,** 3217-3230.

SZOSTAK, J. W., ORR-WEAVER, T. L., ROTHSTEIN, R. J. & STAHL, F. W. 1983. The double-strand-break repair model for recombination. *Cell,* 33**,** 25-35.

TAGLIALATELA, A., ALVAREZ, S., LEUZZI, G., SANNINO, V., RANJHA, L., HUANG, J. W., MADUBATA, C., ANAND, R., LEVY, B., RABADAN, R., CEJKA, P., COSTANZO, V. & CICCIA, A. 2017. Restoration of Replication Fork Stability in BRCA1- and BRCA2-Deficient Cells by Inactivation of SNF2-Family Fork Remodelers. *Mol Cell,* 68**,** 414-430 e8.

TAMAI, T., REGINATO, G., OJIRI, R., MORITA, I., AVRUTIS, A., CEJKA, P., SHINOHARA, M. & SUGIMOTO, K. 2024. Sae2 controls Mre11 endo- and exonuclease activities by different mechanisms. *Nat Commun,* 15**,** 7221.

TAVARES, E. M., WRIGHT, W. D., HEYER, W. D., LE CAM, E. & DUPAIGNE, P. 2019. In vitro role of Rad54 in Rad51-ssDNA filament-dependent homology search and synaptic complexes formation. *Nat Commun,* 10**,** 4058.

THORSLUND, T., MCILWRAITH, M. J., COMPTON, S. A., LEKOMTSEV, S., PETRONCZKI, M., GRIFFITH, J. D. & WEST, S. C. 2010. The breast cancer tumor suppressor BRCA2 promotes the specific targeting of RAD51 to single-stranded DNA. *Nat Struct Mol Biol,* 17**,** 1263-5.

TONG, J., SONG, J., ZHANG, W., ZHAI, J., GUAN, Q., WANG, H., LIU, G. & ZHENG, C. 2024. When DNA-damage responses meet innate and adaptive immunity. *Cell Mol Life Sci,* 81**,** 185.

TRAN, P. T., ERDENIZ, N., DUDLEY, S. & LISKAY, R. M. 2002. Characterization of nuclease-dependent functions of Exo1p in Saccharomyces cerevisiae. *DNA Repair (Amst),* 1**,** 895-912.

TRUJILLO, K. M., YUAN, S. S., LEE, E. Y. & SUNG, P. 1998. Nuclease activities in a complex of human recombination and DNA repair factors Rad50, Mre11, and p95. *J Biol Chem,* 273**,** 21447-50.

TSE, Y. C., KIRKEGAARD, K. & WANG, J. C. 1980. Covalent bonds between protein and DNA. Formation of phosphotyrosine linkage between certain DNA topoisomerases and DNA. *J Biol Chem,* 255**,** 5560-5.

TSENG, H. M. & TOMKINSON, A. E. 2002. A physical and functional interaction between yeast Pol4 and Dnl4-Lif1 links DNA synthesis and ligation in nonhomologous end joining. *J Biol Chem,* 277**,** 45630-7.

TSUKAMOTO, Y., MITSUOKA, C., TERASAWA, M., OGAWA, H. & OGAWA, T. 2005. Xrs2p regulates Mre11p translocation to the nucleus and plays a role in telomere elongation and meiotic recombination. *Mol Biol Cell,* 16**,** 597-608.

TUBBS, A. & NUSSENZWEIG, A. 2017. Endogenous DNA Damage as a Source of Genomic Instability in Cancer. *Cell,* 168**,** 644-656.

USUI, T., OHTA, T., OSHIUMI, H., TOMIZAWA, J., OGAWA, H. & OGAWA, T. 1998. Complex formation and functional versatility of Mre11 of budding yeast in recombination. *Cell,* 95**,** 705-16.

UZIEL, T., LERENTHAL, Y., MOYAL, L., ANDEGEKO, Y., MITTELMAN, L. & SHILOH, Y. 2003. Requirement of the MRN complex for ATM activation by DNA damage. *EMBO J,* 22**,** 5612-21.

VALENCIA, M., BENTELE, M., VAZE, M. B., HERRMANN, G., KRAUS, E., LEE, S. E., SCHAR, P. & HABER, J. E. 2001. NEJ1 controls non-homologous end joining in Saccharomyces cerevisiae. *Nature,* 414**,** 666-9.

VAN DYCK, E., STASIAK, A. Z., STASIAK, A. & WEST, S. C. 2001. Visualization of recombination intermediates produced by RAD52-mediated single-strand annealing. *EMBO Rep,* 2**,** 905-9.

VEAUTE, X., JEUSSET, J., SOUSTELLE, C., KOWALCZYKOWSKI, S. C., LE CAM, E. & FABRE, F. 2003. The Srs2 helicase prevents recombination by disrupting Rad51 nucleoprotein filaments. *Nature,* 423**,** 309-12.

VISSCHER, P. M., WRAY, N. R., ZHANG, Q., SKLAR, P., MCCARTHY, M. I., BROWN, M. A. & YANG, J. 2017. 10 Years of GWAS Discovery: Biology, Function, and Translation. *Am J Hum Genet,* 101**,** 5-22.

WALKER, J. R., CORPINA, R. A. & GOLDBERG, J. 2001. Structure of the Ku heterodimer bound to DNA and its implications for double-strand break repair. *Nature,* 412**,** 607-14.

WAN, L., LOU, J., XIA, Y., SU, B., LIU, T., CUI, J., SUN, Y., LOU, H. & HUANG, J. 2013. hPrimpol1/CCDC111 is a human DNA primase-polymerase required for the maintenance of genome integrity. *EMBO Rep,* 14**,** 1104-12.

WANG, B. 2012. BRCA1 tumor suppressor network: focusing on its tail. *Cell Biosci,* 2**,** 6.

WANG, H., SHI, L. Z., WONG, C. C., HAN, X., HWANG, P. Y., TRUONG, L. N., ZHU, Q., SHAO, Z., CHEN, D. J., BERNS, M. W., YATES, J. R., 3RD, CHEN, L. & WU, X. 2013. The interaction of CtIP and Nbs1 connects CDK and ATM to regulate HR-mediated double-strand break repair. *PLoS Genet,* 9**,** e1003277.

WANG, J. L., DUBOC, C., WU, Q., OCHI, T., LIANG, S., TSUTAKAWA, S. E., LEES-MILLER, S. P., NADAL, M., TAINER, J. A., BLUNDELL, T. L. & STRICK, T. R. 2018. Dissection of DNA double-strand-break repair using novel single-molecule forceps. *Nat Struct Mol Biol,* 25**,** 482-487.

WANG, W., DALEY, J. M., KWON, Y., KRASNER, D. S. & SUNG, P. 2017. Plasticity of the Mre11-Rad50-Xrs2-Sae2 nuclease ensemble in the processing of DNA-bound obstacles. *Genes Dev,* 31**,** 2331-2336.

WANG, Y., GHOSH, G. & HENDRICKSON, E. A. 2009. Ku86 represses lethal telomere deletion events in human somatic cells. *Proc Natl Acad Sci U S A,* 106**,** 12430-5.

WHELAN, D. R. & ROTHENBERG, E. 2021. Super-resolution mapping of cellular double-strand break resection complexes during homologous recombination. *Proc Natl Acad Sci U S A,* 118.

WILLIAMS, R. S., DODSON, G. E., LIMBO, O., YAMADA, Y., WILLIAMS, J. S., GUENTHER, G., CLASSEN, S., GLOVER, J. N., IWASAKI, H., RUSSELL, P. & TAINER, J. A. 2009. Nbs1 flexibly tethers Ctp1 and Mre11-Rad50 to coordinate DNA double-strand break processing and repair. *Cell,* 139**,** 87-99.

WILLIAMS, R. S., MONCALIAN, G., WILLIAMS, J. S., YAMADA, Y., LIMBO, O., SHIN, D. S., GROOCOCK, L. M., CAHILL, D., HITOMI, C., GUENTHER, G., MOIANI, D., CARNEY, J. P., RUSSELL, P. & TAINER, J. A. 2008. Mre11 dimers coordinate DNA end bridging and nuclease processing in double-strand-break repair. *Cell,* 135**,** 97-109.

WILSON, T. E., GRAWUNDER, U. & LIEBER, M. R. 1997. Yeast DNA ligase IV mediates non-homologous DNA end joining. *Nature,* 388**,** 495-8.

WILSON, T. E. & LIEBER, M. R. 1999. Efficient processing of DNA ends during yeast nonhomologous end joining. Evidence for a DNA polymerase beta (Pol4)-dependent pathway. *J Biol Chem,* 274**,** 23599-609.

WILTZIUS, J. J., HOHL, M., FLEMING, J. C. & PETRINI, J. H. 2005. The Rad50 hook domain is a critical determinant of Mre11 complex functions. *Nat Struct Mol Biol,* 12**,** 403-7.

WOLD, M. S. 1997. Replication protein A: a heterotrimeric, single-stranded DNA-binding protein required for eukaryotic DNA metabolism. *Annu Rev Biochem,* 66**,** 61-92.

WOLD, M. S. & KELLY, T. 1988. Purification and characterization of replication protein A, a cellular protein required for in vitro replication of simian virus 40 DNA. *Proc Natl Acad Sci U S A,* 85**,** 2523-7.

WONG, A. K., PERO, R., ORMONDE, P. A., TAVTIGIAN, S. V. & BARTEL, P. L. 1997. RAD51 interacts with the evolutionarily conserved BRC motifs in the human breast cancer susceptibility gene brca2. *J Biol Chem,* 272**,** 31941-4.

WRIGHT, W. D. & HEYER, W. D. 2014. Rad54 functions as a heteroduplex DNA pump modulated by its DNA substrates and Rad51 during D loop formation. *Mol Cell,* 53**,** 420-32.

WU, D., TOPPER, L. M. & WILSON, T. E. 2008. Recruitment and dissociation of nonhomologous end joining proteins at a DNA double-strand break in Saccharomyces cerevisiae. *Genetics,* 178**,** 1237-49.

WU, L. & HICKSON, I. D. 2003. The Bloom's syndrome helicase suppresses crossing over during homologous recombination. *Nature,* 426**,** 870-4.

WU, X., RANGANATHAN, V., WEISMAN, D. S., HEINE, W. F., CICCONE, D. N., O'NEILL, T. B., CRICK, K. E., PIERCE, K. A., LANE, W. S., RATHBUN, G., LIVINGSTON, D. M. & WEAVER, D. T. 2000. ATM phosphorylation of Nijmegen breakage syndrome protein is required in a DNA damage response. *Nature,* 405**,** 477-82.

WU, X., WILSON, T. E. & LIEBER, M. R. 1999. A role for FEN-1 in nonhomologous DNA end joining: the order of strand annealing and nucleolytic processing events. *Proc Natl Acad Sci U S A,* 96**,** 1303-8.

WU, Y., FU, W., ZANG, N. & ZHOU, C. 2023. Structural characterization of human RPA70N association with DNA damage response proteins. *Elife,* 12.

WYATT, H. D., SARBAJNA, S., MATOS, J. & WEST, S. C. 2013. Coordinated actions of SLX1-SLX4 and MUS81-EME1 for Holliday junction resolution in human cells. *Mol Cell,* 52**,** 234-47.

XU, D., GUO, R., SOBECK, A., BACHRATI, C. Z., YANG, J., ENOMOTO, T., BROWN, G. W., HOATLIN, M. E., HICKSON, I. D. & WANG, W. 2008. RMI, a new OB-fold complex

essential for Bloom syndrome protein to maintain genome stability. *Genes Dev,* 22**,** 2843-55.

XU, G., CHAPMAN, J. R., BRANDSMA, I., YUAN, J., MISTRIK, M., BOUWMAN, P., BARTKOVA, J., GOGOLA, E., WARMERDAM, D., BARAZAS, M., JASPERS, J. E., WATANABE, K., PIETERSE, M., KERSBERGEN, A., SOL, W., CELIE, P. H. N., SCHOUTEN, P. C., VAN DEN BROEK, B., SALMAN, A., NIEUWLAND, M., DE RINK, I., DE RONDE, J., JALINK, K., BOULTON, S. J., CHEN, J., VAN GENT, D. C., BARTEK, J., JONKERS, J., BORST, P. & ROTTENBERG, S. 2015. REV7 counteracts DNA double-strand break resection and affects PARP inhibition. *Nature,* 521**,** 541-544.

XU, J., ZHAO, L., XU, Y., ZHAO, W., SUNG, P. & WANG, H. W. 2017. Cryo-EM structures of human RAD51 recombinase filaments during catalysis of DNA-strand exchange. *Nat Struct Mol Biol,* 24**,** 40-46.

YADAV, V. K. & CLAEYS BOUUAERT, C. 2021. Mechanism and Control of Meiotic DNA Double-Strand Break Formation in S. cerevisiae. *Front Cell Dev Biol,* 9**,** 642737.

YANG, S., ZHANG, C., CAO, Y., DU, G., TANG, D., LI, Y., SHEN, Y., YU, H. & CHENG, Z. 2022. FIGNL1 Inhibits Non-homologous Chromosome Association and Crossover Formation. *Front Plant Sci,* 13**,** 945893.

YATES, L. A., TANNOUS, E. A., MORGAN, R. M., BURGERS, P. M. & ZHANG, X. 2023. A DNA damage-induced phosphorylation circuit enhances Mec1(ATR) Ddc2(ATRIP) recruitment to Replication Protein A. *Proc Natl Acad Sci U S A,* 120**,** e2300150120.

YU, T. Y., GARCIA, V. E. & SYMINGTON, L. S. 2019. CDK and Mec1/Tel1-catalyzed phosphorylation of Sae2 regulate different responses to DNA damage. *Nucleic Acids Res,* 47**,** 11238-11249.

YU, T. Y., KIMBLE, M. T. & SYMINGTON, L. S. 2018. Sae2 antagonizes Rad9 accumulation at DNA double-strand breaks to attenuate checkpoint signaling and facilitate end resection. *Proc Natl Acad Sci U S A,* 115**,** E11961-E11969.

YUAN, J. & CHEN, J. 2011. The role of the human SWI5-MEI5 complex in homologous recombination repair. *J Biol Chem,* 286**,** 9888-93.

YUAN, J. & CHEN, J. 2013. FIGNL1-containing protein complex is required for efficient homologous recombination repair. *Proc Natl Acad Sci U S A,* 110**,** 10640-5.

YUAN, S. S., LEE, S. Y., CHEN, G., SONG, M., TOMLINSON, G. E. & LEE, E. Y. 1999. BRCA2 is required for ionizing radiation-induced assembly of Rad51 complex in vivo. *Cancer Res,* 59**,** 3547-51.

YUN, M. H. & HIOM, K. 2009. CtIP-BRCA1 modulates the choice of DNA double-strand-break repair pathway throughout the cell cycle. *Nature,* 459**,** 460-3.

YUZHAKOV, A., KELMAN, Z., HURWITZ, J. & O'DONNELL, M. 1999. Multiple competition reactions for RPA order the assembly of the DNA polymerase delta holoenzyme. *EMBO J,* 18**,** 6189-99.

ZAHID, S., CHAUVAT, J., CEPPI, I., CAPPIELLO, F., PERDICHIZZI, B., FRIT, P., GOMEZ, D., HARDWICK, S. W., LEGRAND, P., KARAZI, J., BACONNAIS, S., PEHAU-ARNAUDET, G., BRITTON, S., CHARBONNIER, J. B., CHAPLIN, A. K., PICHIERRI, P., CEJKA, P., CALSOU, P. & ROPARS, V. 2026. Structural basis of Ku-mediated activation of WRN exonuclease activity. *Nat Commun*.

ZAINU, A., DUPAIGNE, P., BOUCHOUIKA, S., CAU, J., CLEMENT, J. A. J., AUFFRET, P., ROPARS, V., CHARBONNIER, J. B., DE MASSY, B., MERCIER, R., KUMAR, R. & BAUDAT, F. 2024. FIGNL1-FIRRM is essential for meiotic recombination and

prevents DNA damage-independent RAD51 and DMC1 loading. *Nat Commun,* 15**,** 7015.

ZAKHARYEVICH, K., TANG, S., MA, Y. & HUNTER, N. 2012. Delineation of joint molecule resolution pathways in meiosis identifies a crossover-specific resolvase. *Cell,* 149**,** 334-47.

ZHANG, F., MA, J., WU, J., YE, L., CAI, H., XIA, B. & YU, X. 2009. PALB2 links BRCA1 and BRCA2 in the DNA-damage response. *Curr Biol,* 19**,** 524-9.

ZHANG, F., SHI, J., BIAN, C. & YU, X. 2015. Poly(ADP-Ribose) Mediates the BRCA2-Dependent Early DNA Damage Response. *Cell Rep,* 13**,** 678-689.

ZHANG, S., WANG, L., TAO, Y., BAI, T., LU, R., ZHANG, T., CHEN, J. & DING, J. 2017. Structural basis for the functional role of the Shu complex in homologous recombination. *Nucleic Acids Res,* 45**,** 13068-13079.

ZHANG, X. & PAULL, T. T. 2005. The Mre11/Rad50/Xrs2 complex and non-homologous end-joining of incompatible ends in S. cerevisiae. *DNA Repair (Amst),* 4**,** 1281-94.

ZHANG, Y., HEFFERIN, M. L., CHEN, L., SHIM, E. Y., TSENG, H. M., KWON, Y., SUNG, P., LEE, S. E. & TOMKINSON, A. E. 2007. Role of Dnl4-Lif1 in nonhomologous end-joining repair complex assembly and suppression of homologous recombination. *Nat Struct Mol Biol,* 14**,** 639-46.

ZHAO, W., STEINFELD, J. B., LIANG, F., CHEN, X., MARANON, D. G., JIAN MA, C., KWON, Y., RAO, T., WANG, W., SHENG, C., SONG, X., DENG, Y., JIMENEZ-SAINZ, J., LU, L., JENSEN, R. B., XIONG, Y., KUPFER, G. M., WIESE, C., GREENE, E. C. & SUNG, P. 2017. BRCA1-BARD1 promotes RAD51-mediated homologous DNA pairing. *Nature,* 550**,** 360-365.

ZHONG, Q., CHEN, C. F., LI, S., CHEN, Y., WANG, C. C., XIAO, J., CHEN, P. L., SHARP, Z. D. & LEE, W. H. 1999. Association of BRCA1 with the hRad50-hMre11-p95 complex and the DNA damage response. *Science,* 285**,** 747-50.

ZHOU, C., POURMAL, S. & PAVLETICH, N. P. 2015. Dna2 nuclease-helicase structure, mechanism and regulation by Rpa. *Elife,* 4.

ZHOU, H., KAWAMURA, K., YANAGIHARA, H., KOBAYASHI, J. & ZHANG-AKIYAMA, Q. M. 2017. NBS1 is regulated by two kind of mechanisms: ATM-dependent complex formation with MRE11 and RAD50, and cell cycle-dependent degradation of protein. *J Radiat Res,* 58**,** 487-494.

ZHOU, Z., YANG, H., LIANG, X., ZHOU, T., ZHANG, T., YANG, Y., WANG, J. & WANG, W. 2023. C1orf112 teams up with FIGNL1 to facilitate RAD51 filament disassembly and DNA interstrand cross-link repair. *Cell Rep,* 42**,** 112907.

ZHU, Z., CHUNG, W. H., SHIM, E. Y., LEE, S. E. & IRA, G. 2008. Sgs1 helicase and two nucleases Dna2 and Exo1 resect DNA double-strand break ends. *Cell,* 134**,** 981-94.

ZICKLER, D. & KLECKNER, N. 2015. Recombination, Pairing, and Synapsis of Homologs during Meiosis. *Cold Spring Harb Perspect Biol,* 7.

6. Acknowledgements

I would like to thank my supervisor, Prof. Petr Cejka, for giving me the opportunity to work on DNA repair, a topic that I always loved, and for his guidance throughout my PhD. I would also like to thank the past and current members of my committee, Prof. Lorraine Symington, Prof. Grzegorz Ira and Prof. Arianna Calcinotto for their valuable feedback and their availability.

Even though my PhD journey was not always easy, I will be forever thankful for the friends I have found among my colleagues both within the lab and outside of it. We have shared many joyful moments and have supported each other through the most challenging parts of our collective experience. I have met some truly special people in my time here that have become a second family away from home.

My deepest thanks go to all the Cejka lab members, both those who have moved on (Ananya, Giordano, Maria and Francesco) and those who arrived and stayed until the end of my PhD (fellow PhD students Sam, Megha, Akshay, Safa, Kostiiia and Sofifi and postdocs Ila, Ros, Vale and Elda). Thank you for tolerating my bad jokes and all my complaints about Italian cuisine. I will always treasure the coffee and lunch breaks we spent together and all the laughs we shared. I appreciate all the advice you gave me and how much I was taught, both scientifically and personally. I cannot imagine having completed this journey without you around.

A big thanks also goes to the fellow PhD students and postdocs from our institute. Even though I was a bit late to the party, I was embraced by a group of kind-hearted, brilliant and fun people that I am truly proud to call my friends. From parties, to carnivals, to parades in Zurich and boat trips, we have shared many wonderful moments that will stay with me forever.

I am also grateful to my parents for their unconditional love and encouragement throughout my PhD. Although they did not understand what I was working on, they always listened patiently and advised me every time I needed it. I wish I could have spent less time apart from them, but these are the sacrifices that this job painfully demands. All in all, my deepest love goes out to my mom and dad, and they should know that they will always be my number one priority. Vă iubesc nespus de mult!